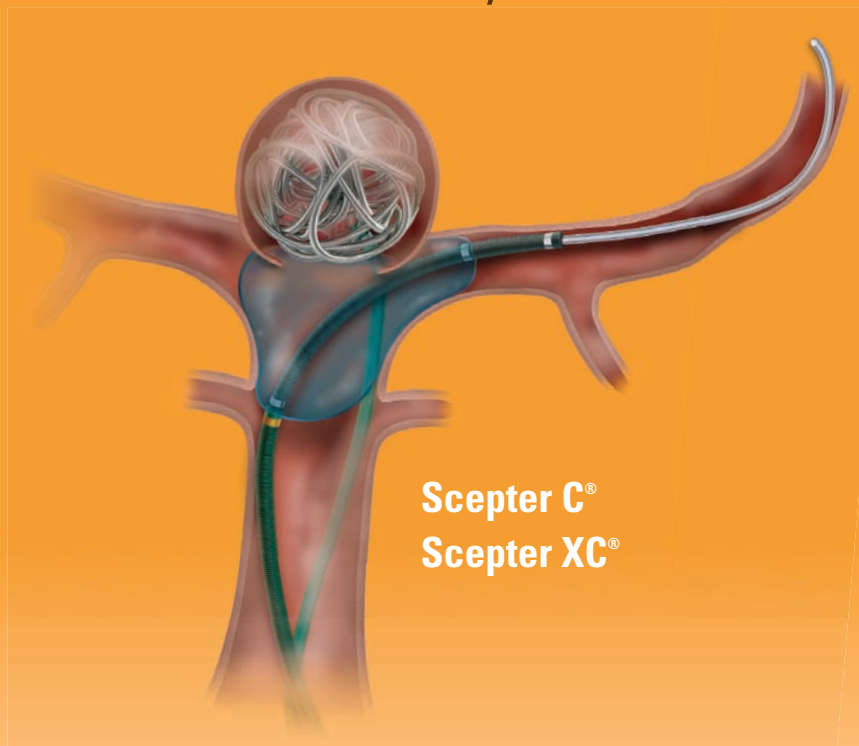


# Versatility

by MicroVention



**Scepter C®**  
**Scepter XC®**

**Scepter**  
Occlusion Balloon  
Catheter

## REDEFINING DELIVERABILITY, VERSATILITY AND CONTROL

MicroVention has developed two occlusion balloon catheters. **Scepter C®** compliant balloon is designed for reliable vessel occlusion yet conforms to vessel anatomy. **Scepter XC®** x-tra compliant balloon conforms to extremely complex anatomies where neck coverage is more challenging.

• Used with



For more information or a product demonstration,  
contact your local MicroVention representative:



**MicroVention, Inc.**

**Worldwide Headquarters**

1311 Valencia Avenue

Tustin, CA 92780 USA

MicroVention UK Limited

MicroVention Europe, S.A.R.L.

MicroVention Deutschland GmbH

PH +1.714.247.8000

PH +44 (0) 191 258 6777

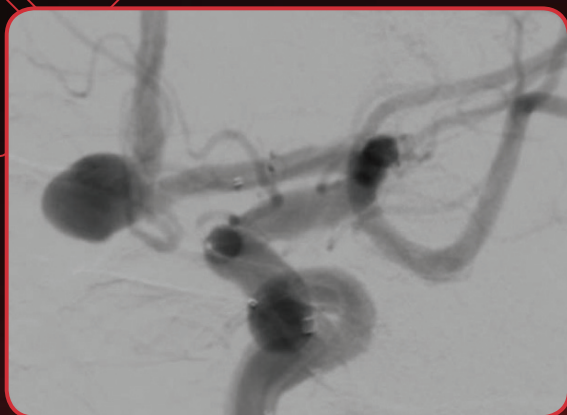
PH +33 (1) 39 21 77 46

PH +49 211 210 798-0

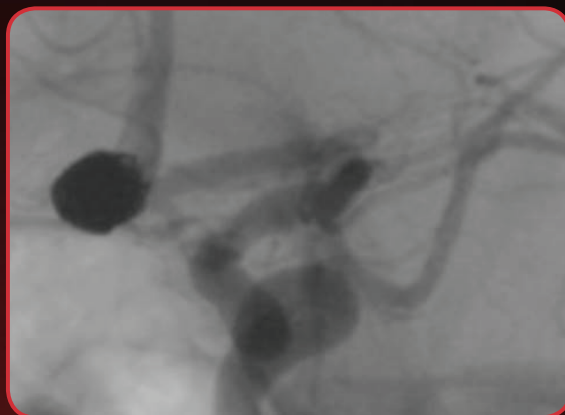
# BARRICADE™ COIL SYSTEM

## COILS THAT PERFORM

STENT ASSISTED COILING OF LEFT ACA ANEURYSM WITH THE BARRICADE COIL SYSTEM



PRE-TREATMENT



POST TREATMENT

“In this tortuous system, the Barricade coils were stable and conforming without issues of catheter kickback, even when working close to the neck, and they filled in the margins of neck very well.”

-Gary R. Duckwiler, M.D.

## COILS THAT SAVE \$

BARRICADE  
COILS  
SAVED  
**\$17,900\***

Images courtesy of Gary R. Duckwiler, M.D.

\* Estimated savings in this case, data on file.

The Barricade Coil System is intended for the endovascular embolization of intracranial aneurysms and other neurovascular abnormalities such as arteriovenous malformations and arteriovenous fistulae. The System is also intended for vascular occlusion of blood vessels within the neurovascular system to permanently obstruct blood flow to an aneurysm or other vascular malformation and for arterial and venous embolizations in the peripheral vasculature. Refer to the instructions for use for complete product information.

18 TECHNOLOGY DRIVE #169, IRVINE CA 92618 | p: 949.788.1443 | f: 949.788.1444  
[WWW.BLOCKADEMEDICAL.COM](http://WWW.BLOCKADEMEDICAL.COM)

MKTG-045 Rev. A

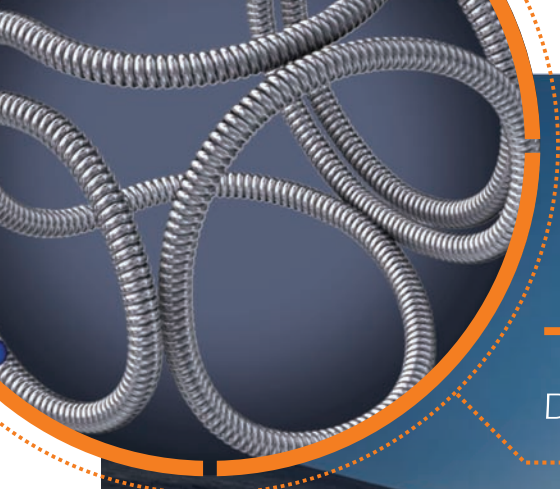


**The brain at your fingertips**

 **Rapid Medical**

[www.rapid-medical.com](http://www.rapid-medical.com) > [comaneci](#)





## Target® DETACHABLE COILS



### Smooth and Stable

Whether you are framing, filling or finishing, Target Detachable Coils deliver consistently smooth deployment and exceptional microcatheter stability. Focused on design, Target Coils feature a host of advantages to ensure the high-powered performance you demand.

For more information, please visit [www.strykerneurovascular.com/Target](http://www.strykerneurovascular.com/Target) or contact your local Stryker Neurovascular sales representative.

**stryker®**  
Neurovascular





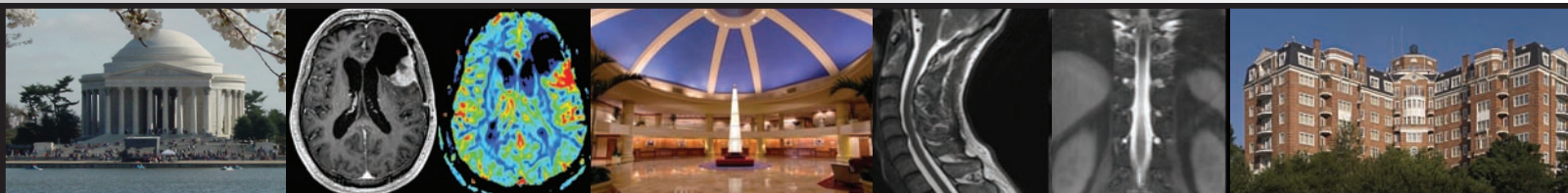
ASFNR • ASHNR • ASPNR • ASSR • SNIS

THE FOUNDATION OF THE ASNR



## THE FOUNDATION OF THE ASNR SYMPOSIUM 2016: EMERGENCY NEURORADIOLOGY MAY 21-22

## ASNR 54<sup>TH</sup> ANNUAL MEETING MAY 23-26



### THE FOUNDATION OF THE ASNR SYMPOSIUM 2016: EMERGENCY NEURORADIOLOGY Symposium 2016:

- Features world-renowned speakers providing a comprehensive review of Emergency Neuroradiology and neuroimaging issues in critical care.
- Features topics Neuroimaging as an indispensable tool for triage and management of both adults and children in emergency settings.
- Review of efficient and appropriate use of CT and MRI that are critical to the urgent management of brain, spine, head & neck, and neurovascular emergencies, all of which will be highlighted by expert faculty.
- Review best practices for traumatic and non-traumatic emergencies, including methods to ensure optimal workflow, image post-processing, PACS integration, telemedicine, safety, and quality.
- Includes discussions of challenges and solutions for providing 24/7 coverage will be presented and debated.

### ASNR 54<sup>TH</sup> ANNUAL MEETING:

- Focused programming on the latest products and services to deliver the highest quality care in the realm of Neuroradiology and allied professions.
- Informative updates on general Neuroradiology and showcase specialty programming from the ASFNR, ASHNR, ASPNR, ASSR, and SNIS.
- Concurrent lectures, original presentations, scientific posters and educational exhibits throughout the week.

**Howard A. Rowley, MD,**  
ASNR 2016 Program Chair/President-Elect  
Programming developed in cooperation with ...

**American Society of Functional Neuroradiology (ASFNR)**  
Christopher G. Filippi, MD

**American Society of Head and Neck Radiology (ASHNR)**  
Lindell R. Gentry, MD

**American Society of Pediatric Neuroradiology (ASPNR)**  
Erin Simon Schwartz, MD

**American Society of Spine Radiology (ASSR)**  
Gregory J. Lawler, MD

**Society of NeuroInterventional Surgery (SNIS)**  
Charles J. Prestigiacomo, MD

### American Society of Neuroradiology (ASNR) Committee Programming:

**Health Policy Committee**  
Robert M. Barr, MD, FACR

**Computer Science and Informatics (CSI) Committee**  
John L. Go, MD, FACR

**Research Scientists Committee**  
Dikoma C. Shungu, PhD and Timothy P.L. Roberts, PhD

### ASNR 54<sup>TH</sup> ANNUAL MEETING

c/o American Society of Neuroradiology  
800 Enterprise Drive, Suite 205  
Oak Brook, Illinois 60523-4216  
Phone: 630-574-0220  
Fax: 630 574-0661  
www.asnr.org/2016

SCAN NOW  
TO VISIT  
OUR WEBSITE



**SAVE THE DATE... MAY 21-26, 2016**  
**WASHINGTON MARRIOTT WARDMAN PARK • WASHINGTON, DC**

*50<sup>th</sup> Annual Meeting*

# American Society of Head & Neck Radiology

Comprehensive Head and Neck Imaging:  
50 Years of Progress



**September 7 - 11, 2016**

Hyatt Regency Washington on Capitol Hill  
Washington, DC

29.25 AMA PRA Category 1 Credit(s)<sup>TM</sup>

Certain sessions of the meeting program  
will be submitted for SAM qualification.

**Hands-on US and US-Guided Biopsy Seminar  
Saturday, September 10, 2016**

Separate Registration Required

Registration is Limited to 20 Attendees Per Session.

Not accredited for AMA PRA Category 1 Credit(s)<sup>TM</sup>

For More Information, visit [www.ashnr.org](http://www.ashnr.org)



American Medical Association **MVP Program**



**The AMA MVP Program:**

*Special offers that fit you and your practice's needs.*

Which savings would benefit you the most? Discounts on pharmaceuticals, medical supplies and equipment? Or on travel, practice financing, and financial and insurance services? Now physicians can save in all of these professional and personal categories and more through the AMA MVP Program.

Please activate your 2016 AMA membership by calling **(800) 262-3211** or visit **[ama-assn.org/go/join](http://ama-assn.org/go/join)**.



\* Subsidiary of the American Medical Association.



## Target® Detachable Coil

**See package insert for complete indications, contraindications, warnings and instructions for use.**

### INTENDED USE / INDICATIONS FOR USE

Target Detachable Coils are intended to endovascularly obstruct or occlude blood flow in vascular abnormalities of the neurovascular and peripheral vessels.

Target Detachable Coils are indicated for endovascular embolization of:

- Intracranial aneurysms
- Other neurovascular abnormalities such as arteriovenous malformations and arteriovenous fistulae
- Arterial and venous embolizations in the peripheral vasculature

### CONTRAINDICATIONS

None known.

### POTENTIAL ADVERSE EVENTS

Potential complications include, but are not limited to: allergic reaction, aneurysm perforation and rupture, arrhythmia, death, edema, embolus, headache, hemorrhage, infection, ischemia, neurological/intracranial sequelae, post-embolization syndrome (fever, increased white blood cell count, discomfort), TIA/stroke, vasospasm, vessel occlusion or closure, vessel perforation, dissection, trauma or damage, vessel rupture, vessel thrombosis. Other procedural complications including but not limited to: anesthetic and contrast media risks, hypotension, hypertension, access site complications.

### WARNINGS

- Contents supplied STERILE using an ethylene oxide (EO) process. Do not use if sterile barrier is damaged. If damage is found, call your Stryker Neurovascular representative.
- For single use only. Do not reuse, reprocess or resterilize. Reuse, reprocessing or resterilization may compromise the structural integrity of the device and/or lead to device failure which, in turn, may result in patient injury, illness or death. Reuse, reprocessing or resterilization may also create a risk of contamination of the device and/or cause patient infection or cross-infection, including, but not limited to, the transmission of infectious disease(s) from one patient to another. Contamination of the device may lead to injury, illness or death of the patient.
- After use, dispose of product and packaging in accordance with hospital, administrative and/or local government policy.
- **This device should only be used by physicians who have received appropriate training in interventional neuroradiology or interventional radiology and preclinical training on the use of this device as established by Stryker Neurovascular.**
- Patients with hypersensitivity to 316LVM stainless steel may suffer an allergic reaction to this implant.
- MR temperature testing was not conducted in peripheral vasculature, arteriovenous malformations or fistulae models.
- The safety and performance characteristics of the Target Detachable Coil System (Target Detachable Coils, InZone Detachment Systems,

delivery systems and accessories) have not been demonstrated with other manufacturer's devices (whether coils, coil delivery devices, coil detachment systems, catheters, guidewires, and/or other accessories). Due to the potential incompatibility of non Stryker Neurovascular devices with the Target Detachable Coil System, the use of other manufacturer's device(s) with the Target Detachable Coil System is not recommended.

- To reduce risk of coil migration, the diameter of the first and second coil should never be less than the width of the ostium.
- In order to achieve optimal performance of the Target Detachable Coil System and to reduce the risk of thromboembolic complications, it is critical that a continuous infusion of appropriate flush solution be maintained between a) the femoral sheath and guiding catheter, b) the 2-tip microcatheter and guiding catheters, and c) the 2-tip microcatheter and Stryker Neurovascular guidewire and delivery wire. Continuous flush also reduces the potential for thrombus formation on, and crystallization of infusate around, the detachment zone of the Target Detachable Coil.
- Do not use the product after the "Use By" date specified on the package.
- Reuse of the flush port/dispenser coil or use with any coil other than the original coil may result in contamination of, or damage to, the coil.
- Utilization of damaged coils may affect coil delivery to, and stability inside, the vessel or aneurysm, possibly resulting in coil migration and/or stretching.
- The fluoro-saver marker is designed for use with a Rotating Hemostatic Valve (RHV). If used without an RHV, the distal end of the coil may be beyond the alignment marker when the fluoro-saver marker reaches the microcatheter hub.
- If the fluoro-saver marker is not visible, do not advance the coil without fluoroscopy.
- Do not rotate delivery wire during or after delivery of the coil. Rotating the Target Detachable Coil delivery wire may result in a stretched coil or premature detachment of the coil from the delivery wire, which could result in coil migration.
- Verify there is no coil loop protrusion into the parent vessel after coil placement and prior to coil detachment. Coil loop protrusion after coil placement may result in thromboembolic events if the coil is detached.
- Verify there is no movement of the coil after coil placement and prior to coil detachment. Movement of the coil after coil placement may indicate that the coil could migrate once it is detached.
- Failure to properly close the RHV compression fitting over the delivery wire before attaching the InZone® Detachment System could result in coil movement, aneurysm rupture or vessel perforation.
- Verify repeatedly that the distal shaft of the catheter is not under stress before detaching the Target Detachable Coil. Axial compression or tension forces could be stored in the 2-tip microcatheter causing the tip to move during coil delivery. Microcatheter tip movement could cause the aneurysm or vessel to rupture.
- Advancing the delivery wire beyond the microcatheter tip once the coil has been detached involves risk of aneurysm or vessel perforation.
- The long term effect of this product on extravascular tissues has not been established so care should be taken to retain this device in the intravascular space.

Damaged delivery wires may cause detachment failures, vessel injury or unpredictable distal tip response during coil deployment. If a delivery wire is damaged at any point during the procedure, do not attempt to straighten or otherwise repair it. Do not proceed with deployment or detachment. Remove the entire coil and replace with undamaged product.

- After use, dispose of product and packaging in accordance with hospital, administrative and/or local government policy.

### CAUTIONS / PRECAUTIONS

- Federal Law (USA) restricts this device to sale by or on the order of a physician.
- Besides the number of InZone Detachment System units needed to complete the case, there must be an extra InZone Detachment System unit as back up.
- Removing the delivery wire without grasping the introducer sheath and delivery wire together may result in the detachable coil sliding out of the introducer sheath.
- Failure to remove the introducer sheath after inserting the delivery wire into the RHV of the microcatheter will interrupt normal infusion of flush solution and allow back flow of blood into the microcatheter.
- Some low level overhead light near or adjacent to the patient is required to visualize the fluoro-saver marker; monitor light alone will not allow sufficient visualization of the fluoro-saver marker.
- Advance and retract the Target Detachable Coil carefully and smoothly without excessive force. If unusual friction is noticed, slowly withdraw the Target Detachable Coil and examine for damage. If damage is present, remove and use a new Target Detachable Coil. If friction or resistance is still noted, carefully remove the Target Detachable Coil and microcatheter and examine the microcatheter for damage.
- If it is necessary to reposition the Target Detachable Coil, verify under fluoroscopy that the coil moves with a one-to-one motion. If the coil does not move with a one-to-one motion or movement is difficult, the coil may have stretched and could possibly migrate or break. Gently remove both the coil and microcatheter and replace with new devices.
- Increased detachment times may occur when:
  - Other embolic agents are present.
  - Delivery wire and microcatheter markers are not properly aligned.
  - Thrombus is present on the coil detachment zone.
- Do not use detachment systems other than the InZone Detachment System.
- Increased detachment times may occur when delivery wire and microcatheter markers are not properly aligned.
- Do not use detachment systems other than the InZone Detachment System.



**Stryker Neurovascular**  
47900 Bayside Parkway  
Fremont, CA 94538-6515

**stryker.com/neurovascular**

Date of Release: FEB/2014

EX\_EN\_US

Copyright © 2014 Stryker  
NV00006677.AA

## Trevo® XP ProVue Retrievers

**See package insert for complete indications, complications, warnings, and instructions for use.**

### INDICATIONS FOR USE

The Trevo Retriever is intended to restore blood flow in the neurovasculature by removing thrombus in patients experiencing ischemic stroke within 8 hours of symptom onset. Patients who are ineligible for intravenous tissue plasminogen activator (IV t-PA) or who fail IV t-PA therapy are candidates for treatment.

### COMPLICATIONS

Procedures requiring percutaneous catheter introduction should not be attempted by physicians unfamiliar with possible complications which may occur during or after the procedure. Possible complications include, but are not limited to, the following: air embolism; hematoma or hemorrhage at puncture site; infection; distal embolization; pain/headache; vessel spasm, thrombosis, dissection, or perforation; emboli; acute occlusion; ischemia; intracranial hemorrhage; false aneurysm formation; neurological deficits including stroke; and death.

### COMPATIBILITY

3x20 mm retrievers are compatible with Trevo® Pro 14 Microcatheters (REF 90231) and Trevo® Pro 18 Microcatheters (REF 90238). 4x20 mm retrievers are compatible with Trevo® Pro 18 Microcatheters (REF 90238). Compatibility of the Retriever with other microcatheters has not been established. Performance of the Retriever device may be impacted if a different microcatheter is used. The Merci® Balloon Guide Catheters are recommended for use during thrombus removal procedures. Retrievers are compatible with the Abbott Vascular DOC® Guide Wire Extension (REF 22260).

### WARNINGS

- Contents supplied STERILE, using an ethylene oxide (EO) process. Nonpyrogenic.
- To reduce risk of vessel damage, adhere to the following recommendations:
  - Take care to appropriately size Retriever to vessel diameter at

intended site of deployment.

- Do not perform more than six (6) retrieval attempts in same vessel using Retriever devices.
- Maintain Retriever position in vessel when removing or exchanging Microcatheter.
- To reduce risk of kinking/fracture, adhere to the following recommendations:
  - Immediately after unsheathing Retriever, position Microcatheter tip marker just proximal to shaped section. Maintain Microcatheter tip marker just proximal to shaped section of Retriever during manipulation and withdrawal.
  - Do not rotate or torque Retriever.
  - Use caution when passing Retriever through stented arteries.
- Do not resterilize and reuse. Structural integrity and/or function may be impaired by reuse or cleaning.
- The Retriever is a delicate instrument and should be handled carefully. Before use and when possible during procedure, inspect device carefully for damage. Do not use a device that shows signs of damage. Damage may prevent device from functioning and may cause complications.
- Do not advance or withdraw Retriever against resistance or significant vasospasm. Moving or torquing device against resistance or significant vasospasm may result in damage to vessel or device. Assess cause of resistance using fluoroscopy and if needed resheath the device to withdraw.
- If Retriever is difficult to withdraw from the vessel, do not torque Retriever. Advance Microcatheter distally, gently pull Retriever back into Microcatheter, and remove Retriever and Microcatheter as a unit. If undue resistance is met when withdrawing the Retriever into the Microcatheter, consider extending the Retriever using the Abbott Vascular DOC guidewire extension (REF 22260) so that the Microcatheter can be exchanged for a larger diameter catheter such as a DAC® catheter. Gently withdraw the Retriever into the larger diameter catheter.
- Administer anti-coagulation and anti-platelet medications per standard institutional guidelines.

### PRECAUTIONS

- Prescription only – device restricted to use by or on order of a physician.
- Store in cool, dry, dark place.
- Do not use open or damaged packages.
- Use by "Use By" date.
- Exposure to temperatures above 54°C (130°F) may damage device and accessories. Do not autoclave.
- Do not expose Retriever to solvents.
- Use Retriever in conjunction with fluoroscopic visualization and proper anti-coagulation agents.
- To prevent thrombus formation and contrast media crystal formation, maintain a constant infusion of appropriate flush solution between guide catheter and Microcatheter and between Microcatheter and Retriever or guidewire.
- Do not attach a torque device to the shaped proximal end of DOC® Compatible Retriever. Damage may occur, preventing ability to attach DOC® Guide Wire Extension.



**Concentric Medical**  
301 East Evelyn  
Mountain View, CA 94041

EC REP

EMERGO Europe  
Molenstraat 15  
2513 BH, The Hague  
The Netherlands

**Stryker Neurovascular**  
47900 Bayside Parkway  
Fremont, CA 94538-6515

**stryker.com/neurovascular**  
**stryker.com/emea/neurovascular**

Date of Release: JUN/2014

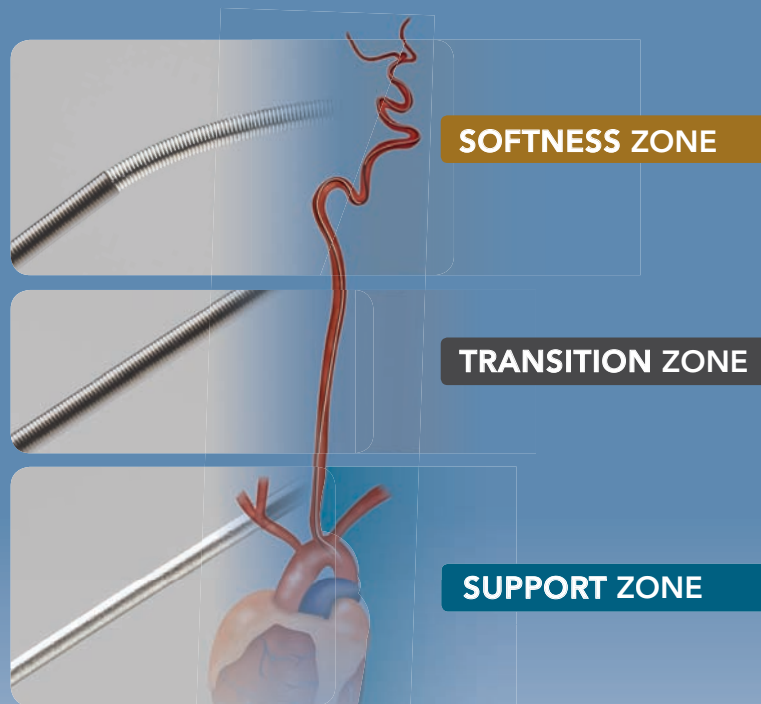
EX\_EN\_GL

Copyright © 2014 Stryker  
NV00009028.AA



# Advanced

by MicroVention



## ENHANCED CONTROL TO MAXIMIZE COIL PERFORMANCE

The **V-Trak® Advanced Coil System**, the next generation to power the performance of our most technically advanced line of coils. Offering the optimal combination of support and flexibility.

[microvention.com](http://microvention.com)

MICROVENTION, V-Trak, Scepter C, Scepter XC and Headway are registered trademarks of MicroVention, Inc. Scientific and clinical data related to this document are on file at MicroVention, Inc. Refer to Instructions for Use, contraindications and warnings for additional information. Federal (USA) law restricts this device for sale by or on the order of a physician. © 2015 MicroVention, Inc. 5/15

CE  
0297

# 66%

of Patients in MR CLEAN  
Were Treated with a  
Trevo® Stent Retriever

**stryker**<sup>®</sup>  
Neurovascular

**Trevo**<sup>®</sup>  
PROVUE RETRIEVER

## MR CLEAN<sup>1</sup>

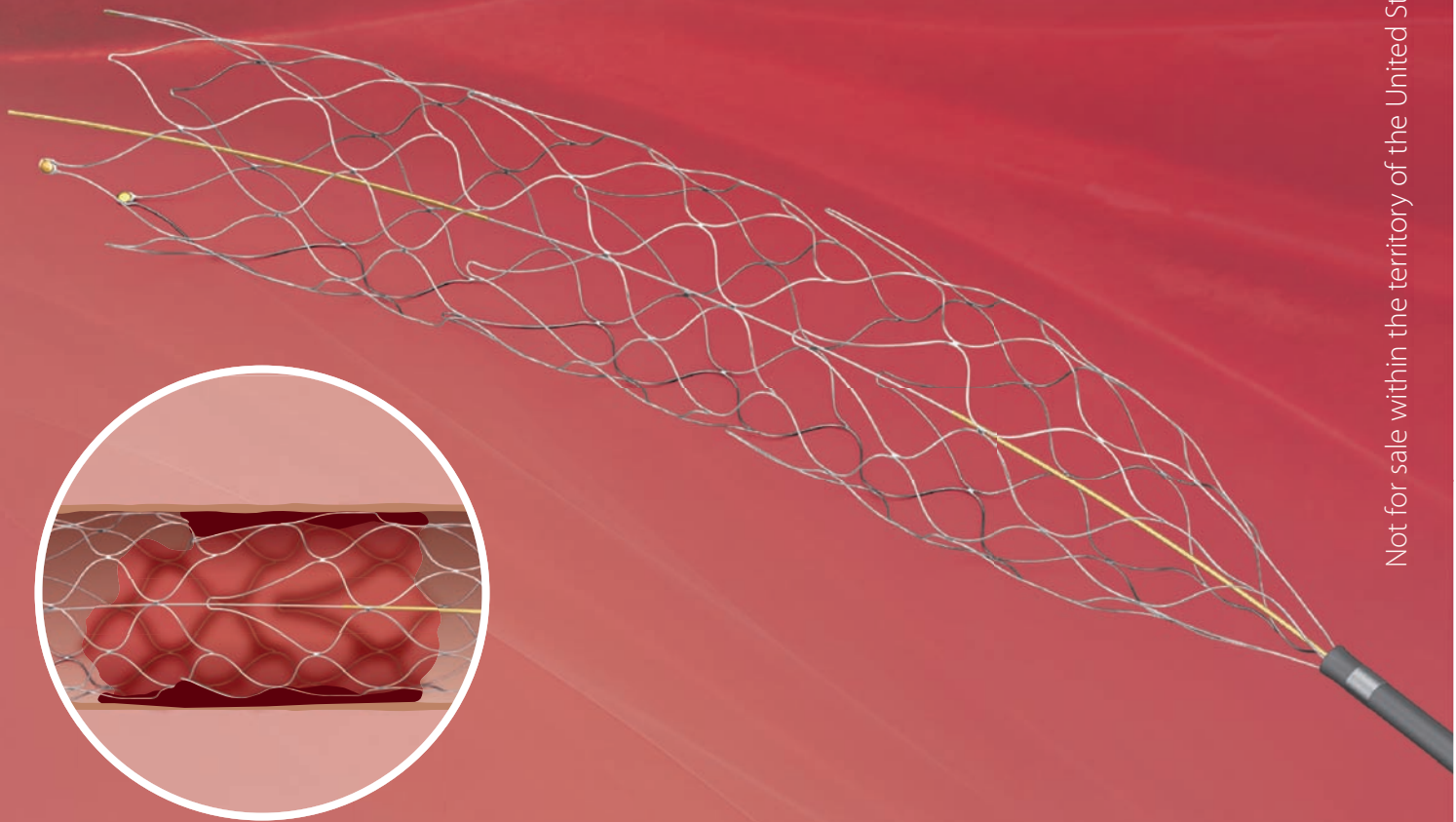
**First clinical evidence for intra-arterial  
treatment with stent retrievers**

- **Largest** of the randomized AIS trials<sup>2</sup>, with over 500 patients enrolled
- The Trevo Retriever was the **#1** device used in the **MR CLEAN** Trial

<sup>1</sup> O.A. Berkhemer et al. A Randomized Trial for Intra-arterial Treatment for Acute Ischemic Stroke. *N Eng J Med* December 2014.

<sup>2</sup> MR CLEAN is the largest AIS Trial in which stent retrievers were used.  
<http://www.mrclean-trial.org/>

## APERIO® Thrombectomy Device



Not for sale within the territory of the United States

### FAST FLOW RESTORATION

- Proven hybrid cell design
- Four sizes for tailored treatment

# AJNR

## AMERICAN JOURNAL OF NEURORADIOLOGY

MARCH 2016  
VOLUME 37  
NUMBER 3  
WWW.AJNR.ORG

Publication Preview at [www.ajnr.org](http://www.ajnr.org) features articles released in advance of print. Visit [www.ajnrblog.org](http://www.ajnrblog.org) to comment on AJNR content and chat with colleagues and AJNR's News Digest at <http://ajnrdigest.org> to read the stories behind the latest research in neuroimaging.

393 **PERSPECTIVES** *M.I. Vargas*

### PRACTICE GUIDELINE



394

**Revised Recommendations of the Consortium of MS Centers Task Force for a Standardized MRI Protocol and Clinical Guidelines for the Diagnosis and Follow-Up of Multiple Sclerosis** *A. Traboulsee, et al.*

**ADULT BRAIN**

### PATIENT SAFETY

402

**Radiation Doses in Patient Eye Lenses during Interventional Neuroradiology Procedures** *R.M. Sánchez, et al.*

**INTERVENTIONAL**

### GENERAL CONTENTS



408

**Diagnostic Accuracy of Transcranial Doppler for Brain Death Confirmation: Systematic Review and Meta-Analysis** *J.J. Chang, et al.*

**ADULT BRAIN**



415

**Utility and Significance of Gadolinium-Based Contrast Enhancement in Posterior Reversible Encephalopathy Syndrome** *S.J. Karia, et al.*

**ADULT BRAIN**



423

**Prominence of Medullary Veins on Susceptibility-Weighted Images Provides Prognostic Information in Patients with Subacute Stroke** *X. Yu, et al.*

**ADULT BRAIN**



430

**Structural Brain Alterations in Community Dwelling Individuals with Chronic Joint Pain** *M. de Kruijf, et al.*

**ADULT BRAIN  
PERIPHERAL  
NERVOUS SYSTEM  
ADULT BRAIN**



439

**Basal Ganglia Iron in Patients with Multiple Sclerosis Measured with 7T Quantitative Susceptibility Mapping Correlates with Inhibitory Control** *P. Schmalbrock, et al.*

**ADULT BRAIN**



447

**Detection of Normal Aging Effects on Human Brain Metabolite Concentrations and Microstructure with Whole-Brain MR Spectroscopic Imaging and Quantitative MR Imaging** *V.V. Eyler, et al.*

**ADULT BRAIN**



455

**High-Resolution 7T MR Imaging of the Motor Cortex in Amyotrophic Lateral Sclerosis** *M. Cosottini, et al.*

**ADULT BRAIN**



462

**MR Elastography Demonstrates Increased Brain Stiffness in Normal Pressure Hydrocephalus** *N. Fattahi, et al.*

**ADULT BRAIN**

468

**Automated Cross-Sectional Measurement Method of Intracranial Dural Venous Sinuses** *S. Lublinsky, et al.*

**ADULT BRAIN**


AJNR (Am J Neuroradiol ISSN 0195-6108) is a journal published monthly, owned and published by the American Society of Neuroradiology (ASNR), 800 Enterprise Drive, Suite 205, Oak Brook, IL 60523. Annual dues for the ASNR include \$170.00 for journal subscription. The journal is printed by Cadmus Journal Services, 5457 Twin Knolls Road, Suite 200, Columbia, MD 21045; Periodicals postage paid at Oak Brook, IL and additional mailing offices. Printed in the U.S.A. POSTMASTER: Please send address changes to American Journal of Neuroradiology, P.O. Box 3000, Denville, NJ 07834, U.S.A. Subscription rates: nonmember \$380 (\$450 foreign) print and online, \$305 online only; institutions \$440 (\$510 foreign) print and basic online, \$875 (\$940 foreign) print and extended online, \$365 online only (basic), extended online \$790; single copies are \$35 each (\$40 foreign). Indexed by PubMed/Medline, BIOSIS Previews, Current Contents (Clinical Medicine and Life Sciences), EMBASE, Google Scholar, HighWire Press, Q-Sensei, RefSeek, Science Citation Index, and SCI Expanded. Copyright © American Society of Neuroradiology.



- 475 **Retrospective Analysis of Delayed Intraparenchymal Hemorrhage after Flow-Diverter Treatment: Presentation of a Retrospective Multicenter Trial** *A. Benaissa, et al.* **INTERVENTIONAL ADULT BRAIN**
- 481 **Intravenous C-Arm Conebeam CT Angiography following Long-Term Flow-Diverter Implantation: Technologic Evaluation and Preliminary Results** *S.C.H. Yu, et al.* **INTERVENTIONAL ADULT BRAIN**
- 487 **Posterior Inferior Cerebellar Artery Patency after Flow-Diverting Stent Treatment** *M.R. Levitt, et al.* **INTERVENTIONAL**
-  490 **In Vitro Evaluation of Intra-Aneurysmal, Flow-Diverter-Induced Thrombus Formation: A Feasibility Study** *K. Gester, et al.* **INTERVENTIONAL**
-  497 **Preclinical Testing of a Novel Thin Film Nitinol Flow-Diversion Stent in a Rabbit Elastase Aneurysm Model** *Y. Ding, et al.* **INTERVENTIONAL**
-  502 **Stent-Assisted Coil Embolization of Intracranial Aneurysms: Complications in Acutely Ruptured versus Unruptured Aneurysms** *R.S. Bechan, et al.* **INTERVENTIONAL**
- 508 **Safety and Efficacy of Intravenous Tirofiban as Antiplatelet Premedication for Stent-Assisted Coiling in Acutely Ruptured Intracranial Aneurysms** *S. Kim, et al.* **INTERVENTIONAL**
-    515 **Applicability of the Sparse Temporal Acquisition Technique in Resting-State Brain Network Analysis** *N. Yakunina, et al.* **FUNCTIONAL**
- 521 **Variability of Forebrain Commissures in Callosal Agenesis: A Prenatal MR Imaging Study** *C. Cesaretti, et al.* **PEDIATRICS**
-    528 **Disorders of Microtubule Function in Neurons: Imaging Correlates** *C.A. Mutch, et al.* **PEDIATRICS ADULT BRAIN**
-  536 **In Utero MR Imaging of Fetal Holoprosencephaly: A Structured Approach to Diagnosis and Classification** *P.D. Griffiths, et al.* **PEDIATRICS**
- 544 **Contrast Leakage Patterns from Dynamic Susceptibility Contrast Perfusion MRI in the Grading of Primary Pediatric Brain Tumors** *C.Y. Ho, et al.* **PEDIATRICS**
-  552 **GABA and Glutamate in Children with Primary Complex Motor Stereotypies: An <sup>1</sup>H-MRS Study at 7T** *A.D. Harris, et al.* **PEDIATRICS**
-  558 **Postoperative MR Imaging of Spontaneous Transdural Spinal Cord Herniation: Expected Findings and Complications** *S. Gaudino, et al.* **SPINE**
- 565 **Normal Venous Phase Documented during Angiography in Patients with Spinal Vascular Malformations: Incidence and Clinical Implications** *D. Eckart Sorte, et al.* **SPINE INTERVENTIONAL**
-   572 **Using Body Mass Index to Predict Needle Length in Fluoroscopy-Guided Lumbar Punctures** *A.P. Nayate, et al.* **SPINE INTERVENTIONAL**
- 579 **3D T2 MR Imaging–Based Measurements of the Posterior Cervical Thecal Sac in Flexion and Extension for Cervical Puncture** *M.P. Bazylewicz, et al.* **SPINE INTERVENTIONAL**
- 584 **35 YEARS AGO IN AJNR**

## ONLINE FEATURES

### LETTERS

-  E20 **Re: The Benefits of High Relaxivity for Brain Tumor Imaging: Results of a Multicenter Intraindividual Crossover Comparison of Gadobenate Dimeglumine with Gadoterate Meglumine (The BENEFIT Study)** *E. Lancelot, et al.*
- E22 **Reply** *A. Spinazzi, et al.*
- E25 **Cerebral Amyloid Angiopathy as an Etiology for Cortical Superficial Siderosis: An Unproven Hypothesis** *H.X. Bai, et al.*
- E26 **Reply** *Y. Inoue, et al.*

- E27 Hemorrhagic Pituitary Adenoma versus Rathke Cleft Cyst: A Frequent Dilemma** *J.-F. Bonneville*
- E29 Reply** *M. Park, et al.*
- E30 In Reply to Antiplatelet Therapy Prior to Temporary Stent-Assisted Coiling** *B. Gory, et al.*

**BOOK REVIEWS** *R.M. Quencer, Section Editor*

Please visit [www.ajnrblog.org](http://www.ajnrblog.org) to read and comment on Book Reviews.



T2-weighted images (top) and surface reconstructions (bottom) in a 21-week gestational age fetus with lobar holoprosencephaly. Interhemispheric fissure formation is present, and there is fusion of the frontal lobes, thalamus, and hypothalamus.



Indicates Editor's Choices selection



Indicates Fellows' Journal Club selection



Indicates open access to non-subscribers at [www.ajnr.org](http://www.ajnr.org)



Indicates article with supplemental on-line table



Indicates article with supplemental on-line photo



Indicates article with supplemental on-line video



Evidence-Based Medicine Level 1



Evidence-Based Medicine Level 2



## AMERICAN JOURNAL OF NEURORADIOLOGY

Publication Preview at [www.ajnr.org](http://www.ajnr.org) features articles released in advance of print.  
Visit [www.ajnrblog.org](http://www.ajnrblog.org) to comment on AJNR content and chat with colleagues  
and AJNR's News Digest at <http://ajnrndigest.org> to read the stories behind the  
latest research in neuroimaging.

MARCH 2016 • VOLUME 37 • NUMBER 3 • WWW.AJNR.ORG

### Official Journal:

American Society of Neuroradiology  
American Society of Functional Neuroradiology  
American Society of Head and Neck Radiology  
American Society of Pediatric Neuroradiology  
American Society of Spine Radiology

### EDITOR-IN-CHIEF

**Jeffrey S. Ross, MD**

*Professor of Radiology, Department of Radiology,  
Mayo Clinic College of Medicine, Phoenix, Arizona*

### SENIOR EDITORS

**Harry J. Cloft, MD, PhD**

*Professor of Radiology and Neurosurgery,  
Department of Radiology, Mayo Clinic College of  
Medicine, Rochester, Minnesota*

**Thierry A.G.M. Huisman, MD**

*Professor of Radiology, Pediatrics, Neurology, and  
Neurosurgery, Chairman, Department of Imaging  
and Imaging Science, Johns Hopkins Bayview,  
Director, Pediatric Radiology and Pediatric  
Neuroradiology, Johns Hopkins Hospital,  
Baltimore, Maryland*

**C.D. Phillips, MD, FACR**

*Professor of Radiology, Weill Cornell Medical  
College, Director of Head and Neck Imaging,  
New York-Presbyterian Hospital, New York,  
New York*

**Pamela W. Schaefer, MD**

*Clinical Director of MRI and Associate Director of  
Neuroradiology, Massachusetts General Hospital,  
Boston, Massachusetts, Associate Professor,  
Radiology, Harvard Medical School, Cambridge,  
Massachusetts*

**Charles M. Strother, MD**

*Professor of Radiology, Emeritus, University of  
Wisconsin, Madison, Wisconsin*

**Jody Tanabe, MD**

*Professor of Radiology and Psychiatry,  
Chief of Neuroradiology,  
University of Colorado, Denver, Colorado*

### STATISTICAL SENIOR EDITOR

**Bryan A. Comstock, MS**

*Senior Biostatistician,  
Department of Biostatistics,  
University of Washington, Seattle, Washington*

### EDITORIAL BOARD

Ashley H. Aiken, *Atlanta, Georgia*  
A. James Barkovich, *San Francisco, California*  
Walter S. Bartynski, *Charleston, South Carolina*  
Barton F. Branstetter IV, *Pittsburgh, Pennsylvania*  
Jonathan L. Brisman, *Lake Success, New York*  
Julie Bykowski, *San Diego, California*  
Donald W. Chakeres, *Columbus, Ohio*  
Asim F. Choudhri, *Memphis, Tennessee*  
Alessandro Cianfoni, *Lugano, Switzerland*  
Colin Derdeyn, *St. Louis, Missouri*  
Rahul S. Desikan, *San Francisco, California*  
Richard du Mesnil de Rochemont, *Frankfurt,  
Germany*  
Clifford J. Eskey, *Hanover, New Hampshire*  
Massimo Filippi, *Milan, Italy*  
David Fiorella, *Cleveland, Ohio*  
Allan J. Fox, *Toronto, Ontario, Canada*  
Christine M. Glastonbury, *San Francisco,  
California*  
John L. Go, *Los Angeles, California*  
Wan-Yuo Guo, *Taipei, Taiwan*  
Rakesh K. Gupta, *Lucknow, India*  
Lotfi Hachein-Bey, *Sacramento, California*  
David B. Hackney, *Boston, Massachusetts*  
Christopher P. Hess, *San Francisco, California*  
Andrei Holodny, *New York, New York*  
Benjamin Huang, *Chapel Hill, North Carolina*  
George J. Hunter, *Boston, Massachusetts*  
Mahesh V. Jayaraman, *Providence, Rhode Island*  
Valerie Jewells, *Chapel Hill, North Carolina*  
Timothy J. Kaufmann, *Rochester, Minnesota*  
Kenneth F. Layton, *Dallas, Texas*  
Ting-Yim Lee, *London, Ontario, Canada*  
Michael M. Lell, *Erlangen, Germany*  
Michael Lev, *Boston, Massachusetts*  
Karl-Olof Lovblad, *Geneva, Switzerland*  
Franklin A. Marden, *Chicago, Illinois*  
M. Gisele Matheus, *Charleston, South Carolina*  
Joseph C. McGowan, *Merion Station,  
Pennsylvania*  
Kevin R. Moore, *Salt Lake City, Utah*  
Christopher J. Moran, *St. Louis, Missouri*  
Takahisa Mori, *Kamakura City, Japan*  
Suresh Mukherji, *Ann Arbor, Michigan*  
Amanda Murphy, *Toronto, Ontario, Canada*  
Alexander J. Nemeth, *Chicago, Illinois*  
Laurent Pierot, *Reims, France*  
Jay J. Pillai, *Baltimore, Maryland*  
Whitney B. Pope, *Los Angeles, California*  
M. Judith Donovan Post, *Miami, Florida*  
Tina Young Poussaint, *Boston, Massachusetts*  
Joana Ramalho, *Lisbon, Portugal*

Otto Rapalino, *Boston, Massachusetts*  
Álex Rovira-Cañellas, *Barcelona, Spain*  
Paul M. Ruggieri, *Cleveland, Ohio*  
Zoran Rumboldt, *Rijeka, Croatia*  
Amit M. Saindane, *Atlanta, Georgia*  
Erin Simon Schwartz, *Philadelphia, Pennsylvania*  
Aseem Sharma, *St. Louis, Missouri*  
J. Keith Smith, *Chapel Hill, North Carolina*  
Maria Vittoria Spampinato, *Charleston, South  
Carolina*  
Gordon K. Sze, *New Haven, Connecticut*  
Krishnamoorthy Thamburaj, *Hershey, Pennsylvania*  
Kent R. Thielen, *Rochester, Minnesota*  
Cheng Hong Toh, *Taipei, Taiwan*  
Thomas A. Tomsick, *Cincinnati, Ohio*  
Aquila S. Turk, *Charleston, South Carolina*  
Willem Jan van Rooij, *Tilburg, Netherlands*  
Arastoo Vossough, *Philadelphia, Pennsylvania*  
Elysa Widjaja, *Toronto, Ontario, Canada*  
Max Wintermark, *Charlottesville, Virginia*  
Ronald L. Wolf, *Philadelphia, Pennsylvania*  
Kei Yamada, *Kyoto, Japan*

### EDITORIAL FELLOW

Hillary R. Kelly, *Boston, Massachusetts*

### SPECIAL CONSULTANTS TO THE EDITOR

#### AJNR Blog Editor

Neil Lall, *Denver, Colorado*

#### Case of the Month Editor

Nicholas Stence, *Aurora, Colorado*

#### Case of the Week Editors

Juan Pablo Cruz, *Santiago, Chile*  
Sapna Rawal, *Toronto, Ontario, Canada*

#### Classic Case Editor

Sandy Cheng-Yu Chen, *Taipei, Taiwan*

#### Facebook Editor

Peter Yi Shen, *Sacramento, California*

#### Health Care and Socioeconomics Editor

Pina C. Sanelli, *New York, New York*

#### Physics Editor

Greg Zaharchuk, *Stanford, California*

#### Podcast Editor

Yvonne Lui, *New York, New York*

#### Twitter Editor

Ryan Fitzgerald, *Little Rock, Arkansas*

### YOUNG PROFESSIONALS

#### ADVISORY COMMITTEE

Asim K. Bag, *Birmingham, Alabama*  
Anna E. Nidecker, *Sacramento, California*  
Peter Yi Shen, *Sacramento, California*

*Founding Editor*

**Juan M. Taveras**

*Editors Emeriti*

**Mauricio Castillo, Robert I. Grossman,  
Michael S. Huckman, Robert M. Quencer**

*Managing Editor*

**Karen Halm**

*Electronic Publications Manager*

**Jason Gantenberg**

*Executive Director, ASNR*

**James B. Gantenberg**

*Director of Communications, ASNR*

**Angelo Artemakis**





Title: Autumn in the Sundgau. This small region, located in the south of Alsace (France), near the border of Switzerland, is known for its many small lakes (or ponds) used for carp farming; "fried carps" is the reputed gastronomic specialty of this region with almost 30 restaurants along the famous "Route of Fried Carps."

*Maria Isabel Vargas, MD, Geneva University Hospitals, Division of Neuroradiology, Geneva, Switzerland*



# Revised Recommendations of the Consortium of MS Centers Task Force for a Standardized MRI Protocol and Clinical Guidelines for the Diagnosis and Follow-Up of Multiple Sclerosis

 A. Traboulsee, J.H. Simon, L. Stone, E. Fisher, D.E. Jones, A. Malhotra, S.D. Newsome, J. Oh,  D.S. Reich, N. Richert, K. Rammohan, O. Khan, E.-W. Radue, C. Ford, J. Halper, and  D. Li



## ABSTRACT

**SUMMARY:** An international group of neurologists and radiologists developed revised guidelines for standardized brain and spinal cord MR imaging for the diagnosis and follow-up of MS. A brain MR imaging with gadolinium is recommended for the diagnosis of MS. A spinal cord MR imaging is recommended if the brain MR imaging is nondiagnostic or if the presenting symptoms are at the level of the spinal cord. A follow-up brain MR imaging with gadolinium is recommended to demonstrate dissemination in time and ongoing clinically silent disease activity while on treatment, to evaluate unexpected clinical worsening, to re-assess the original diagnosis, and as a new baseline before starting or modifying therapy. A routine brain MR imaging should be considered every 6 months to 2 years for all patients with relapsing MS. The brain MR imaging protocol includes 3D T1-weighted, 3D T2-FLAIR, 3D T2-weighted, post-single-dose gadolinium-enhanced T1-weighted sequences, and a DWI sequence. The progressive multifocal leukoencephalopathy surveillance protocol includes FLAIR and DWI sequences only. The spinal cord MR imaging protocol includes sagittal T1-weighted and proton attenuation, STIR or phase-sensitive inversion recovery, axial T2- or T2\*-weighted imaging through suspicious lesions, and, in some cases, postcontrast gadolinium-enhanced T1-weighted imaging. The clinical question being addressed should be provided in the requisition for the MR imaging. The radiology report should be descriptive, with results referenced to previous studies. MR imaging studies should be permanently retained and available. The current revision incorporates new clinical information and imaging techniques that have become more available.

**ABBREVIATIONS:** CIS = clinically isolated syndrome; CMSC = Consortium of MS Centers; PML = progressive multifocal leukoencephalopathy

**M**R imaging of the brain and spinal cord is sensitive for detecting white matter lesions typical of MS. The current diagnostic criteria for MS<sup>1</sup> include specific MR imaging features

(Table 1) to provide evidence for dissemination in space and/or time, allowing an earlier diagnosis of MS after a single clinical syndrome consistent with demyelination (clinically isolated syndrome [CIS]). The newer criteria have good sensitivity and specificity<sup>2</sup> compared with the prior clinical criteria.<sup>3</sup> However, white matter lesions are common in the general population with increasing age, and the MR imaging criteria should be used with caution in patients with atypical symptoms for MS or the onset of symptoms in patients older than 40 years of age. This recommendation is particularly important in the presence of factors known to cause T2 hyperintensities, including hypertension, smoking, diabetes, high cholesterol, and migraines.


MR imaging is also increasingly used to follow patients with a diagnosis of definite MS to determine progression of clinically silent disease activity and to monitor response to therapy. Gadolinium (contrast)-enhancing lesions and/or changes in T2 (hyperintense) lesions are accepted MR imaging biomarkers of new inflammation. New MR imaging activity occurs more frequently than new clinical symptoms (relapses).<sup>4</sup> The ability to monitor patients with MS with MR imaging is hampered by inconsistent protocols and image quality.

Recommendations for a standardized MR imaging protocol and clinical guidelines in MS were previously published.<sup>5</sup> These

From the Department of Medicine (Neurology) (A.T.), University of British Columbia, Vancouver, Canada; Portland VA Research Foundation and Oregon Health and Sciences University (J.H.S.), Portland, Oregon; Mellen Center for MS Treatment and Research (L.S.), Cleveland Clinic, Cleveland, Ohio; Department of Biomedical Engineering, Cleveland Clinic (E.F.), Cleveland, Ohio; Department of Neurology, University of Virginia (D.E.J.), Charlottesville, Virginia; Department of Radiology and Biomedical Imaging, Yale University (A.M.), New Haven, Connecticut; Department of Neurology (S.D.N.), Johns Hopkins School of Medicine, Baltimore, Maryland; St. Michael's Hospital (J.O.), University of Toronto, Toronto, Ontario, Canada; Translational Neuroimaging Unit (D.S.R.), National Institute of Neurological Disorders and Stroke, National Institutes of Health, Bethesda, Maryland; Biogen Idec (N.R.), Cambridge, Massachusetts; University of Miami Multiple Sclerosis Center (K.R.), Miami, Florida; Department of Neurology (O.K.), Wayne State University School of Medicine, Detroit, Michigan; Department of Radiology (E.-W.R.), University Hospital, Basel, Switzerland; University of New Mexico Health Science Center (C.F.), Albuquerque, New Mexico; Consortium of Multiple Sclerosis Centers (J.H.), Hackensack, New Jersey; and Departments of Radiology (D.L.), University of British Columbia, Vancouver, British Columbia Canada.

Organizational support and funding for the meetings were provided by the Consortium of Multiple Sclerosis Centers ([www.msccare.org](http://www.msccare.org)).

Please address correspondence to Anthony Traboulsee, MD, Department of Medicine (Neurology), University of British Columbia, UBC Hospital, 2211 Wesbrook Mall, Room s199, Vancouver, BC, Canada V6T 2B5; e-mail: [t.traboulsee@ubc.ca](mailto:t.traboulsee@ubc.ca)

 Indicates open access to non-subscribers at [www.ajnr.org](http://www.ajnr.org)

<http://dx.doi.org/10.3174/ajnr.A4539>

developed out of a series of meetings sponsored by the Consortium of MS Centers (CMSC), including radiologists and neurologists from academic and community-based MS practices and representatives of the American Academy of Neurology, the Radiological Society of North America, and the American Society of Neuroradiology. The goal of this article is to update the MR imaging protocol and clinical guidelines on the basis of advances in imaging technology and new clinical evidence of the role of MR imaging in the diagnosis and monitoring of MS.

## Methods

Neurologists, radiologists, and imaging scientists with an expertise in MS from North America and Europe, representatives of the American Academy of Neurology, the Radiological Society of North America, the American Society of Neuroradiology, and, more recently, the National Institutes of Health and the North American Imaging in Multiple Sclerosis Cooperative updated the guidelines on the basis of new data, survey results, and expert opinion. Four imaging protocols, routine brain, progressive multifocal leukoencephalopathy (PML) surveillance, spinal cord, and orbits, were developed. Clinical guidelines on the recommended frequency of imaging in diagnosing and monitoring MS were updated.

**Protocol 1: Brain MR Imaging.** The brain MR imaging protocol (Table 2 and Fig 1) provides the minimum required sequence to aid

in the diagnosis and monitoring of MS that can be performed on a variety of clinical scanners and includes 3D T1-weighted, 3D T2-FLAIR, 3D T2-weighted, and post-single-dose gadolinium-enhanced T1-weighted imaging, all with a nongapped section thickness of  $\leq 3$  mm, and a DWI sequence ( $\leq 5$ -mm section thickness). Additional sequences for non-MS pathology can be added, depending on the individual needs of the patient and local preferences.

Scans should be of good quality with adequate SNR and spatial resolution (in-section pixel resolution of  $\leq 1 \times 1$  mm). Reconstruction (interpolation) is recommended at 0.5 mm. This recommendation may be limiting for some older scanners, particularly those operating at lower field strengths. One needs to be aware of the higher lesion-detection rates at 3T compared with 1.5T.<sup>6</sup> Lower field (ie, “open magnet”) should only be used in extenuating circumstances.

Coverage should include the whole brain. Orientation of the axial sequences (acquisition of 2D sequences or reformatting of 3D sequences) should be along the subcallosal line (Fig 1) because consistent repositioning is essential for detecting changes across time.

Most scanners are capable of 3D acquisitions with  $\leq 1.2$ -mm

**Table 1: 2010 Revised McDonald diagnostic criteria for MS<sup>a</sup>**

Minimum MRI Features for DIS (2 of 4 Criteria Required)
1 Infratentorial lesion
1 Juxtacortical lesion (touching the cortex)
1 Periventricular lesion (touching the ventricles)
1 Spinal cord lesion

**Note:**—DIS indicates dissemination in space; DIT, dissemination in time.

<sup>a</sup> MS diagnosis requires clinical and/or MRI evidence for CNS demyelination occurring in multiple locations (DIS) and with multiple events (DIT). The MRI criteria may support the clinical diagnosis of patients with MS with typical symptoms of CNS demyelination after the exclusion of alternative diagnoses. The DIT criterion can be met on MRI with an asymptomatic contrast-enhancing lesion on T1WI sequences (first or follow-up MRI) or newly active T2WI lesions on follow-up MRI. Lesions should be at least 3-mm in diameter and asymptomatic.

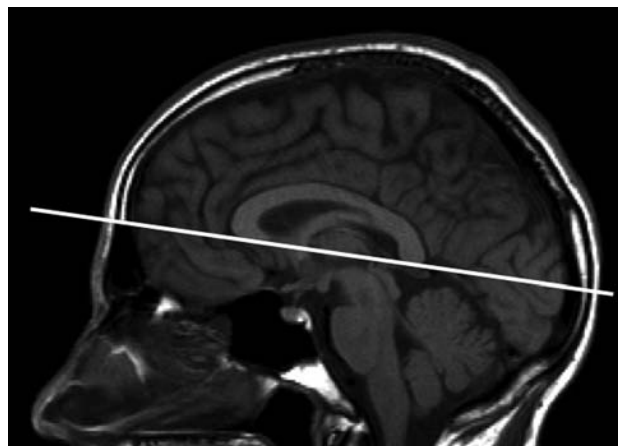


**FIG 1.** Orientation of axial oblique sequences. Orientation of axial oblique sequences should be along the subcallosal line as indicated by the solid line. Axial sections should be  $\leq 3$  mm with no gap.

**Table 2: Standardized brain MRI protocol (diagnosis and routine follow-up of MS)**

Parameters	Description
Field strength	Scans should be of good quality, with adequate SNR and resolution (in-sections, pixel resolution of $\leq 1 \times 1$ mm)
Scan prescription	Use the subcallosal plane to prescribe or reformat axial oblique sections (Fig 1)
Coverage	Whole-brain coverage
Section thickness and gap	$\leq 3$ mm, No gap (for 2D acquisition or 3D reconstruction)
Core sequences	Anatomic 3D inversion recovery-prepared T1 gradient echo (eg, 1.0- to 1.5-mm thickness) Gadolinium single dose, 0.1 mmol/kg given for 30 seconds <sup>a</sup> 3D sagittal T2WI FLAIR <sup>b</sup> (eg, 1.0- to 1.5-mm thickness) 3D T2WI <sup>b</sup> (eg, 1.0- to 1.5-mm thickness) 2D axial DWI ( $\leq 5$ -mm sections, no gap) 3D FLASH (non-IR prep) postgadolinium <sup>b</sup> (eg, 1.0- to 1.5-mm thickness) 3D series would be typically reconstructed to 3-mm thickness for display and subsequent comparison for lesion counts
Optional sequences	Axial proton attenuation Pre- or postgadolinium axial T1 spin-echo (for chronic black holes) SWI for identification of central vein within T2 lesions

**Note:**—IR indicates inversion recovery.

<sup>a</sup> Minimum 5-minute delay before obtaining postgadolinium T1. The 3D sagittal FLAIR may be acquired immediately after contrast injection before the 3D FLASH series.

<sup>b</sup> If unable to perform a 3D acquisition, then perform 2D axial and sagittal FLAIR, axial fast spin-echo proton attenuation/T2, and axial post-gadolinium T1WI spin-echo at  $\leq 3$ -mm section thickness.

**Table 3: PML surveillance brain MRI protocol**

Parameters	Description
Field strength	Scans should be of good quality, with adequate SNR and resolution (in-section pixel resolution of $\leq 1 \times 1$ mm)
Scan prescription	Use the subcallosal plane to prescribe or reformat axial oblique sections (Fig 1)
Coverage	Whole-brain coverage
Sequences	3D sagittal T2WI FLAIR <sup>a</sup> 2D axial DWI (5-mm-thick, no gap)
Section thickness and gap	$\leq 3$ mm, No gap (for 2D acquisition or 3D reconstruction)

<sup>a</sup> If unable to perform a 3D acquisition, then perform 2D axial FLAIR at  $\leq 3$ -mm section thickness.

isotropic voxels.<sup>7</sup> The data can be reformatted to achieve 3-mm axial and/or sagittal sections for clinical readout. If a 2D acquisition is used, the section thickness should be  $\leq 3$  mm and there should be no gap between sections. 3D FLAIR may be equivalent or superior to T2-weighted imaging for posterior fossa lesions. It is recommended that a 3D T2 or a 3-mm axial fast/turbo spin-echo proton attenuation/T2 sequence be acquired for posterior fossa lesion detection as a backup.

The brain MR imaging sequences include a sagittal FLAIR (the 3D acquisition is usually acquired in the sagittal plane) for the detection of MS lesions in the corpus callosum. Although these lesions can be identified on axial images, the sagittal plane provides greater ease of visualization of these, as well as juxtacortical lesions (ie, white matter lesions touching the cortex) and the oval perivenular configuration of lesions.

A thin-section ( $\leq 1.5$ -mm thickness) 3D inversion recovery-prepared, T1-weighted, spoiled gradient-echo sequence is useful for volumetric analysis, which is likely to play an important role in the future. The 3D inversion recovery sequence should be acquired before contrast. This sequence also enables confirmation of juxtacortical and infratentorial lesions. Chronic T1-weighted “black hole” monitoring as a marker of severe axonal injury has only been validated on 2D spin-echo sequences. Because nearly all hyperintense lesions apparent on T2-weighted sequences are hypointense on 3D inversion recovery T1-weighted scans, the specificity of T1 black holes is lost and clinical interpretation requires caution.<sup>8</sup>

The protocol includes a postgadolinium contrast 3D FLASH (non-inversion recovery prep) or axial T1-weighted spin-echo images. Although 3D gradient echo-based T1-weighted imaging could be used as a replacement for T1 spin-echo for identifying postgadolinium contrast enhancement, whether such sequences are less sensitive<sup>9</sup> remains an open question.

Axial DWI (5 mm) is recommended for detecting non-MS pathology, including acute ischemia/infarction and the earlier detection of PML (see below).

The 3D or 2D FLAIR and/or T2-weighted images can be acquired during the minimum 5-minute delay that is required before the postcontrast T1-weighted image. Phased array coils may significantly speed up acquisition time.

Proton attenuation and precontrast 2D spin-echo T1-weighted imaging are considered optional. Subtle lesions can be confirmed on proton attenuation imaging, though the sensitivity of 3D FLAIR may obviate this confirmation.<sup>10</sup>

Gadolinium contrast detects the breakdown of the blood-brain barrier that occurs with new lesion development and reactivation of old lesions. The average duration of enhancement for individual brain lesions is 3 weeks,<sup>11</sup> with most enhancing for

2–6 weeks. Rarely, MS lesions in the brain show persistent enhancement for  $>3$  months with single-dose gadolinium. A standard dose of gadolinium (0.1 mmol/kg) given for 30 seconds and a minimum 5-minute delay before acquiring the postcontrast T1-weighted imaging are recommended. “Triple dose” and longer delays of up to 15 minutes for the postcontrast T1-weighted imaging may detect more lesions but are not necessary for routine clinical practice. Reports of nephrogenic systemic fibrosis/nephrogenic fibrosing dermatopathy in patients with preexisting significant renal impairment have resulted in many centers requiring a recent laboratory assessment of renal function, such as an estimated glomerular filtration rate. Macrocyclic chelates have been recommended by several radiologic societies to minimize this risk.<sup>12,13</sup>

Most newly enhancing lesions will leave residual T2 hyperintensity after the enhancement resolves.<sup>14</sup> Detecting new or enlarging T2 lesions compared with a previous study would also indicate new inflammatory activity even in the absence of gadolinium enhancement. However, to reliably detect new lesions, a standardized MR imaging protocol with similar orientation and other parameters is important. Gadolinium can also be helpful for ruling out alternative diagnoses such as tumors (persistent enhancement) or leptomeningeal disease such as neurosarcoidosis<sup>15,16</sup> or infection.

**Protocol 2: PML Surveillance Brain MR Imaging.** PML is a devastating complication that is rarely seen with some disease-modifying therapies (Table 3). The risk is increased in patients with detectable John Cunningham virus serum antibodies. MR imaging detection of PML in the presymptomatic phase improves outcome and survival.<sup>17</sup> An abbreviated PML surveillance protocol includes 3D (or 2D) FLAIR and DWI sequences.<sup>18</sup> Postcontrast T1 adds little diagnostic value to PML surveillance because  $<50\%$  of early PML lesions show contrast enhancement.<sup>19</sup> Typical PML lesion appearance includes subcortical lesions (48% occur in the frontal lobes) that are hyperintense on T2/FLAIR and hypointense on T1-weighted imaging, with ill-defined borders toward the white matter and sharp borders toward the gray matter and high signal intensity on DWI (absent in about 40% of patients with presymptomatic PML). Lesions can involve the deep gray matter (thalamus and dentate nuclei). Contrast enhancement can be patchy, nodular, or speckled.<sup>18,19</sup>

**Protocol 3: Spinal Cord MR Imaging.** As a minimum, coverage should include the cervical cord (Table 4) because clinically silent MS lesions are more common and better visualized there. It may not be necessary to examine the thoracic cord routinely unless there are clinical symptoms and/or signs at that level. Two sequences are recommended for the detection of subtle lesions, including a sagittal T2-weighted and a proton attenuation, STIR, or

**Table 4: Spinal cord MRI protocol**

Parameter	Description
Field strength	Scans should be of good quality, with adequate SNR and resolution (in-section pixel resolution of $\leq 1 \times 1$ mm) Closed magnets (large bore for patients with claustrophobia) preferred
Coverage	Cervical cord coverage <sup>a</sup>
Core sequences	Sagittal T2 Sagittal proton attenuation, STIR, or PSTI-IR Axial T2 through lesions
Section thickness and gap	Sagittal: $\leq 3$ mm, no gap Axial: 5 mm, no gap
Optional sequences	Axial T2 through complete cervical cord Gadolinium <sup>b</sup> and postgadolinium sagittal T1 Sagittal T1

**Note:**—PSTI-IR indicates phase-sensitive T1 inversion recovery.

<sup>a</sup> Thoracic and conus coverage recommended if symptoms localize to this region to rule out an alternate diagnosis.

<sup>b</sup> Minimum 5-minute delay before obtaining postgadolinium T1. Additional gadolinium does not need to be given for a spinal cord MRI if it follows a contrast brain MRI study.

**Table 5: Clinical guidelines for brain and spinal cord MRI in MS**

Guidelines
Baseline studies for patients with a CIS and/or suspected MS
Brain MRI protocol with gadolinium at baseline and
Spinal cord MRI if transverse myelitis, insufficient features on brain MRI to support diagnosis, or age older than 40 years with nonspecific brain MRI findings
A cervical cord MRI performed simultaneously with the brain MRI would be advantageous in the evaluation of patients with or without transverse myelitis and would reduce the number of patients requiring a subsequent MRI appointment
Orbital MRI if severe optic neuritis with poor recovery
Timing of a follow-up brain MRI protocol for patients with a CIS and/or suspected MS to look for evidence of dissemination in time
6–12 Months for high-risk CIS (eg, $\geq 2$ ovoid lesions on first MRI)
12–24 Months for low-risk CIS (ie, normal brain MRI findings) and/or uncertain clinical syndrome with suspicious brain MRI features (eg, RIS)
Timing of brain MRI protocol with gadolinium for patients with an established diagnosis of MS
No recent prior imaging available (eg, patient with MS transferring to a new clinic)
Postpartum to establish a new baseline
Prior to starting or switching disease-modifying therapy
Approximately 6 months after switching disease-modifying therapy to establish a new baseline on the new therapy
Every 1–2 years while on disease-modifying therapy to assess subclinical disease activity
Unexpected clinical deterioration or reassessment of original diagnosis <sup>a</sup>
Timing of PML surveillance brain MRI protocol
Every 12 months for patients negative for serum JC virus antibody
Every 3–6 months for patients positive for serum JC virus antibody and $\geq 18$ months on natalizumab <sup>b</sup>

**Note:**—JC indicates John Cunningham; RIS, radiologic isolated syndrome.

<sup>a</sup> Routine spinal cord follow-up not required unless syndrome is predominately recurrent transverse myelitis.

<sup>b</sup> The brain MRI protocol for monitoring patients on disease modifying therapies includes the PML surveillance sequences.

T1-weighted inversion recovery sequence with phase-sensitive reconstruction (section thickness,  $\leq 3$  mm).<sup>20</sup> Axial T2 or T2\* and postcontrast axial T1 through the lesions is recommended (section thickness of 5 mm, no gap). A sagittal T1 is of limited value for characterizing intramedullary disease. When spinal cord imaging is performed at the same time as brain imaging with gadolinium, no additional contrast is required.

**Protocol 4: Orbit MR Imaging.** Imaging of the orbit may be clinically indicated to confirm optic neuritis and rule out compressive lesions. Unusual enhancement patterns of the optic nerve and/or sheath might suggest an alternate diagnosis such as sarcoidosis or neuromyelitis optica.<sup>21</sup> The recommended sequences include a coronal STIR or fat-suppressed T2 and a postgadolinium fat-suppressed T1 with a section thickness of  $\leq 2$  mm, with coverage through the optic chiasm.

#### **Clinical Guidelines: Diagnostic Imaging for Suspected MS**

While MR imaging is not absolutely required for the clinical diagnosis of MS (Table 5), it provides important information.<sup>22</sup> A

brain MR imaging with and without gadolinium is recommended for patients suspected of having MS or with an established diagnosis of MS who are new to a clinical practice and do not have recent imaging available for review. A cervical cord MR imaging at the same time would be advantageous in the diagnostic evaluation of patients with or without transverse myelitis and would reduce the number of patients requiring a subsequent MR imaging appointment. Patients suspected of having MS include those with a CIS of optic neuritis, partial transverse myelitis, or brain stem syndromes. Patients with CIS with a brain MR imaging with  $\geq 2$  characteristic lesions ( $\geq 3$  mm in diameter) have a high risk for MS.<sup>23</sup> One-third of patients with CIS (not treated with corticosteroids) will have asymptomatic gadolinium-enhancing lesions and will meet the 2010 McDonald diagnostic criteria for definite MS.<sup>24</sup> Detection of new T2 or gadolinium-enhancing lesions on a follow-up brain MR imaging can be sufficient evidence to fulfill dissemination in time and/or space criteria (Table 1). The recommended timing of the follow-up brain MR imaging is 6–12 months. The proportion of patients with high-risk CIS (younger



**Table 6: Recommendations for communication**

	Recommendations
The clinical requisition for brain MRI should include	
Requesting the CMSC or standardized brain MRI protocol	
Indicating the purpose of the study	
Diagnostic study for CIS or MS (indicate date of symptom onset)	
Treatment-monitoring study (indicate if on disease-modifying therapy)	
PML surveillance study (indicate if high- or low-risk)	
Unexpected clinical decline or reassessment of diagnosis	
Date and location of most recent MRI study (encourage patient to bring a copy of outside images on portable media at the time of MRI appointment)	
The radiology report should include	
For a diagnostic MS study	
Number of gadolinium-enhancing T1 lesions (eg, 0, 1, 2, 3, 4, $\geq 5$ )	
Comparison with previous studies for the number of new T2 lesions (eg, 0, 1, 2, 3, 4, $\geq 5$ )	
The presence of juxtacortical (touching the cortex), periventricular (touching the ventricles), infratentorial, or spinal cord lesions	
The report should avoid a summary statement like “McDonald diagnostic criteria met”	
The interpretation should indicate whether findings are typical, atypical, or not consistent with MS and should provide a differential diagnosis if appropriate	
For a follow-up MS study	
Number of gadolinium-enhancing T1 lesions (eg, 0, 1, 2, 3, 4, $\geq 5$ )	
Comparison with previous studies for the number of new T2 lesions (eg, 0, 1, 2, 3, 4, $\geq 5$ )	
Qualitative assessment of	
Overall T2 lesion-burden severity (eg, mild, moderate, severe)	
Comparison with previous studies for overall worsening of T2 lesion burden and atrophy	
For a PML surveillance study	
Comparison with previous studies for new T2 lesions, hyperintense lesions on DWI	
Presence of PML suspicious features	

than 50 years of age) who develop new lesions by 3, 6, and 12 months is 22%, 51%, and 74%, respectively.<sup>25</sup> By 12–18 months, most patients with high-risk CIS will meet the diagnostic criteria for MS by developing new MR imaging lesions and/or new clinical symptoms.<sup>26</sup> Additional MRIs can be performed according to clinical judgment. Some experts recommend an annual brain MR imaging in patients with CIS with normal brain MR imaging findings for 1–2 years or at the time of development of new symptoms consistent with demyelination.<sup>23,27,28</sup>

Patients suspected of having MS also include those with milder or atypical symptoms or incidental abnormalities on MR imaging that are strongly suspicious for MS (radiologic isolated syndrome).<sup>29</sup> The presence of a spinal cord lesion on MR imaging may be helpful in estimating the risk of conversion to definite multiple sclerosis.<sup>30</sup> A 5-year prospective study of 451 patients with radiologic isolated syndrome demonstrated that the risk of conversion to MS was 34%.<sup>31</sup> In addition to other paraclinical tests such as evoked potentials and CSF analysis, a follow-up MR imaging may support the diagnosis of MS by demonstrating new lesion development in patients suspected of having MS.

In patients with equivocal brain MR imaging findings (ie, not meeting dissemination in space criteria), the detection of lesions on spinal cord imaging can provide additional evidence for disease dissemination in space. Spinal cord lesions have greater specificity for demyelinating disease.<sup>31,32</sup> Nonspecific white matter lesions are extremely uncommon in the spinal cord, in contrast to their frequent occurrence in the brain.<sup>33</sup> Patients may present with a more severe demyelinating or inflammatory syndrome, including tumefactive lesions or acute complete transverse myelitis. A follow-up MR imaging would provide evidence of lesion improvement or resolution supporting an inflammatory process

and/or the detection of new lesions that could aid in the differential diagnosis.<sup>15,34</sup>

Spinal cord imaging, in addition to brain imaging, is recommended if the symptoms involve the spinal cord such as partial transverse myelitis, complete transverse myelitis, or a progressive myelopathy suspicious for primary-progressive MS. Patients with progressive MS may have a chronic, diffuse, extensive abnormal spinal cord signal, though most do not. The detection of a longitudinally extensive spinal cord lesion ( $\geq 3$  segments) with central cord predominance and mass effect in a patient with acute transverse myelitis is suggestive of neuromyelitis optica.<sup>21</sup> The longitudinally extensive involvement of these distinctive lesions is often transient.

#### **Clinical Guidelines: Follow-Up of Established MS**

The 4 common scenarios for requesting a brain MR imaging for patients with an established diagnosis of MS are the following: new baseline evaluation (previous MR imaging unavailable, unacceptable quality, or a long interval since the last MR imaging), routine follow-up for clinically silent disease activity while monitoring treatment response, PML surveillance, and unexpected clinical deterioration or re-evaluation of the diagnosis of MS (Table 6). A baseline spinal cord MR imaging may also be useful, depending on the clinical symptoms.

MR imaging is recommended before the initiation or modification of disease-modifying therapy and approximately 6 months after a treatment switch to allow sufficient time for the new therapy to reach its therapeutic potential. Determining ongoing radiologic stability is based on the presence or absence of new lesions (T2 or contrast-enhancing T1) relative to a posttreatment MR imaging.<sup>35</sup>

MR imaging is the most sensitive tool currently available for monitoring inflammatory disease activity in MS. Clinical assessments far underestimate disease activity and burden compared with MR imaging. A follow-up MR imaging is useful for patients on a disease-modifying therapy to determine the response of subclinical disease activity to treatment. Continued or worsening of MR imaging disease activity while on a disease-modifying therapy may prompt a change in therapy. There is evolving evidence that ongoing MR imaging activity can be indicative of a suboptimal therapeutic response.<sup>36-41</sup>

Many new lesions may be clinically silent, particularly when they occur outside the more functionally eloquent regions of the CNS (spinal cord, optic nerve). However, as more lesions accumulate in the CNS, studies demonstrate a clear relationship between the severity of cognitive dysfunction and lesion burden, even in patients with good mobility. CNS damage also occurs in brain tissue that appears normal on standard conventional imaging (normal appearing brain tissue). This slow, evolving damage can be monitored by nonconventional advanced MR imaging techniques that are mainly restricted to the research realm. New T2 or gadolinium-enhancing lesions are associated with progressive changes in normal appearing brain tissue and global brain atrophy.<sup>42</sup>

The frequency of periodic MR imaging to assess subclinical disease activity will vary depending on the patient's clinical course and other clinical features. For relapsing forms of MS, a follow-up MR imaging should be considered annually for at least the first 2 or 3 years after starting therapy or switching disease-modifying therapy. More frequent surveillance may be indicated in clinically aggressive cases or unusual patterns of MR imaging lesions (eg, tumefactive MS). Clinical judgment and experience may be critical in these settings. While guidelines on a tolerable threshold for new lesion activity that warrants a change in therapy have been proposed,<sup>43,44</sup> individual factors will impact the clinician's decision on the frequency of MR imaging monitoring. The frequency of MR imaging may be higher during the early years for patients with CIS and early relapsing-remitting MS, particularly when patients are on treatment. Fewer MR imaging scans are required in later stages of the disease (secondary-progressive MS) or in primary-progressive MS in which MR imaging activity is low and no effective treatments are as of yet available.<sup>45</sup> Nonetheless, multiple new T2 or contrast-enhancing lesions on surveillance scans in conjunction with the clinical picture, even in primary-progressive MS,<sup>45</sup> should alert the clinician to re-evaluate treatment strategies.

The PML surveillance recommendations by using a shorter protocol depend on John Cunningham virus serum antibody status, length of exposure to natalizumab, and the use of prior immunosuppressive therapy.<sup>46</sup> Higher risk patients (positive for John Cunningham virus serum antibodies) with >18 months of natalizumab exposure should have the PML surveillance MR imaging protocol performed every 3–6 months.<sup>18</sup> Any clinical change suspicious for PML should prompt an urgent MR imaging.

Indications for an unplanned follow-up brain MR imaging in patients with an established diagnosis of MS include the re-assessment of the original diagnosis or to clarify the cause of clinical deterioration that is not otherwise evident by clinical assessment (eg, stroke or tumor).

A spinal cord MR imaging may be indicated when there is significant clinical worsening with few changes on brain MR imaging or to rule out an alternative cause for progressive myelopathy, such as cervical spondylosis or a tumor. Routine follow-up with spinal cord imaging may be useful in rare cases of recurrent transverse myelitis to assess response to therapy or new disease activity.

### **Recommendations for Communication and Storage**

The requisition should ask for standardized brain and/or spinal cord imaging and indicate the clinical question being addressed and include relevant clinical history (eg, CIS localization and symptom duration), current MS disease-modifying therapy, recent high-dose corticosteroids, and date and place of any previous MR imaging (Table 6).

The radiology report should use standardized terminology and include a description of salient findings. These include new T2 or contrast-enhancing T1 lesion numbers and the presence/absence of juxtacortical, periventricular, infratentorial, and spinal cord lesions. The report should avoid a summary statement like "McDonald diagnostic criteria met," because this requires clinical details that may not be available at the time of the radiologic review. The interpretation should indicate whether the findings are typical, atypical, or not consistent with MS, and the radiologist should provide a differential diagnosis, if appropriate. In patients with definite MS, a qualitative assessment of brain volume (atrophy) and overall T2 lesion burden and a comparison with previous studies for new lesion activity and atrophy are useful (Table 6). MR imaging studies should be stored in a standard readable format (DICOM), retained permanently, and available. Patients are encouraged to keep copies of their own studies and have these available if a follow-up MR imaging is performed at a different imaging center.

### **CONCLUSIONS**

The goal of the original guidelines was to provide clinicians with a standardized MR imaging protocol that would be suitable for the initial diagnosis and monitoring of changes with time. The protocol was designed to provide the optimum amount of information that could be acquired within a routine clinical MR imaging setting. The current revision incorporates feedback from centers using the previous protocol and input from radiologists with expertise in MS. 3D FLAIR and 3D T2-weighted imaging are already being introduced into clinical practice. These techniques can provide potentially higher quality data (higher resolution, seamless reformating) and should be comparable with the core 2D approaches. The methodologies for quantification of advanced imaging techniques, such as magnetization transfer imaging, MR spectroscopy, diffusion tensor imaging, and myelin water fraction imaging, require further standardization before their routine clinical use can be recommended. Methods sensitive to gray matter pathology (double inversion recovery and phase-sensitive T1 inversion recovery sequences) are being developed but are still currently investigational. An imaging challenge for the next decade is the continued translation of research methodologies into useful and reliable clinical tools for lesion identification, quantification of T2 lesion burden, and brain and spinal cord atrophy measures.

The revised guidelines provide consensus recommendations for the use of brain and spinal cord MR imaging and the use of gadolinium in the diagnosis of patients with MS. The challenge during the past decade was in reaching a consensus on the frequency of routine imaging to monitor patients with MS. The evidence supporting this role remains incomplete. However, there is consensus that MR imaging provides useful information about subclinical inflammatory activity in the early phase of the disease. It is reasonable for physicians to take these arguments for and against routine MR imaging into consideration when they individualize patient care.

During the past 3 decades, the clinical application of MR imaging in MS and the advances in imaging quality and speed have been remarkable. We anticipate that these guidelines will require future revision as MR imaging technology and our knowledge of MS continue to improve.

## ACKNOWLEDGMENTS

Lori Saslow (Great Neck, New York) assisted in manuscript preparation and editing.

The following individuals participated in workshops and/or reviewed the guidelines: Barry Arnason, Douglas Arnold, Frederik Barkhof, Guy Buckle, Peter Calabresi, Bruce Cohen, Lesley Costley, Patricia Coyle, Virginia Devonshire, Burton Drayer, George Ebers, Massimo Filippi, Joseph Frank, Douglas Graeb, Douglas Goodin, June Halper, Colleen Harris, Stanley Hashimoto, Robert Herndon, George Hutton, Douglas Jeffrey, Ciaran Keogh, Thomas Leist, Geert Lycklama à Nijeholt, Henry McFarland, David Miller, Mary Lou Myles, Paul O'Connor, Joel Oger, Donald Paty, Daniel Pelletier, Michael Phillips, George Rice, John Richert, Jay Rosenberg, Richard Rudick, James Scott, Randall Shapiro, Nancy Sicotte, James Simsarian, Karen Smith, Jay Tsuruda, Brian Weinshenker, Ernest Willoughby, Jerry Wolinsky.

Disclosures: Anthony Traboulsee—*RELATED: Support for Travel to Meetings for the Study or Other Purposes:* CMSC; *UNRELATED: Consultancy:* Chugai Pharmaceuticals, MedImmune, Teva Innovation, Novartis, Hoffman-La Roche, Sanofi-Genzyme, EMD Serono; *Grants/Grants Pending:* Chugai Pharmaceuticals,\* Hoffman-La Roche,\* Sanofi-Genzyme\*; *Payment for Lectures (including service on Speakers Bureaus):* Sanofi-Genzyme. Jack H. Simon—*RELATED: Support for Travel to Meetings for the Study or Other Purposes:* Travel costs were covered for discussion of guidelines by CMSC; *UNRELATED: Consultancy:* Biogen Idec, *Comments:* Consultant, Advisory Board, ad hoc. Lael Stone—*RELATED: Consulting Fee or Honorarium:* CMSC, *Comments:* \$500 honorarium for participation in a meeting held in the fall of 2015; *Support for Travel to Meetings for the Study or Other Purposes:* CMSC, *Comments:* travel to Newark airport and lodging in hotel for 1 night, with meals paid directly to the hotel not to me. Elizabeth Fisher—*RELATED: Consulting Fee or Honorarium:* CMSC, *Comments:* received an honorarium for participating in the CMSC MRI guidelines—development meeting; *Support for Travel to Meetings for the Study or Other Purposes:* CMSC, *Comments:* received travel support to participate in the CMSC MRI guidelines—development meeting; *UNRELATED: Consultancy:* Biogen, Genzyme, Novartis, *Comments:* received payments for consultant work; *Employment:* Biogen (employed as of January 5, 2015). David E. Jones—*RELATED: Consulting Fee or Honorarium:* CMSC; *Support for Travel to Meetings for the Study or Other Purposes:* CMSC; *UNRELATED: Consultancy:* Genzyme, Biogen Idec, Novartis, *Comments:* Although most of the money went to University of Virginia for these activities, I have received personal compensation for some consulting activities with these 3 companies in the past 3 years; *Grants/Grants Pending:* National Multiple Sclerosis Society,\* Biogen Idec,\* *Comments:* Site Principal Investigator for clinical trial with vitamin D; will be site Principal Investigator for Natalizumab as an Efficacy Switch in Participants with Relapsing Multiple Sclerosis After Failure on Other Therapies (ESCALATE); *Payment for Lectures (including service on Speakers Bureaus):* Program of All-inclusive Care for the Elderly, *Comments:* 1 lectured in 2014 (\$500); *Travel/Accommodations/Meeting Expenses Unrelated to Activities Listed:* Multiple Sclerosis Association of America. Jiwon Oh—*RELATED: Grant:* Multiple Sclerosis Society

of Canada\*; *UNRELATED:* EMD Serono, Biogen Idec, Roche, Genzyme; *Grants/Grants Pending:* Biogen Idec,\* Genzyme\*; *Payment for Lectures (including service on Speakers Bureaus):* Teva, EMD Serono, Genzyme, Biogen Idec; *Travel/Accommodations/Meeting Expenses Unrelated to Activities Listed:* Genzyme, EMD Serono. David S. Reich—*UNRELATED: Payment for Development of Educational Presentations:* University of Pennsylvania (grand rounds). Nancy Richert—*UNRELATED: Employment:* Biogen; *Stock/Stock Options:* As a Biogen employee, I received restricted stock options; *Travel/Accommodations/Meeting Expenses Unrelated to Activities Listed:* Biogen pays my travel and accommodations for attending national meetings (eg, American Academy of Neurology, American Society of Neuroradiology, European Committee for Treatment and Research in Multiple Sclerosis). Kottli Rammohan—*UNRELATED: Consultancy:* Novartis, Genentech, Genzyme, Biogen Idec, EMD Serono, Teva Neurosciences; *Grants/Grants Pending:* Novartis,\* Genentech,\* Genzyme,\* EMD Serono,\* Biogen Idec,\* Teva Neurosciences\*; *Payment for Development of Educational Presentations:* Mallinckrodt; *Travel/Accommodations/Meeting Expenses Unrelated to Activities Listed:* CMSC. Omar Khan—*UNRELATED: Consultancy:* Teva, Biogen Idec, Genzyme, Novartis; *Grants/Grants Pending:* Wayne State University. Ernst-Wilhelm Radue—*UNRELATED: Board Membership:* Novartis,\* Biogen\*; *Consultancy:* Novartis, Biogen, Bayer Schering, Merck Serono, Genzyme, Synthon, MorphoSys; *Payment for Lectures (including service on Speakers Bureaus):* Novartis, Biogen, Bayer Schering, Genzyme. Corey Ford—*RELATED: Grant:* Teva Neuroscience,\* *Comments:* research grant for glatiramer acetate clinical trials including 20+ year-long term follow-up study; *Consulting Fee or Honorarium:* Teva Neuroscience, *Comments:* In the past few years, I have consulted with Teva for scientific/medical issues related to MS disease-modifying therapies, including glatiramer acetate; *Support for Travel to Meetings for the Study or Other Purposes:* Teva Neuroscience, *Comments:* travel to meetings for presentation of data and consulting; *Provision of Writing Assistance, Medicines, Equipment, or Administrative Support:* Teva, *Comments:* Teva staff participated in drafting this article and providing data from a data base maintained in multiple clinical trials of glatiramer acetate. I made substantive contributions to the writing, editing, proofing and verification of the content; *UNRELATED: Consultancy:* Novartis, Biogen Idec, *Comments:* I participated in several consulting meetings during the past 3 years. As with Teva, these were advisory-/medical-focused. I do not participate in Speakers Bureaus and all potential conflicts of interest such as these have been reported to the University of New Mexico Health Sciences Center Conflicts of Interest Committee for review and management; *Grants/Grants Pending:* multiple industry sponsors,\* *Comments:* We perform 8–10 clinical trials each year for manufacturers of MS disease-modifying drugs. All are paid to the institution and conducted under appropriate compliance and reporting guidelines; *Payment for Development of Educational Presentations:* CMSC, *Comments:* I have received compensation for the creation of Continuing Medical Education materials for the CMSC in the field of MS clinical care. June Halper—*UNRELATED: Consultancy:* Biogen, *Comments:* Delphi study group. David Li—*UNRELATED: Board Membership:* Opexa Therapeutics (Data Safety Advisory Board); *Consultancy:* Vertex Pharmaceuticals, *Comments:* drug-development testing; *Grants/Grants Pending:* Genzyme,\* Hoffman-La Roche,\* Merck Serono,\* Nuron,\* Perceptives,\* Sanofi-Aventis,\* *Comments:* I am Director of the University of British Columbia MS/MRI Research Group, which has been contracted to provide central MRI analysis for therapeutic trials in multiple sclerosis. \*Money paid to the institution.

## REFERENCES

- Polman CH, Reingold SC, Banwell B, et al. **Diagnostic criteria for multiple sclerosis: 2010 revisions to the McDonald criteria.** *Ann Neurol* 2011;69:292–302 CrossRef Medline
- Dalton CM, Brex PA, Miszkil KA, et al. **Application of the new McDonald criteria to patients with clinically isolated syndromes suggestive of multiple sclerosis.** *Ann Neurol* 2002;52:47–53 CrossRef Medline
- Poser CM, Paty DW, Scheinberg L, et al. **New diagnostic criteria for multiple sclerosis: guidelines for research protocols.** *Ann Neurol* 1983;13:227–31 CrossRef Medline
- Harris JO, Frank JA, Patronas N, et al. **Serial gadolinium-enhanced magnetic resonance imaging scans in patients with early, relapsing-remitting multiple sclerosis: implications for clinical trials and natural history.** *Ann Neurol* 1991;29:548–55 CrossRef Medline
- Simon JH, Li D, Traboulsee A, et al. **Standardized MR imaging protocol for multiple sclerosis: Consortium of MS Centers consensus guidelines.** *AJNR Am J Neuroradiol* 2006;27:455–61 Medline
- Wattjes MP, Barkhof F. **High field MRI in the diagnosis of multiple sclerosis: high field-high yield?** *Neuroradiology* 2009;51:279–92 CrossRef Medline
- Vrenken H, Jenkinson M, Horsfield MA, et al; MAGNIMS Study



- Group. **Recommendations to improve imaging and analysis of brain lesion load and atrophy in longitudinal studies of multiple sclerosis.** *J Neurol* 2013;260:2458–71 CrossRef Medline
8. Barkhof F, Karas GB, van Walderveen MA. **T1 hypointensities and axonal loss.** *Neuroimaging Clin N Am* 2000;10:739–52, ix Medline
9. Rand S, Maravilla KR, Schmiedl U. **Lesion enhancement in radio-frequency spoiled gradient-echo imaging: theory, experimental evaluation, and clinical implications.** *AJNR Am J Neuroradiol* 1994;15:27–35 Medline
10. Gramsch C, Nensa F, Kastrup O, et al. **Diagnostic value of 3D fluid attenuated inversion recovery sequence in multiple sclerosis.** *Acta Radiol* 2015;56:622–27 CrossRef Medline
11. Cotton F, Weiner HL, Jolesz FA, et al. **MRI contrast uptake in new lesions in relapsing-remitting MS followed at weekly intervals.** *Neurology* 2003;60:640–46 CrossRef Medline
12. Nacif MS, Arai AE, Lima JAC, et al. **Gadolinium-enhanced cardiovascular magnetic resonance: administered dose in relationship to United States Food and Drug Administration (FDA) guidelines.** *J Cardiovasc Magn Reson* 2012;14:18 CrossRef Medline
13. Thomsen HS, Morcos SK, Almén T, et al; ESUR Contrast Medium Safety Committee. **Nephrogenic systemic fibrosis and gadolinium-based contrast media: updated ESUR Contrast Medium Safety Committee guidelines.** *Eur Radiol* 2013;23:307–18 CrossRef Medline
14. Miller DH, Rudge P, Johnson G, et al. **Serial gadolinium enhanced magnetic resonance imaging in multiple sclerosis.** *Brain* 1988;111(pt 4):927–39 CrossRef Medline
15. Traboulsee A, Li DK. **Conventional MR imaging.** *Neuroimaging Clin N Am* 2008;18:651–73, x CrossRef Medline
16. Charil A, Yousry TA, Rovaris M, et al. **MRI and the diagnosis of multiple sclerosis: expanding the concept of “no better explanation.”** *Lancet Neurol* 2006;5:841–52 CrossRef Medline
17. Dong-Si T, Richman S, Wattjes MP, et al. **Outcome and survival of asymptomatic PML in natalizumab-treated MS patients.** *Ann Clin Transl Neurol* 2014;1:755–64 CrossRef Medline
18. Wattjes MP, Barkhof F. **Diagnosis of natalizumab-associated progressive multifocal leukoencephalopathy using MRI.** *Curr Opin Neurol* 2014;27:260–70 CrossRef Medline
19. Yousry TA, Pelletier D, Cadavid D, et al. **Magnetic resonance imaging pattern in natalizumab-associated progressive multifocal leukoencephalopathy.** *Ann Neurol* 2012;72:779–87 CrossRef Medline
20. Poonawalla AH, Hou P, Nelson FA, et al. **Cervical spinal cord lesions in multiple sclerosis: T1-weighted inversion-recovery MR imaging with phase-sensitive reconstruction.** *Radiology* 2008;246:258–64 CrossRef Medline
21. Wingerchuk DM, Banwell B, Bennett JL, et al. **International consensus diagnostic criteria for neuromyelitis optica spectrum disorders.** *Neurology* 2015;85:177–89 CrossRef Medline
22. McDonald WI, Compston A, Edan G, et al. **Recommended diagnostic criteria for multiple sclerosis: guidelines from the International Panel on the Diagnosis of Multiple Sclerosis.** *Ann Neurol* 2001;50:121–27 CrossRef Medline
23. Brex PA, Ciccarelli O, O’Riordan JI, et al. **A longitudinal study of abnormalities on MRI and disability from multiple sclerosis.** *N Engl J Med* 2002;346:158–64 CrossRef Medline
24. Kang H, Metz LM, Traboulsee AL, et al; Minocycline in CIS Study Group. **Application and a proposed modification of the 2010 McDonald criteria for the diagnosis of multiple sclerosis in a Canadian cohort of patients with clinically isolated syndromes.** *Mult Scler* 2014;20:458–63 CrossRef Medline
25. Edan G, Kappos L, Montalbán X, et al; BENEFIT Study Group. **Long-term impact of interferon beta-1b in patients with CIS: 8-year follow-up of BENEFIT.** *J Neurol Neurosurg Psychiatry* 2014;85:1183–89 CrossRef Medline
26. Beck RW, Chandler DL, Cole SR, et al. **Interferon beta-1a for early multiple sclerosis: CHAMPS trial subgroup analyses.** *Ann Neurol* 2002;51:481–90 CrossRef Medline
27. The Optic Neuritis Study Group. **Multiple sclerosis risk after optic neuritis: final optic neuritis treatment trial follow-up.** *Arch Neurol* 2008;65:727–32 doi: CrossRef Medline
28. Fisniku LK, Brex PA, Altmann DR, et al. **Disability and T2 MRI lesions: a 20-year follow-up of patients with relapse onset of multiple sclerosis.** *Brain* 2008;131(pt 3):808–17 CrossRef Medline
29. Okuda DT, Mowry EM, Beheshtian A, et al. **Incidental MRI anomalies suggestive of multiple sclerosis: the radiologically isolated syndrome.** *Neurology* 2009;72:800–05 CrossRef Medline
30. Okuda DT, Mowry EM, Cree BA, et al. **Asymptomatic spinal cord lesions predict disease progression in radiologically isolated syndrome.** *Neurology* 2011;76:686–92 CrossRef Medline
31. Okuda DT, Siva A, Kantarci O, et al. **Radiologically isolated syndrome: 5-year risk for an initial clinical event.** *PLoS One* 2014;9:e90509 CrossRef Medline
32. Sombekke MH, Wattjes MP, Balk LJ, et al. **Spinal cord lesions in patients with clinically isolated syndrome: a powerful tool in diagnosis and prognosis.** *Neurology* 2013;80:69–75 CrossRef Medline
33. Bot JC, Barkhof F, Polman CH, et al. **Spinal cord abnormalities in recently diagnosed MS patients: added value of spinal MRI examination.** *Neurology* 2004;62:226–33 CrossRef Medline
34. Miller DH, Weinshenker BG, Filippi M, et al. **Differential diagnosis of suspected multiple sclerosis: a consensus approach.** *Mult Scler* 2008;14:1157–74 CrossRef Medline
35. Simon JH, Bermel RA, Rudick RA. **Simple MRI metrics contribute to optimal care of the patient with multiple sclerosis.** *AJNR Am J Neuroradiol* 2014;35:831–32 CrossRef Medline
36. Rudick RA, Lee JC, Simon J, et al. **Significance of T2 lesions in multiple sclerosis: a 13-year longitudinal study.** *Ann Neurol* 2006;60:236–42 CrossRef Medline
37. Sormani MP, Bonzano L, Roccatagliata L, et al. **Magnetic resonance imaging as a potential surrogate for relapses in multiple sclerosis: a meta-analytic approach.** *Ann Neurol* 2009;65:268–75 CrossRef Medline
38. Prosperini L, Gallo V, Petsas N, et al. **One-year MRI scan predicts clinical response to interferon beta in multiple sclerosis.** *Eur J Neurol* 2009;16:1202–09 CrossRef Medline
39. Bermel RA, You X, Foulds P, et al. **Predictors of long-term outcome in multiple sclerosis patients treated with interferon  $\beta$ .** *Ann Neurol* 2013;73:95–103 CrossRef Medline
40. Sormani MP, Rio J, Tintoré M, et al. **Scoring treatment response in patients with relapsing multiple sclerosis.** *Mult Scler* 2013;19:605–12 CrossRef Medline
41. Rio J, Castelló J, Rovira A, et al. **Measures in the first year of therapy predict the response to interferon beta in MS.** *Mult Scler* 2009;15:848–53 CrossRef Medline
42. Chard DT, Brex PA, Ciccarelli O, et al. **The longitudinal relation between brain lesion load and atrophy in multiple sclerosis: a 14 year follow up study.** *J Neurol Neurosurg Psychiatry* 2003;74:1551–54 CrossRef Medline
43. Multiple Sclerosis Therapy Consensus Group (MSTCG), Wiendl H, Toyka KV, Rieckmann P, et al. **Basic and escalating immunomodulatory treatments in multiple sclerosis: current therapeutic recommendations.** *J Neurol* 2008;255:1449–63 CrossRef Medline
44. Freedman MS, Selchen D, Arnold DL, et al; Canadian Multiple Sclerosis Working Group. **Treatment optimization in MS: Canadian MS Working Group updated recommendations.** *Can J Neurol Sci* 2013;40:307–23 CrossRef Medline
45. Hawker K, O’Connor P, Freedman MS, et al; OLYMPUS trial group. **Rituximab in patients with primary progressive multiple sclerosis: results of a randomized double-blind placebo-controlled multicenter trial.** *Ann Neurol* 2009;66:460–71 CrossRef Medline
46. Bloomgren G, Richman S, Hotermans C, et al. **Risk of natalizumab-associated progressive multifocal leukoencephalopathy.** *N Engl J Med* 2012;366:1870–80 CrossRef Medline



# Radiation Doses in Patient Eye Lenses during Interventional Neuroradiology Procedures

 R.M. Sánchez,  E. Vañó,  J.M. Fernández,  S. Rosati, and  L. López-Ibor

## ABSTRACT

**BACKGROUND AND PURPOSE:** Eye lenses are among the most sensitive organs to x-ray radiation and may be considered at risk during neurointerventional radiology procedures. The threshold dose to produce eye lens opacities has been recently reduced to 500 mGy by the International Commission on Radiologic Protection. In this article, the authors investigated the radiation doses delivered to patients' eyes during interventional neuroradiology procedures at a university hospital.

**MATERIALS AND METHODS:** Small optically stimulated luminescence dosimeters were located over patients' eyes during 5 diagnostic and 31 therapeutic procedures performed in a biplane x-ray system. Phantom measurements were also made to determine the level of radiation to the eye during imaging runs with conebeam CT.

**RESULTS:** The left eye (located toward the lateral C-arm x-ray source) received a 4.5 times greater dose than the right one. The average dose during embolization in the left eye was 300 mGy, with a maximum of 2000 mGy in a single procedure. The patient who received this maximum eye dose needed 6 embolization procedures to treat his high-volume AVM. If one took into account those 6 embolizations, the eye dose could be 2-fold. Sixteen percent of the embolizations resulted in eye doses of >500 mGy.

**CONCLUSIONS:** A relevant fraction of patients received eye doses exceeding the threshold of 500 mGy. A careful optimization of the procedures and follow-up of these patients to evaluate potential lens opacities should be considered.

**ABBREVIATIONS:** CBCT = conebeam CT; DAP = dose-area product; ICRP = International Commission on Radiological Protection; INR = interventional neuro-radiology; OSLD = optically stimulated luminescence dosimeter

Interventional neuroradiology (INR) activity has increased in recent years, providing important benefits to patients, but the use of ionizing radiation adds risks that must be evaluated and minimized. Concerning eye lens irradiation during INR procedures particularly, little research has been conducted, yet it is important for physicians to know the level of risk for this organ in these kinds of procedures. The International Commission on Radiological Protection (ICRP) has recently published a report on the effects of radiation in tissues and organs, in which it recognizes that eye lenses may be more sensitive to ionizing radiation than previously thought.<sup>1</sup> Until recently, the dose threshold suggested for the formation of lens opacities was 5 Gy in case of acute irradiation of the eye lens.<sup>2</sup> However, as a result of new epidemiologic

evidence,<sup>3,4</sup> this threshold value has been reduced to 0.5 Gy,<sup>1</sup> the legislation on radiation protection of workers has been amended, and the dose limits for the lens of the eye reduced in the International Basic Safety Standards<sup>5</sup> and in the new European regulation.<sup>6</sup> In the case of patients, to optimize procedures and reduce radiation doses, the new European legislation<sup>6</sup> requires that the information relative to patient exposure be included in the medical report. In addition, radiation doses averaged from patient samples have to be compared with national diagnostic reference levels, and if relevant deviations are detected, optimization actions should be taken. As in the case of the authors' country, there may be no formal national diagnostic reference levels available. In such a case, other regional or local diagnostic reference levels could be used until the national diagnostic reference levels are established.

There is little information in the literature regarding the eye lens dose received by patients during INR procedures. Moritake et al<sup>7</sup> reported average doses in patients' eyes of 380 mGy, with a maximum of 2079 mGy during cerebral embolizations, 4 times the threshold level of 500 mGy recommended by the ICRP. Sandborg et al<sup>8</sup> reported mean and maximum doses in the eye of 71

Received May 13, 2015; accepted after revision August 6.

From the Departments of Physics (R.M.S., E.V., J.M.F.) and Neuroradiology (S.R., L.L.-I.), Hospital Clínico San Carlos, Madrid, Spain; and Department of Radiology (E.V., J.M.F.), Universidad Complutense de Madrid, Madrid, Spain.

Please address correspondence to Roberto M Sánchez, MD, Medical Physics Department, Hospital Clínico San Carlos, IdISSC. Prof. Martín Lagos sn, 28040 Madrid, Spain; e-mail: robertomariano.sanchez@salud.madrid.org

<http://dx.doi.org/10.3174/ajnr.A4549>

and 515 mSv, respectively, also during cerebral embolizations. The variability of doses found then underlines the need for further investigations into the risks associated with these medical practices. Practitioners also need to know the order of magnitude of the radiation doses delivered to patients' eyes during INR procedures. These data will allow physicians to optimize radiation protection during clinical procedures, to better manage the information about the risks of radiation-induced lens opacities, and to give patients the appropriate counseling on the follow-up.

This article presents the measurement of patient eye lens doses, by using optically stimulated luminescence dosimeters (OSLDs). Eye doses were measured in a sample of diagnostic and therapeutic procedures performed in an interventional neuroradiology laboratory at a university hospital. The contribution of conebeam CT (CBCT) to eye lens doses was also investigated.

## MATERIALS AND METHODS

Cases of cerebral angiography ( $n = 5$ ) and therapeutic ( $n = 31$ ) procedures were randomly selected for this study. The therapeutic procedures consisted of embolizations of AVMs ( $n = 13$ ) mainly with grades IV and V (Spetzler-Martin<sup>9</sup>); fistulas ( $n = 2$ ); and aneurysm coiling ( $n = 16$ ). All procedures were performed in the neuroradiology room equipped with an Allura FD 10/20 (Philips Healthcare, Best, the Netherlands) biplane x-ray unit at the Hospital Clinico San Carlos in Madrid, Spain. The diagonals of the flat detectors were 40 cm for the frontal C-arm and 25 cm for the lateral one. The lateral C-arm has its x-ray focus at the patient's left side (supine). When the patient's head is located at isocenter with the image detectors 10 cm from the patient's head and no collimation, the frontal detector covers the patient's surface area of approximately  $27 \times 27 \text{ cm}^2$ , and the lateral detector,  $14 \times 14 \text{ cm}^2$ . Both C-arms have transmission ionization chambers installed at the x-ray tube exit to monitor the radiation dose delivered to patients; the dose is included in the patient's dose reports. In most procedures, the digital subtraction angiography series was obtained at 2 images per second in the first 10 seconds and at 1 image per second in the remaining time.

The system, by using the conebeam CT technique, has the ability to acquire volumetric images. Depending on the CBCT mode selected, low dose or high resolution, 313 or 622 images can be acquired over a  $240^\circ$  arc rotation for volumetric reconstruction. The CBCT is performed by rotating the arc around the posterior side of the patient (in a supine position), with a rotation angle from  $-120^\circ$  to  $120^\circ$ , minimizing irradiation to the patient's face. During CBCT acquisitions, the generator settings are as follows: 120 kV, 250 mA, 5 ms, 0.4-mm copper (Cu) + 1-mm aluminum (Al) of added filtration. The maximum field size of  $27 \times 27 \text{ cm}^2$  is set at the isocenter. At least 1 CBCT series was acquired during the therapeutic procedures. The x-ray system was submitted to regular quality control and calibration programs by the medical physics service, as recommended by the national guidelines. The neuroradiologists in charge have received training in radiation protection as required by national regulation.

The radiation dose at the eye lens was estimated by measur-



**FIG 1.** Position of the dosimeters on patient eyes.

ing the entrance surface air kerma with small OSLDs. For simplicity, from now on, the word “dose” will refer to the entrance surface air kerma at the eye lens. For each patient, 2 OSLDs were located over the eyelids as shown in Fig 1. The OSLDs used were the nanoDot model (Landauer, Glenwood, Illinois). They are composed of a small disk of 4-mm diameter of optically stimulated luminescent material ( $\text{Al}_2\text{O}_3\text{:C}$ ), which forms the active area, encased in a light-tight plastic protector of  $10 \times 10 \times 2 \text{ mm}^3$ . Their small size makes them suitable for use near patients' eyes. OSLDs have been previously used to measure patient doses in different clinical situations,<sup>10-12</sup> but when used with diagnostic energies, special attention must be paid to limitations such as energy and angular dependence.

In neuroradiology procedures, the x-ray beam quality may change with kilovolt settings and filtration. Kilovolt settings are adjusted by automatic dose control of the flat detector, depending on patient thickness. For the neuroradiology protocols programmed in Allura, the beam kilovolt is nearly constant around 70–80 kV. However, filtration may change depending on the operation mode selected by the user and may range from 0.1 mm of copper plus 1 mm of aluminum with the digital subtraction angiography mode to 0.9 mm of Cu plus 1 mm of Al with the fluoroscopic low-dose mode. The OSLDs have been calibrated “in house” by using typical clinical beam qualities from our interventional x-ray unit and verified by the Centro Nacional de Dosimetría in Valencia, Spain, a standard calibration laboratory. With these user x-ray beams, a difference of 6% in the calibration factor for 70 and 80 kV was observed for the same filtration, while a difference of 16% was measured for different filtrations. The uncertainty resulting from the response of OSLDs to kilovolt variation (6%) was assumed acceptable, but the effect of different filtration in the OSLD response had to be corrected. To reduce the influence of the different added filtration of the x-ray beams in the OSLD response, we used the information included in the patient dose report about the air kerma area product.<sup>13</sup>

The air kerma area product, commonly called dose-area product (DAP), is one of the standard magnitudes used to monitor patient doses in some x-ray modalities. Modern interventional x-ray equipment provides the DAP in both DICOM

headers and patient dose reports and can be used as a patient dose indicator, provided it is duly calibrated. In this case, the DAP meter had a deviation of  $-10\%$ , and all DAP values had been duly corrected. Our x-ray unit produces patient dose reports that provide the fraction of the DAP delivered with fluoroscopy (high added filtration) and with DSA (low added filtration). This information was used to calculate a corrected calibration factor for each procedure, by combining the calibration factors for fluoroscopic and DSA beams proportionally to the fraction of fluoroscopic and DSA DAP included in the dosimetric report. Once the calibration factor had been derived for each procedure, the OSLD reading was then translated into dose. Regarding angular dependence and for the beam qualities used in this study, angular dependence has been measured and resulted in a difference in response of  $-15\%$  in the worst case (beam incidence of  $-90^\circ$  in the lower energetic

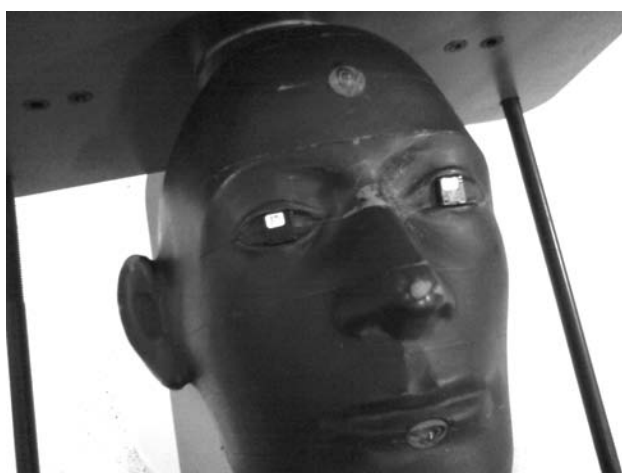


**FIG 2.** Anthropomorphic phantom with OSLDs over the eyes.

beam) and  $-3\%$  for high-filtered beams. Besides the eye dose, other relevant parameters were recorded, such as the dose at the patient entrance reference point,<sup>14</sup> the fluoroscopy time, the number of DSA and CBCT series, and the number of images.

To measure the dose contribution to the eyes during CBCT runs, we performed a phantom simulation. We laid down an anthropomorphic phantom model, Rando (The Phantom Laboratory, Salem, New York), over the examining couch, centering the phantom head at the isocenter. Optically stimulated luminescence dosimeters were attached over the phantom eyes (Fig 2). Doses at the phantom eyes were measured with the 2 modes of operation available in this x-ray system: low dose and high resolution. Both modes of operation have been described previously in this section. The specific calibration factor for the CBCT beam quality was measured for the OSLDs.

Regression analysis between the eye dose and DAP was performed with the statistical package SPSS, Version 12 (IBM, Armonk, New York).

An independent local ethics committee approved this study under the title “Radiologic Risks in Fluoroscopy Guided Procedures” (code B-09/20). Patients agreed to allow anonymous dosimetric information to the investigation.

## RESULTS

Of 36 procedures measured, 5 were diagnostic and 31 were therapeutic. Table 1 summarizes the main results of patient doses. The maximum doses delivered to the left eye, liable to receive direct radiation from the lateral C-arm, resulted in 81 mGy for diagnostic procedures and 2080 mGy for therapeutic ones. Five of the 31 embolizations (16%) resulted in doses in the left eye greater than the threshold of 500 mGy. Table 2 shows the main dosimetric parameters of those procedures. The linear regression between the DAP (in grays  $\times$  square

**Table 1: Main statistics for parameters related to patient dose for diagnostic and therapeutic procedures**

	DAP (Gy $\times$ cm <sup>2</sup> )	Fluoroscopy Time (sec)	No. of DSA Images	Right Eye K (mGy)	Left Eye K (mGy)
Diagnostic (n = 5)					
Min	36	169	87	17	24
Max	86	1581	958	28	81
Mean $\pm$ SD	56 $\pm$ 21	657 $\pm$ 560	484 $\pm$ 421	20 $\pm$ 11	67 $\pm$ 32
Median	44	407	293	23	67
1stQ	44	362	165	21	52
3rdQ	72	768	920	24	77
Therapeutic (n = 31)					
Min	63	680	112	9	32
Max	479	5250	2410	173	2084
Mean $\pm$ SD	203 $\pm$ 120	1680 $\pm$ 900	1030 $\pm$ 460	62 $\pm$ 37	303 $\pm$ 409
Median	164	1400	1000	57	172
1stQ	115	1120	750	42	77
3rdQ	248	2200	1180	76	315

**Note:**—1stQ indicates first quartile; 3rdQ, third quartile; K, air kerma; Min, minimum; Max, maximum.

**Table 2: The dosimetric data for the 5 therapeutic procedures with left eye doses >500 mGy**

Procedure	DAP (Gy $\times$ cm <sup>2</sup> )	Fluoroscopy Time (sec)	No. of Images	AK <sub>R</sub> Frontal (mGy)	AK <sub>R</sub> Lateral (mGy)	Right Eye Dose (mGy)	Left Eye Dose (mGy)
AVM	227	1407	1283	2388	599	—	671
Aneurysm	271	2412	1020	1978	880	58	614
Aneurysm	214	1956	2412	2314	714	118	936
AVM	466	5254	979	3801	1711	129	2080
AVM	423	1801	1801	2220	724	173	911

**Note:**—AK<sub>R</sub> indicates the air kerma in the patient entrance reference point for the frontal and lateral C-arms.

centimeters) and the dose at the left eye (in milligrays) resulted in an expression  $\text{Dose at Eye} = 2.1 \times \text{DAP}$ , with a correlation coefficient of  $r^2 = 0.63$  ( $P < .001$ ). Figure 3 shows the left and right eye dose histogram for cerebral embolizations.

During a CBCT irradiation, the doses at the patient entrance reference point were 32 and 64 mGy for the low dose and high resolution, respectively. On the anthropomorphic

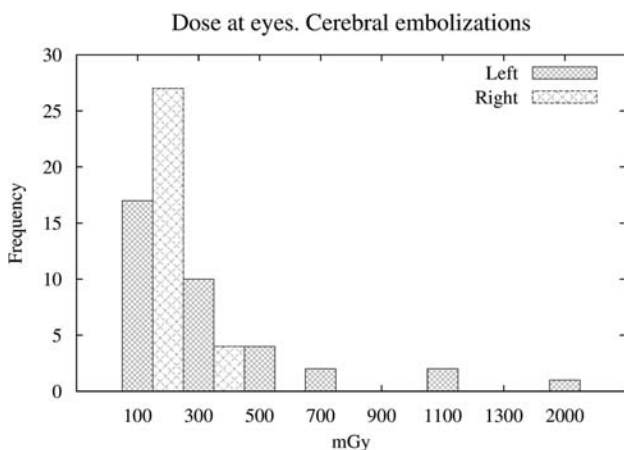


**FIG 3.** Left and right eye doses measured with OSLDs during cerebral embolizations.

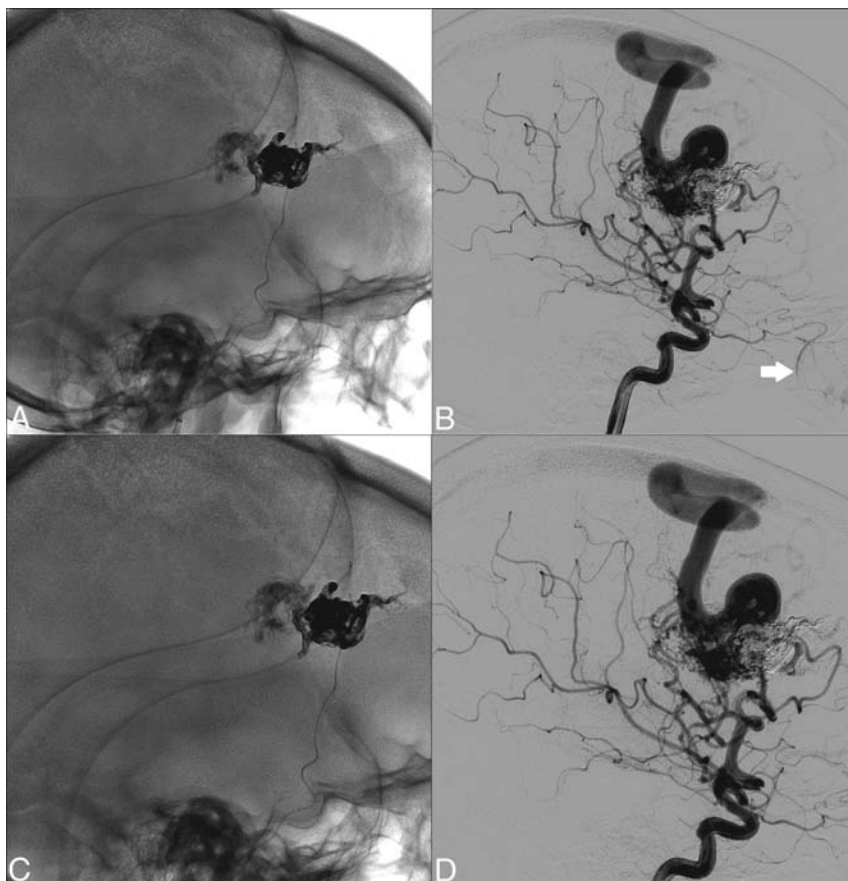


**FIG 4.** A and B, Nonoptimal lateral projection without and with subtraction where the left eye is irradiated. C and D, The proposed collimation to avoid eye irradiation. The arrow in B indicates some contrast in colloids via the ophthalmic artery that may be chosen as the edge to collimate the lateral beam.

phantom's eyes, the doses were 10 mGy in the CBCT low-dose mode and 20 mGy for the high resolution.

## DISCUSSION

The dose values at the phantom's eyes of 10 and 20 mGy measured for this x-ray unit during the CBCT acquisitions correspond to 3%–6% of the average left eye dose for a therapeutic procedure and 15%–30% for a cerebral angiography. Compared with the dose at the patient entrance reference point reported by the x-ray system during a CBCT run, the eye dose resulted in a fraction of 30%. The values in our x-ray system are of the same order of magnitude as the ones reported by Koyama et al,<sup>15</sup> who measured 20 mGy in eye lenses using diodes.

In diagnostic cases, patient DAPs were lower than those in therapeutic cases:  $56 \pm 21 \text{ Gy} \times \text{cm}^2$  versus  $203 \pm 120 \text{ Gy} \times \text{cm}^2$  (mean  $\pm$  SD). These values of DAP are even lower than the ones reported by several authors<sup>16–18</sup> who showed average DAPs from 68 to 158  $\text{Gy} \times \text{cm}^2$  for angiography and from 215 to 382  $\text{Gy} \times \text{cm}^2$  for embolization. Sandborg et al,<sup>8</sup> who also included eye doses, reported 55 and 190  $\text{Gy} \times \text{cm}^2$  for angiographies and embolizations, respectively (ie, doses similar to those found in this investigation). The maximum eye dose recorded during a cerebral angiography was 81 mGy, much lower than the threshold of 500 mGy.

The OSLD located at the left eye (in front of the lateral C-arm x-ray tube) read an average dose 4.8 times greater than the one located at the right eye. The average dose of 300 mGy measured at the left eye can be considered important compared with the threshold recommended by ICRP (500 mGy). This mean value is of the same order of magnitude as the one reported by Moritake et al<sup>7</sup> (380 mGy) but much higher than the one reported by Sandborg et al<sup>8</sup> (71 mGy). The sample of Sandborg et al had a mean DAP similar to ours (190 versus 203  $\text{Gy} \times \text{cm}^2$ ) for embolizations, but in comparison, the eye doses were drastically lower (71 mGy versus our 300 mGy). In our sample, 5 cases (16%) of the 31 therapeutic procedures measured resulted in doses of  $>500$  mGy at the left eye. With such a level of radiation, the possibility of producing opacities or cataracts in patients' eyes should be considered, especially in patients requiring several procedures to be treated properly. At the right eye, the dose measured was below 200 mGy, a value unlikely to produce opacities.

The maximum radiation dose measured at the left eye was 2080 mGy during an AVM located in the anterior fossa, with a DAP of 466  $\text{Gy} \times \text{cm}^2$  (88 fluoroscopy minutes and 979 images).



In such a case, opacities in this eye are likely to occur; 4.4 mGy in the left eye per  $\text{Gy} \times \text{cm}^2$  is an extreme case well above the average tendency of 2.1 mGy/( $\text{Gy} \times \text{cm}^2$ ). This uncommonly high dose may certainly result from the patient's pathology being located in the anterior fossa, close to the eye. This particular patient, with a high-volume AVM, needed 6 INR procedures within 18 months, with a total cumulative DAP of 800  $\text{Gy} \times \text{cm}^2$ . It was not possible to measure the eye dose with OSLDs in the course of the 6 procedures, but if we assume that no additional measures could be taken to protect the eyes, this patient might have received almost 4000 mGy. This patient and his relatives were informed of the risks of developing cataracts and of how to proceed should this happen.

Another case of interest, with a high DAP of 480  $\text{mGy} \times \text{cm}^2$  but with a very low eye dose of 94 mGy, was an embolization located at the posterior side of the head, during which the neuro-radiologist had taken precautions to protect the patient's eye lenses from the lateral beam in most DSA series. This example shows that even during complex procedures with a large DAP, it is still possible to reduce the eye dose when clinically compatible, provided proper collimation in the lateral beam is used to protect the eye. After further analysis of the sample of procedures, we concluded that in some cases, collimation could be optimized. Figure 4A, -B shows a nonoptimal lateral projection from an AVM embolization in which the left eye was irradiated. Figure 4C, -D shows the optimal proposal based on a retrospective analysis during a joint optimization session by neuroradiologists and medical physicists. This collimation provides eye protection while keeping enough FOV to monitor and prevent possible iatrogenic embolizations.

The correlation between DAP, probably the most frequently used dose indicator, and the dose at the left eye was small ( $r^2 = 0.6$ ), certainly limited by the influence of other factors like the collimation of the lateral beam and the lesion location (close or distant from the eyes). The combination of these 3 variables should, therefore, be taken into account to evaluate the risk of producing lens opacities.

So far the radiation dose has been analyzed during 1 single INR procedure, but it is, however, common for a patient to undergo >1 procedure. This hospital is a reference center for the treatment of AVMs of grades IV and V (Spetzler-Martin): 95% of the AVMs performed here are grades 4 and 5 and all of them require several procedures. In fact, only 6 (17%) of the 36 patients in this sample had undergone only 1 INR procedure at the time; 11 patients (30%) had undergone 3 or 4 procedures; 10 patients (28%), 5 or 6 procedures; and 9 patients (25%),  $\geq 6$  procedures. It was not possible to measure the eye doses in all these cases, but all the DAPs were recorded, giving an average of 566  $\text{Gy} \times \text{cm}^2$ , with 17 patients (47%) with  $>300 \text{ Gy} \times \text{cm}^2$ . This value of 300  $\text{Gy} \times \text{cm}^2$  is the DAP obtained from the linear regression equation that may produce eye lens doses over the threshold of 500 mGy. The average age of this patient sample was 59 years, with 9 patients (25%) younger than 50 years of age, therefore with a long life expectancy.

Finally, the difference of 10% in calibration factors used for the various procedures indicates that uncertainties due to the response of OSLDs to beam quality have been reduced. Never-

theless and despite the corrections made, other factors arose from the calibration process and the angular dependence of the dosimeters, which could increase the uncertainty to 20%.

## CONCLUSIONS

During INR therapeutic procedures in a biplane x-ray system, it is possible to deliver relevant doses to the eye lens. For the sample presented in this article, 16% of the therapeutic procedures measured resulted in eye doses higher than the threshold of 500 mGy for lens opacities. The factors that could modify the eye doses are the DAP delivered, the lesion localization, and the possibility of collimating the lateral x-ray beam to protect the eye. Given that most patients in this sample had undergone several INR procedures, the fraction of patients with a DAP that potentially may result in lens doses over the recommended threshold ( $>300 \text{ Gy} \times \text{cm}^2$ ) was 47%. When optimizing the collimation in the lateral beam to prevent direct eye irradiation, the risk of eye lens opacities is reduced to negligible levels. A follow-up of patients receiving high doses in the eyes should be considered to evaluate potential lens opacities and to decide whether the possibility of producing induced opacities should be included in the informed consent. The most effective actions to minimize eye doses are to collimate to the necessary surgical field, especially in the lateral beam; to avoid unnecessary acquisition series; and to use, when possible, fluoroscopy runs instead of acquisitions.

Disclosures: Roberto M. Sánchez—UNRELATED: Grants/Grants Pending: Consejo de Seguridad Nuclear,\* Comments: research project about eye lens doses for medical professionals; Payment for Lectures (including service on Speakers Bureaus): International Atomic Energy Agency, Comments: participant as lecturer during a workshop on radiation protection in interventional practices. \*Money paid to the institution.

## REFERENCES

1. Stewart FA, Akleyev AV, Hauer-Jensen M, et al; ICRP. ICRP Publication 118: ICRP statement on tissue reactions/early and late effects of radiation in normal tissues and organs: threshold doses for tissue reactions in a radiation protection context. *Ann ICRP* 2012;41:1–322 CrossRef Medline
2. The 2007 recommendations of the International Commission on Radiological Protection: ICRP Publication 103. *Ann ICRP* 2007;37:1–332 CrossRef Medline
3. Nakashima E, Neriishi K, Minamoto, A. A reanalysis of atomic-bomb cataract data, 2000–2002: a threshold analysis. *Health Phys* 2006;90:154–60 CrossRef Medline
4. Neriishi K, Nakashima E, Minamoto A, et al. Postoperative cataract cases among atomic bomb survivors: radiation dose response and threshold. *Radiat Res* 2007;168:404–08 CrossRef Medline
5. International Atomic Energy Agency. Radiation protection and safety of radiation sources. International basic safety standards: IAEA Safety Standards Series. GSR part 3. Vienna IAEA, July 21, 2014. [http://www-pub.iaea.org/MTCD/publications/PDF/Pub1578\\_web-57265295.pdf](http://www-pub.iaea.org/MTCD/publications/PDF/Pub1578_web-57265295.pdf). Accessed October 2, 2015
6. Council Directive 2013/59/EURATOM of 5 December 2013 laying down basic safety standards for protection against the dangers arising from exposure to ionising radiation. Official journal of the European Union 17.1.2014, L13, chapter VII pp. 25–28. <http://eur-lex.europa.eu/legal-content/EN/TXT/HTML/?uri=CELEX:32013L0059&from=EN>. Accessed October 2, 2015
7. Moritake T, Matsumaru Y, Takigawa T, et al. Dose measurement on both patients and operators during neurointerventional proce-

- dures using photoluminescence glass dosimeters. *AJNR Am J Neuroradiol* 2008;29:1910–17 CrossRef Medline
8. Sandborg M, Rossitti S, Pettersson H. **Local skin and eye lens equivalent doses in interventional neuroradiology.** *Eur Radiol* 2010;20:725–33 CrossRef Medline
  9. Spetzler R, Martin N. **A proposed grading system for arteriovenous malformations: 1986.** *J Neurosurg* 2008;108:186–93 CrossRef Medline
  10. Al-Senan RM, Hatab MR. **Characteristics of an OSLD in the diagnostic energy range.** *Med Phys* 2011;38:4396 CrossRef Medline
  11. Jursinic PA. **Characterization of optically stimulated luminescents, OSLDs, for clinical dosimetric measurements.** *Med Phys* 2007;34:4594–604 CrossRef Medline
  12. Yukihiro EG, McKeever SW. **Optically stimulated luminescence (OSL) dosimetry in medicine.** *Phys Med Biol* 2008;53:R351–79 CrossRef Medline
  13. International Commission on Radiation Units and Measurements. **ICRU report 74: patient dosimetry for x rays used in medical imaging.** *J ICRU* 2005;5(2, theme issue):29
  14. International Electrotechnical Commission. **Medical electrical equipment. Part 2–43: particular requirements for the safety of x-ray equipment for interventional procedures. Report IEC 60601-2-43.** Geneva, Switzerland: International Electrotechnical Commission; 2010:25–26
  15. Koyama S, Aoyama T, Oda N, et al. **Radiation dose evaluation in tomography and C-arm cone-beam CT examinations with an anthropomorphic phantom.** *Med Phys* 2010;37:4298–306 CrossRef Medline
  16. D'Ercole LI, Thyron FZ, Bocchiola M, et al. **Proposed local diagnostic reference levels in angiography and interventional neuroradiology and a preliminary analysis according to the complexity of the procedures.** *Phys Med* 2012;28:61–70 CrossRef Medline
  17. Miller DL, Kwon D, Bonavia GH. **Reference levels for patient radiation doses in interventional radiology: proposed initial values for U.S. practice.** *Radiology* 2009;253:753–64 CrossRef Medline
  18. Verdun FR, Aroua A, Trueb R, et al. **Diagnostic and interventional radiology: a strategy to introduce reference dose level taking into account the national practice.** *Radiat Prot Dosimetry* 2005;114:188–91 CrossRef Medline

# Diagnostic Accuracy of Transcranial Doppler for Brain Death Confirmation: Systematic Review and Meta-Analysis

JJ. Chang, G. Tsivgoulis, A.H. Katsanos, M.D. Malkoff, and A.V. Alexandrov



## ABSTRACT

**BACKGROUND AND PURPOSE:** Transcranial Doppler is a useful ancillary test for brain death confirmation because it is safe, noninvasive, and done at the bedside. Transcranial Doppler confirms brain death by evaluating cerebral circulatory arrest. Case series studies have generally reported good correlations between transcranial Doppler confirmation of cerebral circulatory arrest and clinical confirmation of brain death. The purpose of this study is to evaluate the utility of transcranial Doppler as an ancillary test in brain death confirmation.

**MATERIALS AND METHODS:** We conducted a systematic review of the literature and a diagnostic test accuracy meta-analysis to compare the sensitivity and specificity of transcranial Doppler confirmation of cerebral circulatory arrest, by using clinical confirmation of brain death as the criterion standard.

**RESULTS:** We identified 22 eligible studies (1671 patients total), dating from 1987 to 2014. Pooled sensitivity and specificity estimates from 12 study protocols that reported data for the calculation of both values were 0.90 (95% CI, 0.87–0.92) and 0.98 (95% CI, 0.96–0.99), respectively. Between-study differences in the diagnostic performance of transcranial Doppler were found for both sensitivity ( $I^2 = 76\%$ ;  $P < .001$ ) and specificity ( $I^2 = 74.3\%$ ;  $P < .001$ ). The threshold effect was not significant (Spearman  $r = -0.173$ ;  $P = .612$ ). The area under the curve with the corresponding standard error (SE) was  $0.964 \pm 0.018$ , while index Q test  $\pm$  SE was estimated at  $0.910 \pm 0.028$ .

**CONCLUSIONS:** The results of this meta-analysis suggest that transcranial Doppler is a highly accurate ancillary test for brain death confirmation. However, transcranial Doppler evaluates cerebral circulatory arrest rather than brain stem function, and this limitation needs to be taken into account when interpreting the results of this meta-analysis.

**ABBREVIATIONS:** CCA = cerebral circulatory arrest; Q\* = index Q test; QUADAS = Quality Assessment of Diagnostic Accuracy Studies; sROC = summary receiver operating curve; TCD = transcranial Doppler; SE = standard error

The concept and irreversibility of brain death have evolved in the past 50 years, further differentiating it from “irreversible coma” as initially described in 1968.<sup>1</sup> Today, the clinical examination, apnea test, etiology, and ascertainment of irreversibility; radiologic confirmation of a structural lesion; and elimination of

confounding laboratory tests remain the criterion standard for brain death diagnosis.<sup>2</sup>

Ancillary testing for brain death confirmation remains controversial. The latest guidelines from the American Academy of Neurology and American Academy of Pediatrics report insufficient evidence for determining brain death with ancillary tests.<sup>3,4</sup> However, ancillary tests remain essential in brain death confirmation when clinical instability prevents safe use of an apnea test<sup>5,6</sup> or barbiturate therapy or hypothermia precludes proper brain death confirmation.<sup>7</sup> In such circumstances, ancillary testing may complement criterion standard testing and confirm brain death. Transcranial Doppler (TCD) is useful for ancillary brain death confirmation because it is safe and noninvasive. TCD confirms brain death by evaluating cerebral circulatory arrest (CCA), which has distinctive flow patterns: oscillatory flow representing reversal of diastolic flow and systolic spikes representing lack of net forward flow.

Case reports and case series have generally reported good correlations between TCD confirmation of CCA and clinical confir-

Received May 4, 2015; accepted after revision July 11.

From the Department of Neurology (J.J.C., G.T., M.D.M., A.V.A.), University of Tennessee Health Science Center, Memphis, Tennessee; Second Department of Neurology (G.T., A.H.K.), Attikon University Hospital, School of Medicine, University of Athens, Athens, Greece; International Clinical Research Center (G.T.), St. Anne's University Hospital in Brno, Czech Republic; and Department of Neurology (A.H.K.), University of Ioannina, School of Medicine, Ioannina, Epirus, Greece.

Please address correspondence to Jason Chang, MD, Department of Neurology, University of Tennessee Health Science Center, 1325 Eastmoreland, Suite 460, Memphis, TN 38104; e-mail: jjwchang@hotmail.com

Indicates open access to non-subscribers at www.ajnr.org

Indicates article with supplemental on-line appendix and table.

Evidence-Based Medicine Level 2.

<http://dx.doi.org/10.3174/ajnr.A4548>

mation of brain death, with sensitivities ranging from 70.5% to 100%. Most recently, a meta-analysis of 10 studies demonstrated TCD having a sensitivity of 89% and specificity of 99% compared with the criterion standard clinical confirmation of brain death.<sup>8</sup> However, this review omitted key methodologies, including estimation of publication bias and the relative strength of each study, and did not adopt Quality Assessment of Diagnostic Accuracy Studies (QUADAS) methodology that standardizes quality assessment and diagnostic accuracy of individual studies in systematic reviews.<sup>9</sup>

In view of these former considerations, we conducted a systematic review of the literature and a meta-analysis adopting the Preferred Reporting Items for Systematic Reviews and Meta-Analyses guidelines<sup>10</sup> and by using QUADAS methodology<sup>9</sup> for quality assessment of included studies. The aim of this meta-analysis was to compare the sensitivity and specificity of TCD confirmation of CCA with clinical confirmation of brain death.

## MATERIALS AND METHODS

### Data Sources and Study Selection

We searched PubMed, Scopus, and the Cochrane Central data bases for all published studies by using the terms “transcranial Doppler,” “cerebral circulatory arrest,” and “brain death.” Three reviewers (J.J.C., G.T., and A.H.K.) examined the references independently to exclude duplicates. The last literature search was conducted on October 16, 2014. Relevant review articles were examined to identify those that might have been missed in the data base search. We imposed no language limitations on the literature search. Case reports, studies not offering a comparison criterion standard clinical examination, and studies consisting of an exclusively pediatric population or primarily focusing on TCD analysis in populations with structural defects of the cranium were excluded.

### Study Eligibility

All retrieved studies were independently examined by 3 reviewers (J.J.C., G.T., and A.H.K.) to determine overall eligibility. Prospectively collected, retrospective, and case series were included. Inclusion criteria for studies were as follows: 1) clinical confirmation of brain death serving as a criterion standard; 2) insonation window that included a transtemporal, suboccipital, or transorbital approach; 3) studies in which quantitative numbers could be extrapolated to calculate sensitivities and specificities; and 4) ages ranging from neonate to 100 years of age while excluding studies focused solely on pediatric populations.

### Data Extraction

The following information from each study was extracted by the 3 investigators independently: true-positives, false-negatives, true-negatives, false-positives, etiology of neurologic injury, and window used for insonation. When identifying the accuracy of TCD waveforms for sensitivity and specificity analysis, we used the following rules: First, waveforms that could not be obtained through the necessary bone windows on TCD were marked as a false-negative result, ultimately lowering the sensitivity for the study and, in some cases, resulting in a lower sensitivity than that reported by the article. Second, for serial TCD examinations, sensi-

tivity was calculated by using the last TCD examination completed because this would have been closest to CCA and would yield the highest sensitivity.

As recommended by the Cochrane Collaboration (<http://www.cochrane.org/>), the QUADAS-2 tool (<http://www.bris.ac.uk/quadas/quadas-2/>) was used to assess the risk of bias of each primary study that reported both sensitivity and specificity measures.<sup>9,11</sup> The 3 reviewers independently evaluated QUADAS-2 items, and conflicts were resolved by consensus.

### Data Synthesis and Statistical Analysis

Details regarding data synthesis and statistical analyses are provided in the On-line Appendix. In brief, sensitivity and specificity were calculated for individual studies, and a random-effects analysis model (DerSimonian and Laird) was used for the estimation of both pooled sensitivity and specificity.

Heterogeneity between studies was assessed by the Cochran Q test and  $I^2$  statistic. Summary receiver operating curves were also constructed by using the random-effects model. The area under the curve and point of the curve where sensitivity equals specificity index Q test were used to assess and summarize the discriminating ability of the summary receiver operating curve (sROC).

## RESULTS

### Study Selection and Study Characteristics

We searched PubMed and Scopus data bases, initially identifying 310 and 376 studies, respectively, that dated from 1987 to 2014. After removing duplicates, we screened the titles and abstracts from the remaining 455 studies, yielding 36 potentially eligible studies for the meta-analysis. The Cochrane Central data base search retrieved no additional studies. Full-text versions of these 36 studies were obtained, and 14 studies were excluded for the following reasons: 1) They did not offer a comparison criterion standard clinical examination,<sup>12-14</sup> 2) the exact number of patients could not be extrapolated from the methodology or results for analysis,<sup>15,16</sup> 3) the study consisted of an exclusively pediatric population,<sup>17-20</sup> 4) the article was a single-patient case report,<sup>21-23</sup> or 5) the study primarily focused on TCD analysis in populations with structural defects of the cranium (ie, patients with external ventricular devices or postdecompressive hemicraniectomy).<sup>24,25</sup>

In the final presentation of the literature search results, there was no conflict or disagreement between 2 reviewers (J.J.C. and G.T.), and the 22 studies that met the protocol inclusion criteria of the study were included in the present systematic review (Fig 1). The characteristics of the included studies,<sup>26-47</sup> comprising 1596 total patients, are shown in the On-line Table.

### Quality Assessment

The quality assessment of included studies by using QUADAS-2 is presented in the Table. High bias was introduced in all 22 studies when using the risk of bias/index test asking the question “could the conduct or interpretation of the index test have introduced bias?” because TCDs were always performed after confirmation of clinical brain death. Risk of bias/patient selection was introduced in 4 studies because patients were excluded due to either TCD windows being unobtainable<sup>27</sup> or, by study design only, a portion of the patients who were clinically brain dead underwent



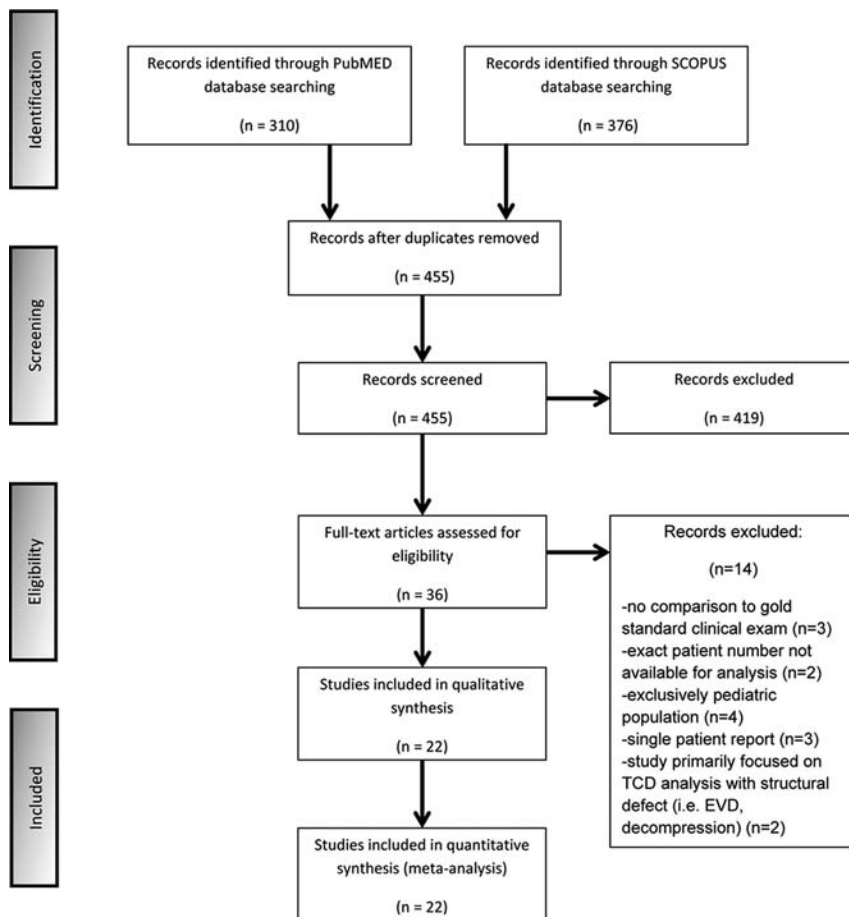


**FIG 1.** Flow chart diagram presenting the selection of eligible studies. EVD indicates external ventricular drain.

TCDs.<sup>34,38,43</sup> High bias was introduced in risk of bias/flow and timing in 3 studies because patients were excluded from analysis due to TCD waveforms being unobtainable despite vasopressor use,<sup>28</sup> bone windows or clinical brain death not being determined,<sup>30</sup> and clinical brain death and even ancillary tests not being performed because of severe clinical instability.<sup>41</sup> Unclear bias was introduced in applicability concerns/patient selection in 6 studies because pediatric patients were included in the analysis.<sup>33,34,37,42,45,47</sup> Finally, high bias was introduced in 1 study in applicability concerns/index test because in addition to the standard TCD transtemporal window, contrast-induced TCD was used.<sup>26</sup> No study had >2 high risks of bias noted.

### Data Synthesis and Statistical Analysis

The sensitivity and specificity values, with the corresponding 95% CIs, were calculated for all included studies. However, overall sensitivity and specificity estimates were pooled from 12 of the 22 study protocols because only these studies reported data for the calculation of both sensitivity and specificity values (Fig 2).

In the pooled analysis of 859 patients (56.1% with clinically confirmed brain death), overall sensitivity was 0.90 (95% CI, 0.87–0.92; Fig 3A) and overall specificity was 0.98 (95% CI, 0.96–0.99; Fig 3B). Between-study differences in the diagnostic performance of TCDs were found for both sensitivity ( $I^2 =$

76%,  $P < .001$ , Fig 3A) and specificity ( $I^2 = 74.3\%$ ,  $P < .001$ , Fig 3B). The threshold effect was not significant (Spearman  $r = -0.173$ ,  $P = .612$ ). The sROC analysis, displaying the individual studies that reported data for the calculation of both sensitivity and specificity and the sROC curve (with its corresponding 95% CI), is presented in Fig 4. The area under the curve of sROC with the corresponding standard error (SE) was  $0.964 \pm 0.018$ , while the  $Q^* \pm SE$  was estimated at  $0.910 \pm 0.028$ .

### DISCUSSION

This study provides the most comprehensive review evaluating the sensitivity and specificity of TCD in confirming brain death. The results of this meta-analysis suggest that TCD is a highly accurate ancillary test for brain death confirmation with a sensitivity and specificity of 90% and 98%, respectively. Moreover, the area under the curve of sROC was estimated at 0.964, underscoring the very satisfactory diagnostic yield of TCD for diagnosing CCA.

The findings of this meta-analysis are roughly in line with the prior meta-analysis of Monteiro et al,<sup>8</sup> with a sensitivity of 89% and specificity of 99% when using TCD for brain death confirmation.

In our meta-analysis, we included all 12 studies used in that article and 10 additional studies. We also improved on the study design by systematically evaluating potential sources of bias and the relative strengths of each study. Moreover, sROC analyses were not performed in the study of Monteiro et al, while  $Q^*$  was also not estimated. Finally, the risk of bias was not systematically addressed by QUADAS methodology. The findings of the present meta-analysis when combined with the study of Monteiro et al argue in favor of using TCD as a standard ancillary test for brain death diagnosis, because TCD remains an inexpensive, easily repeatable, and noninvasive examination.

### Quality of Study

Evaluation of QUADAS elicited several concerns about the quality of the studies that are largely unavoidable given the nonrandomized, observational nature of these individual studies. First, high bias was introduced in all studies regarding the risk of bias/index test. This was inevitable because TCD and any ancillary test will always be measured against and completed after clinical brain death confirmation. Regarding the risk of bias/patient selection, high bias was introduced in 4 studies and unclear bias was introduced in 4 studies. Azevedo et al<sup>27</sup> introduced bias because they did not enroll patients in whom TCDs could not be obtained, while they failed to de-

## Quality assessment of eligible studies

	Risk of Bias				Applicability Concerns		
	Patient Selection	Index Test	Reference Standard	Flow and Timing	Patient Selection	Index Test	Reference Standard
Abadal et al <sup>26</sup>	L	H	L	L	L	H <sup>a</sup>	L
Azevedo et al <sup>27</sup>	H <sup>b</sup>	H	L	L	L	L	L
de Freitas and André <sup>28</sup>	L	H	L	H <sup>c</sup>	L	L	L
Dominguez-Roldan et al <sup>29</sup>	L	H	L	L	L	L	L
Dosemeci et al <sup>30</sup>	L	H	L	H <sup>c</sup>	L	L	L
Ducrocq et al <sup>31</sup>	L	H	L	L	L	L	L
Feri et al <sup>32</sup>	L	H	L	L	L	L	L
Hadani et al <sup>33</sup>	L	H	L	L	U <sup>d</sup>	L	L
Hassler et al <sup>34</sup>	H <sup>e</sup>	H	L	L	U <sup>d</sup>	L	L
Kuo et al <sup>35</sup>	L	H	L	L	L	L	L
Lampl et al <sup>36</sup>	L	H	L	L	L	L	L
Newell et al <sup>37</sup>	L	H	L	L	U <sup>d</sup>	L	L
Orban et al <sup>38</sup>	H <sup>e</sup>	H	L	L	L	L	L
Paolin et al <sup>39</sup>	L	H	L	L	L	L	L
Petty et al <sup>40</sup>	L	H	L	L	L	L	L
Poularas et al <sup>41</sup>	L	H	L	H <sup>c</sup>	L	L	L
Powers et al <sup>42</sup>	L	H	L	L	U <sup>d</sup>	L	L
Su et al <sup>43</sup>	H <sup>e</sup>	H	L	L	L	L	L
Van Velthoven and Calliauw <sup>44</sup>	L	H	L	L	L	L	L
Wang et al <sup>45</sup>	L	H	L	L	U <sup>d</sup>	L	L
Welschehold et al <sup>46</sup>	L	H	L	L	L	L	L
Zuryski et al <sup>47</sup>	L	H	L	L	U <sup>d</sup>	L	L

**Note:**—L indicates low-risk; H, high-risk; U, unclear.

<sup>a</sup> Used alternative TCD index tests: contrast-induced TCD.

<sup>b</sup> Did not enroll patients when TCD windows could not be obtained.

<sup>c</sup> Patients were excluded from analysis.

<sup>d</sup> Subset of the population explored included children (younger than 18 years); not enough information provided to differentiate how many children were included in the study.

<sup>e</sup> Of the total number of patients clinically diagnosed with brain death, only a portion of these patients underwent TCD.

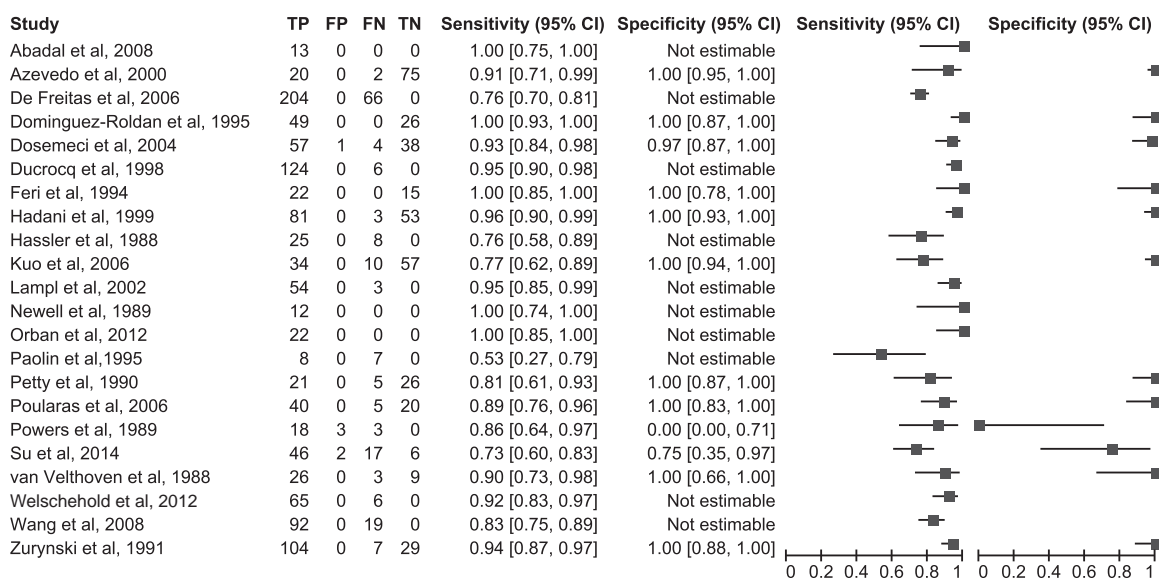


**FIG 2.** Sensitivity and specificity ratios of individual studies, with their corresponding 95% confidence intervals. TP indicates true-positive; FP, positive; FN, false-negative; TN, true-negative.

scribe the number of excluded patients. The other 3 articles introduced high bias in this category because they were primarily designed to use and compare various ancillary tests in brain death confirmation (TCD being used in addition to angiography, electroencephalography, intracranial pressure monitoring, and somatosensory-evoked potentials).<sup>34,38,43</sup> Although high bias was introduced in 3 studies regarding risk of bias/flow and timing, the exclusion of these patients was un-

avoidable due to clinical instability. In all 3 studies, these patients were likely excluded because they had reached an advanced state of brain herniation that left them in multiorgan dysfunction with extreme hemodynamic instability.<sup>28,30,41</sup> Unclear bias was introduced in 5 studies regarding applicability concerns/patient selection because pediatric populations were incorporated and analyzed. Enough details were not provided to individually remove the pediatric patients. Although

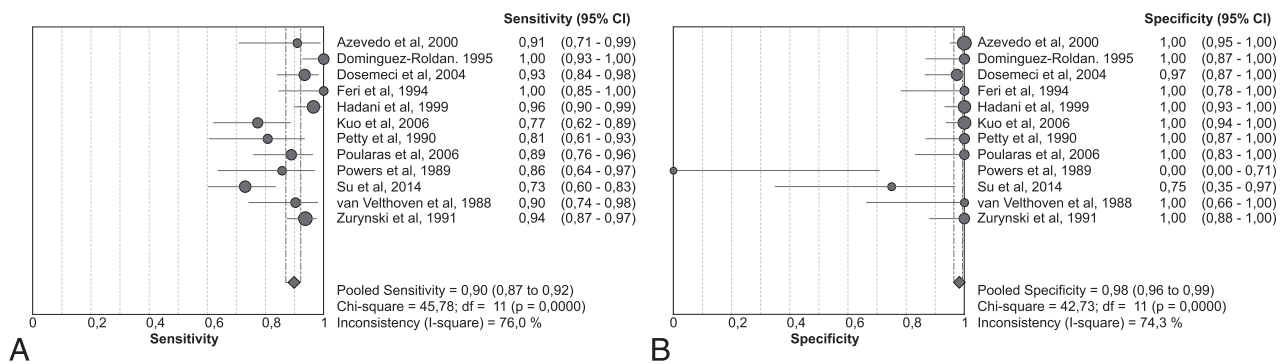


**FIG 3.** Pooled sensitivity (A) and specificity (B) of eligible studies reporting both diagnostic accuracy testing parameters.

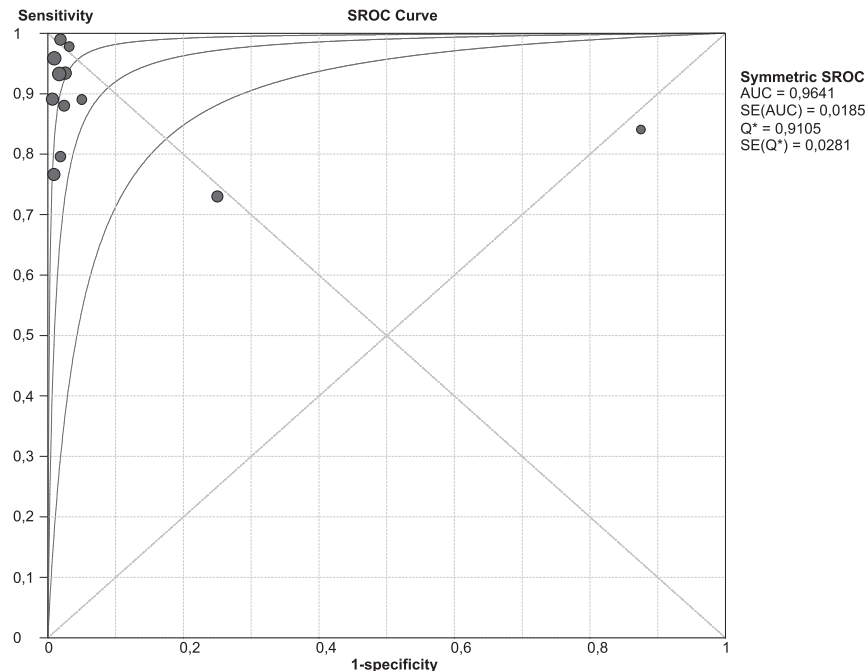


**FIG 4.** The summary receiver operating characteristic curve with its corresponding 95% confidence interval of the diagnostic threshold of transcranial Doppler in the diagnosis of brain death.

unfortunate, as evidenced by mean ages, these populations were primarily adult.<sup>33,34,37,42,45,47</sup> Finally, 1 study introduced high bias in applicability concerns/index test because while using tests that incorporated a standard TCD window (trans-temporal), this study also introduced contrast-induced TCD to increase sensitivity.<sup>26</sup>

### Limitations

Several limitations must be addressed when using TCDs for confirmation of brain death: 1) worse sensitivity of TCD compared with the clinical examination, 2) association between the mechanism of neurologic injury and the sensitivity of TCD, 3) the impossibility of having perfect sensitivity with TCDs, and 4) the impossibility of preventing false-positive results. First, TCD will ultimately have lower sensitivity than clinical confirmation of brain death at earlier time points because blood vessel velocities and patterns demonstrated on TCDs for brain death confirmation depend on CCA. Although isolated case reports exist demonstrating clinical confirmation of brain

death, followed by CCA, and then a rebound improvement in the clinical examination (usually via resumption of respiratory drive),<sup>21</sup> CCA represents a more severe pathologic state than brain death because it is characterized by refractory high intracranial pressures preventing cerebral perfusion. Therefore, CCA should usually temporally occur after brain stem dysfunction. This was shown because serial TCDs conducted on patients who were clinically brain dead always resulted in the best sensitivities occurring at later time points.<sup>30,33,38,41</sup> In addition, the accuracy of TCD evaluation for brain death may also be subject to brain death criteria used in different countries, the largest difference being inclusion of apnea testing which was present in 59% of countries surveyed<sup>48</sup> and would likely result in lower TCD sensitivities.

Second, confirmation of brain death via TCD is influenced by the mechanism of neurologic injury. The classic neurologic injury leading to brain death is a supratentorial mass lesion with downward herniation into the brain stem.<sup>49</sup> Because herniation continues due to increased intracranial pressure, cerebral perfusion will wane and finally be absent, resulting in CCA and corresponding TCD waveforms. Other etiologies that result in global cerebral edema (diffuse anoxic brain injury, leukoencephalopathy from toxin ingestion, poor-grade subarachnoid hemorrhage, and diffuse traumatic brain injury) will also lead to refractory intracranial pressures and CCA whose waveform patterns can be detected by TCD.

Third, TCDs will never offer perfect sensitivities because structural abnormalities will inevitably arise, primarily with obtaining adequate bone windows. Sixty-four patients were reported to have unobtainable bone windows during TCD examination in 8 studies of this meta-analysis (On-line Table), giving a corresponding insufficient insonation rate of 8.4% (range, 2.8%–16%). These patients were evaluated as false-negatives, and this decreased the sensitivity measure. In addition, due to unilateral supratentorial lesions, cases will occur in which 1 large vessel will

demonstrate a CCA pattern on TCD without this occurring in the contralateral vessel.<sup>39</sup> In addition, abnormalities of the cranium, primarily manifested by postsurgical procedures such as decompressive hemicraniectomy<sup>24,25</sup> or external ventricular device placement,<sup>24</sup> or the more malleable cranium of infants and young children,<sup>23</sup> will lead to decreased sensitivities. The most likely mechanism for this was increased pulsatile arterial blood flow introduced by relief of intracranial pressure.

Fourth, although having an extremely high specificity, false-positive results with TCDs are still possible and occurred in 3 studies. In Powers et al,<sup>42</sup> 2 of these false-positive cases occurred because though TCD confirmation did precede clinical brain death, unanticipated cardiopulmonary arrest prevented the inevitable confirmation of clinical brain death. The last false-positive result occurred in a 31-year-old woman with a gunshot wound to the head who had retrograde diastolic flow velocities noted on TCD but who also had extremely high net flow velocities. Her neurologic function improved, and she was ultimately discharged from the hospital.<sup>42</sup> In Su et al,<sup>43</sup> 2 false-positives occurred; however, details behind these results were not evaluated in the article. Finally, Dosemeci et al<sup>30</sup> had 1 false-positive brain death result with TCD, which was associated with a patient with TCD waveforms suggestive of CCA but who still had weak respiratory movements elicited by an apnea test.

Finally, no adjustment was reported in the individual study protocols, thus providing only the unadjusted sensitivity/specificity measures in the published reports of the included studies. Therefore pooling of unadjusted sensitivity/specificity measures can neither eliminate the risk of potential confounder existence in the included study protocols nor exclude their accession to the pooled estimates.

### Topics of Future Study

Several topics may help clinicians better understand the limitations associated with TCD use in brain death confirmation. One such topic may be trying to better understand the mechanism and pathophysiology associated with CCA. This would include gaining a better understanding of the time lag that occurs from brain death to CCA. Such knowledge may assist in determining the earliest time to use TCD as ancillary confirmation of brain death. Other future studies would evaluate how TCD velocity changes relative to skull defects or abnormalities. Future studies would likely need to segregate infants and young children from adults because of their malleable skulls.

### CONCLUSIONS

In our meta-analysis, TCD as ancillary testing for brain death was found to be highly sensitive and specific with rates of 89% and 98%, respectively. However, the main limitation of TCD is that it detects CCA rather than brain stem dysfunction, which will inevitably result in less sensitivity than the clinical examination. As a result, TCD is still best suited for an ancillary test to be performed when clinical conditions or medications make the clinical examination unsuitable.

Disclosures: Georgios Tsivgoulis—UNRELATED: Grants/Grants Pending: I was supported by the European Regional Development Fund—Project St. Anne's University

Hospital, Brno International Clinical Research Center (FNUSA-ICRC) (No. CZ.1.05/1.1.00/02.0123).

### REFERENCES

1. A definition of irreversible coma: Report of the Ad Hoc Committee of the Harvard Medical School to Examine the Definition of Brain Death. *JAMA* 1968;205:337–40 CrossRef Medline
2. Wijdicks EF. The diagnosis of brain death. *N Engl J Med* 2001;344:1215–21 CrossRef Medline
3. Wijdicks EF, Varelas PN, Gronseth GS, et al; American Academy of Neurology. Evidence-based guideline update: determining brain death in adults: report of the Quality Standards Subcommittee of the American Academy of Neurology. *Neurology* 2010;74:1911–18 CrossRef Medline
4. Nakagawa TA, Ashwal S, Mathur M, et al; Society of Critical Care Medicine, Section on Critical Care and Section on Neurology of the American Academy of Pediatrics, Child Neurology Society. Guidelines for the determination of brain death in infants and children: an update of the 1987 Task Force recommendations. *Crit Care Med* 2011;39:2139–55 CrossRef Medline
5. Datar S, Fugate J, Rabinstein A, et al. Completing the apnea test: decline in complications. *Neurocrit Care* 2014;21:392–96 CrossRef Medline
6. Goudreau JL, Wijdicks EF, Emery SF. Complications during apnea testing in the determination of brain death: predisposing factors. *Neurology* 2000;55:1045–48 Medline
7. Bayliff CD, Schwartz ML, Hardy BG. Pharmacokinetics of high-dose pentobarbital in severe head trauma. *Clin Pharmacol Ther* 1985;38:457–61 CrossRef Medline
8. Monteiro LM, Bollen CW, van Huffelen AC, et al. Transcranial Doppler ultrasonography to confirm brain death: a meta-analysis. *Intensive Care Med* 2006;32:1937–44 CrossRef Medline
9. Whiting PF, Rutjes AW, Westwood ME, et al; QUADAS-2 Group. QUADAS-2: a revised tool for the quality assessment of diagnostic accuracy studies. *Ann Intern Med* 2011;155:529–36 CrossRef Medline
10. Liberati A, Altman DG, Tetzlaff J, et al. The PRISMA statement for reporting systematic reviews and meta-analyses of studies that evaluate health care interventions: explanation and elaboration. *J Clin Epidemiol* 2009;62:e1–34 CrossRef Medline
11. Reitsma JB, Rutjes AW, Whiting P, et al. Chapter 9: assessing methodological quality. In: Deeks JJ, Bossuyt PM, Gatsonis C, eds. *Cochrane Handbook for Systematic Reviews of Diagnostic Test Accuracy*. The Cochrane Collaboration, 2009. <http://srdta.cochrane.org/>. Accessed September 30, 2014
12. Dominguez-Roldan JM, Garcia-Alfaro C, Jimenez-Gonzalez PI, et al. Brain death due to supratentorial masses: diagnosis using transcranial Doppler sonography. *Transplant Proc* 2004;36:2898–900 CrossRef Medline
13. Sharma D, Souter MJ, Moore AE, et al. Clinical experience with transcranial Doppler ultrasonography as a confirmatory test for brain death: a retrospective analysis. *Neurocrit Care* 2011;14:370–76 CrossRef Medline
14. Shiogai T, Sato E, Tokitsu M, et al. Transcranial Doppler monitoring in severe brain damage: relationships between intracranial haemodynamics, brain dysfunction and outcome. *Neurol Res* 1990;12:205–13
15. Vakilian A, Iranmanesh F. Comparison of cerebral blood flow pattern by transcranial Doppler in patients with diffuse and focal causes of brain death. *J Res Med Sci* 2012;17:1156–60
16. Llompert-Pou JA, Abadal JM, Velasco J, et al. Contrast-enhanced transcranial color sonography in the diagnosis of cerebral circulatory arrest. *Transplant Proc* 2009;41:1466–68 CrossRef Medline
17. Kirkham FJ, Levin SD, Padayachee TS, et al. Transcranial pulsed Doppler ultrasound findings in brain stem death. *J Neurol Neurosurg Psychiatry* 1987;50:1504–13 CrossRef Medline
18. Qian SY, Fan XM, Yin HH. Transcranial Doppler assessment of brain death in children. *Singapore Med J* 1998;39:247–50 Medline



19. Vicenzini E, Pulitano P, Cicchetti R, et al. **Transcranial Doppler for brain death in infants: the role of the fontanelles.** *Eur Neurol* 2010; 63:164–69 CrossRef Medline
20. Rodriguez RA, Cornel G, Alghofaili F, et al. **Transcranial Doppler during suspected brain death in children: potential limitation in patients with cardiac “shunt.”** *Pediatr Crit Care Med* 2002;3:153–57 CrossRef Medline
21. Budohoski KP, Aries MJ, Kirkpatrick PJ, et al. **Protracted cerebral circulatory arrest and cortical electrical silence coexisting with preserved respiratory drive and flexor motor response.** *Br J Anaesth* 2012;109:293–94 CrossRef Medline
22. Eder KE, Haussen DC, Searls DE, et al. **Reverberating TCD flow pattern in brain death.** *Neurology* 2012;79:e79 CrossRef Medline
23. Mata-Zubillaga D, Oulego-Erroz I. **Persistent cerebral blood flow by transcranial Doppler ultrasonography in an asphyxiated newborn meeting brain death diagnosis: case report and review of the literature.** *J Perinatal* 2012;32:473–75 CrossRef Medline
24. Thompson BB, Wendell LC, Potter NS, et al. **The use of transcranial Doppler ultrasound in confirming brain death in the setting of skull defects and extraventricular drains.** *Neurocrit Care* 2014;21: 534–38 CrossRef Medline
25. Cabrer C, Dominguez-Roldan JM, Manyalich M, et al. **Persistence of intracranial diastolic flow in transcranial Doppler sonography exploration of patients in brain death.** *Transplant Proc* 2003;35: 1642–43 CrossRef Medline
26. Abadal JM, Llompарт-Pou JA, Homar J, et al. **Ultrasonographic cerebral perfusion in assessment of brain death: a preliminary study.** *J Ultrasound Med* 2008;27:791–94 Medline
27. Azevedo E, Teixeira J, Neves JC, et al. **Transcranial Doppler and brain death.** *Transplant Proc* 2000;32:2579–81 CrossRef Medline
28. de Freitas GR, André C. **Sensitivity of transcranial Doppler for confirming brain death: a prospective study of 270 cases.** *Acta Neurol Scand* 2006;113:426–32 CrossRef Medline
29. Dominguez-Roldan JM, Murillo-Cabezas F, Muñoz-Sanchez A, et al. **Changes in the Doppler waveform of intracranial arteries in patients with brain-death status.** *Transplant Proc* 1995;27:2391–92 Medline
30. Dosemeci L, Dora B, Yilmaz M, et al. **Utility of transcranial Doppler ultrasonography for confirmatory diagnosis of brain death: two sides of the coin.** *Transplantation* 2004;77:71–75 CrossRef Medline
31. Ducrocq X, Braun M, Debouverie M, et al. **Brain death and transcranial Doppler: experience in 130 cases of brain dead patients.** *J Neurol Sci* 1998;160:41–46 CrossRef Medline
32. Feri M, Ralli L, Felici M, et al. **Transcranial Doppler and brain death diagnosis.** *Crit Care Med* 1994;22:1120–26 CrossRef Medline
33. Hadani M, Bruk B, Ram Z, et al. **Application of transcranial Doppler ultrasonography for the diagnosis of brain death.** *Intensive Care Med* 1999;25:822–28 CrossRef Medline
34. Hassler W, Steinmetz H, Gawlowski J. **Transcranial Doppler ultrasonography in raised intracranial pressure and in intracranial circulatory arrest.** *J Neurosurg* 1988;68:745–51 Medline
35. Kuo JR, Chen CF, Chio CC, et al. **Time dependent validity in the diagnosis of brain death using transcranial Doppler sonography.** *J Neurol Neurosurg Psychiatry* 2006;77:646–49 CrossRef Medline
36. Lampl Y, Gilad R, Eschel Y, et al. **Diagnosing brain death using the transcranial Doppler with a transorbital approach.** *Arch Neurol* 2002;59:58–60 CrossRef Medline
37. Newell DW, Grady MS, Sirotta P, et al. **Evaluation of brain death using transcranial Doppler.** *Neurosurgery* 1989;24:509–13 CrossRef Medline
38. Orban JC, El-Mahjoub A, Rami L, et al. **Transcranial Doppler shortens the time between clinical brain death and angiographic confirmation: a randomized trial.** *Transplantation* 2012;94:585–88 CrossRef Medline
39. Paolin A, Manuali A, Di Paola F, et al. **Reliability in diagnosis of brain death.** *Intensive Care Med* 1995;21:657–62 CrossRef Medline
40. Petty GW, Mohr JP, Pedley TA, et al. **The role of transcranial Doppler in confirming brain death: sensitivity, specificity, and suggestions for performance and interpretation.** *Neurology* 1990;40: 300–03 CrossRef Medline
41. Poularas J, Karakitsos D, Kouraklis G, et al. **Comparison between transcranial color Doppler ultrasonography and angiography in the confirmation of brain death.** *Transplant Proc* 2006;38:1213–17 CrossRef Medline
42. Powers AD, Graeber MC, Smith RR. **Transcranial Doppler ultrasonography in the determination of brain death.** *Neurosurgery* 1989; 24:884–89 CrossRef Medline
43. Su Y, Yang Q, Liu G, et al. **Diagnosis of brain death: confirmatory tests after clinical test.** *Chin Med J (Engl)* 2014;127:1272–77 Medline
44. Van Velthoven V, Calliauw L. **Diagnosis of brain death: transcranial Doppler sonography as an additional method.** *Acta Neurochir (Wien)* 1988;95:57–60 CrossRef Medline
45. Wang K, Yuan Y, Xu ZQ, et al. **Benefits of combination of electroencephalography, short latency somatosensory evoked potentials, and transcranial Doppler techniques for confirming brain death.** *J Zhejiang Univ Sci B* 2008;9:916–20 CrossRef Medline
46. Welschehold S, Boor S, Reuland K, et al. **Technical aids in the diagnosis of brain death: a comparison of SEP, AEP, EEG, TCD and CT angiography.** *Dtsch Arztebl Int* 2012;109:624–30 CrossRef Medline
47. Zurynski Y, Dorsch N, Pearson I, et al. **Transcranial Doppler ultrasound in brain death: experience in 140 patients.** *Neurol Res* 1991; 13:248–52 Medline
48. Wijedicks EF. **Brain death worldwide: accepted fact but no global consensus in diagnostic criteria.** *Neurology* 2002;58:20–25 CrossRef Medline
49. Ropper AH. **A preliminary MRI study of the geometry of brain displacement and level of consciousness with acute intracranial masses.** *Neurology* 1989;39:622–27 CrossRef Medline

# Utility and Significance of Gadolinium-Based Contrast Enhancement in Posterior Reversible Encephalopathy Syndrome

S.J. Karia, J.B. Rykken, Z.J. McKinney, L. Zhang, and A.M. McKinney



## ABSTRACT

**BACKGROUND AND PURPOSE:** Posterior reversible encephalopathy syndrome is a clinicroadiologic syndrome. Literature regarding associated factors and the prognostic significance of contrast enhancement in posterior reversible encephalopathy syndrome is sparse. This study set out to evaluate an association between the presence of enhancement in posterior reversible encephalopathy syndrome and various clinical factors in a large series of patients with this syndrome.

**MATERIALS AND METHODS:** From an MR imaging report search that yielded 176 patients with clinically confirmed posterior reversible encephalopathy syndrome between 1997 and 2014, we identified 135 patients who had received gadolinium-based contrast. The presenting symptoms, etiology, clinical follow-up, and maximum systolic and diastolic blood pressures within 1 day of MR imaging were recorded. MRIs were reviewed for parenchymal hemorrhage, MR imaging severity, and the presence and pattern of contrast enhancement. Statistical analyses evaluated a correlation between any clinical features and the presence or pattern of enhancement.

**RESULTS:** Of 135 included patients (67.4% females; age range, 7–82 years), 59 (43.7%) had contrast enhancement on T1-weighted MR imaging, the most common pattern being leptomeningeal ( $n = 24$ , 17.8%) or leptomeningeal plus cortical ( $n = 21$ , 15.6%). Clinical outcomes were available in 96 patients. No significant association was found between the presence or pattern of enhancement and any of the variables, including sex, age, symptom, MR imaging severity, blood pressure, or outcome (all  $P > .05$  after Bonferroni correction).

**CONCLUSIONS:** The presence or pattern of enhancement in posterior reversible encephalopathy syndrome is not associated with any of the tested variables. However, an association was found between MR imaging severity and clinical outcome.

**ABBREVIATIONS:** DBP<sub>max</sub> = maximum diastolic blood pressure; PRES = posterior reversible encephalopathy syndrome; SBP<sub>max</sub> = maximum systolic blood pressure

Posterior reversible encephalopathy syndrome (PRES) is a clinical and radiographic syndrome that may result from various etiologies but is most commonly associated with hypertension, eclampsia, or treatment with immunosuppressant medications.<sup>1–4</sup> The exact pathophysiology of this condition remains uncertain, but it has been postulated to relate to dysfunction in cerebral autoregulation or endothelial injury. Contrast enhancement can variably be present on MR imaging in patients with

PRES, having been described in up to 38% of patients, but the significance of this is unclear. The presence of contrast enhancement implies dysfunction of the blood-brain barrier, and it has been postulated that the presence of enhancement in many patients with PRES may further point to endothelial injury as a possible cause.<sup>4–8</sup>

Whether the presence or pattern of contrast enhancement is related to disease severity, etiology, or prognosis is currently unknown because the umbrella of PRES encompasses a vast array of etiologies and imaging appearances. While the clinical picture of PRES is variable, not all cases are fully reversible.<sup>7,8</sup> Typically, the use of gadolinium-based contrast is not necessary to solidify the diagnosis of PRES because the typical imaging appearance of cortical and/or subcortical edema on FLAIR or T2WI, with a corroborative clinical history, is decisive.<sup>1,7,9–13</sup> Meanwhile, although most of the prior literature has described the edema patterns of PRES on FLAIR or T2WI, such studies have hardly focused on the patterns of enhancement or the clinical implications of such enhancement.<sup>7–12</sup> Several smaller series have described the inci-

Received July 22, 2015; accepted after revision August 18.

From the Department of Radiology (S.J.K., J.B.R., A.M.M.) and Clinical and Translational Science Institute (L.Z.), University of Minnesota, Minneapolis, Minnesota; Department of Radiology (A.M.M.) and Clinical Informatics (Z.J.M.), Hennepin County Medical Center, St. Louis Park, Minnesota; and Midwest Center for Occupational Health and Safety/HealthPartners (Z.J.M.), Minneapolis, Minnesota.

Paper previously presented at: American Society of Neuroradiology Annual Meeting and the Foundation of the ASNR Symposium, April 25–30, 2015; Chicago, Illinois.

Please address correspondence to S.J. Karia, MD, University of Minnesota MMC 292, 420 Delaware St SE, Minneapolis, MN 55455; e-mail: karia009@umn.edu

<http://dx.doi.org/10.3174/ajnr.A4563>

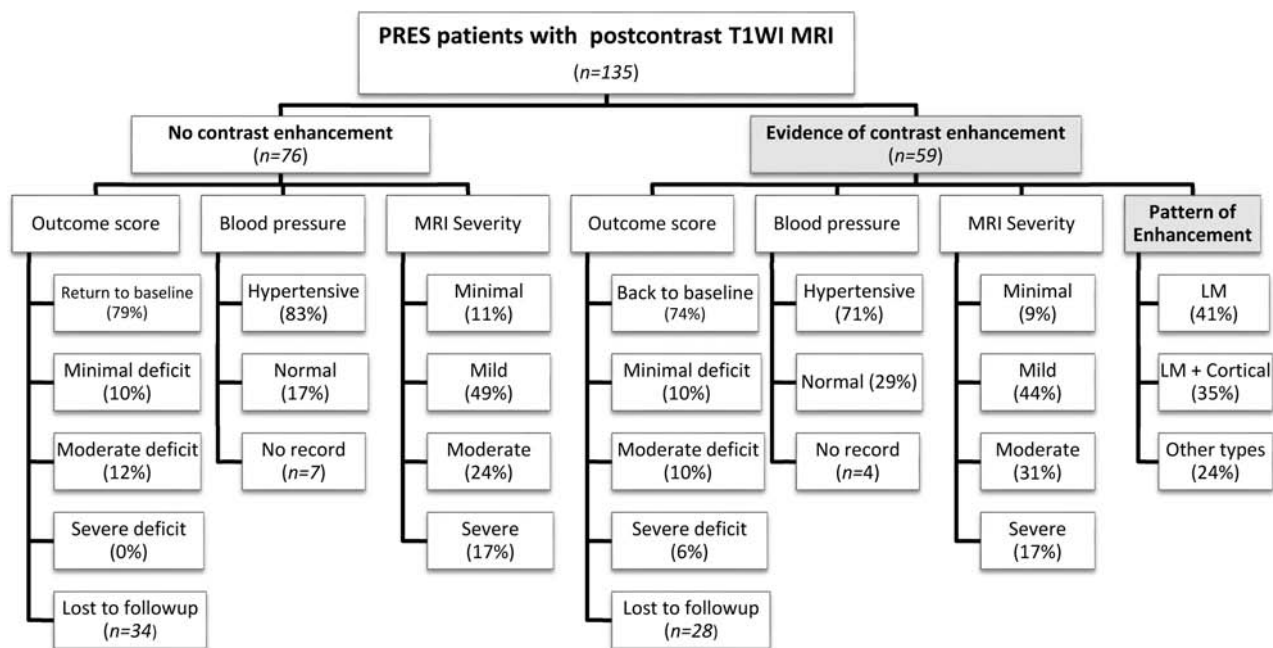


**FIG 1.** Organizational chart of the makeup of the cohort for this study, including MR imaging severity and various clinical factors. LM indicates leptomeningeal.

dence and features of enhancement on MR imaging in PRES, with variable frequency.<sup>3,4,7,8,14,15</sup> Given such variability, this study set out to review a larger series of patients with clinically confirmed PRES to determine whether an association could be made between the presence of contrast enhancement and etiology, prognosis, or a host of other clinical factors.

## MATERIALS AND METHODS

### Patient Selection

This retrospective study was approved by the institutional review boards of 2 hospitals, one being a tertiary care center and the other a level 1 trauma center. An MR imaging data base search was conducted for patients in whom the radiologic and clinical features of PRES were present within a 17-year period (1997–2014), yielding 176 patients with clinically confirmed PRES. The single inclusion criterion was having postcontrast T1WI in addition to the FLAIR images used to diagnose PRES. The exclusion criterion was either the lack of postcontrast T1WI or motion artifacts rendering the MR imaging uninterpretable. Patients with other comorbidities were not excluded, provided they were diagnosed with PRES.

The clinical criteria of PRES were defined as the presence of at least 1 acute neurologic deficit and clinical corroboration of suspected PRES on MR imaging. The radiologic features of PRES were defined by the presence of edema in characteristic distributions, as described previously.<sup>7,9,10</sup> The medical records of these patients were also reviewed to retrieve patient demographics and clinical data, including sex, age, primary presenting symptom, presumed etiology, maximum systolic blood pressure (SBP<sub>max</sub>) and maximum diastolic blood pressure (DBP<sub>max</sub>) (both within 1 day of the MR imaging examination), and clinical outcome (if clinical follow-up was available). Regarding the clinical follow-up, the goal was a clinical examination performed at least 60 days after the initial presentation.

### Clinical Severity and Outcome Scoring

Five categories of clinical outcome based on the follow-up evaluation were established on the basis of a prior study of PRES and acute toxic leukoencephalopathy, which consisted of the following: return to baseline clinical condition (grade 0); minimal residual cognitive deficit (grade 1); mild persistent neurologic deficit (grade 2); moderate persistent neurologic deficit (grade 3); and severe outcome including no improvement (eg, persistent), seizures, coma, or death (grade 4).<sup>16</sup>

### MR Imaging Sequence Protocols

The MR imaging examinations were performed on 6 different scanners (4 with 1.5T magnet strength and 2 with 3T magnet strength) during the 17-year period, which routinely included axial T1WI, T2WI, T2 FLAIR images, DWI, and postcontrast T1WI.

### Radiologic Severity and Grading

Retrospective review by consensus by 2 staff neuroradiologists (A.M.M., J.B.R.), with 12 and 4 years of experience respectively, was performed to evaluate the presence of intracranial hemorrhage, the pattern of radiologic severity, and the presence and pattern of contrast enhancement. Analysis of the clinical details of each case was performed separately, but with joint (consensus) grading of MR imaging severity. The grading of radiologic severity generally follows that previously used in the literature, with the addition of a new “minimal” grade (grade 1) to account for an earlier or milder form of PRES that has occurred with improving recognition of the disorder.<sup>4,7,9</sup> This minimal grade was defined as symmetric, cortical involvement of only 1 lobe (frontal, temporal, parietal, or occipital) without involvement of the basal ganglia, brain stem, or deep white matter. The remaining degrees of “mild,” “moderate,” and “severe” grades adhere to the system previously described.<sup>7,9</sup>

**Table 1: Summary statistics for variables of interest by presence/absence of enhancement**

Variable and Category	Contrast Enhancement		P Value
	Positive (n = 59)	Negative (n = 76)	
Sex			
Male	15 (25%)	29 (38%)	.14
Female	44 (75%)	47 (62%)	
Age			
Median	43	44	.753
Mean	41	42	
MRI severity			
Minimal	5 (8.5%)	8 (10.5%)	.854
Mild	26 (44%)	37 (48.7%)	
Moderate	18 (30.5%)	18 (23.7%)	
Severe	10 (17%)	13 (17.1%)	
Symptom			
Seizure	37 (62.7%)	48 (63.2%)	.481
AMS	12 (20.3%)	20 (26.3%)	
Others	10 (17%)	8 (10.6%)	
IPH			
Yes	8 (13.6%)	6 (7.9%)	.395
No	51 (86.4%)	70 (92.1%)	
SBP <sub>max</sub> (mean)	159.9	168.8	.178
DBP <sub>max</sub> (mean)	94.31	97.23	.386
Outcome score			
Missing +4	28	34	.522
0	23 (74.2%)	33 (78.6%)	
1	3 (9.7%)	4 (9.5%)	
2	3 (9.7%)	5 (11.9%)	
3	2 (6.5%)	0	

**Note:**—IPH indicates intraparenchymal hemorrhage; AMS, altered mental status.

When assessing the presence and pattern type of contrast enhancement, we further categorized the included patients as having leptomeningeal, cortical, or parenchymal nodular patterns of enhancement or a combination of any of these patterns, similar to that previously described.<sup>7</sup>

### Statistical Analysis

An analysis of variance was performed to investigate whether sex, age, clinical presentation (symptom), DBP<sub>max</sub>, SBP<sub>max</sub>, MR imaging severity, or clinical outcome was associated with patterns of contrast enhancement and as an analysis to evaluate a correlation between the radiologic severity and clinical outcomes. *P* values were calculated from the 2-sample *t* test/1-way ANOVA for continuous variables and the Fisher exact test for categorical variables when comparing variables of interest by contrast enhancement. Thereafter, the mean and its 95% confidence intervals were calculated for continuous variables regarding the types of enhancement. A pair-wise comparison was performed after applying a Bonferroni adjustment for association with statistical significance, setting the *P* value at <.017 (*P* = .05/3). We applied a logistic regression to investigate predictors of contrast enhancement, calculating odds ratios and 95% confidence intervals. Notably, regarding outcome scoring, the grade 4 category (death) was merged with the “no follow-up” category to prevent the potential introduction of bias because most patients died from reasons other than PRES.

### RESULTS

Of the 176 patient records reviewed, 41 patients were excluded from the dedicated MR imaging review due to the lack of post-contrast T1WI. A summary of the 135 included patients is presented in the form of an organizational chart in Fig 1, illustrating the patient cohort, and particularly showing the percentage of patients with the various MR imaging severity grades (exemplified in Figs 2–5) and clinical outcome grades in both the contrast-enhancing and nonenhancing subgroups.

### Clinical Findings

Of the 135 patients with PRES, the ages ranged from 7 to 82 years (mean, 40 ± 20 years; range, 3–80 years), 67.4% being female, as shown in Table 1. The most common primary attributable etiology of PRES was immunosuppressant or chemotherapeutic medications (*n* = 60), followed by the following: essential hypertensive emergency (*n* = 21), sepsis (*n* = 14), eclampsia (*n* = 12), systemic lupus erythematosus (*n* = 7), and multidrug use including cocaine abuse or alcohol withdrawal resulting in hypertensive crisis (*n* = 7). Other individual causes in-

**Table 2: Summary statistics for variables of interest by pattern of contrast enhancement**

Variable and Category	Negative (n = 76)	Contrast Enhancement		Others (n = 14)	P Value
		LM (n = 24)	Cortical + LM (n = 21)		
Sex					
Male	29 (38.2%)	4 (16.7%)	5 (23.8%)	6 (42.9%)	.154
Female	47 (61.8%)	20 (83.3%)	16 (76.2%)	8 (57.1%)	
Age					
Median	44	45	24	57	.011
Mean	42	40	32	55	
MRI severity					
Minimal	8 (10.5%)	2 (8.3%)	2 (9.5%)	1 (7.1%)	.942
Mild	37 (48.7%)	10 (41.7%)	10 (47.6%)	6 (42.9%)	
Moderate	18 (23.7%)	6 (25%)	6 (28.6%)	6 (42.9%)	
Severe	13 (17.1%)	6 (25%)	3 (14.3%)	1 (7.1%)	
Symptom					
Seizure	48 (63.2%)	12 (50%)	16 (76.2%)	9 (64.3%)	.322
AMS	20 (26.3%)	5 (20.8%)	3 (14.3%)	4 (28.6%)	
Others	8 (10.5%)	7 (29.2%)	2 (9.5%)	1 (7.1%)	
IPH					
Yes	6 (7.9%)	5 (20.8%)	1 (4.8%)	2 (14.3%)	.233
No	70 (92.1%)	19 (79.2%)	20 (95.2%)	12 (85.7%)	
SBP <sub>max</sub> (mean)	168.8	166.7	142.8	172.8	.037
DBP <sub>max</sub> (mean)	97.23	96.74	88.11	99.08	.260
Outcome score					
Missing +4	34	13	7	8	.305
0	33 (78.6%)	8 (72.7%)	10 (71.4%)	5 (83.3%)	
1	4 (9.5%)	1 (9.1%)	2 (14.3%)	8	
2	5 (11.9%)	0	2 (14.3%)	1 (16.7%)	
3	0	2 (18.2%)	0	0	

**Note:**—LM indicates leptomeningeal; IPH, intraparenchymal hemorrhage; AMS, altered mental status.



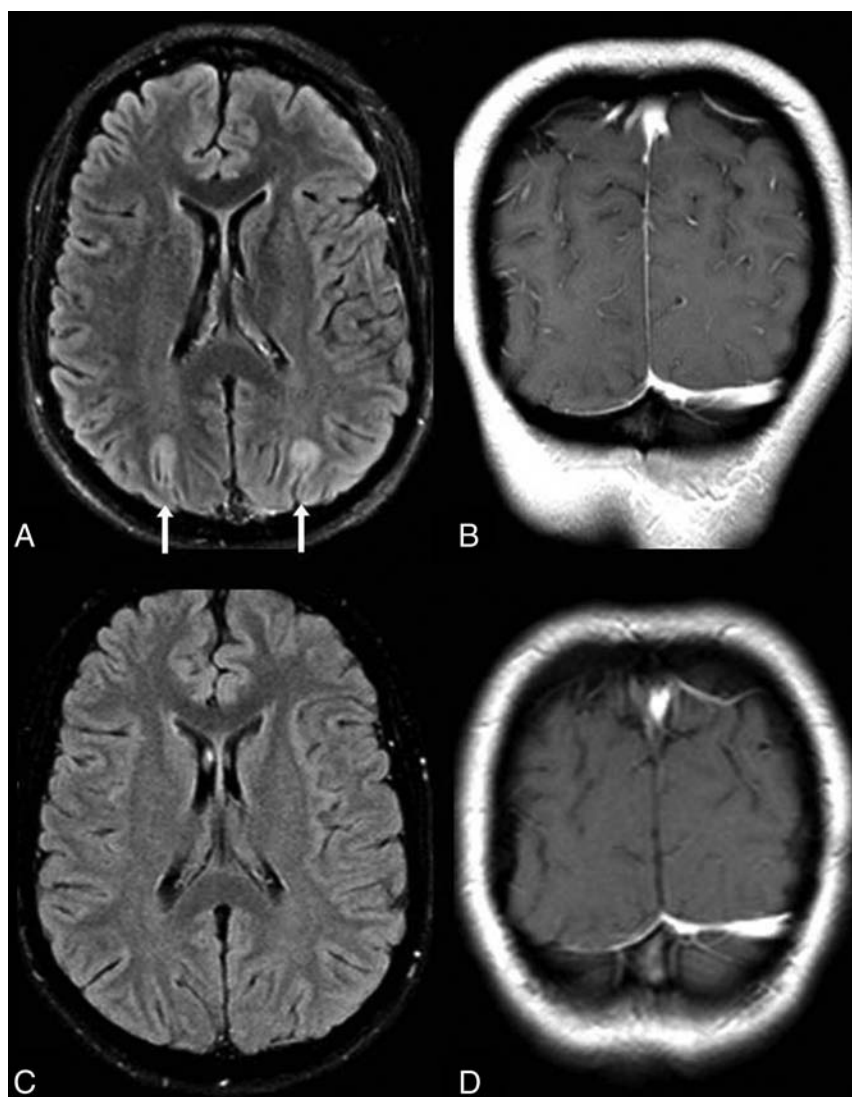


**FIG 2.** No enhancement in “minimal” PRES. A 22-year-old woman with end-stage renal disease presented with seizure, with SBP<sub>max</sub> and DBP<sub>max</sub> of 201/119 mm Hg within 1 day of MR imaging. “Minimal” cortical edema is noted on FLAIR (arrows, A) in the occipital regions, without abnormal contrast enhancement on postcontrast coronal T1WI (B). On a 3-month follow-up 1.5T MR imaging, the edema has resolved on FLAIR (C), and there is no enhancement on T1WI (D).

cluded dysautonomia, nortriptyline overdose, and adult respiratory distress syndrome, also resulting in hypertensive crisis ( $n = 4$ ). In 10 patients, the cause of PRES was unclear.

The recorded SBP<sub>max</sub> and DBP<sub>max</sub> within 1 day before and after the reference MR imaging were available in 124 patients; of these, 23% were normotensive ( $n = 29$ ). The most common primary presenting symptom was seizures, present in 63% ( $n = 85$ ), followed by altered mental status in 24% ( $n = 32$ ). Other primary presenting symptoms included focal neurologic deficits (8.8%,  $n = 12$ ) and headaches (4.4%,  $n = 6$ ).

Clinical follow-up was available in 96 patients. In the remaining 39, no follow-up was available from the medical records. In 58% of the patients with a clinical follow-up ( $n = 56$ ), there was a return to clinical baseline with no persistent neurologic deficit at follow-up, 7% had minimal residual neurologic deficit ( $n = 7$ ), 8% had mild persistent neurologic deficits ( $n = 8$ ), and 2% had a

moderate persistent neurologic deficit ( $n = 2$ ). Five percent of patients re-presented with seizures ( $n = 5$ ). Nineteen percent of patients died in the short-term ( $n = 18$ ), though only 1 patient died with causes attributable to PRES/seizures.

### Radiologic Findings

Of the 135 included patients, 59 (43.7%) demonstrated evidence of contrast enhancement, 75% of these patients being females as shown in Table 2. Figure 2 shows an example of a case of PRES without evidence of enhancement, a pattern found in 76 patients (56.3%). The most common pattern of enhancement was leptomeningeal, identified in 76% ( $n = 45$ , Fig 3), whether isolated (41%,  $n = 24$ ) or combined with a purely cortical pattern of enhancement (35%,  $n = 21$ ; Fig 5). A purely nodular pattern of enhancement was visible in 3 patients (Fig 4), while 3 others exhibited both nodular and leptomeningeal patterns. Within the group of patients positive for contrast enhancement, 14% had radiologic evidence of intraparenchymal hemorrhage ( $n = 8$ ) versus 8% in the group without evidence of intraparenchymal hemorrhage ( $n = 6$ ). When we compared radiologic severity, patients with evidence of contrast enhancement were graded with minimal severity in 8% of cases ( $n = 5$ ), mild in 44% ( $n = 26$ ), moderate in 31% ( $n = 18$ ), and severe in 17% ( $n = 10$ ) versus 11%, 49%, 24%, and 17% ( $n = 8, 37, 18, 13$ ), respectively, in the group of patients with no evidence of enhancement.

No significant difference was found between the presence of contrast enhancement and any of the tested variables (Table 1). When enhancement was present, an association was suggested between increased age and SBP<sub>max</sub> and one of the described patterns of enhancement ( $P = .011$  and  $.037$ , respectively) (Table 2). However, pair-wise comparison after Bonferroni correction (for  $P = .05/3$ ) rejected this hypothesis for SBP<sub>max</sub> ( $P = .029$ ), whereas with respect to age, it failed to demonstrate which group was responsible for this result (leptomeningeal pattern versus cortical + leptomeningeal pattern groups,  $P = .187$ ; cortical + leptomeningeal pattern versus other types of enhancement,  $P = .002$ ; leptomeningeal versus other types of enhancement,  $P = .038$ ). This analysis was thus interpreted as a type I error.

A statistically significant association between radiologic severity and clinical outcomes was found ( $P = .026$ ), as shown in Table 3.

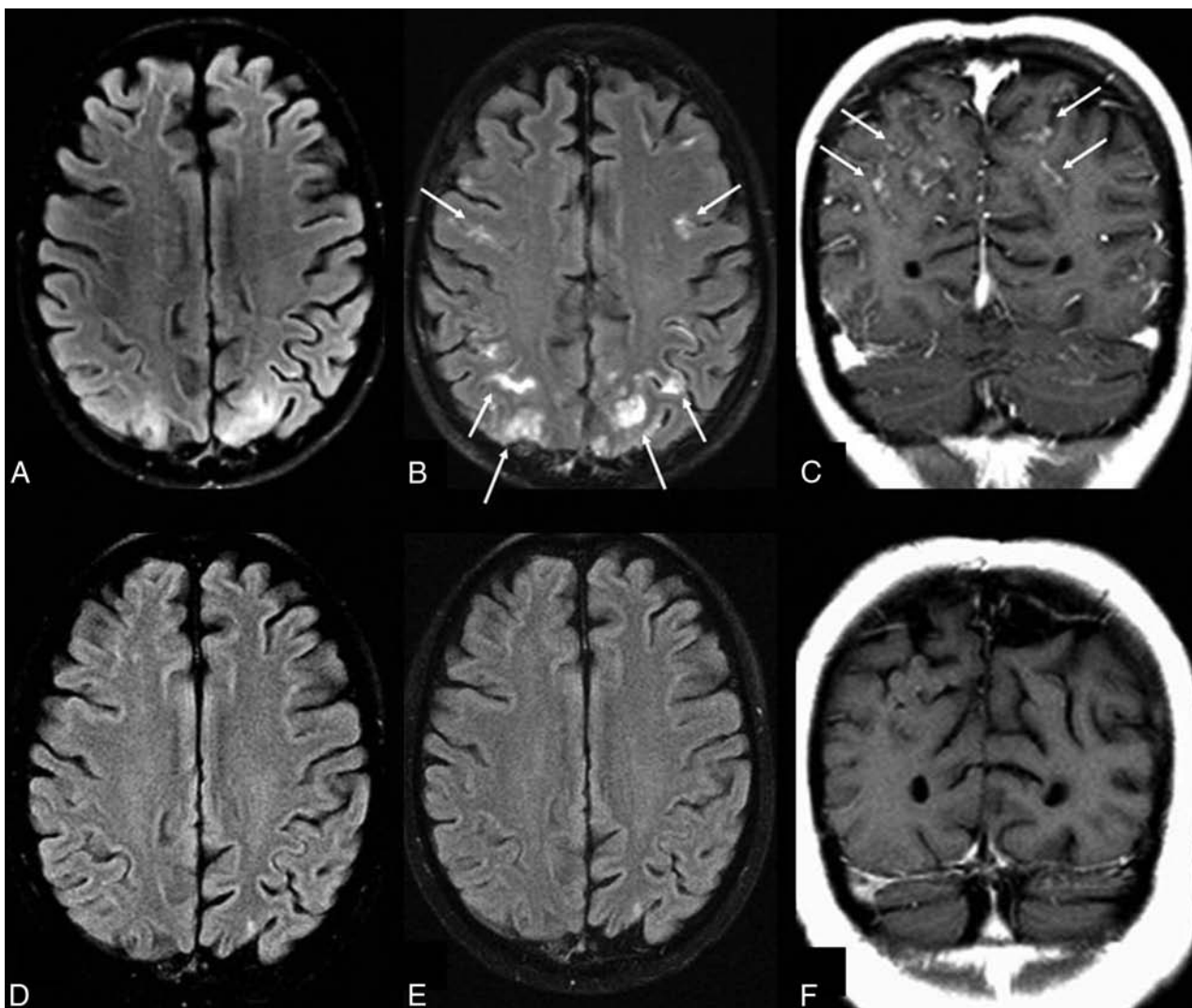


**FIG 3.** Leptomeningeal enhancement pattern in “mild” PRES. A 19-year-old woman with a history of systemic lupus erythematosus and pancytopenia presented with a seizure (blood pressure unavailable). A 1.5T MR imaging demonstrates mild parieto-occipital edema on FLAIR (A), with moderate leptomeningeal enhancement (*thin arrows*) on both gadolinium-enhanced FLAIR (B) and T1WI (C). D–F, A follow-up MR imaging 2 months later shows that both the mild cortical and subcortical edema on FLAIR (D) has resolved as well as the leptomeningeal enhancement on gadolinium-enhanced FLAIR (E) and T1WI (F). While gadolinium-enhanced FLAIR was not used to score the degree of edema or enhancement, the use of postcontrast FLAIR in this example demonstrates how enhancement can occur in areas lacking edema on noncontrast FLAIR, perhaps due to transient blood-brain barrier injury.

## DISCUSSION

This study set out to determine the significance of contrast enhancement in PRES and to determine whether there was any association between the presence or type of enhancement and various clinical factors, including etiology, sex, maximum systolic or diastolic blood pressure, or clinical outcome. No such associations were evident between those recorded clinical factors and enhancement, suggesting that the presence or absence of enhancement does not affect prognosis. Also no association was found between the MR imaging severity score or the presence of hemorrhage and the presence of enhancement, which corroborates the findings of a prior study.<sup>7</sup> Hence, intravenous gadolinium-based contrast is likely not necessary to evaluate the severity or extent of PRES, though studies with control groups would be necessary to truly prove this finding. The utility of postcontrast imaging would be in situations in which etiologies other than PRES are important considerations in the differential diagnosis,

such as infectious meningitis in an immunocompromised patient, subacute phase of posterior circulation infarctions (especially if bilateral), or vasculitis/cerebritis; such entities could also exhibit leptomeningeal or cortical enhancement.

How does enhancement fit into the pathophysiology of PRES, if at all? Enhancement is generally considered to represent breakdown or increased permeability of the blood-brain barrier.<sup>17</sup> The lack of a statistically significant pattern of enhancement with the different etiologies is of uncertain significance, and the pathophysiologic mechanism for these patterns of enhancement remains unclear. The presence or absence of enhancement could indicate different stages in the integrity of the blood-brain barrier, perhaps even being a temporal phenomenon, with cases lacking enhancement possibly being in a later stage at a point when the barrier has regained impermeability. By this rationale, a high incidence of enhancement would be expected in patients who are receiving drugs that are directly toxic to the endothelium, such as

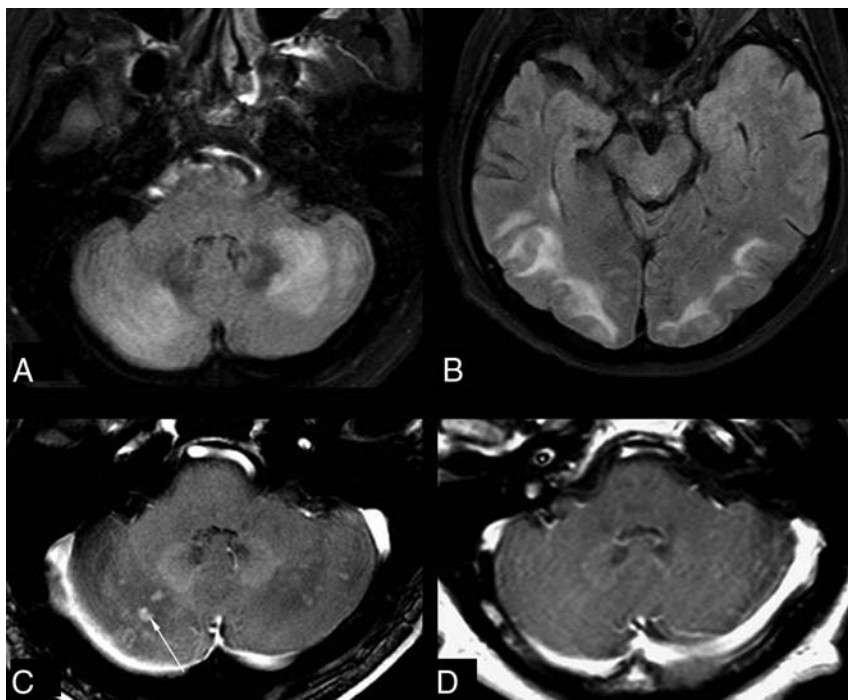


**FIG 4.** Nodular enhancement pattern in “moderate” PRES. A 58-year-old man, on a multiple chemotherapy regimen for metastatic renal cancer with sepsis, developed seizures. The patient was hypotensive, with  $SBP_{max}$  and  $DBP_{max}$  of 92/67 mm Hg. The initial 3T MR imaging demonstrates moderate edema from PRES, graded moderate due to the degree of cerebellar and parieto-occipital edema on FLAIR (A and B); there is also nodular enhancement on postcontrast T1WI (C), demonstrated in multiple planes. D, On a follow-up MR imaging 7 days later, the enhancing cerebellar nodular lesions have resolved.

immunosuppressants.<sup>7,18,19</sup> In this regard, 50% of the patients who were immunosuppressed in this study (who had received cyclosporine, tacrolimus, interferon, or mycophenolate) demonstrated at least 1 of the patterns of contrast enhancement, a finding not described previously, to our knowledge. The presence of increased permeability of the blood-brain barrier in certain etiologies or MR imaging patterns of PRES could perhaps be further evaluated by dynamic susceptibility contrast MR perfusion, perhaps with measurement of a permeability leakage coefficient such as K<sub>2</sub>, but this evaluation is beyond the scope of the current study. In this regard, though, a prior study by Brubaker et al<sup>20</sup> did describe a normal K<sub>2</sub> compared with controls, but that study comprised only 8 patients with PRES; thus, it may not have been large enough to adequately evaluate this phenomenon.<sup>21</sup> Therefore, overall, the significance of contrast enhancement in PRES remains unclear but appears related to a transient impairment in function of the blood-brain barrier.

The traditional theory regarding the underlying pathophysiology of PRES is that a failure of cerebral autoregulation leads to a state of cerebral hyperperfusion through which the blood-brain barrier becomes permeable and that the resultant extravasation of macromolecules and other changes in the extracellular environment of the brain may induce seizures.<sup>22–26</sup> A second theory is that hypoperfusion from exaggerated vasoconstriction/vasospasm as part of an autoregulatory mechanism leads to ischemia, followed by edema, with the ischemic changes affecting endothelial function and thus blood-brain barrier integrity. Accordingly, most studies of patients with PRES by using MR per-

fusion or hexamethylpropyleneamine oxime SPECT noted focal regions of reduced perfusion, with decreased cerebral blood flow.<sup>10,20,27–29</sup> Another study did demonstrate rather focal areas of increased flow on hexamethylpropyleneamine oxime SPECT, though in a single patient of 2 included in the study, perhaps due to comorbidities or the delayed timing of the scan and concomitant therapeutic institution.<sup>30</sup> A more recently proposed theory has been that of endothelial dysfunction due to a multitude of potential causes. Accordingly, recent studies of the effects of immunosuppressant medications on the endothelium suggest that endothelial cell injury and subsequent blood-brain barrier impairment may cause edema and microhemorrhage.<sup>7,18,19,31,32</sup> Such impairment may explain the high rate of contrast enhancement, which often reverses, and may also explain the high incidence of microhemorrhages, which are seen in up to half of patients on SWI.<sup>32</sup> The fact that both enhancement and microhemorrhages occur in normotensive patients from a variety of etiologies suggests that the mechanisms of hyperperfusion or hypoperfusion are

not comprehensive explanations and that endothelial injury is more likely a common thread.<sup>1,7,10,13,19,31,32</sup>

The current study found the frequency of enhancement to be approximately 44%, previously reported to be 21%–38%.<sup>7,8</sup> Such discrepancies among studies could relate to varying statistical power or varying reviewer sensitivities to contrast enhancement. As to differences in the composition of etiologies, the largest subset was patients with immunosuppression, showing similar percentages (44% in the current study; 45% and 50% in a study by Fugate et al<sup>8</sup> and McKinney et al,<sup>7</sup> respectively). Thus, it is unlikely that the makeup of etiologies accounts for differences in the described rates of enhancement.

In attributing a severity grade to the MR images of the patients in our cohort, we attempted, as a secondary end point, to associate the radiologic severity with clinical outcomes. A significant statistical association was found ( $P = .0255$ ). Covarrubias et al<sup>3</sup> previously demonstrated an association between poor clinical outcome and the extent of T2 signal abnormalities. This statistical association further corroborates this finding and lends credence to the idea of using an MR imaging severity grading system, as used in the current and prior studies, to quantify radiologic severity. Such descriptions of MR imaging severity could eventually aid in determining the prognosis of patients with PRES.<sup>3,7</sup>

Even though this study includes one of the largest cohorts of patients with PRES in the literature, it remains limited by being a retrospective study, with data flaws including the absence of or less well-defined clinical outcomes for some patients and the lack



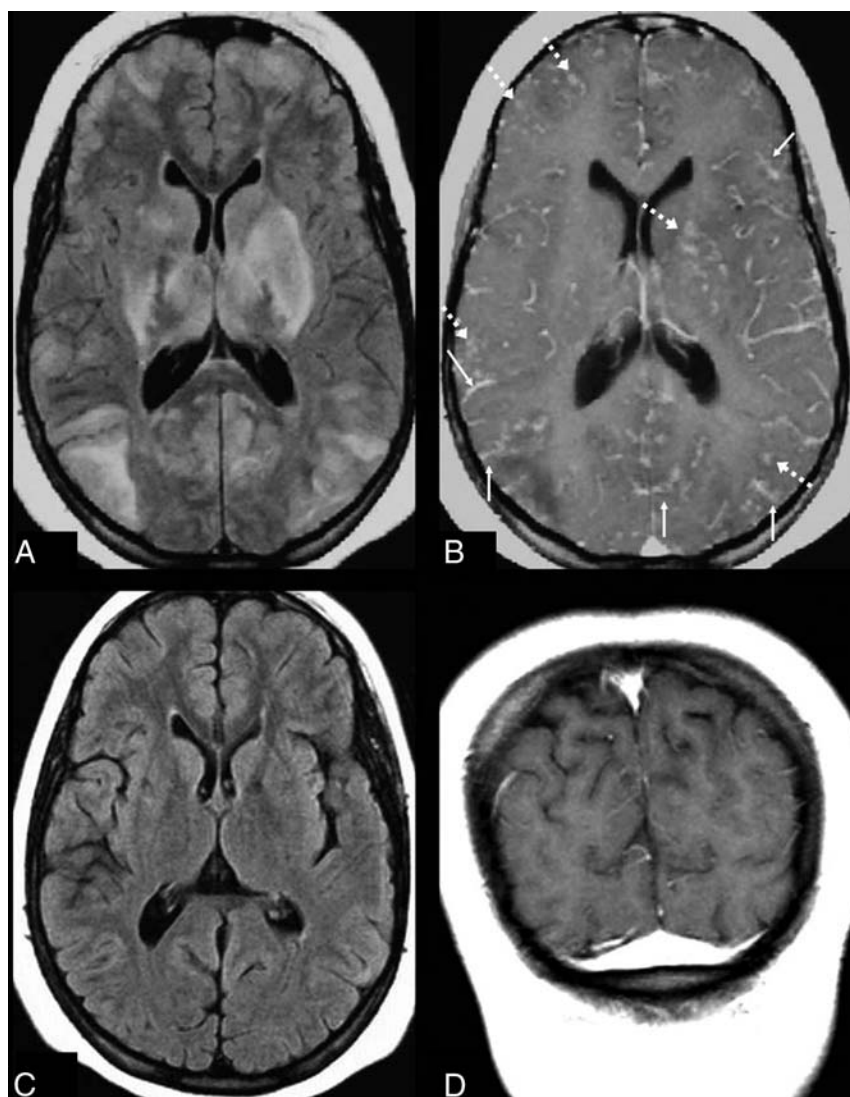


**FIG 5.** Leptomeningeal and cortical enhancement pattern in “severe” PRES. A 14-year-old girl with systemic lupus erythematosus presented with seizures. SBP<sub>max</sub> and DBP<sub>max</sub> were normal (136/83 mm Hg). The initial 1.5T MR imaging demonstrates severe edema on FLAIR (A), involving the basal ganglia, thalami, and brain stem (not shown), while there is diffusely thickened leptomeningeal enhancement (*thin arrows*) and cortical and parenchymal enhancement (*dashed arrows*) on postcontrast T1WI (B). Vessels are seen both within and outside of areas of vasogenic edema and remain an important consideration for these appearances, perhaps due to slow flow or endothelial dysfunction. On a follow-up 1.5T MR imaging 5 months later, the findings have entirely resolved on FLAIR (C) and postcontrast T1WI (D).

**Table 3: Association between radiologic severity and clinical outcome score<sup>a</sup>**

Radiologic Severity	Outcome Score			
	0	1	2	3
Minimal	8 (11%)	0	0	0
Mild	29 (39.7%)	3 (4.1%)	2 (2.7%)	0
Moderate	14 (19.2%)	3 (4.1%)	2 (2.7%)	0
Severe	5 (6.9%)	1 (1.4%)	4 (5.5%)	2 (2.7%)

<sup>a</sup> P value from the Fisher exact test = .026.

of consistent follow-up in all patients. In several patients, clinical outcome may have been biased by the existence of concomitant pathologies at the time of the diagnosis of PRES, including the presence of intracranial hemorrhage and associated brain infarction.

## CONCLUSIONS

PRES can be readily identified on standard MR imaging, and contrast enhancement is not necessary during the evaluation of suspected PRES because it is associated with neither the MR imaging severity nor the clinical outcome. Additionally, other clinical factors such as presenting symptoms, age, sex, maximum blood pressure (systolic or diastolic), and etiology are not associated with the presence or pattern of contrast enhancement. A prospective study would better confirm these findings. The use of intravenous contrast may, nevertheless, be helpful in the evaluation of differential diagnoses. However, this study does suggest a strong association between the radiologic severity and clinical outcome and brings value to the use of an MR imaging grading scale in the prognosis of patients with PRES to estimate its reversibility.

Disclosures: Alexander M. McKinney—UNRELATED: Consultancy: Vital Images, Minnetonka, Minnesota (a division of Toshiba Medical); CVRx (Brooklyn Park, Minnesota), Comments: <\$5000 total reimbursement per year from Vital Images, <\$500 total reimbursement per year from CVRx.

## REFERENCES

1. Bartynski WS. Posterior reversible encephalopathy syndrome, part 1: fundamental imaging and clinical features. *AJNR Am J Neuroradiol* 2008;29:1036–42 CrossRef Medline
2. Hinchey J, Chaves C, Appignani B, et al. A reversible posterior leukoencephalopathy syndrome. *N Engl J Med* 1996;334:494–500 CrossRef Medline
3. Covarrubias DJ, Luetmer PH, Campeau NG. Posterior reversible encephalopathy syndrome: prognostic utility of quantitative diffusion-weighted MR images. *AJNR Am J Neuroradiol* 2002;23:1038–48 Medline
4. McKinney AM, Kieffer SA, Paylor RT, et al. Acute toxic leukoencephalopathy: potential for reversibility clinically and on MRI with diffusion-weighted and FLAIR imaging. *AJR Am J Roentgenol* 2009;193:192–206 CrossRef Medline
5. Larsson HB, Stubgaard M, Frederiksen JL, et al. Quantitation of blood-brain barrier defect by magnetic resonance imaging and gadolinium-DTPA in patients with multiple sclerosis and brain tumors. *Magn Reson Med* 1990;16:117–31 CrossRef Medline
6. Stone LA, Smith ME, Albert PS, et al. Blood-brain barrier disruption on contrast-enhanced MRI in patients with mild relapsing-remitting multiple sclerosis: relationship to course, gender, and age. *Neurology* 1995;45:1122–26 CrossRef Medline
7. McKinney AM, Short J, Truwit CL, et al. Posterior reversible encephalopathy syndrome: incidence of atypical regions of involvement and imaging findings. *AJR Am J Roentgenol* 2007;189:904–12 CrossRef Medline
8. Fugate JE, Claassen DO, Cloft HJ, et al. Posterior reversible enceph-



- alopathy syndrome: associated clinical and radiologic findings. *Mayo Clin Proc* 2010;85:427–32 CrossRef Medline
9. Casey SO, Sampaio RC, Michel E, et al. **Posterior reversible encephalopathy syndrome: utility of fluid-attenuated inversion recovery MR imaging in the detection of cortical and subcortical lesions.** *AJNR Am J Neuroradiol* 2000;21:1199–206 Medline
10. Bartynski WS, Boardman JF. **Catheter angiography, MR angiography, and MR perfusion in posterior reversible encephalopathy syndrome.** *AJNR Am J Neuroradiol* 2008;29:447–55 CrossRef Medline
11. Jones BV, Egelhoff JC, Patterson RJ. **Hypertensive encephalopathy in children.** *AJNR Am J Neuroradiol* 1997;18:101–06 Medline
12. Schwartz RB, Feske SK, Polak JF, et al. **Preeclampsia-eclampsia: clinical and neuroradiographic correlates and insights into the pathogenesis of hypertensive encephalopathy.** *Radiology* 2000;217:371–76 CrossRef Medline
13. Rykken JB, McKinney AM. **Posterior reversible encephalopathy syndrome.** *Semin Ultrasound CT MR* 2014;35:118–35 CrossRef Medline
14. Ugurel MS, Hayakawa M. **Implications of post-gadolinium MRI results in 13 cases with posterior reversible encephalopathy syndrome.** *Eur J Radiol* 2005;53:441–49 CrossRef Medline
15. Mukherjee P, McKinstry RC. **Reversible posterior leukoencephalopathy syndrome: evaluation with diffusion-tensor MR imaging.** *Radiology* 2001;219:756–65 CrossRef Medline
16. McKinney AM, Lohman BD, Sarikaya B, et al. **Acute hepatic encephalopathy: diffusion-weighted and fluid-attenuated inversion recovery findings, and correlation with plasma ammonia level and clinical outcome.** *AJNR Am J Neuroradiol* 2010;31:1471–79 CrossRef Medline
17. Smirniotopoulos JG, Murphy FM, Rushing EJ, et al. **Patterns of contrast enhancement in the brain and meninges.** *Radiographics* 2007;27:525–51 CrossRef Medline
18. Wilasrusmee C, Da Silva M, Singh B, et al. **Morphological and biochemical effects of immunosuppressive drugs in a capillary tube assay for endothelial dysfunction.** *Clin Transplant* 2003;17:6–12 CrossRef Medline
19. Benigni A, Morigi M, Perico N, et al. **The acute effect of FK506 and cyclosporine on endothelial cell function and renal vascular resistance.** *Transplantation* 1992;54:775–80 CrossRef Medline
20. Brubaker LM, Smith JK, Lee YZ, et al. **Hemodynamic and permeability changes in posterior reversible encephalopathy syndrome measured by dynamic susceptibility perfusion-weighted MR imaging.** *AJNR Am J Neuroradiol* 2005;26:825–30 Medline
21. Weisskoff RM, Boxerman JL, Sorensen AG, et al. **Simultaneous blood volume and permeability mapping using a single Gd-based contrast injection.** In: *Proceedings of the Second Meeting of the International Society of Magnetic Resonance in Medicine*, San Francisco, California. August 6–12, 1994:279
22. MacKenzie ET, Strandgaard S, Graham DI, et al. **Effects of acutely induced hypertension in cats on pial arteriolar caliber, local cerebral blood flow, and the blood-brain barrier.** *Circ Res* 1976;39:33–41 CrossRef Medline
23. Iijima T, Kubota Y, Kuroiwa T, et al. **Blood-brain barrier opening following transient reflex sympathetic hypertension.** *Acta Neurochir Suppl* 1994;60:142–44 Medline
24. Ivens S, Gabriel S, Greenberg G, et al. **Blood-brain barrier breakdown as a novel mechanism underlying cerebral hyperperfusion syndrome.** *J Neurol* 2010;257:615–20 CrossRef Medline
25. Marchi N, Angelov L, Masaryk T, et al. **Seizure-promoting effect of blood-brain barrier disruption.** *Epilepsia* 2007;48:732–42 CrossRef Medline
26. Seiffert E, Dreier JP, Ivens S, et al. **Lasting blood-brain barrier disruption induces epileptic focus in the rat somatosensory cortex.** *J Neurosci* 2004;24:7829–36 Medline
27. Sánchez-Carpintero R, Narbona J, López de Mesa R, et al. **Transient posterior encephalopathy induced by chemotherapy in children.** *Pediatr Neurol* 2001;24:145–48 CrossRef Medline
28. Naidu K, Moodley J, Corr P, et al. **Single photon emission and cerebral computerised tomographic scan and transcranial Doppler sonographic findings in eclampsia.** *Br J Obstet Gynaecol* 1997;104:1165–72 CrossRef Medline
29. Engelter ST, Petrella JR, Alberts MJ, et al. **Assessment of cerebral microcirculation in a patient with hypertensive encephalopathy using MR perfusion imaging.** *AJR Am J Roentgenol* 1999;173:1491–93 CrossRef Medline
30. Schwartz RB, Jones KM, Kalina P, et al. **Hypertensive encephalopathy: findings on CT, MR imaging, and SPECT imaging in 14 cases.** *AJR Am J Roentgenol* 1992;159:379–83 CrossRef Medline
31. Zoja C, Furci L, Ghilardi F, et al. **Cyclosporin-induced endothelial cell injury.** *Lab Invest* 1986;55:455–62 Medline
32. McKinney AM, Sarikaya B, Gustafson C, et al. **Detection of microhemorrhage in posterior reversible encephalopathy syndrome using susceptibility-weighted imaging.** *AJNR Am J Neuroradiol* 2012;33:896–903 CrossRef Medline

# Prominence of Medullary Veins on Susceptibility-Weighted Images Provides Prognostic Information in Patients with Subacute Stroke

X. Yu, L. Yuan, A. Jackson, J. Sun, P. Huang, X. Xu, Y. Mao, M. Lou, Q. Jiang, and M. Zhang



## ABSTRACT

**BACKGROUND AND PURPOSE:** The demonstration of prominent medullary veins in the deep white matter ipsilateral to acute ischemic stroke has been shown to predict poor clinical outcome. We have investigated the prognostic implications of prominent medullary veins in patients with subacute stroke who present outside the therapeutic window for revascularization therapy.

**MATERIALS AND METHODS:** Forty-three consecutive patients with ischemic stroke in the middle cerebral artery territory presenting within 3–7 days of ictus were enrolled. The presence of prominent medullary veins in the periventricular white matter of the ipsilateral and contralateral medullary vein hemispheres was recorded. Perfusion-weighted imaging was used to calculate differences in hemispheric CBF from corresponding areas. Clinical outcome was classified as good if the modified Rankin Scale score was <3.

**RESULTS:** Prominent medullary veins were observed in 24/43 patients with 14 ipsilateral medullary veins and 10 contralateral medullary veins. The ipsilateral medullary vein was independently associated with poor outcome (odds ratio, 11.19;  $P = .046$ ). The contralateral medullary vein was not independently predictive of outcome but was significantly more common in patients with good outcome (90.0% contralateral medullary veins). A mean 64.5% decrease and a 52.4% increase of differences in hemispheric CBF were found in ipsilateral medullary veins and contralateral medullary veins, respectively.

**CONCLUSIONS:** The ipsilateral medullary vein was a significant predictive biomarker of poor clinical outcome after stroke and was associated with hypoperfusion. The contralateral medullary vein was associated with good clinical outcome, and we hypothesize that prominent contralateral medullary veins indirectly reflect increased CBF in the ipsilateral hemisphere due to spontaneous recanalization or collateral flow.

**ABBREVIATIONS:**  $\Delta$ CBF = differences in hemispheric CBF; MV = medullary veins; MVc = contralateral medullary veins; MVi = ipsilateral medullary veins; Norm = normal appearances; TIMI = Thrombolysis in Myocardial Infarction

In recent years, several groups, by using SWI in patients with acute ischemic stroke, have observed prominent cerebral medullary veins (MV) in the centrum semiovale and corona

radiata.<sup>1–3</sup> It has been hypothesized that the prominence of MV may be due to increased deoxyhemoglobin content due to an increase in regional oxygen extraction in the drainage territory<sup>1,4–6</sup> and/or dilation of cerebral veins in response to ischemia.<sup>3,7</sup> Subsequent studies have shown that abnormal hypointensity of the MV is correlated with a prolonged mean transit time, a large perfusion defect,<sup>7</sup> and increased cerebral blood volume.<sup>8</sup> The presence of prominent dilated MV in the periventricular white matter on SWI has been called the “brush sign.”

Identification of patients with acute stroke in whom misery perfusion results in increases in oxygen extraction is potentially important as a stratification and predictive biomarker. One recent study of 36 patients with acute stroke reported a significantly higher incidence of hemorrhagic transformation in patients with prominent MV (64% versus 18%,  $P = .028$ ).<sup>2</sup> Our recent study of 54 patients undergoing thrombolytic therapy found that asymmetry of the MV, combined with the size of the diffusion defect, was highly predictive of favorable out-

Received May 18, 2015; accepted after revision July 29.

From the Departments of Radiology (X.Y., J.S., P.H., X.X., M.Z.) and Neurology (Y.M., M.L.), Second Affiliated Hospital of Zhejiang University School of Medicine, Hangzhou, China; Department of Biomedical Engineering and Instrument Science (L.Y.), Key Laboratory for Biomedical Engineering of Education Ministry of China, Zhejiang University, Hangzhou, China; Wolfson Molecular Imaging Centre (A.J.), University of Manchester, Manchester, United Kingdom; and Department of Neurology (Q.J.), Henry Ford Health System, Detroit, Michigan.

This work was supported by the National Natural Science Foundation of China (No. 81271530) and the Zhejiang Provincial Natural Science Foundation of China (No. LZ14H180001).

Please address correspondence to Minming Zhang, MD, PhD, Department of Radiology, Second Affiliated Hospital of Zhejiang University School of Medicine, No. 88 Jiefang Rd, Shangcheng District, Hangzhou, China, 310009; e-mail: zhangminming@zju.edu.cn

Indicates open access to non-subscribers at [www.ajnr.org](http://www.ajnr.org)

<http://dx.doi.org/10.3174/ajnr.A4541>

come for reperfusion and recanalization with an accuracy greater than that of perfusion-diffusion mismatch.<sup>9</sup>

Prominence of the MV is also seen in the subacute stage of ischemic stroke.<sup>10</sup> In clinical practice, we have noted that prominent MV may be seen ipsilateral or contralateral to infarction. Such imaging signs may provide important prognostic information to guide clinicians toward the application of tissue-rescue therapies (such as recanalization or vasodilation) to prevent stroke progression during the subacute phase. We have therefore used SWI combined with dynamic contrast-enhanced MR imaging to test the following hypotheses: 1) Prominent ipsilateral MV are prognostic biomarkers of poor outcome in patients with subacute ischemic stroke; 2) prominent ipsilateral MV are associated with hypoperfusion; and 3) prominent contralateral MV provide additional prognostic information.

## MATERIALS AND METHODS

### Patients

The study was approved by the Medical Ethics Committee of the Second Affiliated Hospital of Zhejiang University School of Medicine, and written informed consent was obtained from all subjects.

Recruitment took place between March 2012 and January 2014. Inclusion criteria were the following: first-ever ischemic stroke, involving the vascular territory of the unilateral middle cerebral artery, without hemorrhagic infarction; age older than 18 years; admission between 3 and 7 days after stroke onset; and National Institutes of Health Stroke Scale score of 5–21 on admission. Exclusion criteria were any evidence of previous stroke on initial brain MRI. No patients were treated with thrombolytic or recanalization therapies. Demographic information and vascular risk factors, including age, sex, diabetes mellitus, hypertension, hyperlipidemia, and smoking and drinking histories, were recorded. Neurologic impairment on admission was assessed by using the NIHSS score. Clinical outcome at 3 months was evaluated by using the modified Rankin Scale<sup>11</sup>: (good outcome = mRS <3). The NIHSS and mRS were assessed by an experienced stroke neurologist who was blinded to the imaging findings.

### MR Imaging Protocol

Brain MR images were obtained on a 3T scanner (Signa Excite; GE Healthcare, Milwaukee, Wisconsin) by using an 8-channel brain phased array coil. Susceptibility-weighted images were acquired by using a 3D high-resolution flow-compensated multiecho gradient-echo sequence (TR/TE = 45/5–35 ms, 6 echoes with an echo spacing of 6.048 ms, flip angle = 25°, section thickness = 2 mm, matrix = 384 × 320 interpolated into 512 × 512, FOV = 24 cm). MRA was acquired by using a 3D time-of-flight sequence (TR/TE = 20/3.2 ms, flip angle = 15°, section thickness = 1.4 mm, matrix = 320 × 224, FOV = 24 cm). DWI was acquired by using an echo-planar imaging sequence (TR/TE = 4000/78.5 ms, flip angle = 90°, section thickness = 4 mm, section gap = 1 mm, matrix = 256 × 256, FOV = 24 cm) by using a single b-value of 1000 s/mm<sup>2</sup> applied in 3 orthogonal directions. PWI was performed by using a T2\* sensitive gradient-echo EPI sequence (TR/TE = 1700/30 ms, flip angle = 60°, section thickness = 4 mm, section gap = 1 mm, matrix = 128 × 128, FOV = 24 cm). Sixty time points were acquired with a temporal resolution of 1.7 sec-

onds. Contrast agent (Gd-DTPA, Ominscan; GE Healthcare, Piscataway, New Jersey), 0.1-mmol/kg body weight, was administered via an antecubital vein at a rate of 4 mL/s followed by a 20-mL saline flush injected at the same rate following the T1-weighted scan acquisition.

### Image Processing and Analysis

The latter 3 echoes (TE = 23.144, 29.192, and 35.240 ms) of multiecho susceptibility-weighted images were averaged to improve the conspicuity of the MV.<sup>12</sup> Each echo of the SWI was processed by using a high-pass filter (64 × 64) followed by phase multiplication by using a factor of 4 and production of a minimum intensity projection over 3 sections based on the magnitude and phase images by using the signal processing in NMR software (Wayne State University, Detroit, Michigan). The presence of prominent MV was assessed at the level of periventricular white matter (from immediately above the basal ganglia to the highest section including ventricle) on the axial plane of the synthesized MIP susceptibility-weighted images.<sup>9</sup> Prominence of the MV was defined as an increased number of MV in 1 hemisphere with at least 5 more seen in comparison with the contralateral hemisphere. This criterion was adapted from the scoring schema described by Horie et al.<sup>13</sup> We did not use the entire grading scale described by Horie et al because we were interested only in the significance of increased MV, so we adopted their cutoff value of a hemispheric asymmetry of >5. A neurologist and a radiologist, each blinded to the results of the other and to the clinical data and other MR images, performed the assessment. In the case of discrepancies, consensus was reached through discussion. Figure 1 shows the examples of ipsilateral MV (MVi), contralateral MV (MVC), and normal appearances (Norm).

Parametric maps of CBF were derived from PWI by using Perfusion Mismatch Analyzer software (<http://asist.umin.jp/index-e.htm>). CBF was measured in the territory of the medullary veins corresponding to their location on susceptibility-weighted images by using symmetric ROIs between 2.4 and 3.0 cm<sup>3</sup> (red rectangular ROIs shown on the CBF images in Fig 1). The hemispheric perfusion ratio (differences in hemispheric CBF [ΔCBF]) was calculated as:

$$\Delta\text{CBF} = (\text{CBF}_{\text{affected side}} - \text{CBF}_{\text{normal side}}) / \text{CBF}_{\text{normal side}} \times 100\%.$$

Hypoperfusion and hyperperfusion were respectively defined as a decrease or increase of ΔCBF of >20% compared with the contralateral hemisphere.<sup>14</sup>

The size of the ischemic lesion on DWI was determined by using a semiautomated threshold algorithm to identify the area with an intensity greater than the mean plus 2 SDs of the value in the homologous contralateral region.<sup>15</sup>

The vascular status was identified on MRA by 2 radiologists who gave a consensus rating by using the Thrombolysis in Myocardial Infarction (TIMI) grading scale<sup>16</sup>: 0 = complete occlusion, 1 = severe stenosis, 2 = mild or moderate stenosis, and 3 = normal. We categorized vascular status into 3 subgroups: occlusion (TIMI 0), stenosis (TIMI 1–2), and normal (TIMI 3). At the same time, the site of arterial stenosis-occlusion was also evaluated.

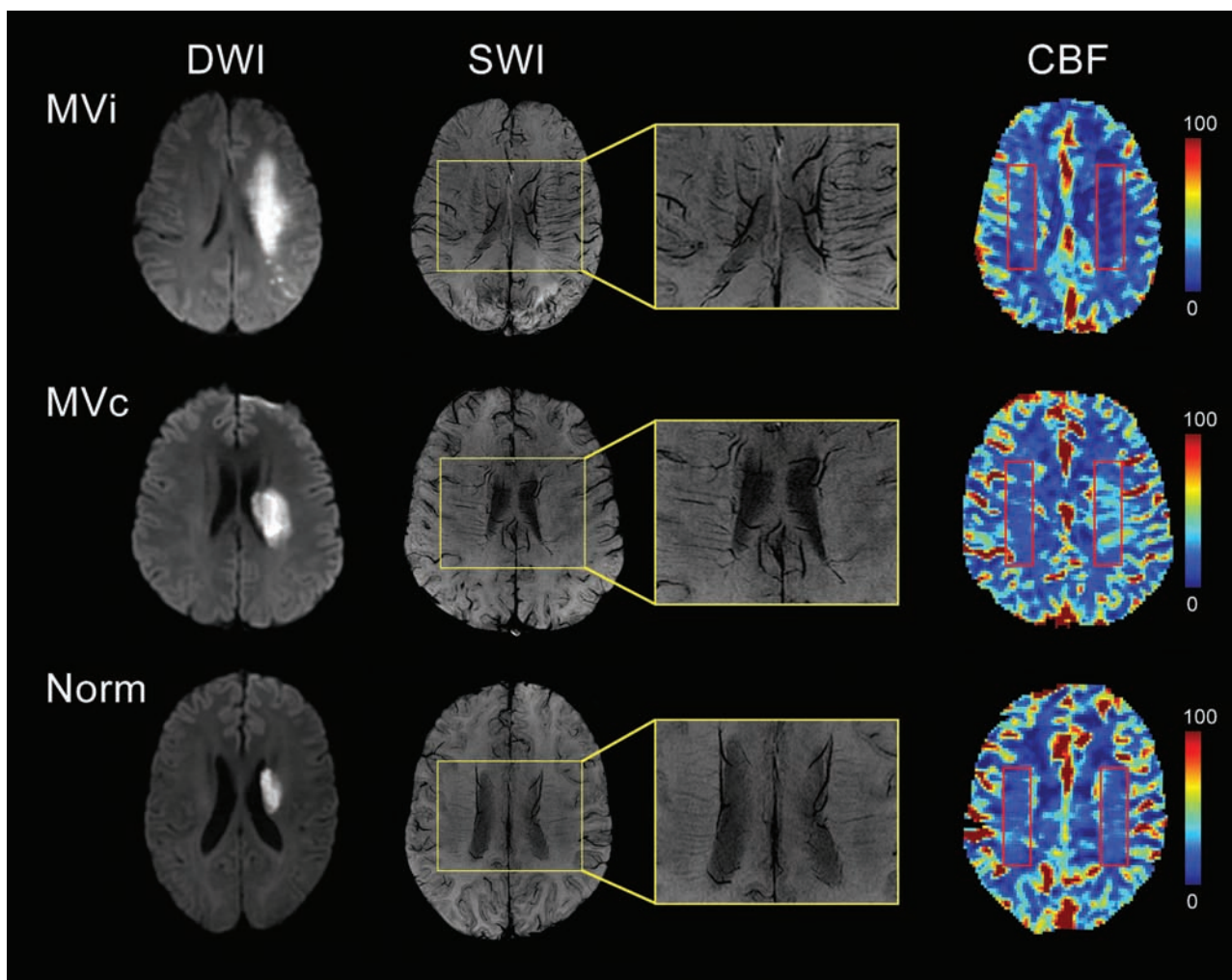


**FIG 1.** Examples of prominent medullary veins on susceptibility-weighted imaging with corresponding diffusion-weighted images and cerebral blood flow maps. *Top row:* Ipsilateral MV are seen in the deep white matter ipsilateral to the diffusion abnormality. CBF maps show decreased white matter perfusion in the corresponding area. *Red rectangles* illustrate the position of the ROIs used for calculation of  $\Delta$ CBF. *Middle row:* Contralateral MV are illustrated in the deep white matter contralateral to the diffusion abnormality. CBF maps show increased white matter perfusion in the corresponding area. *Bottom row:* Normal appearances. Susceptibility-weighted images show no evidence of prominent MV.

### Statistical Analysis

Continuous variables are shown as mean  $\pm$  SD or median (interquartile range), whereas categorical variables are presented as absolute and relative frequencies. Interrater reliability of prominent MV was assessed by using  $\kappa$  statistics. The clinical and imaging variables between good and poor outcome groups were analyzed by using a 2-sample independent  $t$  test or a Mann-Whitney  $U$  test for continuous variables and a Pearson  $\chi^2$  test or Fisher exact test for categorical variables. Univariate and multivariate logistic regression (forward method) models were used to determine the independent contribution of factors to clinical outcome. Specific variables (age, sex, NIHSS, and DWI lesion size) were preselected for entry into the model. Other variables were selected for entry into the model if the differences between good and poor outcome groups were significant at the  $P < .1$  level. The clinical and imaging variables among the 3 groups (MV<sub>i</sub>, MV<sub>c</sub>, and Norm) were compared by using 1-way ANOVA or the Kruskal-Wallis test for continuous variables and the Pearson  $\chi^2$  test or Fisher exact test for categorical variables. The independent factors associated with MV<sub>i</sub> and MV<sub>c</sub> were analyzed by using multivariate logistic regres-

sion analysis. Variables were selected for entry into the model only if the Spearman correlation coefficient was less than a 0.5 level. Odds ratios with their 95% confidence intervals of factors in logistic regression analysis were estimated. A 2-tailed value of  $P < .05$  was considered significant. Statistical analysis was performed by using SPSS 20.0 for Windows software (IBM, Armonk, New York).

## RESULTS

### Patient Characteristics

Forty-three patients were recruited (mean age,  $59.1 \pm 12.4$  years; range, 36 to 80 years); 25/43 (58.1%) were men. The time between MR imaging and symptom onset was  $4.9 \pm 1.4$  days (range, 3–7 days). The NIHSS score on admission was  $9.8 \pm 3.5$  (range, 5–17).

### Interrater Agreement for Evaluation of Prominent MV

Interrater agreement for the evaluation of prominent MV was excellent ( $\kappa = 0.927$ ), as it was for MV<sub>i</sub> ( $\kappa = 0.937$ ) and MV<sub>c</sub> ( $\kappa = 0.922$ ). Prominent MV were seen in 24/43 (55.8%) patients, with 14 (32.6%) MV<sub>i</sub> and 10 (23.2%) MV<sub>c</sub>.



### Factors Associated with Clinical Outcome

Twenty-four of 43 (55.8%) patients were classified as having good outcome, and 19/43 (44.2%), as having poor outcome. There were significant differences between the 2 groups in age ( $P = .008$ ), admission NIHSS score ( $P = .002$ ), site of arterial steno-occlusion ( $P = .085$ ), and prominent MV ( $P = .003$ ) (Table 1). Both MVi ( $P < .01$ ) and MVc ( $P < .05$ ) were significantly different between groups. MVi were significantly more common in the poor outcome group (57.9% versus 12.5%,  $P = .002$ ), and MVc were significantly more common in the good outcome group (37.5% versus 5.3%,  $P = .026$ ). Multivariate regression analysis demonstrated that MVi (OR, 11.19;

95% CI, 1.04–120.03;  $P = .046$ ), age (OR, 1.13; 95% CI, 1.03–1.24;  $P = .013$ ), and admission NIHSS score (OR, 1.67; 95% CI, 1.03–2.69;  $P = .036$ ) were independently associated with poor clinical outcome (Table 2).

### Relationship of Cerebral Blood Flow to MV Prominence

MVi were associated with a mean  $64.5 \pm 18.0\%$  (range, 33.6%–88.3%) decrease in  $\Delta$ CBF; and MVc, with a mean  $52.4 \pm 22.2\%$  (range, 30.1%–102.4%) increase (Fig 2). Subjective review of the CBF images showed that changes in  $\Delta$ CBF reflected decreases in CBF in the ipsilateral hemisphere in the presence of MVi and clear hyperperfusion in the presence of MVc (Fig 1). In addition to

$\Delta$ CBF ( $P < .001$ ), other factors, including admission NIHSS score ( $P = .042$ ), vascular status ( $P = .001$ ), site of arterial steno-occlusion ( $P < .001$ ), and DWI lesion volume ( $P < .001$ ), also showed significant differences among MVi, MVc, and Norm groups (Table 3). Vascular status was highly correlated with  $\Delta$ CBF ( $r = 0.617$ ,  $P < .001$ ) and DWI lesion volume ( $r = 0.736$ ,  $P < .001$ ). The site of arterial steno-occlusion was highly correlated with DWI lesion volume ( $r = 0.583$ ,  $P < .001$ ). Multiple logistic regression analysis showed that  $\Delta$ CBF was negatively related to MVi but positively associated with MVc (OR, 0.91; 95% CI, 0.85–0.97;  $P = .005$ ; and OR, 1.22; 95% CI, 1.01–1.47;  $P = .037$ ; respectively) (Table 4).

### DISCUSSION

The identification of predictive and prognostic biomarkers for patients with ischemic stroke has major potential clinical implications. In recent years, there has been increasing recognition that changes in the appearance of MV on SWI may provide novel, clinically rele-

**Table 1: Clinical and imaging characteristics between patients with good/poor outcome**

Variable	Good Outcome (n = 24)	Poor Outcome (n = 19)	P Value
Age (mean) (yr)	54.7 $\pm$ 11.0	64.6 $\pm$ 12.1	.008 <sup>a</sup>
Men (No.) (%)	12 (50.0)	13 (68.4)	.224
Time to MRI examination (mean) (day)	5.1 $\pm$ 1.4	4.8 $\pm$ 1.4	.489
Admission NIHSS score (mean)	8.4 $\pm$ 3.3	11.5 $\pm$ 2.9	.002 <sup>a</sup>
Vascular risk factors			
Diabetes mellitus (No.) (%)	11 (45.8)	9 (47.4)	.920
Hypertension (No.) (%)	11 (45.8)	7 (36.8)	.553
Hyperlipidemia (No.) (%)	10 (41.7)	12 (63.2)	.161
Smoking (No.) (%)	8 (33.3)	7 (36.8)	.811
Drinking (No.) (%)	6 (25.0)	5 (26.3)	1.000
Lesion left location (No.) (%)	15 (62.5)	8 (42.1)	.183
Vascular status (TIMI)			.285
Occlusion (TIMI 0)	9 (37.5)	11 (57.9)	
Stenosis (TIMI 1–2)	3 (12.5)	3 (15.8)	
Normal (TIMI 3)	12 (50.0)	5 (26.3)	
Site of arterial steno-occlusion			.085 <sup>b</sup>
Intracranial distal ICA	1 (4.2)	5 (26.3)	
MCA M1 segment	7 (29.2)	8 (42.1)	
MCA M2 segment	4 (16.7)	1 (5.3)	
None	12 (50.0)	5 (26.3)	
DWI lesion volume (median) (IQR) (cm <sup>3</sup> )	8.5 (2.5–17.1)	25.3 (3.9–45.5)	.101
Prominent MV			.003 <sup>a</sup>
MVi (No.) (%)	3 (12.5)	11 (57.9)	.002 <sup>a</sup>
MVc (No.) (%)	9 (37.5)	1 (5.3)	.026 <sup>c</sup>
Norm (No.) (%)	12 (50.0)	7 (36.8)	

Note:—IQR indicates interquartile range.

<sup>a</sup>  $P < .01$ .

<sup>b</sup>  $P < .1$ .

<sup>c</sup>  $P < .05$ .

**Table 2: The factors associated with poor clinical outcome**

Variable	Univariate Analysis (OR) (95% CI)	P Value	Multivariate Analysis (OR) (95% CI)	P Value
Age	1.078 (1.016–1.144)	.013 <sup>a</sup>	1.126 (1.026–1.237)	.013 <sup>a</sup>
Sex	2.167 (0.617–7.603)	.227	—	.768
Admission NIHSS score	1.368 (1.088–1.721)	.007 <sup>b</sup>	1.668 (1.033–2.694)	.036 <sup>a</sup>
DWI lesion volume	1.000 (1.000–1.000)	1.126	—	.201
Prominent MV		.009 <sup>b</sup>	—	.029 <sup>a</sup>
Norm	Reference	Reference	Reference	Reference
MVi	6.286 (1.294–30.538)	.023 <sup>a</sup>	11.188 (1.043–120.031)	.046 <sup>a</sup>
MVc	0.190 (0.020–1.837)	.152	0.025 (0.000–2.180)	.106
Site of arterial steno-occlusion		.120		.637
None	Reference	Reference	Reference	Reference
Intracranial distal ICA	12.000 (1.103–130.580)	.041	—	.334
MCA M1 segment	2.743 (0.640–11.753)	.174	—	.880
MCA M2 segment	0.600 (0.053–6.795)	.680	—	.491

Note:— indicates not applicable.

<sup>a</sup>  $P < .05$ .

<sup>b</sup>  $P < .01$ .

vant biomarkers. SWI is a relatively novel technique that maximizes sensitivity to susceptibility differences, caused by the presence of paramagnetic substances, by combining a long TE, high-resolution, fully flow-compensated sequence with a 3D gradient-echo sequence. Magnitude and phase data are both used in image reconstruction, and the technique is very sensitive for the detection of microhemorrhage but also for the detection of deoxygenated venous blood.<sup>17-19</sup> The sensitivity of SWI to high concentrations of deoxyhemoglobin produces high contrast between normal brain and venous structures, which has led to increasing interest in cerebral venous structures and venous abnormalities.

The initial observation by Morita et al<sup>1</sup> in 2008 of prominent MV in the ipsilateral hemisphere of patients with acute stroke was rapidly confirmed and given the name of the “brush sign.” Subsequent studies have shown a strong relationship between the presence of ipsilateral prominent MV and hemorrhagic transformation and outcome in patients undergoing thrombolytic therapy for hyperacute or acute stroke.<sup>2,3,9</sup>

The mechanisms producing increased prominence of MV reflect increased deoxyhemoglobin content within the imaged vox-

els. This may, in part, reflect an increase in venous volume due to vasodilation induced by regional ischemia.<sup>3,7</sup> However, it will also occur if the venous deoxyhemoglobin concentration is increased as a result of increases in oxygen extraction in the venous drainage territory.<sup>1,4-6</sup> A relationship between prominent MV and continuing ischemia in the drainage territory is in keeping with the observed relationships with poor clinical outcome and hemorrhagic transformation.

In the present study, we examined the implications of prominent MV in patients with subacute ischemic stroke, diagnosed after the therapeutic window for revascularization or recanalization therapies. Our initial clinical observations demonstrated that prominent MV are seen in this scenario but also that they may be seen in the hemisphere either ipsilateral or contralateral to the stroke.

Our first hypothesis, based on the results of previous studies, was that prominent ipsilateral MV are prognostic biomarkers of poor outcome in patients with subacute ischemic stroke. This is based on an assumption that prominent MV in the ipsilateral hemisphere reflect increased oxygen extraction due to continuing ischemia in the venous drainage territory. The findings supported this hypothesis, demonstrating that MV<sub>i</sub> were an independent prognostic feature for clinical outcome with an odds ratio of >11 (95% CI, 1.04–120.03; *P* < .05). Our second hypothesis was that prominent ipsilateral MV are associated with hypoperfusion. Once again the findings support the hypothesis, with significant decreases in  $\Delta$ CBF seen in association with prominent MV<sub>i</sub>. These findings suggest that in the subacute setting, a subgroup of patients with stroke identified by the presence of MV<sub>i</sub>, have poorer clinical outcomes resulting from continued ischemia of sufficient severity to require an increase in the oxygen extraction fraction. The poor clinical outcome may result from cellular bioenergetic failure, blood-brain barrier dysfunction, and postisch-

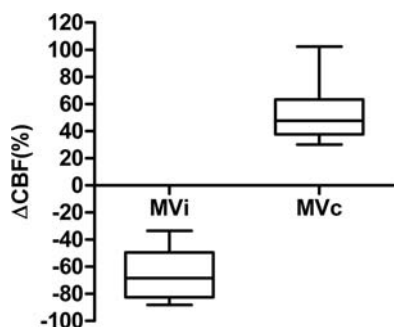


**FIG 2.** Changes in cerebral blood flow associated with ipsilateral and contralateral prominence of the medullary veins.

**Table 3: Clinical and imaging characteristics among MV<sub>i</sub>, MV<sub>c</sub>, and Norm groups**

Variable	MV <sub>i</sub> (n = 14)	MV <sub>c</sub> (n = 10)	Norm (n = 19)	P Value
Age (mean) (yr)	57.4 ± 12.2	53.5 ± 11.2	63.2 ± 12.4	.113
Men (No.) (%)	10 (71.4)	5 (50.0)	10 (52.6)	.528
Time to MRI examination (mean) (day)	4.6 ± 1.6	5.5 ± 1.4	4.9 ± 1.2	.312
Admission NIHSS score (mean)	11.5 ± 3.5	9.9 ± 4.3	8.5 ± 2.4	.042 <sup>a</sup>
Vascular risk factors				
Diabetes mellitus (No.) (%)	7 (50.0)	3 (30.0)	10 (52.6)	.501
Hypertension (No.) (%)	6 (42.9)	5 (50.0)	7 (36.8)	.858
Hyperlipidemia (No.) (%)	9 (64.3)	3 (30.0)	10 (52.6)	.287
Smoking (No.) (%)	6 (42.9)	4 (40.0)	5 (26.3)	.651
Drinking (No.) (%)	5 (35.7)	2 (20.0)	4 (21.1)	.662
Lesion left location (No.) (%)	6 (42.9)	8 (80.0)	9 (47.4)	.117
Vascular status (TIMI)				.001 <sup>b</sup>
Occlusion (TIMI 0)	12 (85.7)	2 (20.0)	6 (31.6)	
Stenosis (TIMI 1–2)	2 (14.3)	1 (10.0)	3 (15.8)	
Normal (TIMI 3)	0 (0.0)	7 (70.0)	10 (52.6)	
Site of arterial steno-occlusion				<.001 <sup>b</sup>
Intracranial distal ICA	4 (28.6)	1 (10.0)	1 (5.3)	
MCA M1 segment	9 (64.3)	1 (10.0)	6 (26.3)	
MCA M2 segment	1 (7.1)	1 (10.0)	3 (15.8)	
None	0 (0.0)	7 (70.0)	10 (52.6)	
DWI lesion volume (median) (IQR) (cm <sup>3</sup> )	30.2 (16.4–46.4)	9.5 (7.5–20.8)	3.3 (2.2–8.5)	<.001 <sup>b</sup>
$\Delta$ CBF (mean) (%)	−64.5 ± 18.0	52.4 ± 22.2	4.8 ± 9.9	<.001 <sup>b</sup>

**Note:**—IQR indicates interquartile range.

<sup>a</sup>*P* < .05.

<sup>b</sup>*P* < .01.

**Table 4: Results of multiple logistic regression analysis for the MV prominence**

Variable	P Value	OR	95% CI	
MVi				
Admission NIHSS score	.987	1.004	0.604	1.671
DWI lesion volume	.217	1.000	1.000	1.000
ΔCBF	.005 <sup>a</sup>	0.910	0.851	0.972
MVc				
Admission NIHSS score	.116	2.213	0.822	5.961
DWI lesion volume	.023 <sup>b</sup>	1.000	1.000	1.000
ΔCBF	.037 <sup>b</sup>	1.217	1.012	1.464

<sup>a</sup>  $P < .01$ .<sup>b</sup>  $P < .05$ .

emic inflammation, all of which are related to poor clinical outcome.<sup>20</sup>

Our third hypothesis was that prominent contralateral MV may provide additional prognostic information. Although MVc did not provide independent significant predictive power for clinical outcome, there was a significant difference in the incidence between outcome groups with MVc, seen in 37.5% of patients with good outcome and only 5.3% of patients with poor outcome ( $P < .05$ ). Prominent MVc were associated with a significant increase in ΔCBF, reflecting hyperperfusion in the ipsilateral hemisphere. The presence of perilesional hyperperfusion in the early postinfarct stage has been recognized for >20 years.<sup>21,22</sup> Hyperperfusion occurs in the ischemic penumbra following recanalization or reperfusion and is seen in up to 50% of patients with a mean delay of 5.8 days from ictus.<sup>23,24</sup> There is extensive evidence that hyperperfusion causes a decreased oxygen extraction fraction and is associated with improved clinical outcome.<sup>22,23,25-27</sup> However, there is also a link between hyperperfusion and increased risk of hemorrhagic transformation.<sup>28</sup> The mechanism of hyperperfusion is incompletely understood, but regional increases in cerebral metabolism have been demonstrated by using MR spectroscopy, leading to the suggestion that local metabolic changes produce local vasodilation.<sup>25</sup> Vasodilation induced by early recanalization may decrease the resistance to blood flow, allowing an increase in CBF. Other works have suggested that cerebrovascular autoregulation fails to re-establish for a time following reperfusion.<sup>23</sup> Whatever the underlying mechanism, it is likely to represent regional decreases in cerebrovascular resistance. These unilateral changes in cerebrovascular resistance, particularly in the presence of proximal arterial occlusions, will promote collateral flow via the circle of Willis or leptomeningeal vessels. We hypothesize that prominent MVc indirectly reflect increased CBF in the ipsilateral hemisphere due to spontaneous recanalization or collateral flow, resulting in relatively decreased deoxyhemoglobin concentration in the draining veins due to excessive oxygen delivery and thus an increase in signal intensity within the medullary veins.

Our study is limited by its relatively small sample size ( $n = 43$ ) and cross-sectional design; therefore, our results should be interpreted cautiously. Second, both SWI and MRA data were collected at the same time point; thus, the causal relationship between change of vascular status and prominence of MV cannot be answered in the current study.

## CONCLUSIONS

This study shows that prominence of MV on SWI in the hemisphere ipsilateral to stroke has significant power to predict clinical outcome, similar to that seen in patients in the acute stroke setting. We have described the relationship between the prominence of MV in the contralateral hemisphere and good clinical outcome which, we hypothesize, reflects the development of penumbral hypoperfusion in combination with spontaneous recanalization or active collateral flow via the circle of Willis or leptomeningeal vessels.

Disclosures: Peiyu Huang—UNRELATED: Grants/Grants Pending: National Natural Science Foundation of China.\* Quan Jiang—UNRELATED: National Institutes of Health (R01 NS64134). Minming Zhang—RELATED: National Natural Science Foundation of China (No. 81271530) and the Zhejiang Provincial Natural Science Foundation of China (No. LZ14H180001); UNRELATED: Grants/Grants Pending: National Natural Science Foundation of China. \*Money paid to the institution.

## REFERENCES

- Morita N, Harada M, Uno M, et al. Ischemic findings of T2\*-weighted 3-Tesla MRI in acute stroke patients. *Cerebrovasc Dis* 2008; 26:367–75 CrossRef Medline
- Terasawa Y, Yamamoto N, Morigaki R, et al. Brush sign on 3-T T2\*-weighted MRI as a potential predictor of hemorrhagic transformation after tissue plasminogen activator therapy. *Stroke* 2014;45: 274–76 CrossRef Medline
- Rosso C, Belleville M, Pires C, et al. Clinical usefulness of the visibility of the transcerebral veins at 3T on T2\*-weighted sequence in acute stroke patients. *Eur J Radiol* 2012;81:1282–87 CrossRef Medline
- Tamura H, Hatazawa J, Toyoshima H, et al. Detection of deoxygenation-related signal change in acute ischemic stroke patients by T2\*-weighted magnetic resonance imaging. *Stroke* 2002;33:967–71 CrossRef Medline
- Kesavadas C, Santhosh K, Thomas B. Susceptibility weighted imaging in cerebral hypoperfusion: can we predict increased oxygen extraction fraction? *Neuroradiology* 2010;52:1047–54 CrossRef Medline
- Haacke EM, Xu Y, Cheng YC, et al. Susceptibility weighted imaging (SWI). *Magn Reson Med* 2004;52:612–18 CrossRef Medline
- Hermier M, Nighoghossian N, Derex L, et al. Hypointense transcerebral veins at T2\*-weighted MRI: a marker of hemorrhagic transformation risk in patients treated with intravenous tissue plasminogen activator. *J Cereb Blood Flow Metab* 2003;23:1362–70 Medline
- Hermier M, Nighoghossian N, Derex L, et al. Hypointense leptomeningeal vessels at T2\*-weighted MRI in acute ischemic stroke. *Neurology* 2005;65:652–53 CrossRef Medline
- Lou M, Chen Z, Wan J, et al. Susceptibility-diffusion mismatch predicts thrombolytic outcomes: a retrospective cohort study. *AJNR Am J Neuroradiol* 2014;35:2061–67 CrossRef Medline
- Reinhard M, Roth M, Guschlbauer B, et al. Dynamic cerebral autoregulation in acute ischemic stroke assessed from spontaneous blood pressure fluctuations. *Stroke* 2005;36:1684–89 CrossRef Medline
- Kasner SE. Clinical interpretation and use of stroke scales. *Lancet Neurol* 2006;5:603–12 CrossRef Medline
- Denk C, Rauscher A. Susceptibility weighted imaging with multiple echoes. *J Magn Reson Imaging* 2010;31:185–91 CrossRef Medline
- Horie N, Morikawa M, Nozaki A, et al. “Brush sign” on susceptibility-weighted MR imaging indicates the severity of Moyamoya disease. *AJNR Am J Neuroradiol* 2011;32:1697–702 CrossRef Medline
- Jørgensen HS, Sperling B, Nakayama H, et al. Spontaneous reperfusion of cerebral infarcts in patients with acute stroke: incidence,

- time course, and clinical outcome in the Copenhagen Stroke Study. *Arch Neurol* 1994;51:865–73 CrossRef Medline
15. Neumann-Haefelin T, Wittsack HJ, Fink GR, et al. **Diffusion- and perfusion-weighted MRI: influence of severe carotid artery stenosis on the DWI/PWI mismatch in acute stroke.** *Stroke* 2000;31:1311–17 CrossRef Medline
  16. Fiebach JB, Al-Rawi Y, Wintermark M, et al. **Vascular occlusion enables selecting acute ischemic stroke patients for treatment with desmoteplase.** *Stroke* 2012;43:1561–66 CrossRef Medline
  17. Haddad D, Haacke E, Sehgal V, et al. **Susceptibility weighted imaging: theory and applications** [in French]. *J Radiol* 2004;85: 1901–08 CrossRef Medline
  18. Mittal S, Wu Z, Neelavalli J, et al. **Susceptibility-weighted imaging: technical aspects and clinical applications, part 2.** *AJNR Am J Neuroradiol* 2009;30:232–52 Medline
  19. Haacke EM, Mittal S, Wu Z, et al. **Susceptibility-weighted imaging: technical aspects and clinical applications, part 1.** *AJNR Am J Neuroradiol* 2009;30:19–30 Medline
  20. Brouns R, De Deyn P. **The complexity of neurobiological processes in acute ischemic stroke.** *Clin Neurol Neurosurg* 2009;111:483–95 CrossRef Medline
  21. Marchal G, Serrati C, Rioux P, et al. **PET imaging of cerebral perfusion and oxygen consumption in acute ischaemic stroke: relation to outcome.** *Lancet* 1993;341:925–27 CrossRef Medline
  22. Marchal G, Furlan M, Beaudouin V, et al. **Early spontaneous hyperperfusion after stroke: a marker of favourable tissue outcome?** *Brain* 1996;119:409–19 CrossRef Medline
  23. Bivard A, Stanwell P, Levi C, et al. **Arterial spin labeling identifies tissue salvage and good clinical recovery after acute ischemic stroke.** *J Neuroimaging* 2013;23:391–96 CrossRef Medline
  24. Bowler JV, Wade JP, Jones BE, et al. **Natural history of the spontaneous reperfusion of human cerebral infarcts as assessed by 99mTc HMPAO SPECT.** *J Neurol Neurosurg Psychiatry* 1998;64:90–97 CrossRef Medline
  25. Bivard A, Krishnamurthy V, Stanwell P, et al. **Spectroscopy of reperfused tissue after stroke reveals heightened metabolism in patients with good clinical outcomes.** *J Cereb Blood Flow Metab* 2014;34: 1944–50 CrossRef Medline
  26. Takamatsu H, Tsukada H, Kakiuchi T, et al. **Detection of reperfusion injury using PET in a monkey model of cerebral ischemia.** *J Nucl Med* 2000;41:1409–16 Medline
  27. Kaku Y, Iihara K, Nakajima N, et al. **Cerebral blood flow and metabolism of hyperperfusion after cerebral revascularization in patients with moyamoya disease.** *J Cereb Blood Flow Metab* 2012;32:2066–75 CrossRef Medline
  28. Yu S, Liebeskind DS, Dua S, et al; UCLA Stroke Investigators. **Post-ischemic hyperperfusion on arterial spin labeled perfusion MRI is linked to hemorrhagic transformation in stroke.** *J Cereb Blood Flow Metab* 2015;35:630–37 CrossRef Medline



# Structural Brain Alterations in Community Dwelling Individuals with Chronic Joint Pain

M. de Kruijf, D. Bos, F.J.P.M. Huygen,  W.J. Niessen, H. Tiemeier,  A. Hofman, A.G. Uitterlinden,  M.W. Vernooij,  M.A. Ikram, and J.B.J. van Meurs



## ABSTRACT

**BACKGROUND AND PURPOSE:** Central sensitization in chronic pain involves structural brain changes that influence vulnerability to pain. Identifying brain regions involved in pain processing and sensitization can provide more insight into chronic pain. This study examines structural brain changes in chronic pain and experimental pain in a large population-based study.

**MATERIALS AND METHODS:** For 3892 participants in the Rotterdam study, global and regional MR imaging brain volumes were automatically segmented and quantified. Chronic joint pain was defined as pain for more than half of all days during the past 6 weeks. Heat pain thresholds were measured in a subset of 1538 individuals. The association between the presence of chronic joint pain and global and lobar brain volumes was studied. Subsequently, literature was reviewed and the association of chronic pain and heat pain thresholds with 11 brain regions associated with musculoskeletal pain in previous publications was studied.

**RESULTS:** Total gray matter volume was smaller in women with chronic pain ( $\beta = -0.066$ ,  $P = .016$ ). This effect was primarily driven by lower gray matter volume in the temporal lobe ( $\beta = 0.086$ ,  $P = .005$ ), the frontal lobe ( $\beta = -0.060$ ,  $P = .039$ ), and the hippocampus ( $\beta = -0.099$ ,  $P = .002$ ). In addition, we observed that a lower heat pain threshold was associated with smaller volumes of the hippocampus ( $\beta = 0.017$ ,  $P = .048$ ), the thalamus ( $\beta = 0.018$ ,  $P = .009$ ), and the anterior cingulate cortex ( $\beta = -0.016$ ,  $P = .037$ ). In men, no significant associations were observed.

**CONCLUSIONS:** The primary identified brain areas, the temporal and frontal lobes and the hippocampus, indicated involvement of emotional processing. The volumetric differences found indicated a sex-specific neuroplasticity in chronic pain. These results emphasized sex-specific and multidisciplinary pain treatment.

Chronic musculoskeletal pain is very common in the general elderly population, with a prevalence up to 50%–60%. Experienced chronic joint pain does not always reflect the extent of

objective pathology.<sup>1–4</sup> Central sensitization plays an important role in the development of chronic joint pain. Chronic pain and central sensitization result in higher vulnerability for developing chronic pain at multiple sites and higher sensitivity for painful stimuli.<sup>5</sup> Differences in pain processing may be expressed in functional and structural changes in the nervous system. MR imaging allows us to identify brain regions involved in this process of central sensitization, which can provide more insight into chronic pain.


Previous studies that examined structural brain alterations in chronic pain focused on a variety of pain phenotypes, such as migraine, back pain, osteoarthritis, and fibromyalgia.<sup>6–15</sup> Typically, the study size was small; the largest studies included approximately 100 subjects. The small sample sizes of these studies led to a modest statistical power, thereby influencing the reproducibility of the results.<sup>16</sup> In addition, all previous reports had a case-control design, which selected individuals who were referred to the clinic as chronic pain cases. As a result, many different areas were shown to associate with a particular pain phenotype but only a few areas of the brain showed consistent associations. For example,


Received January 17, 2015; accepted after revision July 11.

From the Departments of Internal Medicine (M.d.K., A.G.U., J.B.J.v.M.), Anaesthesiology (M.d.K., F.J.P.M.H.), Radiology (D.B., W.J.N., M.W.V., M.A.I.), Epidemiology (D.B., H.T., A.H., A.G.U., M.W.V., M.A.I.), Medical Informatics (W.J.N.), and Neurology (M.A.I.), Erasmus MC, University Medical Center, Rotterdam, the Netherlands; and Faculty of Applied Sciences (W.J.N.), Delft University of Technology, Delft, the Netherlands.

This study was funded by the Netherlands Society for Scientific Research VIDI Grant 917103521. The Rotterdam Study is funded by Erasmus Medical Center and Erasmus University (Rotterdam), Netherlands Organization for the Health Research and Development, the Research Institute for Diseases in the Elderly, the Ministry of Education, Culture and Science, the Ministry for Health, Welfare and Sports, the European Commission (DG XII), and the Municipality of Rotterdam.

Please address correspondence to Joyce van Meurs, PhD, Genetic Laboratory Department of Internal Medicine, Room Ee579b, Erasmus MC, MC PO Box 1738, 3000 DR Rotterdam, the Netherlands; e-mail: j.vanmeurs@erasmusmc.nl

 Indicates open access to non-subscribers at [www.ajnr.org](http://www.ajnr.org)

 Indicates article with supplemental on-line table.

<http://dx.doi.org/10.3174/ajnr.A4556>

the thalamus was found to be positively associated with chronic low back pain by Schmidt-Wilcke et al.<sup>17</sup> but negatively associated with chronic low back pain by Apkarian et al.<sup>18</sup> Regions that are part of the limbic system and signaling pathway were among the identified pain-associated brain areas. Furthermore, each different pain phenotype showed different patterns of structural brain changes, with some overlapping regions, for example, the hippocampus.<sup>7</sup> Despite the possible identification of structural brain alterations in these selected clinical cases, it remains unclear which brain regions are morphologically altered in chronic pain in the general population. Therefore, in this study, after review of the existing literature, we attempted to replicate previous identified regions to find brain structures robustly associated with musculoskeletal pain.

Individuals with chronic pain are shown to be more sensitive to experimental pain stimuli. Central sensitization can be detected by lower pain thresholds.<sup>19–21</sup> The stimulus response curve is shifted to the left, which results in lower pain thresholds or higher reported pain intensity scores for a stimulus. The spread of central sensitization, manifested because general hyperalgesia is one of the fundamental processes in the development of chronic pain.<sup>22–25</sup> Lower pain thresholds, as part of central sensitization, might be associated with structural brain changes. Thus far, the relation between experimental pain and structural brain alterations has only been studied in 1 study of 80 healthy individuals.<sup>26</sup> In addition, Seminowicz et al.<sup>27</sup> showed, in a rat model for long-term neuropathic pain, that thermal and mechanical hyperalgesia is associated with structural brain changes.

Given the high prevalence of chronic musculoskeletal pain in the elderly and the burden of chronic musculoskeletal pain on quality of life, more insight into the pathophysiology is necessary to understand chronic pain in the general population and improve treatment options. In this study, we examined, in a large population-based cohort study, the association of chronic musculoskeletal pain and heat pain thresholds with MR imaging-based structural brain changes. We studied changes in global and lobar brain volumes and, in addition, specific brain regions previously reported to be associated with musculoskeletal pain phenotypes.

## MATERIALS AND METHODS

### **Study Population: The Rotterdam Study**

The Rotterdam Study is a large prospective population-based cohort study of persons ages 45 years and older. The study design and rationale are described elsewhere in detail.<sup>28</sup> In summary, the objective of the Rotterdam Study is to investigate the determinants, incidence, and progression of chronic disabling diseases in the elderly. The first cohort, Rotterdam Study I consisted of 7983 persons ages  $\geq 55$  years and was initiated in 1989. This study population was extended in 2000, which added 3011 participants in Rotterdam Study II and, in 2005, added another 3932 subjects ages  $\geq 45$  years in Rotterdam Study III. All the participants were examined in detail at baseline. In summary, a home interview was conducted, and the subjects had an extensive set of examinations at the research center.

The participants in the study as presented here were derived from the Rotterdam Scan Study,<sup>29</sup> an ongoing population-

based cohort study that investigated brain changes on MR imaging, which is embedded in the Rotterdam Study. The Rotterdam Study has been approved by the medical ethics committee according to the Population Study Act Rotterdam Study executed by the Ministry of Health, Welfare and Sports of the Netherlands. Written informed consent was obtained from all the participants.

### **MR Imaging Acquisition and Processing**

MR imaging scanning was performed on a 1.5T-scanner with an 8-channel head coil (GE Healthcare, Milwaukee, Wisconsin). An extensive description of the scan protocol is provided elsewhere.<sup>29</sup> In short, the protocol included a T1-weighted sequence, a proton-attenuation weighted sequence, and a fluid-attenuated inversion recovery sequence.<sup>29</sup>

Automated brain tissue classification based on a k-nearest-neighbor-classifier algorithm extended with white matter lesion segmentation<sup>30,31</sup> was used to quantify global and lobar brain volume, gray matter volume, white matter volume, and intracranial volume (in mL<sup>3</sup>). This method has been optimized and validated for the Rotterdam Scan Study and includes a standardized and validated image analysis workflow to enable objective, accurate, and reproducible extraction of brain volumes.<sup>29</sup> Segmentation and labeling of smaller specific brain regions was performed by FreeSurfer version 4.5 (<http://surfer.nmr.mgh.harvard.edu/>).<sup>26</sup> This procedure automatically assigns a neuroanatomic label to each voxel in an MR imaging volume based on probabilistic information obtained from a manually labeled training set. FreeSurfer was used with the default parameters, including skull-stripping and using the automatically generated brain mask.

### **Review of the Literature and Selection of Candidate Replication Regions**

We systematically searched the literature by using the PubMed data base on July 7, 2014, with search terms “structural and brain and MR imaging and chronic and pain.” In addition, we screened the references of included articles to extend the search. The review of literature identified 83 articles, of which 68 articles were excluded based on the following selection criteria: 1) the article represents original data, and 2) the trait of interest is musculoskeletal pain. Finally, 15 studies were included in the total review.

### **Assessment of Chronic Joint Pain**

All the participants completed a pain homunculus to report chronic painful sites in the body. The pain homunculus showed a picture of the front and the back of the human body. The participants were asked the following question, “Did you have pain anywhere in your body, for at least half of the days, during the last six weeks?” Circles were drawn by the participant around the painful areas. The homunculi were scored by using a template that assigned 14 different joint pain regions (eg, neck, shoulders, elbows, hands, low back, hips, knees, feet). Chronic joint pain was defined as subjects having one or more painful sites. Furthermore, participants should have visited a medical physician at least once for this chronic joint

**Table 1: Selected brain regions for analysis**

Brain Region	Reference	+/-	N	Chronic Pain Disorder
Thalamus	Apkarian et al, 2004 <sup>18</sup>	—	52	CLBP
	Schmidt-Wilcke et al, 2006 <sup>17</sup>	+	36	CLBP
	Schmidt-Wilcke et al, 2007 <sup>40</sup>	—	42	Fibromyalgia
	Ivo et al, 2013 <sup>9</sup>	—	28	CLBP
S1	Rodriguez-Raecke et al, 2009 <sup>39</sup>	—	32	Hip OA
	Seminowicz et al, 2011 <sup>41</sup>	—	34	CLBP
	Kong et al, 2013 <sup>36</sup>	+	36	CLBP
Insular cortex	Kuchinad et al, 2007 <sup>37</sup>	—	20	Fibromyalgia
	Rodriguez-Raecke et al, 2009 <sup>39</sup>	—	32	Hip OA
	Valet et al, 2009 <sup>42</sup>	—	39	Pain syndrome (DSM IV)
	Robinson et al, 2011 <sup>11</sup>	—	25	Fibromyalgia
	Seminowicz et al, 2011 <sup>41</sup>	—	34	CLBP
Anterior cingulate cortex	Burgmer et al, 2009 <sup>34</sup>	—	28	Fibromyalgia
	Valet et al, 2009 <sup>42</sup>	—	39	Pain syndrome (DSM IV)
	Rodriguez-Raecke et al, 2009 <sup>39</sup>	—	32	Hip OA
	Seminowicz et al, 2011 <sup>41</sup>	—	34	CLBP
Midcingulate cortex	Jensen et al, 2013 <sup>35</sup>	—	39	Fibromyalgia
	Kuchinad et al, 2007 <sup>37</sup>	—	20	Fibromyalgia
	Buckalew et al, 2008 <sup>33</sup>	—	16	CLBP
	Wood et al, 2009 <sup>43</sup>	—	14	Fibromyalgia
	Robinson et al, 2011 <sup>11</sup>	—	25	Fibromyalgia
Prefrontal cortex dorsolateral	Ivo et al, 2013 <sup>9</sup>	—	28	CLBP
	Apkarian et al, 2004 <sup>18</sup>	—	52	CLBP
	Seminowicz et al, 2011 <sup>41</sup>	—	34	CLBP
Prefrontal cortex ventrolateral	Ivo et al, 2013 <sup>9</sup>	—	28	CLBP
	Rodriguez-Raecke et al, 2009 <sup>39</sup>	—	32	Hip OA
	Burgmer et al, 2009 <sup>34</sup>	—	28	Fibromyalgia
Posterior cingulate cortex	Seminowicz et al, 2011 <sup>41</sup>	—	34	CLBP
	Kuchinad et al, 2007 <sup>37</sup>	—	20	Fibromyalgia
	Valet et al, 2009 <sup>42</sup>	—	39	Pain syndrome (DSM IV)
	Wood et al, 2009 <sup>43</sup>	—	14	Fibromyalgia
Orbitofrontal cortex	Robinson et al, 2011 <sup>11</sup>	—	25	Fibromyalgia
	Schmidt-Wilcke et al, 2007 <sup>40</sup>	+	42	Fibromyalgia
	Valet et al, 2009 <sup>42</sup>	—	39	Pain syndrome (DSM IV)
	Rodriguez-Raecke et al, 2009 <sup>39</sup>	—	32	Hip OA
Hippocampus	Seminowicz et al, 2011 <sup>41</sup>	—	34	CLBP
	Lutz et al, 2008 <sup>38</sup>	—	60	Fibromyalgia
Amygdala	Zimmerman et al, 2009 <sup>14</sup>	—	20	Chronic pain
	Burgmer et al, 2009 <sup>34</sup>	—	28	Fibromyalgia
	Rodriguez-Raecke et al, 2009 <sup>39</sup>	—	32	Hip OA

**Note:**—+ indicates larger volume in chronic pain; —, smaller volume in chronic pain; CLBP, chronic low back pain; OA, osteoarthritis; DSMIV, *Diagnostic and Statistical Manual of Mental Disorders, 4th Edition*.

**Table 2: Baseline characteristics of the study population**

	Total (n = 3376)	Men (n = 1525)	Women (n = 1851)
Mean age, y	60.3 ± 8.7	60.4 ± 8.7	60.1 ± 8.7
Chronic pain, no. (%)	1191 (35.3)	414 (27.1)	777 (42.0)
Mean intracranial volume, mL	1126 ± 119	1203 ± 102	1062 ± 91
Positive CESD, no. (%)	328 (8.5)	81 (4.6)	247 (11.7)
Mean heat pain threshold, °C (n = 1538)	47.2 ± 3.2	48.0 ± 2.7	46.6 ± 3.4

**Note:**—CESD indicates Center for Epidemiologic Studies Depression scale.

pain. This information was derived from the questionnaire during the home interview.

In addition, because we used a more heterogenic pain phenotype compared with previous studies, we defined 3 chronic pain phenotypes to be able to compare our results better with previous literature. The phenotypes examined in the studies, also selected for the review, were fibromyalgia, chronic low back pain, and hip osteoarthritis pain. Because we did not have data on fibromyalgia, we used chronic widespread pain as a proxy. Chronic widespread pain was defined as subjects having

pain in the left side of the body, in the right side of the body, above the waist, below the waist, and in the axial skeleton (by following the Fibromyalgia Criteria of the American College of Rheumatology).<sup>32</sup> Hip osteoarthritis pain was defined as a Kellgren-Lawrence score of  $\geq 2$  and chronic pain in the same hip. Controls in these analyses were individuals without chronic pain.

### Heat Pain Threshold Measurement

For the measurement of heat pain threshold, we used a commercially available thermosensory analyzer, the TSA II (Medoc Advanced Medical Systems, Durham, North Carolina). The probe, with a surface of 2 cm by 2 cm was placed on the ventral site of the nondominant forearm. The start temperature of the probe was 32°C. The temperature increased by 2°C per second, and the participant was asked to push a large quiz button when the temperature became painful. This measurement was repeated 5 times; the mean of the last 3 measurements was used. Because this was measured approximately 5 years after the brain MR imaging was acquired, we included only those individuals with a stable pain state. Individuals with chronic pain at both the time of brain MR imaging and chronic pain at the time of the heat pain threshold measurement were considered as cases, individuals without chronic pain at both time points were considered as controls.

### Population for Analysis

A total of 4898 participants who were part of Rotterdam Study I, Rotterdam Study II, or Rotterdam Study III were invited to undergo an MR imaging. We excluded individuals who had dementia

(n = 30) or had MR imaging contraindications (n = 389). Of 4479 eligible persons, 4082 (91%) participated. Due to physical inability, imaging could not be performed in 44 individuals. Of 4038 persons with complete MR imaging examinations, 59 had to be excluded because of motion artifacts or susceptibility artifacts on their scans, which left 3979 persons with complete brain MR imaging. Pain data were not available for 87 of these persons, whereas data on the need for medical treatment for the pain medication was not available for 516 individuals, which left 3376 persons for the analyses. For the association analysis with the heat

pain threshold measurements, a subset of 839 individuals with a stable pain state as described above was used.

### Statistical Analysis

Linear regression models were used to test the association between chronic musculoskeletal pain, heat pain thresholds, and brain volumes. We calculated  $z$  scores  $(X - \text{mean}/\text{SD})$  of the brain volumes to allow direct comparability between the various effect estimates for the analyses between pain and the different brain structures.  $Z$  score standardization is done in the common way by  $(\text{brain volume} - \text{mean brain volume})/\text{SD}$ .

Because previous studies found differences on pain-associated regions between the sexes, we stratified for sex and adjusted for age, intracranial volume, and the presence of depression according to the self-reporting Center for Epidemiologic Studies Depression scale, defined by a score of  $>16$ . SPSS version 21.0 (SPSS Statistics for Windows; IBM, Armonk, New York) was used for the association analysis. The null hypothesis tested was that there is no difference in brain volumes in the studied structures between individuals without chronic musculoskeletal and those with chronic musculoskeletal pain. The second hypothesis tested was that brain volumes of the studied structures are not associated with heat pain thresholds. A  $P$  value of  $<.05$  was considered statistically significant.

### Association Analysis with Chronic Musculoskeletal Pain and Heat Pain Threshold

First, we performed an association analysis without hypothesizing where to expect structural alterations in the brain in chronic joint pain. Therefore, we investigated the association of global volumes of gray and white matter with chronic joint pain. Next, we segmented the brain into the 4 main lobes (frontal, temporal, parietal, and occipital). Gray and white matter volumes in the different lobes were then studied for the association with chronic joint pain. Subsequently, we investigated the association of chronic joint pain with the volumes of the selected regions reported in the literature (Table 1).

In the effort to replicate previous findings, we examined the association of chronic widespread pain as a proxy for fibromyalgia, chronic low back pain, and hip osteoarthritis pain with brain region volumes in our sample. In addition, we investigated the association of the brain region volumes with heat pain thresholds.

## RESULTS

Population characteristics for the 3892 persons with brain MR imaging and chronic pain information are shown in Table 2. The prevalence of chronic pain and depression was higher in women compared with men, and the total intracranial volume was smaller in women. Heat pain thresholds were higher in men compared with women ( $48.0^{\circ}\text{C}$  vs  $46.6^{\circ}\text{C}$ ).

### Chronic Joint Pain and Global and Lobar Brain Volumes

The associations between chronic musculoskeletal pain and global and lobar brain volumes are shown in Fig 1. No significant association between chronic musculoskeletal pain and total brain volume was observed in the overall population.

When we stratified according to sex, we observed a significant association with total gray matter in the women. Total gray matter was smaller in women with chronic pain (difference in  $Z$  score,  $\beta = -0.066$ ;  $P = .016$ ). When we divided the brain into the 4 main lobes, this lower gray matter volume was found to be primarily located in the temporal lobe ( $\beta = -0.086$ ,  $P = .005$ ) and the frontal lobe ( $\beta = -0.060$ ,  $P = .039$ ). In the men, we did not find differences in global brain volumes between participants with and those without chronic pain. Excluding participants with depression defined by a Center for Epidemiologic Studies Depression scale score of  $>16$  (81 men, 247 women) in the sensitivity analysis did not alter these effects.

### Chronic Joint Pain and Predefined Brain Regions

Next, we focused our analysis on volumes of specific brain regions that were previously reported in the literature as being associated with musculoskeletal pain phenotypes (Table 1). These regions were selected on the basis of a systematic review. In total, 15 studies that assessed the relationship between brain structures and chronic pain were included in this review.<sup>9,11,14,17,33-43</sup> All brain regions previously reported to be significantly associated with chronic pain are shown in the On-line Table, together with the direction of the effect. We decided to include the brain regions that were reported to be associated with musculoskeletal pain at least twice. The 11 selected regions are shown in Table 1, together with the sample size of each study, which were all fewer than 100 individuals. Segmentation of the 11 brain regions was done in 4898 individuals with the use of FreeSurfer software. We observed a significantly smaller hippocampal volume in women with chronic musculoskeletal pain ( $\beta = -0.099$ ,  $P = .002$ ), whereas men showed a similar trend, though this did not reach significance (Fig 2). When data for men and women were analyzed together, a highly significant association was seen ( $\beta = -0.092$ ,  $P = 4.69 \times 10^{-4}$ ).

We next studied specific pain subtypes to mimic earlier reports. We studied chronic widespread pain, chronic low back pain, and hip osteoarthritis pain separately as determinants for brain region volumes. For the analyses of chronic widespread pain and hip osteoarthritis pain, we observed similar effect directions for hippocampal volume but only for chronic low back pain was statistical significance reached ( $\beta = -0.115$ ,  $P = .033$ ).

Among the subset with heat pain threshold measurements, we observed only in the women, a positive association between heat pain thresholds and hippocampal volume, thalamic volume, and the volume of the anterior cingulate cortex (Fig 3), which indicated that lower pain sensitivity thresholds, which represent central sensitization, were indeed coinciding with smaller hippocampal, thalamic, and anterior cingulate cortex volumes.

## DISCUSSION

In this large population-based cohort of individuals with ages  $\geq 45$  years, we observed that chronic musculoskeletal pain was associated with a smaller global gray matter volume in the women. This smaller volume was primarily found in the temporal lobe, more specifically, in the hippocampus, part of the limbic system. In addition, again in the women, a lower heat



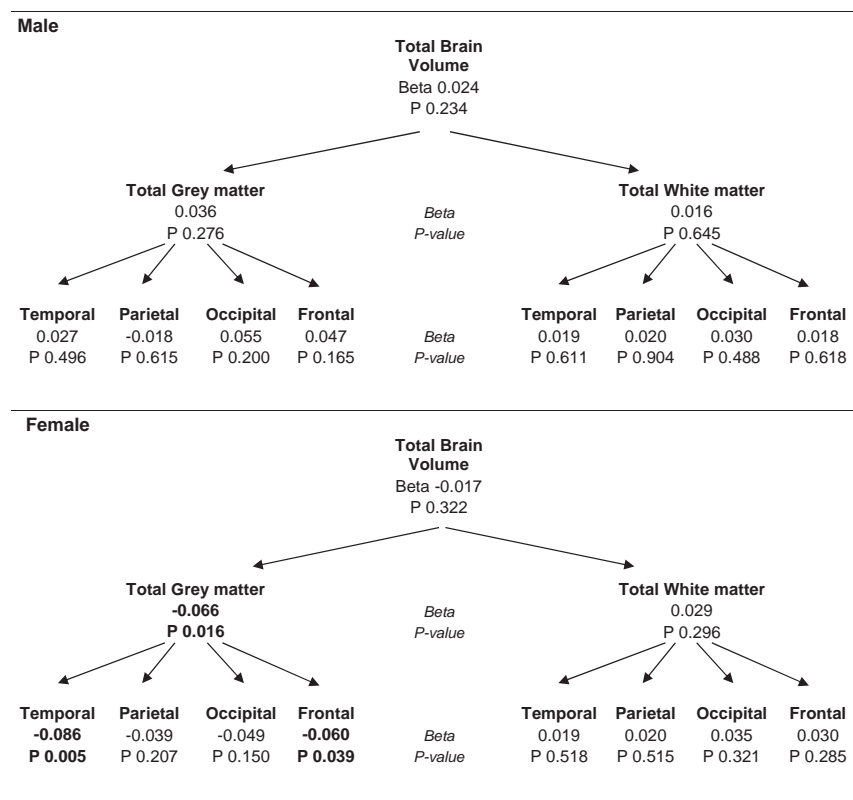


**FIG 1.** Chronic musculoskeletal pain and global brain volumes. Analyses adjusted for age, intracranial volume and depression.  $\beta$  is the difference in standardized brain volume for individuals with chronic joint pain compared with those without chronic joint pain.

pain threshold, which indicates higher (central) pain sensitivity, was associated with smaller volumes of the hippocampus, thalamus, and anterior cingulate cortex, regions that are involved in the limbic system and descending pain processing pathways. In the men, no significant associations between chronic joint pain or heat pain thresholds and brain volumes were observed.

To our knowledge, this is the first study that examined the association between chronic joint pain and structural brain changes in a population-based study. The number of studied patients was approximately 30 times larger than any previous study that examined the relationship between chronic pain and structural brain changes. Previous studies that examined structural brain alterations in pain consisted mostly of small and very specific clinical patient populations.<sup>6–13,15</sup> We used a hierarchical approach in studying brain structural differences. We first examined global brain tissue volumes and lobar volumes. Subsequently, we investigated those brain regions that were reported at least twice in the previous literature to be associated with chronic musculoskeletal pain. This strategy was chosen because previous studies showed inconsistent findings, which might be due to the different clinical pain phenotypes and low power that led to conflicting results, as highlighted previously.<sup>16</sup> Indeed, we were unable to replicate most of the previously implicated brain regions, which indicated that these brain regions are not consistently associated with chronic musculoskeletal pain.

The development of the brain is sex specific and influenced by

sex hormones. It is shown that sex differences are also present with respect to pain processing.<sup>44–48</sup> Therefore, we stratified our analyses according to sex. In women, gray matter in the temporal lobe and, especially, in the hippocampus was smaller in those with chronic pain. The hippocampus has previously been suggested as one of the altered structures in the brain in several pain states.<sup>6,7</sup> In women, this involvement of the limbic system, therefore, could indicate a more emotional coping of pain.

Smaller volumes of the hippocampus, thalamus, and anterior cingulate cortex were also associated with lower heat pain thresholds in women in our study. The thalamus is important in the descending inhibitory signaling, which is known to be compromised in central sensitization in chronic pain,<sup>5,7</sup> which makes our findings more plausible. To our knowledge, this is the first study that examined the association between heat pain thresholds and brain structure volumes. A limitation of the analysis of heat pain threshold and brain volumes was that the 2 measurements were done during 2 different visits, with several

years in between. To minimize this time bias, we examined only those participants who had chronic pain at both visits versus those who had no chronic pain at both visits.

In this study, we examined both the presence of chronic musculoskeletal pain and also heat pain sensitivity thresholds and their relationship to structural brain alterations. The presence of chronic musculoskeletal pain is a very subjective phenotype because it is determined by using questionnaires, and there is no test to measure pain. Heat pain thresholds are closely related to the sensitivity for developing chronic pain and for having chronic pain, which, therefore, makes it a more objective measure for chronic pain. The combined use of questionnaire data and heat pain thresholds to find associations with structural brain alterations, therefore, strengthens the results.

A possible disadvantage of population-based studies is the more heterogeneous pain phenotype compared with the selected clinical populations. However, this reflects the situation in the general population and shows that central sensitization occurs not only in a selected patient population. In addition, chronic pain in community-dwelling subjects represents a huge problem, which affected 35.3% of our study population. However, its nature and cause is poorly understood, and often no apparent reason can be assigned to the chronic pain state. Studying pain in an unselected population without the selection bias of clinical reference could provide new insight in possible pathways involved in any chronic pain state.

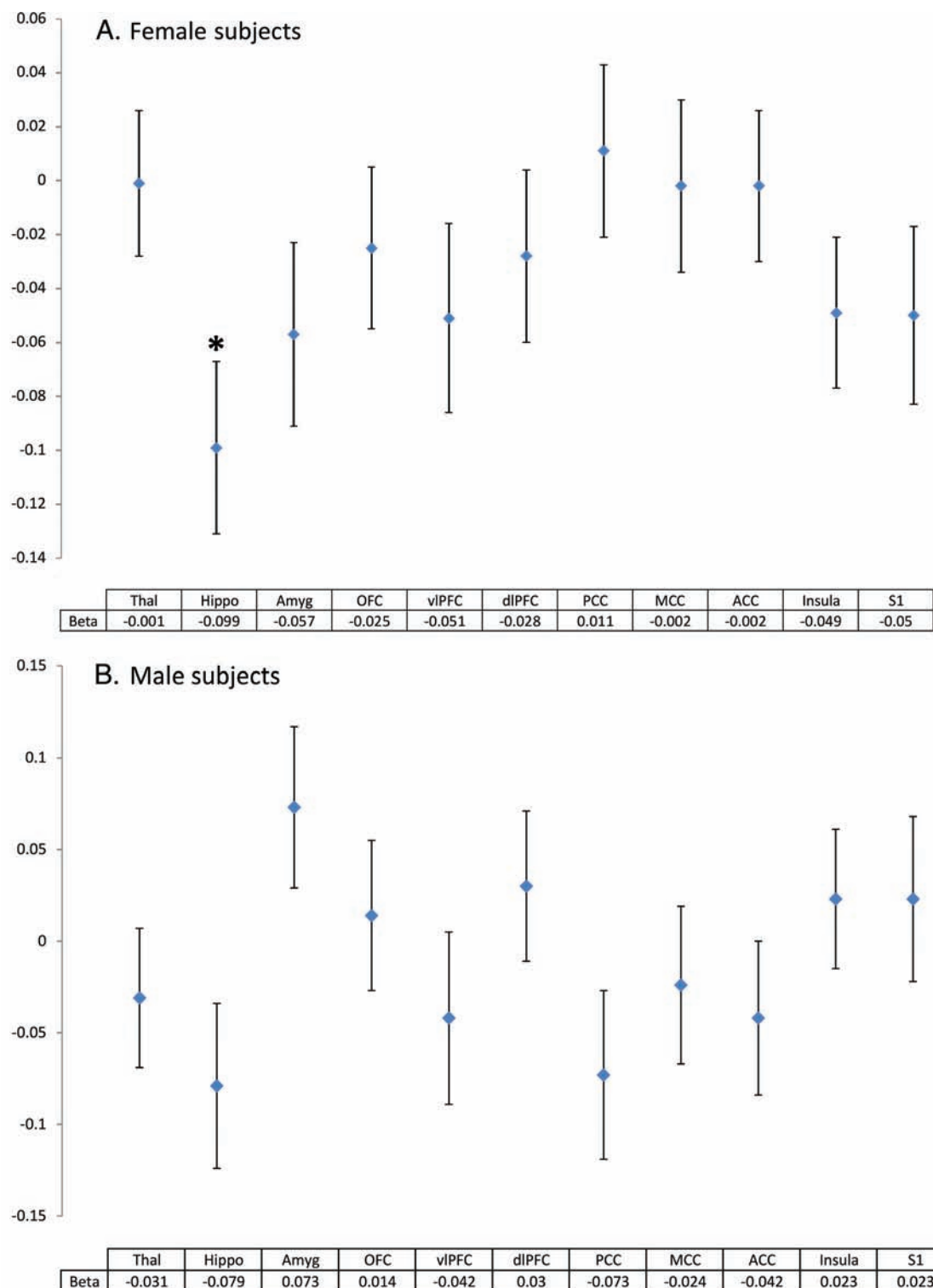


**FIG 2.** Brain volumes in regions of the limbic system and signal processing in relation to chronic musculoskeletal pain in (A) female and (B) male subjects. Plots represent  $\beta$  and standard error.  $\beta$  is the difference in standardized brain volume for individuals with chronic joint pain compared with those without chronic joint pain. Analyses were adjusted for age, intracranial volume, and depression.  $*P = .002$ . Thal indicates thalamus; Hippo, hippocampus; Amyg, amygdala; OFC, orbitofrontal cortex; vIPFC, ventrolateral prefrontal cortex; dIPFC, dorsolateral prefrontal cortex; PCC, posterior cingulate cortex; MCC, midcingulate cortex; ACC, anterior cingulate cortex; Insula, insular cortex; S1, primary somatosensory cortex.

The cross-sectional aspect of this study made us unable to speculate on the brain volume changes being a cause or an effect in the pathology of chronic pain. A previous study on structural

brain changes in pain related to severe hip osteoarthritis showed normalization of these differences after hip replacement surgery, which indicates that the pain is causing structural brain changes,<sup>39</sup>

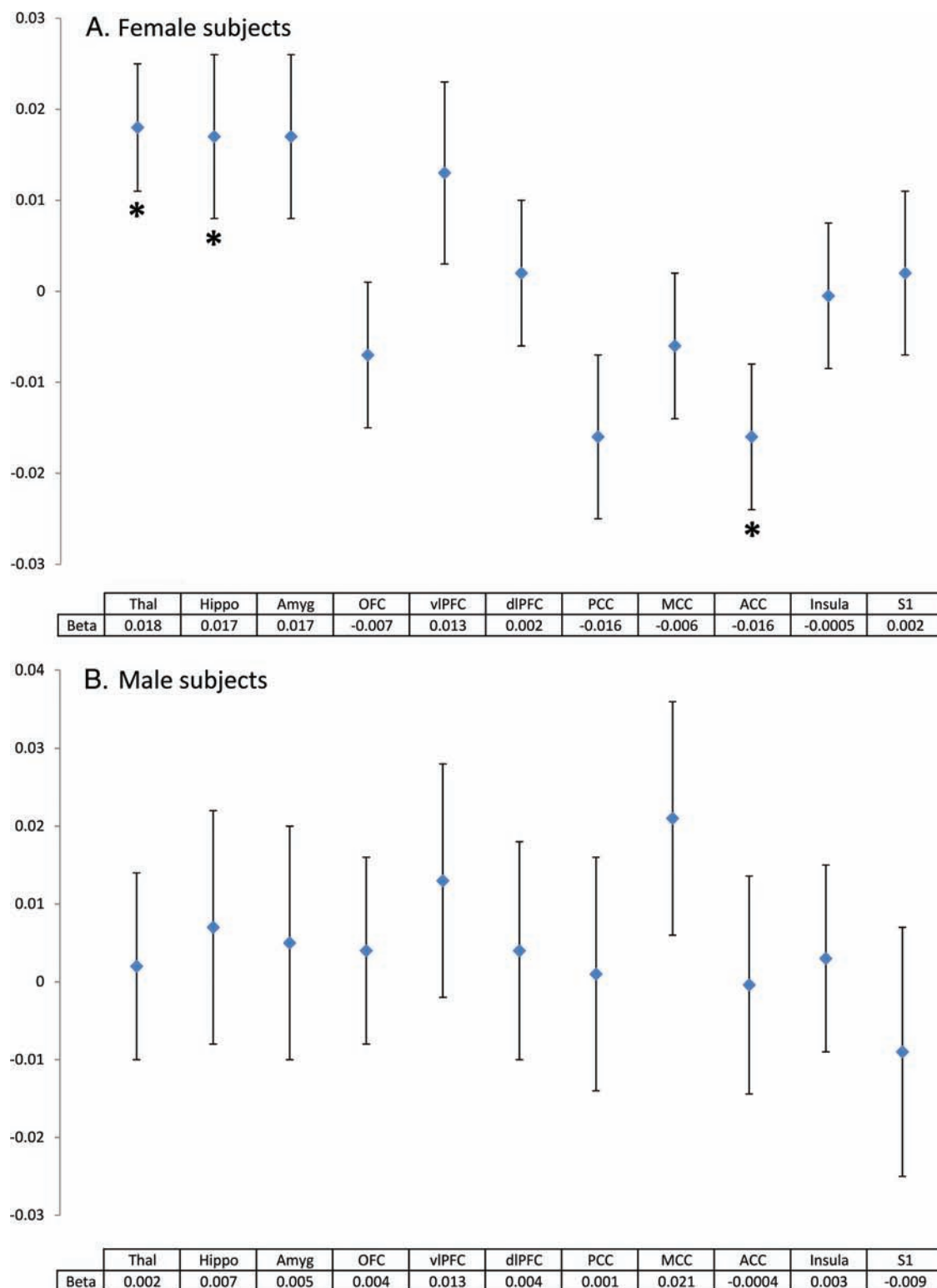


**FIG 3.** Quantitative sensory testing (heat pain threshold) and structural brain alterations in (A) female and (B) male subjects. Plots represent  $\beta$  and standard error.  $\beta$  is the difference in standardized brain volume per degree of temperature (Celsius); analyses were adjusted for age, intracranial volume, and depression.  $*P < .05$ . Thal indicates thalamus; Hippo, hippocampus; Amyg, amygdala; OFC, orbitofrontal cortex; vIPFC, ventrolateral prefrontal cortex; dIPFC, dorsolateral prefrontal cortex; PCC, posterior cingulate cortex; MCC, midcingulate cortex; ACC, anterior cingulate cortex; Insula, insular cortex; S1, primary somatosensory cortex.

but larger longitudinal studies are necessary for confirmation because sample size was small in this study ( $n = 10$ ).

Depression coincides with chronic musculoskeletal pain, and,

because both might affect the limbic system,<sup>11</sup> we adjusted the analysis for the presence of depression. In addition, excluding persons with depression from the model did not change the re-

sults, which indicated that our findings were not influenced by the presence of depression.

Because we started our study hypothesis-free and continued examining smaller regions, we performed a considerable amount of tests, which might have led to spurious findings. If we would have used a Bonferroni correction for the statistically significant *P* value for the brain structures, then this would result in a *P* value of  $.05/11 = .004$ ; this is when assuming independency of the tests. Many results would still be considered statistically significant. However, not all of the tests were independent because the smaller regions were included in the larger lobes. Therefore, deciding which exact *P* value to use would have been challenging. In addition, the performed analyses were not hypothesis-free because we tried to replicate previous published results. Moreover, especially in the women, we showed very consistent and robust findings, with increasing effect sizes when we narrowed the examined regions.

## CONCLUSIONS

In this large population-based study, we found that chronic musculoskeletal pain was associated with structural changes in parts of the limbic system in the brain. The hippocampus, especially, showed a very consistent and strong relationship with chronic joint pain and heat pain thresholds in women, which indicated a key role in the development of central sensitization and chronic pain. Structural alterations in the brain in individuals with chronic pain support the presence of central sensitization. This process of central sensitization increases the risk for a longer period of chronic pain and increases the risk for developing chronic pain at other sites.<sup>5</sup> These results stress the importance of a multidisciplinary and sex-specific therapeutic approach to improve successful treatment.

Disclosures: Wiro Niessen—RELATED: Grant: Dutch Science Foundation,\* EU,\* Comments: We have grants from the Netherlands Science Foundation and EU (7th framework programme) supporting our work in neuroimage analysis; UNRELATED: Consultancy: Quantib BV,\* Comments: I am cofounder, and scientific director of Quantib BV, an Erasmus MC spin-off. I am detached as consulted to this company for 0.2 fte; Stock/Stock Options: I am cofounder and stock-holder of Quantib BV. Henning Tiemeier—RELATED: Grant: Dutch Medical Research Council,\* ZonMw VIDI,\* Comments: Governmental research funding agency; UNRELATED: Grants/Grants Pending: Grants unrelated to work, all from nonprivate agencies such as EU,\* Dutch Medical Research agency\* or Sophia Foundation for Scientific Research,\* a local nonprofit body. \*Money paid to the institution.

## REFERENCES

1. Bedson J, Croft PR. **The discordance between clinical and radiographic knee osteoarthritis: a systematic search and summary of the literature.** *BMC Musculoskelet Disord* 2008;9:116 CrossRef Medline
2. Dieppe PA, Lohmander LS. **Pathogenesis and management of pain in osteoarthritis.** *Lancet* 2005;365:965–73 CrossRef Medline
3. Hunter DJ, McDougall JJ, Keefe FJ. **The symptoms of osteoarthritis and the genesis of pain.** *Rheum Dis Clin North Am* 2008;34:623–43 CrossRef Medline
4. Lawrence JS, Bremner JM, Bier F. **Osteo-arthritis. Prevalence in the population and relationship between symptoms and x-ray changes.** *Ann Rheum Dis* 1966;25:1–24 Medline
5. Woolf CJ. **Central sensitization: implications for the diagnosis and treatment of pain.** *Pain* 2011;152(3 suppl):S2–15 CrossRef Medline
6. Baliki MN, Schnitzer TJ, Bauer WR, et al. **Brain morphological signatures for chronic pain.** *PLoS One* 2011;6:e26010 CrossRef Medline
7. Davis KD, Moayedi M. **Central mechanisms of pain revealed through functional and structural MRI.** *J Neuroimmune Pharmacol* 2013;8:518–34 CrossRef Medline
8. Harvey AK, Taylor AM, Wise RG. **Imaging pain in arthritis: advances in structural and functional neuroimaging.** *Curr Pain Headache Rep* 2012;16:492–501 CrossRef Medline
9. Ivo R, Nicklas A, Dargel J, et al. **Brain structural and psychometric alterations in chronic low back pain.** *Eur Spine J* 2013;22:1958–64 CrossRef Medline
10. May, A. **Chronic pain may change the structure of the brain.** *Pain* 2008;137:7–15 CrossRef Medline
11. Robinson ME, Craggs JG, Price DD, et al. **Gray matter volumes of pain-related brain areas are decreased in fibromyalgia syndrome.** *J Pain* 2011;12:436–43 CrossRef Medline
12. Smallwood RF, Laird AR, Ramage AE, et al. **Structural brain anomalies and chronic pain: a quantitative meta-analysis of gray matter volume.** *J Pain* 2013;14:663–75 CrossRef Medline
13. Tracey I, Bushnell MC. **How neuroimaging studies have challenged us to rethink: is chronic pain a disease?** *J Pain* 2009;10:1113–20 CrossRef Medline
14. Zimmerman ME, Pan JW, Hetherington HP, et al. **Hippocampal correlates of pain in healthy elderly adults: a pilot study.** *Neurology* 2009;73:1567–70 CrossRef Medline
15. Henry DE, Chiodo AE, Yang W. **Central nervous system reorganization in a variety of chronic pain states: a review.** *PM R* 2011;3:1116–25 CrossRef Medline
16. Button KS, Ioannidis JP, Mokrysz C, et al. **Power failure: why small sample size undermines the reliability of neuroscience.** *Nat Rev Neurosci* 2013;14:365–76 CrossRef Medline
17. Schmidt-Wilcke T, Leinisch E, Gänssbauer S, et al. **Affective components and intensity of pain correlate with structural differences in gray matter in chronic back pain patients.** *Pain* 2006;125:89–97 CrossRef Medline
18. Apkarian AV, Sosa Y, Sonty S, et al. **Chronic back pain is associated with decreased prefrontal and thalamic gray matter density.** *J Neurosci* 2004;24:10410–105 CrossRef Medline
19. Puta C, Schulz B, Schoeler S, et al. **Enhanced sensitivity to punctate painful stimuli in female patients with chronic low back pain.** *BMC Neurol* 2012;12:98 CrossRef Medline
20. Staud R, Weyl EE, Price DD, et al. **Mechanical and heat hyperalgesia highly predict clinical pain intensity in patients with chronic musculoskeletal pain syndromes.** *J Pain* 2012;13:725–35 CrossRef Medline
21. Suokas AK, Walsh DA, McWilliams DF, et al. **Quantitative sensory testing in painful osteoarthritis: a systematic review and meta-analysis.** *Osteoarthritis Cartilage* 2012;20:1075–85 CrossRef Medline
22. Arendt-Nielsen L, Yarnitsky D. **Experimental and clinical applications of quantitative sensory testing applied to skin, muscles and viscera.** *J Pain* 2009;10:556–72 CrossRef Medline
23. Bouwense SA, Olesen SS, Drewes AM, et al. **Effects of pregabalin on central sensitization in patients with chronic pancreatitis in a randomized, controlled trial.** *PLoS One* 2012;7:e42096 CrossRef Medline
24. O'Neill S, Manniche C, Graven-Nielsen T, et al. **Generalized deep-tissue hyperalgesia in patients with chronic low-back pain.** *Eur J Pain* 2007;11:415–20 CrossRef Medline
25. Wilder-Smith, OH. **Chronic pain and surgery: a review of new insights from sensory testing.** *J Pain Palliat Care Pharmacother* 2011;25:146–59 CrossRef Medline
26. Erpelding N, Moayedi M, Davis KD. **Cortical thickness correlates of pain and temperature sensitivity.** *Pain* 2012;153:1602–09 CrossRef Medline
27. Seminowicz DA, Laferriere AL, Millevamps M, et al. **MRI structural brain changes associated with sensory and emotional function in a rat model of long-term neuropathic pain.** *Neuroimage* 2009;47:1007–14 CrossRef Medline



28. Hofman A, Darwish Murad S, van Duijn CM, et al. **The Rotterdam Study: 2014 objectives and design update.** *Eur J Epidemiol* 2013;28:889–926 CrossRef Medline
29. Ikram MA, van der Lugt A, Niessen WJ, et al. **The Rotterdam Scan Study: design and update up to 2012.** *Eur J Epidemiol* 2011;26:811–24 CrossRef Medline
30. de Boer R, Vrooman HA, van der Lijn F, et al. **White matter lesion extension to automatic brain tissue segmentation on MRI.** *Neuroimage* 2009;45:1151–61 CrossRef Medline
31. Vrooman HA, Cocosco CA, van der Lijn F, et al. **Multi-spectral brain tissue segmentation using automatically trained k-nearest-neighbor classification.** *Neuroimage* 2007;37:71–81
32. Wolfe F, Smythe HA, Yunus MB, et al. **The American College of Rheumatology 1990 Criteria for the Classification of Fibromyalgia. Report of the Multicenter Criteria Committee.** *Arthritis Rheum* 1990;33:160–72 CrossRef Medline
33. Buckalew N, Haut MW, Morrow L, et al. **Chronic pain is associated with brain volume loss in older adults: preliminary evidence.** *Pain Med* 2008;9:240–48 CrossRef Medline
34. Burgmer M, Gaubitz M, Konrad C, et al. **Decreased gray matter volumes in the cingulo-frontal cortex and the amygdala in patients with fibromyalgia.** *Psychosom Med* 2009;71:566–73 CrossRef Medline
35. Jensen KB, Srinivasan P, Spaeth R, et al. **Overlapping structural and functional brain changes in patients with long-term exposure to fibromyalgia pain.** *Arthritis Rheum* 2013;65:3293–303 CrossRef Medline
36. Kong J, Spaeth RB, Wey HY, et al. **S1 is associated with chronic low back pain: a functional and structural MRI study.** *Mol Pain* 2013;9:43 CrossRef Medline
37. Kuchinad A, Schweinhardt P, Seminowicz DA, et al. **Accelerated brain gray matter loss in fibromyalgia patients: premature aging of the brain?** *J Neurosci* 2007;27:4004–07 CrossRef Medline
38. Lutz J, Jäger L, de Quervain D, et al. **White and gray matter abnormalities in the brain of patients with fibromyalgia: a diffusion-tensor and volumetric imaging study.** *Arthritis Rheum* 2008;58:3960–69 CrossRef Medline
39. Rodriguez-Raecke R, Niemeier A, Ihle K, et al. **Brain gray matter decrease in chronic pain is the consequence and not the cause of pain.** *J Neurosci* 2009;29:13746–50 CrossRef Medline
40. Schmidt-Wilcke T, Luerding R, Weigand T, et al. **Striatal grey matter increase in patients suffering from fibromyalgia—a voxel-based morphometry study.** *Pain* 2007;132(suppl 1):S109–16 CrossRef Medline
41. Seminowicz DA, Wideman TH, Naso L, et al. **Effective treatment of chronic low back pain in humans reverses abnormal brain anatomy and function.** *J Neurosci* 2011;31:7540–50 CrossRef Medline
42. Valet M, Gündel H, Sprenger T, et al. **Patients with pain disorder show gray-matter loss in pain-processing structures: a voxel-based morphometric study.** *Psychosom Med* 2009;71:49–56 CrossRef Medline
43. Wood PB, Glabus MF, Simpson R, et al. **Changes in gray matter density in fibromyalgia: correlation with dopamine metabolism.** *J Pain* 2009;10:609–18 CrossRef Medline
44. Henderson LA, Gandevia SC, Macefield VG. **Gender differences in brain activity evoked by muscle and cutaneous pain: a retrospective study of single-trial fMRI data.** *Neuroimage* 2008;39:1867–76 CrossRef Medline
45. Labus JS, Naliboff BN, Fallon J, et al. **Sex differences in brain activity during aversive visceral stimulation and its expectation in patients with chronic abdominal pain: a network analysis.** *Neuroimage* 2008;41:1032–43 CrossRef Medline
46. Lombardo MV, Ashwin E, Auyeung B, et al. **Fetal testosterone influences sexually dimorphic gray matter in the human brain.** *J Neurosci* 2012;32:674–80 CrossRef Medline
47. McCarthy MM, Auger AP, Bale TL, et al. **The epigenetics of sex differences in the brain.** *J Neurosci* 2009;29:12815–23 CrossRef Medline
48. Peper JS, Koolschijn PC. **Sex steroids and the organization of the human brain.** *J Neurosci* 2012;32:6745–46 CrossRef Medline

# Basal Ganglia Iron in Patients with Multiple Sclerosis Measured with 7T Quantitative Susceptibility Mapping Correlates with Inhibitory Control

P. Schmalbrock, R.S. Prakash, B. Schirda, A. Janssen, G.K. Yang, M. Russell, M.V. Knopp, A. Boster, J.A. Nicholas, M. Racke, and D. Pitt



## ABSTRACT

**BACKGROUND AND PURPOSE:** T2 hypointensity in the basal ganglia of patients with MS has been associated with clinical progression and cognitive decline. Our objectives were the following: 1) to compare signal in T2WI, R2 (ie,  $1/T_2$ ), and R2\* (ie,  $1/T_2^*$ ) relaxation rates and quantitative susceptibility mapping; and 2) to investigate the associations among MR imaging, clinical scores, and cognitive measures of inhibitory control linked to basal ganglia functioning.

**MATERIALS AND METHODS:** Twenty-nine patients with MS underwent a battery of neuropsychological tests including the Flanker and Stroop tasks. 7T MR imaging included 3D gradient-echo and single-echo multishot spin-echo EPI. Quantitative susceptibility mapping images were calculated by using a Wiener filter deconvolution algorithm. T2WI signal was normalized to CSF. R2 and R2\* were calculated by log-linear regression. Average MR imaging metrics for the globus pallidus, putamen, and caudate were computed from manually traced ROIs including the largest central part of each structure.

**RESULTS:** Marked spatial variation was consistently visualized on quantitative susceptibility mapping and T2/T2\*WI within each basal ganglia structure. MR imaging metrics correlated with each other for each basal ganglia structure individually. Notably, caudate and putamen quantitative susceptibility mapping metrics were similar, but the putamen R2 was larger than the caudate R2. This finding suggests that tissue features contribute differently to R2 and quantitative susceptibility mapping. Caudate and anterior putamen quantitative susceptibility mapping correlated with the Flanker but not Stroop measures; R2 did not correlate with inhibitory control measures. Putamen quantitative susceptibility mapping and caudate and putamen R2 correlated with the Expanded Disability Status Scale.

**CONCLUSIONS:** Our study showed that quantitative susceptibility mapping and R2 may be complementary indicators for basal ganglia tissue changes in MS. Our findings are consistent with the hypothesis that decreased performance of basal ganglia-reliant tasks involving inhibitory control is associated with increased quantitative susceptibility mapping.

**ABBREVIATIONS:** BG = basal ganglia; EDSS = Expanded Disability Status Scale; GP = globus pallidus; QSM = quantitative susceptibility mapping; R2 = relaxation rate (ie,  $1/T_2$ ); R2\* = relaxation rate (ie,  $1/T_2^*$ )

Several studies have reported changes in T2, T2\*, and quantitative susceptibility mapping (QSM) in the basal ganglia (BG) of patients with MS compared with healthy controls based on T2 hypointensity. Quantitative CSF-normalized T2 measurements correlated with brain atrophy as measured by volumetric analyses

and with white matter lesion load,<sup>1-3</sup> and with measures of MS disease burden such as the Expanded Disability Status Scale (EDSS), the timed 25-foot walk test,<sup>4,5</sup> and cognitive performance.<sup>6</sup> Change in T2WI hypointensity was reported to be a better predictor of MS disease progression than brain atrophy<sup>5,7</sup> and thus may serve as a biomarker for progression and as an outcome measure to assess treatment efficacy.<sup>8</sup>

Although frequently used as a marker for BG iron, T2WI signal is affected not only by iron content but also by a number of other factors, most notably free water mobility. In addition, T2

Received March 5, 2015; accepted after revision July 31.

From the Departments of Radiology (P.S., G.K.Y., M. Russell, M.V.K.), Psychology (R.S.P., B.S., A.J.), and Neurology (A.B., J.A.N., M. Racke), The Ohio State University, Columbus, Ohio; and Department of Neurology (D.P.), Yale School of Medicine, New Haven, Connecticut.

This work was supported by Biogen (US-TSY-10-10047) and the Wright Center of Innovation in Biomedical Imaging at The Ohio State University.

Paper previously presented in part at: European Committee for Treatment and Research in Multiple Sclerosis–Americas Committee for Treatment and Research in Multiple Sclerosis, September, 10–13, 2014; Boston, Massachusetts; and International Society for Magnetic Resonance in Medicine, May 30–June 5, 2015; Toronto, Ontario, Canada.

Please address correspondence to Petra Schmalbrock, PhD, 395 W 12th Ave, 412, Columbus, OH 43210; e-mail: petra.schmalbrock@osumc.edu; @WCIBMI999

Indicates open access to non-subscribers at www.ajnr.org

Indicates article with supplemental on-line tables.

Indicates article with supplemental on-line photos.

<http://dx.doi.org/10.3174/ajnr.A4599>

measures may be compromised by fluid motion when the CSF signal is used for normalization. Consequently, a number of other MR imaging methods that are thought to be more sensitive to tissue iron have been pursued, including T2 relaxometry,<sup>3,9</sup> T2\* measurement,<sup>10</sup> high-pass filtered-phase MR imaging,<sup>11</sup> and quantitative susceptibility mapping.<sup>12</sup> These studies and MR imaging–histology comparisons<sup>13</sup> demonstrated that higher iron content is a prominent factor in BG abnormality in patients with MS.

Furthermore, it has been increasingly recognized that BG structures play a role in both somatomotor and cognitive control processes associated with localized functional topography.<sup>14,15</sup> Specifically, the BG are implicated in action selection by influencing and modulating activity of the motor cortex and descending motor pathways through inhibitory control.<sup>16</sup> As such, the abnormal iron increase in the BG of patients with MS may be related to cognitive decline, specifically to deficits in inhibitory control. However, to our knowledge, only 1 study has linked BG iron to cognition in MS.<sup>6</sup> Additionally, direct comparison between T2 and QSM for measuring BG iron in patients with MS has not yet been published, to our knowledge.

Our study had 2 objectives: 1) to compare T2, T2\*, and QSM for assessing BG changes; and 2) to correlate T2, T2\*, and QSM to physical and cognitive measures. Specifically, given that the BG play an important role in tasks of inhibitory control, which require suppression of task-irrelevant information to engage correctly in goal-directed, task-relevant behavior, we hypothesized a negative association between iron deposits and neuropsychological measures of inhibitory control.

## MATERIALS AND METHODS

### Patient Selection

Twenty-nine individuals with relapsing-remitting MS participating in an ongoing longitudinal study were recruited (see On-line Table 1 for demographics and clinical characteristics). All patients signed institutional review board–approved consent forms. EDSS scores were obtained by a neurologist. Thirteen patients were treated with natalizumab; 11, with glatiramer acetate; 3, with interferon  $\beta$ ; and 2 were newly diagnosed. On average, patients treated with natalizumab were younger and had shorter MS durations than patients treated with glatiramer acetate. EDSS scores were not significantly different among treatment groups.

### MR Imaging Acquisition and Image Processing

All patients were scanned at 7T (Achieva; Philips Healthcare, Best, the Netherlands) by using a head volume transmit/16-channel receive coil (Nova Medical, Wilmington, Massachusetts). 3D-multiecho gradient-echo images covering the entire brain were acquired by using TR/flip angle = 24 ms/5°, 4 bipolar gradient echoes with TE = 4–20 ms, acquired voxel size of 0.5 × 0.5 mm in-plane and 1-mm section thickness (interpolated to 0.5-mm isotropic), and 9-minute scan time. Complex multicoil data were combined by using scanner software, and real and imaginary data were exported for relaxation rate (ie, 1/T2\*; R2\*) and QSM processing. T2 data were acquired as 4 separately acquired single-echo multishot spin-echo EPI scans by using TR = 5000 ms; TE = 13.5, 21, 36, and 50 ms; 1 × 1 × 3 mm; and scan times of 1 minute

each. Three axial sections through the central part of the BG were acquired. The single-echo sequence was chosen over multiecho to avoid interference from stimulated echoes and because it is more sensitive to diffusion in the inhomogeneous field from tissue microstructure.

Phase maps were calculated from the complex data and unwrapped (FSL PRELUDE, <http://www.fmrib.ox.ac.uk/fsl><sup>17</sup>). To avoid echo shifts introduced by using a bipolar gradient readout, we used difference images between echo 1 and echo 3 for all further processing. Background field removal was done with a Projection onto Dipole Field.<sup>18</sup> Image data were masked more tightly than in the published algorithm to handle stronger phase changes near air-tissue interfaces at 7T. Quantitative susceptibility maps were calculated by using Wiener filter deconvolution (Figs 1 and 2).<sup>19</sup> ROIs in the central part of the right and left globus pallidus (GP), putamen, and caudate were manually traced on 10 sections, including the entire structure seen in the section (Fig 2). ROIs contained 1000–3000 voxels. In addition, the putamen region was split in half, and the anterior and posterior sections were analyzed separately. ROI masks were saved and used to compute average QSM (and SD) and T2\*WI signal at the 4 different TEs. Mean T2\* and SDs were computed from the average signals with log-linear regression.

For T2 analysis, ROIs were manually traced on the TE = 36 ms images. These ROIs were used to calculate signal for all TEs. Quantitative T2 mean and SDs were computed by log-linear regression. To compare quantitative relaxometry with CSF-normalized T2-weighting,<sup>1,2,4,6</sup> we also traced ROIs in the anterior horns of the ventricles on the TE = 36 ms images and computed the ratio of BG over CSF signal (ratio =  $S_{BG} / S_{CSF}$ ) and its SD.

### Neuropsychological Testing

All participants completed neuropsychological assessments designed to measure general cognitive functioning and specific measures that assess functioning on tasks that are subserved by the BG. To examine general cognitive decline, primarily relevant for the ongoing longitudinal study, we administered the Mini-Mental State Examination, the Wechsler Test of Adult Reading, and the Brief Repeatable Battery (On-line Table 2),<sup>20,21</sup> establishing a cognitive baseline for each participant. Participants additionally underwent testing with computerized versions of Flanker and Stroop tasks to assess inhibitory control (On-line Table 3).<sup>21</sup>

### Statistical Analysis

Statistical analyses were performed with Matlab (MathWorks, Natick, Massachusetts). All demographic, MR imaging, and neuropsychological data were tested for outliers, defined as any  $z$  score deviation of >2.5 SDs from the mean. Normality was checked by using the Shapiro-Wilk test. In our data, disease duration and Flanker interference were found to be positively skewed and were corrected with a square root transformation. EDSS data on 1 participant were missing, and we estimated the EDSS of this participant by using the fitted linear regression between disease duration and EDSS. Data from 2 participants were excluded from the neuropsychological analyses, 1 for the Flanker task and 1 for the Stroop task, due to patients performing below chance on all conditions of the task.

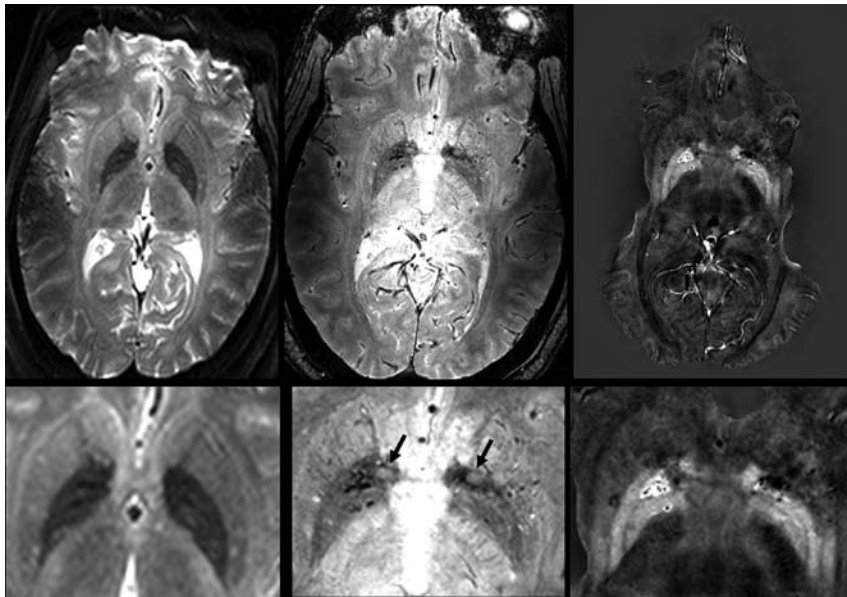


**FIG 1.** T2-weighted (TE = 36 ms), T2\*-weighted (TE = 14 ms), and QSM images (left, middle, right) of a 44-year-old female patient with MS (EDSS = 3; duration, 1.7 years). The T2WI multishot spin-echo EPI and T2\*WI have some distortion due to susceptibility near air spaces in the sinus. A significant part of the temporal lobes is masked in QSM to avoid processing artifacts, but the BG are not obscured. Magnified T2/T2\*-weighted and QSM images show many subtle structures. The internal and external GPs are clearly separated, especially on QSM. In this younger patient, putamen iron is higher only in posterolateral regions. Veins are dark on T2\*WI and bright on QSM. Several high-iron regions (dark on T2WI and T2\*WI, bright on QSM) are seen in the globus pallidus. Bright spots in the putamen and GP are dark on QSM and may be arterial inflow or small high T2 lesions (mobile water). Two areas at the anterior GP edge (arrows, gray on T2\*WI, dark on QSM) are WM regions of the anterior commissure; they are not seen on T2WI due to the larger section thickness.

Pearson correlations were computed between all measured variables. QSM, R2 (ie,  $1/T_2$ ), and R2\* (ie,  $1/T_2^*$ ) relaxation rates increased with age, and the EDSS score increased with disease duration. To remove these dependencies, we subtracted a linear regression fit of QSM, R2/R2\* with age, and EDSS with duration from the measured data. Semipartial correlations were conducted between cognitive (Flanker), duration-adjusted physical (EDSS), and age-adjusted MR imaging measures.

## RESULTS

### Visual Assessment of the MR Imaging Data

**Image Quality.** QSM processing produced high-quality images rich in anatomic details with minimal blurring and artifacts (Figs 1 and 2 and On-line Fig 1). Some streaking from QSM processing was especially visible in coronal reformatted images (On-line Fig 1). Because we chose a very conservative threshold for the background field removal algorithm,<sup>18</sup> significant parts of temporal lobes and hippocampal regions were masked, but the BG were retained. Motion artifacts were observed in some patients but did not preclude quantitative analysis. Multishot T2-weighted EPI had significant distortion near air/tissue interfaces (Fig 1). This occasionally led to banding artifacts extending into the brain, but they did not hinder quantitative T2 analysis.

**Image Characteristics.** QSM and signal on T2/T2\*WI were not homogeneous throughout the GP, putamen, and caudate. Internal and external GPs could be distinguished on original axial and reformatted coronal images in most patients (Figs 1 and 2 and

On-line Fig 1). In the GP, bright “spots” were frequently seen on QSM with values 1–3 SDs higher than those of surrounding tissue. These regions were dark on T2/T2\*WI (Figs 1 and 2 and On-line Fig 1). Sometimes, it was possible to follow these bright-QSM/dark-T2 features through adjacent sections, thus identifying them as vasculature, but often they appeared isolated. Compared with superior GP regions, inferior regions were darker on T2/T2\*WI and brighter on QSM (Fig 2 and On-line Fig 1). In the putamen, bright or dark spots were also observed, but most notably, there was a gradual change in signal from darker posterolateral to brighter anteromedial regions on T2/T2\*WI, with an analogous pattern from bright to dark in QSM. In the caudate, the posteromedial tips were dark on T2/T2\*WI and bright on QSM and seemed to connect to fine vessels visibly extending into the caudate.

These spatial patterns were seen with all imaging methods, T2/T2\*WI and QSM, and remained stable with time (On-line Fig 1), ascertaining that regional variations within each BG structure reflected true tissue differences and

were not merely due to SNR limitations, artifacts, or processing errors.

### Comparison of Quantitative Measures for QSM, T2, and T2\*

**Measurement Precision.** To assess measurement variability, we calculated the average coefficient of variation over all patients and all structures. The coefficient of variation was highest for CSF-normalized T2WI (20%) and lowest for T2 and T2\* relaxometry (both 3%). At 11.5%, the coefficient of variation for QSM was fairly high because local differences were amplified in QSM.

**Relations among MR Imaging Measures.** Table 1 shows mean QSM, R2\*, and R2. Note that the putamen and caudate QSM were similar, whereas caudate R2 was lower than the putamen R2. Table 2 lists correlation coefficients between MR imaging measures; all were high ( $P$  values  $< 10^{-3}$ , data in On-line Fig 2). Most interesting, correlation coefficients between R2 and QSM were lowest, and linear regression slopes were significantly different among GP structures (On-line Fig 2). Also note that correlation coefficients and linear regression slopes were lower for the caudate than the GP and putamen. Last, high correlation between CSF-normalized T2WI and quantitative T2 indicated that simple normalization can be a valid measure, albeit with higher measurement error.

Table 2 also lists fit coefficients for multivariable linear regres-



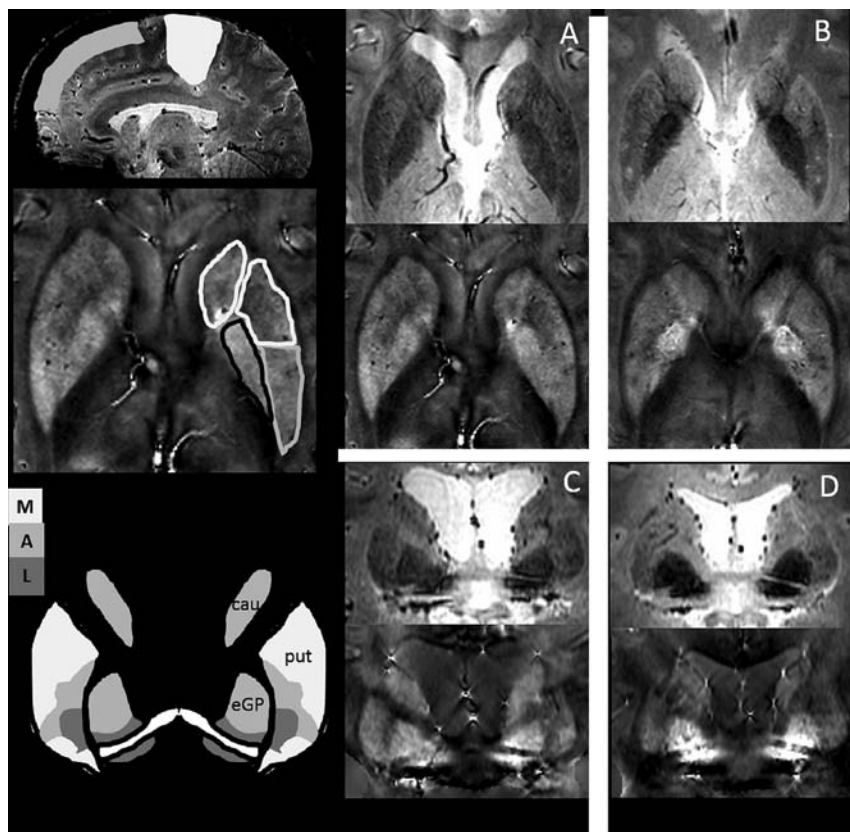


**FIG 2.** Schematic representation of published basal ganglia–cortical connections<sup>14,15</sup> and sample T2\*-weighted and QSM images for 4 different patients. On the left side is a schematic representation of frontal and sensorimotor areas indicated on a sagittal view (top); sample ROIs used for the analysis in this study are shown on an axial view (middle). As indicated, the putamen ROI was split in half into anterior and posterior sections, which were separately analyzed. At the left bottom is a schematic representation of BG functional areas sketched from published calbindin stains.<sup>14</sup> Our GP and putamen ROIs were typically selected on more inferior axial sections than the caudate ROIs so that GP and putamen areas included mixed functional areas, whereas our caudate ROI was predominantly in a cognitive area. The schematic depictions are contrasted with data from 4 different patients on the right. Patient A (a 33-year-old woman; EDSS = 4; Flanker, 37 ms) has lower physical but slightly higher cognitive performance than patient B (a 30-year-old woman; EDSS = 2; Flanker, 57 ms). QSM is higher in the posterior putamen for patient A. Coronal reformatted images of patient C (a 50-year-old woman; EDSS = 5; Flanker, 22 ms) who has worse motor but better cognitive function than patient D (a 50-year-old woman; EDSS = 0; Flanker, 108 ms) show higher QSM in the putamen, but lower QSM in the external GP for patient C compared with patient D. Again, there is some spatial correspondence between high QSM and functional deficits in these patients.

**Table 1: Mean QSM, R2, and R2\* for BG substructures across patients**

	GP	Putamen	Caudate	Aput	Pput
QSM	0.159 ± 0.031	0.064 ± 0.023	0.068 ± 0.019	0.050 ± 0.019	0.095 ± 0.038
R2*	0.096 ± 0.013	0.061 ± 0.011	0.051 ± 0.009	0.059 ± 0.010	0.066 ± 0.016
R2	0.049 ± 0.004	0.036 ± 0.004	0.029 ± 0.002	0.034 ± 0.004	0.039 ± 0.0050

**Note:**—Aput indicates cognitive anterior part of putamen, region predominantly connected to frontal cortex; Pput, motor posterior part of putamen, region predominantly connected to sensorimotor cortex.

sion of R2\* with both QSM and R2 (by using intercept zero). These coefficients were used to estimate the relative contribution from R2 and QSM to R2\* (Table 2). Remarkably, QSM contributed most prominently to R2\* in the GP and (motor cortex–connected) posterior putamen, whereas R2 dominated in the caudate and (cognitive cortex–connected) anterior putamen. Taken together, the observed relations between the different MR imaging measures indicated that QSM and R2 carried somewhat different information about tissue microstructure, whereas R2\* was a mixed measure.

**Associations among Demographic, Clinical, and Neuropsychological Parameters.** Only disease duration and EDSS were strongly correlated; neither Flanker nor Stroop measures correlated with age, disease duration, or EDSS (Table 3). Notably, in our cohort of patients with MS, Flanker and Stroop measures did not correlate.

**Associations among MR Imaging Metrics and Demographic, Clinical, and Inhibitory Control Measures.** Significant correlations with age and QSM were observed for all regions and for R2 for the GP and putamen but not the caudate (Table 4). Associations were weaker for R2\*. Age-related trends followed published data for healthy subjects in the age range of 30–60 years.<sup>22</sup> Compared with published data,<sup>22</sup> GP and caudate QSM were higher in patients with MS than in controls (On-line Fig 3). 7T data for R2 are not available, but age-related trends have been shown at a lower field strength. Caudate QSM also correlated with disease duration (Table 4).

EDSS correlated significantly with R2 in the caudate and putamen, but not the GP (Table 4). Most interesting, no bivariate correlations between EDSS and QSM or R2\* were found without controlling for covariates. After we corrected for age in MR imaging measures and duration in EDSS, stronger correlations were revealed (Table 5). There was a significant correlation between EDSS and R2 for the caudate and putamen (with both putamen subregions). Additional associations between EDSS and QSM ensued and were most prominent for the posterior putamen connected to the motor cortex (Table 5). Still, no correlations were found between EDSS and QSM in the anterior (cognitive) putamen and caudate (On-line Fig 4).

Regarding associations between measures of inhibitory control and MR imaging, bivariate analyses without correction for covariates showed only an association between the Flanker measure and QSM in the caudate and anterior putamen (Table 4). We did not find any associations between QSM and the Stroop task. R2 and R2\* did not correlate with Flanker or Stroop measures for any BG structure. After we corrected QSM and R2 for age, correlations between the Flanker measure and the caudate and anterior putamen QSM became stronger, but still there was no association with R2 (Table 5 and On-line Fig 4).

**Table 2: Bivariate Pearson correlation coefficients between MRI measures and multivariable linear regression of R2\* with QSM and R2 using zero intercept ( $R2^* = a1QSM + a2R2$ )**

	GP	Putamen	Caudate	Aput	Pput
MRI					
R2 (QSM)	0.51 <sup>a</sup>	0.72 <sup>b</sup>	0.52 <sup>a</sup>	0.67 <sup>a</sup>	0.72 <sup>a</sup>
R2* (QSM)	0.73 <sup>b</sup>	0.81 <sup>b</sup>	0.47 <sup>a</sup>	0.71 <sup>a</sup>	0.83 <sup>a</sup>
R2* (R2)	0.55 <sup>b</sup>	0.78 <sup>b</sup>	0.48 <sup>a</sup>	0.75 <sup>a</sup>	0.75 <sup>a</sup>
CSF-T2WI (T2)	0.71 <sup>b</sup>	0.85 <sup>b</sup>	0.59 <sup>b</sup>	0.79 <sup>b</sup>	0.87 <sup>b</sup>
Multivariable linear regression for R2*					
a <sub>1</sub>	0.28 ± 0.04 <sup>b</sup>	0.22 ± 0.04 <sup>b</sup>	0.15 ± 0.06 <sup>c</sup>	0.21 ± 0.05 <sup>a</sup>	0.25 ± 0.04 <sup>b</sup>
a <sub>2</sub>	1.05 ± 0.14 <sup>b</sup>	1.31 ± 0.07 <sup>b</sup>	1.42 ± 0.16 <sup>b</sup>	1.42 ± 0.08 <sup>b</sup>	1.08 ± 0.10 <sup>b</sup>
Fractional Contributions	QSM: 47% R2: 53%	QSM: 23% R2: 77%	QSM: 20.0% R2: 80.0%	QSM: 18% R2: 82%	QSM: 36% R2: 64%

**Note:**—Aput indicates cognitive anterior part of putamen, region predominantly connected to frontal cortex; Pput, motor posterior part of putamen, region predominantly connected to sensorimotor cortex.

<sup>a</sup>  $P < 10^{-3}$ .

<sup>b</sup>  $P < 10^{-6}$ .

<sup>c</sup>  $P = .02$ .

**Table 3: Pearson correlation coefficients (P values) for demographic and neuropsychological measures**

	Age	Duration	EDSS	Flanker	Stroop
Age	1				
Duration	0.36 (.06)	1			
EDSS <sup>a</sup>	0.30 (.11)	0.61 (.0005) <sup>d</sup>	1		
Flanker <sup>b</sup>	0.01 (.95)	0.26 (.18)	0.23 (.23)	1	
Stroop <sup>c</sup>	0.07 (.74)	−0.08 (.68)	−0.02 (.94)	0.03 (.90)	1

<sup>a</sup> Using estimates for missing EDSS scores.

<sup>b</sup> For the Flanker task, 1 participant performed below chance ( $n = 28$ ).

<sup>c</sup> For the Stroop task, data for 1 participant were lost, and 1 performed below chance ( $n = 27$ ).

<sup>d</sup> Statistically significant at  $P < .05$ .

**Table 4: Bivariate Pearson correlation coefficients (P values) ( $n = 29$  except as noted)**

	Age	Duration <sup>a</sup>	EDSS	Flanker <sup>b</sup>	Stroop <sup>c</sup>
QSM					
GP	0.36 (.059)	0.10 (.60)	0.06 (.75)	0.25 (.20)	−0.18 (.36)
Put	0.57 (.001) <sup>f</sup>	0.04 (.85)	0.31 (.09)	0.3 (.12)	0.01 (.97)
Cau	0.41 (.02) <sup>f</sup>	0.42 (.02) <sup>f</sup>	0.24 (.20)	0.47 (.01) <sup>f</sup>	0.13 (.50)
Aput	0.55 (.0015) <sup>f</sup>	0.05 (.81)	0.30 (.11)	0.38 (.045) <sup>f</sup>	0.00 (.99)
Pput	0.57 (.001) <sup>f</sup>	0.09 (.65)	0.35 (.06)	0.23 (.25)	−0.01 (.94)
R2					
GP <sup>d</sup>	0.32 (.12)	0.08 (.68)	0.18 (.38)	0.32 (.11)	0.065 (.76)
Put <sup>e</sup>	0.47 (.01) <sup>f</sup>	0.09 (.65)	0.43 (.02) <sup>f</sup>	0.31 (.11)	0.21 (.34)
Cau <sup>e</sup>	0.37 (.06)	0.29 (.15)	0.58 (.001) <sup>f</sup>	0.31 (.11)	0.07 (.75)
Aput <sup>e</sup>	0.44 (.02) <sup>f</sup>	0.12 (.54)	0.48 (.01) <sup>f</sup>	0.35 (.08)	0.17 (.44)
Pput <sup>e</sup>	0.47 (.01) <sup>f</sup>	0.01 (.96)	0.32 (.04) <sup>f</sup>	0.21 (.29)	0.28 (.18)
R2*					
GP	0.14 (.45)	−0.23 (.22)	−0.20 (.29)	0.2 (.3)	−0.24 (.22)
Put	0.38 (.047) <sup>f</sup>	−0.12 (.51)	0.25 (.19)	0.34 (.075)	−0.02 (.92)
Cau	0.29 (.12)	−0.02 (.90)	0.24 (.20)	0.29 (.13)	0.27 (.17)
Aput	0.30 (.11)	−0.15 (.43)	0.26 (.16)	0.37 (.055)	−0.04 (.84)
Pput	0.45 (.01) <sup>f</sup>	−0.06 (.74)	0.17 (.36)	0.23 (.23)	−0.00 (.99)

**Note:**—Cau indicates caudate; Put, putamen; Aput, cognitive anterior part of putamen, region predominantly connected to frontal cortex; Pput, motor posterior part of putamen, region predominantly connected to sensorimotor cortex.

<sup>a</sup> Using square root transformation for non-normal duration data.

<sup>b</sup> Using square root transformation for non-normal Flanker measure ( $n = 28$ ).

<sup>c</sup> Stroop measure ( $n = 27$ ).

<sup>d</sup> For GP R2  $n = 27$  so that R2–GP versus Flanker ( $n = 26$ ).

<sup>e</sup> For putamen and caudate R2  $n = 28$  so that R2–Put, R2–Cau versus Flanker ( $n = 27$ ).

<sup>f</sup> Statistically significant at  $P < .05$ .

In summary, the cognitive measure, Flanker interference, showed a stronger association with QSM in the caudate and anterior putamen, whereas the physical measure, EDSS, showed a stronger association with R2 but not R2\*.

## DISCUSSION

Our study had 2 goals: first, to compare QSM, T2\*, and T2 for assessing BG changes in patients with MS and second to study

associations among MR imaging metrics, clinical scores, and cognitive measures of inhibitory control.

### Comparison of MR Imaging Measures

Our study found visual correspondence (ie, similar spatial patterns within each BG region) among QSM, T2\*WI, and T2WI. MR imaging measures increased with age, and the correlation among the MR imaging metrics was high. Notably, the dynamic range of QSM was twice as high as that of R2 and R2\*.

However, there were several prominent differences. The caudate QSM was higher than the putamen QSM, whereas the caudate R2 was lower than putamen R2. Postmortem studies of tissue iron showed the highest iron content in the GP, followed by the putamen, and the lowest iron content in the caudate.<sup>13</sup> This order was maintained in QSM studies of healthy subjects.<sup>12,23</sup> Similar to our study findings, Rudko et al<sup>23</sup> demonstrated higher caudate QSM in patients with MS, though overall, their QSM values were lower in their younger subject population. Conversely, the study of Langkammer et al<sup>12</sup> did not show the relative increase in caudate QSM in patients with MS. Furthermore, we observed almost a 2-fold higher QSM in the posterior compared with the anterior putamen, whereas R2 was only 15% higher (Table 1).

An increase in QSM may be due to higher iron or lower myelin content, whereas larger R2 and R2\* are due to higher iron and higher myelin. Thus our finding of relatively higher QSM in the caudate is consistent with increased iron content and/or decreased myelin, both suggesting greater tissue damage in the caudate. Increased QSM in the posterior compared with the anterior putamen suggests higher iron content in the posterior putamen.

Multivariate linear regression of R2\* with QSM and R2 (Table 2) suggests that R2\* is a mixed measure. Even though our simple linear model does not reflect the complexities of the true relationships among R2, R2\*, and QSM, our analysis, nevertheless, demonstrates that different BG structures have very different relative contributions from QSM and R2. It also suggests that R2\* is a less sensitive measure than QSM, whereas R2 may provide complementary information. Thus, our finding that CSF-normalized T2WI correlates well with T2-relaxometry is of interest because it indicates that fast and simple T2WI can serve as a substitute for time-consuming T2 relaxometry.

**Table 5: Correlation coefficients (P values) for semipartial correlations after adjusting MRI parameters for age and EDSS for disease duration**

	GP	Put	Cau	Aput	Pput
Sqrt (Flanker) vs age-adjusted QSM	0.26 (.18)	0.36 (.063)	0.51 (.0058) <sup>a</sup>	0.45 (.016) <sup>a</sup>	0.26 (.17)
Sqrt (Flanker) vs age-adjusted R2	0.33 (.09)	0.34 (.08)	0.31 (.11)	0.37 (.056)	0.23 (.25)
Duration-adjusted EDSS vs age-adjusted QSM	0.00 (.98)	0.39 (.036) <sup>a</sup>	0.01 (.95)	0.34 (.07)	0.40 (.032) <sup>a</sup>
Duration-adjusted EDSS vs age-adjusted R2	0.16 (.43)	0.51 (.0059) <sup>a</sup>	0.46 (.014) <sup>a</sup>	0.51 (.0054) <sup>a</sup>	0.44 (.019) <sup>a</sup>

**Note:**—Sqrt indicates the square root transformation used for the non-normal distributed Flanker test metrics; Cau, caudate; Put, putamen; Aput, cognitive anterior part of putamen, region predominantly connected to frontal cortex; Pput, motor posterior part of putamen, region predominantly connected to sensorimotor cortex.

<sup>a</sup> Statistically significant at  $P < .05$ .

In summary, both the larger dynamic range and the small fractional contribution of QSM to  $R2^*$  suggest that QSM is a more sensitive and perhaps more specific measure than  $R2^*$ . Future studies modeling  $R2$ ,  $R2^*$ , and QSM based on tissue microstructure, including paramagnetic iron predominantly located in oligodendrocytes and diamagnetic myelin, may further elucidate the relative importance of QSM versus  $R2$ .

### Association of MR Imaging with Clinical and Cognitive Measures

An interesting finding of our study was that cognitive performance measured by the Flanker test was associated with QSM but not  $R2$  in the caudate and anterior putamen, whereas EDSS was preferentially associated with  $R2$ .

**Association of EDSS with MR Imaging Metrics.** EDSS is a measure of physical disability in MS. In our population, the EDSS score was strongly correlated with disease duration. We found that EDSS was associated with  $R2$  for the caudate and putamen, with QSM in the posterior putamen, but not the globus pallidus. Conversely, Rudko et al<sup>23</sup> found an association between EDSS for both QSM and  $R2^*$  in all BG regions. This discrepancy may be due to differences in population characteristics; the patients of Rudko et al were younger and had shorter disease duration; these features were not associated with EDSS. Additionally, their average ROI analysis included the full BG structures as defined by atlas data, whereas our study evaluated the central part seen on axial images. Thus, our MR imaging measures may have included specific functionally connected BG regions, whereas the data of Rudko et al included a mixture of all functional BG regions.

**Association of the Flanker Task with MR Imaging.** We found a positive association between the Flanker task performance and QSM for the caudate and anterior putamen, but not for the posterior putamen and GP. No associations were found with  $R2$ .

These findings are consistent with preferential connectivity patterns linking the caudate and anterior putamen to frontal brain areas necessary for inhibitory control processing (Fig 2).<sup>14,15</sup> In contrast, the posterior putamen is connected to the motor-sensory cortex, and the GP is linked to motor, cognitive, and limbic areas.<sup>14,15</sup> In addition, comparison of MR imaging metrics suggests that QSM is perhaps most sensitive for the detection of tissue damage, especially in the caudate. To the best of our knowledge, only 1 prior study has examined associations between T2 hypointensity and cognitive performance, finding an association between a composite neuropsychological score and CSF-normalized T2WI in the GP.<sup>6</sup> Differences in the neuropsychological battery may have contributed to the observed discrepancy.

Future studies are needed to confirm our initial results. First,

our group of patients with MS ( $n = 29$ ) is too small to firmly establish the validity of associations observed in our study. Studies with a larger MS population and/or longitudinal studies are needed. Furthermore, our study did not include healthy subjects, though our MR imaging metrics followed previously published trends.<sup>22-26</sup> However, the notion that changes in QSM and  $R2$  in BG areas preferentially connected to cognitive cortical areas, which may relate to cognitive performance, needs to be further established in healthy subjects.

**Flanker versus Stroop Tasks.** We expected to find associations between Flanker and Stroop task measures and MR imaging metrics. In contrast, our results did not provide evidence for an association between Flanker and Stroop measures or for the Stroop and any MR imaging measure. Although both the Flanker and Stroop tasks are subsumed under the umbrella term of “inhibitory control,” these 2 widely used measures tap into interrelated facets of interference suppression and response inhibition, respectively. “Interference suppression” refers to the ability to suppress task-irrelevant information in favor of task-relevant information, whereas “response inhibition” taps into the ability to suppress a dominant response in favor of a nondominant response.<sup>27,28</sup> Although both of these facets of inhibitory control rely on the frontal-striatal circuitry<sup>29</sup> and the BG have been implicated in behavioral performance on these measures, we did not find an association between MR imaging metrics in BG and Stroop performance. This dissociation suggests that there may be some specificity to BG functioning in individuals with MS, and future research could more clearly parse the involvement of the BG substructures in different facets of inhibitory control for this population.

### Regional Variability

Another prominent feature in our high-resolution 7T data was the pronounced spatial variability observed in QSM and T2/T2\*WI, specifically the posterolateral-to-anteromedial signal change in the putamen and focal signal differences most often seen in the GP. Earlier studies by using low-resolution T2WI did not report such findings.<sup>1,2,5,6</sup> However, several more recent studies described analogous spatial variability in healthy aging<sup>22,24,26</sup> and related it to cognitive decline in aging.<sup>25</sup> A study by Zivadinov et al,<sup>11</sup> using analysis methods emphasizing focal high iron over global/average iron in the BG, found a strong differentiation between healthy controls and patients with MS. Rudko et al<sup>23</sup> also found similar patterns in voxelwise  $z$  score maps comparing healthy controls and patients with MS. Mechanisms for variable iron deposition are not known, but it was suggested that they coincide with lenticulostriate arterioles penetrating the BG,<sup>26,30</sup>



indicative of mineralization, including iron encrustation and/or calcification near vessels.

In future studies, it will be instructive to examine how these observed regional MR imaging changes relate to BG functional connections and clinical and cognitive decline in MS. For example, the cases in Fig 2 may suggest that it is feasible to find a visual scoring system for characterizing signal change in BG subregions defined by prior knowledge of BG functional subdivisions.<sup>14,15</sup> Better yet, subject-specific BG-cortex connections could be identified by simultaneous DTI studies and used to define specific ROIs for QSM and R2 tissue characterization. Finally, voxelwise correlation of MR imaging with clinical and cognitive measures could be used in future studies to better establish BG functionality as a biomarker of disease progression.

We expect that future work by using data analyses that takes into account both local patterns of iron increase and BG functional topography will be the key to gaining additional insight into the role of BG iron in MS-related clinical and cognitive decline and disease progression. High-resolution 7T is uniquely suited for this purpose.

## CONCLUSIONS

Our study showed that both QSM and R2 are indicators for tissue changes in the BG of patients with MS and may provide somewhat complementary information. QSM is more sensitive than R2\*, which is a composite measure of R2 and QSM. We substantiated our hypothesis that QSM-based BG assessment can reveal tissue changes that are implicated in BG-reliant tasks of inhibitory control. If the results from our initial cross-sectional study are replicated in future research with larger populations and/or are extended through longitudinal studies, QSM-based MR imaging can be established as a sensitive biomarker for cognitive decline in MS and serve as an outcome measure to determine treatment efficacy.

Disclosures: Petra Schmalbrock—RELATED: Grant: Biogen Idec\*; Support for Travel to Meetings for the Study or Other Purposes: Biogen Idec.\* Ruchika S. Prakash—RELATED: Grant: Biogen Idec (partial funding); Support for Travel to Meetings for the Study or Other Purposes: Biogen Idec (partial funding). Brittny Schirda—RELATED: Grant: Biogen Idec\*; Support for Travel to Meetings for the Study or Other Purposes: Biogen Idec (partial funding).\* Alisha Janssen—RELATED: Grant: Biogen Idec\*; Fees for Participation in Review Activities such as Data Monitoring Boards, Statistical Analysis, Endpoint Committees, and the Like: Biogen Idec.\* Grant K. Yang—RELATED: Grant: Goldwater Scholarship Program. Mary Russell—RELATED: Grant: Biogen Idec\*; Support for Travel to Meetings for the Study or Other Purposes: Biogen Idec grant.\* Michael V. Knopp—RELATED: Grant: Ohio Third Frontier TECH II-044.\* Aaron Boster—UNRELATED: Consultancy/Honoraria: Teva, Biogen, Novartis, Genzyme, Mallinckrodt, Medtronic. Jacqueline A. Nicholas—UNRELATED: Consultancy: Novartis, Teva, Genzyme, Biogen Idec; Grants/Grants Pending: National Multiple Sclerosis Society\*; Payment for Lectures (including service on Speakers Bureaus): Novartis, Teva, Biogen Idec, Genzyme. Michael Racke—UNRELATED: Board Membership: Editorial Boards: *Annals of Neurology*, *JAMA Neurology*, *Annals of Clinical and Translational Neurology*, *Journal of Neuroimmunology* (editor-in-chief), *Therapeutic Advances in Neurologic Disorders*; Other: 2013–15 Research Program Advisory Committee of the National Multiple Sclerosis Society, 2015 Americas Committee for Treatment and Research in Multiple Sclerosis Advisory Committee, International Society of Neuroimmunology Advisory Board, Consortium of Multiple Sclerosis Centers (Treasurer/Executive Committee, 2010–present), MS Section of the American Academy of Neurology (Executive Committee, 2014–15), Comments: Other boards unpaid but travel/lodging often supported to attend meetings; Grants/Grants Pending: Novartis,\* Genentech,\* DioGenix,\* Comments: Money paid to Ohio State for participation in clinical trials; Consulting Fee or Honorarium: Novartis, Genentech, Biogen Idec, Teva Neuroscience, Comments: Honoraria received for consulting; Other: *Journal of Neuroimmunology*, *JAMA Neurol-*

*ogy*, Comments: Money received for serving as editor-in-chief (JN) or editorial board member (JAMA Neuro); Payment for Lectures (including service on Speakers Bureaus): Honoraria, travel, and/or lodging from multiple institutions for giving lectures (University of Texas–Houston, CME Outfitters, National Institutes of Health, American Academy of Neurology, Allegheny General Hospital, Consortium of Multiple Sclerosis Centers, European Academy of Neurology, Lingnan International Neurological Summit Forum, Hunan Central University, Peking Union Medical College). David Pitt—UNRELATED: Payment for Lectures (including service on Speakers Bureaus): Biogen Idec.\* Money paid to the institution.

## REFERENCES

1. Bakshi R, Benedict RHB, Bermel RA, et al. T2 hypointensity in the deep gray matter of patients with multiple sclerosis: a quantitative magnetic resonance imaging study. *Arch Neurol* 2002;59:62–68 CrossRef Medline
2. Bermel RA, Puli SR, Rudick AA, et al. Prediction of longitudinal brain atrophy in multiple sclerosis by gray matter magnetic resonance imaging T2 hypointensity. *Arch Neurol* 2005;62:1371–76 CrossRef Medline
3. Zhou FQ, Zee CS, Gong HH, et al. Differential changes in deep and cortical gray matters in patients with MS: a quantitative magnetic resonance imaging study. *J Comput Assist Tomog* 2010;34:413–36 CrossRef Medline
4. Toja CW, Benedict RH, Weinstock-Guttman B, et al. MRI T2 hypointensity of the dentate nucleus is related to ambulatory impairment in multiple sclerosis. *J Neurol Sci* 2005;234:17–24 CrossRef Medline
5. Zhang Y, Metz LM, Yong VW, et al. 3T deep gray matter T2 hypointensity correlates with disability over time in stable relapsing-remitting multiple sclerosis: a 3-year pilot study. *J Neurol Sci* 2010; 297:76–81 CrossRef Medline
6. Brass SD, Benedict RH, Weinstock-Guttman B, et al. Cognitive impairment is associated with subcortical magnetic resonance imaging grey matter T2 hypointensity in multiple sclerosis. *Mult Scler* 2006;12:437–44 CrossRef Medline
7. Neema M, Arora A, Healy BC, et al. Deep gray matter involvement on brain MRI scans is associated with clinical progression in multiple sclerosis. *J Neuroimaging* 2009;19:3–8 CrossRef Medline
8. Pawate S, Wang L, Song Y, et al. Analysis of T2 intensity by magnetic resonance imaging of deep gray matter nuclei in multiple sclerosis patients: effect of immunomodulatory therapies. *J Neuroimaging* 2012;22:137–44 CrossRef Medline
9. Burgetova A, Seidl Z, Krasensky J, et al. Multiple sclerosis and the accumulation of iron in the basal ganglia: quantitative assessment of brain iron using MRI T2 relaxometry. *Eur Neurol* 2010;63: 136–43 CrossRef Medline
10. Walsh AL, Blevins G, Lebel RM, et al. Longitudinal MR imaging of iron in multiple sclerosis: an imaging marker of disease. *Radiology* 2014;270:186–96 CrossRef Medline
11. Zivadinov R, Heininen-Brown M, Shirda CV, et al. Abnormal subcortical deep-gray matter susceptibility-weighted imaging filtered phase measurement in patients with MS: a case-control study. *Neuroimage* 2012;59:331–39 CrossRef Medline
12. Langkammer C, Liu T, Khalil M, et al. Quantitative susceptibility mapping in multiple sclerosis. *Radiology* 2013;267:551–59 CrossRef Medline
13. Langkammer C, Schweser F, Krebs B, et al. Quantitative susceptibility mapping (QSM) as a means to measure brain iron? A post mortem validation study. *Neuroimage* 2012;62:1593–99 CrossRef Medline
14. Karachi C, François C, Parain K, et al. Three-dimensional cartography of functional territories in the human striatopallidal complex by using calbindin immunoreactivity. *J Comp Neurol* 2002;450: 122–34 CrossRef Medline
15. Lehericy S, Ducros M, Van de Moortele PF, et al. Diffusion tensor fiber tracking shows distinct corticostriatal circuits in humans. *Ann Neurol* 2004;55:522–29 CrossRef Medline
16. Middleton FA, Strick PL. Basal ganglia output and cognition: evi-



- dence from anatomical, behavioral, and clinical studies. *Brain Cogn* 2000;42:183–20 CrossRef Medline
17. Jenkins M. **Fast automated, N-dimensional phase-unwrapping algorithm.** *Magn Reson Med* 2003;49:193–97 CrossRef Medline
  18. Liu T, Khalidov I, de Rochefort L, et al. **A novel background field removal method for MRI using projection onto dipole fields (PDF).** *NMR Biomed* 2011;24:1129–36 CrossRef Medline
  19. Yang GK. *Computing Magnetic Susceptibility Maps from Gradient Recalled Echo MRI for use in Multiple Sclerosis Studies* [thesis]. Columbus: Ohio State University; 2013
  20. Rao SM; Cognitive Function Study Group of the National Multiple Sclerosis Society. *A Manual for the Brief Repeatable Battery of Neuropsychological Tests in Multiple Sclerosis*. New York: National Multiple Sclerosis Society; 1990
  21. Janssen A, Boster A, Lee H, et al. **The effects of video-game training on broad cognitive transfer in multiple sclerosis: a pilot randomized controlled trial.** *J Clin Exp Neuropsychol* 2015;37:285–302 CrossRef Medline
  22. Li W, Wu B, Batrachenko A, et al. **Differential developmental trajectories of magnetic susceptibility in human brain gray and white matter over the lifespan.** *Hum Brain Mapp* 2014;35:2698–713 CrossRef Medline
  23. Rudko DA, Solovey I, Gati JS, et al. **Multiple sclerosis: improved identification of disease-relevant changes in gray and white matter by using susceptibility-based MR imaging.** *Radiology* 2014; 272: 851–64 CrossRef Medline
  24. Harder SL, Hopp KM, Ward H, et al. **Mineralization of the deep gray matter with age: a retrospective review with susceptibility-weighted MR imaging.** *AJNR Am J Neuroradiol* 2008;29:176–83 CrossRef Medline
  25. Penke L, Valdés Hernández MC, Maniega SM, et al. **Brain iron deposits are associated with general cognitive ability and cognitive aging.** *Neurobiol Aging* 2012;33:510–17.e2 CrossRef Medline
  26. Glatz A, Valdés Hernández MC, Kiker AJ, et al. **Characterization of multi-focal T2\*-weighted MRI hypointensities in the basal ganglia of elderly community-dwelling subjects.** *Neuroimage* 2013;82: 470–80 CrossRef Medline
  27. Nigg JT. **On inhibition/disinhibition in developmental psychopathology: views from cognitive and personality psychology and a working inhibition taxonomy.** *Psychol Bull* 2000;126:220–46 CrossRef Medline
  28. Brydges CR, Anderson M, Reid CL, et al. **Maturation of cognitive control: delineating response inhibition and interference suppression.** *PLoS One* 2013;8:e69826 CrossRef Medline
  29. Bunge SA, Dudukovic NM, Thomason ME, et al. **Immature frontal lobe contributions to cognitive control in children: evidence from fMRI.** *Neuron* 2002;33:301–11 CrossRef Medline
  30. Feekes JA, Cassell MD. **The vascular supply of the functional compartments of the human striatum.** *Brain* 2006;129:2189–201 CrossRef Medline

# Detection of Normal Aging Effects on Human Brain Metabolite Concentrations and Microstructure with Whole-Brain MR Spectroscopic Imaging and Quantitative MR Imaging

V.V. Eyler,  A.A. Maudsley,  P. Bronzlik, P.R. Dellani, H. Lanfermann, and X.-Q. Ding



## ABSTRACT

**BACKGROUND AND PURPOSE:** Knowledge of age-related physiological changes in the human brain is a prerequisite to identify neurodegenerative diseases. Therefore, in this study whole-brain <sup>1</sup>H-MRS was used in combination with quantitative MR imaging to study the effects of normal aging on healthy human brain metabolites and microstructure.

**MATERIALS AND METHODS:** Sixty healthy volunteers, 21–70 years of age, were studied. Brain maps of the metabolites NAA, creatine and phosphocreatine, and Cho and the tissue irreversible and reversible transverse relaxation times T2 and T2' were derived from the datasets. The relative metabolite concentrations and the values of relaxation times were measured with ROIs placed within the frontal and parietal WM, centrum semiovale, splenium of the corpus callosum, hand motor area, occipital GM, putamen, thalamus, pons ventral/dorsal, and cerebellar white matter and posterior lobe. Linear regression analysis and Pearson correlation tests were used to analyze the data.

**RESULTS:** Aging resulted in decreased NAA concentrations in the occipital GM, putamen, splenium of the corpus callosum, and pons ventral and decreased creatine and phosphocreatine concentrations in the pons dorsal and putamen. Cho concentrations did not change significantly in selected brain regions. T2 increased in the cerebellar white matter and decreased in the splenium of the corpus callosum with aging, while the T2' decreased in the occipital GM, hand motor area, and putamen, and increased in the splenium of the corpus callosum. Correlations were found between NAA concentrations and T2' in the occipital GM and putamen and between creatine and phosphocreatine concentrations and T2' in the putamen.

**CONCLUSIONS:** The effects of normal aging on brain metabolites and microstructure are region-dependent. Correlations between both processes are evident in the gray matter. The obtained data could be used as references for future studies on patients.

**ABBREVIATIONS:** B5d = pons dorsal; B5v = pons ventral; HK = hand motor area; SCC = splenium of the corpus callosum; tCr = creatine and phosphocreatine

As a prerequisite to identify neurodegenerative diseases, the knowledge of age-related physiologic changes in the human brain becomes more important in a society with increasing life expectancy. <sup>1</sup>H-MR spectroscopy and quantitative MR imaging of brain tissue are both useful tools to study these changes. <sup>1</sup>H-MR spectroscopy enables detection of brain metabolites, which, for example, reflect neuronal attenuation and

integrity (NAA), relate to the turnover of cell membranes (Cho), or serve as a marker of energy metabolism (creatine and phosphocreatine [tCr]). Thus, <sup>1</sup>H-MR spectroscopy has often been applied to study age-associated neurometabolism<sup>1</sup> or pathology in the human brain.<sup>2</sup> Due to limitations in the spatial coverage of standard acquisition techniques, most of the <sup>1</sup>H-MR spectroscopy studies have been performed by using just 1 or a few small brain regions.<sup>1</sup> In recent years, a whole-brain <sup>1</sup>H-MRS technique with high spatial resolution has been established and has been used to study metabolic aging effects by deriving mean metabolite concentrations within each brain lobe.<sup>3</sup> However, the evaluation of aging effects in multiple, more differentiated anatomic structures in human brain remains unreported, to our knowledge.


Quantitative MR imaging methods can be used to quantify relaxation processes of brain tissue, such as transverse relaxation due to spin-spin interactions characterized by the irreversible relaxation time (T2), local magnetic field inhomoge-

Received March 16, 2015; accepted after revision July 26.

From the Institute of Diagnostic and Interventional Neuroradiology (V.V.E., P.B., P.R.D., H.L., X.-Q.D.), Hannover Medical School, Hannover, Germany; and Department of Radiology (A.A.M.), University of Miami School of Medicine, Miami, Florida.

This work was partially supported by Deutsche Forschungsgemeinschaft and by the National Institutes of Health grants R01 EB016064 and R01 EB008222 (A.A.M.).

Please address correspondence to Xiao-Qi Ding, MD, Institute of Diagnostic and Interventional Neuroradiology, Hannover Medical School, Carl-Neuberg-Str One, 30625 Hannover, Germany; e-mail: ding.xiaoqi@mh-hannover.de

 Indicates open access to non-subscribers at [www.ajnr.org](http://www.ajnr.org)

<http://dx.doi.org/10.3174/ajnr.A4557>

neity characterized by the reversible relaxation time ( $T_2'$ ), or both mechanisms together characterized by an effective relaxation time ( $T_2^*$ ), with the relation of  $1/T_2^* = 1/T_2 + 1/T_2'$ . The variations of transverse relaxation times reflect influences from the molecular environment within the tissue and provide a measure of microstructural changes in the maturing or aging brain<sup>4-6</sup> and brain diseases.<sup>7,8</sup>

In this prospective study, NAA, tCr, and Cho concentrations and  $T_2$  and  $T_2'$  values were measured simultaneously in selected brain structures by using whole-brain  $^1\text{H}$ -MRS and quantitative MR imaging with the aim of detecting physiologic changes of the metabolism and microstructure of the human brain related to normal aging and possible correlations among metabolic and microstructural changes, which may provide insight into the effects of aging.

## MATERIALS AND METHODS

### Subjects

Sixty-eight healthy volunteers were recruited from the local population. Based on a self-reporting interview, all subjects had no history of brain trauma, neurologic disorder, or other systemic diseases. Each subject received 2 screening tests (DemTect and the Beck Depression Inventory II) to exclude cognitive or psychiatric impairments.<sup>9,10</sup> Sixty subjects 21–70 years of age (mean age,  $44 \pm 14$  years; 6 men and 6 women in each age group—ie, 21–30 years, group 1; 31–40 years, group 2; 41–50 years, group 3; 51–60 years, group 4; and 61–70 years, group 5) were included in the study. Eight subjects were excluded after the screening tests or due to incomplete MR imaging examination findings. The study was approved by local institution review board, and written consent was obtained from all subjects before the examinations.

### MR Imaging Examinations

All MR imaging examinations were performed at 3T (Verio; Siemens, Erlangen, Germany). A 12-channel phased array head coil was used. The MR imaging protocol included a  $T_2$ -weighted turbo spin-echo sequence with 3 echoes (triple TE) (TR/TE, 6640/8.7/70/131 ms;  $150^\circ$  flip angle; 3-mm section thickness;  $256 \times 208$  matrix;  $256 \times 208$  mm FOV; acceleration factor, 2), a  $T_2^*$ -weighted gradient-echo sequence with triple TEs (TR/TE, 1410/6.42/18.42/30.42 ms;  $20^\circ$  flip angle; 3-mm section thickness;  $256 \times 208$  matrix;  $256 \times 208$  mm FOV; acceleration factor, 2), and volumetric spin-echo-planar spectroscopic imaging (TR/TE, 1710/70 ms) acquisition by using an FOV of  $280 \times 280 \times 180$  mm<sup>3</sup> and a slab of 135 mm, with a resolution of approximately 1 mL.<sup>11</sup> The spin-echo-planar spectroscopic imaging acquisition included a second dataset obtained without water suppression that provided a water reference signal with spatial parameters identical to those of the metabolite MR spectroscopy. The water reference MR spectroscopic imaging was used for several processing functions, including measurement and correction of the resonance frequency offset at each voxel location, correction of line shape distortions, and providing an internal signal reference for the normalization of metabolite concentrations.<sup>12</sup> In addition, a  $T_1$ -weighted 3D MPRAGE image was obtained at 1-mm isotropic resolution for anatomic reference. The spin-echo-planar spectroscopic imaging, MPRAGE, TSE, and gradient-echo scans were

obtained with the same angulation so that the same anatomic structures could be identified. The total scan time was approximately 36 minutes.

### Data Processing

$T_2$ - and  $T_1$ -weighted images were inspected by 2 experienced neuroradiologists to exclude subjects with morphologic abnormalities.

**Whole-Brain  $^1\text{H}$ -MRS and Metabolite Maps.** Reconstructions of the metabolite and water reference images were made as described by Maudsley et al,<sup>3</sup> on which the spin-echo-planar spectroscopic imaging data were analyzed by using the Metabolic Imaging and Data Analysis software to determine volumetric maps of the metabolites NAA, tCr, and Cho, with metabolite signal-intensity normalization by using tissue water as an internal reference and the corresponding maps of spectral line width. All resultant maps were spatially transformed and interpolated to a standard spatial reference at 2-mm isotropic resolution.

**Maps of Relaxation Times.**  $T_2$  and  $T_2^*$  maps were obtained on the fly on the MR imaging system with an extended image reconstruction provided by the manufacturer, by using monoexponential fitting to the signal-intensity decay curves of the triple TE data acquired with TSE and gradient-echo sequences, respectively.  $T_2'$  values were calculated according to the relationship  $1/T_2' = 1/T_2^* - 1/T_2$ .

**ROI Analysis.** Local metabolite concentrations NAA, tCr, and Cho, as a ratio to tissue water, together with the spectral line width and tissue relaxation times  $T_2$  and  $T_2'$ , were determined by using mean values over ROIs at 13 locations within each hemisphere: the frontal and parietal WM, centrum semiovale, splenium of the corpus callosum (SCC), hand motor cortex (HK), occipital GM, putamen, pallidum, thalamus, pons ventral (BSv), pons dorsal (BSd) at the level of the upper pons, and cerebellar white matter at the axial level of the midcerebellar peduncle and cerebellar posterior lobe. Metabolite values obtained from spectra with a line width of  $>12$  Hz or with a signal-to-noise ratio of  $<5$  were not sampled. Paired  $t$  tests showed that there were significant differences ( $P < .05$ ) of up to 10% between the bihemispheric values at several ROIs. However, considering the limitations of the sample size related to the handedness (54 for right-handed versus 6 for left-handed), the left and right values for each ROI were averaged for further analysis. Due to local magnetic field distortion caused by neighboring structures containing bone and air, ROIs at the genu of the corpus callosum and caudate nucleus were not considered. All ROIs were carefully drawn within a single section on  $T_1$ -weighted images (for metabolite measurements) and  $T_2$ -weighted images (for quantitative MR imaging measurements) as a circle with an area of  $29 \pm 4$  mm<sup>2</sup>, which was manually located according to anatomic landmarks to exclude partial volume effects. ROI measurements on the relaxation time maps were made by using ImageJ software (National Institutes of Health, Bethesda, Maryland),<sup>13</sup> while those on the metabolites were done with the ROI tool in the Metabolic Imaging and Data Analysis software. No CSF correction was made considering that the ROIs were placed within brain tissue.

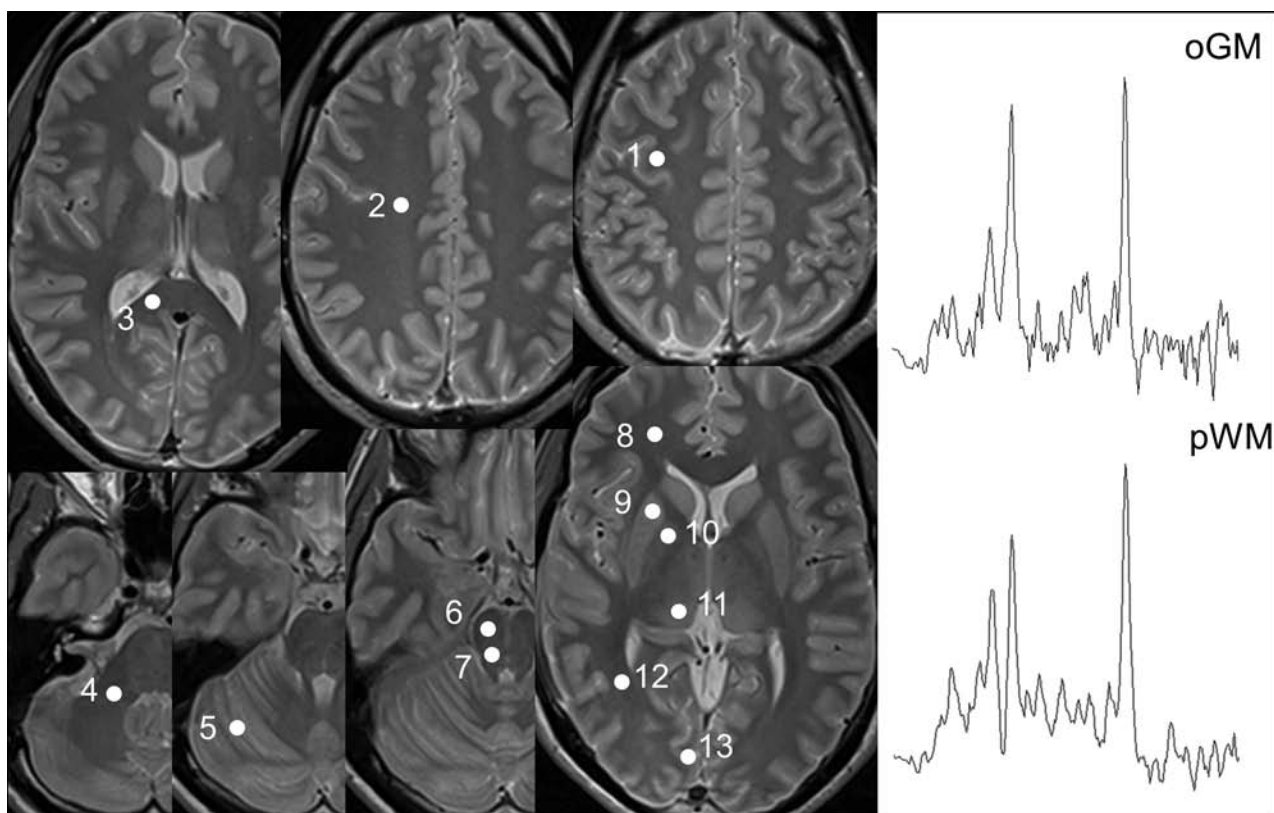


**FIG 1.** Locations of each selected ROI in the right brain hemisphere displayed as *white filled circles* on the T2-weighted images, respectively, and sample spectra from the parietal white matter and occipital gray matter of a 31-year-old volunteer. The numbering represents the ROIs in the hand motor cortex (1), centrum semiovale (2), splenium of the corpus callosum (3), cerebellar white matter (4) and posterior lobe (5), brain stem ventral (6) and dorsal (7), frontal white matter (8), putamen (9), pallidum (10), thalamus (11), parietal white matter (pWM, 12), and occipital gray matter (oGM, 13), respectively.

### Statistical Analysis

For each ROI, the 2-sided  $t$  tests with Bonferroni correction (significance level,  $\alpha = .05/3 = .017$ ) were used to estimate sex differences of the measured local metabolite concentrations or transverse relaxation times. A linear regression analysis was used to estimate the age-dependence of the measured values, and the Pearson correlation test was used to test for possible correlations between changes of local metabolite concentrations and local transverse relaxation times (ie, to quantify the degree to which they are related). For linear regression analysis and for the Pearson correlation test, a low significance level of .01 was used to avoid accidental associations. Statistical analyses were performed with SPSS, Version 21 (IBM, Armonk, New York).

### RESULTS

Locations of each selected ROI in the right-brain hemisphere are shown in Fig 1 as white filled circles on the T2-weighted images of a 31-year-old volunteer, where sample spectra in the parietal white matter and occipital gray matter are also shown. Metabolite maps of NAA, Cho, and tCr and maps of transverse relaxation times were obtained for all subjects for further ROI analyses.

The values of NAA, Cho, tCr concentrations, and T2 and T2' were measured at each ROI on the corresponding maps of metabolites or relaxation times for all subjects. The group mean values of each age group obtained in corresponding ROIs are shown in Fig 2, where both metabolite concentrations and the transverse

relaxation times show clear differences between the ROIs, indicating that the brain metabolite content or relaxation times are brain region-dependent.

Two-sided  $t$  tests revealed no significant sex differences for most measures with the exceptions of NAA concentrations and T2' in BSD, tCr concentrations in HK, and T2' in the cerebellar posterior lobe and centrum semiovale. Therefore, values for male and female subjects were combined for most ROIs, and those showing significant sex differences were analyzed separately for men and women. While the spectral line width at all ROIs did not reveal any significant correlation to age, linear regression analysis revealed significant ( $P < .01$ ) changes of metabolite concentrations and transverse relaxation times with age in most of the selected brain structures, as shown in the Table: NAA concentration was significantly decreased in the occipital GM, putamen, SCC, and BSv, with amounts varying from  $-16\%$  to  $-26\%$  within the observed 5 decades, and showed a trend of reduced values in the centrum semiovale ( $R = -0.292$ ,  $P = .024$ ) and parietal WM ( $R = -0.288$ ,  $P = .026$ ) and the thalamus ( $R = -0.301$ ,  $P = .019$ ) (not shown). tCr concentration was reduced significantly in the putamen ( $-17\%$ ) and dorsal brain stem ( $-16\%$ ) and showed a tendency of increase in frontal WM ( $R = 0.27$ ,  $P = .044$ ) (not shown). Cho concentration in selected ROIs did not change significantly with age but had a small increase in frontal WM ( $R = 0.261$ ,  $P = .054$ ). T2 decreased with age in the SCC ( $-14\%$ ) and



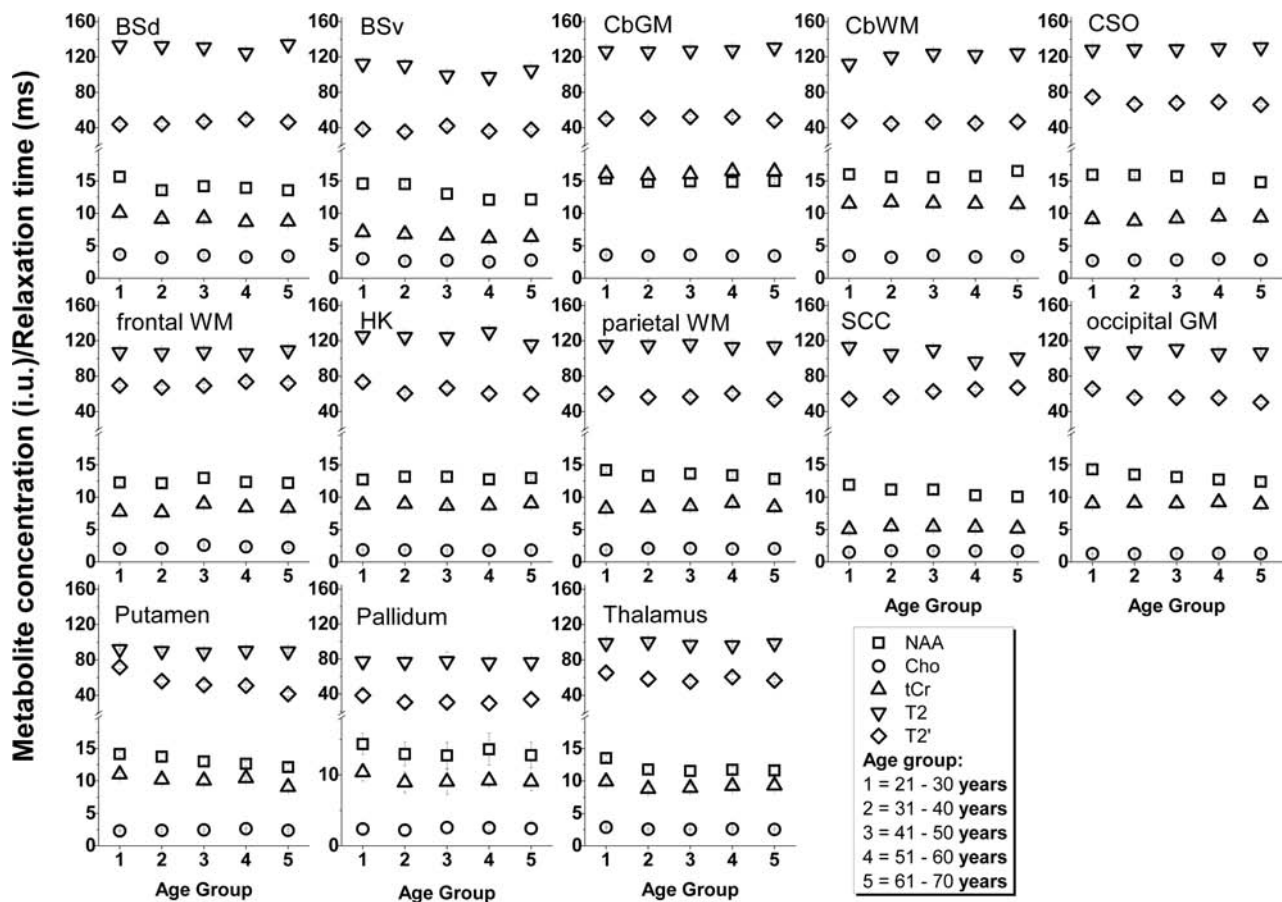


**FIG 2.** Group mean values of metabolite concentrations and tissue transverse relaxation times (y axis) with SDs for age group 1 (21–30 years), group 2 (31–40 years), group 3 (41–50 years), group 4 (51–60 years), and group 5 (61–70 years) are shown. The ROIs are as described in Fig 1.

**Significant associations ( $P < .01$ ) of the regional metabolite concentrations and transverse relaxation times with age, derived with linear regressions**

ROI	Parameter	Mean <sup>a</sup>	SD	R	P	No. <sup>b</sup>	Intercept	Slope	Variation in 50 Yr (%) <sup>c</sup>
Occipital GM	NAA	13.2	1.6	−0.40	.002	59	15.16	−0.04	−16
	T2'	56.7	9.4	−0.45	.000	60	69.67	−0.30	−23
Putamen	NAA	13.2	1.5	−0.51	.000	60	15.54	−0.05	−19
	tCr	10.2	1.4	−0.39	.002	60	11.89	−0.04	−17
Pallidum <sup>d</sup>	T2'	55.1	13.1	−0.68	.000	60	83.44	−0.66	−47
	T2'	32.3	6.4	−0.34	.005	40	41.53	−0.24	−26 <sup>e</sup>
HK	T2'	63.6	10.5	−0.35	.007	60	76.72	−0.28	−20
	T2'	63.6	10.5	−0.35	.007	60	76.72	−0.28	−20
SCC	NAA	10.9	1.9	−0.36	.005	60	13.01	−0.05	−19
	T2	105.1	9.3	−0.47	.000	60	118.50	−0.31	−14
CbWM	T2'	57.5	7.4	0.40	.002	60	45.14	0.36	35
	T2	120.5	8.3	0.45	.000	60	108.93	0.26	12
BSv	NAA	13.4	2.4	−0.42	.003	50	16.73	−0.08	−26
BSd	tCr	9.2	1.3	−0.35	.010	53	10.64	−0.03	−16

**Note:**—R indicates the Pearson correlation coefficient.

<sup>a</sup> In ratio to internal water for metabolites and in milliseconds for relaxation times.

<sup>b</sup> Values of several ROIs were not sampled for all subjects ( $n < 60$ ) due to artifacts.

<sup>c</sup> In ratio to the values at 20 years of age.

<sup>d</sup> The values for subjects older than 60 years were not sampled for linear regression.

<sup>e</sup> Variation in 40 years. Significant linear relation of T2' to age in the pallidum was found for the ages between 20 and 60 years ( $P < .01$ ), but not for the whole age range (21–70 years,  $P > .01$ ).

increased in the cerebellar white matter (12%), and T2' decreased in occipital GM (−23%), putamen (−47%), and hand motor cortex (−20%) and increased in the SCC (35%) with age.

In Fig 3, the values of metabolite concentrations (top) and tissue transverse relaxation times (bottom) measured at the ROIs of the occipital GM, putamen, and pallidum are drawn according

to age, together with the corresponding results of linear regression analysis: The NAA and T2' in the occipital GM and the NAA, tCr, and T2' in the putamen revealed linear reductions with age ( $P < .01$ , Table), while tCr, Cho, and T2 in the occipital GM and Cho and T2 in the putamen did not show any age dependence. The results measured in the pallidum showed a tendency of de-

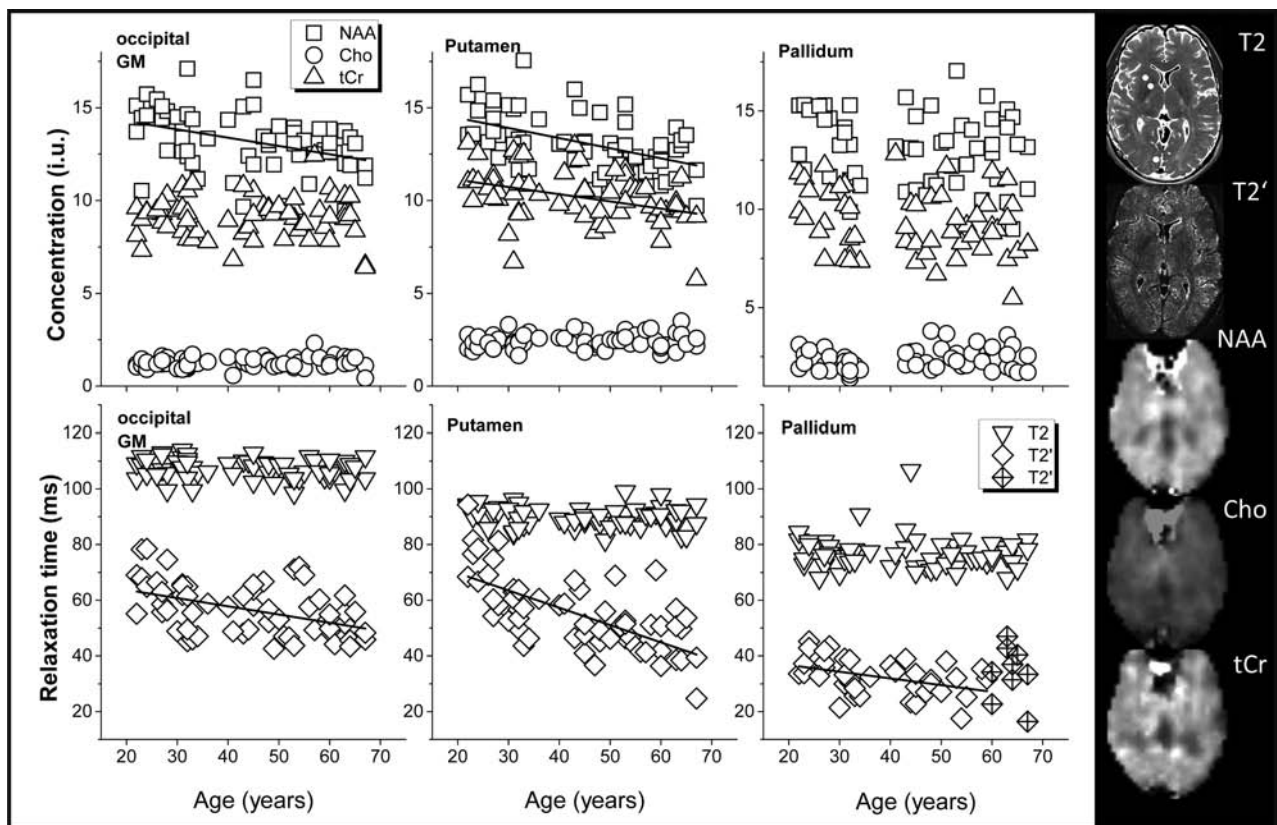


**FIG 3.** Values of the metabolite concentrations (top) and tissue transverse relaxation times (bottom) of all subjects measured at the ROIs of occipital GM, putamen, and pallidum drawn according to the age, where NAA and T2' in the occipital GM and NAA, tCr, and T2' in the putamen reveal linear reductions with age ( $P < .01$  with the value of each slope being given in the Table), while tCr, Cho, and T2 in the occipital GM and Cho and T2 in putamen do not show an age dependence. No significant age correlations were found in the pallidum both for metabolites and relaxation times, but a significant linear reduction of T2' with age was found up to 60 years of age ( $P < .01$  with the value of each slope being given in the Table).

creased tCr with age ( $R = -0.28$ ,  $P = .04 > .01$ ) and no significant age correlation for NAA, Cho, and T2. T2' values in the pallidum were the lowest ones in comparison with all other ROIs and revealed a linear reduction with ages from 20 to 60 years ( $-26\%$ ) ( $P < .01$ , Table), though without further significant reduction for older than 60 years of age ( $P = .73$ ). The Pearson correlation tests showed significant positive correlations ( $R = 0.53$ ,  $P < .01$ ) between NAA concentrations and T2' in the occipital cortical gray matter, between NAA concentrations and T2' ( $R = 0.55$ ,  $P < .01$ ), and between tCr concentration and T2' ( $R = 0.50$ ,  $P < .01$ ) in the putamen. Weak correlations between NAA concentrations and T2 ( $R = 0.30$ ,  $P = .02$ ) and between NAA concentrations and T2' ( $R = -0.27$ ,  $P = .03$ ) were found in the SCC.

## DISCUSSION

Previous studies have examined associations of brain metabolite concentrations with age in selected brain structures with varying results,<sup>1</sup> but few of these studies have examined a large number of brain anatomic structures. To our knowledge, no previous studies have examined possible associations with tissue relaxation times. The metabolite concentrations determined in this study agree in general with those reported by using single-voxel spectroscopy, with NAA being the largest component in the cerebrum and tCr, the largest component in cerebellum, while the Cho concentration is the smallest in both regions,<sup>14,15</sup> though in this study the

measurements were obtained in multiple regions by using only a single MR spectroscopic acquisition. The T2 and T2' values found in this study are also comparable with those previously published, with T2' being shortest in the supratentorial deep gray matter, and T2, longest in the cerebellum.<sup>6,16</sup>

With combined whole-brain <sup>1</sup>H-MRSI and quantitative MR imaging measurements, this study determined for the first time, simultaneously, the age-related metabolite concentrations and tissue transverse relaxation times at multiple supratentorial and infratentorial structures in the healthy human brain, which have the potential to provide a reference basis for future studies to identify pathologic alterations in patients. Additionally, with a significance level of .01, variable age dependences of the metabolite concentrations and the tissue relaxation times within the brain have been found. With increasing age, NAA changed the most among the 3 metabolites, with concentrations decreasing significantly in 4 ROIs (occipital GM, putamen, SCC, and BSv), while the tCr concentration decreased significantly in 2 ROIs (putamen, BSd). Cho concentration revealed only a tendency to increased values in the frontal white matter. Although the metabolite T2s were not directly measured, the observations of no significant correlations between age and spectral line width for all ROIs indicate that the changes in metabolite T2s with age are negligible. Thus, the possible influence on local metabolite concentrations

caused by variations of metabolite T2s with age was not considered. For transverse relaxation times, the aging effect was most obvious for T2', which showed significant age-related changes in 4 ROIs, the occipital GM, putamen, hand motor cortex, and SCC, and some changes in the pallidum, while T2 significantly changed with age in only 2 ROIs (SCC and cerebellar white matter).

These observations indicate that NAA and T2' are sensitive to brain aging. Moreover, the observed age-related metabolic and microstructural changes were strongly brain region-dependent: The most significant changes occurred in the putamen (reducing NAA and tCr concentrations and T2') and the SCC (reducing NAA concentrations and T2, and increasing T2'), indicating that both structures are vulnerable to metabolic and microstructural aging. These observations are in line with previous reports that both the putamen and corpus callosum play important roles concerning age-related cognitive and motor impairment.<sup>17,18</sup>

Decreased brain NAA with age in several brain structures has also been reported previously by different authors.<sup>3,19,20</sup> It has been suggested that decreased NAA concentrations reflect reduced neuronal attenuation or neuronal function.<sup>19,21</sup> Both reasons could be responsible for our observations of age-related NAA concentration reductions. While the age-related reductions of NAA concentration are frequently reported, findings for Cho and tCr in relation to the age reported until now are more divergent. Raininko and Mattsson,<sup>22</sup> in a single-voxel spectroscopy study at 1.5T, found age-related reduction of NAA concentration, but age-independent Cho concentrations and tCr concentrations in cerebral supraventricular white matter. Charles et al<sup>20</sup> found lower NAA, Cho, and tCr concentrations in the cortical and subcortical gray matter of older subjects but not in the white matter. In a single-voxel spectroscopy study at 1.5T on 50 healthy subjects 20–70 years of age, Brooks et al<sup>19</sup> found that the NAA decreased significantly with age in the interhemispheric tissue of the medial frontal lobe, with an overall decrease of 12% between the third and seventh decades, and the concentrations of Cr and Cho did not change significantly with age. Similar to our findings in the brain stem (decreased NAA concentrations at the BSv and decreased tCr concentrations at the BSd), an age-related decline of NAA and a trend toward decreased tCr concentrations in the upper brain stem were also observed by Moreno-Torres et al<sup>23</sup> in a single-voxel spectroscopy study on 57 healthy subjects from 23 to 79 years of age. Therefore, more MR spectroscopy studies under standardized conditions will be necessary to obtain more precise and comparable values for multicenter studies to clarify these divergent findings.

It is interesting to compare our results with the lobar mean metabolite content derived by Maudsley et al,<sup>3</sup> with the same spin-echo-planar spectroscopic imaging technique on a different sample of healthy volunteers. While our ROI measurements in the frontal WM for NAA (reduced with age), Cho, and tCr concentrations (both showed a tendency of increase with age) are consistent with their observations of age-related reduction of lobar mean NAA concentrations and an increase of lobar mean tCr and Cho concentrations,<sup>3</sup> we found that the tCr concentration was reduced with increasing age in the BSd and putamen, whereas the Cho concentration did not show significant age-related changes in the selected ROIs. These discrepancies may be caused by a

regional dependence of age-related metabolic distributions within the lobar structures that was observable only for ROI measurements, as revealed also by a study using both 2D-MR spectroscopy and single-voxel spectroscopy. With 2D MR spectroscopy in the centrum semiovale, Gruber et al<sup>24</sup> found a decrease of 3.1% per decade for NAA and an increase of 3.6% per decade for Cho, while with single-voxel spectroscopy located in the frontal lobe, they found a positive correlation between tCr and age, but only a trend of increased Cho with age in the frontal lobe, indicating again the inhomogeneity of metabolite distributions even within a brain lobe.

The tissue transverse relaxation parameters reflect molecular-level relaxation mechanisms and are sensitive to microstructural variations in tissue, such as changes of the free water content. For example, reduced free water corresponds to shortened T2 in the maturing brain,<sup>4,25</sup> while pathologic demyelination or neurodegeneration resulting in increased free water content is associated with prolonged T2.<sup>26–28</sup> In line with these facts, our observations of age-related increase of T2 in cerebellar white matter ( $R = 0.45$ ) may, therefore, reflect an age-related increase of free water within this region, whereas the decrease of T2 at SCC ( $R = -0.47$ ) may indicate a loss of free water content within that region, though the exact mechanism behind these changes is not yet clear. Siemonsen et al<sup>5</sup> found, in a retrospective study of 55 adults (12–90 years of age; mean age,  $54 \pm 20$ ), an age-related decrease of T2' in the lentiform nucleus ( $R = -0.69$ ) and no age correlation in the thalamus and parietal white matter, which are consistent with our observations that T2' showed a strong negative linear correlation to age in the putamen ( $R = -0.68$ ) and no correlation with age in the thalamus and parietal white matter.

Our findings that T2 and T2' values in the motor and occipital cortices were comparable and lowest in the pallidum are consistent with an earlier study on T2 by Jara et al<sup>29</sup> and with regional distribution of nonheme iron in the report by Hallgren and Sourander,<sup>30</sup> in which the iron content in the motor and occipital cortices was similar while the pallidum had the largest amount of iron. A decrease of T2' in the deep gray matter has been suggested as a marker of increased iron deposition,<sup>5,7,8</sup> while cortical T2' is considered to provide information about the local concentration of deoxyhemoglobin, which is reduced due to age-related variations of cerebral autoregulation and increased deoxyhemoglobin in elderly subjects.<sup>31–33</sup> An increase of T2' in the normal-appearing white matter of patients with multiple sclerosis was attributed to reduced metabolism.<sup>7</sup> Correspondingly, our observations of correlated decreases of T2' and NAA concentrations ( $R = 0.53$ ) in the occipital GM may indicate an association of an age-related increase of deoxyhemoglobin and reductions of neuronal attenuation and/or function in the occipital gray matter. The correlated decreases of T2' with NAA and tCr concentrations ( $R = 0.55$  and  $0.50$ , respectively) in the putamen may indicate associations of age-related increase of iron deposition (decreased T2') and reductions of neuronal attenuation and/or function (reduced NAA concentrations) and a decrease of energy metabolism (reduced tCr concentrations) in the deep gray matter, while the observed increase of T2' with age in the white matter of the SCC may reflect reduced metabolism with age,



consistent with the observations of an age-related reduction of NAA concentrations and T2 in the SCC. Also our observation of a smaller change in T2' values in the pallidum for ages older than 60 could be an indication of the metabolic function slowing with increased age. The evidence of an age-related increase of iron deposition with reduced neuronal function and energy metabolism in the putamen and age-related reduction of neuronal function, metabolism, and free water in the SCC may make the putamen and corpus callosum more vulnerable to neurodegenerative diseases.

There are several limitations to this study. The differences between the left and right hemispheres and the possible effect of handedness were not considered because of the limited sample size. Due to differences of section thickness (interpolated section thickness of 5.6 mm for metabolite maps versus 3 mm for T2 maps), the spatial volumes of ROIs obtained on metabolite maps did not match exactly those on quantitative MR imaging maps. The effect of partial volume contributions from neighboring structures and CSF was also not taken into account. This was, however, minimized by using a small ROI that was visually placed to avoid these contributions. An additional limitation is that subjects older than 70 years were not included due to difficulties in subject recruitment. To overcome these limitations, a study with a larger sample size and more selected brain-specific structures is necessary.

## CONCLUSIONS

This study has demonstrated that age-related metabolic and microstructural changes in the human brain are regionally dependent and more apparent in the cerebrum than in the cerebellum. Correlations between both processes are evident in the gray matter. These results could be used as references for future study on patients.

Disclosures: Andrew A. Maudsley—RELATED: Grant: National Institutes of Health\*; UNRELATED: Travel/Accommodations/Meeting Expenses Unrelated to Activities Listed: Helmholtz Association, Comments: International Scholars Award for travel to the Helmholtz research site in Germany. Heinrich Lanfermann—UNRELATED: Expert Testimony: Oberlandesgericht Braunschweig; Grants/Grants Pending: Acandis, Penumbra\*; Payment for Lectures (including service on Speakers Bureaus): Bender Imaging, Radiopharm; Payment for Development of Educational Presentations: Institut für medizinische und pharmazeutische Prüfungsfragen; Travel/Accommodations/Meeting Expenses Unrelated to Activities Listed: German Society of Neuroradiology, German Society of Radiology, Friedrich-Schiller-Universität Jena, Johann Wolfgang Goethe-Universität Frankfurt am Main. Xiao-Qi Ding—RELATED: Grant: German Research Foundation.\*Money paid to the institution.

## REFERENCES

- Haga KK, Khor YP, Farrall A, et al. **A systematic review of brain metabolite changes, measured with 1H magnetic resonance spectroscopy, in healthy aging.** *Neurobiol Aging* 2009;30:353–63 CrossRef Medline
- Barker PB, Bizzi A, De Stefano N, et al. *Clinical MR Spectroscopy: Techniques and Applications*. 1st ed. Cambridge: Cambridge University Press, 2009
- Maudsley AA, Govind V, Arheart KL. **Associations of age, gender and body mass with 1H MR-observed brain metabolites and tissue distributions.** *NMR Biomed* 2012;25:580–93 CrossRef Medline
- Ding XQ, Kucinski T, Wittkugel O, et al. **Normal brain maturation characterized with age-related T2 relaxation times: an attempt to develop a quantitative imaging measure for clinical use.** *Invest Radiol* 2004;39:740–46 CrossRef Medline
- Siemonsen S, Finsterbusch J, Matschke J, et al. **Age-dependent normal values of T2\* and T2' in brain parenchyma.** *AJNR Am J Neuroradiol* 2008;29:950–55 CrossRef Medline
- Sedlacik J, Boelmans K, Löbel U, et al. **Reversible, irreversible and effective transverse relaxation rates in normal aging brain at 3T.** *Neuroimage* 2014;84:1032–41 CrossRef Medline
- Holst B, Siemonsen S, Finsterbusch J, et al. **T2' imaging indicates decreased tissue metabolism in frontal white matter of MS patients.** *Mult Scler* 2009;15:701–07 CrossRef Medline
- Miszkiel KA, Paley MN, Wilkinson ID, et al. **The measurement of R2, R2\* and R2' in HIV-infected patients using the prime sequence as a measure of brain iron deposition.** *Magn Reson Imaging* 1997;15:1113–19 CrossRef Medline
- Steer RA, Clark DA, Beck AT, et al. **Common and specific dimensions of self-reported anxiety and depression: the BDI-II versus the BDI-IA.** *Behav Res Ther* 1999;37:183–90 CrossRef Medline
- Kalbe E, Kessler J, Calabrese P, et al. **DemTect: a new, sensitive cognitive screening test to support the diagnosis of mild cognitive impairment and early dementia.** *Int J Geriatr Psychiatry* 2004;19:136–43 CrossRef Medline
- Maudsley AA, Domenig C, Sherif S. **Reproducibility of serial whole-brain MR spectroscopic imaging.** *NMR Biomed* 2010;23:251–56 CrossRef Medline
- Barker PB, Soher BJ, Blackband SJ, et al. **Quantitation of proton NMR spectra of the human brain using tissue water as an internal concentration reference.** *NMR Biomed* 1993;6:89–94 CrossRef Medline
- Abramoff MD, Magalhães PJ, Ram SJ. **Image processing with ImageJ.** *Biophotonics International* 2004;11:36–42
- Baker EH, Basso G, Barker PB, et al. **Regional apparent metabolite concentrations in young adult brain measured by (1)H MR spectroscopy at 3 Tesla.** *J Magn Reson Imaging* 2008;27:489–99 CrossRef Medline
- Pouwels PJ, Brockmann K, Kruse B, et al. **Regional age dependence of human brain metabolites from infancy to adulthood as detected by quantitative localized proton MRS.** *Pediatr Res* 1999;46:474–85 CrossRef Medline
- Kumar R, Delshad S, Woo MA, et al. **Age-related regional brain T2-relaxation changes in healthy adults.** *J Magn Reson Imaging* 2012;35:300–08 CrossRef Medline
- Li W, Langkammer C, Chou YH, et al. **Association between increased magnetic susceptibility of deep gray matter nuclei and decreased motor function in healthy adults.** *Neuroimage* 2015;105:45–52 CrossRef Medline
- Ryberg C, Rostrup E, Paulson OB, et al. **LADIS study group. Corpus callosum atrophy as a predictor of age-related cognitive and motor impairment: a 3-year follow-up of the LADIS study cohort.** *J Neurol Sci* 2011;307:100–05 CrossRef Medline
- Brooks JC, Roberts N, Kemp GJ, et al. **A proton magnetic resonance spectroscopy study of age-related changes in frontal lobe metabolite concentrations.** *Cereb Cortex* 2001;11:598–605 CrossRef Medline
- Charles HC, Lazeyras F, Krishnan KR, et al. **Proton spectroscopy of human brain: effects of age and sex.** *Prog Neuropsychopharmacol Biol Psychiatry* 1994;18:995–1004 CrossRef Medline
- Chao LL, Mueller SG, Buckley ST, et al. **Evidence of neurodegeneration in brains of older adults who do not yet fulfill MCI criteria.** *Neurobiol Aging* 2010;31:368–77 CrossRef Medline
- Raininko R, Mattsson P. **Metabolite concentrations in supraventricular white matter from teenage to early old age: a short echo time 1H magnetic resonance spectroscopy (MRS) study.** *Acta Radiol* 2010;51:309–15 CrossRef Medline
- Moreno-Torres A, Pujol J, Soriano-Mas C, et al. **Age-related metabolic changes in the upper brainstem tegmentum by MR spectroscopy.** *Neurobiol Aging* 2005;26:1051–59 CrossRef Medline
- Gruber S, Pinker K, Riederer F, et al. **Metabolic changes in the normal ageing brain: consistent findings from short and long**



- echo time proton spectroscopy.** *Eur J Radiol* 2008;68:320–27 CrossRef Medline
25. Holland BA, Haas DK, Norman D, et al. **MRI of normal brain maturation.** *AJNR Am J Neuroradiol* 1986;7:201–08 Medline
  26. Dawe RJ, Bennett DA, Schneider JA, et al. **Ex vivo T2 relaxation: associations with age-related neuropathology and cognition.** *Neurobiol Aging* 2014;35:1549–61 CrossRef Medline
  27. Ding XQ, Wittkugel O, Goebell E, et al. **Clinical applications of quantitative T2 determination: a complementary MRI tool for routine diagnosis of suspected myelination disorders.** *Eur J Paediatr Neurol* 2008;12:298–308 CrossRef Medline
  28. Weissenborn K, Bültmann E, Donnerstag F, et al. **Quantitative MRI shows cerebral microstructural damage in hemolytic-uremic syndrome patients with severe neurological symptoms but no changes in conventional MRI.** *Neuroradiology* 2013;55:819–25 CrossRef Medline
  29. Jara H, Sakai O, Mankal P, et al. **Multispectral quantitative magnetic resonance imaging of brain iron stores: a theoretical perspective.** *Top Magn Reson Imaging* 2006;17:19–30 CrossRef Medline
  30. Hallgren B, Sourander P. **The effect of age on the non-haemin iron in the human brain.** *J Neurochem* 1958;3:41–51 CrossRef Medline
  31. Wagner M, Jurcoane A, Volz S, et al. **Age-related changes of cerebral autoregulation: new insights with quantitative T2'-mapping and pulsed arterial spin-labeling MR imaging.** *AJNR Am J Neuroradiol* 2012;33:2081–87 CrossRef Medline
  32. Wagner M, Magerkurth J, Volz S, et al. **T2'- and PASL-based perfusion mapping at 3 Tesla: influence of oxygen-ventilation on cerebral autoregulation.** *J Magn Reson Imaging* 2012;36:1347–52 CrossRef Medline
  33. Seals DR, Jablonski KL, Donato AJ. **Aging and vascular endothelial function in humans.** *Clin Sci (Lond)* 2011;120:357–75 CrossRef Medline

# High-Resolution 7T MR Imaging of the Motor Cortex in Amyotrophic Lateral Sclerosis

M. Cosottini, G. Donatelli, M. Costagli, E. Caldarazzo Ienco, D. Frosini, I. Pesaresi, L. Biagi, G. Siciliano, and M. Tosetti



## ABSTRACT

**BACKGROUND AND PURPOSE:** Amyotrophic lateral sclerosis is a progressive motor neuron disorder that involves degeneration of both upper and lower motor neurons. In patients with amyotrophic lateral sclerosis, pathologic studies and ex vivo high-resolution MR imaging at ultra-high field strength revealed the co-localization of iron and activated microglia distributed in the deep layers of the primary motor cortex. The aims of the study were to measure the cortical thickness and evaluate the distribution of iron-related signal changes in the primary motor cortex of patients with amyotrophic lateral sclerosis as possible in vivo biomarkers of upper motor neuron impairment.

**MATERIALS AND METHODS:** Twenty-two patients with definite amyotrophic lateral sclerosis and 14 healthy subjects underwent a high-resolution 2D multiecho gradient-recalled sequence targeted on the primary motor cortex by using a 7T scanner. Image analysis consisted of the visual evaluation and quantitative measurement of signal intensity and cortical thickness of the primary motor cortex in patients and controls. Qualitative and quantitative MR imaging parameters were correlated with electrophysiologic and laboratory data and with clinical scores.

**RESULTS:** Ultra-high field MR imaging revealed atrophy and signal hypointensity in the deep layers of the primary motor cortex of patients with amyotrophic lateral sclerosis with a diagnostic accuracy of 71%. Signal hypointensity of the deep layers of the primary motor cortex correlated with upper motor neuron impairment ( $r = -0.47$ ;  $P < .001$ ) and with disease progression rate ( $r = -0.60$ ;  $P = .009$ ).

**CONCLUSIONS:** The combined high spatial resolution and sensitivity to paramagnetic substances of 7T MR imaging demonstrate in vivo signal changes of the cerebral motor cortex that resemble the distribution of activated microglia within the cortex of patients with amyotrophic lateral sclerosis. Cortical thinning and signal hypointensity of the deep layers of the primary motor cortex could constitute a marker of upper motor neuron impairment in patients with amyotrophic lateral sclerosis.

**ABBREVIATIONS:** ALS = amyotrophic lateral sclerosis; ALSFRS-R = ALS Functional Rating Scale-Revised; DPR = disease progression rate; HS = healthy subjects; M1 = primary motor cortex; UHF = ultra-high field; UMN = upper motor neuron

Amyotrophic lateral sclerosis (ALS) is a progressive motor neuron disorder that entails degeneration of both upper and lower motor neurons,<sup>1</sup> producing fasciculation, muscle wasting and weakness, increased spasticity, and hyperreflexia.

Upper motor neuron (UMN) impairment in ALS can be detected from clinical signs such as brisk reflexes and spasticity; however, the masking effect of the lower motor neuron involvement that reduces muscle strength and reflexes may make it hard

to reveal clinical evidence of pyramidal involvement. Electrophysiologic investigations, such as prolongation of central motor conduction time in motor-evoked potentials in transcranial magnetic stimulation, may detect the upper motor neuron involvement, but results are conflicting and these measures are not a sensitive tool or a useful indicator of disease severity or prognosis.<sup>2–4</sup> Therefore, a robust in vivo biomarker of UMN impairment, though desirable,<sup>5</sup> is not available.

The hallmark of UMN pathology in ALS is depopulation of the Betz cells in the motor cortex and axonal loss within the descend-

Received June 26, 2015; accepted after revision August 12.

From the Department of Translational Research and New Technologies in Medicine and Surgery (M.Cosottini) and Neurology Unit, Department of Clinical and Experimental Medicine (E.C.I., D.F., G.S.), University of Pisa, Pisa, Italy; Neuroradiology Unit (G.D., I.P.), Department of Diagnostic and Interventional Radiology, Azienda Ospedaliero-Universitaria Pisana, Pisa, Italy; IMAGO7 Foundation (M.Costagli), Pisa, Italy; and IRCCS Stella Maris (L.B., M.T.), Pisa, Italy.

This work is part of the protocol "Clinical Impact of Ultra-High Field MRI in Neurodegenerative Diseases Diagnosis" (RF RF-2009-1546281) approved and funded by the Italian Ministry of Health and cofunded by the Health Service of Tuscany.

Please address correspondence to Mirco Cosottini, MD, Via Paradisa 2, 56124 Cisanello, Pisa, Italy; e-mail: mircocosottini@libero.it

Indicates open access to non-subscribers at www.ajnr.org

Indicates article with supplemental on-line tables.

Indicates article with supplemental on-line photos.

<http://dx.doi.org/10.3174/ajnr.A4562>

ing motor pathway associated with myelin pallor and gliosis of the corticospinal tracts.<sup>6</sup>

Conversely, also, characteristic of ALS pathology similar to that in other neurodegenerative disorders is the occurrence of a neuroinflammatory reaction, consisting of activated glial cells, mainly microglia and astrocytes, and T-cells.<sup>7</sup> In transgenic mouse models of mutant *SOD1*-associated familial ALS, reactive microglial cells and astrocytes actively contribute to the death of motor neurons.<sup>7</sup>

Moreover, a significant association between cortical microglia and UMN damage has been described by using PET with a radioligand for microglia.<sup>8</sup>

Recently, an ex vivo study with Perls' DAB staining detected intracellular and extracellular iron deposits in the motor cortex of patients with ALS. Iron in the form of ferritin is detected in activated microglia (CD68+) in the middle and deep layers of the motor cortex, sparing the superficial layers.<sup>9</sup>

Gradient recalled-echo T2\* sequences, which can provide signal magnitude, phase, and their combination in susceptibility-weighted imaging,<sup>10</sup> are considered the most appropriate technique to visualize small amounts of uniformly distributed iron, such as ferritin,<sup>11,12</sup> and are the most sensitive sequences for detecting the low signal intensity in the precentral cortex in patients with ALS.<sup>13</sup>

The introduction of ultra-high field (UHF) MR imaging equipment greatly increases the sensitivity to susceptibility phenomena and allows obtaining in vivo spatial resolution of approximately 200  $\mu\text{m}$ , which enables determination of the cortical layers.<sup>14</sup>

The aims of our study were to measure the thickness of the primary motor cortex (M1) and to describe the distribution of the iron-related signal changes in the M1 of patients with ALS as a possible in vivo biomarker of UMN impairment by using targeted high-resolution gradient recalled-echo T2\* sequences at UHF.

## MATERIALS AND METHODS

### Patients and Controls

Twenty-two patients (5 women and 17 men; mean age,  $61 \pm 10$  years) with a diagnosis of definite ALS (limb onset) according to the revised El Escorial diagnostic criteria<sup>15</sup> were enrolled (On-line Table 1). Patients with dementia were excluded by administering the Mini-Mental State Examination<sup>16</sup> and the Frontal Assessment Battery,<sup>17</sup> as short and rapid bedside tests for a screening of cognitive, behavioral, and global executive dysfunction. Clinical history and standard neurologic and psychiatric assessment were used to rule out possible neuropsychiatric comorbidities and other neurodegenerative diseases.

Patients underwent CSF and plasma laboratory analysis to respectively assess concentration of  $\beta$ -amyloid,  $\tau$ , and p- $\tau$  neuronal proteins and some peripheral oxidative stress biomarkers such as advanced oxidation protein products, ferric-reducing ability of plasma, and thiols.<sup>18</sup> Neurophysiologic investigation included motor-evoked potentials with calculations of central conduction time, cortical latency, and cortical silent period. Disease severity was evaluated by using the ALS Functional Rating Scale-Revised (ALSFRS-R) (range, 0–48),<sup>19</sup> the Medical Research Council scale for segmentary muscle strength (range, 0–130),<sup>20</sup> and a compos-

ite semiquantitative arbitrary score of UMN burden (UMN score; range, 0–33) (On-line Table 2).<sup>8,21,22</sup> Disease duration was expressed in months from symptom appearance to MR imaging acquisition, while disease progression rate (DPR) was calculated according the following formula:  $(48 - \text{ALSFRS-R})/\text{Disease Duration}$ .<sup>23</sup>

Fourteen right-handed healthy subjects (HS), age-matched with patients (8 women and 6 men; mean age,  $58 \pm 12$  years), were enrolled to compare the cerebral motor cortex morphology with respect to patients with ALS. HS were volunteers who had no history of psychiatric and neurologic disorders; their neurologic examination findings were normal.

All patients and controls gave their informed consent to the enrollment and diagnostic procedures on the basis of the adherence to an experimental protocol "Clinical Impact of Ultra-High Field MR Imaging in Neurodegenerative Diseases Diagnosis" (RF-2009-1546281) approved and funded by Italian Ministry of Health and cofunded by the Health Service of Tuscany. The study was approved by the local competent ethics committee.

### MR Imaging Acquisition

MR imaging experiments were performed on a 7T MR950 scanner (GE Healthcare, Milwaukee, Wisconsin) equipped with a 2CH-TX/32CH-RX head coil (Nova Medical, Wilmington, Massachusetts).

The MR imaging protocol included a high-resolution 2D multiecho gradient-recalled sequence with TE = 10 ms and 20 ms, TR = 500 ms, flip angle = 15°, NEX = 2, section thickness = 2 mm, FOV = 112 mm, and in-plane resolution = 250  $\mu\text{m}$ , targeted to the M1, oriented in the axial plane, and covering the cerebrum from the vertex to the internal capsule. The total acquisition time was 7 minutes 32 seconds.

### Image Analysis

**Visual Inspection and Subjective Assessment.** Two expert neuroradiologists (M.Cosottini and I.P.) blinded to the clinical status of subjects visually evaluated, independently, images on the basis of morphologic criteria.

The M1 in the precentral gyrus was identified on UHF MR images for the presence of the "hand knob."<sup>24</sup> The anatomy of the cerebral motor cortex at the level of the M1 was evaluated on the basis of accepted cognition sourcing from anatomic atlases<sup>25</sup> and MR imaging studies<sup>26,27</sup> and atlases<sup>28</sup> at UHF. The normal anatomy of the M1 at UHF MR imaging consists of deeper cortical layers identified as a slight hypointense band immediately subjacent to a thinner superficial hyperintense layer. The subcortical hypointense line corresponding to U-fibers appears smooth, and the gray-white junction, poorly demarcated (Fig 1A, -B).

When the M1 anatomy differed from such configurations, and namely the M1 deeper layers were particularly thin<sup>23,29</sup> and/or hypointense<sup>9,30</sup> (Fig 1D, -E), images were judged as belonging to patients with ALS.

Sensitivity, specificity, positive predictive value, negative predictive value, and diagnostic accuracy in distinguishing patients and HS were calculated for each reader. Interobserver agreement was calculated with the Cohen  $\kappa$  statistic.

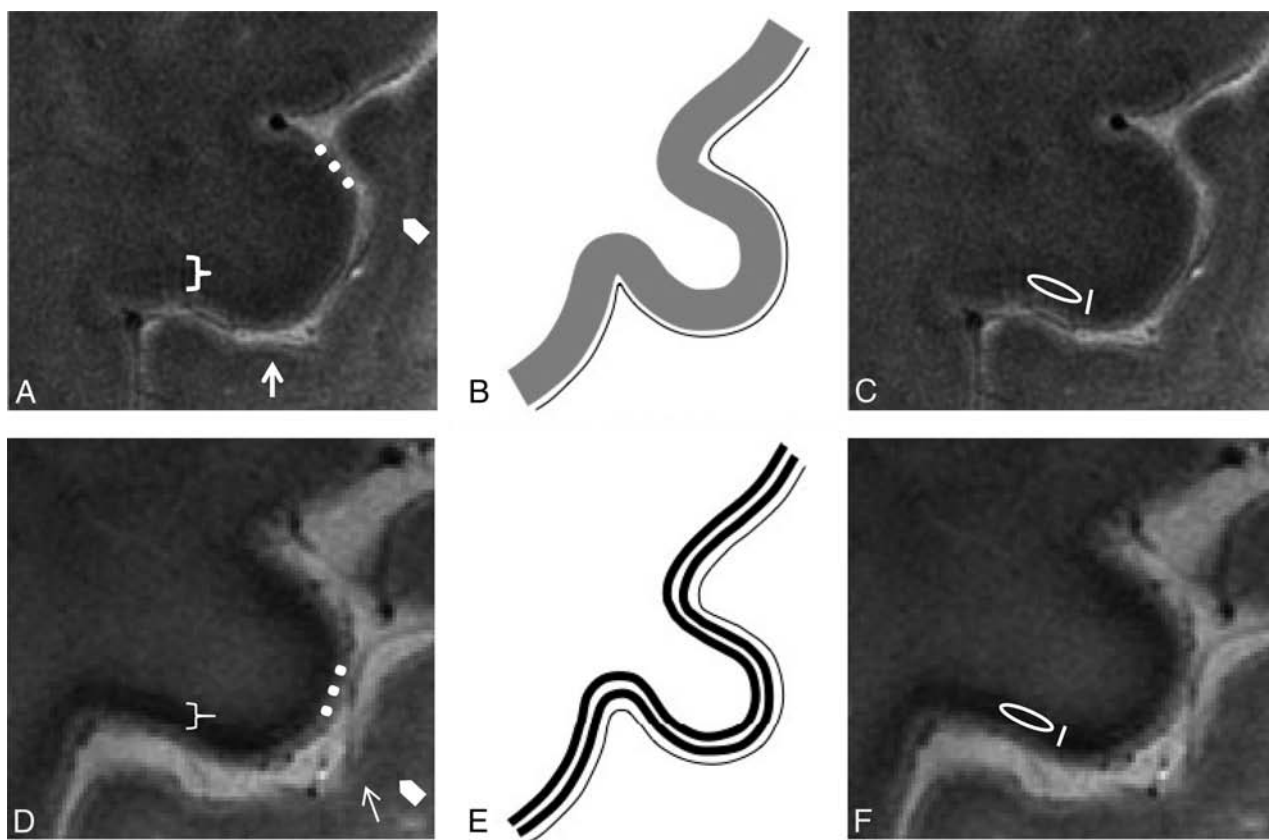


**FIG 1.** Normal anatomy. In vivo UHF high-resolution gradient recalled-echo T2\* sequence acquisition of the pre- and postcentral gyri (A) and its schematic representation (B) in healthy subjects. The postcentral gyrus resembles the classic ex vivo UHF MR imaging appearance of the unimodal sensory cortices: a low signal intensity tier corresponding to heavily myelinated intracortical layer IV (external band of Baillarger) (arrows) and a subcortical hypointensity (arrowheads) corresponding to arcuate U-fibers demarcating the gray-white matter junction.<sup>56</sup> The cortical ribbon of M1 (bracket) as the functional counterpart of Brodmann area 4<sup>35</sup> is thicker than S1<sup>57</sup> because it is agranular<sup>36</sup> and contains the giant Betz pyramidal cells. The superficial hyperintense layer in MR imaging (dots) is due to the lightly myelinated superficial layers relative to the more heavily myelinated deep layers.<sup>58</sup> M1 does not have an intermediate sharp hypointense line as in S1 but shows a more widespread slight hypointensity of the deeper cortical layer corresponding to its astriate myeloarchitecture.<sup>59,60</sup> The deeper layers of M1 are not easily distinguished from the underlying white matter due to the heavily myelinated M1 cortex.<sup>32,58</sup> **ALS features.** UHF high-resolution gradient recalled-echo T2\* sequence acquisition of the pre- and postcentral gyri in a patient with ALS (D) and the corresponding schematic view (E). Beneath a preserved superficial cortical layer (dots), the deep layers in M1 are thinner and more hypointense (bracket) than those in healthy subjects and show an inconstant track appearance. The M1 signal hypointensity in ALS could be due to paramagnetic effects of the iron-containing microglia within the deep motor cortex. The method adopted for quantitative measurement of signal intensity and thickness in a healthy subject (C) and in patients with ALS (F) is reported. Quantitative assessments of the deep layers of M1 are obtained by drawing an oval ROI within them for the signal intensity measurement and a line with an electronic caliper for the thickness quantification.

Differences in UMN scores between correctly diagnosed and misdiagnosed patients were evaluated by a Mann-Whitney *U* test.

**Quantitative Assessment.** For each cerebral hemisphere, thickness and signal intensity of the deeper layers of the M1 were measured in 4 anatomic regions corresponding to the Penfield's areas of foot, leg, hand, and face (Fig 1C, -F).<sup>31</sup> Signal intensities were measured by using oval ROIs of 4 mm<sup>2</sup> and were normalized with respect to those of the superficial cerebral cortex of the left precuneus. Measurement of cortical thickness was obtained by tracing, with an electronic caliper, a line encompassing the deep layer of the M1. The measurements of signal intensity and cortical thickness for each subject were then averaged to obtain mean values from both cerebral hemispheres.

Quantitative data of cortical thickness and the signal intensity of the M1 were compared between patients and HS by using a Mann-Whitney *U* test. In the group of patients, the relationship between morphometric parameters (mean values of cortical

thickness and signal intensity) and clinical scores (ALSFRS-R, Medical Research Council scale, disease duration, and DPR) and the electrophysiologic (central conduction time, cortical latency, cortical silent period) and laboratory (ferric reducing ability of plasma, advanced oxidation protein products, plasma thiols) data was evaluated by the Spearman rank correlation coefficient. Cortical thickness and signal intensity of the M1 for each Penfield's area of hand, leg, and foot were correlated to the correspondent UMN score by using the Spearman rank correlation coefficient.

Using the median of DPR as a cutoff, we divided patients on the basis of the progression rate into 2 groups: "faster" and "slower." A Mann-Whitney *U* test was applied to investigate differences in morphometric parameters between the 2 groups.

## RESULTS

Four patients and 1 healthy control subject were excluded from the analysis due to the presence of severe motion artifacts.



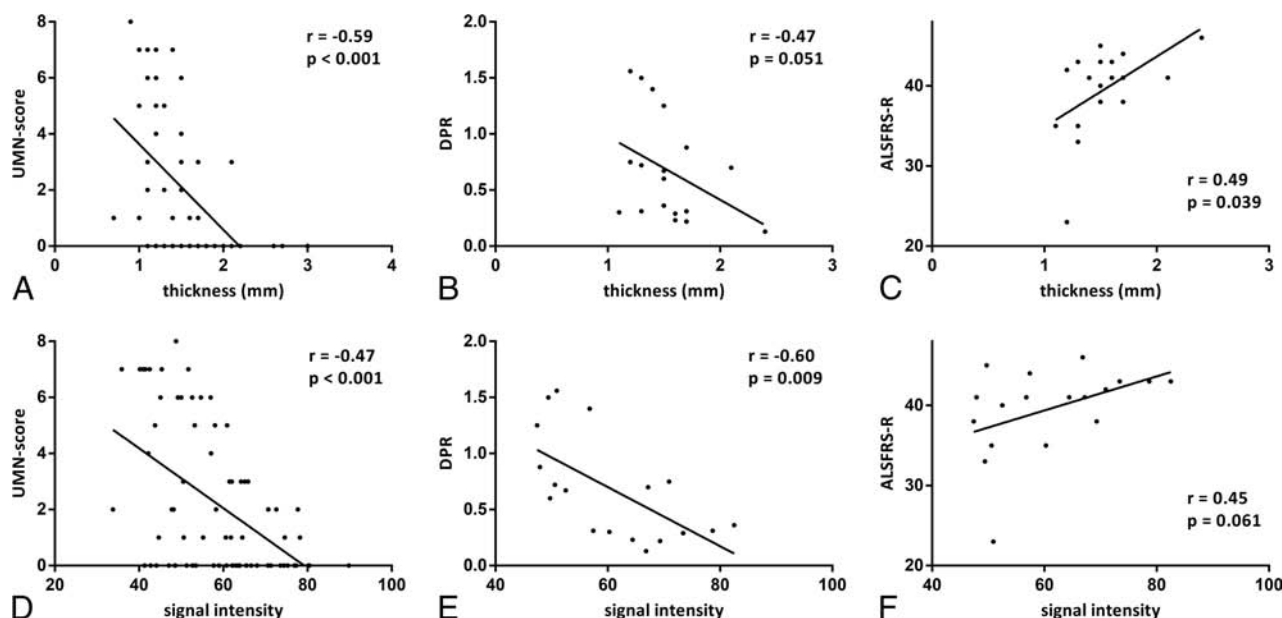


**FIG 2.** Correlations in patients with ALS between morphometric parameters (thickness and signal intensity of deeper layers of M1) and clinical scores (UMN score, DPR, and ALSFRS-R). The UMN score ranges from zero to 8 because it refers to a single limb and not to the overall evaluation. Correlations between morphometric parameters and UMN score were calculated by taking into account the clinical score of each limb of every patient and signal intensity and thickness of the corresponding areas of M1.

In the remaining 18 patients, the mean values were  $40 \pm 5$  for ALSFRS-R,  $9 \pm 10$  for the UMN score,  $118 \pm 13$  for the Medical Research Council scale,  $16 \pm 12$  for disease duration, and  $0.68 \pm 0.47$  for DPR.

#### Visual Inspection and Subjective Assessment

At visual inspection, reader 1 detected hypointensity and thinning of the deeper layers of the M1 in 12 of 18 patients with ALS and in 3 of 13 HS. Sensitivity, specificity, positive predictive value, negative predictive value, and diagnostic accuracy in distinguishing patients and HS on the basis of morphologic criteria were 67%, 77%, 80%, 63%, and 71%, respectively.

Reader 2 detected hypointensity and thinning of the deeper layers of the M1 in 9 of 18 patients with ALS and in zero of 13 HS. Sensitivity, specificity, positive predictive value, negative predictive value, and diagnostic accuracy in distinguishing patients and HS on the basis of morphologic criteria were 50%, 100%, 100%, 59%, and 71%, respectively.

The Interobserver agreement was good (0.61, Cohen  $\kappa$  statistic).

On the basis of both readings, the UMN score was significantly higher ( $P = .003$  and  $P = .028$ , respectively) in correctly diagnosed patients ( $13 \pm 10$  and  $14 \pm 10$ , respectively) than in misdiagnosed ones ( $1 \pm 1$  and  $4 \pm 8$ , respectively) (On-line Fig 1A, -B and On-line Tables 3–6).

Also, the DPR was higher on the basis of both readings ( $P = .019$  and  $P = .066$ , respectively) in correctly diagnosed patients ( $0.85 \pm 0.48$  and  $0.87 \pm 0.49$ , respectively) than in misdiagnosed ones ( $0.33 \pm 0.20$  and  $0.48 \pm 0.38$ , respectively).

#### Quantitative Assessment

Cortical thickness was significantly ( $P < .001$ ) lower in patients (mean value = 1.5 mm) than in HS (mean value = 2 mm)

(On-line Fig 1C) and showed a moderate correlation with the UMN score ( $r = -0.59$ ;  $P < .001$ ) (Fig 2A). Cortical thickness had a weaker correlation with DPR ( $r = -0.47$ ;  $P = .051$ ) and ALSFRS-R ( $r = 0.49$ ;  $P = .039$ ) (Fig 2B, -C).

Signal intensity did not differ between patients with ALS and HS (On-line Fig 1D) but correlated with UMN score ( $r = -0.47$ ;  $P < .001$ ), DPR ( $r = -0.60$ ;  $P = .009$ ), and ALSFRS-R ( $r = 0.45$ ;  $P = .061$ ) (Fig 2D–F).

Signal intensity in the subgroup of patients with faster DPR was significantly lower than that in the slower DPR subgroup ( $P = .024$ ), while no significant difference in cortical thickness was found between subgroups of patients (On-line Fig 2).

No significant correlations were found between morphometric parameters and either motor-evoked potential indices (central motor conduction time and cortical silent period) or the ferric-reducing ability of plasma, advanced oxidation protein products, and thiols.

## DISCUSSION

#### UHF MR Signal in M1 of Controls and Patients with ALS

UHF MR imaging allows an in vivo evaluation of the inner structure of the cerebral motor cortex of patients with ALS and controls. The gradient recalled-echo T2\* sequence at 7T provides information on the architectural organization of the human cortex in vivo,<sup>32</sup> due to the iron and myelin contribution to T2\* contrast.<sup>26</sup> Because myelin and iron in the form of ferritin are strongly co-localized in the intracortical myelinated fibers,<sup>33</sup> the MR signals across the cortical gray matter reflect myelin content and myeloarchitecture.<sup>34</sup> The normal anatomy of the M1 (Brodmann area 4)<sup>35</sup> at UHF depends on its peculiar architecture: The large cortical thickness, inconspicuous lamination pattern, low cell density, and the absence of a clear boundary between layer VI

and white matter<sup>36</sup> correspond to the MR imaging findings of the motor cortex as shown in Fig 1A, -B.

In patients with ALS, in accordance with previous ex vivo UHF images of the affected cerebral cortices,<sup>9</sup> we revealed a rim of signal hypointensity with an inconstant track appearance beneath a preserved superficial hyperintense cortical layer (Fig 1D, -E).

The decreased signal intensity of the motor cortex on T2\*-weighted images in patients with ALS may represent ferritin because at postmortem examination, the precentral cortex showed intensely stained microglia and macrophages after antiferritin antibody staining.<sup>13</sup> Until now, cortical hypointensity in vivo seemed to involve the motor cortex in a full-thickness fashion at both conventional<sup>37</sup> and UHF<sup>9</sup> MR imaging. Our targeted UHF MR imaging high-resolution study, as well as the ex vivo UHF imaging, demonstrated that in patients with ALS, the signal hypointensity is confined to the deeper layers of the cerebral cortex, the same structures in which several studies have shown an increased number of microglial cells resulting from local proliferation of resident microglia.<sup>38</sup>

PET with radioligand-binding biomarkers of activated microglia revealed that areas with the highest microglial activation in patients with ALS were the motor cortices,<sup>39</sup> thus corresponding to the distribution of signal changes and atrophy that we have detected in our group of patients.

### **Cortical Thickness in the M1 of Patients with ALS**

Cortical atrophy in ALS has been revealed in several voxel-based morphometry works<sup>40-42</sup> by manual or automated measurements of the cortical thickness and has been interpreted as a structural surrogate of UMN degeneration.<sup>23</sup> In particular, the regional grade of atrophy in different areas of M1 corresponds to a somatotopic functional disability supporting the concepts of cortical focality and motor phenotype heterogeneity.<sup>43</sup> In line with previous results, our data confirmed the thinning of the M1 in patients with ALS and the correlation between the cortical atrophy and the UMN burden, but we observed that the alteration is confined to the deeper cortical layers rather than the full-thickness cortex. Moreover, cortical atrophy and signal hypointensity of the M1 in patients with ALS are in line, respectively, with the reduction of *N*-acetylaspartate and the increase of myo-inositol<sup>44</sup> as an expression of the neurodegenerative phenomena and gliosis.

### **MR Imaging of M1: Biomarker for Diagnosis or Prognosis**

Several conventional MR imaging studies subjectively evaluated the cortical morphology and signal changes in patients with ALS.<sup>37,45-49</sup> These studies using full-thickness measures of cortical signal changes were limited by low specificity because similar findings are age-related and can also be detected in subjects without ALS.<sup>50</sup> Although our approach permitted the evaluation of the inner structure of the cerebral motor cortex, the diagnostic accuracy (71%) and the sensitivity (67% and 50% for reader 1 and reader 2, respectively) of M1 morphologic changes remain unsatisfactory.

Unlike electrophysiologic data, in which a correlation with UMN impairment has never been demonstrated,<sup>51</sup> in our study, the quantitative analysis showed that increased image hypointensity and the atrophic deep motor cortex both correspond to

greater UMN involvement. The correlation between the signal intensity and the UMN score and the fact that the UMN score was significantly higher in correctly diagnosed patients than in misdiagnosed ones support the hypothesis that hypointensity is a marker of UMN degeneration rather than of ALS.

This relationship influences the diagnostic accuracy of MR imaging, which remains modest because the correct diagnosis of ALS based on cortical signal changes depends on the amount of UMN impairment in sampled patients. The variable impairment of UMNs in ALS explains why decreased signal intensity in ALS has been reported at a variable extent, ranging from 93%<sup>37</sup> to 30%.<sup>13</sup>

The cortical signal intensity correlates with DPR and could constitute a prognostic marker of the disease. Although we interpret signal intensity as an expression of activated microglia, we do not know the pathologic mechanism that regulates the disease progression in our patients.

Translational research in mutant *SOD1* transgenic mice shows that microglial cells become activated before motor neurons disappear and well before clinical disease onset.<sup>52</sup> Moreover *SOD* mutant levels in microglia regulate the rate of disease progression.<sup>53</sup> The correlation between cortical signal hypointensity as a presumptive marker of activated microglia and DPR could constitute the basis of a longitudinal study of microgliosis in patients with ALS, widening the pathogenic scenario of the causes of this disease and offering novel targets for therapeutic development. To understand whether the neuroinflammatory reaction could be a therapeutic target in ALS, a reliable biomarker able to investigate and monitor the neuroinflammatory response to motor-neuron degeneration with time would be desirable. Besides laboratory inflammatory markers in the CSF<sup>54</sup> and PET studies by using microglial ligands, high-resolution UHF MR imaging might provide alternative relevant information on neuroinflammation.

In ALS, biomarkers of disease or prognosis would be paramount for patient management and therapeutic implications.<sup>5</sup> Advanced neuroimaging techniques provide an opportunity to assess disease pathophysiology and promise new biomarkers.<sup>55</sup> The introduction of the UHF MR imaging of the cerebral cortex in evaluating patients with ALS could be an adjunctive tool in a multimodal approach to the research of biomarkers.<sup>5</sup>

The main limitation of the present study is the small sample of patients, which affects the statistical power. A further limitation is the impossibility of enrolling patients with advanced disease for logistic reasons related to their disability, which would probably have provided information on the course of the disease.

### **CONCLUSIONS**

The combined high spatial resolution and sensitivity to paramagnetic substances of 7T MR imaging demonstrate in vivo signal changes of the cerebral motor cortex that resemble the distribution of activated microglia within the cortex of patients with ALS. Reduced cortical thickness and signal hypointensity of the M1 deep layers could constitute a marker of UMN impairment in patients with ALS. Further studies with a larger sample of patients would be desirable to confirm the UHF MR imaging results in motor neuron disorders.

Disclosures: Ilaria Pesaresi—RELATED: Grant: Ministry of Health.\* Gabriele Siciliano—UNRELATED: Board Membership: Baxter International, Comments: clinical trial board membership; Expert Testimony: CSL Behring.\* Comments: therapeutic trial testimony; Payment for Lectures (including service on Speakers Bureaus): Baxter International, Grunenthal, Grifols; Payment for Manuscript Preparation: Baxter International; Payment for Development of Educational Presentations: Baxter International; Travel/Accommodations/Meeting Expenses Unrelated to Activities Listed: Kedrion, CSL Behring, Comments: meeting expenses. \*Money paid to the institution.

## REFERENCES

- Strong M, Rosenfeld J. **Amyotrophic lateral sclerosis: a review of current concepts.** *Amyotroph Lateral Scler Other Motor Neuron Disord* 2003;4:136–43 CrossRef Medline
- Claus D, Brunhölzl C, Kerling FP, et al. **Transcranial magnetic stimulation as a diagnostic and prognostic test in amyotrophic lateral sclerosis.** *J Neurol Sci* 1995;129(suppl):30–34 CrossRef Medline
- de Carvalho M, Dengler R, Eisen A, et al. **Electrodiagnostic criteria for diagnosis of ALS.** *Clin Neurophysiol* 2008;119:497–503 CrossRef Medline
- Vucic S, Kiernan MC. **Utility of transcranial magnetic stimulation in delineating amyotrophic lateral sclerosis pathophysiology.** *Handb Clin Neurol* 2013;116:561–75 CrossRef Medline
- Chiò A, Pagani M, Agosta F, et al. **Neuroimaging in amyotrophic lateral sclerosis: insights into structural and functional changes.** *Lancet Neurol* 2014;13:1228–40 CrossRef Medline
- Ince PG, Evans J, Knopp M, et al. **Corticospinal tract degeneration in the progressive muscular atrophy variant of ALS.** *Neurology* 2003;60:1252–58 CrossRef Medline
- Philips T, Robberecht W. **Neuroinflammation in amyotrophic lateral sclerosis: role of glial activation in motor neuron disease.** *Lancet Neurol* 2011;10:253–63 CrossRef Medline
- Turner MR, Cagnin A, Turkheimer FE, et al. **Evidence of widespread cerebral microglial activation in amyotrophic lateral sclerosis: an [11C](R)-PK11195 positron emission tomography study.** *Neurobiol Dis* 2004;15:601–09 CrossRef Medline
- Kwan JY, Jeong SY, Van Gelderen P, et al. **Iron accumulation in deep cortical layers accounts for MRI signal abnormalities in ALS: correlating 7 Tesla MRI and pathology.** *PLoS One* 2012;7:e35241 CrossRef Medline
- Haacke EM, Mittal S, Wu Z, et al. **Susceptibility-weighted imaging: technical aspects and clinical applications, part 1.** *AJNR Am J Neuroradiol* 2009;30:19–30 Medline
- Liu M, Habib C, Miao Y, et al. **Measuring iron content with phase.** In: Haacke EM, Reichenbach JR, eds. *Susceptibility Weighted Imaging in MRI: Basic Concept and Clinical Applications*. 10th ed. Hoboken: John Wiley & Sons; 2011:369–401
- Duyn JH. **High-field MRI of brain iron.** *Methods Mol Biol* 2011;711:239–49 CrossRef Medline
- Adachi Y, Sato N, Saito Y, et al. **Usefulness of SWI for the detection of iron in the motor cortex in amyotrophic lateral sclerosis.** *J Neuroimaging* 2015;25:443–51 CrossRef Medline
- Fischl B. **Estimating the location of Brodmann areas from cortical folding patterns using histology and ex vivo MRI.** In: Geyer S, Turner R, eds. *Microstructural Parcellation of the Human Cerebral Cortex: From Brodmann's Post-Mortem Map to in Vivo Mapping with High-Field Magnetic Resonance Imaging*. Berlin: Springer-Verlag; 2013:129–56
- Brooks BR, Miller RG, Swash M, et al; World Federation of Neurology Research Group on Motor Neuron Disease. **El Escorial revisited: revised criteria for the diagnosis of amyotrophic lateral sclerosis.** *Amyotroph Lateral Scler Other Motor Neuron Disord* 2000;1:293–99 CrossRef Medline
- Folstein MF, Folstein SE, McHugh PR. **"Mini-mental state": a practical method for grading the cognitive state of patients for the clinician.** *J Psychiatr Res* 1975;12:189–98 CrossRef Medline
- Appollonio I, Leone M, Isella V, et al. **The frontal assessment battery (FAB): normative values in an Italian population sample.** *Neurol Sci* 2005;26:108–16 CrossRef Medline
- Siciliano G, Piazza S, Carlesi C, et al. **Antioxidant capacity and protein oxidation in cerebrospinal fluid of amyotrophic lateral sclerosis.** *J Neurol* 2007;254:575–80 CrossRef Medline
- Cedarbaum JM, Stambler N, Malta E, et al. **The ALSFRS-R: a revised ALS functional rating scale that incorporates assessments of respiratory function: BDNF ALS Study Group (Phase III).** *J Neurol Sci* 1999;169:13–21 CrossRef Medline
- Florence JM, Pandya S, King WM, et al. **Intrarater reliability of manual muscle test (Medical Research Council scale) grades in Duchenne's muscular dystrophy.** *Phys Ther* 1992;72:115–22; discussion 122–26 Medline
- Ashworth B. **Preliminary trial of carisoprodol in multiple sclerosis.** *Practitioner* 1964;192:540–42 Medline
- Woo JH, Wang S, Melhem ER, et al. **Linear associations between clinically assessed upper motor neuron disease and diffusion tensor imaging metrics in amyotrophic lateral sclerosis.** *PLoS One* 2014;9:e105753 CrossRef Medline
- Walhout R, Westeneng HJ, Verstraete E, et al. **Cortical thickness in ALS: towards a marker for upper motor neuron involvement.** *J Neurol Neurosurg Psychiatry* 2015;86:288–94 CrossRef Medline
- Yousry TA, Schmid UD, Alkadhi H, et al. **Localization of the motor hand area to a knob on the precentral gyrus: a new landmark.** *Brain* 1997;120:141–57 CrossRef Medline
- Zilles K, Amunts K. **Architecture of the cerebral cortex.** In: Mai JK, Paxinos G, eds. *The Human Nervous System*. 3rd ed. London: Elsevier; 2012:836–95
- Duyn JH, van Gelderen P, Li TQ, et al. **High-field MRI of brain cortical substructure based on signal phase.** *Proc Natl Acad Sci U S A* 2007;104:11796–801 CrossRef Medline
- Geyer S, Weiss M, Reimann K, et al. **Microstructural parcellation of the human cerebral cortex: from Brodmann's post-mortem map to in vivo mapping with high-field magnetic resonance imaging.** *Front Hum Neurosci* 2011;5:19 CrossRef Medline
- Geyer S, Turner R. **Microstructural Parcellation of the Human Cerebral Cortex: From Brodmann's Post-Mortem Map to in Vivo Mapping with High-Field Magnetic Resonance Imaging.** Berlin: Springer-Verlag; 2013
- Verstraete E, Veldink JH, Hendrikse J, et al. **Structural MRI reveals cortical thinning in amyotrophic lateral sclerosis.** *J Neurol Neurosurg Psychiatry* 2012;83:383–88 CrossRef Medline
- Ignjatović A, Stević Z, Lavrić S, et al. **Brain iron MRI: a biomarker for amyotrophic lateral sclerosis.** *J Magn Reson Imaging* 2013;38:1472–79 CrossRef Medline
- Penfield W, Rasmussen T. *The Cerebral Cortex of Man: A Clinical Study of Localization of Function*. New York: Macmillan; 1950
- Cohen-Adad J, Polimeni JR, Helmer KG, et al. **T<sub>2</sub>\* mapping and B<sub>0</sub> orientation-dependence at 7 T reveal cyto- and myeloarchitecture organization of the human cortex.** *Neuroimage* 2012;60:1006–14 CrossRef Medline
- Fukunaga M, Li TQ, van Gelderen P, et al. **Layer-specific variation of iron content in cerebral cortex as a source of MRI contrast.** *Proc Natl Acad Sci U S A* 2010;107:3834–39 CrossRef
- Turner R. **MRI methods for in-vivo cortical parcellation.** In: Geyer S, Turner R, eds. *Microstructural Parcellation of the Human Cerebral Cortex: From Brodmann's Post-Mortem Map to in Vivo Mapping with High-Field Magnetic Resonance Imaging*. Berlin: Springer-Verlag; 2013:197–220
- Brodmann K. *Vergleichende Lokalisationslehre der Grosshirnrinde*. Leipzig: Barth; 1909
- Brodmann K. *Beiträge zur histologischen Lokalisation der Grosshirnrinde: Erste Mitteilung—Die Regio Rolandica.* *J Psychol Neurol* 1903;2:79–107
- Oba H, Araki T, Ohtomo K, et al. **Amyotrophic lateral sclerosis: T2 shortening in motor cortex at MR imaging.** *Radiology* 1993;189:843–46 CrossRef Medline
- Gowing G, Philips T, Van Wijmeersch B, et al. **Ablation of proliferating microglia does not affect motor neuron degeneration in**

- amyotrophic lateral sclerosis caused by mutant superoxide dismutase. *J Neurosci* 2008;28:10234–44 CrossRef Medline
39. Corcia P, Tauber C, Vercoullie J, et al. **Molecular imaging of microglial activation in amyotrophic lateral sclerosis.** *PLoS One* 2012;7:e52941 CrossRef Medline
  40. Agosta F, Pagani E, Rocca MA, et al. **Voxel-based morphometry study of brain volumetry and diffusivity in amyotrophic lateral sclerosis patients with mild disability.** *Hum Brain Mapp* 2007;28:1430–38 CrossRef Medline
  41. Mezzapesa DM, Ceccarelli A, Dicuonzo F, et al. **Whole-brain and regional brain atrophy in amyotrophic lateral sclerosis.** *AJNR Am J Neuroradiol* 2007;28:255–59 Medline
  42. Cosottini M, Pesaresi I, Piazza S, et al. **Structural and functional evaluation of cortical motor areas in amyotrophic lateral sclerosis.** *Exp Neurol* 2012;234:169–80 CrossRef Medline
  43. Bede P, Bokde A, Elamin M, et al. **Grey matter correlates of clinical variables in amyotrophic lateral sclerosis (ALS): a neuroimaging study of ALS motor phenotype heterogeneity and cortical focality.** *J Neurol Neurosurg Psychiatry* 2013;84:766–73 CrossRef Medline
  44. Foerster BR, Pomper MG, Callaghan BC, et al. **An imbalance between excitatory and inhibitory neurotransmitters in amyotrophic lateral sclerosis revealed by use of 3-T proton magnetic resonance spectroscopy.** *JAMA Neurol* 2013;70:1009–16 CrossRef Medline
  45. Goodin DS, Rowley HA, Olney RK. **Magnetic resonance imaging in amyotrophic lateral sclerosis.** *Ann Neurol* 1988;23:418–20 CrossRef Medline
  46. Ishikawa K, Nagura H, Yokota T, et al. **Signal loss in the motor cortex on magnetic resonance images in amyotrophic lateral sclerosis.** *Ann Neurol* 1993;33:218–22 CrossRef Medline
  47. Cheung G, Gawel MJ, Cooper PW, et al. **Amyotrophic lateral sclerosis: correlation of clinical and MR imaging findings.** *Radiology* 1995;194:263–70 CrossRef Medline
  48. Thorpe JW, Moseley IF, Hawkes CH, et al. **Brain and spinal cord MRI in motor neuron disease.** *J Neurol Neurosurg Psychiatry* 1996;61:314–17 CrossRef Medline
  49. Hecht MJ, Fellner F, Fellner C, et al. **Hyperintense and hypointense MRI signals of the precentral gyrus and corticospinal tract in ALS: a follow-up examination including FLAIR images.** *J Neurol Sci* 2002;199:59–65 CrossRef Medline
  50. Cosottini M, Cecchi P, Piazza S, et al. **Mapping cortical degeneration in ALS with magnetization transfer ratio and voxel-based morphometry.** *PLoS One* 2013;8:e68279 CrossRef Medline
  51. Yokota T, Yoshino A, Inaba A, et al. **Double cortical stimulation in amyotrophic lateral sclerosis.** *J Neurol Neurosurg Psychiatry* 1996;61:596–600 CrossRef Medline
  52. Hall ED, Oostveen JA, Gurney ME. **Relationship of microglial and astrocytic activation to disease onset and progression in a transgenic model of familial ALS.** *Glia* 1998;23:249–56 CrossRef Medline
  53. Boillée S, Yamanaka K, Lobsiger CS, et al. **Onset and progression in inherited ALS determined by motor neurons and microglia.** *Science* 2006;312:1389–92 CrossRef Medline
  54. Mitchell RM, Freeman WM, Randazzo WT, et al. **A CSF biomarker panel for identification of patients with amyotrophic lateral sclerosis.** *Neurology* 2009;72:14–19 CrossRef Medline
  55. Foerster BR, Welsh RC, Feldman EL. **25 years of neuroimaging in amyotrophic lateral sclerosis.** *Nat Rev Neurol* 2013;9:513–24 CrossRef Medline
  56. Fatterpekar GM, Naidich TP, Delman BN, et al. **Cytoarchitecture of the human cerebral cortex: MR microscopy of excised specimens at 9.4 Tesla.** *AJNR Am J Neuroradiol* 2002;23:1313–21 Medline
  57. Meyer J, Roychowdhury S, Russell EJ, et al. **Location of the central sulcus via cortical thickness of the precentral and postcentral gyri on MR.** *AJNR Am J Neuroradiol* 1996;17:1699–706 Medline
  58. Glasser MF, Van Essen DC. **Mapping human cortical areas in vivo based on myelin content as revealed by T1- and T2-weighted MRI.** *J Neurosci* 2011;31:11597–616 CrossRef Medline
  59. Vogt O. **Die myeloarchitektonische Felderung des Menschlichen Stirnhirns.** *J Psychol Neurol* 1910;15:221–32
  60. Braitenberg V. **Die Gliederung der Stirnhirnrinde auf Grund ihres Markfaserbaus (Myeloarchitektonik).** In: Rehwald E, ed. *Das Hirn-trauma*. Stuttgart: Thieme; 1956:183–203



# MR Elastography Demonstrates Increased Brain Stiffness in Normal Pressure Hydrocephalus

 N. Fattahi,  A. Arani,  A. Perry,  F. Meyer,  A. Manduca,  K. Glaser,  M.L. Senjem,  R.L. Ehman, and  J. Huston



## ABSTRACT

**BACKGROUND AND PURPOSE:** Normal pressure hydrocephalus is a reversible neurologic disorder characterized by a triad of cognitive impairment, gait abnormality, and urinary incontinence that is commonly treated with ventriculoperitoneal shunt placement. However, multiple overlapping symptoms often make it difficult to differentiate normal pressure hydrocephalus from other types of dementia, and improved diagnostic techniques would help patient management. MR elastography is a novel diagnostic tool that could potentially identify patients with normal pressure hydrocephalus. The purpose of this study was to assess brain stiffness changes in patients with normal pressure hydrocephalus compared with age- and sex-matched cognitively healthy individuals.

**MATERIALS AND METHODS:** MR elastography was performed on 10 patients with normal pressure hydrocephalus and 21 age- and sex-matched volunteers with no known neurologic disorders. Image acquisition was conducted on a 3T MR imaging scanner. Shear waves with 60-Hz vibration frequency were transmitted into the brain by a pillowlike passive driver. A novel postprocessing technique resistant to noise and edge artifacts was implemented to determine regional brain stiffness. The Wilcoxon rank sum test and linear regression were used for statistical analysis.

**RESULTS:** A significant increase in stiffness was observed in the cerebrum ( $P = .001$ ), occipital lobe ( $P < .001$ ), parietal lobe ( $P = .001$ ), and the temporal lobe ( $P = .02$ ) in the normal pressure hydrocephalus group compared with healthy controls. However, no significant difference was noted in other regions of the brain, including the frontal lobe ( $P = .07$ ), deep gray and white matter ( $P = .43$ ), or cerebellum ( $P = .20$ ).

**CONCLUSIONS:** This study demonstrates increased brain stiffness in patients with normal pressure hydrocephalus compared with age- and sex-matched healthy controls; these findings should motivate future studies investigating the use of MR elastography for this condition and the efficacy of shunt therapy.

**ABBREVIATIONS:** NPH = normal pressure hydrocephalus; MRE = MR elastography

Normal pressure hydrocephalus (NPH) is a potentially treatable condition characterized by cognitive impairment, gait abnormality, and urinary incontinence. A recent large epidemiologic study reported a dramatic increase in the prevalence of NPH after 80 years of age with only a minority of these cases undergoing treatment.<sup>1</sup> With the progressive aging of our population, a continued increase in the prevalence of NPH can be expected in the future.

Multiple overlapping signs and symptoms among different types of cognitive impairment, such as NPH, Alzheimer disease, and vascular dementia<sup>2-4</sup> create diagnostic challenges in these patients. These challenges will motivate the development and investigation of novel noninvasive imaging techniques to serve as diagnostic tools for identifying patients with NPH. The reversibility of neurologic symptoms after shunt tube placement supports the theory that deranged CSF circulation could play a role in NPH pathophysiology. Hypothetically, CSF accumulation may lead to local compression on the brain and can be the cause of this disorder.<sup>4</sup> Therefore, recent studies have targeted hemodynamic and CSF circulation alterations and are investigating their role in intracranial pressure changes, which may be the cause of neurologic symptoms in NPH.<sup>5-7</sup>


Although there is variability in the diagnosis of NPH, a high-volume lumbar tap with improvement of clinical symptoms as-

Received June 11, 2015; accepted after revision July 23.

From the Department of Radiology, Mayo Clinic, Rochester, Minnesota.

This research was supported by the Theodore W. Batterman Family Foundation and R01 grant EB001981 (R.L.E.).

Please address correspondence to John Huston III, MD, Mayo Clinic 200 1st St SW #W4, Rochester, MN 55905; e-mail: jhuston@mayo.edu

 Indicates open access to non-subscribers at [www.ajnr.org](http://www.ajnr.org)

<http://dx.doi.org/10.3174/ajnr.A4560>

**Table 1: Patient distribution based on clinical manifestations and clinical response to treatment**

Manifestation	Distribution
Clinical symptoms	100% Gait disturbance 80% Cognitive problems 50% Urinary incontinence
High volume CSF tap	100% Improvement of clinical symptoms
Response to shunt treatment	90% Improvement of clinical symptoms 10% No improvement

essed by video studies obtained before and after the procedure is considered the most sensitive test for NPH at our institution. Several groups have shown that there is a strong correlation between surgical outcomes of shunt placement and a patient's response to a high-volume lumbar tap.<sup>5,8-13</sup> However, several factors, including time intervals between CSF taps, CSF leaks, and the subjective nature of both the diagnosis and therapeutic response, may result in ambiguity in the interpretation of the results. Another disadvantage of a lumbar tap is the invasive nature of the test, with associated potential complications such as headache, infection, and CSF leakage.<sup>14</sup> Neuroimaging currently has a prominent role in the diagnosis, assessment of therapy response, and monitoring of disease progression in patients with NPH. Disproportionate enlargement of cerebral ventricles, the Sylvian fissure, and the basal cistern in relation to the degree of cortical atrophy is the conventional MR imaging finding suggestive of NPH.<sup>15</sup>

MR elastography (MRE) is an MR imaging–based technique that noninvasively measures the mechanical properties of tissues *in vivo*. It has been shown that pressure changes that alter tissue elasticity are detectable by MRE.<sup>16,17</sup> Therefore, the purpose of this study was to investigate possible brain stiffness changes in patients with NPH compared with age- and sex-matched healthy controls.

## MATERIALS AND METHODS

This study was approved by our institutional review board, and all subjects provided informed written consent before recruitment and imaging.

### Subjects

Ten patients with NPH (5 women and 5 men) with a mean age of 71 years (range, 67–79 years) were studied. All subjects were diagnosed with NPH on the basis of clinical symptoms and enlarged ventricles out of proportion to the size of the sulci (anatomic MR imaging) and improvement of symptoms following high-volume lumbar tap (Table 1). After undergoing MRE, all patients underwent CSF shunt surgery, and 9 of 10 patients experienced a remarkable improvement in symptoms after the procedure, which further supports the NPH diagnosis. Twenty-one cognitively healthy individuals without known neurologic disorders, 11 women and 10 men with a mean age 74 years (range, 67–80 years), served as the healthy control group. The healthy control group was obtained from a subset of subjects previously recruited from a longitudinal study of aging who were imaged with MRE.<sup>18,19</sup>

### MRE

Studies were performed on a 3T scanner (GE Healthcare, Milwaukee, Wisconsin) by using a single-shot, flow-compensated, spin-echo EPI pulse sequence. Shear waves were introduced into the brain from an active driver engine located outside the scan room through a soft pillowlike passive driver placed under the subject's head within an 8-channel receive-only head coil.<sup>20</sup> The frequency of vibration was 60 Hz, and the MRE sequence was performed by using the following parameters: TR/TE = 3600/62 ms; FOV = 24 cm; bandwidth =  $\pm 250$  kHz;  $72 \times 72$  imaging matrix reconstructed to  $80 \times 80$ ;  $3 \times$  parallel imaging acceleration; frequency encoding in the anteroposterior direction; 48 contiguous 3-mm-thick axial sections; one 4-G/cm 18.2-ms zero- and first-order moment nulled motion-encoding gradient on each side of the refocusing radiofrequency pulse synchronized to the motion; motion encoding in the positive and negative x, y, and z directions; and 8 phase offsets sampled during 1 period of the 60-Hz motion (the acquisition time was <7 minutes). The acquired images had 3-mm isotropic resolution.

### Image Processing

We applied a previously published MRE postprocessing pipeline that masks out voxels with contributions from CSF, minimizes partial volume and edge effects, attempts to correct areas of low MR signal-to-noise ratio and low wave amplitude, and has previously been shown to have a coefficient of variation of <1% for global brain stiffness and <2% for the lobes of the brain and the cerebellum.<sup>21</sup> Key features of the processing are the following: registration of the MRE data to a standard anatomic atlas, applying the vector curl operation on the first temporal harmonic of the acquired displacement field to reduce the effects of longitudinal waves and boundaries; adaptive filters for all derivative calculations to reduce partial volume effects at boundaries; and careful masking of the results from regional boundaries to minimize edge effects and contamination from CSF. The curl is a mathematic operation on a vector field (in this case, the displacement field with motion in all 3 directions). It is a combination of derivatives that quantifies rotational deformation (eg, shear waves), which is the only signal of interest in MRE, but suppresses all compressional deformation (eg, longitudinal waves). Last, an elastogram (map of stiffness, defined as wave speed squared times attenuation) was calculated by applying the direct inversion algorithm to the smoothed curl wave field. Additionally 2-phase offset images were acquired with zero motion amplitude to calculate the signal-to-noise ratio. We calculated the median stiffness of different ROIs in the brain. Each ROI was generated by applying a warped lobar atlas to a T1-weighted image. ROIs were then registered to the magnitude data obtained from the MRE as described previously.<sup>22</sup> The full postprocessing pipeline to produce elastograms was applied separately to each ROI. The ROIs investigated in this study included the cerebrum (whole brain excluding cerebellum); frontal, temporal, parietal, occipital lobes; deep gray matter/white matter (GM/WM) (insula, deep gray nuclei, and white matter tracts); and the cerebellum.

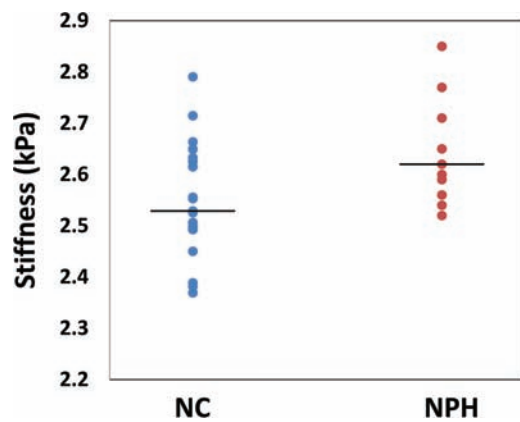


**FIG 1.** Summary of cerebral stiffness for the healthy controls (NC) and patients with normal pressure hydrocephalus. Lines represent the average stiffness for each group, and the circles represent the cerebral median stiffness for each individual patient.

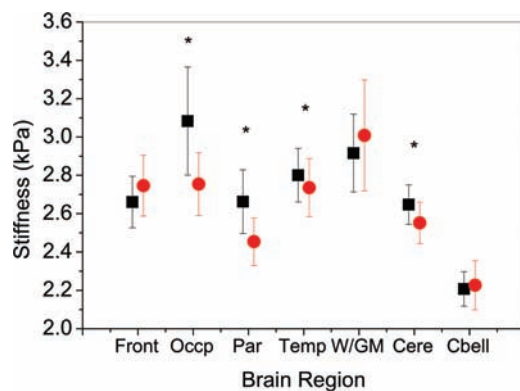


**FIG 2.** Mean of the median stiffness and SD of brain regions in patients with normal pressure hydrocephalus (black squares) and healthy controls (red circles). Asterisks indicate regions of significant stiffness difference between the NPH group and the healthy controls. Front indicates frontal lobe; Occp, occipital lobe; Par, parietal lobe; Temp, temporal lobe; W/GM, deep white/gray matter; Cere, cerebrum; Cbell, cerebellum.

### Statistical Analysis

To compare brain tissue stiffness between patients with NPH and healthy controls, we used a Wilcoxon rank sum test; a  $P$  value  $< .05$  was considered statistically significant. A linear regression test was used to determine whether sex and age introduced a significant bias in the brain stiffness of the healthy control cohort.

### RESULTS

The average median stiffness value of the cerebrum among patients with NPH was  $2.64 \pm 0.1$  kPa, which was significantly higher than the stiffness of the cerebrum in healthy controls ( $2.55 \pm 0.1$  kPa) ( $P = .001$ ) (Fig 1). Significant increased stiffness was also observed in the occipital lobe ( $P < .001$ ), the parietal lobe ( $P = .001$ ), and the temporal lobe ( $P = .02$ ) in the NPH group (Figs 2 and 3). However, no significant difference was noted in other regions of the brain including the frontal lobe ( $P = .07$ ), deep GM/WGM ( $P = .43$ ), or the cerebellum ( $P = .20$ ) (Table 2). Brain stiffness of the healthy control group was fitted to a linear regression model to assess possible confounding factors of age and sex in the specific age range. A trend with age was found as in previous work,<sup>19</sup> though in this age range it did not reach statis-

tical significance ( $P = .1$ ). There was no significant linear relationship between sex and brain stiffness in our healthy control group ( $P = .8$ ).

### DISCUSSION

In our study, patients with NPH demonstrated a significant increase of stiffness in the cerebrum and occipital, parietal, and temporal lobes compared with age- and sex-matched healthy controls. Although there is a significant difference between patients with NPH and healthy controls (Fig 1), there is too much overlap between the groups to be useful on an individual patient basis. Our findings stand in contrast to those of Streitberger et al,<sup>23</sup> who observed a significant decrease in the cerebral stiffness in patients with NPH compared with age- and sex-matched healthy controls. This discrepancy may be attributed to differences in the acquisition and postprocessing techniques. In our study, we reported 3-mm isotropic full-volume datasets segmented into anatomic lobes, while Streitberger et al took 3 adjacent 6-mm-thick sections and segmented them into global and periventricular regions. A considerable volume of the ROIs of Streitberger et al included the frontal lobes, which, in our work, showed a trend toward decreased stiffness in patients with NPH (though it did not reach significance). Other differences between the technique of Streitberger et al and ours, including differences in scanner hardware; processed data resolutions ( $1.5 \times 1.5 \times 6$  mm versus  $3 \times 3 \times 3$  mm); TE (149 versus  $\sim 60$  ms); number of time points (32 versus 8); and a processing approach that attempts to minimize CSF contamination and edge effects in this study, could potentially introduce SNR differences and stiffness estimation variations between the 2 techniques.

The physiology of NPH is dynamic, complex, and not well-understood, which makes it difficult to deduce a concrete mechanism behind the brain stiffening observed in this study. NPH generally refers to ventricular enlargement with normal opening pressure on lumbar puncture. However, overnight intermittent elevation of the intracranial pressure has been detected in patients with NPH, suggesting that increased intracranial pressure may play a role in the pathophysiology of NPH.<sup>24</sup> In addition, Alperin et al<sup>25</sup> reported a linear pressure-volume relationship between the volumetric blood flow rate and intracranial pressure changes with a consistent elastance index. On the basis of these findings, ventricular dilation is thought to occur at the expense of the compressible compartment as interstitial and intracellular fluids are “squeezed” out of parenchymal pores. Brain tissue compression can cause tissues to move into the nonlinear elastic regime, causing stiffening, which would support our findings. Furthermore, corresponding cellular changes, such as a higher ratio of cytoskeletal matrix to interstitial and intracellular fluid has been reported, as well as a more compressed capillary and venous channel matrix, all of which could contribute to parenchymal stiffening and a loss of compliance.<sup>26,27</sup>

In this study, we found a significant increase in stiffness in the occipital, parietal, and temporal lobes, while lower elasticity values were measured in the frontal lobe and deep GM/WGM areas in patients with NPH compared with healthy controls. Although these latter findings did not reach significance, it attracted our attention toward possible underlying changes that may contrib-

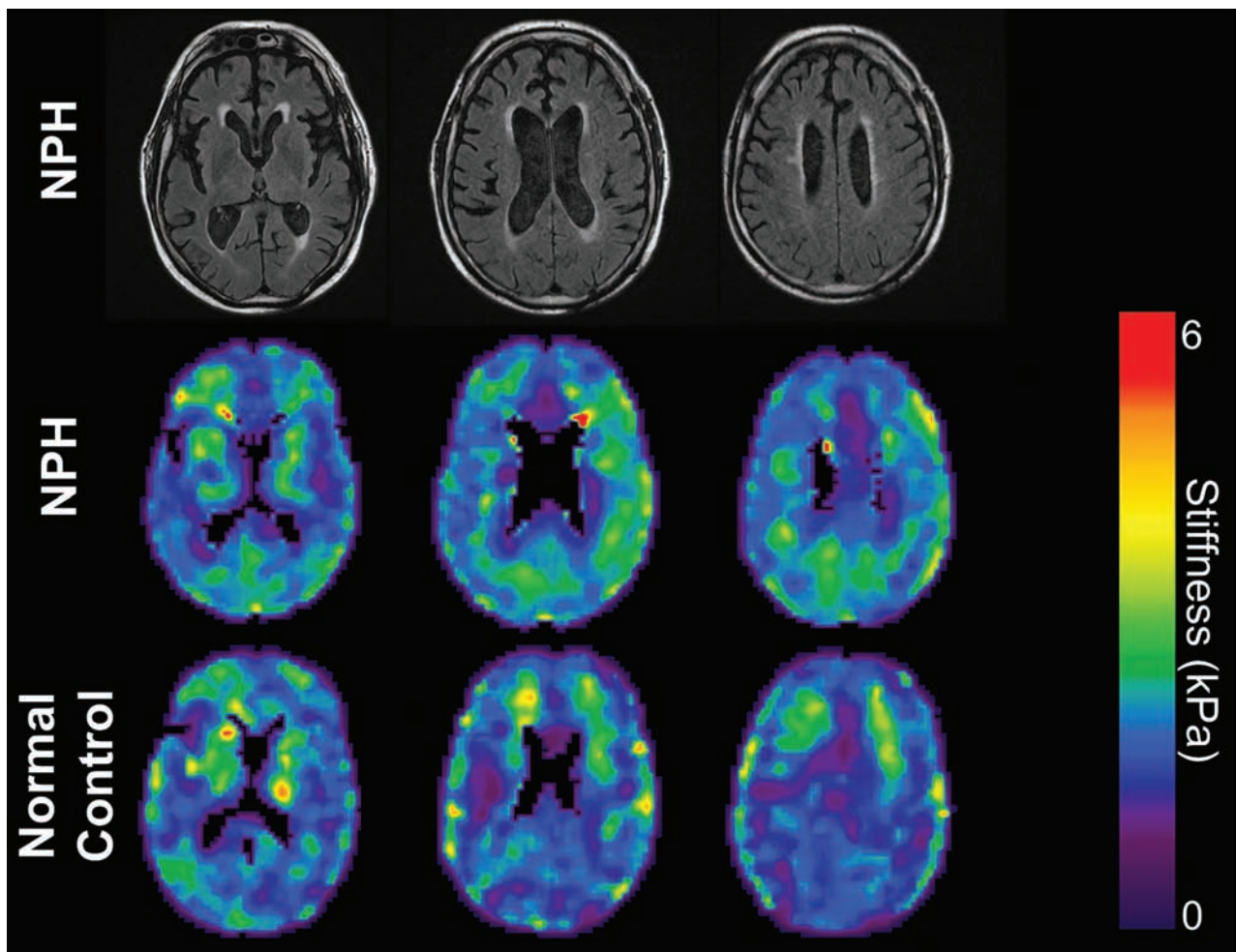


**FIG 3.** MRE image comparison of patients with NPH and healthy controls. T2 FLAIR images (*top row*) and MRE images (*middle row*) of a 67-year-old man with NPH. MRE of age- and sex-matched healthy controls (*bottom row*) shows increased stiffness in the patients with NPH compared with the healthy controls, especially in the parietal and occipital regions.

**Table 2: MRE stiffness results**

	Healthy Control Brain Stiffness (kPa)	NPH Brain Stiffness (kPa)	P Value
Frontal lobe	2.75 ± 0.16	2.66 ± 0.13	.07
Occipital lobe	2.75 ± 0.16	3.08 ± 0.28	<.001
Parietal lobe	2.45 ± 0.12	2.66 ± 0.17	.001
Temporal lobe	2.73 ± 0.15	2.80 ± 0.14	.02
Deep GM/WM	3.01 ± 0.29	2.91 ± 0.20	.43
Cerebrum	2.55 ± 0.11	2.65 ± 0.10	.001
Cerebellum	2.23 ± 0.13	2.21 ± 0.09	.20

ute to brain softening. Several imaging and histopathologic studies reported brain tissue degeneration beyond the paraventricular area, which was shown to be associated with acute or chronic hydrocephalus.<sup>28-30</sup> Ziegelitz et al<sup>31</sup> illustrated a significant reduction in cerebral blood flow, not only in the paraventricular area but also in the basal medial frontal cortex and deep gray matter in patients with NPH compared with healthy controls. In addition, they reported a positive correlation between decreased cerebral blood flow and the severity of clinical symptoms. Bugalho and Alves<sup>32</sup> suggested that predominant frontal lobe white matter lesions observed by T2-weighted MR imaging may be a cause of

irreversible symptoms in NPH. Therefore, the combination of factors such as reduced blood flow, tissue degeneration, and the development of white matter lesions could result in tissue softening in some regions, which may be overcompensation for compressional stiffening effects.

Further evidence of these competing factors can be found in the diffusion-tensor imaging literature. DTI studies investigating microstructural changes in NPH have illustrated region-dependent neuronal changes throughout the brain. They have reported that neuronal integrity changes in the periventricular area, including the corticospinal tract, are consistent with changes secondary to mechanical compression and tend to reverse after shunt treatment. However, neuronal integrity changes in the frontal lobe white matter, corpus callosum, and deep gray matter are compatible with degenerative changes, which remain unchanged after treatment.<sup>6,7,29,32-34</sup> Furthermore, previous brain MRE studies on Alzheimer disease and multiple sclerosis have illustrated that decreased brain tissue stiffness is associated with neurodegenerative changes.<sup>20,33,34</sup> Similarly, in this study, we hypothesized that the decreased stiffness in the frontal lobe and deep GM/WM may be attributed to the underlying neurodegenerative process resulting from NPH or reduced blood flow.<sup>13,24,35,36</sup> In-



creased pressure in these areas, producing elevated stiffness, due to ventricle enlargement may also contribute to a limited measurable reduction in stiffness. This theory is also compatible with clinical and neuroanatomic studies suggesting that cognitive impairment in NPH corresponds to irreversible changes in the deep GM/WM frontal subcortical areas, which is unlikely to improve after shunt treatment.<sup>37,38</sup> Also, Freimann et al<sup>39</sup> have reported no significant change in stiffness after shunt tube placement in patients with NPH. These results should motivate future investigation into the relationship between regional brain stiffness and shunt placement outcomes.

## CONCLUSIONS

Brain MRE of patients with NPH revealed increased brain tissue stiffness in the cerebrum and the occipital, parietal, and temporal lobes compared with age- and sex-matched healthy controls. Although not significant, decreased stiffness was observed in the frontal lobe and deep GM/WM of patients with NPH compared with healthy controls. This specific pattern of stiffness alteration will motivate future studies investigating the role of compressibility and degenerative changes in the development of NPH. In the future, MRE could potentially be implemented as a valuable diagnostic and prognostic tool for NPH and therapy response.

Disclosures: Nikoo Fattahi—RELATED: Grant: Theodore W. Batterman Family Foundation.\* Armando Manduca—UNRELATED: Stock/Stock Options: stockholder in Resoundant, which works in the general area of MR elastography. Kevin Glaser—RELATED: Grant: NIH R01 EB001981\*; UNRELATED: Patents (planned, pending or issued): MR elastography\*; Royalties: licensing of MR Elastography intellectual property; Stock/Stock Options: Resoundant. Matthew Senjem—RELATED: Grant: NIH.\* Richard L. Ehman—RELATED: Grant: NIH (EB001981)\*; UNRELATED: Board Membership: Resoundant (CEO, uncompensated); Grants/Grants Pending: Resoundant; Patents (planned, pending, or issued): R.L.E. and the Mayo Clinic have patents and intellectual property rights related to MRE; Royalties: Resoundant, Comments: Resoundant has licensed MRE technology from Mayo Clinic. Resoundant pays a licensing fee to Mayo Clinic, which is shared, in part, with R.L.E. and other inventors, pursuant to the Bayh-Dole act; Stock/Stock Options: Resoundant\*; OTHER RELATIONSHIPS: The Mayo Clinic and R.L.E. have intellectual property rights and a financial interest in technologies used in this research. R.L.E. serves as CEO of Resoundant. This research was conducted under the oversight and in compliance with Mayo Clinic Conflict of Interest Review Board. John Huston—RELATED: Grant: NIH (NIH R01 grant EB001981)\* Theodore W. Batterman Family Foundation\*; UNRELATED: Patents (planned, pending or issued): MR elastography brain patents planned; Stock/Stock Options: Resoundant.\* Money paid to the institution.

## REFERENCES

1. Jaraj D, Rabiei K, Marlow T, et al. **Prevalence of idiopathic normal-pressure hydrocephalus.** *Neurology* 2014;82:1449–54 CrossRef Medline
2. Leinonen V, Koivisto AM, Alafuzoff I, et al. **Cortical brain biopsy in long-term prognostication of 468 patients with possible normal pressure hydrocephalus.** *Neurodegener Dis* 2012;10:166–69 CrossRef Medline
3. Bech-Azeddine R, Høgh P, Juhler M, et al. **Idiopathic normal-pressure hydrocephalus: clinical comorbidity correlated with cerebral biopsy findings and outcome of cerebrospinal fluid shunting.** *J Neurol Neurosurg Psychiatry* 2007;78:157–61 CrossRef Medline
4. Chakravarty A. **Unifying concept for Alzheimer's disease, vascular dementia and normal pressure hydrocephalus: a hypothesis.** *Med Hypotheses* 2004;63:827–33 CrossRef Medline
5. Bateman GA. **The pathophysiology of idiopathic normal pressure hydrocephalus: cerebral ischemia or altered venous hemodynamics?** *AJNR Am J Neuroradiol* 2008;29:198–203 CrossRef Medline
6. Kamiya K, Hori M, Miyajima M, et al. **Axon diameter and intra-axonal volume fraction of the corticospinal tract in idiopathic nor-**

- mal pressure hydrocephalus measured by q-space imaging.** *PLoS One* 2014;9:e103842 CrossRef Medline
7. Klinge PM, Brooks DJ, Samii A, et al. **Correlates of local cerebral blood flow (CBF) in normal pressure hydrocephalus patients before and after shunting: a retrospective analysis of [(15)O]H(2)O PET-CBF studies in 65 patients.** *Clin Neurol Neurosurg* 2008;110:369–75 CrossRef Medline
8. Wikkelsø C, Andersson H, Blomstrand C, et al. **The clinical effect of lumbar puncture in normal pressure hydrocephalus.** *J Neurol Neurosurg Psychiatry* 1982;45:64–69 CrossRef Medline
9. Damasceno BP, Carelli EF, Honorato DC, et al. **The predictive value of cerebrospinal fluid tap-test in normal pressure hydrocephalus.** *Arq Neuropsiquiatr* 1997;55:179–85 CrossRef Medline
10. Marmarou A, Bergsneider M, Klinge P et al. **The value of supplemental prognostic tests for the preoperative assessment of idiopathic normal-pressure hydrocephalus.** *Neurosurgery* 2005;57(3 suppl):S17–28; discussion ii-v Medline
11. Calcagni ML, Taralli S, Mangiola A, et al. **Regional cerebral metabolic rate of glucose evaluation and clinical assessment in patients with idiopathic normal-pressure hydrocephalus before and after ventricular shunt placement: a prospective analysis.** *Clin Nucl Med* 2013;38:426–31 CrossRef Medline
12. Lundin F, Ledin T, Wikkelsø C, et al. **Postural function in idiopathic normal pressure hydrocephalus before and after shunt surgery: a controlled study using computerized dynamic posturography (EquiTest).** *Clin Neurol Neurosurg* 2013;115:1626–31 CrossRef Medline
13. Lundin F, Ulander M, Svanborg E, et al. **How active are patients with idiopathic normal pressure hydrocephalus and does activity improve after shunt surgery? A controlled actigraphic study.** *Clin Neurol Neurosurg* 2013;115:192–96 CrossRef Medline
14. Kahlon B, Sundbärg G, Rehn Crona S. **Comparison between the lumbar infusion and CSF tap tests to predict outcome after shunt surgery in suspected normal pressure hydrocephalus.** *J Neurol Neurosurg Psychiatry* 2002;73:721–26 CrossRef Medline
15. Kitagaki H, Ishii K, Yamaji S, et al. **CSF spaces in idiopathic normal pressure hydrocephalus: morphology and volumetry.** *AJNR Am J Neuroradiol* 1998;19:1277–84 Medline
16. Hirsch S, Beyer F, Guo J, et al. **Compression-sensitive magnetic resonance elastography.** *Phys Med Biol* 2013;58:5287–99 CrossRef Medline
17. Mousavi SR, Fehlnér A, Streitberger KJ, et al. **Measurement of in vivo cerebral volumetric strain induced by the Valsalva maneuver.** *J Biomech* 2014;47:652–57 CrossRef
18. Roberts RO, Geda YE, Knopman DS, et al. **The Mayo Clinic Study of Aging: design and sampling, participation, baseline measures and sample characteristics.** *Neuroepidemiology* 2008;30:58–69 CrossRef Medline
19. Arani A, Murphy MC, Glaser KJ, et al. **Measuring the effects of aging and sex on regional brain stiffness with MR elastography in healthy older adults.** *Neuroimage* 2015;111:59–64 CrossRef Medline
20. Murphy MC, Huston J 3rd, Jack CR Jr, et al. **Decreased brain stiffness in Alzheimer's disease determined by magnetic resonance elastography.** *J Magn Reson Imaging* 2011;34:494–98 CrossRef Medline
21. Murphy MC, Huston J 3rd, Jack CR Jr, et al. **Measuring the characteristic topography of brain stiffness with magnetic resonance elastography.** *PLoS One* 2013;8:e81668 CrossRef Medline
22. Jack CR, Jr, Lowe VJ, Senjem ML, et al. **11C PiB and structural MRI provide complementary information in imaging of Alzheimer's disease and amnesic mild cognitive impairment.** *Brain* 2008;131(pt 3):665–80 CrossRef Medline
23. Streitberger KJ, Wiener E, Hoffmann J, et al. **In vivo viscoelastic properties of the brain in normal pressure hydrocephalus.** *NMR Biomed* 2011;24:385–92 CrossRef Medline
24. Eide PK, Brean A. **Cerebrospinal fluid pulse pressure amplitude during lumbar infusion in idiopathic normal pressure hydroceph-**

- alus can predict response to shunting. *Cerebrospinal Fluid Res* 2010; 7:5 CrossRef Medline
25. Alperin NJ, Lee SH, Loth F, et al. **MR-intracranial pressure (ICP): a method to measure intracranial elastance and pressure noninvasively by means of MR imaging: baboon and human study.** *Radiology* 2000;217:877–85 CrossRef Medline
  26. Sklar FH, Diehl JT, Beyer CW Jr, et al. **Brain elasticity changes with ventriculomegaly.** *J Neurosurg* 1980;53:173–79 CrossRef Medline
  27. Levine DN. **The pathogenesis of normal pressure hydrocephalus: a theoretical analysis.** *Bull Math Biol* 1999;61:875–916 CrossRef Medline
  28. Del Bigio MR, Cardoso ER, Halliday WC. **Neuropathological changes in chronic adult hydrocephalus: cortical biopsies and autopsy findings.** *Can J Neurol Sci* 1997;24:121–26 Medline
  29. Tarnaris A, Toma AK, Pullen E, et al. **Cognitive, biochemical, and imaging profile of patients suffering from idiopathic normal pressure hydrocephalus.** *Alzheimers Dement* 2011;7:501–08 CrossRef Medline
  30. Assaf Y, Ben-Sira L, Constantini S, et al. **Diffusion tensor imaging in hydrocephalus: initial experience.** *AJNR Am J Neuroradiol* 2006;27:1717–24 Medline
  31. Ziegelitz D, Starck G, Kristiansen D, et al. **Cerebral perfusion measured by dynamic susceptibility contrast MRI is reduced in patients with idiopathic normal pressure hydrocephalus.** *J Magn Reson Imaging* 2014;39:1533–42 CrossRef Medline
  32. Bugalho P, Alves L. **Normal-pressure hydrocephalus: white matter lesions correlate negatively with gait improvement after lumbar puncture.** *Clin Neurol Neurosurg* 2007;109:774–78 CrossRef Medline
  33. Murphy MC, Curran GL, Glaser KJ, et al. **Magnetic resonance elastography of the brain in a mouse model of Alzheimer's disease: initial results.** *Magn Reson Imaging* 2012;30:535–39 CrossRef Medline
  34. Streitberger KJ, Sack I, Krefting D, et al. **Brain viscoelasticity alteration in chronic-progressive multiple sclerosis.** *PLoS One* 2012;7:e29888 CrossRef Medline
  35. Qvarlander S, Lundkvist B, Koskinen LO et al. **Pulsatility in CSF dynamics: pathophysiology of idiopathic normal pressure hydrocephalus.** *J Neurol Neurosurg Psychiatry* 2013;84:735–41 CrossRef Medline
  36. Hamlat A, Adn M, Sid-ahmed S, et al. **Theoretical considerations on the pathophysiology of normal pressure hydrocephalus (NPH) and NPH-related dementia.** *Med Hypotheses* 2006;67:115–23 CrossRef Medline
  37. Poca MA, Mataró M, Matarín M, et al. **Good outcome in patients with normal-pressure hydrocephalus and factors indicating poor prognosis.** *J Neurosurg* 2005;103:455–63 CrossRef Medline
  38. Kazui H. **Cognitive impairment in patients with idiopathic normal pressure hydrocephalus [in Japanese].** *Brain Nerve* 2008;60:225–31 Medline
  39. Freimann FB, Streitberger KJ, Klatt D, et al. **Alteration of brain viscoelasticity after shunt treatment in normal pressure hydrocephalus.** *Neuroradiology* 2012;54:189–96 CrossRef Medline

# Automated Cross-Sectional Measurement Method of Intracranial Dural Venous Sinuses

S. Lublinsky, A. Friedman, A. Kesler, D. Zur, R. Anconina, and I. Shelef

## ABSTRACT

**BACKGROUND AND PURPOSE:** MRV is an important blood vessel imaging and diagnostic tool for the evaluation of stenosis, occlusions, or aneurysms. However, an accurate image-processing tool for vessel comparison is unavailable. The purpose of this study was to develop and test an automated technique for vessel cross-sectional analysis.

**MATERIALS AND METHODS:** An algorithm for vessel cross-sectional analysis was developed that included 7 main steps: 1) image registration, 2) masking, 3) segmentation, 4) skeletonization, 5) cross-sectional planes, 6) clustering, and 7) cross-sectional analysis. Phantom models were used to validate the technique. The method was also tested on a control subject and a patient with idiopathic intracranial hypertension (4 large sinuses tested: right and left transverse sinuses, superior sagittal sinus, and straight sinus). The cross-sectional area and shape measurements were evaluated before and after lumbar puncture in patients with idiopathic intracranial hypertension.

**RESULTS:** The vessel-analysis algorithm had a high degree of stability with <3% of cross-sections manually corrected. All investigated principal cranial blood sinuses had a significant cross-sectional area increase after lumbar puncture ( $P \leq .05$ ). The average triangularity of the transverse sinuses was increased, and the mean circularity of the sinuses was decreased by  $6\% \pm 12\%$  after lumbar puncture. Comparison of phantom and real data showed that all computed errors were <1 voxel unit, which confirmed that the method provided a very accurate solution.

**CONCLUSIONS:** In this article, we present a novel automated imaging method for cross-sectional vessels analysis. The method can provide an efficient quantitative detection of abnormalities in the dural sinuses.

**ABBREVIATIONS:** IIH = idiopathic intracranial hypertension; LP = lumbar puncture

Idiopathic intracranial hypertension (IIH) (also known as “pseudotumor cerebri”) is a disorder of increased intracranial pressure without clinical, laboratory, or radiologic evidence of an intracranial space-occupying lesion or cerebral sinus vein thrombosis, predominantly affecting women of childbearing age with obesity. The annual incidence of IIH in the general population is estimated between 1 and 2 per 100,000. However, the incidence has risen to 3.5–12 per 100,000 in women 20–44 years of age, and among women with obesity in this age group, it has climbed to 7.9–21 per 100,000.<sup>25,30</sup>

To rule out occlusion or stenosis in patients with IIH, performing CTV and cerebral MRV is now accepted. However, drawbacks to CTV include concerns about radiation exposure, potential for iodine contrast material allergy, and issues related to the use of contrast in the setting of poor renal function. In some settings, MRV is preferable to CTV because of these concerns.<sup>27</sup> Doppler sonography is not considered a standard for the current study.<sup>26</sup>

Cross-sectional changes in the cerebral venous system in patients with IIH have received increased attention in recent years. In >90% patients with IIH, there is stenosis in the transverse dural sinuses,<sup>1–5</sup> and after medical treatment and normalization of the intracranial pressure in patients with IIH, there is no change in venous diameter.<sup>6</sup> However, another study presented cases of IIH in which an increase in venous diameter occurred after lumbar puncture (LP); in 1 patient, there was a decrease in venous diameter after stopping a CSF leak with a blood patch.<sup>7</sup> In agreement with a previous study, another study showed narrowing of the transverse sinuses on MRV in all patients with IIH and an

Received June 30, 2015; accepted after revision July 20.

From the Zolotowsky Neuroscience Center (S.L., A.F.), Ben-Gurion University, Beer-Sheva, Israel; Department of Medical Neuroscience (A.F.), Dalhousie University, Halifax, Nova Scotia, Canada; Ophthalmology Department (A.K., D.Z.), Tel Aviv Sourasky Medical Center, Tel Aviv, Israel; and Diagnostic Imaging Department (R.A., I.S.), Soroka University Medical Center, Beer-Sheva, Israel.

Please address correspondence to Ilan Shelef, MD, Soroka University Medical Center, Diagnostic Imaging Department, PO Box 151, Beer-Sheva 84101, Israel; e-mail: shelef@bgu.ac.il

<http://dx.doi.org/10.3174/ajnr.A4583>

increased diameter of the cerebral sinuses after LP.<sup>1,8</sup> This change was different for all patients and was more prominent at the right than left transverse sinus. All venous sinuses had an increased diameter in response to LP, and this change was not confined to the transverse sinuses.<sup>8</sup> In some patients with IIH, all dural sinuses appeared narrowed over long distances; this appearance gave the impression that these sinuses were compressed.<sup>9-11</sup> After we normalized against intracranial hypertension, the sinus volumes increased to normal values. However, there is controversy about the observation of the dynamic behavior of the sinus diameter.<sup>12-15</sup>

A novel "venous distension sign" for the diagnosis of intracranial hypotension<sup>30</sup> has recently been introduced. The cross-sectional contour of the transverse sinus normally has a triangular inferior border. In cases of intracranial hypotension, the inferior border acquires a distended appearance with a convex bulging. However, the estimation of the venous distension sign was performed on the basis of whether the latter was present or absent for each image set. In the present study, we propose using circularity and triangular-shape characteristics to quantify contour changes of the dural sinuses.

MRV is an important tool for blood vessel imaging and for the evaluation of stenosis (abnormal narrowing), occlusion, or aneurysms. Yet no accurate image-processing tool for quantitative measurement of the size and shape of the sinuses has so far been developed, to our knowledge. In previous reports, the sinuses were only estimated by using a descriptive, subjective method (ie, according to the impression of the radiologist). The main purpose of this study was to develop a technique for the accurate point-to-point assessment of cross-sectional alterations in cerebral sinuses before and after LP in patients with IIH. The method was validated by using computer models. A single control CT and MRV data were used for validating the technique. The method was implemented in 4 patients with IIH who were internally controlled against themselves (before and after LP).

## MATERIALS AND METHODS

### Subjects

Images of 4 female patients with IIH were retrospectively included in the study. The mean age of the examinees was  $33.7 \pm 10$  years; mean body mass index,  $27.9 \pm 7.6$ . Patients with IIH were diagnosed according to modified Dandy criteria.<sup>7,28</sup> Each participant underwent 2 MR imaging examinations: One was performed before the LP and another after. The timeframe for obtaining the second MR imaging was not to exceed 48 hours post-LP. Opening pressure on LP was  $>250$  mm H<sub>2</sub>O in all patients. The LP was performed by a neurologist with the patient under local anesthesia with lidocaine 1%, with the patient lying in the lateral decubitus position. Opening pressure was measured, and 10 mL of CSF was withdrawn. This study was conducted according to a protocol approved by the local ethics committee at Soroka University Medical Center, Diagnostic Imaging Department (Beer-Sheva, Israel).

### Image Acquisition

A patient with IIH, a control subject, and 2 phantoms each had MR imaging performed with a 1.5T scanner (Intera; Philips Healthcare, Best, the Netherlands) by using a 6-channel head coil for sensitivity encoding. A contrast-enhanced 3D spoiled gradi-

ent-echo sequence (T1WI) was used for imaging. The sequence parameters were the following: TR, 5.7 ms; TE, 1.75 ms; section width, 2 mm (reconstructed to 1 mm); in-plane resolution,  $0.74 \times 1.05$  mm; flip angle, 40°; sensitivity encoding reduction factor, 2.5; and scan time, 40.8 seconds. In addition, a single control subject and phantoms were used for validating the technique. The former had both an MR imaging and a contrast-enhanced head CT scan (in-plane resolution, 0.556 mm; section thickness, 1 mm; iopromide, Ultravist [Bayer HealthCare, Berlin, Germany], 300 mg/mL with a dose of 2 mL per kg; scan delay, 40 seconds after injector application).

The algorithm for vessel cross-sectional analysis included 7 main steps: 1) image registration, 2) masking, 3) segmentation, 4) skeletonization, 5) cross-sectional planes, 6) clustering, and 7) cross-section analysis.

The implementation of the algorithm used Matlab (MathWorks, Natick, Massachusetts).

### Image Processing

**Image Registration (Step 1).** The MRV images before and after LP from patients with IIH were used. The images were mapped to a standard brain<sup>29</sup> to avoid artifacts due to head movements and to allow accurate pixel-based comparison among scans and even among patients for group study analysis. The registration method applied mutual information (that measured the amount of information that one variable contained about the other) to measure statistical dependence between image intensities of corresponding voxels in both images (SPM12; <http://www.fil.ion.ucl.ac.uk/spm/software/spm12>; Matlab). Mutual information was assumed maximal when the images were geometrically aligned. Image transformation was restricted to rigid-body transformation only.

**Masking (Step 2).** A masking procedure was used to extract sinuses from the brain volume and separate them from other tissues of similar intensity. The brain mask was created by using a segmentation routine (SPM12). Three objects were created because of this procedure: gray matter, white matter, and CSF. These objects were combined. Morphologic closing, simply defined as dilation followed by erosion with the same structuring element for both operations, was applied to create a solid brain mask by removing all remaining gaps and inner spaces of the combined object.

**Segmentation (Step 3).** This step included segmentation of sinuses in the brain mask volume of interest. The integrated segmentation procedure developed in this study combined global and local image information (Fig 1).

Before applying the segmentation method, noise was reduced by filtering the data with a 3D Gaussian smoothing function with support and  $\sigma$  that approximated the size of background texture (support = 1 voxel;  $\sigma$  = 2 voxels).

The set of edges, detected with the Canny method<sup>17</sup> combined with the globally segmented region,<sup>16</sup> was used as an initial seed object. Starting with the seed object, the final vessel region was iteratively grown by appending to each seed the neighboring voxels that had intensities similar to the seed. To this end, the original gray-scale intensities of the seed object were dilated in 3D with a sphere-shaped structuring element that had a small radius (2 voxels). The gray-scale dilation was used to compute the local maxi-



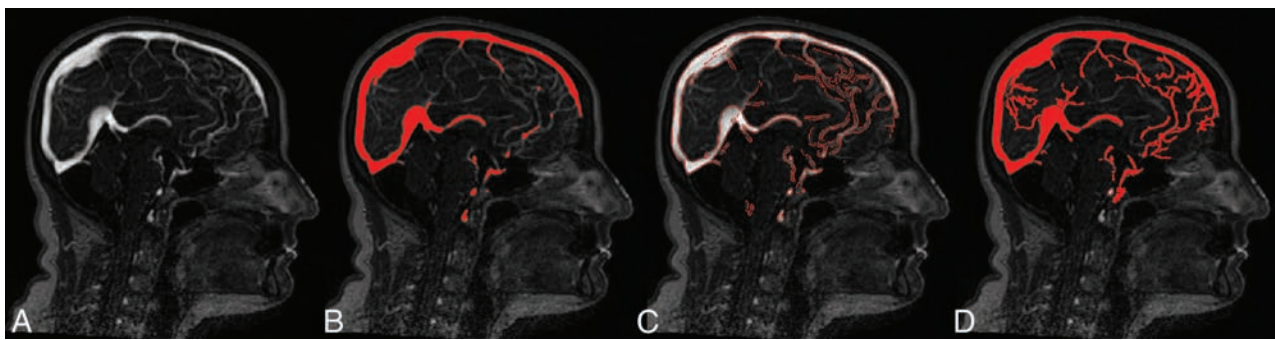


**FIG 1.** Integrated segmentation procedure. A, Gray-scale image. B, Global threshold region (red). Only thick sinuses could be detected by using this method. C, Edge detection. D, Region-growing segmentation. The method allowed the detection of most of the thin, low-intensity sinuses.

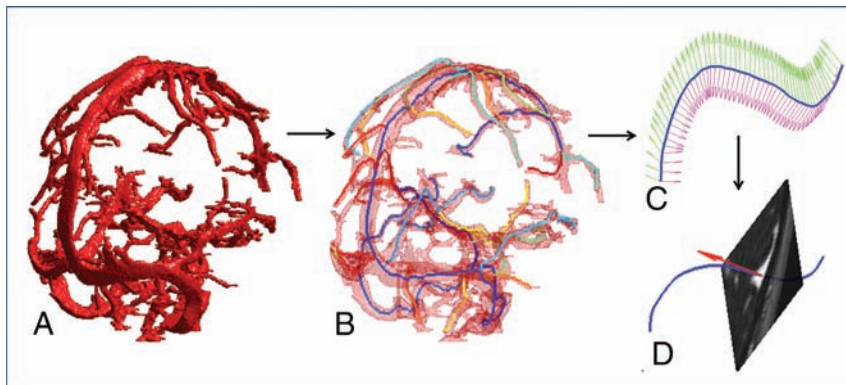


**FIG 2.** Segmentation and skeletonization. A, Segmented sinus object. B, Superimposition of skeleton branches (shown in different colors) with the segmented vessel object (transparent red). C, Typical definition of the cross-sectional planes for a single skeleton branch (blue line). D, Typical extraction of a cross-sectional plane from image volume.

imum-intensity values in every structuring element for the 26-neighborhood. The Gaussian-weighted values of dilated intensities served as local thresholds. Voxels connected to the seed object with gray values higher than the local threshold values were appended to the seed object. The described procedure was run iteratively until no more voxels could be added. This region-growing part of the algorithm was adapted, in part, from a method previously described.<sup>18,19</sup>

The edge inclusion criteria were developed to reduce the risk of thickening the sinuses. Only strong edges were considered true edges and included in the final vessel object (Fig 2).

**Skeletonization (Step 4).** The 3D MultiStencils Fast Marching Method was applied to extract a central path of the segmented vessel object (Fig 2).<sup>20–22</sup> The method was used to calculate the shortest distance from a list of points to all other voxels in the image by solving the Eikonal equation. This method gave more accurate distances by using second-order derivatives and cross-neighbors. The skeletonization procedure was implemented in custom-built code (Matlab) and C code. The number of skeleton branches was determined automatically from the maximum diameter of the vessel object. The termination condition for the new branched search occurred when the length of the new branch was smaller than the diameter of the largest vessel.

**Cross-Sectional Planes (Step 5).** Each skeleton branch was smoothed by using a cubic smoothing spline to provide continuous derivatives at every point. The moving reference frame of the

orthonormal vectors of Serret<sup>23</sup> and Frenet<sup>23,24</sup> was used to describe a branch curve  $\gamma(t)$ :

$$T(t) = \gamma'(t) / \|\gamma'(t)\|,$$

where  $T(t)$  was the unit tangent vector at every point  $t$ .

The unit normal vector to the cross-sectional plane took the form

$$N(t) = T(t).$$

The cross-sectional plane at every skeleton point  $t (x_t, y_t, z_t)$  was determined by the point itself and  $N(t)$  at that point (Fig 2). To minimize computational time, we extracted cross-sections from small portions of the segmented vessel object by application of a disc-shaped mask at each point  $t$ . To define

the size of the disc-shaped mask, we calculated the Euclidean distance transform map of the vessel object. To this end, each skeleton voxel was assigned a number that was the distance between the voxel itself and the nearest background (zero) voxel. The diameter of the disc-shaped mask was estimated as  $4 \times$  the distance transform value at point  $t$ .

**Clustering (Step 6).** Some vessel cross-sections may have included an intersection with other sinuses; therefore, to separate a single-vessel cross-section from the other sinuses, we developed a special clustering procedure. Component labeling was applied to select the connected vessel object with the centroid at point  $t$ . This operation allowed detection of an initial vessel shape by removing all disconnected elements. The attached components were separated from the initial vessel object (Fig 3).

This procedure included several substeps. The Euclidean distance transform map of the vessel object was calculated (Fig 3). To create catchment basins for the further watershed transform, we calculated differences between the maximal distance transform value and the distance transform map. All nonobject pixels were set to zero. The watershed transform was performed (Fig 3), and the watershed region containing the central point  $t$  was identified. An overlay of the outer boundary of the vessel object onto a gray-scaled plane was used for visual inspection of separation.

**Cross-Section Analysis (Step 7).** The boundary points of vessel cross-sections detected in the previous step were used to derive

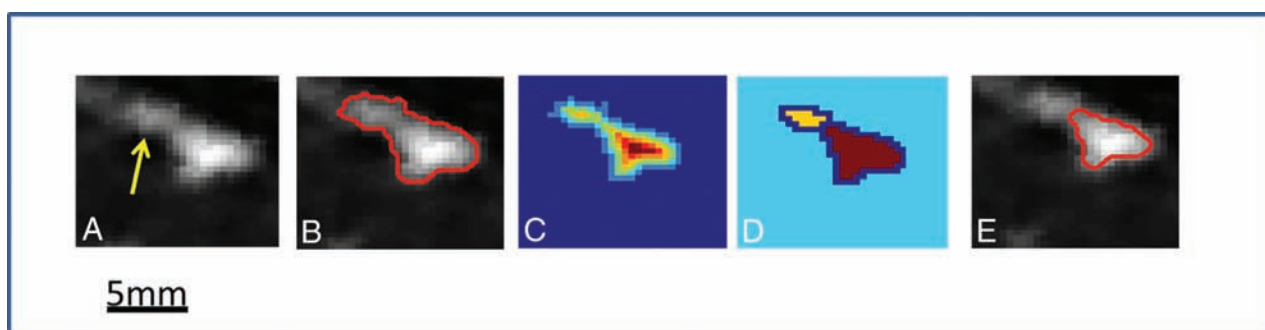


**FIG 3.** Clustering procedure for removal of intersecting or touching sinuses (yellow arrow points to adjacent components). *A*, A single cross-sectional plane extracted from the image volume. The vessel object had an attached component. *B*, An overlay of the initial segmented vessel object onto a gray-scaled image at the extracted cross-sectional plane. *C*, The Euclidean distance transform map. *D*, The watershed transform. *E*, The final result of the separation procedure (red line) overlaid onto the original data.

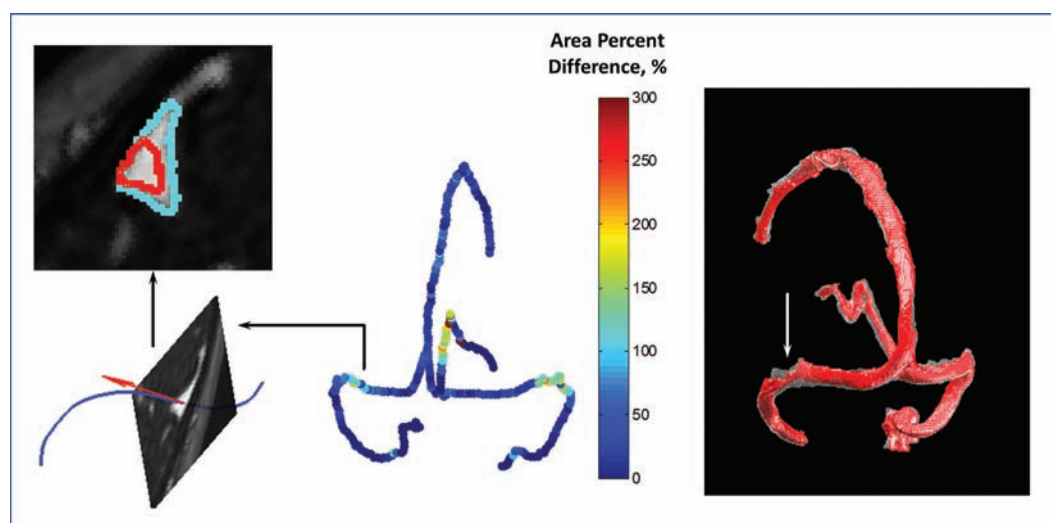


**FIG 4.** Changes in cross-sectional areas between images before and after LP in IIH. *Left*: Typical shape-changed areas for a single cross-section (red line, before LP; cyan line, after LP). *Middle*: Each skeleton point was assigned with a value of percentage difference of cross-sectional areas before and after LP. *Right*: Superimposition of before (red, nontransparent) and after (transparent) LP vessel objects reconstructed for the 4 main sinuses (right and left transverse sinuses, superior sagittal sinus, and straight sinus). No cross-sectional data analysis was performed at vessel intersections (shown as gaps).

**Table 1: Cross-sectional area measurements in the principal cerebral sinuses<sup>a</sup>**

Sinus	Cross-Sectional Area (mm <sup>2</sup> )			
	Before LP		After LP	
Right transverse	40 ± 21 <sup>b</sup>	(4–76)	52 ± 22	(6–79)
Left transverse	45 ± 20 <sup>b</sup>	(7.5–78)	52 ± 23	(8–78)
Superior sagittal	52 ± 21 <sup>b</sup>	(17–88)	54 ± 21	(17–88)
Straight	23 ± 13 <sup>b</sup>	(2–45)	30 ± 16	(4–48)

<sup>a</sup> *N* = 4 patients. Data are reported as mean (range).

<sup>b</sup> Significant difference (*P* ≤ .05) between measurements before and after LP.

geometric measurements, including circumference, area, circularity, and triangularity. The circumference ( $L_t$ ) and area ( $A_t$ ) were directly calculated as polygon length and area. Circularity, which was a parameter of shape compactness, was defined as

$$\text{Circularity} = 4 \pi A_t / L_t^2.$$

Triangularity of the vessel cross-section was estimated as

$$\text{Triangularity} = A_{t\_fit} / A_t,$$

where  $A_{t\_fit}$  was the area of the largest triangle inscribed in the polygon.

### Validation of the Method

Validation experiments were performed to evaluate the performance of the presented algorithm. The method was validated with 2 phantom silicon catheters filled with the contrast agent Gd-DTPA and 1 digitally created phantom. The silicon catheters had inner diameters of 1.5 and 3 mm and were scanned at an isometric resolution of 0.5 mm.

The diameters of all phantoms were digitally expanded by 5 mm each. The expansion of the catheters was done by morphologic dilation by using a spheric structural element (radius = 2.5 mm). The automatic procedure described (steps 3–7) was applied to reconstruct phantom cross-sections with altered diameters.

To test the accuracy, potential bias, and reproducibility of the calculation routine, we compared the actual phantom diameters with the computed ones.

### Method Application

The sinus analysis algorithm was initially tested on 4 patients. Only 4 large sinuses were chosen for the analysis (right and left transverse sinuses, superior sagittal sinus, and straight sinus). The images before and after LP were aligned with standard brain, and

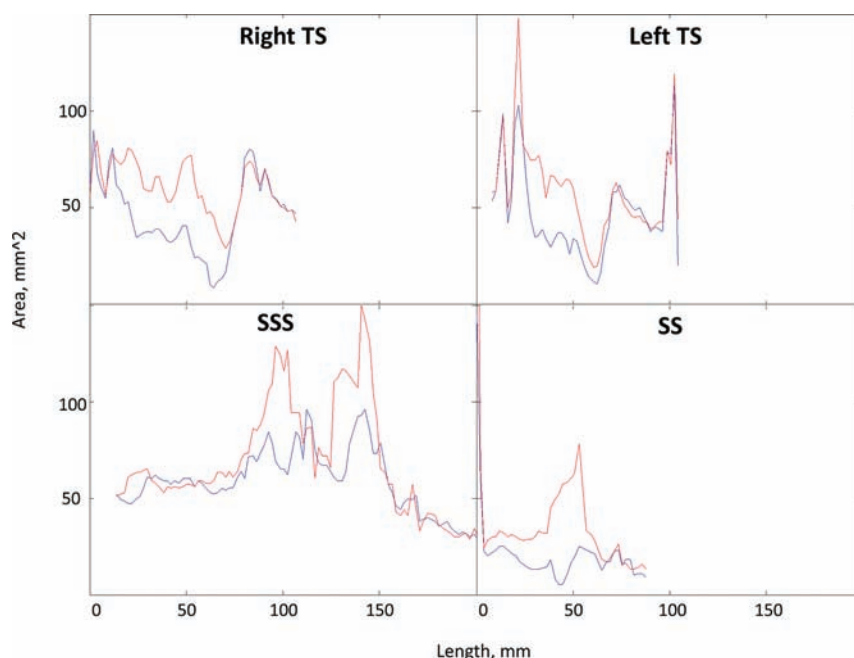


**FIG 5.** Typical cross-sectional area plot along 4 principal cranial blood sinuses before (blue) and after (red) LP.

**Table 2: Cross-sectional shape-change measurements in the principal cerebral sinuses<sup>a</sup>**

Sinus	Cross-Sectional Shape Measurement (mm <sup>2</sup> )			
	Before LP		After LP	
	Circularity	Triangularity	Circularity	Triangularity
Right transverse	72 ± 11	61 ± 9	66 ± 13	64 ± 11
Left transverse	75 ± 11 <sup>b</sup>	59 ± 8	71 ± 12	62 ± 10
Superior sagittal	77 ± 10	60 ± 8	77 ± 12	59 ± 8
Straight	84 ± 16 <sup>b</sup>	60 ± 6	78 ± 17	62 ± 9

<sup>a</sup> N = 4 patients. Data are reported as means.

<sup>b</sup> Significant differences ( $P \leq .05$ ) between measurements before and after LP.

the skeletonization procedure was applied only to the segmented vessel object after LP. To minimize computational time, we performed the cross-sectional calculations at every other skeleton point of the sinuses selected for analysis (step distance, 2 mm between skeleton points).

### Statistical Methods

The comparison of the cross-sectional area, triangularity, and circularity between before and after LP was performed with a *t* test.  $P < .05$  was considered significant.

### RESULTS

The sinus analysis algorithm showed a high degree of stability with <3% of cross-sections manually corrected. The automated algorithm was completed in <10 minutes, including all steps of the cross-sectional analysis in which 350 cross-sections were analyzed for each patient.

Distribution of the percentage difference before and after LP (Fig 4) showed that the patient with IIH had bilateral narrowing of the lateral part of the transverse sinus, with a more prominent right-than-left transverse sinus. All investigated principal cranial blood sinuses had a significant cross-sectional area increase after LP ( $P \leq .05$ ) (Table 1). Typical behavior of the cross-sectional

area measured along blood sinuses showed narrowing regions in all 4 investigated sinuses before LP, which were expanded after LP (Fig 5).

As an application of the method, statistical distribution of the sinus cross-sectional circularity and triangularity was tested; the shape of the sinuses became slightly more triangular after LP. The mean triangularity of the transverse sinuses was increased, and the mean circularity of the sinuses was decreased by  $6\% \pm 12\%$  after LP (Table 2).

In addition, cross-sectional vessel analysis was performed for CT and MR imaging data of a control patient (Fig 6). The mean percentage difference of the calculated areas along 4 large sinuses was  $12\% \pm 14\%$ .

To evaluate the accuracy of the algorithm, we compared the diameters calculated from the phantom images and real ones. There were >100 cross-sections calculated along each phantom skeleton curve. All computed errors were <1 voxel unit, which showed that this method provided a very accurate solution (Table 3). In addition, the behavior of the algorithm was tested by altering the size of the phantoms. For this purpose, the phantoms were digitally expanded by morphologic dilation with a spheric structural element. The relative diameter changes were calculated at each cross-section across the phantom skeletons. To various degrees, all errors in measurement were dependent on the phantom diameter. Phantoms with wider diameters were associated with smaller measurement errors. This was reasonable because the segmentation and calculation errors depended on image resolution and object size.

### DISCUSSION

The principal aim of this study was to develop an automated method for the point-to-point cross-sectional analysis and comparison of blood sinuses. The accuracy of the sinus segmentation was determined by visual assessment. For this purpose, an overlay of a segmented image onto the gray-scale image was examined for each section. The advantage of the proposed hybrid segmentation method is that it combined global and local image statistical information. The global segmentation method made use of global optimality criteria and might produce significant results but typically might have poor localization of the regional boundaries. This outcome occurred because the criteria used were based on statistics obtained from all pixels in the entire image region and did not reflect local characteristics. In contrast, the local region-growing method offered accurate boundary localization but usually did not have sufficient global information.

The goal of the proposed integrated segmentation method was to combine global and regional edge information to enable the use of both image-wide statistics and local edge responses. The results of this method were segmented regions with accurate boundary

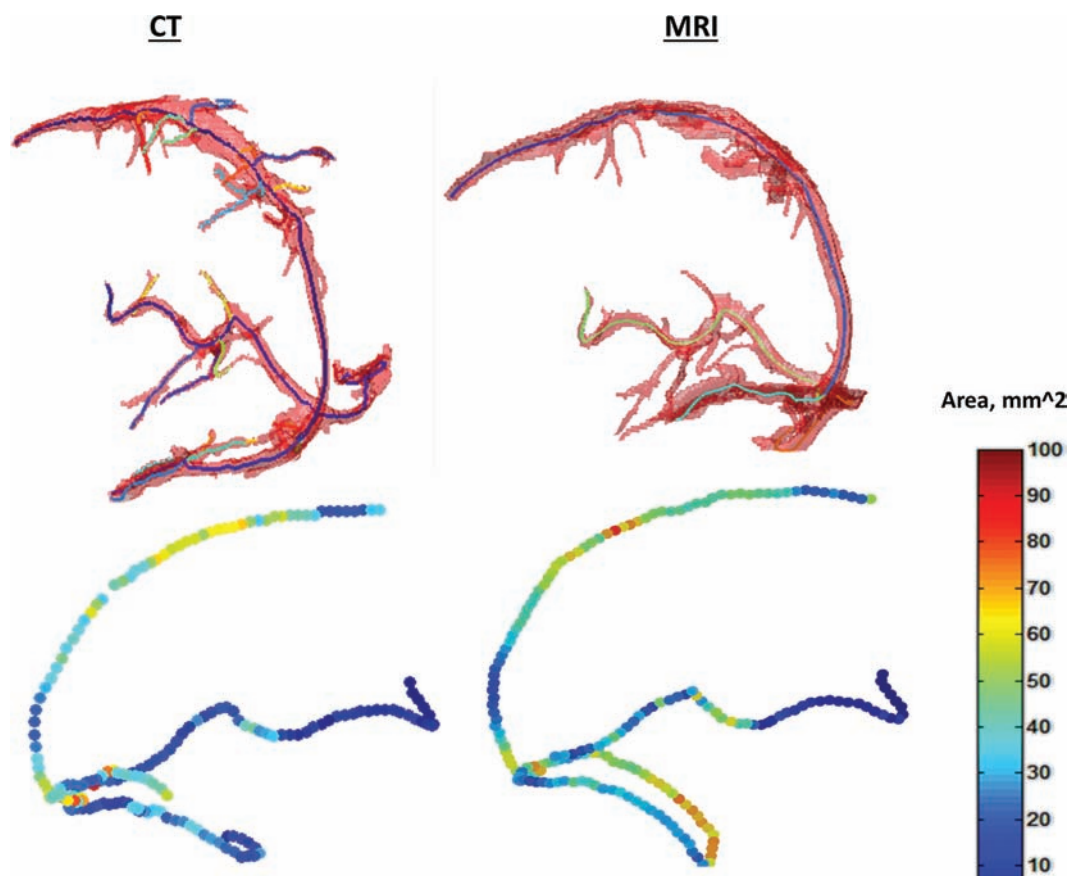


**FIG 6.** Cross-sectional vessel analysis for both CT and MR imaging data of a control patient. *Top:* Segmented sinus object with an overlaid central line. *Bottom:* Calculated cross-sectional areas along central lines of the sinuses. *Right:* MR imaging data. *Left:* CT data.

**Table 3: Average error, SD, and maximum error for phantom data used to validate the methods<sup>a</sup>**

Phantom Catheter	ID (mm)	Diameter Measurement		Relative Diameter Change after Digital Expansion		Image Resolution (mm)
		Mean (mm)	Maximum Error (mm)	Mean (mm)	Maximum Error (mm)	
1.5-mm catheter	1.5	0.2 ± 0.3	0.46	0.1 ± 0.2	0.31	0.5
3.0-mm catheter	3	0.06 ± 0.2	0.23	0.04 ± 0.08	0.16	0.5

**Note:**—ID indicates inner diameter of catheter.

<sup>a</sup> Data are reported as mean or value.

localizations at places where the edge-detection operators produced reasonably strong responses.

This proposed segmentation technique helped create connected and homogeneous segmented sinus objects.

Precise detection of the centerline of the vessel object (skeleton) is important for the accurate detection of cross-sectional planes across the vessel objects. The skeletonization method used in this study computed subvoxel precise skeletons by using a fast-marching method. The very robust, fully automatic technique did not depend on the complexity of the skeleton structure (number and curvature of branches) and was not limited to tubular structures with roughly circular cross-sections.

The present automated algorithm may run without user intervention. Therefore, a special 2-step clustering technique was developed for rendering the vessel cross-sectional circumference. The technique was tested across all analyzed cross-sections by visual inspection of the automatically detected clusters overlaid onto vessel cross-sectional planes. Qualitatively, visual inspection showed a high capability for accurate identification of vessel cir-

cumference. Furthermore, the method was automatic and did not require fine-tuning of the initially determined input parameters such as filters, global thresholds, and morphologic distances for each sample or patient in the study. These input parameters may vary with different scan protocols and may be affected by scan resolution. Thus, preliminary adjustment of the input parameters may be necessary before applying the procedure to a study.

As an additional input option during the skeletonization step, the user is asked to select a specific sinus (skeleton branches) for further analysis. There are several methods of vessel selection, including automatic (vessel length, maximal diameter, or the entire skeleton) and manual selection. In addition, the user can define the calculation step or distance value between the 2 next skeleton points where the cross-sectional data will be calculated.

All 4 sinuses increased their diameter in response to LP, not only the transverse sinuses. In agreement with a previous report,<sup>8</sup> this finding suggests that intracranial pressure and volume changes influence all sinuses.

The recently discovered venous distension sign phenomenon



was not yet given for quantification.<sup>27</sup> The recognition of the venous distension sign was somewhat subjective on the basis of reader interpretation and was categorized as absent or present. The proposed shape quantification circularity and triangularity parameters can provide a quantitative measure of the phenomena. In addition, the venous distension sign can also be measured by estimation of whether the shape is more concave or convex. In agreement with a previous review,<sup>30</sup> the shape of the sinuses tends to become slightly more triangular (or less circular) after LP. Potentially, the technique can be applied for evaluation of normal cross-sectional contour variation of the normal dural sinuses.

Cross-sectional area plots before and after LP demonstrate changes along the vessels. They can be helpful in revealing the most prominent cross-sectional change regions following LP. The presented method can be applied to characterize the sinuses of a healthy population with normal MR imaging findings and create normograms of them. Therefore, comparison of the IIH sinus characteristics with the norm can be critical in establishing pathologic conditions with changes in the intracranial pressure.

We have developed the special clustering procedure for separation of a single-vessel cross-section from the other sinuses. However, there still could be some complicit intersections defined. This definition may result in some sharp peaks on cross-sectional area plots, but one can remove the peaks by smoothing them out.

The limitation of the presented method is related to the small number of patients enrolled in the study. Therefore, a larger scale study is warranted to validate our findings.

## CONCLUSIONS











A quantitative method to evaluate the size of the dural sinuses of the brain has not been described yet, and estimation of change in the size of the sinuses—whether the sinus is narrow or wide—is decided subjectively according to the impression of the reader in a descriptive method. The method presented and tested here is fast and accurate and can be used in cross-sectional vessel analysis in different vascular systems. Implementation of the technique can provide new insight on the mechanisms underlying the development of IIH.

## REFERENCES

- Farb RI, Vanek I, Scott JN, et al. **Idiopathic intracranial hypertension: the prevalence and morphology of sinovenous stenosis.** *Neurology* 2003;60:1418–24 CrossRef Medline
- Ahlsgog JE, O'Neill BP. **Pseudotumor cerebri.** *Ann Intern Med* 1982; 97:249–56 CrossRef Medline
- Corbett JJ, Thompson HS. **The rational management of idiopathic intracranial hypertension.** *Arch Neurol* 1989;46:1049–51 CrossRef Medline
- Smith JL. **Whence pseudotumor cerebri?** *J Clin Neuroophthalmol* 1985;5:55–56 Medline
- Pickard JD, Czosnyka Z, Czosnyka M, et al. **Coupling of sagittal sinus pressure and cerebrospinal fluid pressure in idiopathic intracranial hypertension: a preliminary report.** *Acta Neurochir Suppl* 2008;102: 283–85 CrossRef Medline
- Bono F, Giliberto C, Mastrandrea C, et al. **Transverse sinus stenoses persist after normalization of the CSF pressure in IIH.** *Neurology* 2005;65:1090–93 CrossRef Medline
- Wall M. **Idiopathic intracranial hypertension.** *Neurol Clin* 2010;28: 593–617 CrossRef Medline

- Horev A, Hallevy H, Plakht Y, et al. **Changes in cerebral venous sinuses diameter after lumbar puncture in idiopathic intracranial hypertension: a prospective MRI study.** *J Neuroimaging* 2013;23: 375–78 CrossRef Medline
- Rohr A, Bindeballe J, Riedel C, et al. **The entire dural sinus tree is compressed in patients with idiopathic intracranial hypertension: a longitudinal, volumetric magnetic resonance imaging study.** *Neuroradiology* 2012;54:25–33 CrossRef Medline
- Rohr A, Dorner L, Stinge R, et al. **Reversibility of venous sinus obstruction in idiopathic intracranial hypertension.** *AJNR Am J Neuroradiol* 2007;28:656–59 Medline
- Biousse V, Ameri A, Bousser MG. **Isolated intracranial hypertension as the only sign of cerebral venous thrombosis.** *Neurology* 1999;53: 1537–42 CrossRef Medline
- Baryshnik DB, Farb RI. **Changes in the appearance of venous sinuses after treatment of disordered intracranial pressure.** *Neurology* 2004; 62:1445–46 CrossRef Medline
- Walker RW. **Idiopathic intracranial hypertension: any light on the mechanism of the raised pressure?** *J Neurol Neurosurg Psychiatry* 2001;71:1–5 CrossRef Medline
- Karahalios DG, Rekeate HL, Khayata MH, et al. **Elevated intracranial venous pressure as a universal mechanism in pseudotumor cerebri of varying etiologies.** *Neurology* 1996;46:198–202 CrossRef Medline
- Soler D, Cox T, Bullock P, et al. **Diagnosis and management of benign intracranial hypertension.** *Arch Dis Child* 1998;78:89–94 CrossRef Medline
- Otsu N. **A threshold selection method from gray-level histograms.** *IEEE Trans Syst Man Cybern* 1979;9:62–66 CrossRef
- Canny J. **A computational approach to edge detection.** *IEEE Trans Pattern Anal Mach Intell* 1986;8:679–98 Medline
- Waarsing JH, Day JS, Weinans H. **An improved segmentation method for in vivo microCT imaging.** *J Bone Miner Res* 2004;19: 1640–50 CrossRef Medline
- Lublinsky S, Ozcivici E, Judex S. **An automated algorithm to detect the trabecular-cortical bone interface in micro-computed tomographic images.** *Calcif Tissue Int* 2007;81:285–93 CrossRef Medline
- Barentzen JA. **On the implementation of fast marching methods for 3D lattices.** *Math Model* 2001;13:1–19
- Hassouna MS, Farag AA. **Multi-stencils fast marching methods: a highly accurate solution to the Eikonal equation on Cartesian domains.** *IEEE Trans Pattern Anal Mach Intell* 2007;29:1563–74 CrossRef Medline
- Van Uiter R, Bitter I. **Subvoxel precise skeletons of volumetric data based on fast marching methods.** *Med Phys* 2007;34:627–38 CrossRef Medline
- Serret JA. **Sur quelques formules relatives à la théorie des courbes à double courbure.** *J. de Math* 1851;16
- Frenet F. **Sur les courbes à double courbure.** Thèse. Toulouse, 1847. Abstract in *J. de Math* 1852;17
- Durcan FJ, Corbett JJ, Wall M. **The incidence of pseudotumor cerebri: population studies in Iowa and Louisiana.** *Arch Neurol* 1988;45:875–77 CrossRef Medline
- Gur AY, Kesler A, Shopin L, et al. **Transcranial Doppler for evaluation of idiopathic intracranial hypertension.** *Acta Neurol Scand* 2007;116:239–42 CrossRef Medline
- Agid R, Shelef I, Scott JN, et al. **Imaging of the intracranial venous system.** *Neurologist* 2008;14:12–22 CrossRef Medline
- Friedman DI, McDermott MP, Kiebertz K, et al; NORDIC IIHTT Study Group. **The idiopathic intracranial hypertension treatment trial: design considerations and methods.** *J Neuroophthalmol* 2014; 34:107–17 CrossRef Medline
- Talairach J, Tournoux P. *Co-Planar Stereotaxic Atlas of the Human Brain: 3-Dimensional Proportional System: An Approach to Cerebral Imaging.* New York: Thieme; 1988
- Radhakrishnan K, Ahlsgog JE, Garrity JA, et al. **Idiopathic intracranial hypertension.** *Mayo Clin Proc* 1994;69:169–80 CrossRef Medline

# Retrospective Analysis of Delayed Intraparenchymal Hemorrhage after Flow-Diverter Treatment: Presentation of a Retrospective Multicenter Trial

 A. Benaissa,  C. Tomas,  F. Clarençon,  N. Sourour,  D. Herbreteau,  L. Spelle,  S. Gallas,  A.-C. Januel,  A.L. Gaultier, and  L. Pierot

## ABSTRACT

**BACKGROUND AND PURPOSE:** Intracranial aneurysm treatment with flow diverters has shown satisfying results in terms of aneurysm occlusion, and while some cases of delayed intraparenchymal hemorrhage have been described, no systematic analysis of the risk factors affecting its occurrence has been conducted in a large series of patients. This retrospective analysis of delayed intraparenchymal hemorrhage after flow-diverter treatment is a multicenter, retrospective study using a large series of treated patients to analyze factors affecting the occurrence of delayed intraparenchymal hemorrhage.

**MATERIALS AND METHODS:** Patients treated with flow diverters and presenting with delayed intraparenchymal hemorrhage were included from December 2007 to December 2014 in 7 participating centers in France. Patient and aneurysm characteristics were recorded as were characteristics of bleeding (size, lateralization, and time to bleed), treatment, and clinical outcome after 1, 3, and 6 months.

**RESULTS:** Delayed intraparenchymal hemorrhage occurred in 11 patients between 1 and 21 days after the procedure. In 10 of these patients, hemorrhages were ipsilateral to the treated aneurysms. Five of the 11 underwent surgery, and 9 of the 11 had good clinical outcomes at 6 months (mRS  $\leq 2$ ).

**CONCLUSIONS:** The pathogenesis of delayed intraparenchymal hemorrhage occurring after flow-diverter treatment remains unclear. The multidisciplinary management of delayed intraparenchymal hemorrhage yields a relatively low morbidity-mortality rate compared with the initial clinical presentation.

**ABBREVIATIONS:** FD = flow diverter; DIPH = delayed intraparenchymal hemorrhage

During recent decades, endovascular treatment has become the first-line treatment for intracranial aneurysms.<sup>1-3</sup> Nevertheless, treatment of giant, wide-neck, and fusiform aneurysms remains difficult and has evolved with the use of balloon- or stent-assisted coiling, flow diverters (FDs), and flow disrupters.<sup>4</sup> The use of FDs has shown promising results in the treatment of complex and recanalized aneurysms.<sup>5,6</sup> However, thromboembolic complications and aneurysm rupture can occur during and after

FD treatment.<sup>7-10</sup> More recently, cases of delayed intraparenchymal hemorrhage (DIPH) have also been reported with potential serious worsening.<sup>11-15</sup> To date, the clinical presentation, etiology, and management of this complication are not well-understood, and published series of DIPH cases have included a limited number of patients and did not analyze precisely aneurysm, procedural, and postprocedural factors that may affect the occurrence of such complications.

The aim of this retrospective study was to describe and analyze the clinical presentation, modalities of treatment, and outcomes in a series of 11 patients who presented with DIPH.

## MATERIALS AND METHODS

### Patient Selection

From 2007 to 2014, patients treated with a flow diverter and who presented with DIPH after treatment were retrospectively included from 7 French interventional neuroradiologic centers (Pitié-Salpêtrière, Tours, Reims, Nantes, Créteil, Toulouse, and Beaujon). Because of the study design, informed consent was waived. Flow-diverter treatment was decided after a mul-

Received May 28, 2015; accepted after revision July 29.

From the Department of Neuroradiology (A.B., C.T., L.P.), Centres Hospitaliers Universitaires de Reims, Reims, France; Department of Neuroradiology (F.C., N.S.), Centres Hospitaliers Universitaires of Pitié-Salpêtrière, Paris, France; Department of Neuroradiology (D.H.), Centres Hospitaliers Universitaires of Tours, Tours, France; Department of Neuroradiology (L.S.), Centres Hospitaliers Universitaires of Beaujon, Clichy, France; Department of Neuroradiology (S.G.), Centres Hospitaliers Universitaires of Créteil, Créteil, France; Department of Neuroradiology (A.-C.J.), Centres Hospitaliers Universitaires of Toulouse, Toulouse, France; and Department of Neuroradiology (A.L.G.), Centres Hospitaliers Universitaires of Nantes, Nantes, France.

Please address correspondence to Laurent Pierot, MD, Service de Neuroradiologie, Hôpital Maison Blanche, 45, Rue Cognacq Jay, 51092 Reims Cedex, France; e-mail: lpierot@chu-reims.fr

<http://dx.doi.org/10.3174/ajnr.A4561>

tidisciplinary decision-making process. The study received institutional review board approval.

### **Endovascular Procedure**

For all patients, the treatment was performed with the patient under general anesthesia by an experienced interventional neuro-radiologist with at least 5 years' experience. The 3D reconstruction and 2D working projections were used to measure the parent artery, allowing selection of the FD size. A 6F long sheath or a 6F guiding catheter was used via transfemoral access. The precise type of introducer sheath and/or guiding catheter used during the procedure was not systematically registered in the procedure reports. A coaxial system catheter was used for stent navigation, with a guiding catheter (or sheath) in which a delivery microcatheter was inserted. A 0.027-inch inner diameter Marksman microcatheter (Covidien, Irvine, California) was used for the Pipeline Embolization Device (Covidien), a 0.040-inch inner diameter Surpass microcatheter (Stryker Neurovascular, Kalamazoo, Michigan) was used for the Surpass FD, and a 0.021-inch inner diameter Vasco +21 microcatheter (Balt Extrusion, Montmoryncy, France) was used for the Silk FD (Balt Extrusion). The FD was used to cover the aneurysm neck. The correct deployment was controlled by DSA and CT angiography.

One periprocedural complication was described (initial misdeployment of the FD that further opened spontaneously). No immediate postprocedural complications were observed. No perforation of a distal vessel or hemorrhagic or thromboembolic events were encountered.

### **Short-Term and Midterm Clinical and Imaging Follow-Up**

We reviewed the following characteristics of the DIPH: time to bleed, location, lateralization, size, associated lesions, clinical signs, and treatment. Clinical outcomes of each patient were evaluated according to mRS scores before FD treatment and at 1, 3, and 6 months. All patients underwent brain imaging during their hospital stay (CT or MR imaging).

## **RESULTS**

### **Population**

From 2007 to 2014, 449 patients were treated with FDs in the 7 participating French university centers. Among these, 11 (2.4%) presented with DIPH after FD treatment and were retrospectively included. A precedent series including 4 of these 11 patients has already been published.<sup>14</sup>

The group consisted in 4 men and 7 women ranging in age from 30 to 61 years (mean,  $46.1 \pm 9.9$  years; median, 46.0 years). Five had known histories of arterial hypertension, and 7 were smokers. All had mRS scores of zero before FD treatment. Nine aneurysms treated with FDs in these participating centers were unruptured.

**Aneurysm Data.** Nine aneurysms were situated in the ICA (3 cavernous ICAs and 6 supracavernous ICAs), and 2 were situated in the posterior cerebral circulation (1 basilar artery and 1 vertebral artery; Fig 1). Eight aneurysms were saccular, and 3 were fusiform. Four were small ( $<10$  mm), and 7 were large or giant ( $>10$  mm). The 8 saccular aneurysms ranged in size from 4.2 to 30 mm (mean,  $12.4 \pm 7.7$  mm; median, 11 mm), and the necks of the

aneurysms ranged from 2.5 to 13 mm. Three had already been treated with coils (2 patients) or coils and a stent (1 patient), and 2 were initially ruptured.

### **Flow Diverters**

We used 3 types of FDs: Pipeline (Covidien), Surpass (Stryker Neurovascular), and Silk (Balt Extrusion). The 11 aneurysms were treated with 15 FDs (9 by using a single FD, 1 with 2 FDs, and 1 with 4 FDs). Among the 15 FDs used, 11 were Pipeline, 3 were Surpass, and 1 was Silk, used in 8, 2, and 1 patient, respectively.

### **Antiplatelet Regimen**

**Preprocedure.** Six patients had a dual-antiplatelet regimen (clopidogrel and aspirin), and 5 had single clopidogrel therapies. Among the 6 patients with dual-antiplatelet therapy, aspirin was started 1–7 days before the procedure in variable doses. Clopidogrel was started 5–6 days before the procedure at 75 mg/day in 9 patients. In the remaining 2, clopidogrel was started 1 day before the procedure with a loading dose of 450 mg. The efficacy of the antiaggregation therapy was checked in 5 patients (Multiplate analyzer; Roche, Basel, Switzerland). Among these 5 patients, 4 had normal platelet function response. In the remaining patient, moderate resistance led to an increase in the clopidogrel dose.

**Perprocedure.** Periprocedural heparinization was used in all cases. Six patients had a loading dose of aspirin at the beginning of the procedure (including the 5 patients who had single antiplatelet treatment before the procedure and 1 patient who received dual-antiplatelet therapy before treatment).

**Postprocedure.** Dual-antiplatelet therapy (75 mg/day of clopidogrel and 160 mg/day of aspirin) was continued postprocedurally. Postprocedural heparinization was maintained in 6 patients during the 24 hours following the procedure. The clinical status of all patients remained unchanged after the FD procedure. Three patients underwent CT after the procedure and showed no hemorrhagic complications. Two had MRI showing no immediate ischemic complications.

### **Intraparenchymal Hemorrhage Characteristics**

DIPH occurred between 1 and 21 days (mean,  $7.7 \pm 6.6$  days; median, 7 days) after FD treatment. Hemorrhage was revealed by hemiparesis in 6 patients, aphasia in 4, headache in 2, and visual acuity loss in 1 patient. All hemorrhages were anatomically remote from the treated aneurysm (Fig 1). In 10 patients, the hematomas were located in the same region and on the same side. In 1 patient, the hematoma was located in the left superficial temporal lobe after the treatment of a sacciform basilar artery aneurysm.

The average size of the greater length of the intraparenchymal hematomas was 50.5 mm (range, 17–90 mm; median,  $50 \pm 20.8$  mm). In 5 patients, the DIPH was associated with a subdural or extradural hematoma. In all the patients with DIPH, clopidogrel was stopped and aspirin was maintained (75 mg/day) to prevent FD thrombosis. Five patients underwent surgery after receiving platelet transfusion.

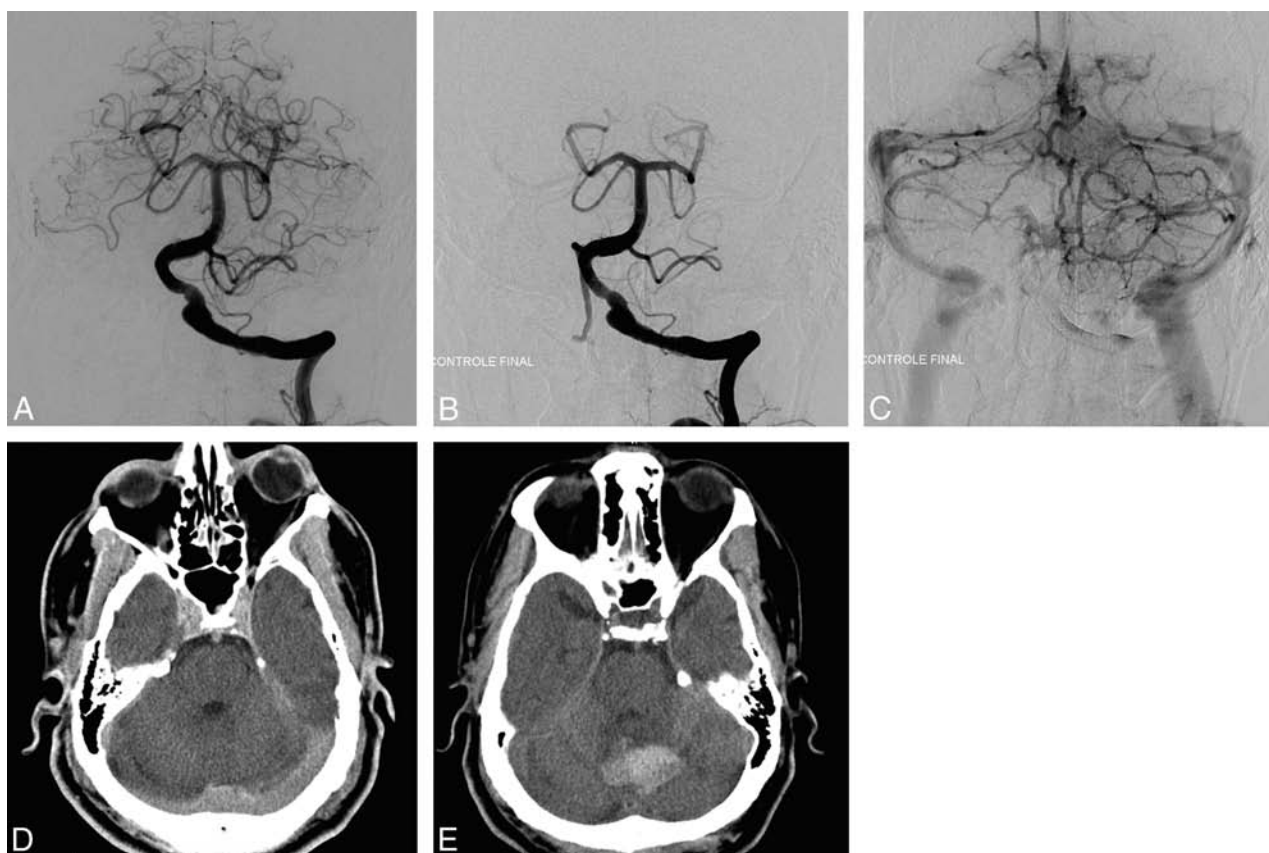


**FIG 1.** A, Pretreatment angiography shows a left vertebral fusiform aneurysm. B and C, Posttreatment angiography shows the placement and the permeability of the FD. D, Posttreatment CT shows no postprocedural complications, mainly no intracranial bleeding. E, CT performed 7 days later for headache and aphasia reveals a vermian hematoma.

### Clinical Course

Nine patients had good clinical outcomes at 6 months (mRS  $\leq 2$ ). A severe disability remained in 1 patient (mRS 5) who had a right temporal voluminous hematoma treated by surgery. One patient died (mRS 6). Five were treated surgically by craniectomy and hematoma evacuation. Among them, 4 had good clinical outcomes at 6 months. The remaining patient had a severe disability (mRS 5). Among the 6 patients with conservative treatments, 5 had good clinical outcomes. The remaining patient died (mRS 6). In the 10 surviving patients, vascular imaging control performed at least 6 months after the procedure showed the FD to be patent.

### DISCUSSION

To date, the occurrence of DIPH after FD treatment is a serious adverse event that appears unpredictable. In the literature, DIPH seems to be more frequent than delayed aneurysm rupture after the use of an FD.<sup>13,16</sup> In our study, the frequency of DIPH was 2.4%. Our findings are concordant with those in the literature, which reported a rate of DIPH between 1.1% and 8.5%.<sup>11,13,14,16-18</sup> In a recently published study including 793 patients with 906 aneurysms treated with the Pipeline Embolization Device, the rate of intracranial hemorrhage, not including aneurysm rupture, was 2.4%.<sup>19</sup>

In our study, DIPHs were revealed by headaches or focal neurologic deficit (hemiparesis, aphasia, or a decrease of visual acuity). The occurrence of DIPH seems to be independent of the preprocedural antiplatelet regimen or the type or number of FDs

used for aneurysm treatment. The decision about whether and when to operate in cases of DIPH remains controversial. The surgical treatment of DIPH depends on the size and the location of the hematoma, the degree of mass effect, and the clinical presentation. Options available for neurosurgical treatment include hematoma evacuation and/or craniectomy, depending on the imaging features and on the neurosurgeon's habits. In our series, 5 patients were treated surgically, and all had craniectomies. In patients with severe clinical deterioration, elevated intracranial pressure, and/or mass effect seen on CT scans, hematoma evacuation is usually performed. The major advantages of craniectomy are adequate exposure for removal of the clot and prevention of complications such as hydrocephalus and mass effect of the blood clot. The major disadvantage is that it may lead to further brain damage.<sup>20</sup> However, elevated intracranial pressure and poor cerebral perfusion pressure are associated with poor outcome, which, in these cases, supports a possible benefit from surgical intervention. Despite the International Surgical Trial in Intracerebral Hemorrhage results, craniectomy in intracerebral hemorrhage remains a matter of debate.<sup>21</sup> Nevertheless, a recent small-sample-size study showed that decompressive craniectomy was possible in patients with intracerebral hematoma and it may reduce mortality.<sup>22</sup> Prospective studies are needed to clarify the benefit of surgery in the treatment of intracerebral hematoma.

Because all patients treated with FDs have antiplatelet regimens, hemorrhagic complications resulting from surgical treat-



ment may occur. Then, the neurosurgical treatment decision has to be made carefully. Before surgical treatment of DIPH, platelet transfusion and stopping clopidogrel appear logical, even if no consensus about the management of this complication is available. In our study, all of the patients who underwent an operation had platelet transfusion and stopped clopidogrel. Aspirin was maintained to prevent FD thrombosis.

### ***Etiology and Pathogenesis***

The cause of DIPH remains unclear and a matter of debate, but some hypotheses have been advocated to explain the occurrence of this complication. All hemorrhages found in this study were remote from the treated aneurysm, and most were located in the same region and on the same side. The location of these hemorrhages may be explained by the association of locoregional mechanisms, including flow modification, hemorrhagic transformation of ischemic lesions, or venous lesions. However, given that a single superficial temporal DIPH occurred after treatment of a posterior circulation aneurysm, the occurrence of DIPH may not be explained by only local or regional hypotheses. General mechanisms have to be taken into account, such as the antiplatelet regimen, to explain such hemorrhages. Therefore, DIPH is probably a consequence of the association of locoregional and general mechanisms.

### ***Inflammatory Reactions***

In a recent study, Hu et al<sup>15</sup> performed postmortem analysis in 3 patients who had fatal DIPHs. Microscopic analyses revealed foreign material occluding the small arteries within the hemorrhagic area. The Fourier transform infrared spectroscopies showed that this material was polyvinylpyrrolidone, a substance used in the coating on a variety of interventional devices. No clinical ictus preceding death and no large vascular cerebral infarcts on the postmortem examination were observed. Thus, based on interventional cardiology literature, which described granulomas in the perivascular soft tissues after using polyvinylpyrrolidone, the potential role of the foreign body in the weakening and disruption of the arterial wall leading to vessel rupture and DIPH was suggested. However, neither granulomas nor inflammatory reactions were observed in the histologic analyses of these 3 patients.

Hu et al<sup>15</sup> suggested that polyvinylpyrrolidone was coming from the introducer sheath used in the patients reported in this series. Unfortunately, the precise reference of introducer sheaths and guiding catheters used in the 7 participating centers was, in most cases, not reported in the procedure files, making analysis of the potential responsibility of polyvinylpyrrolidone in our cases impossible.

Systematic anatomic-pathologic analysis of the DIPH in surgically treated patients or postmortem analysis might confirm this hypothesis or help find an explanation for this type of complication. Unfortunately, no histopathologic analysis was performed in our cases.

Most interesting, a recent study reported 7 patients who developed MR imaging enhancing brain lesions after endovascular cerebral aneurysm treatment. These lesions were mostly in the vascular territory of the catheterized arteries, located in the corticostriatal region where small emboli usually get lodged.

On the basis of the imaging and clinical characteristics, the authors suggested that these brain lesions might be the consequence of a foreign body reaction such as aseptic abscess and granulomas. These foreign bodies might be linked to dislodgment of the hydrophilic coating of the catheters used in endovascular treatment.<sup>23</sup> However, no DIPH was observed in this series.

### ***Hemorrhagic Conversion of Ischemic Infarcts***

Occurrence of DIPH can be a consequence of hemorrhagic transformation of an ischemic lesion. Stroke can be the result of either thromboembolic events during the procedure or microemboli caused by foreign bodies.<sup>14,15,24</sup> This mechanism may be a possible explanation for DIPH because 11 of 12 hemorrhages were ipsilateral to the treated aneurysm. However, no clinical symptom of an eventual cerebral stroke was described in our patients before hemorrhage occurred. Moreover, no ischemic lesion was observed on the postoperative MR imaging performed before bleeding in 2 patients in our series.

### ***Post-Flow Diversion Hyperperfusion Phenomenon***

Flow diverters permit the treatment of complex or giant intracranial aneurysms by using the concept of blood flow diversion, allowing the conservation of the parent artery and collateral vessels. Blood flow is modified not only in the aneurysm but also in the parent artery and side branches.<sup>10</sup>

Using FDs for the treatment of aneurysms changes the blood pressure waveform with a larger pulse pressure, which increases the pressure transmitted to the aneurysm and the distal cerebral arteries, leading to hemorrhagic complications.<sup>11</sup>

In their recent study, Gascou et al<sup>25</sup> hypothesized that DIPH might be a result of hyperperfusion syndrome. This syndrome is related to a sudden increase in regional cerebral blood flow secondary to loss of cerebrovascular autoregulation. It has already been described after surgical treatment (clipping) and endovascular stent placement of intracranial aneurysms.<sup>26,27</sup>

Murakami et al<sup>28</sup> suggested that giant aneurysms are responsible for the blood flow reduction in the parent artery. After FD treatment, the blood flow suddenly increases in the parent artery, increasing the pressure transmitted to the distal artery, exceeding cerebral autoregulation abilities and leading to cerebral hyperperfusion. This hyperperfusion could be a cause of intraparenchymal distal bleeding and then DIPH. However, in our series, DIPH occurred in 4 of 11 patients who had aneurysms with diameters of <10 mm, making this hypothesis less relevant.

### ***Antiplatelet Regimen, FD, and Stent***

Antiplatelet treatment is known to increase the risk of hemorrhagic events and to increase the size of intraparenchymal hematomas.<sup>29</sup> Lately, antiplatelet treatment with hypertension has been associated with the occurrence of intracranial hemorrhages.<sup>29</sup> Even if hemorrhagic complications occur after stent placement, their incidence is low, about 2.2%; no intraparenchymal hemorrhage has been described remote from an aneurysm treated with stents. Therefore, the FD probably has a specific mechanism that may lead to intraparenchymal hemorrhage and that could be amplified by the antiplatelet regimen. Clopidogrel hyper-response or resistance is associated with hemorrhagic and

thromboembolic complications, respectively, in patients treated with stents.<sup>30,31</sup> The evaluation of the antiplatelet response may improve the clinical outcomes of patients treated with stents and FDs. Unfortunately, no consensus exists about the type of test or about how to use the results of these tests. Even if these tests were performed systematically before FD treatment, no consensual strategy of management is available on how to modify the preoperative antiplatelet regimen.

### Venous Lesion

In their study, Hu et al<sup>15</sup> also performed anatomic-pathologic analysis of the hematomas that showed attenuation of the tunica media of postcapillary venules with extravasated erythrocytes, suggesting a rise in the venule pressure and a potential venous mechanism in the occurrence of DIPH.

Cerebral venous thrombosis is a cause of parenchymal brain hemorrhage in both children and adults.<sup>32</sup> Cerebral venous thrombosis is known to often be associated with an increase of the capillary pressure, which leads to cerebral edema, increased blood-brain barrier permeability, and hemorrhage.<sup>33</sup> By modifying the postcapillary pressure, FD placement may also induce a higher venous pressure and then intraparenchymal hematoma. An FD-induced venous lesion (thrombosis or pressure modification) might be a potential explanation of hemorrhagic lesions in DIPH. Nevertheless such hemodynamic modifications were not clearly demonstrated, and FD placement has not been shown to modify venous pressure. This potential mechanism is probably the most difficult to demonstrate; thus, it is less relevant.

### Limitations of the Study

First, our study included a small number of patients. However, the frequency of DIPH is low, and this study included a higher number of patients with DIPH. Second, because of its retrospective nature, our data remain subject to the biases of retrospective review. Third, because of the different heparinization procedures linked to a multicenter retrospective study, we did not discuss the impact of heparin therapy on the occurrence of DIPH. Fourth, this study analyzed the small subgroup of patients treated with FDs and presenting with DIPH. It is indeed not representative of the whole population in terms of periprocedural complications. Fifth, because our goal was to describe and analyze patients with DIPH, we have not analyzed the patients who are not known to have DIPH. Therefore patients lost to follow-up and potentially having a DIPH were not included, so the rate of DIPH is potentially underestimated.

Evaluation of the antiplatelet response was not performed in all patients included in the study because at the time of their treatment, all the participating centers did not include such evaluations in their routine management of FD treatment. Since 2014, evaluation of the antiplatelet response has been performed in most the centers.

### CONCLUSIONS

Flow-diverting devices offer an alternative treatment for large and complex aneurysms. Nevertheless, DIPH seems to be an unexpected potential complication. The pathogenesis of this complication remains unclear, even though new hypotheses have

emerged in the past few years. The multidisciplinary management of DIPH provides a relatively low morbidity-mortality rate compared with the initial clinical presentation.

Disclosures: Nader Sourour—UNRELATED: Consultancy: Covidien, Stryker. Laurent Spelle—UNRELATED: Consultancy: Sequent, Stryker, Medtronic; Payment for Lectures (including service on Speakers Bureaus): Sequent, Stryker, Medtronic; Travel/Accommodations/Meeting Expenses Unrelated to Activities Listed: Sequent, Stryker, Medtronic. Laurent Pierot—UNRELATED: Consultancy: Codman, Covidien/ev3, MicroVention, Neuravi, Sequent Medical.

### REFERENCES

1. Molyneux A, Kerr R, Stratton I, et al; International Subarachnoid Aneurysm Trial (ISAT) Collaborative Group. **International Subarachnoid Aneurysm Trial (ISAT) of neurosurgical clipping versus endovascular coiling in 2143 patients with ruptured intracranial aneurysms: a randomized trial.** *J Stroke Cerebrovasc* 2002;11:304–14 CrossRef Medline
2. Pierot L, Spelle L, Vitry F, et al; ATENA investigators. **Immediate anatomic results after the endovascular treatment of unruptured intracranial aneurysms: analysis of the ATENA series.** *AJNR Am J Neuroradiol* 2010;31:140–44 CrossRef Medline
3. Pierot L, Cognard C, Ricolfi F, et al; CLARITY investigators. **Mid-term anatomic results after endovascular treatment of ruptured intracranial aneurysms with Guglielmi detachable coils and Matrix coils: analysis of the CLARITY series.** *AJNR Am J Neuroradiol* 2012;33:469–73 CrossRef Medline
4. Pierot L, Wakhloo AK. **Endovascular treatment of intracranial aneurysms: current status.** *Stroke* 2013;44:2046–54 CrossRef Medline
5. Chalouhi N, Tjoumakaris S, Starke RM, et al. **Comparison of flow diversion and coiling in large unruptured intracranial saccular aneurysms.** *Stroke* 2013;44:2150–54 CrossRef Medline
6. Benaissa A, Januel AC, Herbreteau D, et al. **Endovascular treatment with flow diverters of recanalized and multitreated aneurysms initially treated by endovascular approach.** *J Neurointerv Surg* 2015;7:44–49 CrossRef Medline
7. Pierot L. **Flow diverter stents in the treatment of intracranial aneurysms: where are we?** *J Neuroradiol* 2011;38:40–46 CrossRef Medline
8. Mustafa W, Kadziolka K, Anxionnat R, et al. **Direct carotid-cavernous fistula following intracavernous carotid aneurysm treatment with a flow-diverter stent: a case report.** *Interv Neuroradiol* 2010;16:447–50 Medline
9. Turowski B, Macht S, Kulcsár Z, et al. **Early fatal hemorrhage after endovascular cerebral aneurysm treatment with a flow diverter (SILK-Stent): do we need to rethink our concepts?** *Neuroradiology* 2011;53:37–41 CrossRef Medline
10. Cebral JR, Mut F, Raschi M, et al. **Aneurysm rupture following treatment with flow-diverting stents: computational hemodynamics analysis of treatment.** *AJNR Am J Neuroradiol* 2011;32:27–33 CrossRef Medline
11. Cruz JP, Chow M, O’Kelly C, et al. **Delayed ipsilateral parenchymal hemorrhage following flow diversion for the treatment of anterior circulation aneurysms.** *AJNR Am J Neuroradiol* 2012;33:603–08 CrossRef Medline
12. Kulcsár Z, Houdart E, Bonafé A, et al. **Intra-aneurysmal thrombosis as a possible cause of delayed aneurysm rupture after flow-diversion treatment.** *AJNR Am J Neuroradiol* 2011;32:20–25 CrossRef Medline
13. The ESMINT Retrospective Analysis of Delayed Aneurysm Ruptures after Flow Diversion (RADAR) study. <http://www.ejmint.org/original-article/1244000088>. Accessed October 29, 2014
14. Tomas C, Benaissa A, Herbreteau D, et al. **Delayed ipsilateral parenchymal hemorrhage following treatment of intracranial aneurysms with flow diverter.** *Neuroradiology* 2014;56:155–61 CrossRef Medline
15. Hu YC, Deshmukh VR, Albuquerque FC, et al. **Histopathological**

assessment of fatal ipsilateral intraparenchymal hemorrhages after the treatment of supraclinoid aneurysms with the Pipeline Embolization Device. *J Neurosurg* 2014;120:365–74 CrossRef Medline

16. Saatci I, Yavuz K, Ozer C, et al. Treatment of intracranial aneurysms using the Pipeline flow diverter embolization device: a single-center experience with long-term follow-up results. *AJNR Am J Neuroradiol* 2012;33:1436–46 CrossRef Medline
17. Becske T, Kallmes DF, Saatci I, et al. Pipeline for incoilable or failed aneurysms: results from a multicenter clinical trial. *Radiology* 2013;267:858–68 CrossRef Medline
18. Fischer S, Vajda Z, Aguilar Perez M, et al. Pipeline embolization device (PED) for neurovascular reconstruction: initial experience in the treatment of 101 intracranial aneurysms and dissections. *Neuroradiology* 2012;54:369–82 CrossRef Medline
19. Kallmes DF, Hanel R, Lopes D, et al. International retrospective study of the Pipeline embolization device: a multicenter aneurysm treatment study. *AJNR Am J Neuroradiol*, 2015;36:108–15 CrossRef Medline
20. Broderick JP, Adams HP Jr, Barsan W, et al. Guidelines for the management of spontaneous intracerebral hemorrhage: a statement for healthcare professionals from a special writing group of the Stroke Council, American Heart Association. *Stroke* 1999;30:905–15 CrossRef Medline
21. Mendelow AD, Gregson BA, Fernandes HM, et al; STICH investigators. Early surgery versus initial conservative treatment in patients with spontaneous supratentorial intracerebral haematomas in the International Surgical Trial in Intracerebral Haemorrhage (STICH): a randomised trial. *Lancet* 2005;365:387–97 CrossRef Medline
22. Fung C, Murek M, Z'Graggen WJ, et al. Decompressive hemicraniectomy in patients with supratentorial intracerebral hemorrhage. *Stroke* 2012;43:3207–11 CrossRef Medline
23. Cruz JP, Marotta T, O'Kelly C, et al. Enhancing brain lesions after endovascular treatment of aneurysms. *AJNR Am J Neuroradiol* 2014;35:1954–58 CrossRef Medline
24. Shannon P, Billbao JM, Marotta T, et al. Inadvertent foreign body embolization in diagnostic and therapeutic cerebral angiography. *AJNR Am J Neuroradiol* 2006;27:278–82 Medline
25. Gascou G, Lobotesis K, Brunel H, et al. Extra-aneurysmal flow modification following Pipeline embolization device implantation: focus on regional branches, perforators, and the parent vessel. *AJNR Am J Neuroradiol* 2015;36:725–31 CrossRef Medline
26. Kuroki K1, Taguchi H, Yukawa O. Hyperperfusion syndrome after clipping of an unruptured aneurysm: case report. *Neurol Med Chir (Tokyo)* 2006;46:248–50 Medline
27. Maruya J, Nishimaki K, Minakawa T. Hyperperfusion syndrome after neck clipping of a ruptured aneurysm on a dolichoectatic middle cerebral artery. *J Stroke Cerebrovasc Dis* 2011;20:260–63 CrossRef Medline
28. Murakami HI, Inaba M, Nakamura A, et al. Ipsilateral hyperperfusion after neck clipping of a giant internal carotid artery aneurysm: case report. *J Neurosurg* 2002;97:1233–36 CrossRef Medline
29. Toyoda K, Yasaka M, Iwade K, et al; Bleeding with Antithrombotic Therapy (BAT) Study Group. Dual antithrombotic therapy increases severe bleeding events in patients with stroke and cardiovascular disease: a prospective, multicenter, observational study. *Stroke* 2008;39:1740–45 CrossRef Medline
30. Fifi JT, Brockington C, Narang J, et al. Clopidogrel resistance is associated with thromboembolic complications in patients undergoing neurovascular stenting. *AJNR Am J Neuroradiol* 2013;34:716–20 CrossRef Medline
31. Comin J, Kallmes DF. Platelet-function testing in patients undergoing neurovascular procedures: caught between a rock and a hard place. *AJNR Am J Neuroradiol* 2013;34:730–34 CrossRef Medline
32. Huang AH, Robertson RL. Spontaneous superficial parenchymal and leptomeningeal hemorrhage in term neonates. *AJNR Am J Neuroradiol* 2004;25:469–75 Medline
33. Nagai M, Terao S, Yilmaz G, et al. Roles of inflammation and the activated protein C pathway in the brain edema associated with cerebral venous sinus thrombosis. *Stroke* 2010;41:147–52 CrossRef Medline

# Intravenous C-Arm Conebeam CT Angiography following Long-Term Flow-Diverter Implantation: Technologic Evaluation and Preliminary Results

 S.C.H. Yu,  K.T. Lee,  T.W.W. Lau,  G.K.C. Wong,  V.K.Y. Pang, and  K.Y. Chan

## ABSTRACT

**BACKGROUND AND PURPOSE:** A noninvasive investigation with high spatial resolution and without metal artifacts is necessary for long-term imaging follow-up after flow-diverter implantation. We aimed to evaluate the diagnostic value of conebeam CT angiography with intravenous contrast enhancement in the assessment of vascular status following implantation of the Pipeline Embolization Device and to analyze the preliminary results of vascular status following long-term Pipeline Embolization Device implantation.

**MATERIALS AND METHODS:** This was an ongoing prospective study of consecutive patients with intracranial aneurysms treated with the Pipeline Embolization Device. Patients with a modified Rankin Scale score of 4–5 were excluded. The median and interquartile range of the time interval of Pipeline Embolization Device implantation to conebeam CT angiography with intravenous contrast enhancement were 56.6 and 42.9–62.4 months, respectively. Conebeam CT angiography with intravenous contrast enhancement was performed with the patient fully conscious, by using a C-arm CT with a flat panel detector.

**RESULTS:** There were 34 patients and 34 vascular segments. In all 34 cases, contrast effect and image quality were good and not substantially different from those of intra-arterial conebeam CTA. Metal artifacts occurred in all 14 cases with coil masses; the Pipeline Embolization Device was obscured in 3 cases. In all 34 cases, there was no residual aneurysm, no vascular occlusion, 1 vascular stenosis (50%), good Pipeline Embolization Device apposition to the vessel, and no Pipeline Embolization Device–induced calcification. All 28 Pipeline Embolization Device–covered side branches were patent.

**CONCLUSIONS:** Conebeam CT angiography with intravenous contrast enhancement is potentially promising and useful for effective evaluation of the vascular status following intracranial flow diverters. The Pipeline Embolization Device for intracranial aneurysms is probably safe and promising for long-term placement, with favorable morphologic outcome and without delayed complications.

**ABBREVIATIONS:** CBCT = conebeam CT; CBCTA = conebeam CT angiography; IACBCTA = conebeam CT angiography with intra-arterial contrast enhancement; IVCBCTA = conebeam CT angiography with intravenous contrast enhancement; PED = Pipeline Embolization Device

The Pipeline Embolization Device (PED; Covidien, Irvine, California) as a flow diverter has been introduced for the treatment of intracranial aneurysms.<sup>1–6</sup> To date, knowledge on the anatomic status of the post-PED vascular segment as revealed on DSA is mainly limited to within 6–12 months.<sup>1,2,4,5,7,8</sup> Follow-up DSA with a longer duration of 18–24 months has been reported in only 2 studies.<sup>6,9</sup> Beyond 24 months, post-PED

vascular status has been studied only with MR imaging,<sup>10</sup> but CT angiography or MR angiography is not desirable for this purpose owing to metal artifacts from the PED and suboptimal spatial resolution.<sup>11,12</sup> The long-term status of the post-PED vascular segment and the covered side branches beyond 24 months remains unknown. The use of DSA to assess long-term post-PED vascular status is probably not practical because patients tend to refuse an invasive investigation when they do not see an immediate clinical need; such limitations could be an important cause of lack of long-term angiographic data. There

Received April 28, 2015; accepted after revision July 29.

From the Department of Imaging and Interventional Radiology (S.C.H.Y., K.T.L., T.W.W.L.) and Division of Neurosurgery (G.K.C.W.), Department of Surgery, The Chinese University of Hong Kong, Prince of Wales Hospital, Shatin, Hong Kong SAR; Department of Neurosurgery (V.K.Y.P.), Pamela Youde Nethersole Eastern Hospital, Hong Kong, SAR; and Department of Neurosurgery (K.Y.C.), Kwong Wah Hospital, Yaumatei, Kowloon, Hong Kong, SAR.

This research was supported by funding from the Vascular and Interventional Radiology Foundation.

Please address correspondence to Simon Chun Ho Yu, MBBS, MD, FRCR, Department of Imaging and Interventional Radiology, The Chinese University of Hong Kong, Room 2A061, Department of Imaging and Interventional Radiology, Level 2, Main Clinical Block; and Trauma Centre, Prince of Wales Hospital, 30–32 Ngan Shing St, Shatin, Hong Kong SAR; e-mail: simonyu@cuhk.edu.hk

<http://dx.doi.org/10.3174/ajnr.A4558>



is, therefore, a need for a noninvasive technique with multiplanar cross-sectional imaging capability for simultaneous visualization of the PED and the vessel lumen, to allow adequate examination of the PED-paved vascular segment.

The use of conebeam CT angiography with intravenous contrast enhancement (IVCBCTA) for patient monitoring following placement of flow diverters has been reported and found to be feasible and potentially useful.<sup>13-15</sup> We aimed to evaluate the diagnostic value of IVCBCTA in the assessment of post-PED vascular status and to analyze the preliminary results of vascular status following long-term PED implantation.

## MATERIALS AND METHODS

### Study Design

This was part of a prospective study that aimed to evaluate the long-term radiologic outcome of PED implantation. The study had been approved by the institutional review board, conducted in accordance to the Declaration of Helsinki and the International Conference on Harmonisation Good Clinical Practice. Consecutive patients with intracranial aneurysms treated with the PED between September 2008 and December 2011 were invited to participate in this study according to the chronologic order of the date of PED implantation. Patients who gave consent to the study were included. Patients with a modified Rankin Scale score of 4 or 5 at the time of this study, between October and December of 2014, were excluded because it is unethical to overburden this group of patients with an investigation that does not directly benefit them; moreover, the increased risk of motion artifacts due to the increased likelihood of restlessness and noncompliance among these patients was also a concern. The study objectives were to evaluate the diagnostic value of IVCBCTA in the assessment of post-PED vascular status and to analyze the preliminary results of vascular status following long-term PED implantation.

### Imaging Protocol

The patients were positioned supine with the head placed on a rubber head mold for stability. The patient's head and the rubber mold were bound to the floating tabletop with 3 external immobilization straps set on the forehead and mandible. The contrast arrival time from the right antecubital vein to the cervical carotid arteries was predetermined specifically for each individual patient with a test dose of 15 mL of iohexol (Omnipaque, 350 mg I/mL; GE Healthcare, Piscataway, New Jersey) delivered at 4 mL/s through an 18-ga catheter by using a power injector. DSA was performed at 1 frame/s in the frontal projection. Before conebeam CT (CBCT), 80 mL of Omnipaque, 350 mg I/mL, was injected at a rate of 4 mL/s. CBCT scanning was activated following contrast injection at a time lag equivalent to the contrast arrival time. CBCT was performed by using biplane DSA equipment (Allura FD20/20; Philips Healthcare, Best, the Netherlands) that consisted of a C-arm-mounted CT unit and a digital flat panel detector. A nontruncated CT volume was created at a detector format of 48 cm, a projection matrix of  $1024 \times 792$  pixels without pixel binning,  $2464 \times 1904$  photodiodes, scintillator thickness of 550- $\mu$ m, scanning time of 20 seconds, 622 projections, an ac-

quisition range of  $240^\circ$ , and  $0.38^\circ$  angular increment. The detector entrance-dose setting was 149.0 nGy/projection. The respective raw data were transferred to the XperCT (Philips Healthcare) workstation for reconstruction. At the default zoom factor of 140% and default resolution of  $384^3$ , voxels of  $467 \mu\text{m}^3$  were created at a pixel pitch of 254  $\mu\text{m}$ . A second reconstruction on a specific area of interest was performed at 33% zoom and  $384^3$  resolution to create voxels of  $65 \mu\text{m}^3$ . Reconstruction took approximately 30 seconds. The isotropic volume data of the PED-paved vascular segment were displayed at a thickness of 0.2–0.27 mm, examined at multiplanar cross-sectional projections, and included the longitudinal and axial sections of the vascular segment, with manipulation of the parameters of metal or soft-tissue algorithms. 3D imaging was used to define the location of the PED in relation to bone structures, the location of embolization coils in relation to the PED, and the orientation of beam-hardening artifacts in relation to the PED.

### Control Conebeam CT Angiography with Intra-Arterial Contrast

The image quality of IVCBCTA was evaluated by comparing IVCBCTA with conebeam CTA with intra-arterial contrast enhancement (IACBCTA), which was performed on another date in 10 randomly selected patients as a control. The IACBCTA was performed with the internal carotid artery or the proximal vertebral artery catheterized for contrast delivery and the patient under general anesthesia. Omnipaque, 30 mg I/L 40 mL, was delivered with a power injector at 2 mL/s for 20 seconds. The scanning time was 20 seconds. The difference in image quality of IVCBCTA compared with IACBCTA was evaluated by 2 neuroradiologists who were blinded to the nature of the images and drew conclusions by consensus. Each of the 10 pairs of conebeam CT angiography (CBCTA) images was rated as “no difference or subtle difference” or “substantial difference” regarding the quality of contrast enhancement, motion artifacts, and metal artifacts due to the PED. Interobserver agreement on the ratings was estimated with  $\kappa$  statistics.<sup>16</sup>

### Study Subjects

There were 34 patients, including 12 men and 22 women. The average age was  $61.9 \pm 10.3$  years. The mean, median, and interquartile range of PED insertion to IVCBCTA time interval was  $54.2 \pm 11.3$ , 56.6, and 42.9–62.4 months, respectively. Thirty-four vascular segments were involved, 32 of them located at the internal carotid artery C2–3, C3–4, C4–5, C6, or C4–6. The other 2 were located at segments 3–4 of the vertebral artery. Seven vascular segments were covered with 2 PEDs, and 27 segments were covered with 1 PED. In 28 of these 34 cases, 1 or 2 side branches were covered by the PED; in total, 32 side branches were covered. In 11 of these 34 vascular segments that had been treated with the PED for cerebral aneurysms, coil embolization had been performed for the same cerebral aneurysm. The average aneurysm size was  $7 \pm 5.3$  mm. IVCBCTA was successfully completed in all 34 patients without adverse effects.

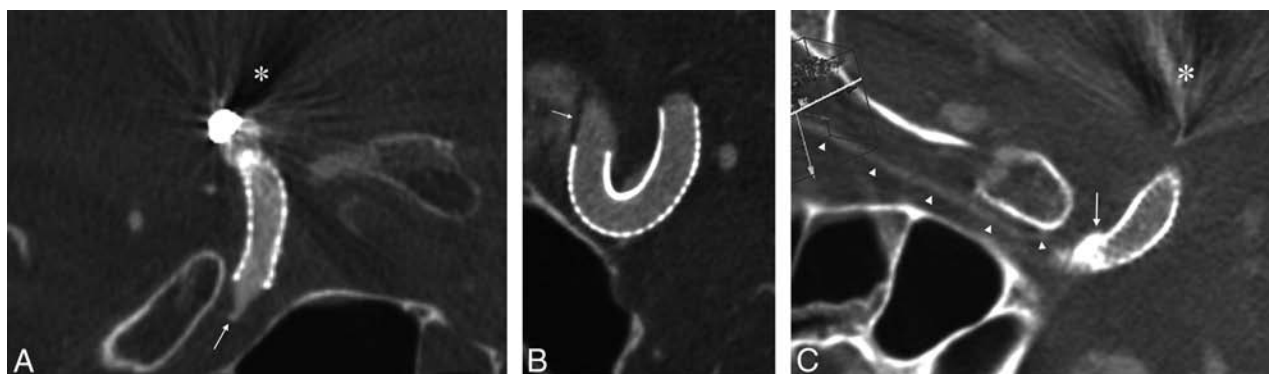


**FIG 1.** CBCTA with intra-arterial contrast shows the absence of motion artifacts and good contrast opacification of the vascular structures. The same image quality is also observed with IVCBCTA. *A*, Metal artifacts (asterisk) and the origin of ophthalmic artery (white arrow) are depicted on intra-arterial CBCTA. *B*, Features of contrast enhancement within the internal carotid artery and the hypoattenuated wall of the internal carotid artery (white arrow) within the enhanced cavernous sinus are indistinguishable from those depicted on intravenous CBCTA. *C*, In a 59-year-old man who underwent implantation of 1 PED 68 months ago, IVCBCTA shows the presence of metal artifacts (white asterisk) not affecting the PED-paved vascular segment to be assessed. Focal calcification can be depicted near the lower end of the PED (white arrow). The ophthalmic artery covered by the PED is well-preserved and well-depicted (white arrowheads).

### Study Parameters

The study end points for the diagnostic value of IVCBCTA included the quality of intravascular contrast that was rated as “good” or “suboptimal,” the presence of motion artifacts, and the presence of metal artifacts due to the PED. The study end points for post-PED vascular status included the presence of residual aneurysms, the presence of vascular occlusion or stenosis, good PED apposition to vessel wall without any gapping, the presence of intimal calcification of the PED-paved segment, and the patency of the PED-covered vascular branch. Imaging findings were reviewed by 2 neuroradiologists who drew conclusions by consensus. Interobserver agreement on the evaluation of the diagnostic value of CBCTA and post-PED vascular status was estimated with the  $\kappa$  statistics.<sup>16</sup>

### Statistical Analysis

Descriptive statistics were performed on the variables of patient demographics, the time interval of PED implantation to IVCBCTA, and all the study parameters. Interobserver agreement on the rating of the image quality of IVCBCTA compared with IACBCTA, the evaluation of the diagnostic value of CBCTA, and the evaluation of the post-PED vascular status was estimated with  $\kappa$  statistics, in which a  $\kappa$  value of 0.81–0.99 signified almost perfect agreement.<sup>16</sup>

## RESULTS

### Comparison of IVCBCTA and IACBCTA

In the 10 pairs of images, there was no substantial difference between IVCBCTA and IACBCTA regarding the quality of contrast enhancement, motion artifacts, and metal artifacts due to the PED (Fig 1). There was perfect agreement between the 2 neuroradiologists on the ratings.

### Diagnostic Value of CTA

In all 34 cases, the quality of the intravascular contrast effect of IVCBCTA was good ( $\kappa = 1$ ) and there were no motion artifacts ( $\kappa = 1$ ) (Table). In all 20 cases in which there were no embolization coils in the cerebral aneurysm, metal artifacts were not present ( $\kappa = 1$ ). In all 14 cases in which embolization coils were

### Study results

Study End Points (Total No. of Cases for Assessment)	Result	$\kappa$
Diagnostic value of IVCBCTA		
Good contrast quality (34)	34 (100%)	1
Motion artifacts present (34)	0	1
Obscuration of PED-paved segment due to metal artifact		
Embolization coil present (14)	3	1
Embolization coil absent (20)	0	1
Post-PED vascular status		
Presence of residual aneurysm (31)	0	1
Presence of vascular occlusion (31)	0	1
Presence of vascular stenosis (31)	1 (3.2%)	1
Good PED apposition to vessel wall (31)	31 (100%)	1
Intimal calcification of the PED-paved segment (31)	0	1
Patency vascular branch (28)	28 (100%)	1

present, metal artifacts were present ( $\kappa = 1$ ). The metal artifacts were due to the coil mass, extended from the coil mass, and were orientated in the plane parallel to the direction of x-ray beams (Fig 2). In 3 of these 14 cases, all or part of the PED-paved vascular segment was oriented within the plane of metal artifacts and was obscured by the metal artifacts so that the status of these vascular segments could not be assessed. In the other 11 cases with metal artifacts due to the coil mass, the PED-paved vascular segment could still be well-depicted on CBCT ( $\kappa = 1$ ) (Fig 2).

### Post-PED Vascular Status

Apart from the 3 vascular segments that were obscured by metal artifacts, all of the other 31 vascular segments could be assessed with IVCBCTA for vascular status (Table). There was no evidence of residual aneurysms in all 31 cases ( $\kappa = 1$ ) (Fig 3). Vascular occlusion was absent in all cases ( $\kappa = 1$ ). Vascular stenosis of any degree occurred in only 1 case in a 79-year-old man 40 months after PED implantation ( $\kappa = 1$ ). The stenosis was 46% (residual lumen, 1.4 mm; normal segment, 2.6 mm) and was located at the distal end of the PED at C6 of the internal carotid artery (Fig 4). The PED was well-apposed to the vessel wall and conformed to

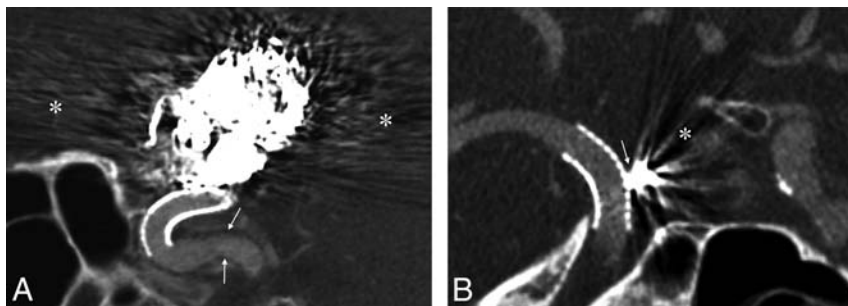


**FIG 2.** How the PED-paved vascular segment can still be depicted in the presence of coil-induced metal artifacts is illustrated in the following 2 cases. *A*, In a 67-year-old woman who had a giant aneurysm at C6 and received coil embolization 4 times with 23 coils (total length, 275 cm), including 1 stent-assisted coil embolization, the aneurysm recurred and was treated with 2 PEDs implanted at C4–6. IVCBCTA was performed 55 months after PED implantation. Although the large coil mass in close proximity induced intense metal artifacts, the PED-paved vascular segment is not affected because it lies outside the plane of metal artifacts (white asterisks) parallel to the direction of the conebeam x-ray. The PED is seen well-apposed to the vessel wall and conforming to the vascular curvature. The hypoattenuated wall of the internal carotid artery (white arrow) allows the vessel to be differentiated from the contrast-enhanced cavernous sinus. *B*, In a 57-year-old man who underwent coil embolization (total length, 20 cm) for a cerebral aneurysm and subsequently underwent PED implantation at C6 for aneurysm recurrence, IVCBCTA was performed 72 months afterward, which showed the PED-paved vascular segment unaffected by metal artifacts (white asterisk), despite the presence of the coil mass (white arrow) in close proximity. The PED is seen well-apposed to the vessel wall and conforming to the vascular curvature.

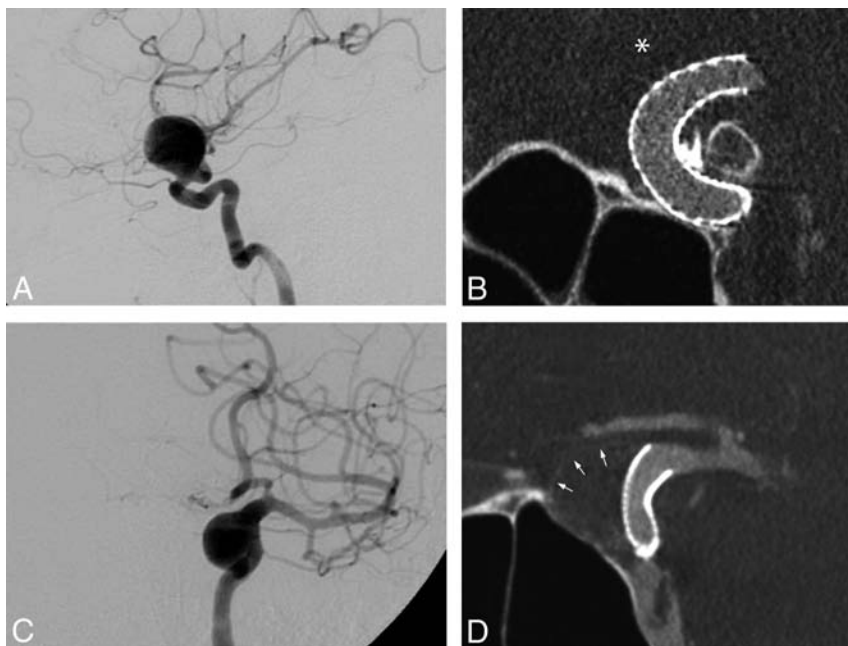


**FIG 3.** In a 68-year-old woman with a 21-mm saccular aneurysm located at the ophthalmic segment (C6) of the internal carotid artery as shown on DSA (*A*), follow-up IVCBCTA 56 months after PED implantation shows no evidence of residual cavity or wall of the aneurysm (white asterisk, *B*). In a 69-year-old woman with a 13-mm saccular aneurysm located at the communicating segment (C7) of the internal carotid artery as shown on DSA (*C*), follow-up IVCBCTA 52 months after PED shows no evidence of a residual cavity of the aneurysm but evidence of a residual wall of the aneurysm (white arrows, *D*).

the vascular curvature in all cases ( $\kappa = 1$ ) (Fig 5). Focal calcification of 2–4.4 mm in length occurred in 5 cases, all located at the vessel wall outside the PED ( $\kappa = 1$ ) (Figs 2C and 5A, -B). Calcifications occurred bilaterally at corresponding sites in all 5 cases. All were present on the plain CT before PED implantation. These features signified atherosclerotic calcification rather than PED-induced calcification. Four of 32 PED-covered side branches were

obscured by metal artifacts, and their patency could not be assessed; all of the other 28 PED-covered side branches were patent ( $\kappa = 1$ ) (Figs 2C and 5B–D).

## DISCUSSION

Compared with multidetector row CT, CBCT can provide superior spatial resolution, which is distinctly advantageous for imaging intracranial vessels, especially those with calcified atherosclerotic plaques, cerebral aneurysms, and endovascular stents.<sup>17,18</sup> CBCT has a similar contrast resolution for high-contrast structures but a slightly inferior contrast resolution for low-contrast structures compared with multidetector row CT, though the difference is negligible for most clinical applications.<sup>17,19</sup> The radiation dose of CBCT for the head is generally lower than that of multidetector row CT.<sup>20</sup> For example, in sinus imaging, the effective radiation doses of CBCT and multidetector row CT were 0.17 and 0.87 mSv, respectively.<sup>18</sup> However, the image noise in CBCT images was 54.8%–70.6% higher than that in multidetector row CT images.<sup>19</sup> CT number uniformity and accuracy were also worse with the CBCT scanner.<sup>21</sup>

Noncontrast CBCT has been used for intraoperative monitoring of neuroendovascular interventional procedures<sup>22,23</sup>; it was found useful for visualization and characterization of intracranial stents that are notoriously low-profile and radiopaque.<sup>24</sup> In-stent restenosis, calcified plaque, and stent-vessel interface that are not visualized by radiography or DSA can be depicted with CBCT.<sup>24</sup>

Intra-arterial CBCTA has been used to image intracranial stents and was found to be useful in simultaneous imaging of the stent and the parent vessel.<sup>25</sup> In the assessment of the degree of in-stent restenosis following a nitinol stent, intra-arterial CBCTA was found to correlate well with histology in an *in vivo* swine experiment.

Intracranial CBCTA also correlated well with DSA in assessing in-stent restenosis following intracranial stents or PEDs in clinical studies.<sup>26</sup> The accuracy of intra-arterial CBCTA in assessing the status of PED apposition to the vessel wall has been validated with catheter-based optical coherence tomography endoscopy in *in vivo* canine models.<sup>27</sup> The use of IVCBCTA as a noninvasive imaging alternative for the assessment of the



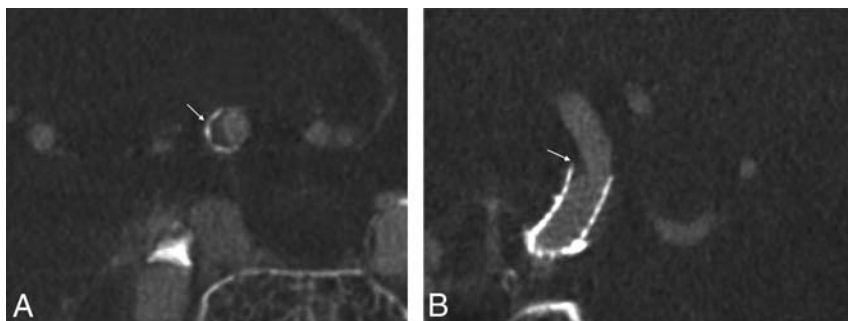


**FIG 4.** The only case of vascular stenosis occurred in a 79-year-old man who underwent implantation of 1 PED at 40 months before IVCBCTA. The stenosis (*white arrow*) can be well-depicted between the PED and the contrast-enhanced arterial lumen when the vascular segment C6 is examined in cross-sections perpendicular to the long axis (A) or in a longitudinal section (B).

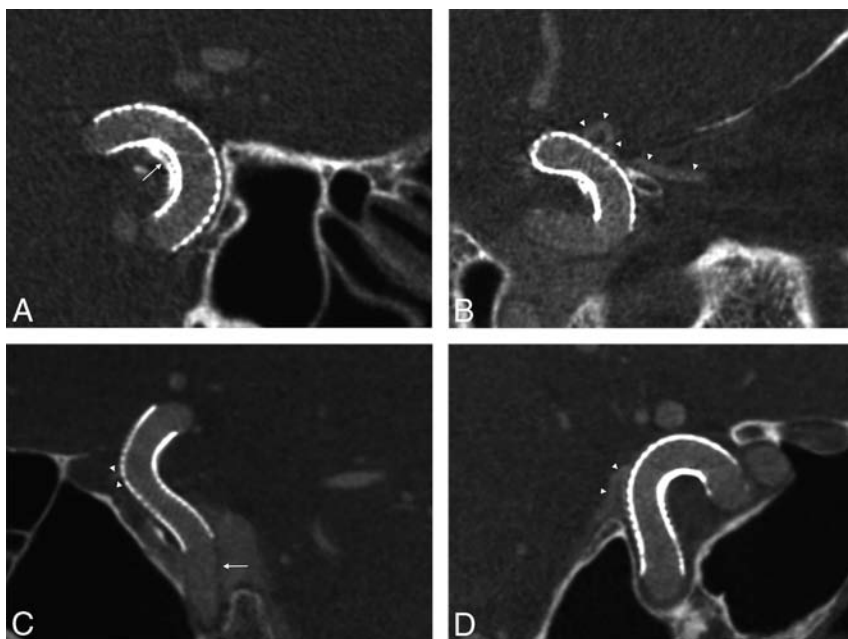


**FIG 5.** Good PED apposition to the vessel wall, good PED conformity to the vascular curvature, and preservation of the covered side branch can be illustrated in the following 3 patients. In a 66-year-old woman who underwent implantation of 1 PED 42 months ago, IVCBCTA (A) shows good PED apposition to the vessel wall and good conformity to the vascular curvature, with focal calcification at the wall of C5 outside the PED (*white arrow*). B, Good PED apposition to the vessel wall and good conformity to the vascular curvature, in which the ophthalmic artery covered by the PED is well-preserved and well-depicted (*white arrowheads*). C, In a 68-year-old woman who underwent implantation of 1 PED 52 months ago, IVCBCTA shows good PED apposition to the vessel wall and good conformity to the vascular curvature. The hypotenuated wall of the internal carotid artery (*white arrow*) allows the vessel to be differentiated from the contrast-enhanced cavernous sinus. D, In an 81-year-old woman who underwent implantation of 1 PED 51 months ago, IVCBCTA shows good PED apposition to the vessel wall and good conformity to the vascular curvature. The ophthalmic artery covered by the PED is well-preserved and well-depicted (*white arrowheads*).

vascular status following flow diverters is an attractive idea that has been put into practice recently.<sup>13-15</sup>

To date, the experience of intravenous CBCTA on the assessment of flow diverters is still very limited; it is restricted to 14 patients in 3 reports.<sup>13-15</sup> In 2 of these reports that originated from the same group, IVCBCTA was acquired with a 10-second program (Axion Artis dBA, Siemens AG, Healthcare Sector, Forchheim, Germany).<sup>13,14</sup> In the other report, a 20-second program (Allura FD20/20; Philips Healthcare), the same as that being used in the current study, was used.<sup>15</sup> A longer acquisition time of 20

seconds instead of 10 seconds allows a better image signal producing a better image quality, while there is an increased chance of image-quality degradation due to motion artifacts, especially in the absence of general anesthesia.

The results of the current study showed that with the use of a 20-second program (Allura FD20/20; Philips Healthcare), the contrast effect of IVCBCTA was good and not substantially different from that of IACBCTA in assessing PED-paved vascular segments. Despite a long acquisition time of up to 20 seconds, the images could be free of motion artifacts with the use of external immobilization straps, which was demonstrated consistently in all 34 patients without exception.

The problem of motion artifacts due to long acquisition times could likely be solved. We, therefore, believe that intravenous CBCTA is potentially a promising technique useful for effective evaluation of intracranial vessels following implantation of flow diverters in an outpatient setting without general anesthesia. However, metal artifacts due to beam-hardening, scattered radiation, sampling, and noise artifacts remain a problem in CBCT in the presence of embolization coils.<sup>25</sup> When the ROI is located in proximity to the coils and becomes obscured by metal artifacts, the diagnostic value of CBCT is greatly diminished, though the presence of a coil mass in close proximity to a vascular segment does not necessarily preclude the possibility of good-quality imaging of the vascular segment with IVCBCTA, provided the vascular segment is oriented outside the plane of metal artifacts when CT is performed. The possibility of good quality imaging of the vascular segment despite the presence of metal artifacts was demonstrated in 11 of 14 patients with intracranial coil masses

(Fig 2). If the location of the coil mass in relation to the PED-paved vascular segment can be identified and taken into account in the positioning of the patient's head in relation to the x-ray beam for CBCTA, the detrimental effect of metal artifacts on the CT image of the vascular segment can be reduced. Moreover, techniques to reduce metal artifacts due to the coil mass in CBCT are being developed.<sup>28,29</sup>

The post-PED vascular status following long-term PED implantation has been evaluated in 34 cases by using intravenous CBCTA as part of an ongoing study. These preliminary results



showed very promising outcomes of complete aneurysm occlusion in all cases, absence of parent artery occlusion, a low stenosis (46% stenosis) rate of 3.2% (1/31), complete PED apposition to vessel wall in all cases, absence of PED-induced calcification, and absence of occlusion of the PED-covered side branch. These findings indicated very favorable morphologic outcome and absence of delayed complications following long-term PED placement.

The small number of cases in the current report was a limitation for the assessment of post-PED vascular status; there was also a selection bias in patients with modified Rankin Scale scores of 4 or 5. We present these early findings because we believe the findings are conclusive and unlikely to differ significantly when the entire ongoing study is completed.

## CONCLUSIONS

IVCBCTA is potentially a promising technique that is useful for effective evaluation of the status of intracranial arteries following implantation of flow diverters; the PED for intracranial aneurysms is probably promising and safe for long-term placement, with very favorable morphologic outcome without delayed complications.

Disclosures: Vincent Kai Yuen Pang—UNRELATED: Expert Testimony: preparing an expert report about a case (potential medicolegal case); Travel/Accommodations/Meeting Expenses Unrelated to Activities Listed: Pamela Youde Netherlands Eastern Hospital Doctors Association (source: MicroVention), Comments: travel to Asian-Australasian Federation of Interventional and Therapeutic Neuroradiology in 2014, European Congress of Neurological Surgery in 2014.

## REFERENCES

1. Lylyk P, Miranda C, Ceratto R, et al. Curative endovascular reconstruction of cerebral aneurysms with the Pipeline embolization device: the Buenos Aires experience. *Neurosurgery* 2009;64:632–42; discussion 642–3; quiz N6 CrossRef Medline
2. Szikora I, Berentei Z, Kulcsar Z, et al. Treatment of intracranial aneurysms by functional reconstruction of the parent artery: the Budapest experience with the Pipeline embolization device. *AJNR Am J Neuroradiol* 2010;31:1139–47 CrossRef Medline
3. Nelson PK, Lylyk P, Szikora I, et al. The Pipeline embolization device for the intracranial treatment of aneurysms trial. *Am J Neuroradiol* 2011;32:34–40 CrossRef Medline
4. Fischer S, Vajda Z, Aguilar Perez M, et al. Pipeline embolization device (PED) for neurovascular reconstruction: initial experience in the treatment of 101 intracranial aneurysms and dissections. *Neuroradiol* 2012;54:369–82 CrossRef Medline
5. McAuliffe W, Wycoco V, Rice H, et al. Immediate and midterm results following treatment of unruptured intracranial aneurysms with the Pipeline embolization device. *AJNR Am J Neuroradiol* 2012;33:164–70 CrossRef Medline
6. Yu SCH, Kwok CK, Cheng PW, et al. Intracranial aneurysms: mid-term outcome of Pipeline embolization—a prospective study in 143 patients with 178 aneurysms. *Radiology* 2012;265:893–901 CrossRef Medline
7. Zanaty M, Chalouhi N, Tjoumakaris SI, et al. Flow-diversion panacea or poison? *Front Neurol* 2014;5:21 CrossRef Medline
8. Gascou G, Lobotesis K, Brunel H, et al. Extra-aneurysmal flow modification following Pipeline embolization device implantation: focus on regional branches, perforators, and the parent vessel. *AJNR Am J Neuroradiol* 2015;36:725–31 CrossRef Medline
9. Saatci I, Yavuz K, Ozer C, et al. Treatment of intracranial aneurysms using the Pipeline flow-diverter embolization device: a single-center experience with long-term follow-up results. *AJNR Am J Neuroradiol* 2012;33:1436–46 CrossRef Medline
10. Briganti F, Napoli M, Leone G, et al. Treatment of intracranial aneurysms by flow diverter devices: long-term results from a single center. *Eur J Radiol* 2014;83:1683–90 CrossRef Medline
11. Curtin KR, Walker MT, Shaibani A. Appearance of the Neuroform stent on computed tomography angiographic images: imaging pitfall—case illustration. *J Neurosurg* 2007;107:1249 CrossRef Medline
12. Lövblad KO, Yilmaz H, Chouiter A, et al. Intracranial aneurysm stenting: follow-up with MR angiography. *J Magn Reson Imaging* 2006;24:418–22 CrossRef Medline
13. Struffert T, Saake M, Ott S, et al. Intravenous flat detector CT angiography for non-invasive visualisation of intracranial flow diverter: technical feasibility. *Eur Radiol* 2011;21:1797–801 CrossRef Medline
14. Saake M, Struffert T, Goeltz P, et al. Angiographic CT with intravenous contrast agent application for monitoring of intracranial flow diverting stents. *Neuroradiology* 2012;54:727–35 CrossRef Medline
15. Kizilkilic O, Kocer N, Metaxas GE, et al. Utility of VasoCT in the treatment of intracranial aneurysm with flow-diverter stents. *J Neurosurg* 2012;117:45–49 CrossRef Medline
16. Viera AJ, Garrett JM. Understanding interobserver agreement: the kappa statistic. *Fam Med* 2005;37:360–63 Medline
17. Gupta R, Cheung AC, Bartling SH, et al. Flat-panel volume CT: fundamental principles, technology, and applications. *Radiographics* 2008;28:2009–22 CrossRef Medline
18. Miracle AC, Mukherji SK. Conebeam CT of the head and neck, part 2: clinical applications. *AJNR Am J Neuroradiol* 2009;30:1285–92 CrossRef Medline
19. Bai M, Liu B, Mu H, et al. The comparison of radiation dose between C-arm flat-detector CT (DynaCT) and multi-slice CT (MSCT): a phantom study. *Eur J Radiol* 2012;81:3577–80 CrossRef Medline
20. Mettler FA Jr, Huda W, Yoshizumi TT, et al. Effective doses in radiology and diagnostic nuclear medicine: a catalog. *Radiology* 2008;248:254–63 CrossRef Medline
21. Yu L, Vrieze TJ, Bruesewitz MR, et al. Dose and image quality evaluation of a dedicated cone-beam CT system for high-contrast neurologic applications. *AJR Am J Roentgenol* 2010;194:W193–201 CrossRef Medline
22. Engelhorn T, Struffert T, Richter G, et al. Flat panel detector angiographic CT in the management of aneurysmal rupture during coil embolization. *AJNR Am J Neuroradiol* 2008;29:1581–84 CrossRef Medline
23. Pfaff J, Struffert T, Göltz P, et al. Angiographic CT for intraprocedural monitoring of complex neuroendovascular procedures. *AJNR Am J Neuroradiol* 2013;34:E77–80 CrossRef Medline
24. Benndorf G, Strother CM, Claus B, et al. Angiographic CT in cerebrovascular stenting. *AJNR Am J Neuroradiol* 2005;26:1813–18 Medline
25. Patel NV, Gounis MJ, Wakhloo AK, et al. Contrast-enhanced angiographic cone-beam CT of cerebrovascular stents: experimental optimization and clinical application. *AJNR Am J Neuroradiol* 2011;32:137–44 CrossRef Medline
26. Flood TF, van der Bom IM, Strittmatter L, et al. Quantitative analysis of high-resolution, contrast-enhanced, cone-beam CT for the detection of intracranial in-stent hyperplasia. *J Neurointerv Surg* 2015;7:118–25 CrossRef Medline
27. van der Marel K, Gounis M, King R, et al. P-001 high-resolution optical and angiographic CT imaging of flow-diverter stents for assessment of vessel wall apposition. *J Neurointerv Surg* 2014;6(suppl 1):A21 CrossRef
28. Psychogios MN, Scholz B, Rohkohl C, et al. Impact of a new metal artefact reduction algorithm in the noninvasive follow-up of intracranial clips, coils, and stents with flat-panel angiographic CTA: initial results. *Neuroradiology* 2013;55:813–18 CrossRef Medline
29. van der Bom IM, Hou SY, Puri AS, et al. Reduction of coil mass artifacts in high-resolution flat detector conebeam CT of cerebral stent-assisted coiling. *AJNR Am J Neuroradiol* 2013;34:2163–70 CrossRef Medline

# Posterior Inferior Cerebellar Artery Patency after Flow-Diverting Stent Treatment

M.R. Levitt, M.S. Park, F.C. Albuquerque, K. Moon, M.Y.S. Kalani, and C.G. McDougall

## ABSTRACT

**BACKGROUND AND PURPOSE:** The rate of PICA occlusion after flow-diverting stent placement for vertebral and vertebrobasilar artery aneurysms is not known. The purpose of this study is to determine the medium-term rate of PICA patency and risk factors for occlusion after such aneurysm treatment.

**MATERIALS AND METHODS:** Patients were identified who had vertebral or vertebrobasilar artery aneurysms and who were treated by placing a flow-diverting stent across the PICA ostium. Demographic and procedural factors associated with stent placement were recorded. Patency of the PICA was evaluated immediately after stent placement and on follow-up angiography.

**RESULTS:** Thirteen patients with vertebral or vertebrobasilar artery aneurysms were treated in the study period, of whom 4 presented with subarachnoid hemorrhage. The average number of devices that spanned the PICA ostium was 1.77 (range, 1–3), with no immediate PICA occlusions. There were no postoperative strokes in the treated PICA territory, although there was 1 contralateral PICA-territory stroke of unclear etiology without clinical sequelae. In 11 patients with follow-up angiography at a mean of 10.6 months (range, 0.67–27.9 months), the PICA patency rate remained 100%.

**CONCLUSIONS:** Flow-diverting stent placement across the PICA ostium in the treatment of vertebral and vertebrobasilar artery aneurysms may not result in immediate or midterm PICA occlusion.

**ABBREVIATION:** FDS = flow-diverting stent

The initial studies of safety and efficacy of flow-diverting stents (FDSs), such as the Pipeline Embolization Device (Covidien, Irvine, California), for the treatment of intracranial aneurysms primarily focused on anterior circulation aneurysms.<sup>1</sup> The application of an FDS in posterior circulation aneurysms remains controversial due to an increased risk of thrombotic and hemorrhagic complications.<sup>2–4</sup> The location of some vertebral and vertebrobasilar aneurysms in relation to the PICA often necessitates stent placement across the arterial ostium, theoretically risking PICA occlusion with resultant brain stem infarction. The immediate and midterm rate of branch occlusion of the PICA after FDS placement has not been described.

## MATERIALS AND METHODS

This study was approved by the institutional review board of St. Joseph's Hospital and Medical Center. Review of our prospective endovascular data base was performed, and all the patients with vertebral and vertebrobasilar artery aneurysms who were treated between May 2011 and May 2015 with an FDS in which one or more devices spanned the ostium of the PICA were identified. Patient demographics, aneurysm rupture status, the number of stent devices deployed, the presence of adjunctive aneurysm coiling, antiplatelet medication reactivity testing, and the postoperative stroke rate were recorded. Initial postprocedure and follow-up angiography images were reviewed to determine the immediate and midterm PICA patency rate after FDS placement.

All but one of the patients with unruptured aneurysms were pretreated with aspirin (325 mg/day) and clopidogrel (75 mg/day) for at least 3 days before the procedure. Patients with ruptured aneurysms were treated with a single 0.125 mg/kg intraprocedural bolus of intravenous or intra-arterial abciximab after stent placement instead of dual antiplatelet pretreatment. Platelet inhibition testing was used to determine patient response to aspirin and clopidogrel. All the patients

Received June 17, 2015; accepted after revision August 12.

From the Division of Neurological Surgery (M.R.L., F.C.A., K.M., M.Y.S.K., C.G.M.), Barrow Neurological Institute, St. Joseph's Hospital and Medical Center, Phoenix, Arizona, and Departments of Neurosurgery and Radiology (M.S.P.), University of Utah, Salt Lake City, Utah.

Please address correspondence to Felipe C. Albuquerque, MD, c/o Neuroscience Publications, Barrow Neurological Institute, St. Joseph's Hospital and Medical Center, 350 W Thomas Rd, Phoenix, AZ 85013; e-mail: Neuropub@dignityhealth.org

<http://dx.doi.org/10.3174/ajnr.A4550>

were maintained on antiplatelet therapy for 6 months after the index procedure, after which only aspirin (81 mg/day) was continued.

The technique of FDS deployment has been described previously.<sup>5</sup> All endovascular procedures were performed with the patient under general anesthesia, with neurophysiologic monitoring, and via transfemoral transarterial access. Intravenous heparin was administered to maintain an activated clotting time of at least 250 seconds. Multiple devices were placed at the discretion of the surgeon for optimal aneurysm coverage. In cases in which aneurysm coils were placed, a separate microcatheter was jailed within the aneurysm dome before FDS placement.

## RESULTS

Thirteen patients (mean age,  $61.3 \pm 12.4$  years) met inclusion criteria. The average aneurysm size was  $9.3 \pm 4.9$  mm in maximal dimension, and 4 of 13 (30.8%) were ruptured at presentation. There were no instances of AICA-PICA complex. One of the 9 patients with an unruptured aneurysm refused clopidogrel pretreatment and only took aspirin 325 mg/day. Platelet inhibition testing results showed that no patients had aspirin resistance and that 3 patients had clopidogrel resistance. Two of these 3 patients were switched to prasugrel (10 mg/day), and 1 patient with a history of deep venous thrombosis was maintained on preoperative warfarin (5 mg/day).

In 6 patients (46%), the aneurysm involved the PICA origin (4 in whom the PICA origin arose from the neck of the aneurysm, and 2 in whom the PICA arose from the dome of the aneurysm); in the remaining 7 patients (54%), the PICA origin was either distinctly proximal or distal to the aneurysm. Between 1 and 3 FDS devices (mean, 1.77) were implanted. Two of 13 procedures (15.4%) included adjuvant aneurysm coiling; both were only partially coiled because both aneurysms incorporated the PICA origin into the aneurysm dome. There were no periprocedural neurologic complications.

A review of the angiography immediately after stent deployment demonstrated PICA patency in all 13 procedures. Two patients were lost to follow-up, and the remaining 11 patients underwent follow-up angiography (mean, 10.6 months; range, 0.67–27.9 months). There were no instances of PICA occlusion or stenosis on follow-up angiography. The rate of aneurysm obliteration at follow-up was 72.7% (8/11 patients), and there was 1 case (9.1%) of a patient with mild in-stent stenosis.

## DISCUSSION

We showed that the rate of immediate and midterm patency of the PICA was high after FDS treatment of vertebral and vertebrobasilar artery aneurysms. There were no clinical sequelae from spanning the PICA ostium with one or more devices and no specific risk factors associated with PICA occlusion.

Branch occlusion after FDS placement is an uncommon occurrence. A large series of 178 aneurysms treated with FDSs found a 1.4% (2/140) rate of branch occlusion at follow-up, in both cases posterior communicating arteries.<sup>6</sup> Similarly, Moon et al<sup>7</sup> reported an ophthalmic artery occlusion rate of 3.5% (1/29) in a series of periophthalmic artery aneurysms treated by FDS that remained clinically silent. However, other researchers reported a

higher occlusion rate. Puffer et al<sup>8</sup> studied 20 patients after FDS placement for internal carotid artery aneurysms and found that 15% of ophthalmic arteries had slow or absent flow immediately after FDS placement, with subsequent occlusion in 21% at follow-up angiography. No patients developed any clinical deficit from ophthalmologic occlusion. Another study, of 49 patients with 68 carotid aneurysms, found an overall branch occlusion rate of 4.4% (4% of ophthalmic and 7.1% of posterior communicating arteries) without clinical sequelae at follow-up angiography.<sup>9</sup> A study of 11 patients with 13 carotid aneurysms in which the posterior communicating artery ostium was covered by one or more FDSs found an occlusion rate of 27%, with an additional 18% with diminished flow.<sup>10</sup> Finally, 2 reports with a combined total of 43 anterior choroidal arteries spanned by at least 1 FDS in the treatment of carotid aneurysms documented 2 branch occlusions (4.7%) at follow-up, without clinical sequelae.<sup>11,12</sup> No study found a significant association between branch occlusion and the number of FDS devices placed across vessel ostia.

There are limited studies of posterior circulation aneurysms treated with FDSs, only one of which (Gascou et al<sup>13</sup>) specifically reported the patency of the PICA. This series of 59 patients with 66 aneurysms in various locations found a 3% overall occlusion rate and 16.2% branch vessel stenosis rate at follow-up. The FDS spanned the PICA ostium in 6 patients (9.1%); none of these PICAs were occluded on immediate or follow-up angiography, though stenosis was seen in 2 of 6 patients at the 12-month follow-up. In contrast, we did not observe any PICA stenosis in the 11 patients with follow-up angiography, though our average follow-up was only 10.6 months.

Neurologic deficit is rare after branch occlusion by FDS placement.<sup>13–15</sup> Two patients in the series from Gascou et al<sup>13</sup> had infarction after coverage of the middle cerebral artery perforators and the anterior division of the middle cerebral artery bifurcation, respectively. Three patients with basilar tip aneurysms (in which the FDS was placed from the P1 segment to the midbasilar artery) had brain stem perforator-related infarction among a series of 32 posterior circulation aneurysms treated by FDS.<sup>15</sup> Finally, a patient with a complex A1 segment aneurysm treated by FDS awoke from the procedure with perforator-related infarction.<sup>14</sup> Despite acute or subacute presentation of infarction, perforator occlusion was not observed during angiography at the time of FDS placement in any of the above complications.

The low rate of PICA occlusion after FDS placement is likely related to the small size of the FDS wire diameter (30  $\mu$ m)<sup>16</sup> compared with the PICA diameter (mean, 1.23 mm; range, 0.5–2.5 mm).<sup>17</sup> The average diameter of the ophthalmic artery is reported to be between 1.75 and 2.9 mm,<sup>18,19</sup> but it carries a substantially higher reported rate of immediate and long-term stenosis or occlusion after FDS placement. The higher radius of curvature at the origin of the ophthalmic artery would be expected to increase, rather than reduce, stent porosity<sup>16</sup> compared with the relatively straight vertebral artery segment from which the PICA originates. Animal studies indicate a minimal but increased incidence of branch occlusion with lower stent porosity,<sup>20</sup> such as what might be found after FDS implantation across the PICA ostium and with multiple overlapping stents.<sup>21</sup> However, our study and others did not find an association between the number of devices and branch

occlusion. Animal studies indicate that the perfusion demand of tissue supplied by branch vessels that are covered by the FDS maintains branch vessel patency.<sup>22</sup> We hypothesized that the increased volume of tissue supplied by the PICA alone demands a higher flow rate from this artery at its ostium compared with the relatively small amount of tissue perfused by the ophthalmic artery, and the rich collateral arterial network in the orbit may, in addition, reduce the demand on the ophthalmic artery. However, further animal studies are required to confirm this theory, and caution should be exercised in the presence of aneurysms that involve an AICA-PICA complex, the thrombosis of which could cause significant neurologic morbidity.

## CONCLUSIONS

In this small series, FDS placement across the PICA ostium in the treatment of vertebral and vertebrobasilar artery aneurysms did not result in immediate or midterm PICA occlusion.

Disclosures: Cameron McDougall—UNRELATED: Consultancy: Covidien, MicroVention Inc.

## REFERENCES

1. Becske T, Kallmes DF, Saatci I, et al. **Pipeline for uncoilable or failed aneurysms: results from a multicenter clinical trial.** *Radiology* 2013; 267:858–68 CrossRef Medline
2. Siddiqui AH, Abila AA, Kan P, et al. **Panacea or problem: flow diverters in the treatment of symptomatic large or giant fusiform vertebrobasilar aneurysms.** *J Neurosurg* 2012;116:1258–66 CrossRef Medline
3. Ertl L, Holtmannspotter M, Patzig M, et al. **Use of flow-diverting devices in fusiform vertebrobasilar giant aneurysms: a report on periprocedural course and long-term follow-up.** *AJNR Am J Neuroradiol* 2014;35:1346–52 CrossRef Medline
4. Albuquerque FC, Park MS, Abila AA, et al. **A reappraisal of the Pipeline embolization device for the treatment of posterior circulation aneurysms.** *J Neurointerv Surg* 2015;7:641–45 CrossRef Medline
5. Nelson PK, Lylyk P, Szikora I, et al. **The Pipeline embolization device for the intracranial treatment of aneurysms trial.** *AJNR Am J Neuroradiol* 2011;32:34–40 CrossRef Medline
6. Yu SC, Kwok CK, Cheng PW, et al. **Intracranial aneurysms: mid-term outcome of Pipeline embolization device—a prospective study in 143 patients with 178 aneurysms.** *Radiology* 2012;265:893–901 CrossRef Medline
7. Moon K, Albuquerque FC, Ducruet AF, et al. **Treatment of ophthalmic segment carotid aneurysms using the Pipeline embolization device: clinical and angiographic follow-up.** *Neurol Res* 2014;36: 344–50 CrossRef Medline
8. Puffer RC, Kallmes DF, Cloft HJ, et al. **Patency of the ophthalmic artery after flow diversion treatment of paraclinoid aneurysms.** *J Neurosurg* 2012;116:892–96 CrossRef Medline
9. Vedantam A, Rao VY, Shaltoni HM, et al. **Incidence and clinical implications of carotid branch occlusion following treatment of internal carotid artery aneurysms with the Pipeline embolization device.** *Neurosurgery* 2015;76:173–78; discussion 178 CrossRef Medline
10. Brinjikji W, Lanzino G, Cloft HJ, et al. **Patency of the posterior communicating artery after flow diversion treatment of internal carotid artery aneurysms.** *Clin Neurol Neurosurg* 2014;120:84–88 CrossRef Medline
11. Raz E, Shapiro M, Becske T, et al. **Anterior choroidal artery patency and clinical follow-up after coverage with the Pipeline embolization device.** *AJNR Am J Neuroradiol* 2015;36:937–42 CrossRef Medline
12. Brinjikji W, Kallmes DF, Cloft HJ, et al. **Patency of the anterior choroidal artery after flow-diversion treatment of internal carotid artery aneurysms.** *AJNR Am J Neuroradiol* 2015;36:537–41 CrossRef Medline
13. Gascou G, Lobotesis K, Brunel H, et al. **Extra-aneurysmal flow modification following Pipeline embolization device implantation: focus on regional branches, perforators, and the parent vessel.** *AJNR Am J Neuroradiol* 2015;36:725–31 CrossRef Medline
14. van Rooij WJ, Sluzewski M. **Perforator infarction after placement of a Pipeline flow-diverting stent for an unruptured A1 aneurysm.** *AJNR Am J Neuroradiol* 2010;31:E43–E44 CrossRef Medline
15. Phillips TJ, Wenderoth JD, Phatouros CC, et al. **Safety of the Pipeline embolization device in treatment of posterior circulation aneurysms.** *AJNR Am J Neuroradiol* 2012;33:1225–31 CrossRef Medline
16. Shapiro M, Raz E, Becske T, et al. **Variable porosity of the Pipeline embolization device in straight and curved vessels: a guide for optimal deployment strategy.** *AJNR Am J Neuroradiol* 2014;35:727–33 CrossRef Medline
17. Pai BS, Varma RG, Kulkarni RN, et al. **Microsurgical anatomy of the posterior circulation.** *Neurol India* 2007;55:31–41 CrossRef Medline
18. Erdogmus S, Govsa F. **Anatomic features of the intracranial and intracanalicular portions of ophthalmic artery: for the surgical procedures.** *Neurosurg Rev* 2006;29:213–18 CrossRef Medline
19. Govsa F, Erturk M, Kayalioglu G, et al. **Neuro-arterial relations in the region of the optic canal.** *Surg Radiol Anat* 1999;21:329–35 CrossRef Medline
20. Hong B, Wang K, Huang Q, et al. **Effects of metal coverage rate of flow diversion device on neointimal growth at side branch ostium and stented artery: an animal experiment in rabbit abdominal aorta.** *Neuroradiology* 2012;54:849–55 CrossRef Medline
21. Dai D, Ding YH, Kadirvel R, et al. **Patency of branches after coverage with multiple telescoping flow-diverter devices: an in vivo study in rabbits.** *AJNR Am J Neuroradiol* 2012;33:171–74 CrossRef Medline
22. Kallmes DF, Ding YH, Dai D, et al. **A new endoluminal, flow-disrupting device for treatment of saccular aneurysms.** *Stroke* 2007;38: 2346–52 Medline



# In Vitro Evaluation of Intra-Aneurysmal, Flow-Diverter-Induced Thrombus Formation: A Feasibility Study

K. Gester, I. Lüchtefeld, M. Büsen, S.J. Sonntag, T. Linde, U. Steinseifer, and  G. Cattaneo



## ABSTRACT

**BACKGROUND AND PURPOSE:** Intracranial aneurysm treatment by flow diverters aims at triggering intra-aneurysmal thrombosis. By combining in vitro blood experiments with particle imaging velocimetry measurements, we investigated the time-resolved thrombus formation triggered by flow diverters.

**MATERIALS AND METHODS:** Two test setups were built, 1 for particle imaging velocimetry and 1 for blood experiments, both generating the same pulsatile flow and including a silicone aneurysm model. Tests without flow diverters and with 2 different flow-diverter sizes (diameter: 4.5 and 4.0 mm) were performed. In the blood experiments, the intra-aneurysmal flow was monitored by using Doppler sonography. The experiments were stopped at 3 different changes of the spatial extent of the signal.

**RESULTS:** No thrombus was detected in the aneurysm model without the flow diverter. Otherwise, thrombi were observed in all aneurysm models with flow diverters. The thrombi grew from the proximal side of the aneurysm neck with fibrin threads connected to the flow diverter and extending across the aneurysm. The thrombus resulting from the 4.0-mm flow diverter grew along the aneurysm wall as a solid and organized thrombus, which correlates with the slower velocities near the wall detected by particle imaging velocimetry. The thrombus that evolved by using the 4.5-mm flow diverter showed no identifiable growing direction. The entire thrombus presumably resulted from stagnation of blood and correlates with the central vortex detected by particle imaging velocimetry.

**CONCLUSIONS:** We showed the feasibility of in vitro investigation of time-resolved thrombus formation in the presence of flow diverters.

**ABBREVIATIONS:** FD = flow-diverter; PIV = particle imaging velocimetry

Intracranial aneurysm treatment by flow diverters (FDs) aims at blood clotting in the aneurysm, triggered by the reduction or elimination of intra-aneurysmal blood flow. This therapeutic approach offers an alternative treatment for larger wide-neck aneurysms, in which coil embolization is associated with high recurrence.<sup>1,2</sup> Otherwise, a longer delay to complete intra-aneurysmal thrombosis and documented cases of postprocedural bleeding<sup>3-5</sup> suggest that the FD-driven mechanism of thrombus formation is

considerably different from that using coils. In previous studies, it has been hypothesized that aneurysm rupture occurring in patients after treatment with FDs is a consequence of uncontrolled flow-driven clot formation resulting in thrombus-associated autolysis<sup>4</sup> or mural destabilization of the aneurysm wall due to thrombus evolution.<sup>6</sup>

The influence of FDs on hemodynamic properties was investigated in several in vitro experiments by particle imaging velocimetry (PIV). Especially, the influence of the geometry of the aneurysm,<sup>7,8</sup> the stent porosity,<sup>7,9-12</sup> the number of stents, and the stent material<sup>8,13</sup> on intra-aneurysmal velocity fields was extensively studied. All investigations were performed with water-glycerol mixtures as a blood analog fluid. The use of a transparent fluid is inevitable because PIV is an optical method, but it fore-stalls the possibility of investigate clotting effects. Therefore, because the thrombus-growing process influences the flow behavior, PIV investigations only represent the flow conditions directly after the insertion of FDs.


The goal of our study was the in vitro investigation of time-

Received December 10, 2014; accepted after revision August 10, 2015.

From the Department of Cardiovascular Engineering (K.G., I.L., M.B., S.J.S., T.L., U.S.), Institute of Applied Medical Engineering, Helmholtz Institute–RWTH Aachen University, Aachen, Germany; and Acandis GmbH & Co KG (G.C.), Pforzheim, Germany.

This project was funded by the German Federal Ministry for Economic Affairs and Energy.

Please address correspondence to Kathrin Gester, PhD, Department of Cardiovascular Engineering, Institute of Applied Medical Engineering, Helmholtz Institute–RWTH Aachen University, Pauwelsstr 20, D-52074, Aachen, Germany; e-mail: kathrin.gester@rwth-aachen.de

 Indicates open access to non-subscribers at [www.ajnr.org](http://www.ajnr.org)

<http://dx.doi.org/10.3174/ajnr.A4555>

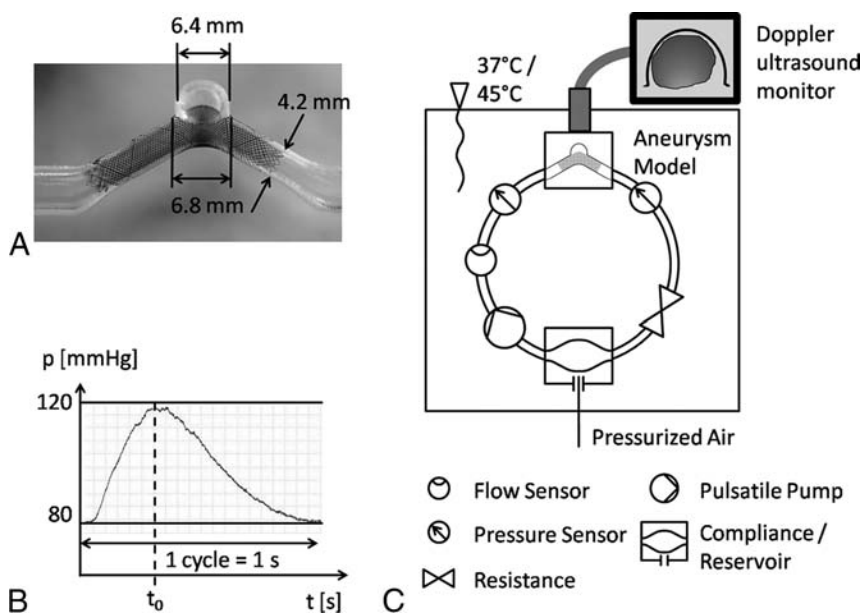


**FIG 1.** A, Silicone model with an inserted FD. B, Pressure curve upstream of the aneurysm model. C, Flow loop.

resolved formation of thrombi triggered by FDs. Although biologic mechanisms, triggered by the aneurysm wall, are not depicted in the new *in vitro* model, the location and shape of thrombus during the forming and growing process, as well as the composition of the thrombus, were investigated for 2 different FD configurations. Moreover, we correlated the results with PIV measurements.

## MATERIALS AND METHODS

### *In Vitro* Aneurysm Model and Flow-Loop Setup

A simplified geometry of a lateral aneurysm was used in this study to limit the geometric variables. The aneurysm was spheric with an inner diameter of 6.4 mm and an oval neck of  $6.8 \times 5.4$  mm. These dimensions are in agreement with those in the clinical literature.<sup>14</sup> The parent vessel had an inner diameter of 4.2 mm with an angle of  $120^\circ$  at the aneurysm neck (Fig 1A). The aneurysm models were blocks, made from silicone by a casting technique using male casts of the aneurysm model manufactured by rapid prototyping (Objet Eden 350V; Stratasys, Eden Prairie, Minnesota). We used 2 different kinds of silicone: Elastosil RT 601 (Wacker Chemie, Munich, Germany) for PIV measurements due to opacity requirements and Elastosil RT 625 (Wacker Chemie) for blood experiments due to hemocompatibility. For all models, the FD Derivo Embolization Device (Acandis GmbH & Co. KG, Pforzheim, Germany) with inner diameters of 4.5 and 4.0 mm (called FD-4.5 and FD-4.0) was used. The device is composed of 24 nitinol wires with a diameter of  $40 \mu\text{m}$  and an electropolished and annealed surface, characterized by approximately a 50-nm thin layer of oxides and nitrides/oxy-nitrides. The wires at the distal end of the FD run in loops back to the proximal end, where the wires end openly, resulting in a mesh of  $2 \times 24$  wires.

For the PIV measurements, 3 models were used (empty and loaded with FD-4.5 and FD-4.0, respectively). For blood experiments, we used 10 models: 4 empty, 2 loaded with FD-4.5, and 4 loaded with FD-4.0. The FD-4.5 was oversized and axially

stretched, which led to an increase of cell size, whereas the FD-4.0 was fitted with an outer diameter of approximately 4.2 mm within the parent vessel without radial compression. With a braiding angle of  $75^\circ$  in the completely expanded state, mean porosities within the model were 72% and 65% for FD-4.5 and FD-4.0, respectively, according to geometric calculation, whereas manual loading of the devices in the model led to heterogeneities and variability of local porosity. The models were placed in a flow loop, which consisted of a pulsatile-operated blood pump (deltastream DP3; Medos Medizintechnik, Stolberg, Germany) and a compliance/reservoir (Fig 1C). All components were connected by PVC tubing and connectors made of polycarbonate. Pump, compliance pressure, and resistance were adjusted to achieve an average volume flow rate of

$$\dot{V} = 220 \frac{\text{mL}}{\text{min}},$$

according to a flow rate between that of the internal carotid artery and the media carotid artery<sup>15-17</sup> and a pressure curve behind the pump between 80 and 120 mm Hg, as shown in Fig 1B. The average volume flow rate (T110; Transonic Systems, Ithaca, New York) was recorded directly behind the pump; and the pressure curve (SP844; Memscap, Crolles, France) upstream, downstream of the aneurysm model, and both was accordingly adjusted. The intraluminal mean Reynolds number, Womersley number, and pulsatility index as defined in Hoi et al,<sup>15</sup> were 358, 6.0, and 1.19, respectively. The whole test setup was temperature-controlled at  $45^\circ\text{C}$  for PIV measurements and  $37^\circ\text{C}$  for blood experiments.

### PIV Measurements

A PIV system (Dantec Dynamics, Skovlunde Denmark) was added to the test setup described above. The PIV system included an Nd:Ylf laser (Pegasus; NewWave, Fremont, California), a light sheet optic (80X70, Dantec Dynamics, Skovlunde, Denmark), and a CMOS camera ( $1280 \times 1024$  pixels, Redlake, X3 mol/L-M-4; IDT, Tallahassee, Florida) positioned perpendicular to the laser light sheet and a traverse for microaccurate movement of the whole system.

A mixture of glycerol and distilled water (55.8%–44.2% by weight) at  $45^\circ\text{C}$  was used as working fluid. At these parameters, the refractive index matches that of silicone ( $n_{\text{silicone}} = n_{\text{water/glycerol}} \approx 1.404$ ); this avoids distortion of the recorded images. Additionally, the viscosity of this fluid [ $\eta_{\text{water-glycerol}} = (3.5395 \pm 0.0417) \text{ mPa}\cdot\text{s}$ ] corresponds to that of high sheared blood ( $\eta_{\text{blood}} = 3.6 \text{ mPa}\cdot\text{s}$ ), allowing similar flow properties.<sup>18</sup>

Neutrally buoyant polystyrene tracer particles,  $10 \mu\text{m}$  in diameter and containing Rhodamine B (MF-RhB-polymer particles; Microparticles, Berlin, Germany), were added to the water-glycerol mixture. The particles were illuminated by a laser light sheet, and particle images were captured with the

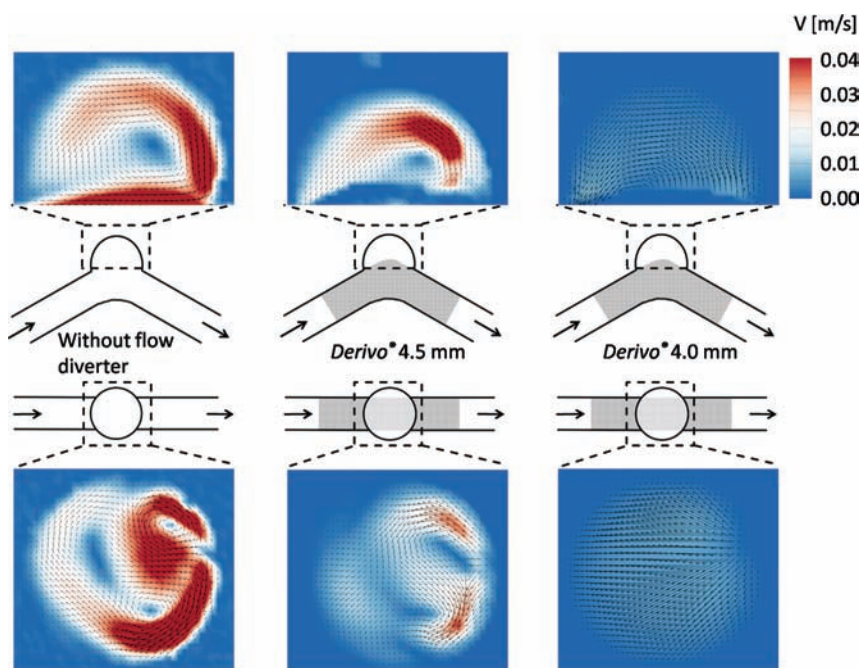


**FIG 2.** Results of the PIV measurements. The velocity fields for the systolic flow are recorded in the sagittal and transverse planes.

camera. The maximum fluorescence emission wavelength of the tracer particles was 584 nm. With a suitable filter, the laser light with a wavelength of 527 nm could be filtered to increase image quality. Ten pump cycles were recorded. Measurements without the FD were recorded in “single image mode” with a frequency of 100 Hz, and measurements with the FD in double-image mode with a time difference between the 2 images varied from 100 to 950  $\mu$ s. To generate the velocity fields, we divided the recorded images into small areas of interrogation. Using a cross-correlation algorithm, we calculated displacement vectors for each area of interrogation for subsequent images. The resulting vector fields had a resolution of  $70 \times 70 \mu$ m. They were averaged for the 10 pump cycles by using the software Matlab (MathWorks, Natick, Massachusetts). The velocity fields were recorded in the sagittal and transverse planes of the aneurysm, the last 3.2 mm below the top of the aneurysm. In this study, we concentrated on the velocity field at the systolic pressure peak, corresponding to time  $t_0$  of the pressure wave (Fig 1B).

### Blood Experiments

All parts of the test setup were cleaned for 1 hour according to a standardized in-house cleaning procedures with 40% 2-propanol at room temperature and rinsed with distilled water and saline solution.

The blood was collected from the cervical artery of slaughterhouse pigs. It was immediately anticoagulated with Clexane multidoses (Sanofi-Aventis Pharma Deutschland, Frankfurt, Germany) with concentrations of 2000 or 4000 IU/L. Because coagulation activity is very dependent on the blood used, concentration was varied during the study to allow a visualization of thrombus formation in a feasible time window of a maximum duration of 12 hours. However, the influence of the anticoagulant concentration on the thrombus formation was not an aim of this

study, and only the results of experiments with the same anticoagulant concentration were compared. Blood count was determined before and after the blood experiments by using a hematology analyzer (Celltac- $\alpha$  MEK-6450; Nihon Kohden, Tokyo, Japan). Throughout the experiments, the flow in the aneurysm was monitored with the help of a color Doppler sonography system (Vivid I; GE Healthcare, Milwaukee, Wisconsin) by recording changes in the Doppler signal in magnitude and spatial expansion. The sonographic probe was placed on top of the silicone model, allowing monitoring of the whole aneurysm region (Fig 1C).

To analyze the structure of the FD-induced thrombi at different growing phases, 3 study end points were defined on the basis of the changes in the spatial extent of the signal: 1) beginning, 2) approximately 50%, and 3) nearly complete reduction of the spatial extent of

the signal. For 2 FD-4.0s, the tests were stopped at the first end point to investigate the early anchoring of the thrombus to the FD. Additionally, FD-4.5 and FD-4.0 were both investigated at the second and third end points to compare the development of the resulting thrombi for different mesh porosities. For the empty models, in which no thrombus formation was expected, 2 end points were defined at 5 and 12 hours after starting the experiment. After we reached each end point, the time was recorded, the blood flow was interrupted, and the aneurysm model was rinsed with 100 mL of phosphate buffer solution (pH = 7.4), preserved in formaldehyde (4%) for 24 hours, and dehydrated in ascending concentrations of propanol (30%, 50%, 70%, 90%, 100%, 100%). Finally, the silicone model was opened, and pictures were taken. The thrombi arising at the third end point were taken out and embedded in paraffin; sections were cut (HM 360; Thermo Fisher Scientific, Waltham, Massachusetts) and stained with H&E for histology.

## RESULTS

### PIV Measurements

The velocity fields for the systolic flow, recorded in the sagittal and transverse planes, are shown in Fig 2. Without the FD, the fluid entered the aneurysm distally and moved along the aneurysm wall until leaving it at the proximal side on the sagittal plane. The velocities at the distal side were higher than those at the proximal side. The area of the slowest velocities was close to the center of the aneurysm, where a vortex occurred. On the transverse plane, the velocity field was irregular. The maximal flow velocity, detected on the transverse plane, was 0.14 m/s. A similar velocity field on the sagittal plane was observed in the model with FD-4.5. However, the maximum velocities were reduced to 0.04 m/s. The vortex area with the slowest velocities within the aneurysm was smaller and closer to the parent vessel. In the transverse plane, a



## Overview of the performed blood experiment

Name of Trial <sup>a</sup>	FD	Clexane Concentration (IU/L)	Platelet Count, Start of Trial (10 <sup>3</sup> /μL)	Platelet Count, End of Trial (10 <sup>3</sup> /μL)	Hematocrit Value, Start of Trial (%)	Hematocrit Value, End of Trial (%)	Duration	Qualitative Spatial Extent of the Doppler Signal at End of Trials <sup>b</sup>
O-A	None	2000	205	220	41.3	39.5	5 h 2 min	
O-B	None	4000	220	211	45.2	44.3	5 h 1 min	
O-C	None	2000	212	213	39.2	46.4	12 h 2 min	
O-D	None	4000	214	377	41.3	15.0	12 h 4 min	
4.0-A	FD-4.0	2000	235	345	42.6	20.4	4 h 9 min	
4.0-B	FD-4.0	2000	340	290	38.7	40.8	11 h 58 min	
4.0-C	FD-4.0	2000	270	225	38.7	40.1	3 h 4 min	
4.0-D	FD-4.0	4000	245	250	40.1	42.1	12 h 42 min	
4.5-C	FD-4.5	2000	270	355	44.2	38.0	11 h 10 min	
4.5-D	FD-4.5	4000	265	295	36.3	31.8	9 h 51 min	

<sup>a</sup> O-A and O-B are after 5 hours; O-C and O-D are after 12 hours; 4.0-A and 4.0-B are the first end point; 4.0-C and 4.5-C are the second end point; and 4.0-D and 4.5-D indicate no sonography signal at the end of the trial (third end point).

<sup>b</sup> The gray area in the aneurysm represents the spatial extent of the Doppler ultrasound signal.

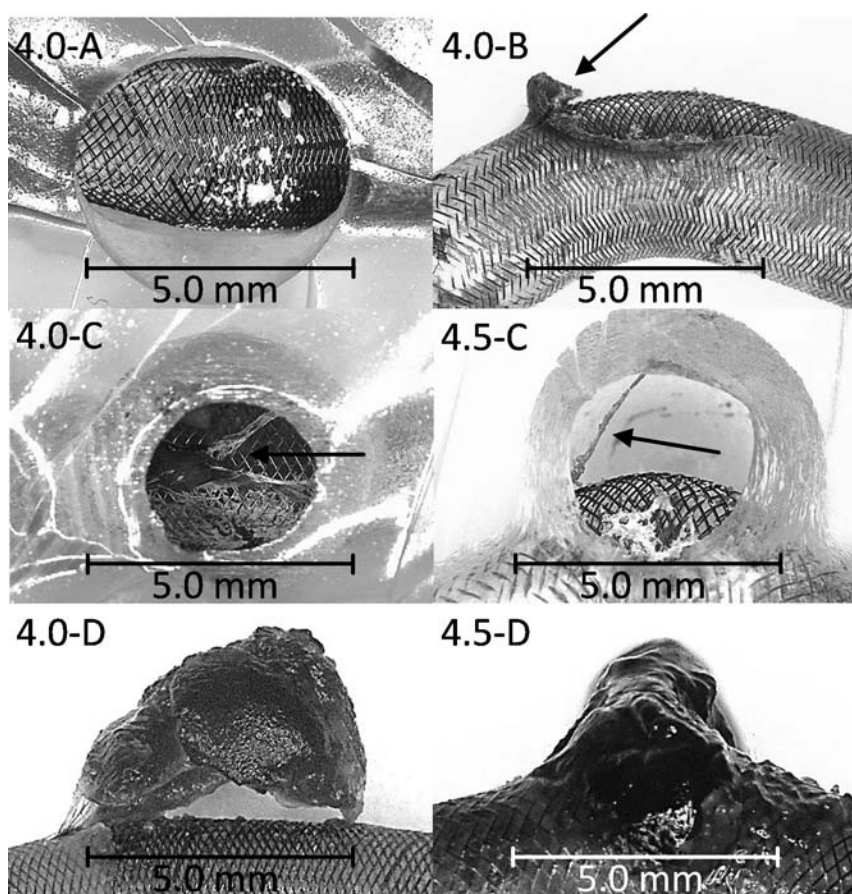


**FIG 3.** Thrombi after the blood experiments. Experiments 4.0-A and 4.0-B show no thrombus or the beginning of a thrombus; 4.0-C and 4.5-C show a fibrin network, anchored at the proximal side of the aneurysm in the FD and extended across the aneurysm up to the upper distal wall; 4.0-D shows a red cap-shaped thrombus that has fibrin strands connected to the proximal part of the FD; and 4.5-D shows an apparently erythrocyte-rich thrombus with a very soft consistency, which almost completely fills the aneurysm. Degree of magnification: 5× (left images), 40× (right images).

very irregular and symmetric velocity field occurred, with a vortex in the distal area of the aneurysm extending across the whole neck width. The FD-4.0 led to a different velocity profile, with the highest velocities appearing symmetric at both distal and proximal sides and closer to the FD compared with both previous models.

In addition, in this model, the fluid entered the aneurysm on the distal side. Furthermore, maximum flow velocities were reduced to 0.005 m/s. The velocity field in the transverse plane was much more symmetric than that without the FD and with FD-4.5, with significant reduction of the velocities.

### Blood Experiments

An overview of the performed experiments is listed in the Table.

Four models without FDs were tested with anticoagulant concentrations of 2000 IU/L (O-A, O-C) and 4000 IU/L (O-B, O-D). No signal change was detected, so the blood flow was interrupted at the end points of 5 hours (O-A, O-B) and 12 hours (O-C, O-D). No thrombi were detected after the models were rinsed.

In experiments with the first end point (4.0-A, 4.0-B), either no thrombus or the beginning of a thrombus at the proximal side was found in the neck area (Fig 3). Second end point experiments (4.0-C, 4.5-C) led to a fibrin network, which anchored to the FD at the proximal side of the aneurysm and extended across the aneurysm to the upper distal wall (Fig 3). This was observed for both FDs, whereas it was more pronounced for FD-4.0. When the sonography signal no longer existed (4.0-D, 4.5-D), a red cap-shaped thrombus could be observed for the FD-4.0. The thrombus had fibrin strands connected to the proximal part of the FD (Fig 3) but showed a gap to the rest of the FD surface, which remained patent. In comparison, the thrombus resulting from the FD-4.5 appeared as erythrocyte-rich, which almost completely filled the aneurysm.



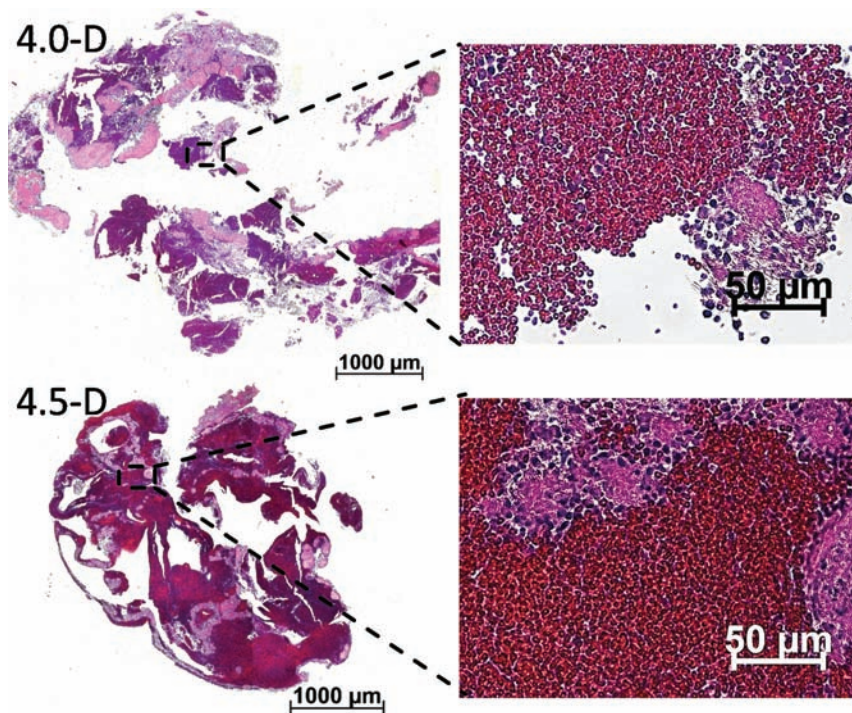


**FIG 4.** H&E-stained sections of the thrombi resulting from experiments 4.0-D and 4.5-D. Erythrocyte-rich areas are stained dark red, whereas fibrin- and platelet-rich areas are stained a light pink. Degree of magnification: 5 $\times$  (left images), 40 $\times$  (right images).

After we removed the silicone model, the thrombus collapsed because it had a very soft consistency.

The sections of both thrombi showed a similar structure (Fig 4). Fibrin- and platelet-rich areas and erythrocyte-rich areas could be identified and could be clearly distinguished from each other. The sections of the thrombus that developed in the experiment with FD-4.5 showed a larger amount of erythrocyte-rich areas in comparison with the thrombus from FD-4.0. However, even here, fibrin- and platelet-rich areas were clearly visible. In all trials with FDs, a thin layer of thrombi on the FD was observed. Mostly, the thrombi appeared as white, fibrin- and platelet-rich and accumulated partially between the stent struts of the FD; but also red, erythrocyte-rich areas could be found sporadically (4.0-B, 4.0-C).

The blood values (Table) of the individual experiments were within the measurement accuracy of the blood count system and the expected change of blood values in an *in vitro* experiment. However, in 2 experiments, the hematocrit value dropped noticeably during the experiment (O-D and 4.0-A), and in 3 experiments, the platelet count increased (O-D, 4.0-A, and 4.5-C).

## DISCUSSION

Many *in vitro* PIV studies investigated the influence of FDs on hemodynamic properties,<sup>7-13</sup> because this method is established for measuring flow behavior. However, when using a water-glycerol mixture, which is transparent and thus enables PIV measurements, one disregards the thrombus formation and its influence on the flow. Therefore, the PIV measurement only represents the flow conditions directly after the insertion of FDs. Moreover, the influence of the FDs on the thrombus formation was further investigated in animal trials.<sup>19-22</sup> However, the dynamics of intra-

aneurysmal thrombosis cannot be observed in the follow-up period, which takes several weeks, because blood flow cannot be abruptly stopped at defined phases of thrombus formation. *In vitro* blood experiments allow arbitrarily accelerating thrombus formation by appropriate anticoagulant concentrations so that we can continuously visualize the different phases of formation and abruptly stop the experiment for thrombus observation based on visualization. We combined PIV measurements and *in vitro* blood experiments monitored by Doppler sonography for the investigation of velocity fields and thrombus formation in silicone aneurysm models.

In the blood experiments, both FDs caused thrombus formation in the aneurysm model in contrast to the experiments with empty aneurysm models. We conjecture that the material triggers the thrombus formation because fibrin- and platelet-rich thrombi were present on the FD surface before any thrombus in the aneurysm was observed. Therefore, blood flow could play an important

role in the mechanism of thrombus formation because the thrombi prevalently arose at the same side of the FD and developed in a similar direction. Experiments that were stopped at the first end point showed that the thrombi formation begins at the proximal side of the aneurysm neck. Fibrin threads with entangled platelets were connected to both FDs and extended across the aneurysm. We presume a combination of flow- and surface-induced coagulation because the velocities on the proximal side were the slowest and the mesh of the FD is a good anchorage point.

After the FDs were anchored on the proximal side of the aneurysm, the further course of thrombi formation was different for both FDs with different sizes and thus porosity. The thrombus, resulting from the FD-4.0 with lower porosity, grew along the aneurysm wall as a solid and organized thrombus with fibrin and erythrocytes included. The thrombus seemed to develop against flow direction detected by PIV, which was from distal to proximal, in the region with lower and uniform velocities. At the neck of the aneurysm, where velocities were higher in PIV, a small thrombus-free gap was observed. The thrombus that evolved when using the FD-4.5 showed no identifiable growing direction. The entire thrombus presumably resulted from stagnation of blood after the formation of fibrin through the aneurysm because it was not very stable or very erythrocyte-rich. This finding is supported by the microtome sections, which showed clearly defined fibrin areas and areas of erythrocytes loosely next to each other and correlate with the central vortex detected by PIV.

The noticeable decrease of the hematocrit value and the simultaneous increase in platelet count indicates hemolysis in the circuit.

The blood count device identifies the individual cell types by their sizes; therefore, cell fragments of destroyed erythrocytes are incorrectly identified as platelets. The hemolysis is probably caused by the pump.

### Limitations

In the PIV test setup, the particles are illuminated by a laser light sheet that has a thickness of approximately 1 mm. Velocity components vertical to that plane are not detected and considered. Furthermore, in this study, only velocity components at the systolic pressure peak were considered and correlated to the results of blood experiments. Otherwise, the velocity fields during the whole pulsatile cycle showed similar profiles despite lower velocities (data are not included in this work).

With the blood experiments, it was possible to investigate the occlusion of an aneurysm after insertion of an FD. The duration of the experiment until thrombus formation was adjusted by anticoagulant concentration. The maximum experiment duration was limited to approximately 12 hours in an attempt to limit the effect of hemolysis, particularly by the use of the pump. Moreover, in the experiments without FDs, no coagulation occurred after the 12-hour test period. Clinical studies report that the aneurysm is never closed by a thrombus at end-of-procedure angiography—that is, after 1 or 2 hours,<sup>23,24</sup> while at 6-month follow-up angiography, complete occlusion was found in 68%–94% of patients.<sup>23,25–31</sup> Although it is difficult to judge when the thrombus formation begins in patients, we suppose that the process is strongly accelerated in the in vitro setup, which potentially influences clotting mechanisms.

Dosed anticoagulation by means of Clexane aimed to allow the in vitro use of blood for several hours and does not depict the clinical standard of antiplatelet therapy with aspirin and clopidogrel.

We set both test setups (PIV and blood), with and without FD, to the same flow and pressure conditions and thus neglected the effect of FDs on flow within the parent vessel. In addition, vessel elasticity was neglected by using nearly rigid silicone blocks. Using standardized aneurysm geometry, we did not consider the effect of complex aneurysm geometry on flow pathways.

Our model does not consider the influence of real vessel biology and, in particular, endothelial cells on flow. First, progressive endothelialization of the FD structure would lead to a decrease in pore size.<sup>32</sup> Second, clotting mechanisms triggered by endothelial cells are not reproduced in the silicone model. By use of FDs, flow deceleration leads to a decrease of shear stress at the aneurysm wall, which is responsible for endothelial cell–induced release of proadhesive and prothrombotic mediators.<sup>33</sup>

In this test series only a limited amount of blood experiments were performed to demonstrate the feasibility of the test setup. To obtain a statistically significant comparison between different FDs, a larger number of experiments are required.

### CONCLUSIONS

In this study, we showed the feasibility of intra-aneurysmal thrombus formation in vitro, comparing 2 different FD sizes with an empty model and correlating the results with PIV measurements. The combination of both methods can potentially im-

prove the understanding of the dynamics of thrombus formation. Furthermore, thrombosis investigation in patient-specific models could also support the treatment decision or device-sizing. Potential improvements of the in vitro setup and extensions of this research field are a more detailed life detection of thrombus formation by MR imaging and the development of a transparent and coagulable PIV fluid, such as a modified platelet-rich plasma.

Disclosures: Kathrin Gester, Ines Luchtefeld, Martin Büsen, Simon Johannes Sonntag, Torsten Linde, Ulrich Steinseifer—RELATED: Grant: This project was funded by the German Federal Ministry for Economic Affairs and Energy.\* Giorgio Cattaneo—RELATED: Grant: Federal Ministry for Economic Affairs and Energy\*; UNRELATED: Employment: Acandis GmbH & Co KG; Grants/Grants Pending: Federal Ministry for Economic Affairs and Energy.\* \*Money paid to the institution.

### REFERENCES

- Byrne JV, Beltechi R, Yarnold JA, et al. **Early experience in the treatment of intra-cranial aneurysms by endovascular flow diversion: a multicentre prospective study.** *PLoS One* 2010;5:e12492 CrossRef Medline
- Becske T, Kallmes DF, Saatci I, et al. **Pipeline for uncoilable or failed aneurysms: results from a multicenter clinical trial.** *Radiology* 2013; 267:858–68 CrossRef Medline
- Cebral JR, Mut F, Raschi M, et al. **Aneurysm rupture following treatment with flow-diverting stents: computational hemodynamics analysis of treatment.** *AJNR Am J Neuroradiol* 2011;32:27–33 CrossRef Medline
- Kulcsár Z, Houdart E, Bonafé A, et al. **Intra-aneurysmal thrombosis as a possible cause of delayed aneurysm rupture after flow-diversion treatment.** *AJNR Am J Neuroradiol* 2011;32:20–25 CrossRef Medline
- Pereira VM, Brina O, Delattre BMA, et al. **Assessment of intra-aneurysmal flow modification after flow diverter stent placement with four-dimensional flow MRI: a feasibility study.** *J Neurointerv Surg* 2014 Oct 3. [Epub ahead of print] CrossRef Medline
- Hampton T, Walsh D, Tolia C, et al. **Mural destabilization after aneurysm treatment with a flow-diverting device: a report of two cases.** *J Neurointerv Surg* 2011;3:167–71 CrossRef Medline
- Augsburger L, Farhat M, Reymond P, et al. **Effect of flow diverter porosity on intraaneurysmal blood flow.** *Klin Neuroradiol* 2009;19: 204–14 CrossRef Medline
- Roselle BN, Gonzalez LF, Babiker MH, et al. **Flow diverter effect on cerebral aneurysm hemodynamics: an in vitro comparison of telescoping stents and the Pipeline.** *Neuroradiology* 2013;55:751–58 CrossRef Medline
- Seong J, Wakhloo AK, Lieber BB. **In vitro evaluation of flow diverters in an elastase-induced saccular aneurysm model in rabbit.** *J Biomech Eng* 2007;129:863–72 CrossRef Medline
- Yu CH, Matsumoto K, Shida S, et al. **A steady flow analysis on a cerebral aneurysm model with several stents for new stent design using PIV.** *J Mechanical Science and Technology* 2012;26:1333–40 CrossRef
- Bouillot P, Brina O, Ouared R, et al. **Particle imaging velocimetry evaluation of intracranial stents in sidewall aneurysm: hemodynamic transition related to the stent design.** *PLoS One* 2014;9: e113762 CrossRef Medline
- Bouillot P, Brina O, Ouared R, et al. **Hemodynamic transition driven by stent porosity in sidewall aneurysms.** *J Biomech* 2015;48:1300–09 CrossRef Medline
- Dorn F, Niedermeyer F, Balasso A, et al. **The effect of stents on intra-aneurysmal hemodynamics: in vitro evaluation of a pulsatile sidewall aneurysm using laser Doppler anemometry.** *Neuroradiology* 2011;53:267–72 CrossRef Medline
- Chalouhi N, Starke RM, Yang S, et al. **Extending the indications of flow diversion to small, unruptured, saccular aneurysms of the anterior circulation.** *Stroke* 2014;45:54–58 CrossRef Medline
- Hoi Y, Wasserman BA, Xie YJ, et al. **Characterization of volumetric**

- flow rate waveforms at the carotid bifurcations of older adults. *Physiol Meas* 2010;31:291–302 CrossRef Medline
16. Zhao M, Amin-Hanjani S, Ruland S, et al. **Regional cerebral blood flow using quantitative MR angiography.** *AJNR Am J Neuroradiol* 2007;28:1470–73 CrossRef Medline
  17. Hendrikse J, van Raamt AF, van der Graaf Y, et al. **Distribution of cerebral blood flow in the circle of Willis.** *Radiology* 2005;235:184–89 CrossRef Medline
  18. Brown RI. **The physics of continuous flow centrifugal cell separation.** *Artif Organs* 1989;13:4–20 CrossRef Medline
  19. Ahlhelm F, Roth C, Kaufmann R, et al. **Treatment of wide-necked intracranial aneurysms with a novel self-expanding two-zonal endovascular stent device.** *Neuroradiology* 2007;49:1023–28 CrossRef Medline
  20. Kallmes DF, Ding YH, Dai D, et al. **A new endoluminal, flow-disrupting device for treatment of saccular aneurysms.** *Stroke* 2007;38:2346–52 CrossRef Medline
  21. Simgen A, Ley D, Roth C, et al. **Evaluation of a newly designed flow diverter for the treatment of intracranial aneurysms in an elastase-induced aneurysm model, in New Zealand white rabbits.** *Neuroradiology* 2014;56:129–37 CrossRef Medline
  22. Wang K, Huang Q, Hong B, et al. **Correlation of aneurysm occlusion with actual metal coverage at neck after implantation of flow-diverting stent in rabbit models.** *Neuroradiology* 2012;54:607–13 CrossRef Medline
  23. Wagner A, Cortsen M, Hauerberg J, et al. **Treatment of intracranial aneurysms: reconstruction of the parent artery with flow-diverting (Silk) stent.** *Neuroradiology* 2012;54:709–18 CrossRef Medline
  24. Fischer S, Vajda Z, Perez MA, et al. **Pipeline embolization device (PED) for neurovascular reconstruction: initial experience in the treatment of 101 intracranial aneurysms and dissections.** *Neuroradiology* 2012;54:369–82 CrossRef Medline
  25. Lubicz B, Collignon L, Raphaeli G, et al. **Flow-diverter stent for the endovascular treatment of intracranial aneurysms: a prospective study in 29 patients with 34 aneurysms.** *Stroke* 2010;41:2247–53 CrossRef Medline
  26. Piano M, Valvassori L, Quilici L, et al. **Midterm and long-term follow-up of cerebral aneurysms treated with flow diverter devices: a single-center experience.** *J Neurosurg* 2013;118:408–16 CrossRef Medline
  27. Saatci I, Yavuz K, Ozer C, et al. **Treatment of intracranial aneurysms using the Pipeline flow-diverter embolization device: a single-center experience with long-term follow-up results.** *AJNR Am J Neuroradiol* 2012;33:1436–46 CrossRef Medline
  28. Ringelstein A, Schlamann M, Goericke SL, et al. **3-year follow-up after endovascular aneurysm treatment with Silk® flow diverter [in German].** *Rofo* 2013;185:328–32 CrossRef Medline
  29. Cinar C, Bozkaya H, Oran I. **Endovascular treatment of cranial aneurysms with the Pipeline flow-diverting stent: preliminary mid-term results.** *Diagn Interv Radiol* 2013;19:154–64 CrossRef Medline
  30. De Vries J, Boogaarts J, Van Norden A, et al. **New generation of flow diverter (Surpass) for unruptured intracranial aneurysms: a prospective single-center study in 37 patients.** *Stroke* 2013;44:1567–77 CrossRef Medline
  31. Maimon S, Gonen L, Nossek E, et al. **Treatment of intra-cranial aneurysms with the SILK flow diverter: 2 years' experience with 28 patients at a single center.** *Acta Neurochir (Wien)* 2012;154:979–87 CrossRef Medline
  32. Kadirvel R, Ding YH, Dai D, et al. **Cellular mechanisms of aneurysm occlusion after treatment with a flow diverter.** *Radiology* 2014;270:394–99 CrossRef Medline
  33. Boussel L, Rayz V, McCulloch C, et al. **Aneurysm growth occurs at region of low wall shear stress: patient-specific correlation of hemodynamics and growth in a longitudinal study.** *Stroke* 2008;39:2997–3002 CrossRef Medline



# Preclinical Testing of a Novel Thin Film Nitinol Flow-Diversion Stent in a Rabbit Elastase Aneurysm Model

Y. Ding, D. Dai, D.F. Kallmes, D. Schroeder, C.P. Kealey, V. Gupta, A.D. Johnson, and R. Kadirvel



## ABSTRACT

**BACKGROUND AND PURPOSE:** Thin film nitinol can be processed to produce a thin microporous sheet with a low percentage of metal coverage (<20%) and high pore attenuation (~70 pores/mm<sup>2</sup>) for flow diversion. We present in vivo results from the treatment of experimental rabbit aneurysms by using a thin film nitinol-based flow-diversion device.

**MATERIALS AND METHODS:** Nineteen aneurysms in the rabbit elastase aneurysm model were treated with a single thin film nitinol flow diverter. Devices were also placed over 17 lumbar arteries to model perianeurysmal branch arteries of the intracranial circulation. Angiography was performed at 2 weeks ( $n = 7$ ), 1 month ( $n = 8$ ), and 3 months ( $n = 4$ ) immediately before sacrifice. Aneurysm occlusion was graded on a 3-point scale (grade I, complete occlusion; grade II, near-complete occlusion; grade III, incomplete occlusion). Toluidine blue staining was used for histologic evaluation. En face CD31 immunofluorescent staining was performed to quantify neck endothelialization.

**RESULTS:** Markedly reduced intra-aneurysmal flow was observed on angiography immediately after device placement in all aneurysms. Grade I or II occlusion was noted in 4 (57%) aneurysms at 2-week, in 6 (75%) aneurysms at 4-week, and in 3 (75%) aneurysms at 12-week follow-up. All 17 lumbar arteries were patent. CD31 staining showed that  $75\% \pm 16\%$  of the aneurysm neck region was endothelialized. Histopathology demonstrated incorporation of the thin film nitinol flow diverter into the vessel wall and no evidence of excessive neointimal hyperplasia.

**CONCLUSIONS:** In this rabbit model, the thin film nitinol flow diverter achieved high rates of aneurysm occlusion and promoted tissue in-growth and aneurysm neck healing, even early after implantation.

**ABBREVIATION:** TFN = thin film nitinol

Flow diverters are a relatively recent advancement in the endovascular treatment of intracranial aneurysms and have expanded the types of aneurysms addressable with endovascular techniques.<sup>1-5</sup> Numerous different flow diverters have been approved in Europe, and several are either approved for use or under investigation in the United States. Each of the flow-diversion devices in current use is

constructed from braided metallic strands, typically nitinol, cobalt chromium, and/or platinum. These devices, while promising, have several relative disadvantages. Aneurysm occlusion may be delayed, precise placement may be challenging because of device shortening, >1 device is often required, and branch arteries covered by the device may undergo occlusion.<sup>6-8</sup>

Thin film nitinol (TFN) is a biomaterial produced in patterned sheets approximately 5  $\mu\text{m}$  thick by using techniques adapted from the microelectronics industry. Previous reports have demonstrated that TFN has unique mechanical properties, excellent biocompatibility, and a low profile that make it well-suited for use in endovascular devices.<sup>9-11</sup> Potential advantages of a flow-diverting stent based on TFN technology include the ability to fabricate devices with much higher pore densities and a lower percentage of metal coverage than is achieved with current-generation devices based on braided wire technology. The purpose of this study was to test a novel TFN-based flow-diverting stent in a rabbit model of saccular aneurysms.

Received June 9, 2015; accepted after revision August 12.

From the Department of Neurointerventional Radiology (Y.D., D.D., D.F.K., D.S., R.K.), Mayo Clinic, Rochester, Minnesota; and NeuroSigma Inc. (C.P.K., V.G., A.D.J.), Los Angeles, California.

This work was supported by NeuroSigma Inc. and a National Institutes of Health Grant (R41 NS074576).

Paper previously presented at: American Society of Neuroradiology Annual Meeting and the Foundation of the ASNR Symposium, April 25–30, 2015; Chicago, Illinois.

Please address correspondence to Yonghong Ding, MD, Department of Radiology, Mayo Clinic, 200 First St SW, Rochester, MN, 55905; e-mail: ding.yonghong@mayo.edu

Indicates open access to non-subscribers at www.ajnr.org

<http://dx.doi.org/10.3174/ajnr.A4568>



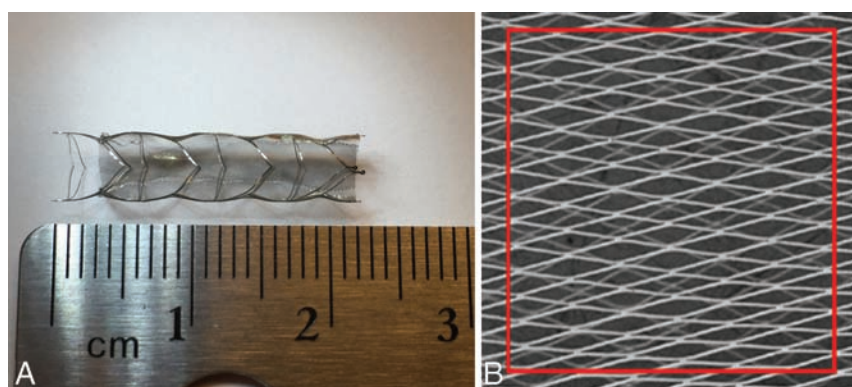


**FIG 1.** A, A prototype TFN flow diverter. B, The scanning electron microscopy image of TFN.

## MATERIALS AND METHODS

Aneurysms ( $n = 19$ ) were created in New Zealand white rabbits. Our Institutional Animal Care and Use Committee approved all animal procedures. The detailed procedure for aneurysm creation has been described previously.<sup>12</sup> Briefly, anesthesia was induced with an intramuscular injection of ketamine (35 mg/kg), xylazine (6 mg/kg), and acepromazine (1.0 mg/kg) and was maintained with 2.5%–3.0% isoflurane conveyed in 100% oxygen. Using a sterile technique, we exposed and ligated the right common carotid artery distally. A 1- to 2-mm bevelled arteriotomy was made, and a 5F AVANTI vascular sheath (Cordis, Miami Lakes, Florida) was advanced retrogradely in the right common carotid artery to a point approximately 3 cm cephalad to the origin of right common carotid artery. Fluoroscopy (Advantx; GE Healthcare, Milwaukee, Wisconsin) was performed by injection of contrast through the sheath retrogradely in the right common carotid artery, to identify the junction between the right common carotid artery and the subclavian and brachiocephalic arteries. A 3F Fogarty balloon (Baxter Healthcare, Irvine, California) was advanced through the sheath to the level of the origin of the right common carotid artery with fluoroscopic guidance and was inflated with iodinated contrast material. Porcine elastase (5.23 units per mg protein, 40.1 mg protein/mL, approximately 200 units/mL; Worthington Biochemical, Lakewood, New Jersey) was incubated within the lumen of the right common carotid artery above the inflated balloon for 20 minutes, after which the balloon and sheath were removed and the right common carotid artery was ligated below the sheath entry site.

Three weeks after creation, patency of all the aneurysms and parent arteries was confirmed by DSA before TFN-device deployment. A 5F sheath was advanced on one side of the femoral artery via cutdown, followed by a 5F Envoy guiding catheter with 0.056-inch ID (Codman & Shurtleff, Raynham, Massachusetts). A distal-access catheter with 0.044-inch ID (Concentric Medical, Mountain View, California) was advanced into the distal end of parent artery (right subclavian artery) over a 0.038-inch guidewire with a hydrophilic coating (Boston Scientific, Natick, Massachusetts) through the guide catheter.

Prototype TFN flow diverters were fabricated and provided for this study by NeuroSigma (Los Angeles, California). Detailed methods for the fabrication of TFN have been published previously.<sup>13–15</sup> In brief, TFN is sputter-deposited on 4-inch

silicon wafers by using a custom DC magnetron sputter system. Silicon wafers are micropatterned by using deep reactive ion etching before the sputter-deposition process. Following deposition, the TFN is removed from the silicon wafer and annealed at 500°C. This process yields a cylindric TFN micro-mesh that is subsequently used to cover a laser-cut nitinol backbone stent (Fig 1). The red box outlines an area of 1 mm<sup>2</sup>. The pore attenuation and percentage of metal coverage of the TFN flow diverter were calculated from scanning electron microscope images of a device at full expansion.

The number of pores in an area of 1 mm<sup>2</sup> was counted from the scanning electron microscope image, and the percentage of metal coverage was calculated from the following formula: 1 – Percent Metal Coverage of Stent Backbone. At full expansion, the TFN flow diverter had a pore attenuation of approximately 70 pores/mm<sup>2</sup> and a percentage of metal coverage of <20%. Results from in vitro and in vivo testing of devices constructed by using similar methods have been reported previously.<sup>9–11</sup>

The first TFN device (4.5-mm outside diameter × 12 mm) was deployed across the aneurysm neck by pushing the device out of the distal access catheter with the 0.038-inch guidewire with hydrophilic coating. The second device (4.5-mm outside diameter × 12 mm) was deployed across a lumbar artery within the abdominal aorta. DSA was performed through the guide catheter immediately after deployment. No damage to the device occurred during deployment. Aspirin (10 mg/kg) and clopidogrel (10 mg/kg) were given daily 2 days before implantation and continued until 30 days after treatment.

Sacrifice was performed at 2 weeks ( $n = 7$ ), 4 weeks ( $n = 8$ ), and 12 weeks ( $n = 4$ ) after treatment. On the day of sacrifice, anesthesia was administered as a cocktail of ketamine (74 mg/kg), xylazine (5 mg/kg), and acepromazine (1 mg/kg). Surgical access of the left common femoral artery was achieved. DSA was performed for both the brachiocephalic trunk and abdominal aorta. Degrees of aneurysm occlusion immediately after device deployment and before sacrifice were graded on a 3-point scale based on DSA images, including grade I (complete flow cessation, no flow within the aneurysm), grade II (near-complete flow, <10% residual flow), and grade III (incomplete occlusion, ≥10% residual flow).<sup>13</sup> Patency of the parent and lumbar arteries (including stenosis or occlusion) was assessed from DSA. Immediately following angiography, the subjects were euthanized by using a lethal injection of pentobarbital. The aneurysm, stented parent artery, and the aorta were harvested and fixed in 10% formalin. Toluidine blue staining was performed to evaluate thrombus organization within the aneurysm and neointima coverage of aneurysm neck and the orifice of lumbar artery.

Gross pathology and en face CD31 immunofluorescent staining were performed on a subset of devices selected at random from each of the follow-up time points to quantify neck endothelialization (1 at 2 weeks, 3 at 4 weeks, 2 at 12 weeks). Whole-mount immunofluorescent staining was performed by using an

anti-CD31 antibody. The coverage percentage of endothelialized neointima across the neck was calculated by using the value of the neck area of endothelialization measured under the microscope and the whole neck area. Histopathology of explanted devices was performed on the device at each of the 3 time points by using plastic-section mounting and toluidine blue staining.

## RESULTS

Mean aneurysm sizes (including aneurysm neck, width, and height) and angiographic outcomes from the 19 aneurysms are shown in the Table.

Grades I or II occlusion rates were noted in 57% ( $n = 4$ ) aneurysms at the 2-week follow-up time point (Fig 2A–C). At the 4-week time point, 6 (75%) aneurysms had complete or near-complete occlusion (grades I or II) (Fig 3A–C). At the 12-week time point, 3 (75%) aneurysms showed grades I or II occlusion. The distal parent artery was occluded in 1 aneurysm immediately after device deployment but reopened at the 3-month follow-up. Overall, grades I or II occlusion rates were achieved in 13 (68%) of the 19 aneurysms. All other parent and lumbar arteries remained patent without stenosis (Figs 2E–G and 3E–G).

For the 6 aneurysms with histologic processing, the average implant duration was 6.3 weeks. The mean neck orifice area was  $6.3 \pm 2.5 \text{ mm}^2$ , and  $75 \pm 16\%$  of the aneurysm neck region was covered by endothelialized tissue at the time of sacrifice (Figs 2D

and 3D). Toluidine blue staining of aneurysms with explanted devices confirmed these findings, which included minimal neointimal hyperplasia and good incorporation of the TFN and support stent. Thrombus formation within the aneurysm was also indicated (Fig 4).

## DISCUSSION

In this study, we demonstrated that a single TFN flow diverter could achieve high rates of complete or near-complete aneurysm occlusion as early as 2 weeks after implantation. Furthermore, rapid and near-complete endothelialization was noted across aneurysm necks, while branch arteries remained patent in all cases. All these results offer evidence that the TFN flow diverter holds substantial promise for clinical use.

Numerous flow-diverting devices have previously been tested in the elastase aneurysm model and have subsequently been applied clinically.<sup>16–22</sup> Aneurysm occlusion, neointimal hyperplasia of the parent artery (stenosis or occlusion), distal parent artery emboli, and patency of the branch artery can be assessed in this aneurysm model. Compared with current flow-diverter devices, the NeuroSigma TFN flow diverter achieves a very high pore attenuation while, at the same time, allowing a low percentage of metal coverage. Thus, very small distances are needed for endothelial cells to cross between structural elements of the TFN.

This study has several limitations. The number of subjects at each time point was relatively small, and the duration of implantation was limited. The aneurysms in this study were small, even though the mean height of the aneurysm was approximately 10 mm. The longest time point for follow-up was only 3 months in this study. Finally, the morphology of

**Aneurysm size and angiographic outcome**

Time Point (Weeks)	Mean Aneurysm Size (mm)			Occlusion Grades		Lumbar Artery Patency (%)
	Neck	Width	Height	I or II	III	
2	$4.0 \pm 1.4$	$4.5 \pm 1.5$	$9.8 \pm 2.4$	57%	43%	100
4	$4.1 \pm 1.0$	$4.1 \pm 1.4$	$9.3 \pm 1.6$	75%	25%	100
12	$4.1 \pm 1.0$	$4.7 \pm 2.1$	$9.5 \pm 2.7$	75%	25%	100

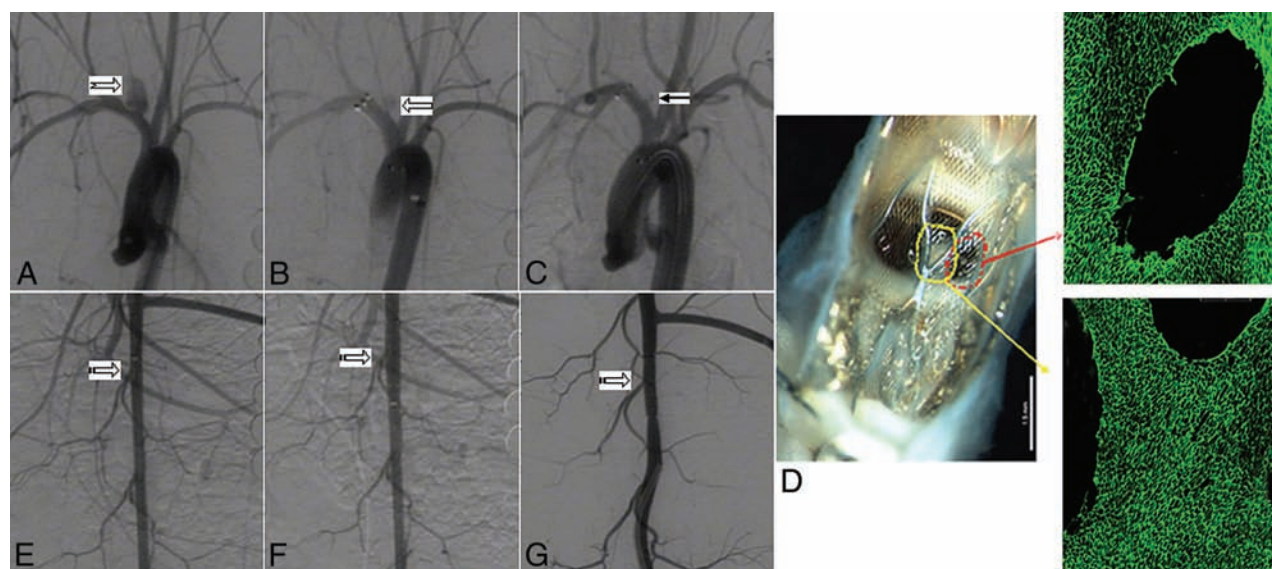


**FIG 2.** A, Digital subtraction angiogram shows the aneurysm before treatment (notched right arrow). B, DSA image immediately after device deployment shows blood flow reduction in the aneurysm (left block arrow). C, DSA image at 2 weeks of deployment shows near-complete aneurysm occlusion (grade II) (left arrow). D, Gross pathology along with en face CD 31 immunofluorescent staining (original magnification water lens 20 $\times$ ) shows that 46% of aneurysm neck area is covered by endothelialized tissue (red and yellow arrows). E, DSA image shows the lumbar arteries before deployment in the abdominal aorta (striped right arrow). F, DSA image immediately after device deployment shows patent lumbar arteries (striped right arrow). G, DSA image at 2 weeks of deployment shows that the lumbar arteries remain patent (striped right arrow).



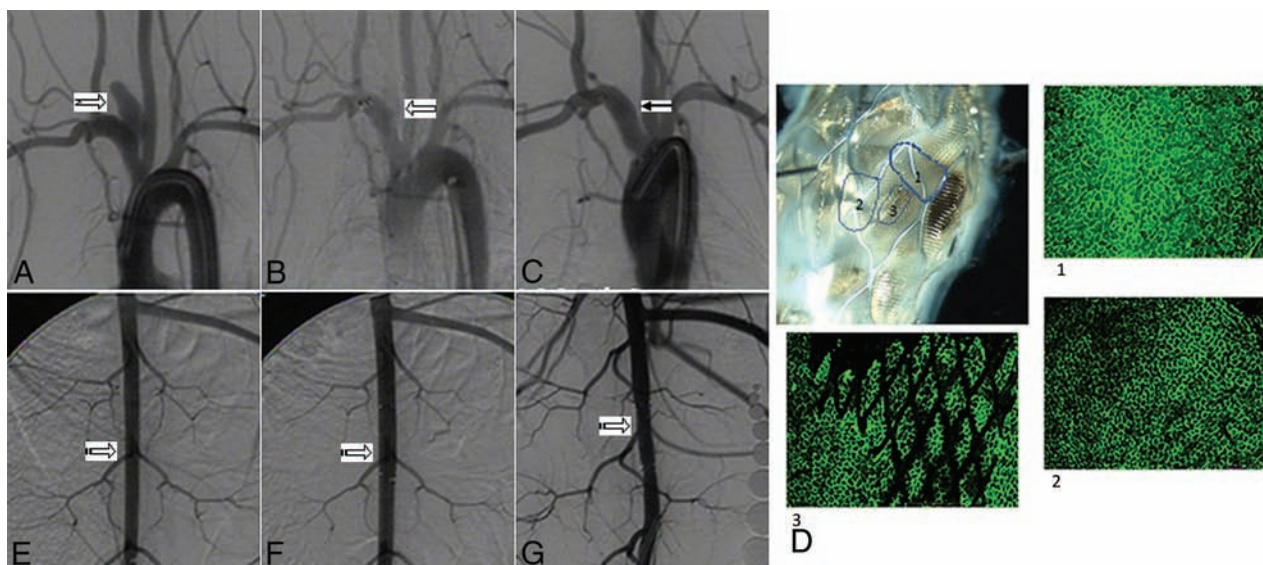


**FIG 3.** A, Digital subtraction angiogram shows the aneurysm before treatment (notched right arrow). B, DSA image immediately after device deployment shows significant blood flow reduction in the aneurysm (left block arrow). C, DSA image at 4 weeks of deployment shows complete aneurysm occlusion (grade I) (left arrow). D, Gross pathology along with en face CD 31 immunofluorescent staining (original magnification water lens 20 $\times$ ) shows that 89% of the aneurysm neck area was covered by endothelialized tissue (areas 1, 2, and 3). E, DSA image shows the lumbar arteries before deployment in the abdominal aorta (striped right arrow). F, DSA image immediately after device deployment shows patent lumbar arteries (striped right arrow). G, DSA image at 4 weeks of deployment shows that the lumbar arteries remain patent (striped right arrow).

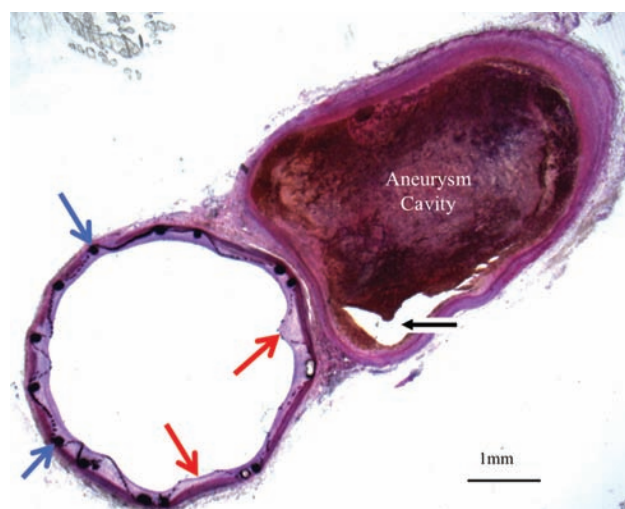


**FIG 4.** Histologic section (toluidine blue staining, original magnification 1.25 $\times$ ) of the TFN flow diverter explanted after 4 weeks. This axial image demonstrates minimal neointimal hyperplasia deep to the TFN (red arrows) and support stent (blue arrows). The aneurysm cavity is partially filled with thrombus in various stages of organization. A small part of the aneurysm lumen is empty (black arrow).

the aneurysms does not provide the range expected clinically, and the tortuosity of the carotid siphon and other vessel territories in humans may cause substantial challenges in achieving adequate wall apposition of the device.

## CONCLUSIONS

In this rabbit model, the TFN devices achieved high rates of acute angiographic occlusion. Vessel branches covered by the devices remained patent. High degrees of endothelialization across the aneurysm neck were achieved, which indicates that in this model, the TFN can promote tissue in-growth and aneurysm neck healing.

Disclosures: Yonghong Ding—RELATED: Grant: This work was partially supported by a National Institutes of Health Small Business Technology Transfer (STTR) grant (IR41NS074576). David F. Kallmes—RELATED: Grant: NeuroSigma.\* Comments: National Institutes of Health Small Business Innovation Research (SBIR) grant subcontract; UNRELATED: Board Membership: GE Healthcare (cost-effectiveness board); Consultancy: ev3/Covidien/Medtronic, Comments: planning and implementing clinical trials; Grants/Grants Pending: MicroVention,\* Sequent,\* SurModics,\* Codman,\* ev3/Covidien/Medtronic,\* Comments: preclinical and clinical research; Royalties: University of Virginia Patent Foundation (Spine Fusion); Travel/Accommodations/Meeting Expenses Unrelated to Activities Listed: ev3/Covidien/Medtronic,\* Comments: travel to the FDA panel meeting. Colin P. Kealey—RELATED: The work was partially funded by a STTR grant from the National Institutes of Health (IR41NS074576)\*; UNRELATED: Employment: NeuroSigma (full-time employee); Patents (planned, pending or issued): I am a coinventor on patents related to this technology that are owned and/or licensed by NeuroSigma\*; Stock/Stock Options: I have stock options in NeuroSigma. Vikas Gupta—RELATED: Grant: National Institutes of Health \*; Consulting Fee or Honorarium: NeuroSigma, Comments: Work during May 2014 to March 2015 was performed as an independent consultant. Since April 2015, the work has been performed as full-time employee; Support for Travel to Meetings for the Study or Other Purposes: NeuroSigma; UNRELATED: Consultancy: NeuroSigma; Employment: NeuroSigma; Stock/Stock Options: NeuroSigma; Travel/Accommodations/Meeting Expenses Unrelated to Activities Listed: NeuroSigma. Alfred David Johnson—RELATED: Grant: National Institutes of Health (IR41NS074576)\*; Support for Travel to Meetings for the Study or Other Purposes: Travel expenses were paid for experiments at the Mayo Clinic by NeuroSigma; UNRELATED: Other: salary from TiNi Alloy Company for work unrelated to the submitted work. Ramanathan Kadirvel—RELATED: Grant: National Institutes of Health (NS076491).\*\*Money paid to the institution.

## REFERENCES

1. Kallmes DF, Hanel R, Lopes D, et al. **International retrospective study of the Pipeline embolization device: a multicenter aneurysm treatment study.** *AJNR Am J Neuroradiol* 2015;36:108–15 CrossRef Medline
2. Saatci I, Yavuz K, Ozer C, et al. **Treatment of intracranial aneurysms using the Pipeline flow-diverter embolization device: a single-center experience with long-term follow-up results.** *AJNR Am J Neuroradiol* 2012;33:1436–46 CrossRef Medline
3. Berge J, Biondi A, Machi P, et al. **Flow-diverter Silk stent for the treatment of intracranial aneurysms: 1-year follow-up in a multicenter study.** *AJNR Am J Neuroradiol* 2012;33:1150–55 CrossRef Medline

4. Lubicz B, Van der Elst O, Collignon L, et al. **Silk flow-diverter stent for the treatment of intracranial aneurysms: a series of 58 patients with emphasis on long-term results.** *AJNR Am J Neuroradiol* 2015; 36:542–46 CrossRef Medline
5. Briganti F, Leone G, Marseglia M, et al. **p64 flow modulation device in the treatment of intracranial aneurysms: initial experience and technical aspects.** *J Neurointerv Surg* 2015 Apr 20. [Epub ahead of print] CrossRef Medline
6. Tan LA, Keigher KM, Munich SA, et al. **Thromboembolic complications with Pipeline embolization device placement: impact of procedure time, number of stents and pre-procedure P2Y12 reaction unit (PRU) value.** *J Neurointerv Surg* 2015;7:217–21 CrossRef Medline
7. Cirillo L, Leonardi M, Dall'olio M, et al. **Complications in the treatment of intracranial aneurysms with Silk stents: an analysis of 30 consecutive patients.** *Interv Neuroradiol* 2012;18:413–25 Medline
8. De Vries JD, Boogaarts J, Van Norden AV, et al. **New generation of flow diverter (Surpass) for unruptured intracranial aneurysms: a prospective single-center study in 37 patients.** *Stroke* 2013;44: 1567–77 CrossRef Medline
9. Shayan M, Chun Y. **An overview of thin film nitinol endovascular devices.** *Acta Biomater* 2015;21:20–34 CrossRef Medline
10. Kealey CP, Chun YJ, Viñuela FE, et al. **In vitro and in vivo testing of a novel, hyperelastic thin film nitinol flow diversion stent.** *J Biomed Mater Res B Appl Biomater* 2012;100:718–25 CrossRef Medline
11. Kealey CP, Whelan SA, Chun YJ, et al. **In vitro hemocompatibility of thin film nitinol in stenotic flow conditions.** *Biomaterials* 2010;31: 8864–71 CrossRef Medline
12. Ding YH, Dai D, Kadirvel R, et al. **Five-year follow-up in elastase-induced aneurysms in rabbits.** *AJNR Am J Neuroradiol* 2010;31: 1236–39 CrossRef Medline
13. Gupta V, Johnson AD, Martynov V, et al. **Nitinol thin film three-dimensional devices: fabrication and applications.** In: Pelton AR, Duerig T, eds. *SMST-2003: Proceedings*. Materials Park: ASM International 2004;639–50
14. Mohanchandra KP, Ho KK, Carman GP. **Compositional uniformity in sputter-deposited NiTi shape memory alloy thin films.** *Materials Lett* 2008;62:3481–83 CrossRef
15. Chun YJ, Levi DS, Mohanchandra KP, et al. **Novel micro-patterning processes for thin film NiTi vascular devices.** *Smart Materials and Structures* 2010;19:105021 CrossRef
16. Brinjikji W, Lanzino G, Cloft HJ, et al. **Patency of the posterior communicating artery after flow diversion treatment of internal carotid artery aneurysms.** *Clin Neurol Neurosurg* 2014;120:84–8 CrossRef Medline
17. Kallmes DF, Ding YH, Dai D, et al. **A new endoluminal, flow-disrupting device for treatment of saccular aneurysms.** *Stroke* 2007;38: 2346–52 CrossRef Medline
18. Kallmes DF, Ding YH, Dai D, et al. **A second-generation, endoluminal, flow-disrupting device for treatment of saccular aneurysms.** *AJNR Am J Neuroradiol* 2009;30:1153–58 CrossRef Medline
19. Simgen A, Ley D, Roth C, et al. **Evaluation of a newly designed flow diverter for the treatment of intracranial aneurysms in an elastase-induced aneurysm model, in New Zealand white rabbits.** *Neuroradiology* 2014;56:129–37 CrossRef Medline
20. Struffert T, Ott S, Kowarschik M, et al. **Measurement of quantifiable parameters by time-density curves in the elastase-induced aneurysm model: first results in the comparison of a flow diverter and a conventional aneurysm stent.** *Eur Radiol* 2013;23:521–27 CrossRef Medline
21. Ionita CN, Natarajan SK, Wang W, et al. **Evaluation of a second-generation self-expanding variable-porosity flow diverter in a rabbit elastase aneurysm model.** *AJNR Am J Neuroradiol* 2011;32:1399–407 CrossRef Medline
22. Sadasivan C, Cesar L, Seong J, et al. **An original flow diversion device for the treatment of intracranial aneurysms: evaluation in the rabbit elastase-induced model.** *Stroke* 2009;40:952–58 CrossRef Medline



# Stent-Assisted Coil Embolization of Intracranial Aneurysms: Complications in Acutely Ruptured versus Unruptured Aneurysms

R.S. Bechan, M.E. Sprengers, C.B. Majoie, J.P. Peluso, M. Sluzewski, and W.J. van Rooij



## ABSTRACT

**BACKGROUND AND PURPOSE:** The use of stents in the setting of SAH is controversial because of concerns about the efficacy and risk of dual antiplatelet therapy. We compare complications of stent-assisted coil embolization in patients with acutely ruptured aneurysms with complications in patients with unruptured aneurysms.

**MATERIALS AND METHODS:** Between February 2007 and March 2015, 45 acutely ruptured aneurysms and 47 unruptured aneurysms were treated with stent-assisted coiling. Patients with ruptured aneurysms were not pretreated with antiplatelet medication but received intravenous aspirin during the procedure. Thromboembolic events and early rebleeds were recorded.

**RESULTS:** In ruptured aneurysms, 9 of 45 patients had thromboembolic complications. Four patients remained asymptomatic, 4 developed infarctions, and 1 patient died. The permanent complication rate in ruptured aneurysms was 11% (95% CI, 4%–24%). Five of 45 patients (11%; 95% CI, 4%–24%) had an early rebleed from the treated aneurysm after 3–45 days, and in 4, this rebleed was fatal. In 46 patients with 47 unruptured aneurysms, thromboembolic complications occurred in 2. One patient remained asymptomatic; the other had a thalamus infarction. The complication rate in unruptured aneurysms was 2.2% (1 of 46; 95% CI, 0.01%–12%). No first-time hemorrhages occurred in 46 patients with 47 aneurysms during 6 months of follow-up.

**CONCLUSIONS:** The complication rate of stent-assisted coiling with early adverse events in ruptured aneurysms was 10 times higher than that in unruptured aneurysms. Early rebleed accounted for most mortality. In ruptured aneurysms, stent-assisted coil embolization is associated with increased morbidity and mortality and should only be considered when less risky options have been excluded.

Endovascular treatment of wide-neck intracranial aneurysms remains a technically challenging procedure due to the risk of coil protrusion into the parent artery and subsequent thrombus formation or parent vessel compromise. There are several techniques to coil wide-neck aneurysms, such as balloon- or stent-assisted coiling,<sup>1–7</sup> flow diversion, and, more recently introduced, the WEB aneurysm embolization system (Sequent Medical, Aliso Viejo, California).<sup>8</sup> With the use of stents or flow diverters, complication rates tend to be higher than with selective coiling or balloon-assisted coiling because of the thrombogenicity of the devices and the need for dual antiplatelet medication with inherent risk in the postop-

erative period.<sup>9–14</sup> Most operators are reluctant to use antiplatelet therapy in the setting of subarachnoid hemorrhage because of the potential need for a ventriculostomy, the potential for infarction secondary to vasospasm, and the high likelihood of future invasive interventions. Therefore, stent placement is generally avoided in acutely ruptured aneurysms in favor of clip ligation or other endovascular techniques that do not mandate dual antiplatelet therapy.

In this observational study with prospectively collected data, we evaluated the incidence of hemorrhagic and thromboembolic complications in patients with acutely ruptured aneurysms treated with stent-assisted coiling. In addition, we compared the complication rates with those of unruptured aneurysms treated with stent assistance during the same period.

## MATERIALS AND METHODS

This observational study with prospectively collected data was compliant with institutional privacy policy. The institutional review board gave exempt status for approval and informed consent.

Received May 18, 2015; accepted after revision July 29.

From Sint Elisabeth Ziekenhuis (R.S.B., J.P.P., M.S., W.J.v.R.), Tilburg, the Netherlands; and Academisch Medisch Centrum (M.E.S., C.B.M.), Amsterdam, the Netherlands.

Please address correspondence to Willem Jan van Rooij, MD, Department of Radiology, Sint Elisabeth Ziekenhuis, Hilvarenbeekseweg 60, 5022GC Tilburg, the Netherlands; e-mail: wjvanrooij@gmail.com

<http://dx.doi.org/10.3174/ajnr.A4542>

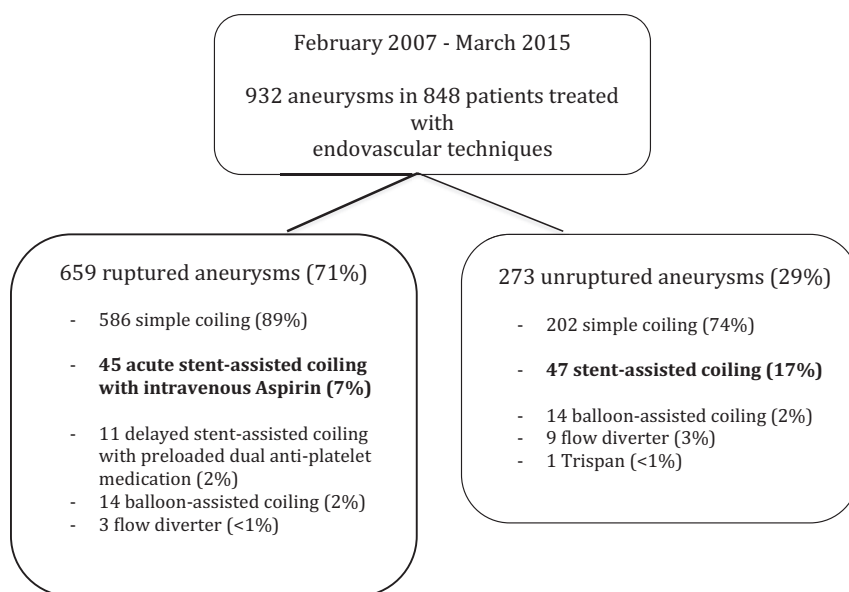


**FIG 1.** Flow chart of 932 aneurysms in 848 patients treated endovascularly between February 2007 and March 2015.

### Patient Population

Between February 2007 and March 2015, 848 patients with 932 aneurysms were treated with endovascular techniques (Fig 1). There were 659 ruptured aneurysms (71%) and 273 unruptured aneurysms (29%). Of 659 ruptured aneurysms, 45 aneurysms in 45 patients were treated with stent-assisted coiling in the acute phase of SAH without pretreatment with antiplatelet medication. Of 273 unruptured aneurysms, 47 in 46 patients were treated with stent-assisted coiling.

### General Indications for Stent-Assisted Coiling

Patients with SAH diagnosed on CT or lumbar puncture underwent angiography of all cerebral vessels on a biplane angiographic system (Integris Allura BN 3000 or Allura FD 20/10; Philips Healthcare, Best, the Netherlands). When a wide-neck ruptured aneurysm (dome-to-neck ratio  $<2$  and/or a neck length of  $\geq 4$  mm) or dissection was identified on 3D angiography, a vascular neurosurgeon was consulted about the best treatment for the individual patient with respect to clinical condition, age, and comorbidities. Stent-assisted coiling in ruptured wide-neck aneurysms was indicated for all aneurysms or dissections located in the posterior circulation and for aneurysms and dissections in the anterior circulation in poor-grade patients who were not surgical candidates.

For unruptured aneurysms, the indications for stent-assisted coiling were determined in a multidisciplinary meeting with neurosurgeons and neurologists.

### Stent-Assisted Coiling Procedure

Coiling was performed with the patient under general anesthesia. First, stent placement was simulated by computer graphics on the 3D dataset by using standard machine software (Philips Healthcare, Best, the Netherlands).<sup>15</sup> The software exactly calculated the diameters and length of the vessel segment where the stent placement was intended. Accordingly, the proper stent length and di-

ameter could be chosen. We aimed at a 10-mm stent overlap on either side of the aneurysm neck.

The aneurysm was passed with a microcatheter (Prowler Plus; Codman & Shurtleff, Raynham, Massachusetts). After stent placement, the delivery microcatheter was removed. A new lower profile microcatheter (Excelsior SL-10; Stryker, Kalamazoo, Michigan) was introduced through the stent struts into the aneurysm, and coils were placed until the aneurysm was occluded. In selected cases, a microcatheter was jailed in the aneurysm by the stent.

Of 45 patients, 34 were treated with an Enterprise self-expanding stent (Codman & Shurtleff); 5, with an Acclino stent (Acandis, Pforzheim, Germany); and 4, with a LVIS stent (MicroVention, Tustin, California). In 2 patients, a LEO stent (Balt Extrusion, Montmorency, France) was used, followed by a Silk flow diverter (Balt

Extrusion), which was coaxially placed.

### Anticoagulation Protocol

During coiling of ruptured aneurysms, heparin was administered via the pressure bags (1000 U per 500 mL of saline). Intravenous aspirin, 500 mg, was administered immediately before stent placement.<sup>14</sup> After the procedure, patients were prescribed a loading dose of 300 mg of clopidogrel (Plavix), followed by 75 mg of clopidogrel daily for 6 months and, life-long, 80 mg of aspirin daily. The clopidogrel loading dose was administered orally or through a gastric tube immediately after the procedure. For 48 hours after the procedure, 7500 U of subcutaneous heparin was given twice daily.

Patients with unruptured aneurysms were preloaded for 4 days with clopidogrel and aspirin and were heparinized during the procedure. Dual antiplatelet therapy was continued for 6 months; and aspirin, 80 mg daily, life-long. Response to antiplatelet therapy was not tested before the procedure.

When a thromboembolic event (angiographically visible thrombus or vessel occlusion) occurred during the endovascular procedure, a loading dose of glycoprotein IIb/IIIa antagonist (tirofiban [Aggrastat]) was administered intravenously or intra-arterially followed by drip infusion for 24 hours. In 1 patient, mechanical thrombectomy with a Solitaire stent (Covidien, Irvine, California) was performed. The decision to perform a thrombectomy depended on the location of the thrombus, and the perception of possible successful removal.

### Clinical and Imaging Outcomes

Procedural complications were defined as visible thrombus or vessel occlusion during the procedure or procedural rupture. Clinical consequences of thromboembolic complications were recorded. If the clinical condition of the patient worsened after the procedure, CT or MR imaging was performed to clarify the cause. In patients with an early rebleed, control angiography was per-

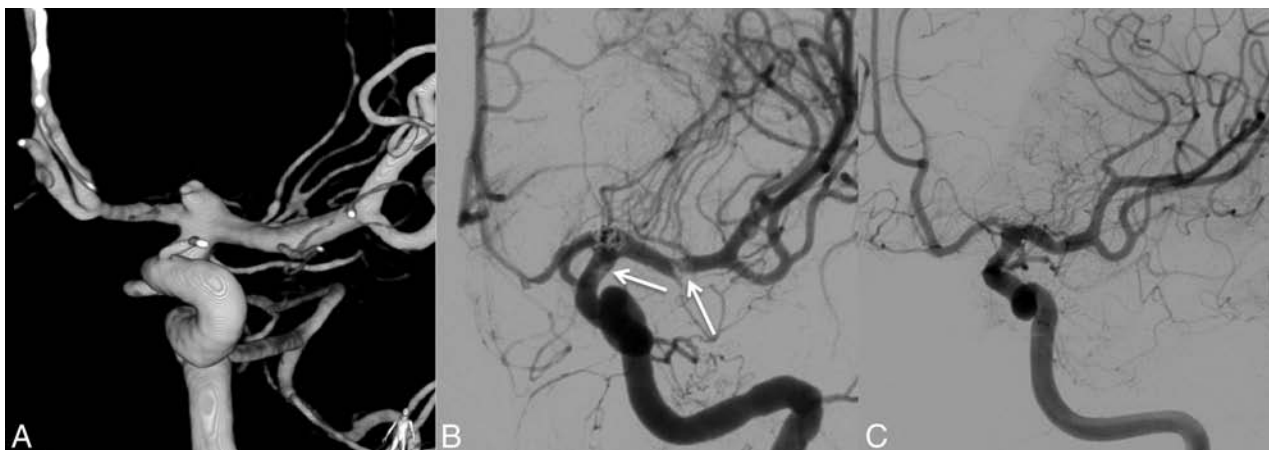


**FIG 2.** Ruptured carotid tip aneurysm in a 58-year-old woman treated with stent-assisted coiling. *A*, 3D angiogram shows a wide-neck aneurysm on the carotid tip. *B*, Anteroposterior left carotid artery angiogram during coiling demonstrates thrombus formation on the proximal and distal ends of the stent (arrows). *C*, Follow-up angiogram at 6 months shows complete aneurysm occlusion and patent distal internal carotid and middle cerebral arteries.

formed if the clinical condition was fair or good. In patients with a thromboembolic complication, a native CT and diffusion-weighted MR imaging were performed.

For all other surviving patients, a follow-up visit, including angiography or MRA imaging, was scheduled at 6 months. The outcome was assessed according to the mRS scale. Extended imaging follow-up was tailored to the individual patient.

Additional coiling was scheduled in cases in which the aneurysm was reopened by coil compaction or resolution of intraluminal thrombus.

### Statistical Analysis

Quantitative variables were expressed with descriptive statistics, and categoric variables were expressed as frequencies or percentages with 95% CIs. The  $\chi^2$  test was used for comparison of proportions. Statistical analysis was performed with MedCalc for Windows, Version 14.12.0 (MedCalc Software, Mariakerke, Belgium).

## RESULTS

### Patients with Ruptured Aneurysms

Forty-five patients with 45 ruptured aneurysms were treated with stent-assisted coiling. There were 33 women (75%) and 12 men (25%), with a mean age of 56 years (median, 58 years; range, 21–79 years). Aneurysm location was the basilar tip in 13, anterior communicating artery in 8, carotid tip in 6, middle cerebral artery in 4, vertebral artery in 4, posterior communicating artery in 2, supraclinoid dissection aneurysm in 2, superior cerebellar artery in 2, basilar trunk in 2, A1 in 1, and PICA dissection in 1. The mean aneurysm size was 8.7 mm (median, 7 mm; range, 2–30 mm). The clinical condition at the time of treatment according to the Hunt and Hess scale (HH) was HH 1–2 in 6 (13%), HH 3 in 21 (47%), and HH 4–5 in 18 (40%). Timing of stent-assisted coiling after SAH was a mean of 1.7 days (median, 1 day; range, 0–11 days). Of 45 patients, 36 (80%) were treated within 24 hours after the onset of SAH.

**Procedural Complications.** Nine patients had thromboembolic complications. In 3 patients with angiographically visible

thrombus on the stent without vessel occlusion and tirofiban treatment, this complication remained without clinical symptoms (Fig 2). In 1 patient with an anterior communicating artery aneurysm, thrombus occluded the middle cerebral artery, mechanical thrombectomy was successful, and the outcome was good.

In 3 patients with visible in-stent thrombus, infarctions developed despite tirofiban treatment (Fig 3). One patient with a basilar tip aneurysm developed an infarction in the posterior cerebral artery after the procedure. One patient with a basilar tip aneurysm died of progressive basilar thrombosis during the procedure.

There were no procedural ruptures.

The overall procedure-related complication rate was 11% (5 of 45; 95% CI, 4%–24%).

**Early Rebleed from the Coiled Aneurysm.** Five of 45 patients (11%; 95% CI, 4%–24%) had an early rebleed from the treated aneurysm after 3, 12, 26, 32, and 45 days (Table). Four of these aneurysms seemed completely occluded (Fig 4), and 1 was incompletely occluded. In 4 of 5 patients, this rebleed was fatal; 1 patient had a good outcome (mRS 2). All 5 recurrent hemorrhages were from saccular aneurysms.

**Additional Surgical Procedures.** Ten patients underwent external ventricular drainage, 7 before and 3 after stent-assisted coiling. One patient had an external lumbar drain; and 1, a lumbo-peritoneal drain after coiling. Two patients underwent a decompressive hemicraniectomy. There were no hemorrhagic complications from surgical procedures and no additional clipping after stent-assisted coiling.

**Overall Clinical and Imaging Outcome in Patients with Ruptured Aneurysms.** Immediate postprocedural angiography showed adequate (complete or near-complete) aneurysm occlusion in 42 patients (93%), and incomplete occlusion in 3 (7%).

At 6 months' follow-up, 13 patients (29%) had died (mRS 6): Seven patients died of the sequelae of SAH; 1, of a thromboembolic complication; 4, of a rebleed; and 1, of a traumatic subdural hematoma at 5 months. A good outcome (mRS 0–1)

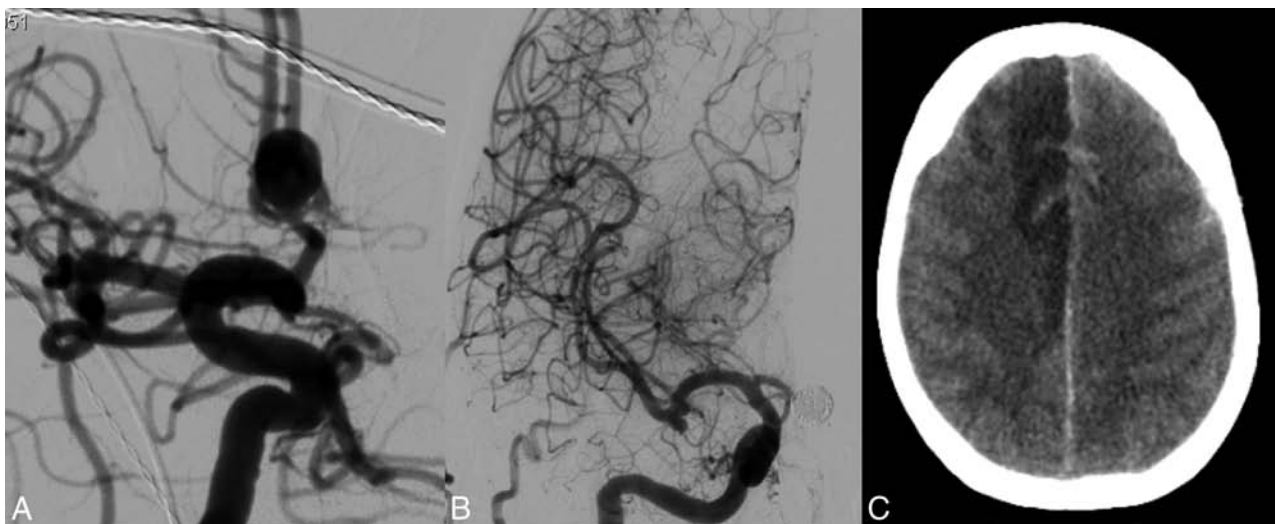


**FIG 3.** Ruptured anterior communicating artery aneurysm in a 64-year-old woman. *A*, Anteroposterior right carotid artery angiogram shows a large anterior communicating artery aneurysm with a relatively wide neck. A stent was placed in the right A1–A2. *B*, After coiling, the right A2 was completely occluded by an in-stent thrombus that did not react to glycoprotein IIb/IIIa antagonist (tirofiban) therapy. *C*, CT scan the next day demonstrates infarction in the right anterior cerebral artery territory.

**Characteristics of 5 patients with an early rebleed after stent-assisted coiling of a ruptured aneurysm**

Patient Sex, Age (yr)	HH Grade	Aneurysm Location and Size	Occlusion Rate	Stent	Timing of Rebleed	Outcome
F, 48	3	PcomA, 4 mm	Complete	Enterprise	45 Days	Death
F, 58	3	SCA, 3 mm	Complete	Enterprise	12 Days	Death
F, 64	4	Carotid tip, 5 mm	Incomplete	Enterprise	32 Days	Death
F, 70	1	Basilar trunk, 30 mm	Complete	LEO	26 Days	Death
F, 54	5	MCA, 11 mm	Complete	LVIS	3 Days	mRS 2

**Note:**—PcomA indicates posterior communicating artery; SCA, superior cerebellar artery; HH, Hunt and Hess.

was achieved in 24 patients (53%), 6 patients had some disability (mRS 2–3), and 2 patients were in a nursing home (mRS 5).

Angiographic (9 patients) or MR imaging follow-up (20 patients) was a mean of 18 months (median, 6 months; range, 6–75 months) in 29 of 30 eligible patients; 1 patient is scheduled for MRA. Reopening of the aneurysm was evident in 6 patients (21%), and these aneurysms were additionally coiled. The other 23 aneurysms remained completely occluded. In 1 asymptomatic patient (3%) with a small carotid tip aneurysm, the A1 showed progressive and severe narrowing by intimal hyperplasia after 1 year (Fig 5).

**Patients with Unruptured Aneurysms**

Forty-six patients with 47 unruptured aneurysms were treated with stent-assisted coiling. There were 34 women (74%) and 12 men (26%) with a mean age of 58.4 years (median, 59 years; range, 27–80 years). Aneurysm size was a mean of 13 mm (median, 11 mm; range, 3–40 mm). Twenty-four aneurysms (51%) were located in the anterior circulation, and 23 (49%), in the posterior circulation.

Thromboembolic complications occurred in 2 patients (4%). One patient responded favorably to tirofiban. The other patient (with a 12-mm basilar tip aneurysm) developed hemiparesis and an infarction in the left thalamus. At 6 months' follow-up, the hemiparesis had improved (outcome mRS of 2). Mortality was 0% (0 of 46; 95% CI, 0%–9.2%), and morbidity was 2.2% (1 of 46;

95% CI, 0.01%–12%). No first-time hemorrhages occurred in 46 patients with 47 aneurysms during 6 months of follow-up.

**Comparison of Complications in Ruptured and Unruptured Aneurysms**

In patients who underwent stent-assisted coiling in the acute period of SAH, the symptomatic complication rate due to this strategy was 22.2% (10 of 45), and in unruptured aneurysms, it was 2.2% (1 of 46). This difference was highly significant ( $P = .001$ ).

**DISCUSSION**

In this study, we found that the complication rate with early adverse events of stent-assisted coiling in patients with ruptured aneurysms was very high and 10 times higher than that in stent-assisted coiling of unruptured aneurysms. The high frequency of early rebleeds (11%, 5 of 45) accounted for the high mortality: In 4 of 5 patients, the rebleed was fatal. In 2 of 5 patients with angiography shortly after the rebleed, the aneurysm seemed completely occluded (Fig 4). Apparently, in these patients, the anticoagulation medication prevented thrombosis of the aneurysm in the days following coiling, despite adequate packing with coils.

SAH in the acute period triggers the coagulation cascade, leading to a hypercoagulable state with a high tendency for clotting or thrombosis. Heparinization in combination with intravenous aspirin did not prevent thrombus formation (on the stent) in all cases: Thromboembolic complications occurred in 20% (9 of 45) with permanent neurologic deficits in 4 and death in 1 patient. Tirofiban was administered in those patients with visible thrombus during the procedure. In our study, 3 of 6 patients with visible thrombus had successful



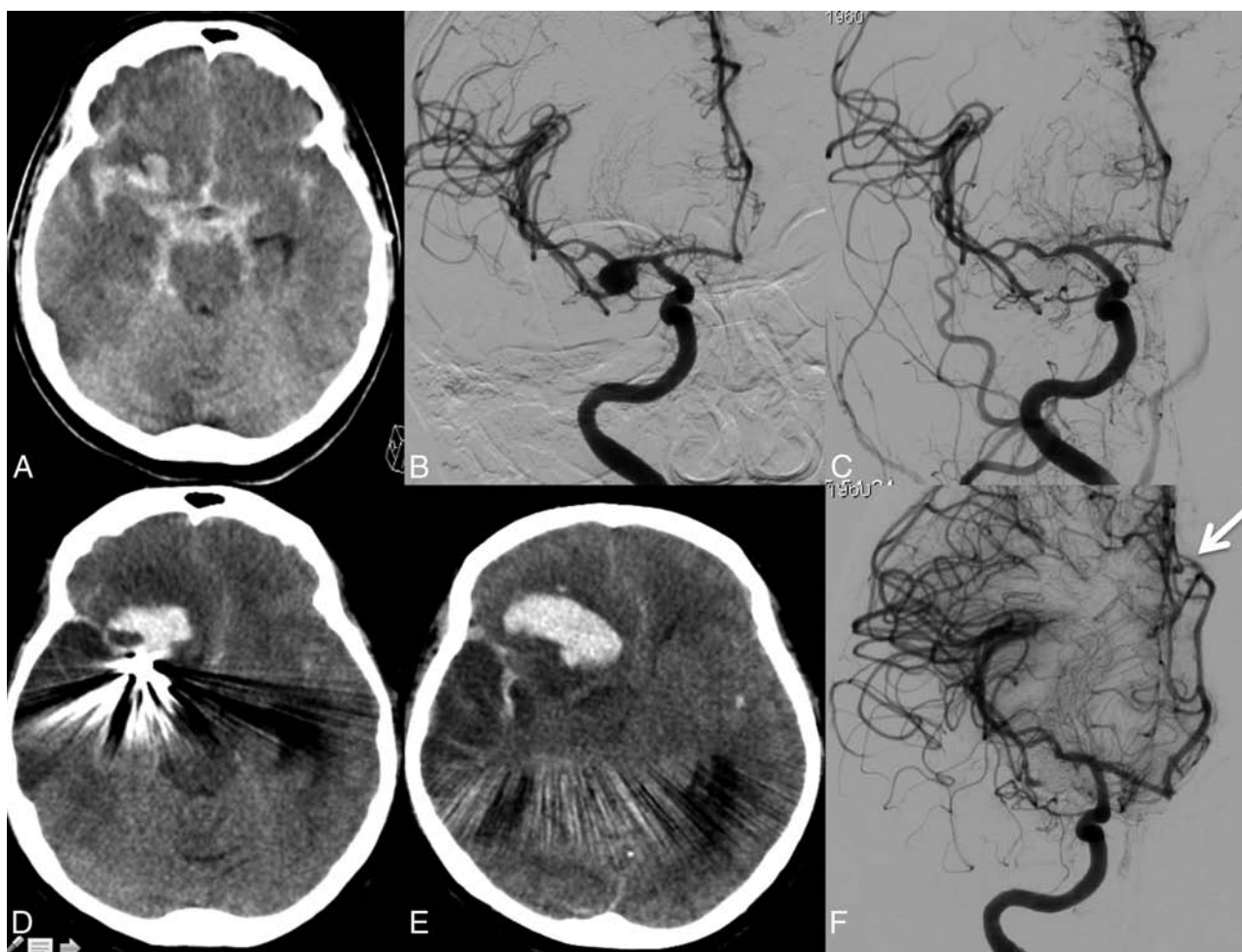


**FIG 4.** Ruptured middle cerebral artery aneurysm in a 54-year-old woman. *A*, CT scan on admission with SAH from the right middle cerebral artery aneurysm. *B*, Anteroposterior carotid artery angiogram shows a wide-neck middle cerebral artery aneurysm. *C*, Angiogram after stent-assisted coiling demonstrates complete aneurysm occlusion. *D* and *E*, CT scan 3 days later reveals recurrent hemorrhage from the aneurysm. *F*, Repeat angiogram the same day confirms complete occlusion of the aneurysm. Note subfalcine herniation of the anterior cerebral artery resulting from a large hematoma (arrow).

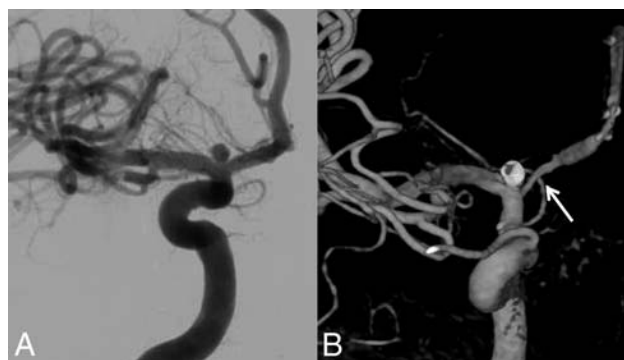


**FIG 5.** Ruptured small carotid tip aneurysm in a 33-year-old man. *A*, Anteroposterior carotid angiogram shows the small carotid tip aneurysm. A coil was placed inside the aneurysm, which seemed unstable, and a stent was subsequently placed across the neck in the A1. *B*, 3D angiogram 1 year later demonstrates severe narrowing of the A1. The patient was asymptomatic.

recanalization after treatment with tirofiban and had a good clinical outcome.

Our disappointing results are in concordance with those in other studies. Chalouhi et al<sup>4</sup> also concluded, from a study of 508

patients, that stent-assisted coiling of ruptured aneurysms was associated with higher complication rates (25% versus 4.7%) and worse outcomes. The morbidity-mortality rate in this study was 13% in patients with a ruptured aneurysm.

Ruptured aneurysms were also independently predictive of complications and poor outcomes in several other studies.<sup>5,6,10</sup> Thus, the safety-efficacy profile of stent-assisted coiling is clearly less favorable in ruptured than in unruptured aneurysms.

Hemorrhagic complications consistently contributed the most to morbidity and mortality rates. In addition to the frequent early rebleeds from the ruptured aneurysms treated with stent-assisted coiling, as seen in our study and others,<sup>1,9,11</sup> fatal hemorrhagic complications may also occur from extraventricular drain placement or even spontaneous remote intracranial hemorrhages.<sup>9,12</sup> Apparently, with dual antiplatelet therapy, coiling does not protect against rebleed and induces hemorrhages from surgical procedures.

In addition to the complications in the periprocedural period, delayed complications may also occur<sup>7,16,17</sup>: In a follow-up study of 213 patients by Mocco et al,<sup>16</sup> 6 percent of patients had delayed (>30 days) angiographic adverse findings, of which, 3% demon-

strated high-grade in-stent stenosis or occlusion. Seven delayed thromboembolic events occurred (3%), along with 2 additional immediate periprocedural events. All 7 delayed events occurred after cessation of dual-antiplatelet therapy. Longer follow-up studies are needed to better understand the long-term effects of stents on the intracranial vasculature.

Our data and those of others indicate that stent-assisted coiling in the acute phase of SAH is associated with many procedural and postprocedural complications, thromboembolic, hemorrhagic, and delayed. In our opinion, this type of therapy and its indications should be reconsidered to significantly decrease the complication rate. We have some suggestions. First, direct surgical clipping can be a valuable and low-risk alternative for coiling in good-grade patients with ruptured wide-neck aneurysms in the anterior circulation. Second, in ruptured wide-neck posterior circulation aneurysms and in poor-grade patients with ruptured wide-neck aneurysms in the anterior circulation, balloon assistance obviates antiplatelet medication and should be preferred over stent placement. Third, the recent introduction of the WEB device<sup>8</sup> is a promising alternative treatment to stent-assisted coiling for wide-neck ruptured aneurysms without the need for antiplatelet medication.

Our study is limited by its absence of randomization between study groups. The results reflect the experience of a single neurovascular center with a specific technique and anticoagulation protocols and may not be readily generalizable to other centers. The individual response to antiplatelet medication was not tested. Because diffusion-weighted imaging was not routinely performed, the incidence of clinically silent infarcts has likely been underestimated. MRA was used in most patients eligible for imaging follow-up. MRA is sufficient to detect reopening, hemorrhage, and infarction but has limitations in detecting in-stent stenosis.

Despite these limitations, this study confirms that stent-assisted coiling in the acute phase in ruptured aneurysms is associated with a high complication rate.

## CONCLUSIONS

In acutely ruptured wide-neck aneurysms treated with stent-assisted coiling, antiplatelet medication without pretreatment does not prevent all thromboembolic complications and, in addition, is a risk factor for hemorrhagic complications in the periprocedural period. Therefore, this treatment should be avoided in favor of other surgical or endovascular treatments without the need for antiplatelet medication.

Disclosures: Charles B. Majoie—UNRELATED: Grants/Grants Pending: Dutch Heart Foundation\*; Payment for Lectures (including service on Speakers Bureaus): Stryker (payment for lectures).\* \*Money paid to the institution.

## REFERENCES

1. Bodily KD, Cloft HJ, Lanzino G, et al. **Stent-assisted coiling in acutely ruptured intracranial aneurysms: a qualitative, systematic review of the literature.** *AJNR Am J Neuroradiol* 2011;32:1232–36 CrossRef Medline
2. Shapiro M, Becske T, Sahlein D, et al. **Stent-supported aneurysm coiling: a literature survey of treatment and follow-up.** *AJNR Am J Neuroradiol* 2012;33:159–63 CrossRef Medline
3. Mocco J, Snyder KV, Albuquerque FC, et al. **Treatment of intracranial aneurysms with the Enterprise stent: a multicenter registry.** *J Neurosurg* 2009;110:5–39 CrossRef Medline
4. Chalouhi N, Jabbour P, Singhal S, et al. **Stent-assisted coiling of intracranial aneurysms: predictors of complications, recanalization, and outcome in 508 cases.** *Stroke* 2013;44:1348–53 CrossRef Medline
5. Piotin M, Blanc R, Spelle L, et al. **Stent-assisted coiling of intracranial aneurysms: clinical and angiographic results in 216 consecutive aneurysms.** *Stroke* 2010;41:110–15 CrossRef Medline
6. Wakhloo AK, Linfante I, Silva CF, et al. **Closed-cell stent for coil embolization of intracranial aneurysms: clinical and angiographic results.** *AJNR Am J Neuroradiol* 2012;33:1651–56 CrossRef Medline
7. Biondi A, Janardhan V, Katz JM. **Neuroform stent-assisted coil embolization of wide-necked intracranial aneurysms: strategies in stent deployment and midterm follow-up.** *Neurosurgery* 2007;61:460–68; discussion 468–69 CrossRef Medline
8. Behme D, Berlis A, Weber W. **Woven EndoBridge intrasaccular flow disrupter for the treatment of ruptured and unruptured wide-neck cerebral aneurysms: report of 55 cases.** *AJNR Am J Neuroradiol* 2015;36:1501–06 CrossRef Medline
9. Chung J, Lim YC, Suh SH, et al. **Stent-assisted coil embolization of ruptured wide-necked aneurysms in the acute period: incidence of and risk factors for periprocedural complications.** *J Neurosurg* 2014;121:4–11 CrossRef Medline
10. Tähtinen OI, Vanninen RL, Manninen HI, et al. **Wide-necked intracranial aneurysms: treatment with stent-assisted coil embolization during acute (<72 hours) subarachnoid hemorrhage: experience in 61 consecutive patients.** *Radiology* 2009;253:199–208 CrossRef Medline
11. Amenta PS, Dalyai RT, Kung D, et al. **Stent-assisted coiling of wide-necked aneurysms in the setting of acute subarachnoid hemorrhage: experience in 65 patients.** *Neurosurgery* 2012;70:1415–29; discussion 1429 CrossRef Medline
12. Tumulán LM, Zhang YJ, Cawley CM, et al. **Intracranial hemorrhage associated with stent-assisted coil embolization of cerebral aneurysms: a cautionary report.** *J Neurosurg* 2008;108:1122–29 CrossRef Medline
13. Brinjikji W, Morales-Valero SF, Murad MH, et al. **Rescue treatment of thromboembolic complications during endovascular treatment of cerebral aneurysms: a meta-analysis.** *AJNR Am J Neuroradiol* 2015;36:121–25 CrossRef Medline
14. Ries T, Buhk JK, Kucinski T, et al. **Intravenous administration of acetylsalicylic acid during endovascular treatment of cerebral aneurysms reduces the rate of thromboembolic events.** *Stroke* 2006;37:1816–21 CrossRef Medline
15. Peluso JP, van Rooij WJ, Sluzewski M, et al. **A new self-expandable nitinol stent for the treatment of wide-neck aneurysms: initial clinical experience.** *AJNR Am J Neuroradiol* 2008;29:1405–08 CrossRef Medline
16. Mocco J, Fargen KM, Albuquerque FC, et al. **Delayed thrombosis or stenosis following Enterprise-assisted stent-coiling: is it safe? Mid-term results of the interstate collaboration of Enterprise stent coiling.** *Neurosurgery* 2011;69:908–13; discussion 913–14 CrossRef Medline
17. Fiorella D, Albuquerque FC, Woo H. **Neuroform in-stent stenosis: incidence, natural history, and treatment strategies.** *Neurosurgery* 2006;59:34–42; discussion 34–42 CrossRef Medline

# Safety and Efficacy of Intravenous Tirofiban as Antiplatelet Premedication for Stent-Assisted Coiling in Acutely Ruptured Intracranial Aneurysms

S. Kim, J.-H. Choi, M. Kang, J.-K. Cha, and J.-T. Huh

## ABSTRACT

**BACKGROUND AND PURPOSE:** Stent-assisted coiling of intracranial aneurysms requires antiplatelet therapy, typically aspirin and clopidogrel to prevent thromboembolic complications. There is a substantial concern that tirofiban may increase the risk of hemorrhage when used as an antiplatelet premedication in ruptured intracranial aneurysms. Our aim was to evaluate the safety and efficacy of intravenous tirofiban administration, instead of oral dual antiplatelet agents, as an antiplatelet premedication for stent-assisted coiling in patients with acutely ruptured intracranial aneurysms.

**MATERIALS AND METHODS:** We conducted a retrospective review of a data base containing a consecutive series of patients who underwent stent-assisted coiling for acutely ruptured intracranial aneurysms between March 2010 and January 2015. Intravenous tirofiban was administered to all patients before stent-assisted coiling, instead of premedication with loading doses of aspirin or clopidogrel.

**RESULTS:** Forty patients with 41 aneurysms received intravenous tirofiban and underwent stent-assisted coiling. None of the patients had a newly developed intracerebral hemorrhage, subarachnoid hemorrhage, or intraventricular hemorrhage. Intraprocedural aneurysmal rupture occurred in 2 patients (5%). Cerebral infarction developed in 2 patients (5%). Ventriculostomy-related hemorrhage was seen in 2 of 10 patients in whom ventriculostomy was performed before or after coiling. Thirty-four (85%) patients had a good outcome (Glasgow Outcome Score of 4 or 5) at the time of discharge, but 1 patient died of cardiac arrest. None of the patients developed thrombocytopenia, retroperitoneal, gastrointestinal, or genitourinary bleeding related to tirofiban administration.

**CONCLUSIONS:** In our study, tirofiban showed a low risk of symptomatic hemorrhagic or thromboembolic complications. Tirofiban may offer a safe and effective alternative as an antiplatelet premedication during stent-assisted coiling of acutely ruptured intracranial aneurysms.

**ABBREVIATIONS:** EVD = external ventricular drain; GOS = Glasgow Outcome Score; HH = Hunt and Hess

Results from the International Subarachnoid Aneurysm Trial showed that the endovascular management of intracranial aneurysm is a safe, effective, and sometimes preferable treatment option.<sup>1</sup> However, endovascular treatment of ruptured wide-neck aneurysms is still a challenge to neurointerventionalists because of the controversy surrounding the use of stent placement as an adjuvant therapy for the coiling of acutely ruptured aneurysms, due to the need for antiplatelet

medications. Stent-assisted procedures are particularly prone to thromboembolic complications, with a reported rate of thromboembolic events of 7%–15% during stent-assisted coiling.<sup>2–4</sup> Therefore, there is a need for preoperative antiplatelet therapy with optimal anticoagulation during the procedures, even with subarachnoid hemorrhage. However, there is no consensus about when and how patients should be loaded with antiplatelet medication before the procedure.

Glycoprotein IIb/IIIa antagonists have attracted attention for the prevention or treatment of thromboembolism during coiling of intracranial aneurysms,<sup>5–7</sup> but the increased risk of intracranial hemorrhage following glycoprotein IIb/IIIa inhibition remains a substantial concern. Moreover, the safety and efficacy data regarding the use of tirofiban in endovascular aneurysm treatment are lacking.

The objective of our study was to evaluate the safety and efficacy of intravenous tirofiban, instead of clopidogrel and aspirin, as an antiplatelet premedication for stent-assisted coiling in patients with acutely ruptured intracranial aneurysms.

Received June 17, 2015; accepted after revision August 13.

From the Departments of Radiology (S.K., M.K.), Neurosurgery (J.-H.C., J.-T.H.), and Neurology (J.-K.C.), Busan-Ulsan Regional Cardio-Cerebrovascular Disease Center, Dong-A University Hospital, Busan, Republic of Korea.

Sanghyeon Kim and Jae-Hyung Choi are co-first authors.

This work was supported by the Dong-A University Research Fund.

Please address correspondence to Myongjin Kang, MD, Department of Radiology, Busan-Ulsan Regional Cardio-Cerebrovascular Disease Center, Dong-A University Hospital, 26 Daesingongwon-ro, Seo-gu, Busan 602-715, Republic of Korea; e-mail: myongjin.kang@gmail.com

<http://dx.doi.org/10.3174/ajnr.A4551>

## MATERIALS AND METHODS

### Patients

We conducted a retrospective review of a neurointerventional data base containing data collected from a consecutive series of patients who underwent stent-assisted coiling of acutely ruptured intracranial aneurysms between March 2010 and January 2015. SAH was diagnosed by using noncontrast brain CT.

The clinical severity of SAH was assessed by using the Hunt and Hess (HH) grading system, and the radiographic grade was classified by using the Fisher grade. Clinical outcomes were assessed at discharge by using the Glasgow Outcome Score (GOS) and classified as follows: 1) dead; 2) vegetative state; 3) severely disabled; 4) moderately disabled; and 5) mildly or not disabled. A GOS of  $\geq 4$  was considered a good clinical outcome. Medical charts were also reviewed to determine clinical or subclinical worsening of radiologic findings after the procedures and to evaluate any possible systemic complications related to tirofiban therapy such as retroperitoneal, gastrointestinal, or genitourinary bleeding and thrombocytopenia.

### Procedures

The decision to use stent-assisted coiling was based on aneurysm morphology, such as a wide-neck aneurysm, defined by a fundus-to-neck ratio of less  $<2$ , a neck diameter of  $\geq 4$  mm, or the need for stent placement after intraprocedural coil prolapse. All procedures were performed with written informed consent. In patients with SAH, the diagnostic angiogram and the coiling procedure were performed on the day of admission. All patients underwent endovascular treatment during a single session under general anesthesia.

Despite the use of aggressive intraoperative antiplatelet therapy, angiographic catheters are contact activators of the coagulation cascade and are significant sources of thromboembolic complications.<sup>8</sup> Thus, to prevent this complication, a solution of 5000 IU of heparin in 1000 mL of 0.9% normal saline was administered continuously through the guiding catheter.

Intravenous tirofiban was administered to all patients, instead of premedication with loading doses of aspirin or clopidogrel, before stent-assisted coiling. The intravenous tirofiban infusion was initiated only after confirming that contrast was not filling the dome (presumed rupture site) of the aneurysm. Patients received a 0.4- $\mu$ g/kg/min loading dose of tirofiban for 30 minutes followed by a 0.10- $\mu$ g/kg/min maintenance infusion. A loading dose of clopidogrel and aspirin (300 mg each) was administered after the tirofiban maintenance infusion, followed by daily doses of 75 mg/day of clopidogrel for 6 months and 100 mg/day of aspirin indefinitely.

We used the "jailing" technique in all patients. The microcatheter was initially positioned within the aneurysm and then coiled within the aneurysm until contrast was no longer filling the dome of the aneurysm; then tirofiban infusion was initiated. The stent was deployed 15 minutes after the initiation of tirofiban administration, and the aneurysm was packed with more coils after stent deployment. Aneurysms were embolized with a variety of bare platinum coils at the operator's discretion.

Stent-assisted coiling was performed by using a Neuroform stent (Stryker Neurovascular, Kalamazoo, Michigan), Enterprise stent (Codman & Shurtleff, Raynham, Massachusetts), or

**Table 1: Clinical and radiologic characteristics of patients**

Characteristics	No. of Cases (%)
Mean age (yr) (range)	57.3 $\pm$ 10.5 (41–84)
Sex (M/F)	12:28
Hunt and Hess grade	
1	5 (12.5)
2	22 (55)
3	8 (20)
4	5 (12.5)
5	0
Fisher grade	
1	2 (5)
2	10 (25)
3	15 (37.5)
4	13 (32.5)
Clinical outcome (GOS)	
1	1 (2.5)
2	1 (2.5)
3	4 (10)
4	4 (10)
5	30 (75)

Solitaire stent (Covidien, Irvine, California). The choice of stent was made on a case-by-case basis according to the operator's preference, anatomic considerations, and specific clinical situations.

All patients underwent brain CT immediately after the procedure to ascertain any new or worsening SAH or intraparenchymal hemorrhage during the acute phase of tirofiban infusion. An external ventricular drain (EVD) was placed in patients experiencing clinical deterioration, in whom developing hydrocephalus was confirmed by follow-up brain CT. Tirofiban was not stopped during the EVD operation.

Postprocedural hemorrhage and infarction were evaluated with brain CT and/or MR imaging. All patients underwent brain CT immediately after the procedure and were followed up for 7 days. Patients were re-evaluated if their clinical condition worsened during hospitalization, and they underwent additional brain CT and/or MR imaging to determine the cause of their deterioration. Cerebral infarction was evaluated depending on the vascular territory involved and the timing of the appearance of neurologic symptoms. The effect of vasospasm due to SAH was also considered.

## RESULTS

Forty patients with 41 aneurysms underwent stent-assisted coiling and received intravenous tirofiban. Of those, 28 (70%) were women and 12 (30%) were men, with a mean age of 57.3  $\pm$  10.5 years (range, 41–84 years). In terms of clinical severity, 5 (12.5%), 22 (55%), 8 (20%), and 5 (12.5%) patients had HH grades of 1, 2, 3, and 4, respectively. The clinical and radiologic characteristics of patients are summarized in Table 1.

The mean aneurysm size was 5.9  $\pm$  2.9 mm (range, 2–13 mm). The location of the aneurysms was the anterior communicating artery in 17 aneurysms, posterior communicating artery in 11 aneurysms, internal carotid artery in 4 aneurysms, vertebrobasilar artery in 4 aneurysms, middle cerebral artery in 3 aneurysms, and anterior cerebral artery in 2 aneurysms. Solitaire, Neuroform, and Enterprise stents were used in 25 (62.5%), 11, and 4 patients, respectively.



## Complications

None of the patients showed a newly developed intracerebral hemorrhage, SAH, or intraventricular hemorrhage on immediate follow-up brain CT after coiling (Table 2).

Intraprocedural aneurysmal rupture occurred in 2 patients (Fig 1) as a result of coil extrusion during coil insertion, after tirofiban injection and stent deployment in 1 patient and by the high tension of the microcatheter before tirofiban injection in the other. In the former patient, we packed the aneurysm with more coils until the bleeding stopped while maintaining tirofiban administration. In the latter, the aneurysm was packed with more coils until the bleeding stopped, but the coils protruded into the parent artery. Thus, we deployed a stent after tirofiban infusion. These 2 cases showed slight worsening of SAH on a brain CT scan performed immediately after the procedure, but patients were discharged without neurologic deficits.

An EVD was placed in 10 patients. Of those, the EVD was placed before the stent-assisted coiling in 5 patients who showed hydrocephalus in the initial brain CT. Ventriculostomy-related hemorrhage was seen in 2 of 5 patients (Fig 2), but the hemorrhage was small and located along the catheter tract. Further follow-up brain CT demonstrated resolution of the hemorrhage.

EVDs were placed on the same day in the other 5 patients who did not show hydrocephalus on the initial brain CT but developed hydrocephalus after stent-assisted coiling. No surgical difficulties or ventriculostomy-related hemorrhages resulting from an increased bleeding tendency due to tirofiban therapy were observed. Of the 10 patients who had undergone EVD, 1 patient underwent EVD after stent-assisted coiling and required permanent CSF di-

version with a ventriculoperitoneal shunt for persistent hydrocephalus. The patient underwent placement of a ventriculoperitoneal shunt 27 days following stent-assisted coiling. The patient was maintained on dual antiplatelet therapy with aspirin and clopidogrel during perioperative ventriculoperitoneal shunt placement, but no new intracranial hemorrhage was observed.

Infarction developed in 2 patients. One patient was treated with coiling for a right posterior communicating artery aneurysm (Fig 3) and underwent brain MR imaging for evaluation because of mild left-sided weakness on postprocedure day 7. Brain MR imaging showed acute infarction in the posterior limb of the right internal capsule, in the territory of the anterior choroidal artery. The left-sided motor weakness improved, and the GOS score was 5 at discharge. The other patient who was treated for an anterior communicating artery aneurysm experienced infarction in the left frontal lobe confirmed by routine follow-up on a day-7 brain CT scan. However, follow-up angiography did not show in-stent thrombosis or vascular occlusion of anterior cerebral artery. This patient showed no infarction-related neurologic sequelae and was discharged with a GOS of 5.

None of the patients developed thrombocytopenia, retroperitoneal, gastrointestinal, or genitourinary bleeding related to tirofiban therapy. No one had additional hemicraniectomy.

## Outcomes

The mean GOS for patients at the time of discharge was 4.5. The individual GOSs were as follows: 30 (75%), 4 (10%), 4 (10%), and 1 (2.5%); and 1 (2.5%) had GOSs of 5, 4, 3, 2, and 1, respectively. Two patients had a GOS of  $\leq 2$ : One presented with an HH grade 4 SAH and failed to achieve neurologic improvement during hospitalization, and the other died 5 days after coiling from causes unrelated to the procedure, such as cardiac and pulmonary disease.

## DISCUSSION

With the advancement in endovascular devices and techniques, stent-assisted coiling has been shown to be safe and efficacious for wide-neck intracranial aneurysms.<sup>9</sup> However, thromboembolic complications are regarded as a major concern of intracranial

**Table 2: Complications**

Complications	No. of Cases (%)
Hemorrhagic complications	
Newly developed ICH, SAH, or IVH	0 (0)
Intraoperative rupture	2 (5)
Ventriculostomy-related hemorrhage	2 (20) <sup>a</sup>
Infarction	2 (5)

**Note:**—ICH indicates intracerebral hemorrhage; IVH, intraventricular hemorrhage.

<sup>a</sup> Percentages were obtained in relation to the number of patients in whom ventriculostomy was placed before or after coiling ( $n = 10$ ), whereas other complications are over the total number of patients ( $n = 40$ ).



**FIG 1.** A 53-year-old woman presented with a Hunt and Hess grade 1 subarachnoid hemorrhage. A, Digital subtraction angiography shows a wide-neck right posterior communicating artery aneurysm of approximately  $15.49 \times 3.72$  mm. B, Angiography shows contrast extravasations during coil insertion after tirofiban injection and stent deployment. We packed the aneurysm with more coils while maintaining tirofiban. C, Immediate posttreatment angiography shows cessation of contrast extravasations and complete occlusion of the aneurysm.

stent placement. Therefore, given the thrombogenicity of endovascular stents, anticoagulation is recommended in patients undergoing stent-assisted procedures to prevent thromboembolic

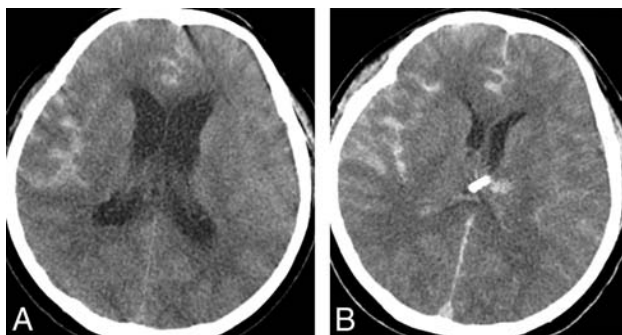


**FIG 2.** A 54-year-old woman presented with a Hunt and Hess grade 4 subarachnoid hemorrhage. **A**, Initial precontrast brain CT scan shows subarachnoid hemorrhage and hydrocephalus. An external ventricular drain was placed before stent-assisted coiling. **B**, Immediate post-treatment precontrast brain CT scan shows asymptomatic ventriculostomy-related hemorrhage. The hemorrhage was small and occurred along the catheter tract. A 7-day follow-up brain CT scan (not shown in Fig 2) shows disappearance of the hemorrhage.

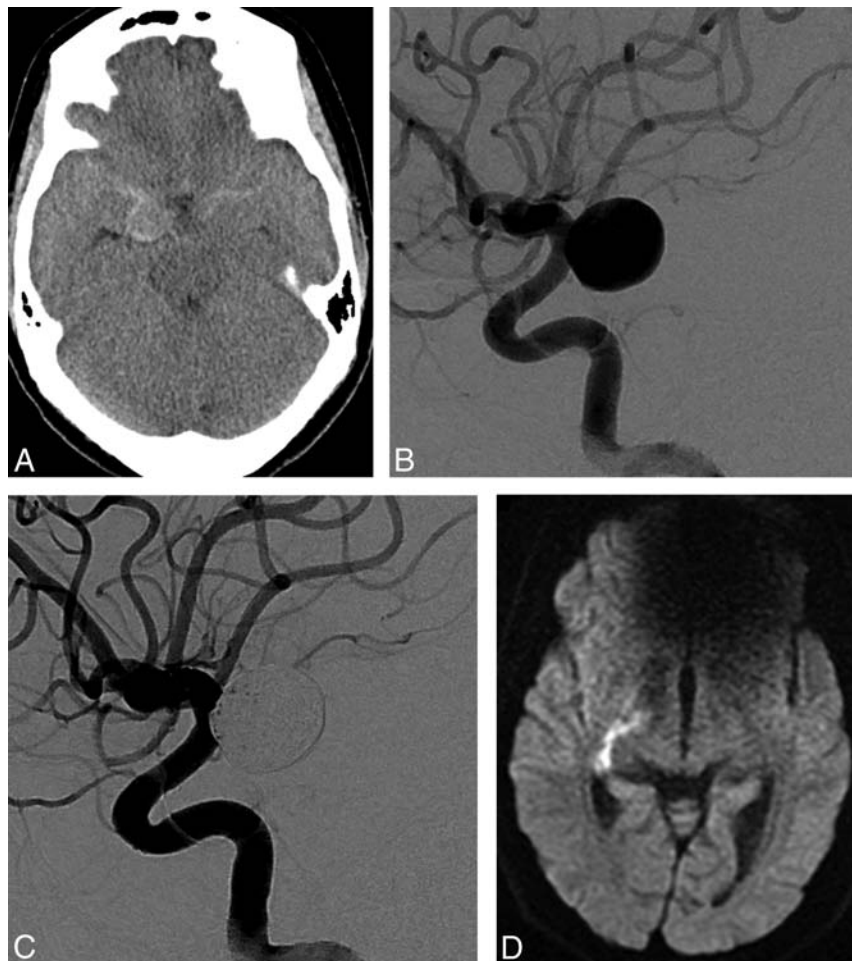


**FIG 3.** A 44-year-old woman presented with a Hunt and Hess grade 2 subarachnoid hemorrhage. **A**, Initial precontrast brain CT scan showed subarachnoid hemorrhage. **B**, Digital subtraction angiography shows a wide-neck right posterior communicating artery aneurysm of approximately  $11.3 \times 12$  mm. **C**, Immediate posttreatment angiography shows complete occlusion of the aneurysm and normal patency of the anterior choroidal artery. **D**, Diffusion-weighted MR imaging shows infarction of the posterior limb of the right internal capsule on postoperative day 7.

events such as in-stent thrombosis. Intra- and postprocedural anticoagulation with heparin and antiplatelet therapy with aspirin or clopidogrel are widely used and reduce thromboembolism rates in patients undergoing coiling for cerebral aneurysms.<sup>10–12</sup> However, antiplatelet drugs take time to reach therapeutic levels. For example, a 600-mg loading dose of clopidogrel provides platelet inhibition of 55%–59% within 4 hours after administration.<sup>13</sup>

In the setting of SAH, the use of a stent is not always anticipated because the decision to place a stent is sometimes made during the procedure and pretreatment with antiplatelet drugs is not always possible. In our center, the diagnostic angiogram and the coiling procedure are performed on the day of admission to minimize the risk of rebleeding in patients with SAH. Hence, the necessity of a stent during coiling cannot be anticipated in these patients; this scenario precludes premedication with aspirin or clopidogrel. Thus, intravenous tirofiban was injected intraprocedurally in all patients to prevent thromboembolic complications, instead of aspirin and clopidogrel, before stent-assisted coiling of acutely ruptured intracranial aneurysms.

Available glycoprotein IIb/IIIa inhibitors include abciximab, tirofiban, and eptifibatide. Abciximab is more commonly used

than tirofiban to treat patients with acute coronary syndrome. However, several studies reported that abciximab and eptifibatide may induce fatal intracerebral hemorrhage.<sup>7,14–16</sup> Moreover, abciximab binds irreversibly to the glycoprotein IIb/IIIa receptor causing platelet-function suppression for almost 48 hours after interruption of the infusion.<sup>17</sup>

Tirofiban acts as a reversible antagonist of fibrinogen by binding to the glycoprotein IIb/IIIa receptor on platelets. Tirofiban has a rapid onset of action (5 minutes).<sup>18</sup> When administered according to the regimen of  $0.4 \mu\text{g/kg/min}$  for 30 minutes followed by a  $0.1 \mu\text{g/kg/min}$  maintenance infusion,  $>90\%$  inhibition of platelet aggregation is attained by the end of the initial 30-minute infusion. Its plasma half-life is 2 hours, and following discontinuation of an infusion of tirofiban,  $0.10 \mu\text{g/kg/min}$ , ex vivo platelet aggregation returns to near baseline in 4–8 hours in approximately 90% of patients.<sup>14,19</sup>

Experience with tirofiban in the neuroendovascular setting has been limited. Chalouhi et al<sup>20</sup> assessed the safety and efficacy of tirofiban in stent-assisted coiling as a prophylactic treatment and as a rescue therapy for thromboembolic events. They reported that the incidence of tirofiban-related hemorrhage and mortality in patients treated with a bolus followed by a maintenance protocol was as high as 18.8% and 12.5%, respec-

tively. However, the study enrolled patients who were presenting with not only ruptured aneurysms but also unruptured aneurysms. Furthermore, in contrast to our study, all patients with aneurysms treated in the setting of SAH were loaded with 600 mg of clopidogrel and 325 mg of aspirin intraprocedurally and infused with tirofiban immediately after stent deployment or placement of the first coil. In this study, we assessed the safety and efficacy of intravenous tirofiban without aspirin and clopidogrel administration as a premedication in stent-assisted coiling of ruptured aneurysms.

In the immediate postrupture period, further bleeding from the aneurysm dome is prevented by a fibrin-platelet plug. On the basis of their pharmacologic properties, glycoprotein IIb/IIIa receptor antagonists may promote breakdown of hydrogen sulfate bonds between platelets, leading to lysis of the platelet-rich clot/thrombus, which then increases the chance of intraprocedural rupture.<sup>21</sup> Furthermore, in the event of iatrogenic aneurysm perforation, the likelihood of a devastating hemorrhage is also increased. In our study, intraprocedural aneurysmal rupture occurred in 2 cases before or after tirofiban infusion and stent deployment. Bleeding was stopped after packing the aneurysm with extra coils. Immediate postprocedural brain CT scans showed slight worsening of the subarachnoid hemorrhage, but patients were discharged without neurologic deficits.

The coexistence of acute hydrocephalus at the time of presentation is an additional complicating factor when considering stent-assisted coiling following SAH. Hemorrhage rates after EVD placement varied widely from 1% to 33%.<sup>22-24</sup> Scholz et al<sup>25</sup> reported a hemorrhage rate of 14.8% in patients who underwent EVD placement after endovascular coil embolization of cerebral aneurysms under anticoagulation or antiplatelet therapy. The risk of ventriculostomy-related hemorrhage is higher in patients with SAH treated with stent-assisted coiling than in those with coiling without a stent.<sup>26</sup>

In this study, an EVD was placed in 10 of 40 patients, with ventriculostomy-related hemorrhage occurring in 2 of 5 patients whose EVD was placed before coiling. The hemorrhage was characterized by small petechial bleeding along the catheter tract, which was <1 cm in diameter, asymptomatic, and temporary. Five patients underwent an additional EVD placement within 1 day without stopping tirofiban after stent-assisted coiling. There were no operational complications or particular difficulties associated with abnormal intraoperative bleeding resulting from the increased bleeding tendency induced by tirofiban therapy, and immediate postoperative brain CTs did not show ventriculostomy-related hemorrhage.

Operations such as EVD placement or decompressive craniectomy are sometimes necessary after coiling, especially in cases of ruptured cerebral aneurysms. With SAH, our experience suggests that tirofiban may not expose patients to a higher risk of hemorrhagic complications, especially those undergoing invasive procedures such as placement of an EVD.

In our study, infarction developed in 2 patients. One patient was admitted with a history of headache and mild left-sided weakness. The patient was treated with stent-assisted coiling for a posterior communicating artery aneurysm, and immediate postprocedural angiography showed no in-stent thrombosis and normal patency of the anterior choroidal artery. Left-sided weakness im-

proved gradually after stent-assisted coiling. Initial brain CT did not show an abnormality in the internal capsule, but a follow-up brain MR imaging 7 days after the procedure revealed infarction in the posterior limb of the internal capsule. Considering the clinical course of left-sided weakness, vasospasm may contribute to infarction. Another possible mechanism is flow disturbance due to the stent. The stent was deployed across the origin of the anterior choroidal artery. Therefore, another possibility as a potential cause is disturbance of blood flow to the anterior choroidal artery by the stent struts. The other patient who was treated for an anterior communicating artery aneurysm developed an infarction in the left frontal lobe. However, follow-up angiography showed normal patency of the intracranial vessel. A possible mechanism is distal emboli into the anterior cerebral artery related to the stent. Additionally, the anterior communicating artery aneurysm had a broad neck, so the exposure of the coil mass alone could contribute to distal emboli into the anterior cerebral artery. Vasospasm of the anterior cerebral artery associated with SAH may be another possible mechanism but is less likely.

Despite infarction and hemorrhagic complications, 34 (85%) patients had a good outcome (GOS of 4 or 5), with only 2 patients (5%) having a GOS of  $\leq 2$  at discharge in this study. In addition, our mortality rate of only 2.5% highlights the potential benefits of tirofiban in stent-assisted coiling of ruptured intracranial aneurysms.

As an alternative to clopidogrel in patients with acute coronary syndromes, the novel platelet P2Y<sub>12</sub> inhibitors, prasugrel and ticagrelor, have been evaluated. Both agents provide stronger and more consistent platelet inhibition than clopidogrel.<sup>27,28</sup> The time to onset of maximal platelet inhibition after administration of loading doses of prasugrel and ticagrelor is 30 minutes and 2 hours, respectively, and both agents are orally administered.<sup>28,29</sup> We believe that the more rapid onset of the antiplatelet effect with tirofiban is more suited to acute intraprocedural decision-making, for example, when intraoperative coil prolapse necessitates the use of a stent. Moreover, intravenous administration of the drug may be more convenient and may decrease the risk of aspiration in patients with decreased consciousness.

In recent years, there has been an increase in the use of flow diverters for intracranial aneurysms. However, because there is no immediate aneurysm occlusion after stent implantation, the need for antiplatelet therapy complicates the use of flow diverters for acute ruptured aneurysms. The treatment of ruptured aneurysms with a flow diverter has been reported, but there are still concerns related to the risk of recurrent SAH during antiplatelet therapy while remodeling is underway.<sup>30,31</sup> Further study regarding a viable acute antiplatelet agent for potential flow-diverter cases is important.

Our study had some limitations. The retrospective and single-arm design of our study may limit it because we did not compare aspirin and clopidogrel with glycoprotein IIb/IIIa receptor antagonists. Therefore, we are unable to determine whether the combination of aspirin and clopidogrel has any clinical advantage over glycoprotein IIb/IIIa receptor antagonists or vice-versa. In addition, the dosage and method of tirofiban administration during coiling of intracranial aneurysms were based on the standard application of the drug for acute coronary syndrome. When we first used tirofiban (in March 2010) for stent-assisted coiling in SAH,



we could not find any articles about tirofiban as a premedication for stent-assisted coiling of acutely ruptured intracranial aneurysms. We, therefore, chose to use the cardiac dose because data on the use of tirofiban at this dose were available. Later, several studies suggested a protocol of 0.1- $\mu$ g/kg/min maintenance infusion without a loading dose for stent placement of intracranial aneurysms.<sup>20,32</sup> The pharmaceutical company Merck & Co. recommended that the infusion should be continued through angiography and for 12–24 hours after angioplasty or atherectomy.<sup>33</sup> Tirofiban infusion was, therefore, continued for 12–24 hours after the procedure in our study. However, a postprocedural bolus and initiation of aspirin and clopidogrel (Plavix) could be a viable alternative method. Further studies to research the optimal dose and application method of the drug are needed.

The small sample size limits some of the conclusions that can be drawn. More data are necessary to determine whether tirofiban increases the risk of hemorrhage after EVD placement.

## CONCLUSIONS

Tirofiban is a fast-acting, fast-deactivated, highly selective non-peptide glycoprotein IIb/IIIa antagonist. In our study, tirofiban showed a low risk of symptomatic hemorrhagic or thromboembolic complications. Thus, tirofiban may offer a safe and effective alternative as an antiplatelet premedication during stent-assisted coiling of acutely ruptured intracranial aneurysms. Larger and randomized trials are needed to further clarify this observation.

## REFERENCES

1. Molyneux AJ, Kerr RS, Yu LM, et al. **International subarachnoid aneurysm trial (ISAT) of neurosurgical clipping versus endovascular coiling in 2143 patients with ruptured intracranial aneurysms: a randomised comparison of effects on survival, dependency, seizures, rebleeding, subgroups, and aneurysm occlusion.** *Lancet* 2005;366:809–17 CrossRef Medline
2. Benitez RP, Silva MT, Klem J, et al. **Endovascular occlusion of wide-necked aneurysms with a new intracranial microstent (Neuroform) and detachable coils.** *Neurosurgery* 2004;54:1359–67; discussion 1368 CrossRef Medline
3. Fiorella D, Albuquerque FC, Han P, et al. **Preliminary experience using the Neuroform stent for the treatment of cerebral aneurysms.** *Neurosurgery* 2004;54:6–16; discussion 16–17 CrossRef Medline
4. Piotin M, Blanc R, Spelle L, et al. **Stent-assisted coiling of intracranial aneurysms: clinical and angiographic results in 216 consecutive aneurysms.** *Stroke* 2010;41:110–15 CrossRef Medline
5. Jeong HW, Jin SC. **Intra-arterial infusion of a glycoprotein IIb/IIIa antagonist for the treatment of thromboembolism during coil embolization of intracranial aneurysm: a comparison of abciximab and tirofiban.** *AJNR Am J Neuroradiol* 2013;34:1621–25 CrossRef Medline
6. Aggour M, Pierot L, Kadziolka K, et al. **Abciximab treatment modalities for thromboembolic events related to aneurysm coiling.** *Neurosurgery* 2010;67(2 suppl operative):503–08 CrossRef Medline
7. Yi HJ, Gupta R, Jovin TG, et al. **Initial experience with the use of intravenous eptifibatide bolus during endovascular treatment of intracranial aneurysms.** *AJNR Am J Neuroradiol* 2006;27:1856–60 Medline
8. Dawson P, Strickland NH. **Thromboembolic phenomena in clinical angiography: role of materials and technique.** *J Vasc Interv Radiol* 1991;2:125–32 CrossRef Medline
9. Pierot L, Spelle L, Vitry F. **Immediate clinical outcome of patients harboring unruptured intracranial aneurysms treated by endovascular approach: results of the ATENA study.** *Stroke* 2008;39:2497–504 CrossRef Medline
10. Bodily KD, Cloft HJ, Lanzino G, et al. **Stent-assisted coiling in acutely ruptured intracranial aneurysms: a qualitative, systematic review of the literature.** *AJNR Am J Neuroradiol* 2011;32:1232–36 CrossRef Medline
11. Meckel S, Singh TP, Undrén P, et al. **Endovascular treatment using predominantly stent-assisted coil embolization and antiplatelet and anticoagulation management of ruptured blood blister-like aneurysms.** *AJNR Am J Neuroradiol* 2011;32:764–71 CrossRef Medline
12. Ries T, Buhk JH, Kucinski T, et al. **Intravenous administration of acetylsalicylic acid during endovascular treatment of cerebral aneurysms reduces the rate of thromboembolic events.** *Stroke* 2006;37:1816–21 CrossRef Medline
13. Müller I, Seyfarth M, Rüdiger S, et al. **Effect of a high loading dose of clopidogrel on platelet function in patients undergoing coronary stent placement.** *Heart* 2001;85:92–93 CrossRef Medline
14. Park JH, Kim JE, Sheen SH, et al. **Intraarterial abciximab for treatment of thromboembolism during coil embolization of intracranial aneurysms: outcome and fatal hemorrhagic complications.** *J Neurosurg* 2008;108:450–57 CrossRef Medline
15. Walsh RD, Barrett KM, Aguilar MI, et al. **Intracranial hemorrhage following neuroendovascular procedures with abciximab is associated with high mortality: a multicenter series.** *Neurocrit Care* 2011;15:85–95 CrossRef Medline
16. Cho YD, Lee JY, Seo JH, et al. **Early recurrent hemorrhage after coil embolization in ruptured intracranial aneurysms.** *Neuroradiology* 2012;54:719–26 CrossRef Medline
17. Tcheng JE, Ellis SG, George BS, et al. **Pharmacodynamics of chimeric glycoprotein IIb/IIIa integrin antiplatelet antibody Fab 7E3 in high-risk coronary angioplasty.** *Circulation* 1994;90:1757–64 CrossRef Medline
18. Dart RC, ed, McCuigan MA, Caravati EM. *Medical Toxicology*. 3rd ed. Philadelphia: Lippincott, Williams & Wilkins; 2003:635–37
19. Highlights of prescribing information: AGGRASTAT (tirofiban hydrochloride). Food and Drug Administration, Silver Spring, Maryland. [http://www.accessdata.fda.gov/drugsatfda\\_docs/label/2013/020912s019s0201bl.pdf](http://www.accessdata.fda.gov/drugsatfda_docs/label/2013/020912s019s0201bl.pdf). Accessed August 7, 2015
20. Chalouhi N, Jabbour P, Kung D, et al. **Safety and efficacy of tirofiban in stent-assisted coil embolization of intracranial aneurysms.** *Neurosurgery* 2012;71:710–14; discussion 714 CrossRef Medline
21. Lodi YM, Latorre JG, El-Zammar Z, et al. **Stent assisted coiling of the ruptured wide necked intracranial aneurysm.** *J Neurointerv Surg* 2012;4:281–86 CrossRef Medline
22. Roitberg BZ, Khan N, Alp MS, et al. **Bedside external ventricular drain placement for the treatment of acute hydrocephalus.** *Br J Neurosurg* 2001;15:324–27 CrossRef Medline
23. Ehtisham A, Taylor S, Bayless L, et al. **Placement of external ventricular drains and intracranial pressure monitors by neurointensivists.** *Neurocrit Care* 2009;10:241–47 CrossRef Medline
24. Binz DD, Toussaint LG 3rd, Friedman JA. **Hemorrhagic complications of ventriculostomy placement: a meta-analysis.** *Neurocrit Care* 2009;10:253–56 CrossRef Medline
25. Scholz C, Hubbe U, Deininger M, et al. **Hemorrhage rates of external ventricular drain (EVD), intracranial pressure gauge (ICP) or combined EVD and ICP gauge placement within 48 h of endovascular coil embolization of cerebral aneurysms.** *Clin Neurol Neurosurg* 2013;115:1399–402 CrossRef Medline
26. Kung DK, Policeni BA, Capuano AW, et al. **Risk of ventriculostomy-related hemorrhage in patients with acutely ruptured aneurysms treated using stent-assisted coiling.** *J Neurosurg* 2011;114:1021–27 CrossRef Medline
27. Wiviott SD, Braunwald E, McCabe CH, et al; TRITON-TIMI 38 Investigators. **Prasugrel versus clopidogrel in patients with acute coronary syndromes.** *N Engl J Med* 2007;357:2001–15 CrossRef Medline
28. Gurbel PA, Bliden KP, Butler K, et al. **Randomized double-blind assessment of the ONSET and OFFSET of the antiplatelet effects of ticagrelor versus clopidogrel in patients with stable coronary artery**



- disease: the ONSET/OFFSET study. *Circulation* 2009;120:2577–85 CrossRef Medline
29. Zhu B, Effron MB, Kulkarni MP, et al. **The onset of inhibition of platelet aggregation with prasugrel compared with clopidogrel loading doses using gatekeeping analysis of integrated clinical pharmacology data.** *J Cardiovasc Pharmacol* 2011;57:317–24 CrossRef Medline
  30. Kulcsár Z, Wetzel SG, Augsburg L, et al. **Effect of flow diversion treatment on very small ruptured aneurysms.** *Neurosurgery* 2010;67:789–93 CrossRef Medline
  31. Aydin K, Arat A, Sencer S, et al. **Treatment of ruptured blood blister-like aneurysms with flow diverter SILK stents.** *J Neurointerv Surg* 2015;7:202–09 CrossRef Medline
  32. Chalouhi N, Zanaty M, Starke R, et al. **O-022: a new protocol for anticoagulation with tirofiban during stenting of intracranial aneurysms.** *J Neurointerv Surg* 2014;6:A11–12 CrossRef
  33. AGGRASTAT (tirofiban hydrochloride). MERCK & CO., INC., West Point, PA. Food and Drug Administration, Silver Spring, Maryland. [http://www.accessdata.fda.gov/drugsatfda\\_docs/label/1998/20913lbl.pdf](http://www.accessdata.fda.gov/drugsatfda_docs/label/1998/20913lbl.pdf). Accessed August 8, 2015

# Applicability of the Sparse Temporal Acquisition Technique in Resting-State Brain Network Analysis

N. Yakunina, T.S. Kim, W.S. Tae, S.S. Kim, and E.C. Nam



## ABSTRACT

**BACKGROUND AND PURPOSE:** The ability of sparse temporal acquisition to minimize the effect of scanner background noise is of utmost importance in auditory fMRI; however, it has considerably lower temporal efficiency and resolution than the conventional continuous acquisition method. The purpose of this study was to determine whether sparse sampling could be applied to resting-state research by comparing its results with those obtained by using continuous acquisition.

**MATERIALS AND METHODS:** We identified resting-state networks by using independent component analysis and measured their functional connectivity strength in 14 healthy subjects who underwent two 6-minute sparse (60 volumes) and continuous (360 volumes) imaging sessions. To account for the sample size difference, an additional continuous dataset was generated by temporally matching the continuous dataset to 60 volumes of the sparse dataset.

**RESULTS:** Consistent resting-state network maps were produced through all 3 datasets. Scanner background noise did not appear to affect the spatial constitution of the networks, whereas a larger sample size influenced it substantially. The strength of the intranetwork connectivity was similar through the 3 datasets.

**CONCLUSIONS:** Our results indicated that continuous acquisition is a recommended technique that should be applied in most of the resting-state studies due to its superior temporal efficiency and increased statistical power. The use of sparse temporal acquisition should be restricted to very particular conditions when continuous scanner noise is unacceptable.

**ABBREVIATIONS:** CA = continuous acquisition; DMN = default mode network; RSN = resting-state network; SBN = scanner background noise; STA = sparse temporal acquisition; ICA = independent component analysis

Resting-state fMRI may be a better alternative for studying mechanisms that underlie certain auditory disorders than stimulation-based studies. For example, in the case of tinnitus, it may be preferred to investigate spontaneous brain activity in the absence of any external auditory stimulation when tinnitus is

more prominent because no acoustic masking or distraction is present. A few recent studies examined resting-state functional connectivity in patients with tinnitus; however, all of the studies used the conventional continuous acquisition (CA) method, which constantly produces scanner background noise (SBN) and may mask tinnitus acoustically or may even cause residual inhibition for several minutes.<sup>1-4</sup>

Sparse temporal acquisition (STA), in contrast, reduces the effect of SBN by using long interacquisition intervals, which allows hemodynamic response induced by acquisition noise to decay completely or close to baseline at the time of the next image acquisition.<sup>5</sup> Practical use of STA in resting-state research has barely been explored. The trade-off required to minimize the SBN effect by using the STA approach is a lower temporal efficiency that allows substantially fewer volumes to be obtained within a limited imaging time, which could affect the analysis of functional maps and functional connectivity. Questions such as whether STA can provide resting-state results comparable with those widely and consistently obtained to date by using CA techniques and, if the results are different, whether the discrepancy is due to

Received November 1, 2014; accepted after revision August 17, 2015.

From the Institute of Medical Science (N.Y.), Department of Radiology (S.S.K.), and Department of Otolaryngology (E.C.N.), Kangwon National University, School of Medicine, Chuncheon, Republic of Korea; and Neuroscience Research Institute (N.Y., W.S.T., S.S.K., E.C.N.) and Department of Otolaryngology (T.S.K.), Kangwon National University Hospital, Chuncheon, Republic of Korea.

This research was supported by the Basic Science Research Program through the National Research Foundation of Korea, funded by the Ministry of Education (2014R1A1A4A01003909).

Please address correspondence to Eui-Cheol Nam, MD, Department of Otolaryngology, School of Medicine, Kangwon National University, One Kangwondaehak-gil, Chuncheon, Kangwon-do, 200-701, Republic of Korea; e-mail: birdynec@kangwon.ac.kr

Indicates open access to non-subscribers at www.ajnr.org

Indicates article with supplemental on-line tables.

Indicates article with supplemental on-line photos.

<http://dx.doi.org/10.3174/ajnr.A4554>

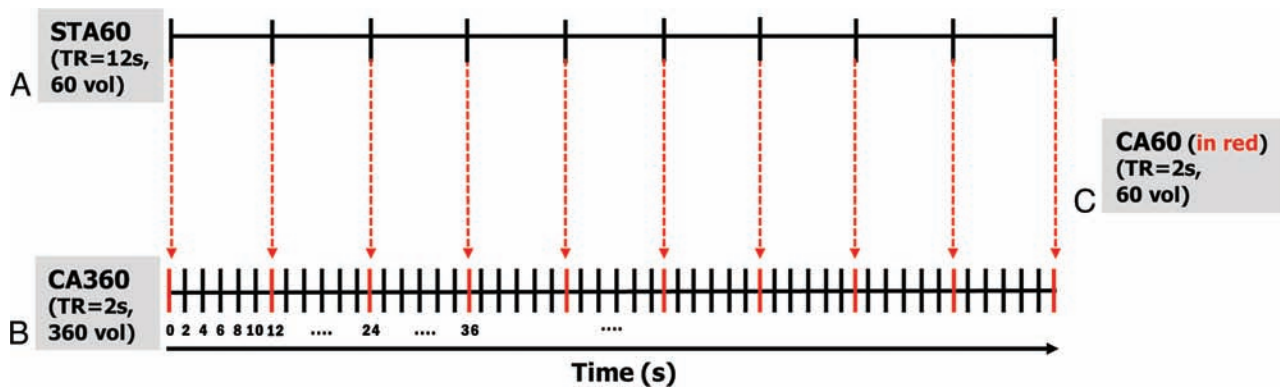


**FIG 1.** Construction of sparse and continuous image acquisition datasets. A, STA (STA60) design. Sixty images were acquired every 12 seconds. B, CA (CA360) design. Three-hundred and sixty images were acquired every 2 seconds. C, CA60 design. The number of volumes in the CA360 data set was matched with the STA60 dataset by selecting every sixth image that corresponded in time to the STA60 acquisitions (CA60; marked with red arrows).

the SBN effect or differences in sample size between the 2 acquisition methods, remain unanswered.

In this study, we separated the effects of SBN and sample-size differences when comparing the STA and CA techniques. Specifically, we compared resting-state networks (RSNs) obtained by the 2 acquisition methods in terms of spatial map constitution and intranetwork functional connectivity strength to establish the applicability of STA to fMRI studies that explore auditory pathophysiology related to alterations in the brain resting state, such as tinnitus or other forms of auditory hyperactivity, in which the noisy environment of CA is unacceptable.

## MATERIALS AND METHODS

### Subjects

This study was approved by the institutional review board of Kangwon National University Hospital. All the subjects gave written informed consent before participation in this study. Fourteen healthy subjects (mean age,  $30.6 \pm 4.7$  years; all right-handed; 8 men) with normal hearing ( $<20$  dB hearing level in a standard audiometric frequency range of 250–8000 Hz) participated in the study. The subjects had no known auditory, neurologic, or neuropsychologic disorders. Before the fMRI session, all the subjects underwent pure-tone audiometry and were examined for loudness discomfort level and dynamic range.

### Data Acquisition

Imaging was performed by using a 3T MR imaging scanner (Achieva TX; Philips Healthcare, Best, the Netherlands) with a 32-channel SENSE head coil. Coronal 3D T1-weighted high-resolution structural images of the whole brain were acquired for anatomic orientation (TR, 9.8 milliseconds; TE, 4.8 milliseconds; flip angle,  $8^\circ$ ; section thickness, 1.0 mm; matrix,  $256 \times 256 \times 195$ ; FOV,  $220 \times 220$  mm; voxel size,  $0.94 \times 0.94$  mm). T2\*-weighted functional images were acquired by using a gradient EPI sequence (30 oblique coronal sections; TE, 35 milliseconds; flip angle,  $90^\circ$ ; section thickness, 5 mm, with a 1-mm gap; matrix,  $80 \times 80$ ; FOV,  $220 \times 220$  mm; voxel size,  $2.75 \times 2.75$  mm). The 19th anterior-most section was positioned to intersect the inferior colliculi and the cochlear nuclei in the brain stem. Each subject underwent four 6-minute resting-state runs: 2 continuous (TR, 2 seconds; 180 volumes per run; acquisition time, 1.88 seconds; no silent gap between

acquisitions) and 2 sparse (TR, 12 seconds; 30 volumes per run; acquisition time, 1.88 seconds; functional acquisitions separated by approximately 10-second silent periods free of scanner noise). The subjects were instructed to rest quietly with their eyes closed. The subjects wore a protective headset that helped to diminish SBN from the original level of 115 dB sound pressure level to 95 dB sound pressure level. The scanner coolant pump was turned off during imaging to further reduce the ambient noise level.

### Data Preprocessing

Preprocessing was performed by using the SPM12 software package (<http://www.fil.ion.ucl.ac.uk/spm/software/spm12>) in the Matlab 7.8 programming environment (MathWorks, Natick, Massachusetts). In each run, the functional images were corrected for head motion, coregistered, normalized to the standard Montreal Neurological Institute T1 template, and spatially smoothed with an 8-mm isotropic Gaussian kernel. Section timing correction was not performed because of the discontinuous nature of the STA data.

### Independent Component Analysis

To eliminate the effect of the difference in sample sizes between the STA dataset (60 volumes, labeled STA60) and CA dataset (360 volumes, labeled CA360), a third matched continuous dataset (CA60) was created by selecting 60 volumes of the CA360 set, which corresponded in time to the STA60 dataset volumes (Fig 1). Three pairs of datasets were compared. The STA60 and CA60 datasets were compared to assess any SBN effect, because they had equal numbers of volumes. A comparison of the CA60 and CA360 datasets was performed to reveal the effect of sample size, because they were equal in terms of continuous SBN effect and differed only in sample size. Finally, the STA60 and CA360 datasets were compared directly.

Spatial independent component analysis (ICA) was performed by using the Group ICA of fMRI Toolbox software (GIFT, ver. 2.0a; <http://mialab.mrn.org/software/gift/>).<sup>6</sup> The ICA order of 33, approximately half of the full temporal dimension of the STA60 and CA60 data, was chosen so as not to overfit the model.<sup>7,8</sup> Group ICA was assessed for concatenated STA60-CA60, CA60-CA360, and STA60-CA360 datasets. Independent components were extracted by using the Infomax algorithm. Twenty iterations of ICA were performed by using the ICASSO

algorithm to verify the stability of the components.<sup>9</sup> All individual components were scaled to represent percentage signal change. Group statistical maps of each component were generated by performing a voxelwise 1-sample *t* test on these individual independent component maps and then thresholded at false discovery rate corrected at  $q < 0.05$ .

The resulting group components for each dataset were subsequently visually examined to determine their neural or artifactual nature. Components were considered to be gray matter components (RSN) if they were found in clusters that matched well with particular gray matter structures rather than being diffusely scattered across large regions or found in the periphery.

### **Statistical Comparison of RSN Spatial Maps and Their Characteristics**

To compare the results of individual analyses, a paired *t* test was performed on individual RSN maps of STA60-CA60, CA60-CA360, and STA60-CA360 analyses. T-contrasts of STA60 > CA60 and CA60 > STA60 were performed to explore the effect of SBN; t-contrasts of CA360 > CA60 and CA60 > CA360 were performed to explore the effect of volume number. T-contrasts of STA60 > CA360 and CA360-STA60 were performed to see how the 2 acquisition methods compared directly. Contrast maps were thresholded at the false discovery rate corrected  $q < 0.05$ .

Statistical analyses were performed by using SPSS software (ver. 19.0; IBM, Armonk, New York). The number of voxels, average percentage signal change, and maximum percentage signal change were calculated for each individual RSN of each pair-wise ICA and compared between STA60 and CA60, CA60 and CA360, and STA60 and CA360 by using the Wilcoxon signed rank test with Bonferroni correction for multiple comparisons.

### **Functional Connectivity Analysis**

Intranetwork RSN functional connectivity strength, another measure of compositional robustness, was compared between the 3 dataset pairs. Connectivity was assessed between ROIs placed in major subregions of each RSN from each dataset. Each RSN was divided into spatially nonoverlapping subareas (eg, left/right, frontal/parietal, left (right)/medial), which resulted in several pairs of coupled subregions. The peak voxel of each subarea was used to create ROIs. ROIs were created as spheres of 3-mm radius. Center voxels for ROIs for each dataset pair comparison were chosen as peak voxels of group ICA maps performed on the corresponding concatenated datasets.

Connectivity analysis was performed by using the CONN functional connectivity toolbox, Version 15.0<sup>10</sup>; <http://www.nitrc.org/projects/conn>) with the CompCor method for estimating and removing physiologic and other sources of noise.<sup>11</sup> The individual motion parameters and a linear term for detrending were included as covariates. The residual blood-oxygen level dependent signal was bandpass-filtered over a low-frequency window of interest (0.01–0.1 Hz). For each dataset and for each ROI, time courses were extracted and averaged over all voxels in the ROI. Pearson correlation coefficients were calculated between the time courses of each pair of ROIs for every subject. Correlation coefficients and correlation maps were converted to Fisher *z* scores and compared pair-wise between STA60 and CA60, CA60

and CA360, and STA60 and CA360 by using a Wilcoxon signed rank test with the Bonferroni correction.

### **Frequency Domain Analysis**

To assess the fundamental fluctuation frequency of each RSN from the CA360 dataset and to determine whether it fell within the frequency range covered by STA with its lower sampling rate, a fast Fourier transform was performed on each RSN time course produced by ICA to obtain its frequency power spectrum. Before performing the Fourier transform, a Butterworth high-pass filter was applied to all time courses, with a lower cutoff frequency of 0.01 Hz.

## **RESULTS**

### **Independent Component Analysis**

All independent components of all 3 datasets had very high stability indices (mean STA60-CA60,  $0.948 \pm 0.055$ ; CA60-CA360,  $0.972 \pm 0.01$ ; STA60-CA360,  $0.975 \pm 0.072$ ). Fourteen RSNs were obtained consistently from the 3 concatenated analyses of paired datasets: auditory, 2 default mode networks (DMNs), salience, dorsal and ventral attentional, 2 frontoparietal, 2 sensorimotor, 3 visual, and cerebellar networks. An additional anterolateral sensorimotor network was produced by STA60-CA60 and STA60-CA360 analyses, and a medial visual network was, in addition, found in CA60-CA360 analysis, which made a total of 15 discovered RSNs in all 3 dataset pairs (Fig 2; On-line Table 1).

### **Statistical Comparison of RSN Spatial Maps and Characteristics**

A comparison of the STA60 and CA60 individual spatial maps revealed a larger auditory network in STA60. A comparison of CA60 and CA360 revealed greater salience, right frontoparietal, and 3 visual networks in the CA360 dataset. A comparison of STA60 and CA360 revealed greater posterior and anterior DMN and lateral visual networks in CA360 (On-line Fig 1).

The 3 investigated RSN characteristics (number of voxels, average and maximum percentage signal changes), a comparison of STA60 to CA60 revealed a greater voxel number for the posterior DMN in CA60. In CA60-CA360 comparison, the CA360 dataset consistently displayed significantly greater values than CA60 for several RSNs, including salience, frontoparietal, sensorimotor, and visual networks. A comparison of STA60 with CA360 showed a greater voxel number for the anterior and posterior DMN in CA360 (On-line Table 2).

### **Functional Connectivity Analysis**

Stronger connectivity of the medial sensorimotor network was observed in STA60 compared with CA60; CA360 showed a more robust posterior DMN compared with CA60 and compared with STA60 (Table).

### **Frequency Domain Analysis**

All RSNs obtained from CA360 exhibited dominant frequencies lower than the Nyquist frequency of the STA's sampling rate (0.0417 Hz) (On-line Fig 2). However, some components had frequencies above the Nyquist frequency, with power comparable with that of the dominant frequency (such as salience or medial sensorimotor).



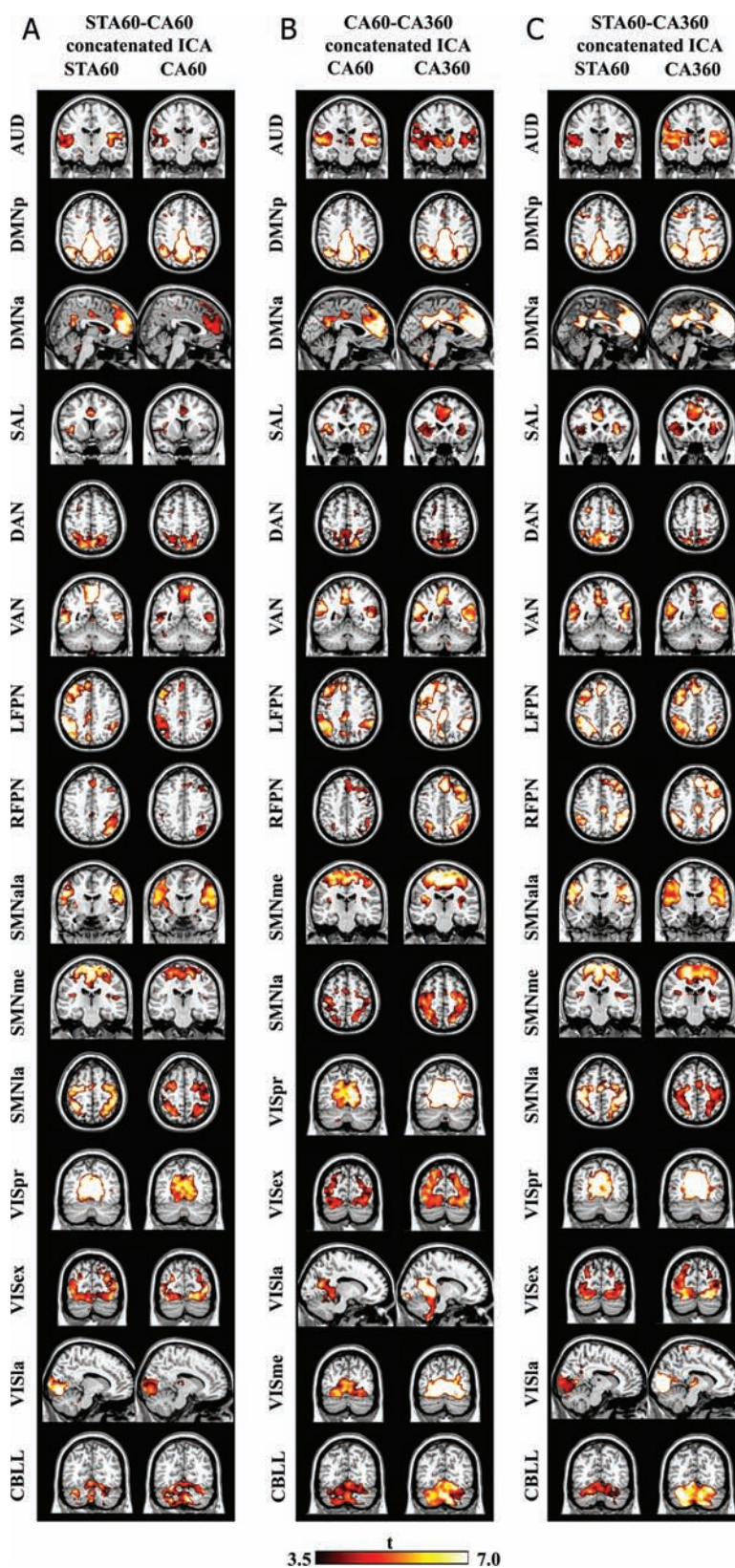


**FIG 2.** ICA results of each dataset pair. A, STA60-CA60 concatenated datasets. B, CA60-CA360 concatenated datasets. C, STA60-CA360 concatenated datasets. A total of 15 networks were identified in each of the analyses; 14 common networks: auditory (AUD), default mode posterior/anterior (DMNp/a), salience (SAL), dorsal/ventral attentional (DAN/VAN), right/left frontoparietal (RFPN/LFPN), sensorimotor medial/lateral (SSMme/la), visual primary/extrastriate/lateral (VISpr/ex/la), and cerebellar (CBLL) networks. In addition, the anterolateral sensorimotor network (SSMala) was identified in STA60-CA60 and STA60-CA360 analyses, and the medial visual network (VISme) was identified in CA60-CA360 analysis. Spatial maps are presented on the most representative section according to a neurologic convention thresholded at false discovery rate corrected  $q < 0.05$ .

# Intranetwork functional connectivity<sup>a</sup>

RSN	Notation	STA60-CA60		CA60-CA360		STA60-CA360	
		STA60	CA60	CA60	CA360	STA60	CA360
Auditory Default mode	AUD_LR	0.17	0.16	0.12	0.25	0.21	0.14
	DMNp_ML	−0.04	0.07	0.18	0.25	0.08	0.11
	DMNp_MR	−0.02	0.04	0.14	0.12	−0.03	0.04
	DMNp_LR	0.20	0.29	0.19	0.26	0.15	0.33 <sup>b</sup>
	DMNa_FP	0.19	0.19	0.18	0.26	0.23	0.25
Salience	SAL_ML	0.13	0.23	0.19	0.15	0.26	0.26
	SAL_MR	0.21	0.23	0.03	0.08	0.21	0.27
	SAL_LR	0.27	0.26	−0.02	−0.02	0.20	0.25
Dorsal/ventral attention	DAN_LR	0.19	0.29	0.20	0.29	0.36	0.36
	VAN_ML	0.27	0.33	0.19	0.24	0.06	0.16
	VAN_MR	0.07	0.12	0.20	0.25	0.22	0.31
	VAN_LR	0.01	0.11	0.09	0.16	0.29	0.37
Frontoparietal	RFPN_FP	0.25	0.11	0.28	0.31	0.09	0.22
	LFPN_FP	−0.06	−0.07	0.04	0.00	0.07	0.17
Sensorimotor	SMNla_LR	0.31	0.13	—	—	0.37	0.27
	SMNme_LR	0.25	0.11	0.27	0.28	0.21	0.23
	SMNla_LR	0.02	−0.01	0.03	0.13	0.28	0.31
	VISpr_LR	0.37	0.41	0.03	0.13	0.68	0.74
Visual	VISex_LR	0.39	0.40	0.02	0.06	0.34	0.28
	VISla_LR	0.27	0.34	0.08	0.15	0.40	0.49
	VISme_LR	—	—	0.39	0.44	—	—
Cerebellum	CBLL_LR	0.01	−0.02	0.05	0.06	0.13	0.04

**Note:**—L indicates left; R, right; M, medial; F, frontal; P, posterior; AUD, auditory; DMNp/a, default mode posterior/anterior; SAL, salience; DAN/VAN, dorsal/ventral attentional; RFPN/LFPN, right/left frontoparietal; SSMLa/me/la, sensorimotor anteromedial/medial/lateral; VISpr/ex/la/me, visual primary/extrastriate/lateral/medial; CBLL, cerebellar networks.

<sup>a</sup> Correlation coefficients between subareas of each RSN were compared for presenting SBN effect (STA60-CA60 comparison), sample size effect (CA60-CA360 comparison), and the direct comparison of the 2 acquisition methods (STA60-CA360 comparison).

<sup>b</sup> Significantly greater than the comparison value of the other dataset ( $P < .05$ , Bonferroni corrected, Wilcoxon signed rank test).

## DISCUSSION

The issue of SBN effects on the resting state of the brain remains poorly explored. To date, 2 reported studies evaluated the SBN effect on the resting state. Rondioni et al<sup>12</sup> used a “silent” EPI sequence, which allowed reduction of SBN by only approximately 12 dB. Although quieter than the original EPI SBN level, this does not seem to provide an adequately “silent” environment suitable for auditory studies. In our study, STA provided approximately 10-second completely silent periods between consecutive image acquisitions, whereas SBN was generated continuously during CA sessions. Another study used STA in comparison with the CA technique for rest and auditory task conditions.<sup>13</sup> Although the researchers used ICA as in this study, there were significant differences: first, we observed and included into the analysis substantially more RSNs for comparison; second, we eliminated the influence of a greater sample size of CA by creating the volume-matched CA60 dataset.

ICA successfully extracted consistent canonical RSNs identified by previous resting-state and task-based studies for each pair of datasets.<sup>14–17</sup> Except for an anterolateral sensorimotor network in STA60-CA60 and STA60-CA360 analyses, and the medial visual network in CA60-CA360 analysis, all identified RSNs matched across the 3 dataset pairs. RSNs identified from all dataset pairs included most of the RSNs provided as templates with the GIFT software<sup>18</sup> and RSNs identified by a multisubject high-order ICA study.<sup>17</sup> All components were highly stable.

A comparison of the STA60 with the CA60 dataset revealed the larger number of voxels for the posterior DMN in CA60 (On-line Table 2). No other differences were found, either in spatial RSN characteristics or in the intranetwork functional connectivity (Table). Therefore, SBN did not seem to affect RSNs significantly.

The CA360 dataset, however, was significantly larger than CA60 in terms of the voxel number and average and maximum percentage signal changes for a number of networks. These results were in line with the comparison of RSN spatial maps, in which the same RSNs had a significantly greater spatial extent in CA360 than those in CA60 (On-line Fig 1). This could indicate that the larger sample size of CA360 had a substantial effect on the spatial distribution of the ICA components. However, the sample size did not appear to have any impact on functional connectivity because no differences between the 2 datasets were found.

Direct comparison of the STA60 with the CA360 dataset revealed a larger number of voxels in the anterior and posterior DMN in CA360 (which agreed with the results of the spatial maps comparison) (On-line Table 2; On-line Fig 1). CA360 also demonstrated stronger functional connectivity for the posterior DMN (Table). Because the effects of SBN and sample size were not separated here, it is unclear how much either was responsible for this difference. Although a larger sample size appeared to have a stronger influence on ICA results after the results of CA60-CA360 comparison, the posterior DMN demonstrated a higher voxel number in CA60 compared with STA60, which means that a larger DMN in CA360 may also be due to the SBN effect. The brain switches into the default mode of ongoing introspective activity when it is not engaged in any immediate attention-demanding task or stimulation.<sup>19,20</sup> In fMRI resting-state studies, there is no active task or stimulus to voluntarily direct attention, which can result in attention being involuntarily drawn to SBN.

Continuous SBN in CA, if recognized as a constant but meaningless and harmless sensory stimulus, would lead to attention system fatigue and send top-down controlling signals to the pe-

ripheral auditory system to discontinue responding.<sup>21</sup> Decreased attention and adaptation (fatigue) to the continuous stimulus (SBN) in CA may result in increased activity in the default mode network. In contrast, the far sparser occurrence of SBN in STA, similar to auditory oddball or novelty stimulation, might evoke an attentional response, which, subsequently, may keep subjects more alert and result in disturbed default mode activity. Note that this might not be the case with task-oriented studies, in which allocation of attentional resources is largely governed by the task at hand, and SBN may not impact attentional and default mode networks in the same manner as in the resting state. Furthermore, although the described mechanism related to regulation of attention by SBN is one possible explanation, other scenarios may exist and should not be ruled out.

Frequency analysis showed that the dominant frequency of all RSNs (which is known to be  $<0.1$  Hz<sup>22,23</sup>) was lower than the Nyquist frequency of the STA's sampling rate (0.0417 Hz), which indicated that the low sampling rate of STA was fast enough to capture low-frequency fluctuations of resting brain networks. However, some components of CA360 had frequencies beyond the Nyquist frequency, which had a comparably strong power. It means that some essential information about temporal dynamics could still be lost in STA, which is a method far inferior to CA for studying temporal behavior of the brain because of its discontinuous nature.

Altogether, SBN did not seem to have any effect on RSN spatial maps and connectivity, except possibly disturbing DMN activity. Thus, CA should be a preferred method of acquisition in general resting-state studies due to its superior temporal resolution, increased statistical power, and less subject-to-subject variability. STA, however, did not appear to have any benefits compared with CA. Its disadvantages, such as increased variability, temporal discontinuity, small sample size, and decreased power, make it a far inferior method to CA. STA may be applicable only in very rare and particular cases, such as when continuous SBN may mask tinnitus or is unbearable by patients with hyperacusis or other auditory disorders.

Regarding the limitations of the current study, it should be noted that SBN may not be the only difference factor between STA60 and CA60 datasets. The 2 datasets may differ in signal-to-noise ratio because the longer interacquisition intervals in STA allow for better T1 recovery and thus greater signal intensity.<sup>5</sup>

## CONCLUSIONS

STA was able to extract the same networks as CA, but it did not display any advantages over the continuous method. SBN did not seem to affect either spatial maps or connectivity of the RSNs. Therefore, apart from very particular cases when continuous SBN is unwanted or unbearable, CA is a recommended acquisition method for most of the resting-state studies, including those of auditory disorders, due to its eminent temporal resolution and high statistical power.

## REFERENCES

- Maudoux A, Lefebvre P, Cabay JE, et al. **Auditory resting-state network connectivity in tinnitus: a functional MRI study.** *PLoS One* 2012;7:e36222 CrossRef Medline
- Ueyama T, Donishi T, Ukai S, et al. **Brain regions responsible for tinnitus distress and loudness: a resting-state fMRI study.** *PLoS One* 2013;8:e67778 CrossRef Medline
- Schmidt SA, Akrofi K, Carpenter-Thompson JR, et al. **Default mode, dorsal attention and auditory resting state networks exhibit differential functional connectivity in tinnitus and hearing loss.** *PLoS One* 2013;8:e76488 CrossRef Medline
- Burton H, Wineland A, Bhattacharya M, et al. **Altered networks in bothersome tinnitus: a functional connectivity study.** *BMC Neurosci* 2012;13:3 CrossRef Medline
- Hall DA, Haggard MP, Akeroyd MA, et al. **"Sparse" temporal sampling in auditory fMRI.** *Hum Brain Mapp* 1999;7:213–23 Medline
- Calhoun VD. **Group ICA of fMRI toolbox (GIFT).** 2004. <http://mialab.mrn.org/software/>. Accessed October 15, 2015.
- Abou Elseoud A, Littow H, Remes J, et al. **Group-ICA model order highlights patterns of functional brain connectivity.** *Front Syst Neurosci* 2011;5:37 CrossRef Medline
- Kiviniemi V, Starck T, Remes J, et al. **Functional segmentation of the brain cortex using high model order group PICA.** *Hum Brain Mapp* 2009;30:3865–86 CrossRef Medline
- Himberg J, Hyvarinen A. **Icasso: software for investigating the reliability of ICA estimates by clustering and visualization.** In: *Proceedings of the IEEE 13th Workshop on Neural Network for Signal Processing*, Toulouse, France, May 17–19, 2003: 259–68
- Whitfield-Gabrieli S, Nieto-Castanon A. **Conn: a functional connectivity toolbox for correlated and anticorrelated brain networks.** *Brain Connect* 2012;2:125–41 CrossRef Medline
- Behzadi Y, Restom K, Liao J, et al. **A component based noise correction method (CompCor) for BOLD and perfusion based fMRI.** *Neuroimage* 2007;37:90–101 CrossRef Medline
- Rondinoni C, Amaro E Jr, Cendes F, et al. **Effect of scanner acoustic background noise on strict resting-state fMRI.** *Braz J Med Biol Res* 2013;46:359–67 CrossRef Medline
- Langers DR, van Dijk P. **Robustness of intrinsic connectivity networks in the human brain to the presence of acoustic scanner noise.** *Neuroimage* 2011;55:1617–32 CrossRef Medline
- Beckmann CF, DeLuca M, Devlin JT, et al. **Investigations into resting-state connectivity using independent component analysis.** *Philos Trans R Soc Lond B Biol Sci* 2005;360:1001–13 CrossRef Medline
- Damoiseaux JS, Rombouts SA, Barkhof F, et al. **Consistent resting-state networks across healthy subjects.** *Proc Natl Acad Sci U S A* 2006;103:13848–53 CrossRef Medline
- De Luca M, Beckmann CF, De Stefano N, et al. **fMRI resting state networks define distinct modes of long-distance interactions in the human brain.** *Neuroimage* 2006;29:1359–67 CrossRef Medline
- Allen EA, Erhardt EB, Damaraju E, et al. **A baseline for the multivariate comparison of resting-state networks.** *Front Syst Neurosci* 2011;5:2 CrossRef Medline
- Shirer WR, Ryali S, Rykhlevskaia E, et al. **Decoding subject-driven cognitive states with whole-brain connectivity patterns.** *Cereb Cortex* 2012;22:158–65 CrossRef Medline
- Raichle ME, Snyder AZ. **A default mode of brain function: a brief history of an evolving idea.** *Neuroimage* 2007;37:1083–90; discussion 1097–99 CrossRef Medline
- Buckner RL, Andrews-Hanna JR, Schacter DL. **The brain's default network: anatomy, function, and relevance to disease.** *Ann NY Acad Sci* 2008;1124:1–38 CrossRef Medline
- Guinan JJ Jr. **Cochlear efferent innervation and function.** *Curr Opin Otolaryngol Head Neck Surg* 2010;18:447–53 CrossRef Medline
- Greicius MD, Krasnow B, Reiss AL, et al. **Functional connectivity in the resting brain: a network analysis of the default mode hypothesis.** *Proc Natl Acad Sci U S A* 2003;100:253–58 CrossRef Medline
- Fransson P. **Spontaneous low-frequency BOLD signal fluctuations: an fMRI investigation of the resting-state default mode of brain function hypothesis.** *Hum Brain Mapp* 2005;26:15–29 CrossRef Medline



# Variability of Forebrain Commissures in Callosal Agenesis: A Prenatal MR Imaging Study

C. Cesaretti, M. Nanni, T. Ghi, C. Parazzini, G. Conte, E. Contro, G. Grisolia, and A. Righini

## ABSTRACT

**BACKGROUND AND PURPOSE:** Agenesis of the corpus callosum, even when isolated, may be characterized by anatomic variability. The aim of this study was to describe the types of other forebrain commissures in a large cohort of randomly enrolled fetuses with apparently isolated agenesis of the corpus callosum at prenatal MR imaging.

**MATERIALS AND METHODS:** All fetuses with apparent isolated agenesis of the corpus callosum undergoing prenatal MR imaging from 2004 to 2014, were evaluated for the presence of the anterior or a vestigial hippocampal commissure assessed in consensus by 2 pediatric neuroradiologists.

**RESULTS:** Overall, 62 cases of agenesis of the corpus callosum were retrieved from our data base. In 3/62 fetuses (4.8%), no forebrain commissure was visible at prenatal MR imaging, 23/62 fetuses (37.1%) presented with only the anterior commissure, and 20/62 fetuses (32.3%) showed both the anterior commissure and a residual vestigial hippocampal commissure, whereas in the remaining 16/62 fetuses (25.8%), a hybrid structure merging a residual vestigial hippocampal commissure and a rudiment of the corpus callosum body was detectable. Postnatal MR imaging, when available, confirmed prenatal forebrain commissure findings.

**CONCLUSIONS:** Most fetuses with apparent isolated agenesis of the corpus callosum showed at least 1 forebrain commissure at prenatal MR imaging, and approximately half of fetuses also had a second commissure: a vestigial hippocampal commissure or a hybrid made of a hippocampal commissure and a rudimentary corpus callosum body. Whether such variability is the result of different genotypes and whether it may have any impact on the long-term neurodevelopmental outcome remains to be assessed.

**ABBREVIATIONS:** AC = anterior commissure; ACC = agenesis of the corpus callosum; CC = corpus callosum; GA = gestational age; HC = hippocampal commissure; HS = hybrid structure

The corpus callosum (CC) is the major white matter forebrain commissure. Agenesis of the corpus callosum (ACC) is among the most common congenital brain anomalies, often co-existing with chromosomal or genetic syndromes and other malformations of the central nervous system or extra-CNS location,<sup>1-4</sup> which may negatively impact the neurodevelopmental outcome.<sup>5-7</sup> MR imaging<sup>8,9</sup> has been introduced in prenatal assessment of suspected ACC as a complementary investigation to

sonography, due to its high performance in evaluating the fetal brain structures and detecting associated anomalies that may be overlooked at sonography but may impact the final outcome.

Both prenatal and postnatal MR imaging may accurately depict the brain features accompanying ACC. For example, the presence or absence of Probst bundles has been extensively addressed in the literature.<sup>10-12</sup> On the contrary, the involvement in ACC of the other forebrain commissures, namely the anterior commissure (AC) and the hippocampal commissure (HC), has been poorly investigated and mainly as sporadic imaging reports in the postnatal setting.<sup>8,13</sup> These postnatal reports did not provide consistent data about how the other forebrain commissures are involved in ACC. These reports are not the result of a random case screening; rather, they are a collection of clinical cases.

Consistent visualization of the other forebrain commissures seems feasible at prenatal MR imaging, albeit very poor data are available regarding the forebrain commissures in fetuses with ACC.

Received July 6, 2015; accepted after revision August 7.

From the Radiology and Neuroradiology Department (C.C., C.P., G.C., A.R.), Children's Hospital V. Buzzi, Milan, Italy; Medical Genetics Unit (C.C.), Fondazione Istituto di Ricovero e Cura a Carattere Scientifico Ca' Granda, Ospedale Maggiore Policlinico, Milan, Italy; Fetal Medicine Unit (M.N., T.G., E.C.), S. Orsola-Malpighi Hospital, University of Bologna, Bologna, Italy; Obstetrics and Gynecology Department (M.N., G.G.), Carlo Poma Hospital, Mantova, Italy; Obstetrics Department (T.G.), Ospedale Maggiore, University of Parma, Parma, Italy; and Department of Health Sciences (G.C.), University of Milan, Milan, Italy.

Please address correspondence to Claudia Cesaretti, MD, Radiologia e Neuroradiologia Pediatrica, Ospedale dei Bambini V. Buzzi, Via Castelvetro 32, 20154 Milan, Italy; e-mail: claudia.cesaretti@gmail.com

<http://dx.doi.org/10.3174/ajnr.A4570>



The aim of this study was to describe the types of other forebrain commissures and to assess their frequency in a large cohort of fetuses with apparent isolated ACC on prenatal MR imaging.

## MATERIALS AND METHODS

The MR imaging data base of our tertiary referral center was retrospectively searched for all cases diagnosed antenatally with isolated ACC between 2004 and 2014. All cases that underwent prenatal MR imaging were referred to our hospital after expert neuroultrasonography examination.

Cases were excluded if additional brain or extra-CNS anomalies were antenatally suspected. Because of the remarkable complexity of ACC etiology and the existence of several heterogeneous syndromes under the “umbrella” definition of callosal agenesis, we chose to limit our investigation field to cases without apparent additional CNS or extra-CNS anomalies. Commonly associated findings with ACC were not considered exclusion criteria (ie, ventriculomegaly). Other features that may be frequently associated with ACC in postnatal imaging, such as hippocampal malrotation or anterior cerebral artery variability, could not be considered in our fetal imaging analysis. The relatively low mean gestational age (GA) (26 weeks) of our population prevented us from a detailed evaluation of such findings (ie, in younger fetuses, the hippocampus is still physiologically incompletely rotated).<sup>14</sup>

In the study period, MR imaging was performed on a 1.5T magnet system (Achieva; Philips Healthcare, Best, the Netherlands) with body phased array coils. Standard MR imaging protocol applied to all studies was the following: a T1-weighted fast spin-echo sequence (TR/TE, 300/14 ms; turbo factor, 5; flip angle, 69°; number of signals acquired, 1; matrix, 256 × 256; FOV, 340 mm; section thickness, 5.5 mm; intersection gap, 4 mm; number of sections, 6; acquisition time, 14 seconds) during maternal apnea; a T2-weighted single-shot fast spin-echo sequence (TR/TE, 3000/180 ms; turbo factor, 85; flip angle, 90°; matrix, 256 × 256; FOV, 260 mm; section thickness, 3–4 mm; intersection gap, 0.1 mm; number of sections, 11; acquisition time, 12 seconds); and a balanced fast-field echo sequence, with 2-mm-thick sections especially on the sagittal plane. All women underwent fetal MR imaging without sedation. The acquisition time of fetal scanning ranged between 20 and 30 minutes.

Despite our cases being collected during an entire decade, the single-shot fast spin-echo T2-weighted image quality has been quite constant with time, because, unfortunately, the technology of single-shot *k*-space sampling has not changed significantly since its introduction, not allowing a progression of in-plane spatial resolution.

Two pediatric neuroradiologists with >10 years' experience (A.R. and C.P.) reviewed the MR imaging examination of each fetus, first confirming the absence of other brain anomalies associated with ACC and then assessing the presence or absence of other forebrain commissures.

The following forebrain commissures were assessed in the 2 planes: the AC (defined as a tubularlike structure connecting the 2 hemispheres and located anterior and inferior to the thalamic mass); the HC (defined as any structure connecting the right and left fornical crura of the hippocampus and located anteriorly and at the level of the thalamic mass convexity); and the hybrid struc-

ture (HS; defined as an ovoid vestigial structure resembling a CC remnant located immediately beside the AC, anterior and well-cranial to the thalamic mass convexity). In the group with the HS, a line intersecting the mammillary body and the AC was traced on the midsagittal section to differentiate an HS from a CC genu remnant, according to the method reported by Kier and Truwit.<sup>15</sup>

The presence of an interthalamic adhesion, an interhemispheric structure that connects the thalami, was also assessed.

Because the occurrence of some degree of ventriculomegaly is frequent in isolated ACC, the hypothesis that commissural variability may correlate with different ventricular sizes was tested. In all cases, the diameter of both lateral ventricles was measured on coronal sections through the atrial level. The average of the ventricle diameters was used for statistical analysis.

If the pregnancy was not terminated, the antenatal findings were reassessed after birth by cerebral sonography or MR imaging. Postnatal MR imaging included at least sagittal T1-weighted and axial and coronal T2-weighted sections.

This retrospective study complied with clinical review study guidelines in use in our institution. A specific signed consent form for prenatal MR imaging retrospective studies was obtained from each woman undergoing prenatal MR imaging.

The Mann-Whitney *U* test was used to compare the medians of variables that were not parametric among different groups. The  $\chi^2$  test was used to compare qualitative data among different groups.  $P < .05$  was considered statistically significant. All statistical analyses were performed by using SPSS, Version 18.0 (IBM, Armonk, New York).

## RESULTS

Overall, 62 fetuses (32 males, 30 females; mean gestational age, 26 weeks; range, 20–35 weeks) with an antenatal diagnosis of isolated ACC at prenatal MR imaging were retrieved from our archive, obtained from 61 pregnancies. Two were twin pregnancies, one with both fetuses showing ACC, the other with only 1 fetus affected.

In all 62 fetuses, ACC was confirmed at imaging review as not being associated with other brain anomalies, with the exception of concomitant colpocephaly and ventriculomegaly, which were identified in 35 cases (56.5%).

From the entire study group, 48 live births were registered, whereas pregnancy was electively terminated upon couple request in 14 cases.

In 32/62 cases (51.6%), the karyotype was obtained by an antenatal invasive procedure or postnatal blood sampling: Thirty showed normal chromosomal analysis findings, while in 2 cases, a trisomy 8 mosaicism was detected. Normal findings on array-comparative genomic hybridization analysis were observed in 2 cases showing normal karyotypes.

All cases were divided into 4 groups (Fig 1) according to the presence or absence of other forebrain commissures. Three cases (4.8%) did not show any forebrain commissure (group 1) (Fig 2); 23 cases (37.1%) presented only the AC (group 2) (Fig 3); 20 cases (32.3%) showed an AC and HC (group 3) (Fig 4); and in the remaining 16 cases (25.8%), the AC and an ovoid HS were detected (group 4) (Fig 5). In all 16 cases, the mentioned ovoid HS appeared to be located well posterior to the line

intersecting the mammillary body and the AC on the midsagittal section, thus excluding the possibility of a CC genu remnant, according to the model of Kier and Truwit.<sup>15</sup>

Interthalamic adhesion was not detected in 14/62 fetuses (22%), 9 of group 2, 2 of group 3, and 3 of group 4, without a statistically significant difference in the prevalence among the 4 groups ( $P = .09$ ).

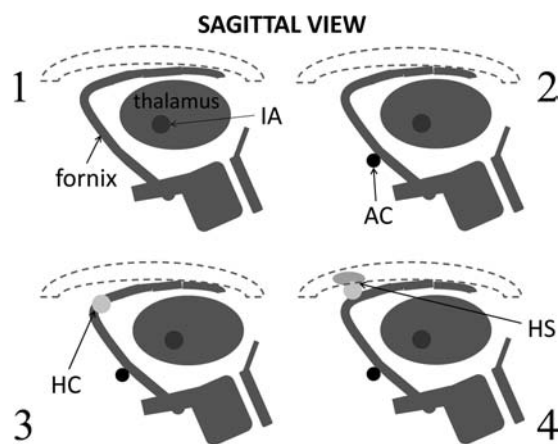


**FIG 1.** A scheme showing 4 sagittal view examples of the corpus callosum putative region, reporting the 4 groups on the basis of forebrain commissures. IA indicates interthalamic adhesion.

Because in our cohort, the major morphologic difference among the 4 groups seemed to be related to the presence or absence of a second commissural structure in addition to the AC itself, we compared group 2 with groups 3 and 4 pooled together in terms of atrial ventricle diameter. The median GA at MR imaging of group 2 (27 weeks; range, 20–34 weeks) and groups 3 and 4 pooled together (23 weeks; range, 20–35 weeks) did not show a statistically significant difference ( $P = .29$ ); the same result ( $P = .12$ ) was obtained comparing the atrial lateral ventricle diameters of group 2 (median, 14 mm; range 5–19 mm) with those of groups 3 and 4 pooled together (median, 11 mm; range, 8–26 mm).

In all neonates, cranial sonography was available and did not show additional brain malformations. A postnatal MR imaging study was available in 22 cases, and in all, the prenatal features related to the commissural structures were confirmed. In 3 cases of group 4, diffusion tensor–based fiber-tracking was obtained and it confirmed that the HS was composed of fibers connecting both the fornical crura and the hemispheric parenchyma (Fig 5).

## DISCUSSION

Our study shows that prenatal MR imaging can identify different classes of isolated ACC on the basis of the presence or absence of other forebrain commissural structures. Because the approach of

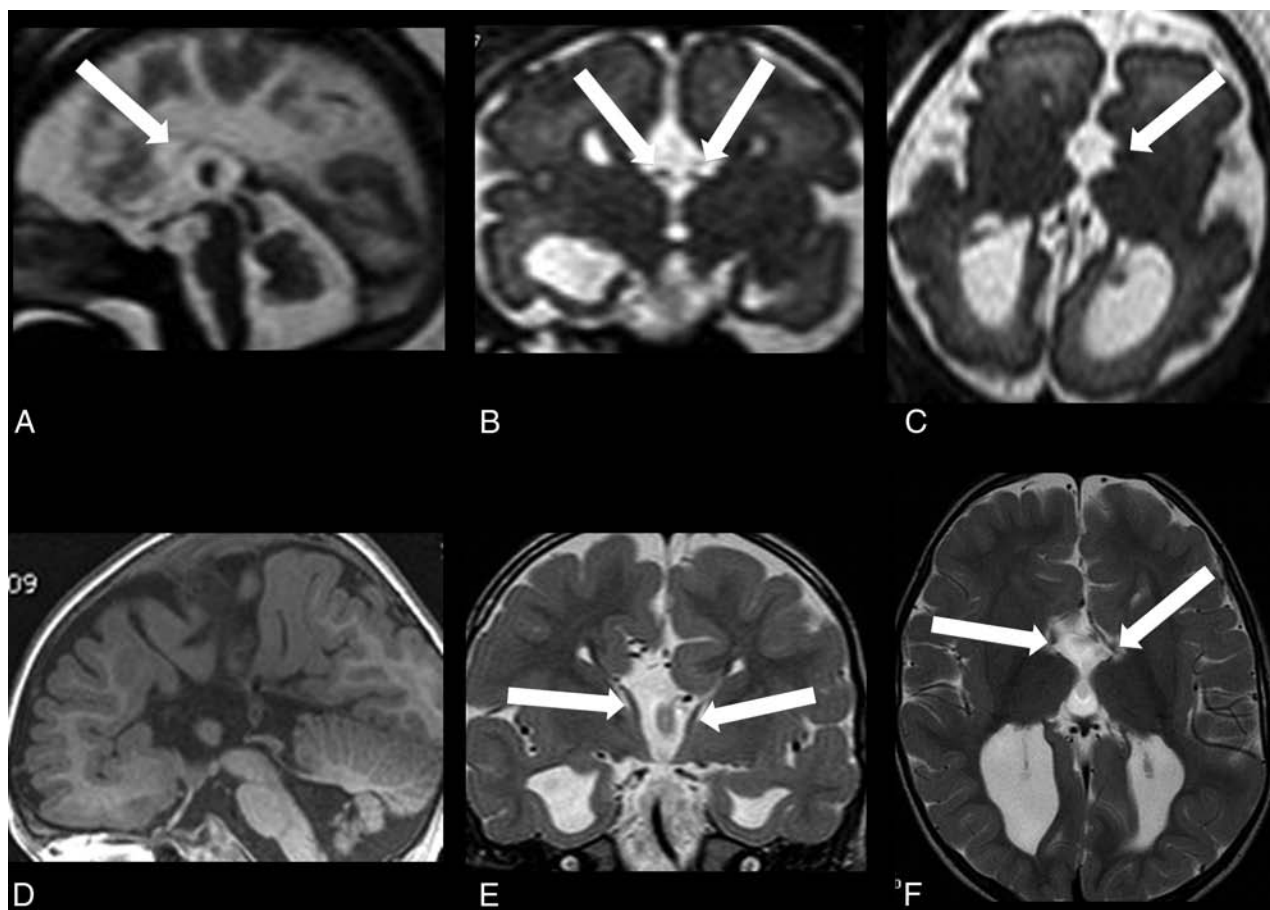


**FIG 2.** Group 1 fetuses. A–C, Sagittal, coronal, and axial single-shot fast spin-echo 3-mm-thick T2-weighted sections from a 32-week-GA study with no visible AC or HC. White arrows show the fornical crura. D–F, Sagittal T1 and coronal and axial T2-weighted sections from a postnatal study confirm the prenatal findings. White arrows show the fornical crura with no HC connecting them.

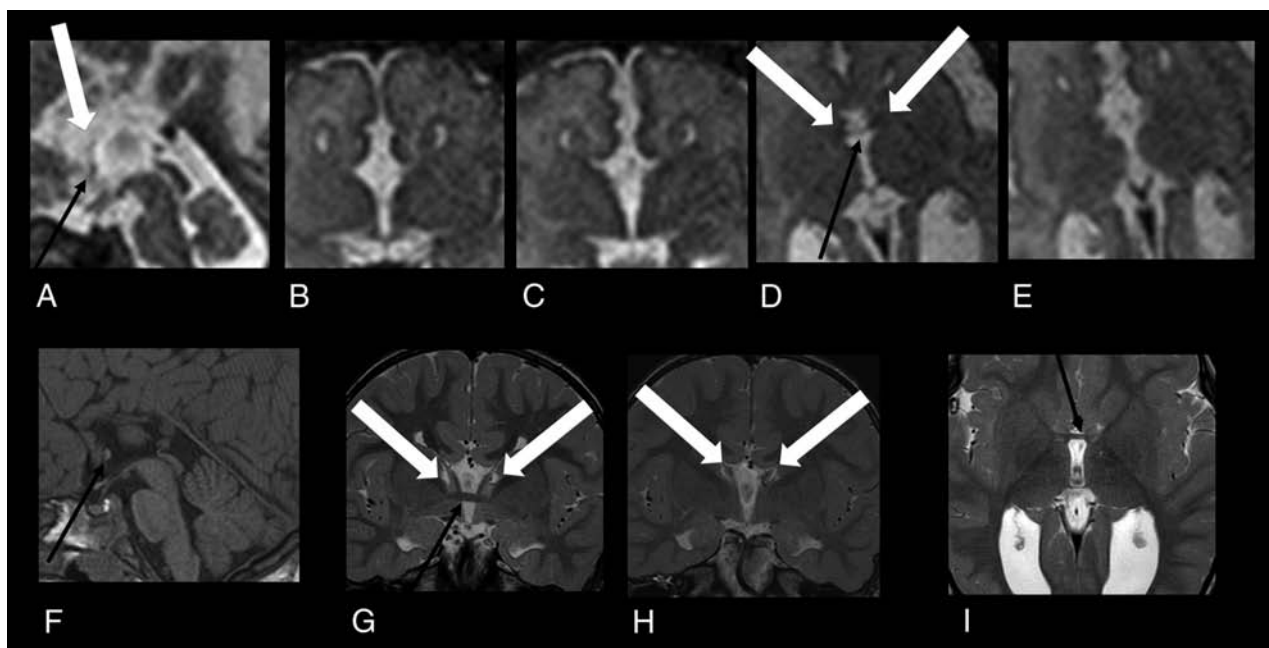


**FIG 3.** Group 2 fetuses. A–E, Sagittal, coronal, and axial single-shot fast spin-echo 3-mm-thick T2-weighted sections from a 30-week-GA study with a visible AC (black arrows) but no HC. White arrows show the fornical crura. F–I, Sagittal T1 and coronal and axial T2-weighted sections from a postnatal study confirm prenatal findings: the presence of only the AC (black arrows). White arrows show the fornical crura with no HC connecting them.

this study was based on randomized recruitment of cases, our data are likely to provide information about the real frequencies of ACC subgroups according to the types of other forebrain commissures.

Commissures are bundles of white matter that cross the midline and connect symmetric structures on the 2 cerebral hemispheres. The CC is the major white matter commissure between the 2 cerebral hemispheres, extending from the frontal lobe anteriorly to above the collicular plate posteriorly. Apart from the CC, there are 2 main interhemispheric forebrain commissures: the AC and the HC, the latter being, in healthy cases, a lamina lying underneath the callosal splenium.<sup>13</sup>

According to the extensive review of Raybaud,<sup>13</sup> there is an intimate relation between the early developing body of the CC and the vestigial HC in the fetal brain, starting from 11–13 weeks of GA. The HC, which is initially located in the anterior third ventricle area, is the archipallian commissure between hemispheres. It assumes tubular (on coronal view) and ovoid (on sagittal view) shapes. Early HC supports the development of the very early body of the CC; the latter is located immediately above the vestigial HC, with interposition of a glial sling. The HC then progressively migrates and elongates toward its final subsplenial position; the body of the CC courses parallel to the HC in its development.

In our series, we identified 4 groups of fetuses with ACC based on the presence or absence of other forebrain commissures: group 1: no forebrain commissure; group 2: AC only; group 3: AC and vestigial HC; and group 4: AC and a HS, with the HS composed of a vestigial HC and an early rudiment of the CC body.

Only 3 of our cases presented without any forebrain commissure (group 1), supporting the hypothesis that this is actually the less common condition with respect to other ACC types.

Among the remaining 3 groups with an AC, a further division was proposed on the basis of the absence (group 2) or presence (groups 3 and 4) of some transverse structures connecting the fornical crura (HC or HS). After matching prenatal and postnatal images, we speculated that the tubular structure joining the hippocampal fornical crura might be a form of vestigial dysmorphic HC that did not complete development toward its final normal laminar shape and its normal location underneath the splenium and posterior third of CC. In this regard, we did not encounter, in our cohort, a single ACC case with a normal laminar-shaped HC. On the other side, the ovoid structure described well above the thalamic mass convexity could represent an HS composed of a very initial underdeveloped CC component (rudiment) merged, in some cases, with a vestigial HC component. In particular, by tracing a line according to the method reported by Kier and Truwit,<sup>15</sup> we demonstrated that this rudimentary structure resides posterior to such a line in all cases of group 4 (Fig 5). This location may suggest that such an abnormal structure is compatible with a very early component of the developing body of the CC, rather than with a genu remnant.

The ovoid structure reported in group 4 has totally different characteristics with respect to the diagonal aberrant oblique tracts reported recently in some cases of CC dysgenesis<sup>11,12</sup>; in our cases, the vestigial structure is clearly orthogonal to the cerebral hemispheres and does not resemble an X-shaped bundle, as confirmed by postnatal fiber-tracking studies (Fig 5).

The interesting work of Kasprian et al,<sup>11</sup> which highlighted the possibility of Probst bundles depicted through fiber-tracking technique during intrauterine life, does not seem to be applicable to study the AC and the vestigial HC because the currently limited diffusion tensor imaging spatial resolution (approximately 2 mm<sup>2</sup>) would not intercept these commissures. Even though our



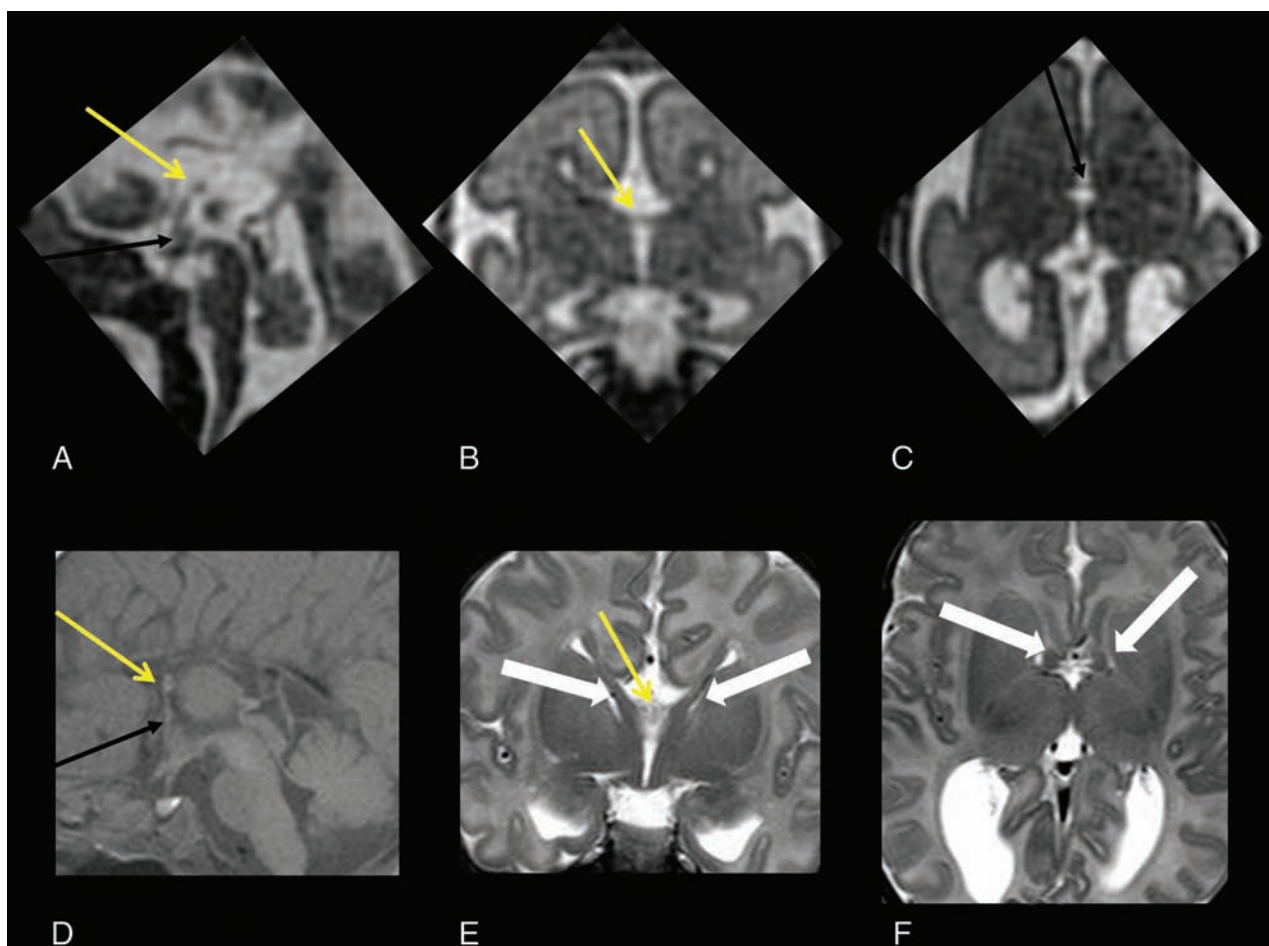


**FIG 4.** Group 3 fetuses. A–C, Sagittal, coronal, and axial single-shot fast spin-echo 3-mm-thick T2-weighted sections from a 27-week-GA study with a visible vestigial HC (yellow arrows). Black arrows show the AC. D–F, Sagittal T1 and coronal and axial T2-weighted sections from the postnatal study confirm the prenatal findings: the presence of the AC (black arrow) and a vestigial HC (yellow arrows), connecting the fornical crura (white arrows).

imaging protocol included sections not thinner than 2 mm, the identification of commissural structures was obtained with confidence by the 2 readers by comparing multiple sets of coronal, axial, and sagittal images, because at least 3 series of sections had been acquired for each plane redundantly. In particular, the AC, which is the thinnest of the commissures, when not clearly appreciable in axial or coronal planes, could be usually visualized on the sagittal plane, taking advantage of the higher in-plane spatial resolution (about 1 mm<sup>2</sup>).

Due to the frequent association of isolated ACC with ventriculomegaly, we further investigated whether this finding could have any relationship with the presence of HC or HS. Our results showed no statistical difference of the atrial width between group 2 and groups 3 and 4 pooled together, thus suggesting that the presence of HC or HS has no impact on the degree of concomitant ventriculomegaly.

Regarding the prevalence of interthalamic adhesion in our cases, we found that our data are very similar to those reported by previous imaging studies, which demonstrated its absence in approximately 22% of healthy subjects.<sup>16</sup> However, we did not find any correlation with commissural variability.

The strength of this study lies in its original content, to our knowledge, being the first time that additional forebrain commis-

ures have been systematically assessed at prenatal MR imaging in a large cohort of fetuses with isolated ACC and enrolled as the result of a prenatal screening.

Very recently, some neurosonographers have demonstrated, in a smaller cohort of fetuses with ACC, that HC identification was feasible by state-of-the-art 3D sonography; however, different from our study, a complete assessment of commissural variability, also including the AC, did not seem achievable.<sup>17</sup>

The major limitation of this study is the lack of postnatal MR imaging in all cases because some neonates were submitted only to cranial sonography and some pregnancies were terminated, with brain deterioration not allowing an accurate postmortem analysis.

The lack of postnatal MR imaging control in all our cases does not allow considering our report as a definite indicator of the diagnostic accuracy of prenatal MR imaging concerning the status of forebrain commissures.

The clinical and prognostic meaning of forebrain commissures variability in isolated ACC needs to be tested by long-term clinical follow-up studies, which may also include global white matter pathway rearrangement evaluation via high-resolution DTI tractography. Very recently, Meoded et al<sup>18</sup> performed a structural connectivity study in children with isolated ACC and



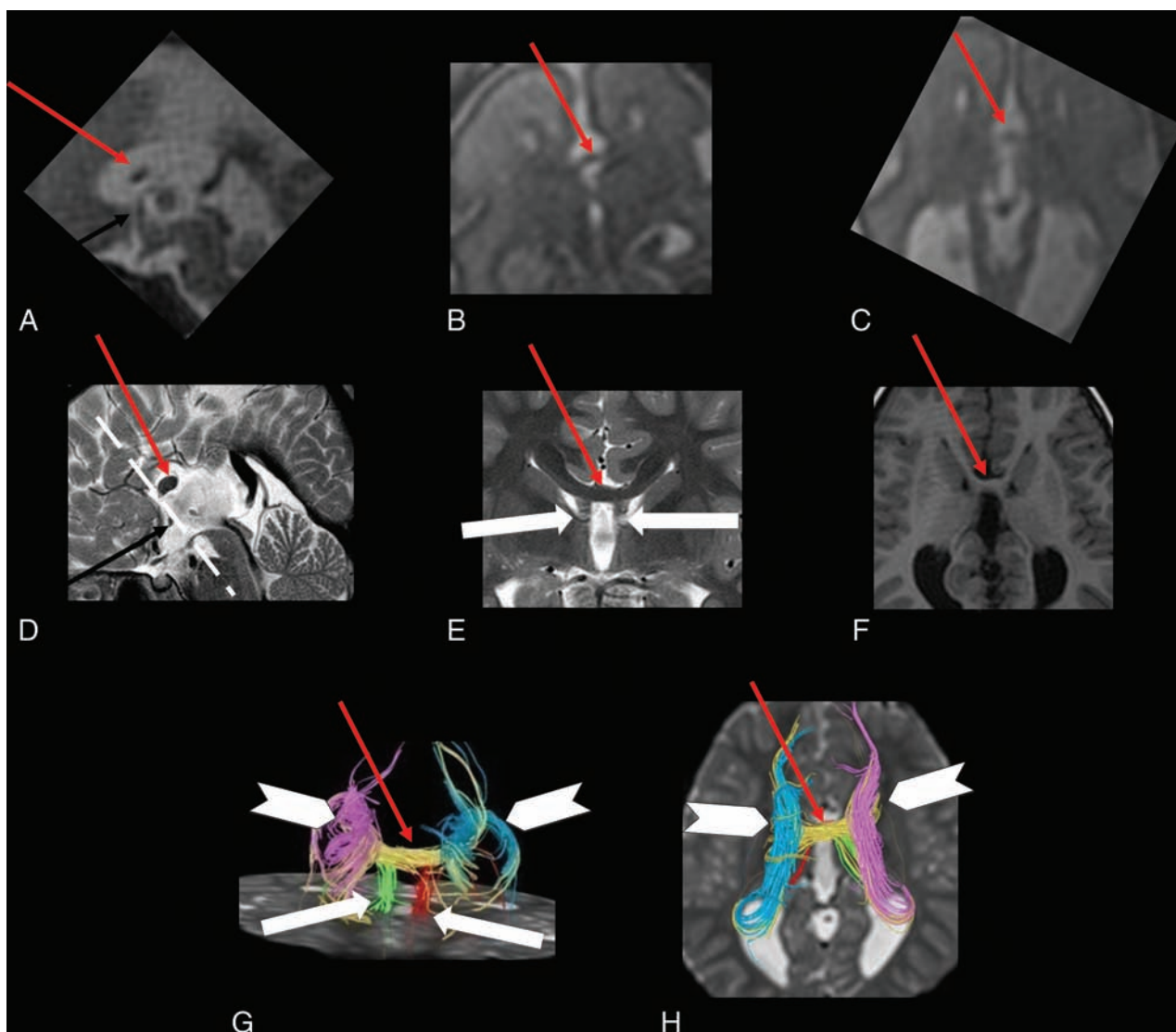


**FIG 5.** Group 4 fetuses. A–C, Sagittal, coronal, and axial single-shot fast spin-echo 3-mm-thick T2-weighted sections from a 25-week-GA study with a visible AC (black arrow) and a putative HS composed of a vestigial HC and an early rudiment of the CC body (red arrows). This putative HS seems to be located slightly more cranially compared with the simple vestigial HC shown in Fig 3. D–F, Sagittal and coronal T2 and axial T1-weighted sections from a postnatal study confirm prenatal findings: the presence of the AC (black arrow) and a putative HS (red arrows). White arrows show the fornical crura; the dotted line in D intersects the mammillary body and the AC, according to the method reported by Kier and Truwit.<sup>15</sup> G and H, Fiber-tracking images from the same study show fibers forming the putative HS (red arrows indicate yellow fibers apparently connecting the cerebral hemispheres and also the fornical crura). Arrowheads indicate Probst bundles (blue and violet fibers), and white arrows show the fornical crura (green and red fibers).

identified hubs in the bilateral insular regions that are connected to each other by the AC, suggesting how brain plasticity may induce alternative pathways for interhemispheric connectivity. However, the clinical impact of these observations is still unknown.

## CONCLUSIONS

Our data demonstrate that prenatal MR imaging may identify different groups of isolated ACC according to the presence or absence of other forebrain commissures, such as the AC, HC, and HS. Most fetuses with apparent isolated ACC showed at least the AC at prenatal MR imaging, and approximately half of these fetuses also showed a second commissure: a vestigial HC or an HS composed of an HC and a rudimental CC body.

Further studies are needed to ascertain whether such variabil-

ity may be associated with different genetic characteristics and if it may have any impact on the long-term neurodevelopmental outcome.

## REFERENCES

1. Grogono JL. Children with agenesis of the corpus callosum. *Dev Med Child Neurol* 1968;10:613–16 Medline
2. Jeret JS, Serur D, Wisniewski K, et al. Frequency of agenesis of the corpus callosum in the developmentally disabled population as determined by computerized tomography. *Pediatr Neurosci* 1985-1986;12:101–03 Medline
3. Glass HC, Shaw GM, Ma C, et al. Agenesis of the corpus callosum in California 1983–2003: a population-based study. *Am J Med Genet A* 2008;146A:2495–500 CrossRef Medline
4. Santo S, D'Antonio F, Homfray T, et al. Counseling in fetal

- medicine: agenesis of the corpus callosum. *Ultrasound Obstet Gynecol* 2012;40:513–21 CrossRef Medline
5. Sotiriadis A, Makrydimas G. **Neurodevelopment after prenatal diagnosis of isolated agenesis of the corpus callosum: an integrative review.** *Am J Obstet Gynecol* 2012;206:337.e1–5 CrossRef Medline
  6. Moutard ML, Kieffer V, Feingold J, et al. **Isolated corpus callosum agenesis: a ten-year follow-up after prenatal diagnosis (how are the children without corpus callosum at 10 years of age?).** *Prenat Diagn* 2012;32:277–83 CrossRef Medline
  7. Noguchi R, Abe K, Hamada H, et al. **Outcomes of patients with prenatally diagnosed agenesis of the corpus callosum in conjunction with ventriculomegaly.** *Arch Gynecol Obstet* 2014;290:237–42 CrossRef Medline
  8. Küker W, Mayrhofer H, Mader I, et al. **Malformations of the midline commissures: MRI findings in different forms of callosal dysgenesis.** *Eur Radiol* 2003;13:598–604 Medline
  9. Manfredi R, Tognolini A, Bruno C, et al. **Agenesis of the corpus callosum in fetuses with mild ventriculomegaly: role of MR imaging.** *Radiol Med* 2010;115:301–12 CrossRef Medline
  10. Tovar-Moll F, Moll J, de Oliveira-Souza R, et al. **Neuroplasticity in human callosal dysgenesis: a diffusion tensor imaging study.** *Cereb Cortex* 2007;17:531–41 Medline
  11. Kasprian G, Brugger PC, Schopf V, et al. **Assessing prenatal white matter connectivity in commissural agenesis.** *Brain* 2013;136:168–79. CrossRef Medline
  12. Edwards TJ, Sherr EH, Barkovich AJ, et al. **Clinical, genetic and imaging findings identify new causes for corpus callosum development syndromes.** *Brain* 2014;137(pt 6):1579–613 CrossRef Medline
  13. Raybaud C. **The corpus callosum, the other great forebrain commissures, and the septum pellucidum: anatomy, development, and malformation.** *Neuroradiology* 2010;52:447–77 CrossRef Medline
  14. Righini A, Zirpoli S, Parazzini C, et al. **Hippocampal infolding angle changes during brain development assessed by prenatal MR imaging.** *AJNR Am J Neuroradiol* 2006;27:2093–97 Medline
  15. Kier EL, Truwit CL. **The normal and abnormal genu of the corpus callosum: an evolutionary, embryologic, anatomic, and MR analysis.** *AJNR Am J Neuroradiol* 1996;17:1631–41 Medline
  16. Nopoulos PC, Rideout D, Crespo-Facorro B, et al. **Sex differences in the absence of massa intermedia in patients with schizophrenia versus healthy controls.** *Schizophr Res* 2001;48:177–85 CrossRef Medline
  17. Contro E, Nanni M, Bellussi F, et al. **The hippocampal commissure: a new finding at prenatal 3D ultrasound in fetuses with isolated complete agenesis of the corpus callosum.** *Prenat Diagn* 2015;35:919–22 CrossRef Medline
  18. Meoded A, Katipally R, Bosemani T, et al. **Structural connectivity analysis reveals abnormal brain connections in agenesis of the corpus callosum in children.** *Eur Radiol* 2015;25:1471–78 CrossRef Medline

# Disorders of Microtubule Function in Neurons: Imaging Correlates

C.A. Mutch, A. Poduri, M. Sahin, B. Barry, C.A. Walsh, and A.J. Barkovich



## ABSTRACT

**BACKGROUND AND PURPOSE:** A number of recent studies have described malformations of cortical development with mutations of components of microtubules and microtubule-associated proteins. Despite examinations of a large number of MRIs, good phenotype-genotype correlations have been elusive. Additionally, most of these studies focused exclusively on cerebral cortical findings. The purpose of this study was to characterize imaging findings associated with disorders of microtubule function.

**MATERIALS AND METHODS:** MRIs from 18 patients with confirmed tubulin mutations (8 *TUBA1A*, 5 *TUBB2B*, and 5 *TUBB3*) and 15 patients with known mutations of the genes encoding microtubule-associated proteins (5 *LIS1*, 4 *DCX*, and 6 *DYNC1H1*) were carefully visually analyzed and compared. Specific note was made of the cortical gyral pattern, basal ganglia, and white matter to assess internal capsular size, cortical thickness, ventricular and cisternal size, and the size and contours of the brain stem, cerebellar hemispheres and vermis, and the corpus callosum of patients with tubulin and microtubule-associated protein gene mutations. Results were determined by unanimous consensus of the authors.

**RESULTS:** All patients had abnormal findings on MR imaging. A large number of patients with tubulin gene mutations were found to have multiple cortical and subcortical abnormalities, including microcephaly, ventriculomegaly, abnormal gyral and sulcal patterns (termed “dysgyria”), a small or absent corpus callosum, and a small pons. All patients with microtubule-associated protein mutations also had abnormal cerebral cortices (predominantly pachygyria and agyria), but fewer subcortical abnormalities were noted.

**CONCLUSIONS:** Comparison of MRIs from patients with known mutations of tubulin genes and microtubule-associated proteins allows the establishment of some early correlations of phenotype with genotype and may assist in identification and diagnosis of these rare disorders.

**ABBREVIATIONS:** MAP = microtubule-associated protein; MT = microtubule

The relationship of lissencephaly and pachygyria to mutations of specific genes, such as *LIS1*,<sup>1</sup> *DCX*,<sup>2</sup> and *ARX*,<sup>3</sup> has been known for >20 years, with some mutations resulting in milder

forms known as double cortex<sup>2</sup> or band heterotopia.<sup>4</sup> Many lissencephalies, in particular lissencephalies associated with significant microcephaly (head circumference of  $\geq 3$  SDs below the mean for age, also called “microlissencephalies”<sup>5</sup>), were not associated with mutations of any of these genes. In the past decade, studies have shown that many lissencephalies (and microlissencephalies) are associated with mutations of genes coding for tubulins, proteins that form the components of microtubules (MTs),<sup>6,7</sup> and microtubule-associated proteins (MAPs)<sup>8</sup> which, interestingly, include *LIS1* and *DCX*. The recent literature has revealed that mutations of genes encoding tubulin and MAPs cause severe developmental delay, epilepsy, and severe anomalies of brain development. Although most mutations of both tubulin and MAP genes cause abnormal sulcation, tubulin gene mutations are associated with severe microcephaly and white matter anomalies, while patients with mutations of MAP genes have small normal brains or mild microcephaly with normal or nearly normal white matter structures. Specific MR imaging phenotype-

Received July 6, 2015; accepted after revision July 7.

From the Department of Radiology and Biomedical Imaging (C.A.M., A.J.B.), University of California, San Francisco, San Francisco, California; Epilepsy Genetics Program (A.P., B.B., C.A.W.), Division of Epilepsy and Clinical Neurophysiology; F.M. Kirby Neurobiology Center (A.P., B.B., C.A.W.), and Division of Genetics and Genomics (B.B., C.A.W.), Department of Medicine, Manton Center for Orphan Disease Research and Howard Hughes Medical Institute, Boston Children's Hospital, Boston, Massachusetts; and Department of Neurology (A.P., M.S., B.B., C.A.W.), Harvard Medical School, Boston, Massachusetts.

This work was funded by the US Department of Health and Human Services—National Institutes of Health—National Institute of Biomedical Imaging and Bioengineering (2T32EB001631-11).

Please address correspondence to James Barkovich, MD, Department of Radiology and Biomedical Imaging, University of California at San Francisco, 505 Parnassus Ave, San Francisco, CA 94143-0628; e-mail: James.Barkovich@ucsf.edu

Indicates open access to non-subscribers at [www.ajnr.org](http://www.ajnr.org)

Indicates article with supplemental on-line photos.

<http://dx.doi.org/10.3174/ajnr.A4552>

genotype correlations have been elusive, despite examinations of large numbers of MR images.<sup>8-10</sup> In this report, we describe the imaging appearances of 18 patients with brain malformations secondary to tubulin mutations and 15 patients with malformations secondary to tubulin-associated protein mutations, including cortical malformations, white matter disorders (corpus callosum, white matter volume, brain stem anomalies), and head size. These data allow establishment of some early correlations of phenotype with genotype.

## MATERIALS AND METHODS

### Imaging

MRIs were retrieved from a large file of imaging studies of >2500 patients with malformations of cortical development that is part of ongoing studies of the genetics of epilepsy and cerebral malformations. The file includes MRIs of patients of all ages who were imaged during the past 30 years, mainly for developmental disorders or epilepsy, and were referred to one of the authors for evaluation; all consented to the use of their studies for research purposes. All patients have mutations identified in specific genes that are thought to be the cause of the malformation. Because these studies were obtained in many different facilities in multiple countries during >25 years, both the MR imaging techniques and the techniques for identifying mutations differed considerably. Most MRIs were obtained at 1.5T, though some recent scans were obtained at 3T. T1WI and T2WI (spin-echo or spoiled gradient-echo in more recent volumetric acquisitions) with section thicknesses ranging from 1 to 3 mm were analyzed. For inclusion, MRIs required 3 orthogonal planes with adequate contrast between the cerebral cortex and (myelinated or unmyelinated) white matter to determine the cortical gyral pattern, basal ganglia, and white matter to visually assess internal capsular presence or absence, cortical thickness (normal, <4 mm), ventricular and cisternal size, and the size and contours of the brain stem, cerebellar hemispheres and vermis, and the corpus callosum.

### Patients

All patients were referred for seizures and developmental anomalies, often associated with microcephaly that was variable in severity. Genetic analyses required that the candidate gene have a logarithm of odds score of  $\geq 3$  or microarray demonstration of abnormal gene expression. Targeted genetic analyses during the past few years revealed 18 patients with confirmed diagnoses of tubulin mutations: 8 with *TUBA1A* mutations, 5 with *TUBB2B* mutations, and 5 with *TUBB3* mutations. No *TUBA8*, *TUBB5*, or *TUBG1* mutations were identified in any of our patients. The MR imaging findings of these patients were carefully analyzed and compared with those of 15 patients with known mutations of the MAP genes *LIS1* (5 patients), *DCX* (4 patients), and *DYNC1H1* (6 patients). Included patients ranged in age from 2 days to 33 years. Although the scans had already been reviewed and findings recorded, all were rereviewed by the authors. Results were then analyzed to determine which imaging features best defined mutations of tubulin and MAP genes, which features overlapped, and which features or combinations of features, if any, allowed specific

diagnoses. Recorded results were determined by unanimous consensus of the authors.

## RESULTS

All patients had abnormal findings on brain MR imaging. In particular, abnormalities of white matter structures/pathways (corpus callosum, internal capsules, and portions of the brain stem), the cerebral cortex (gyral pattern), and the cerebellum (vermis more frequently than hemispheres) were seen in essentially all patients. When the olfactory sulci and bulbs were adequately visualized with coronal images, the sulcal depth and appearance of the bulbs were assessed. Abnormalities of the midbrain tectum were recorded when present.

### Tubulin Mutations

All 18 patients with mutations of tubulin genes had diminished white matter volume, ranging from moderate to severe, associated, in all cases, with microcephaly (by provided clinical history). Ventriculomegaly was present in 8/8 patients with *TUBA1A* mutations, 3/5 patients with *TUBB2B* mutations, and 2/5 patients with *TUBB3* mutations (Table). The degree of enlargement varied considerably, from mild to severe; in more severely affected patients, ventricular enlargement was diffuse (Figs 1 and 2), but in 2 *TUBA1A* mutations, ventriculomegaly was asymmetric (1 left > right, the other right > left). A third patient had colpocephaly with enlarged trigones and occipital horns but normal temporal horns, frontal horns, and ventricular bodies.

All patients had abnormalities of the corpus callosum, dysmorphic or absent in all patients with *TUBA1A* or *TUBB2B* mutations and either dysmorphic (2/5) or abnormally thin (4/5) in patients with *TUBB3* mutations (Figs 1–3 and On-line Fig 3). All patients with tubulin gene mutations also had abnormalities of the basal ganglia, including an enlarged caudate and an absent or diminutive internal capsule dividing the caudate from the putamen, resulting in a fused striatum (Figs 1–3). Additionally, nearly all patients with tubulin gene mutations had a small, often asymmetric brain stem (Table, Fig 2D, and On-line Fig 2) and a small cerebellar vermis; and a number had large midbrain tecta (Figs 2 and 3).

Abnormalities of the cerebral cortex were seen in essentially all patients in this group, ranging from complete agyria to mixtures of agyria and pachygyria to complete “dysgyria” (a term intended to describe a cortex of normal thickness but with an abnormal gyral pattern characterized by abnormalities of sulcal depth or orientation: obliquely oriented sulci directed radially toward the center of the cerebrum and narrow gyri separated by abnormally deep or shallow sulci (Fig 1). Other patients had regions of pachygyria mixed with regions of dysgyria. Of the 5 patients with *TUBB3* mutations, 3 had both dysgyria and pachygyria, with pachygyria located in the Sylvian and supra-Sylvian areas. The cortex in patients with *TUBA1A* mutations ranged from lissencephalic to pachygyric to dysgyric, with pachygyria usually present in the parietal and occipital lobes (Fig 4). Differentiation of regional pachygyria (with a cell sparse zone) from localized band heterotopia was based on the



widths of the gyri and depths of the sulci: For classification, where sulci were deeper than the breadth of the gyri, the diagnosis of band heterotopia was made; and if the sulci were shallower than the breadth of the gyri, pachygyria was diagnosed. Four of the 5 patients with *TUBB3* mutations exhibited dysgyria of varying severity, including 1 patient with both diffuse dysgyria and bifrontal band heterotopia (Fig 2). The fifth patient had nearly normal cerebrocortical morphology. Hypoplastic or absent olfactory bulbs or sulci were noted in 11/16 patients with tubulin mutations (4/6 *TUBA1A*, 3/5 *TUBB2B*, 4/5 *TUBB3*) for which they were adequately evaluated (On-line Fig 1).

#### Features of tubulin and microtubule-associated gene mutations

	Tubulin Mutations			MAP Mutations		
	<i>TUBA1A</i>	<i>TUBB2B</i>	<i>TUBB3</i>	<i>LIS1</i>	<i>DCX</i>	<i>DYNC1H1</i>
Dysmorphic/absent corpus callosum	8/8 <sup>a</sup>	5/5	2/5	5/5 <sup>b</sup>	1/4	6/6 <sup>c</sup>
Thin corpus callosum	4/5	4/5	4/5	0/5	2/4	1/6 <sup>d</sup>
Dysgyric cerebral cortex	4/7 <sup>e</sup>	4/5	5/5	0/5	0/4	0/6
Pachygyric/agyric cerebral cortex	4/7 <sup>e</sup>	0/5	3/5	5/5 <sup>f</sup>	4/4 <sup>g</sup>	6/6 <sup>h</sup>
Small cerebellar vermis	8/8	5/5 <sup>i</sup>	4/5	2/5 <sup>i</sup>	0/4	3/6 <sup>i</sup>
Small cerebellar hemisphere	5/8	1/5	1/5 <sup>j</sup>	0/5	0/4	0/6
Small brain stem	7/8 <sup>k</sup>	5/5 <sup>l</sup>	5/5 <sup>m</sup>	3/5 <sup>n</sup>	0/3 <sup>o</sup>	3/6 <sup>l</sup>
Large tectum	4/8	1/5	1/5	0/5	0/4	0/6
Mild ventriculomegaly	1/8	2/5	0/5	0/5	0/4	2/6
Moderate ventriculomegaly	3/8	1/5	1/5	0/5	0/4	0/6
Severe ventriculomegaly	4/8	0/5	1/5	0/5	0/4	0/6

<sup>a</sup> Corpus callosum absent 3/8.

<sup>b</sup> L-shaped corpus callosum 4/5.

<sup>c</sup> L-shaped corpus callosum 3/6.

<sup>d</sup> Thick corpus callosum 5/6.

<sup>e</sup> In 1 patient, poor gray-white differentiation precludes accurate cortical assessment.

<sup>f</sup> Complete agyria 1/5; posterior agyria and anterior pachygyria 4/5.

<sup>g</sup> Complete agyria 1/4; anterior pachygyria 3/4.

<sup>h</sup> Posterior pachygyria 6/6.

<sup>i</sup> Small anterior vermis in all cases.

<sup>j</sup> Dysmorphic vermis.

<sup>k</sup> Asymmetric 3/8.

<sup>l</sup> Small pons in all cases.

<sup>m</sup> Asymmetric in all cases.

<sup>n</sup> Diffusely thin brain stem 2/5, small pons 1/5.

<sup>o</sup> Brain stem not well-visualized, 1 case.

#### MAP Mutations

Of the 15 patients with mutations of MAPs, the imaging findings were more consistent within groups (Table). Patients with *LIS1* mutations (5 total) had cortical malformations ranging from complete agyria to frontal pachygyria or shallow sulci with nearly normal cortical thickness associated with parietal and occipital pachygyria or agyria. They had anomalies of the corpus callosum, with a small or absent rostrum and inferior genu, normal body, and an unusual, sharp angle at the junction of the body and splenium (Fig 4), with the splenium coursing more caudal than usual (4/5) or a short splenium (1/5). These findings were very similar to the callosal anomaly seen in patients with *DYNC1H1*

mutations (6 total), who also had posterior pachygyria (less severe, overall, than that seen in the patients with *LIS1* mutations, but some cases were indistinguishable by imaging).

Half (3/6) of the patients with *DYNC1H1* mutations had a slightly small anterior cerebellar vermis compared with published norms,<sup>11</sup> compared with 1/5 patients with *LIS1* mutations and no patient with *DCX* mutations. This vermian anomaly and the presence of large caudate heads (found in all 6/6 patients with *DYNC1H1* mutations [Fig 4], but in no [0/5] patients with *LIS1* mutations) were the only consistent differences between patients with *LIS1* and *DYNC1H1* mutations.

The patients with *DCX* mutations had different appearances of the corpus callosum, which were either normal (2/4) or diffusely thin (2/4). The cortex of patients with *DCX* mutations, as has been reported,<sup>12</sup> varied from normal

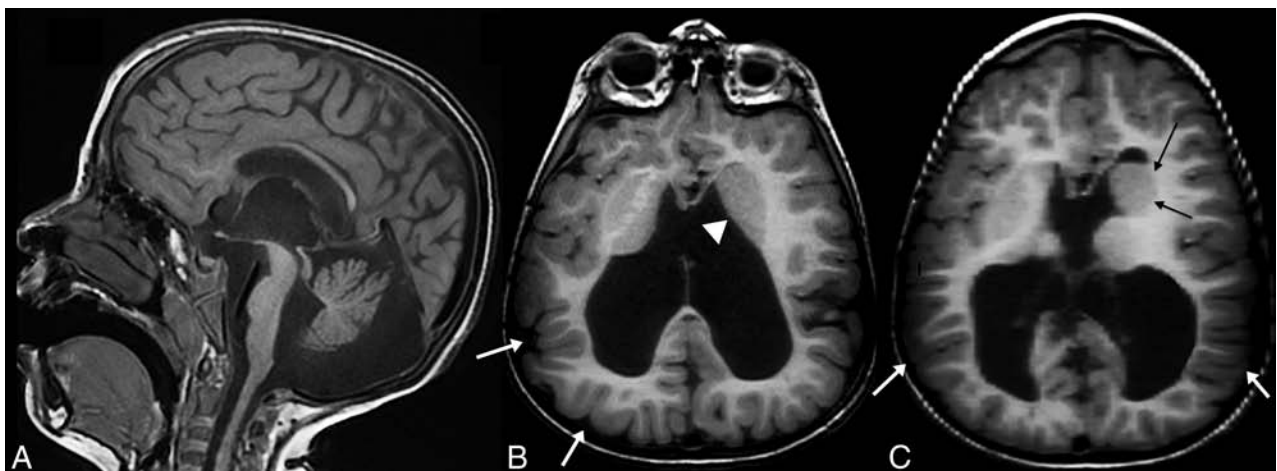


**FIG 1.** A 5-year-old child with a *TUBB3* mutation. Midline sagittal TIWI (A) shows a fully formed but thin corpus callosum, an enlarged third ventricle, a dysmorphic cerebellar vermis with a disproportionately small anterior vermis, and a thin pons. Axial TIWI (B) shows asymmetry of the basal ganglia with an unseparated left striatum (white arrowhead). Note that the gyral pattern is abnormal, with sulci coursing deeply at many different angles and in unusual locations (white arrows). This abnormal pattern is classified as “dysgyria.” Axial TIWI at a slightly higher level of the same patient (C) shows again the dysmorphic, asymmetric basal ganglia with an enlarged left caudate head (black arrows) and marked ventriculomegaly. Cortical dysgyria is again noted (white arrows).

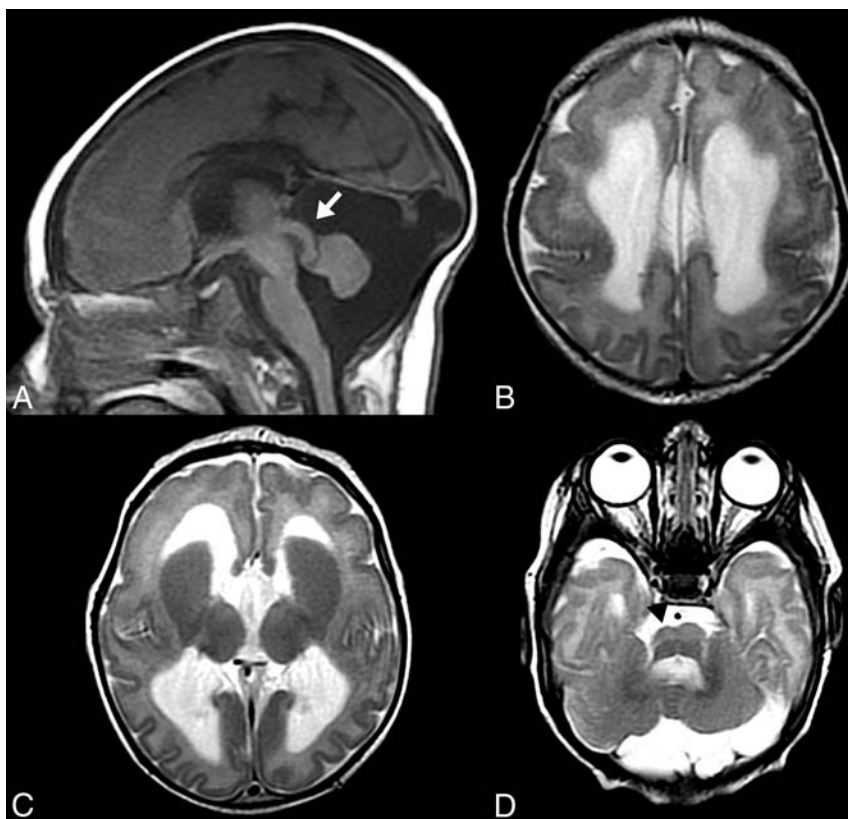


**FIG 2.** A 7-week-old infant with a *TUBB2B* mutation. Midline sagittal T1WI (A) shows a short, thin corpus callosum; a small cerebellar vermis; and a thin pons with a disproportionately large tectum (white arrow). Axial T2WI (B–D from superior to inferior) reveals severe ventriculomegaly. There is diffuse cortical dysgyria with bilateral frontal lobe band heterotopia (B). More inferiorly, there are abnormally enlarged caudates with fused striata (C) and an asymmetric, small pons (D), smaller on the right (black arrowhead) with a central cleft.

thickness to slightly thick, associated with shallow sulci and a layer of neurons (band heterotopia<sup>4</sup>) deep to the cortex; the cortical anomaly was more severe frontally than in the occipital cortex. No cerebellar or brain stem anomalies were identified; however, large caudate heads were identified in 3/4 patients with *DCX* mutations, and cerebral white matter volume was mildly or moderately diminished in 3/4.

## DISCUSSION

Microtubules are filamentous intracellular structures critical for long-range intracellular cargo transport in neurons and, therefore, important in brain formation and function.<sup>13</sup> They have key roles in mitosis, organization of intracellular structure, axonal pathfinding, neuronal migration, protein transport, and ciliary motility.<sup>13–15</sup> Not surprising, disorders of MT formation affect multiple aspects of brain development, resulting in multiple malformations, including microcephaly (presumably from impaired mitosis), lissencephaly, band heterotopia and other types of cortical dysgenesis (impaired neuronal migration), anomalies of white matter pathways (impaired axonal pathfinding), and malformations of the mid-brain and hindbrain (possibly impairment of both neuronal migration and axonal pathfinding); these malformations have some characteristic features that allow them to be recognized on routine MR imaging.<sup>9,15–23</sup>

Similar malformations had been previously reported in patients with mutations of genes encoding MAPs, such as *LIS1* and *DCX1*,<sup>2,12</sup> that bind to MTs and aid long-range intracellular transport into distal axons, dendrites, and leading processes (actin-based transport is more important for short-range transport to synapses and axonal growth cones<sup>24</sup>). Recent revelations on MT functions and their interactions with MAPs in so many developmental processes make it clear that disorders of MT and MAP formation and function cause many developmental brain disorders.<sup>8,13,25–29</sup> Although some MR imaging findings of cortical malformations and cranial neuropathies associated with mutations of tubulins and MAPs have been described, the precise nature of the cortical anomalies (which have been nearly uniformly called “pachygyria” and “polymicrogyria”) and the other aspects of abnormal brain development associated with them, such as callosal anomalies, brain stem anomalies, and cerebellar anomalies, have not been previously compared and contrasted, to our knowledge. In making this comparison, we have discovered several MR imaging findings that

may help narrow the search for genes responsible for malformations.

A brief description of how microtubules form and function may be useful in this discussion. MTs form by polymerization of tubulin heterodimers, which are composed of the 2 main tubulin proteins,  $\alpha$ -tubulin (formed from proteins constructed by transcription and translation of *TUBA* genes) and  $\beta$ -tubulin (from *TUBB* genes), which spontaneously combine (dimerize) to form  $\alpha$ - $\beta$ -heterodimers. To initiate the formation of an MT, heterodimers bind to a  $\gamma$ -tubulin ring complex, composed of  $\gamma$ -tubulins (formed by transcription and translation of *TUBG* genes) bound to  $\gamma$ -tubulin complex proteins in the wall of a centrosome.<sup>25</sup> The  $\gamma$ -tubulin ring complex functions as a scaffold, with exposed  $\gamma$ -tubulin on its periphery, to which  $\alpha$ - $\beta$ -heterodimers bind and begin to polymerize, ultimately forming the MT (Fig 5D).<sup>25</sup> The advancing ends of the MTs, at the growth cone of a pathfinding axon or the leading process of a migrating neuron, follow actin and myosin scaffolding that interacts with chemical signals in the interstitium (Fig 5B, -C).<sup>24</sup> Attractive signals cause rapid growth of the actin in that direction, which quickly stimulates MT polymerization in its wake, whereas repulsive signals cause actin breakdown, quickly followed by MT depolymerization.<sup>24,26</sup>

Thus, the MT plays a critical role in the navigation and formation of axons and neurons through the developing brain.<sup>13,27,28</sup>

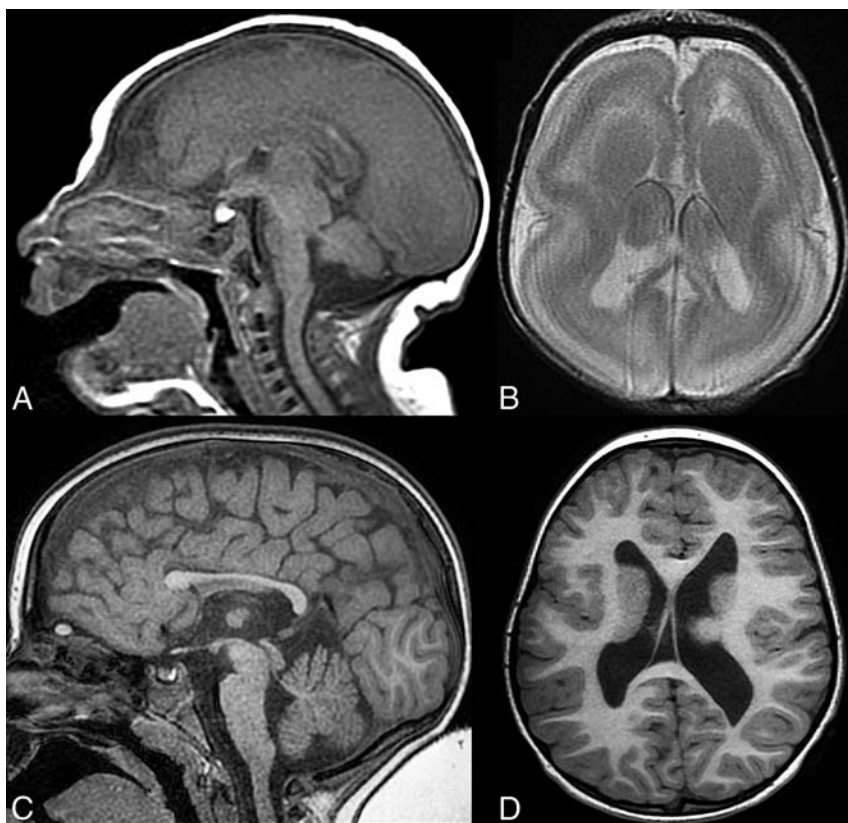


**FIG 3.** Patients with *TUBA1A* mutations. Midline sagittal T1WI in a 2-day-old patient (A) shows a thick, dysmorphic corpus callosum; a small cerebellar vermis; and a thin pons with a disproportionately large tectum. Axial T2WI in the same patient (B) shows cortical lissencephaly with a cell sparse zone, enlarged caudate heads with fused striata, and mild ventriculomegaly. Midline sagittal (C) and axial (D) T1WI from a different 3-year-old patient with *TUBA1A* mutation reveals contrasting dysgyric cortex (D) and a thin corpus callosum with an absent genu and rostrum (C). Again note a thin pons and moderate ventriculomegaly.

The same process occurs during mitosis as the MTs migrate from centrosomes to attach to and separate chromosomes and begin cell division (Fig 5A). Thus, MTs are critical to the processes of mitosis, axon navigation, and neuron migration, all key factors in development. During neuronal migration, an important role is also played by MAPs (in particular *LIS1*, *NuDE*, and *Dynein*), which are critical to the process of nucleokinesis, by which the nucleus of the migrating neuron is pulled forward after its leading process advances<sup>29</sup>; in the absence of nucleokinesis, the neuron does not migrate. The precise role of MAPs in axonal navigation is less well-established, but it is becoming clear that external axonal guidance cues in the brain interstitium couple with other molecules in the axonal growth cone (such as *ROBO3* or *DCC*) to direct microtubule dynamics.<sup>30,31</sup> It is entirely possible (and, indeed, likely) that MAPs participate in this process to some extent.

Knowledge of the developmental functions of MTs and MAPs helps in understanding imaging findings. MTs play a key role in mitosis; therefore, cell proliferation is diminished in patients who have mutations of MT genes. In addition, patients with tubulin mutations (*TUBA1A*, *TUBB2B*, *TUBB3*, *TUBG*, and so forth) almost universally have microcephaly<sup>6,8-10</sup>; the most severely affected do not survive gestation.<sup>32</sup> A review of the recent literature indicates that patients with MT muta-

tions very commonly have severe microcephaly, some profoundly so, and the severity of the microcephaly seems to be directly related to the severity of the brain malformation: most severe in microlissencephaly followed by lissencephaly and pachygyria and least severe with dysgyria (60% of these patients are normocephalic).<sup>9</sup> The microcephaly seems likely to be related to abnormalities of mitosis. In contrast, patients with MAP mutations have much milder impairment of brain growth,<sup>33,34</sup> with most normocephalic, and those with small heads usually mildly affected.

Because neuronal migration is disturbed in tubulinopathies, enlarged or asymmetric basal ganglia, heterotopias, and cortical dysgenesis are common. Pachygyria and agyria appear to be most common in *TUBA1A* and *TUBG* mutations. However, the MR imaging appearance of the cortex in the patients in our study and those described in the literature does not resemble true polymicrogyria. Pathologic analysis of the brains with tubulin mutations showed migration of neurons through gaps in the pial-limiting membrane into the subarachnoid space,<sup>32</sup> which is not found in polymicrogyria. Moreover, the appearance of

a smooth cortical surface with radially oriented sulci, even on high-resolution images, is not consistent with polymicrogyria. Because the appearance in these patients has not been previously described, we have coined the term “dysgyria” to describe a malformation in which sulci course at unusual angles and unusual depths, an appearance that has been illustrated in published MR imaging figures from patients with mutations of all the tubulin genes described at this time<sup>9,17,19,22,23</sup> but not discussed in detail. We suggest that recognition of this characteristic feature aids in the diagnosis of tubulinopathy, especially when associated with microcephaly. In addition, the anterior cerebellar vermis is very commonly small, and the midbrain tectum is often large (which can be a result of abnormal migration of cerebellar granule cells<sup>35</sup>).

Finally, because axonal pathfinding is disturbed, patients with tubulin mutations may have congenital fibrosis of the extraocular muscles or hypoplastic olfactory nerves<sup>18</sup>; hypoplasia or absence of the corpus callosum; a small, often asymmetric brain stem; abnormal-appearing, fused striatum due to the absence of various parts of the internal capsule (most commonly the anterior limb); and diminished overall white matter volume.<sup>8,9</sup> All of these findings were seen in some of our patients, and nearly all were seen in many of the patients with tubulin mutations.



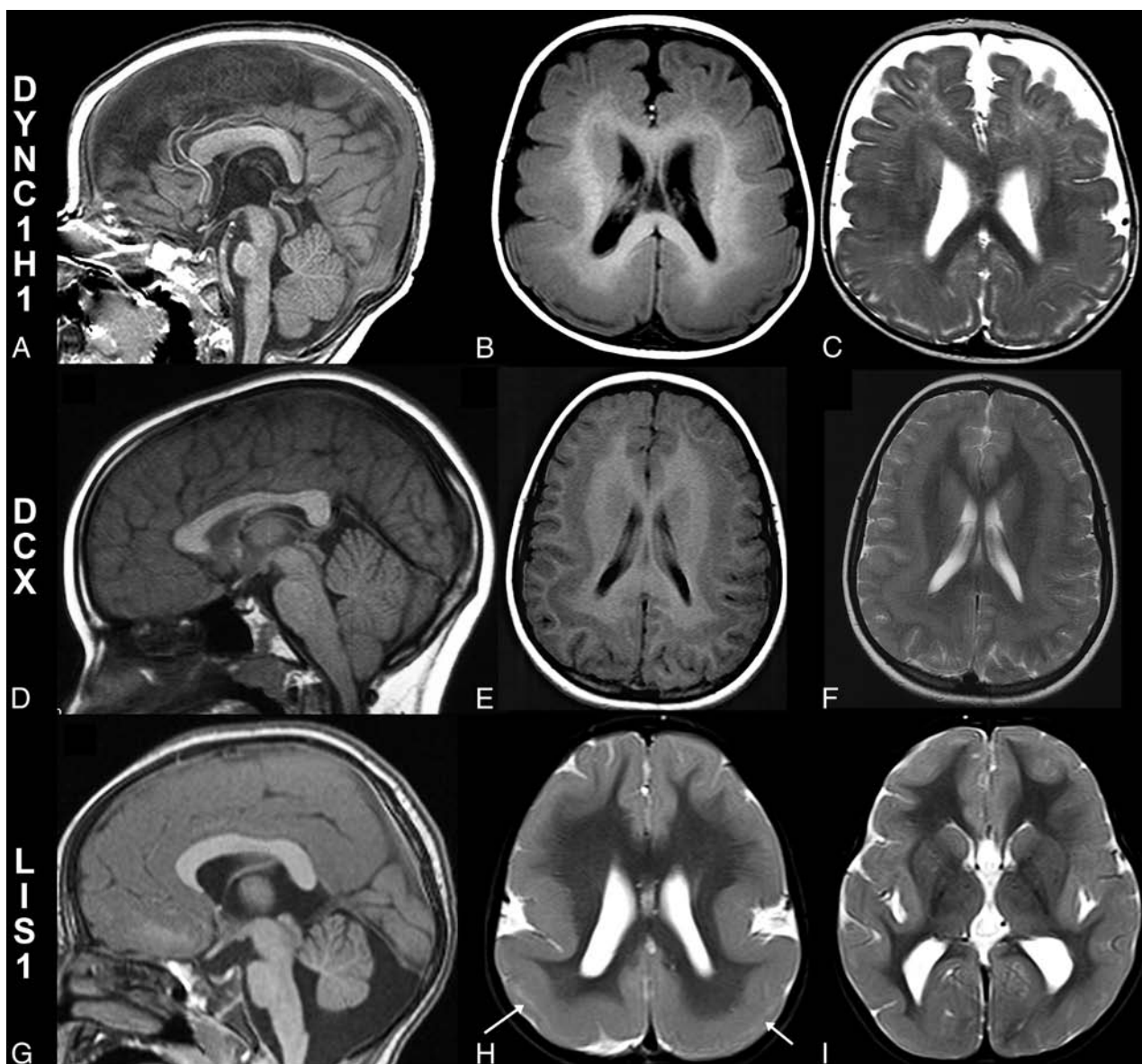


**FIG 4.** Patients with microtubule-associated protein mutations. Midline sagittal T1WI (A), axial T1WI (B), and T2WI (C) in an 8-month-old patient with a *DYNC1H1* mutation. An abnormal corpus callosum with an absent inferior genu and rostrum and an L-shaped angulation of the body and splenium with small pons (A) are noted. Axial images (B and C) reveal parietal pachygyria with a cell sparse zone. Midline sagittal T1WI in a 7-year-old patient with a *DCX* mutation shows normal midline structures, including the corpus callosum, pons, cerebellar vermis, and tectum (D). Axial images from the same patient with a *DCX* mutation (E and F) reveal diffuse shallow sulci consistent with pachygyria and moderate band heterotopia. Midline sagittal T1WI from a 33-year-old patient with a *LIS1* mutation (G) demonstrates a small anterior vermis and pons, with a mildly dysmorphic corpus callosum (small inferior genu and short splenium). Axial T2WI (H and I) from the same patient with a *LIS1* mutation shows a typical cortical anteroposterior gradient with frontal pachygyria progressing to agyria in the parietal and occipital lobes. A thin cell sparse zone is present in the parietal and occipital lobes (H, white arrows). The basal ganglia are normal (I).

Of particular interest in this study is the observation that abnormalities of axon pathfinding were much more common in patients with mutations of MT genes compared with those with MAP genes, while the abnormalities of neuronal migration were not. Therefore, these findings appear to be important in making the differentiation. Eighteen of 19 patients with MT gene mutations had a dysmorphic or absent corpus callosum (in the other, the corpus was uniformly thin). Most of the dysmorphic ones were thin and incompletely formed, with an absent rostrum and inferior genu and a thin, short splenium. One was of normal thickness but very short (rostrocaudally). Although only 2/15 pa-

tients with MAP gene mutations had a normal corpus callosum, 7 of them (4 with *LIS1* mutations and 3 with *DYNC1H1* mutations) had a very similar finding of a rather thick corpus callosum with a small inferior genu, absent rostrum, and a rather sharp angle in the posterior half of the callosal body, resulting in an overly vertical splenium situated within a few millimeters of the superior colliculus (Fig 4A). The brain stem was small in 17/18 patients with MT gene mutations and asymmetric in 8, but a small brain stem was seen in only 6/15 patients with MAP gene mutations and all brain stems were symmetric. Mutations of other axonal pathfinding genes, such as *ROBO3*,<sup>36</sup> can cause similar (though usu-



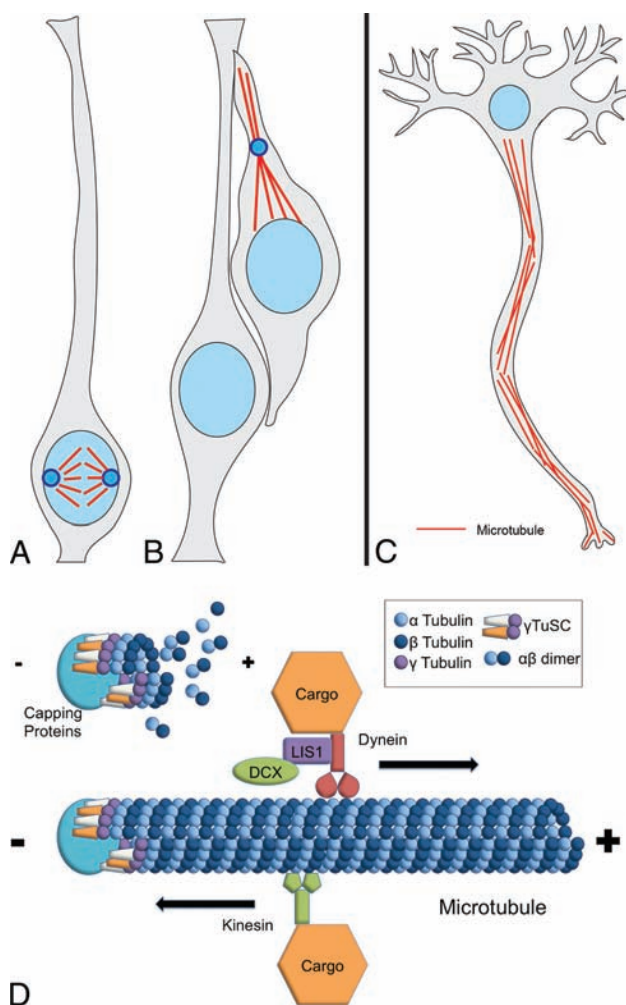


**FIG 5.** Multiple roles of microtubules in development. Schematic illustrates the importance of microtubules in key developmental functions, including mitosis/proliferation (A), migration (B), and axonal pathfinding/transport (C). Microtubules along with their associated proteins form attachments between chromosomes and centrosomes, establishing polarity in dividing neural progenitor cells, such as radial glia (A), during neurogenesis and providing the mechanical apparatus of mitosis and cell division. Following cell division, neuroblasts (immature neurons) migrate (B) from the germinal ventricular zone along the pial process of their mother radial glial cell into the developing cortical plate through the process of nucleokinesis, where the nucleolus are pulled along microtubules following the leading process of neuroblasts. Later in development, microtubules appear to play multiple important functional roles in projection neurons (C), including polarization, axonal pathfinding, synaptogenesis, and transport of intracellular materials along the axon. D. The prevailing “template model” for microtubule polymerization.  $\gamma$ -Tubulin molecules (usually 13) together with their associated scaffolding and capping proteins form the  $\gamma$ -tubulin ring complex, which serves as a template for polymerizing  $\alpha$ -tubulin and  $\beta$ -tubulin dimers, forming a cylindric complex of filaments forming the microtubule. Microtubules are intrinsically polarized with distinct positive and negative ends. Microtubule-associated proteins include the molecular motor dynein (including *DYNC1H1*) and kinesin, which transport intracellular cargo along microtubules toward the positive and negative ends, respectively, as well as proteins such as *LIS1* and *DCX*.

ally symmetric) clefts in the pons and medulla, but they are not associated with cortical malformations. Therefore, a finding of a small, asymmetric brain stem with a midline cleft in the setting of cortical malformations should strongly suggest a tubulin mutation as the cause.

In terms of cortical malformations, areas of dysgyria were present in 13/17 patients with MT gene mutations, in whom the cortex was adequately visualized, while pachygyria was seen in 7. Peri-Sylvian pachygyria was seen in addition to dysgyria in 3/5 patients with *TUBB3* mutations. In contrast, dysgyria was not seen in patients with MAP gene mutations, while pachygyria was present in all, mostly in the posterior parietal/occipital regions. Only 5/15 patients with MAP mutations (3/6 with *DYNC1H1* mutations) had a small vermis (in contrast to 17/18 of patients with tubulin gene mutations); notably, anterior vermis atrophy predominated in both groups. No patients with predominantly posterior vermis atrophy were seen.

## CONCLUSIONS

The human brain is formed in a complex and highly regulated process that includes neurogenesis (proliferation of progenitor cells and production of immature neurons), neuronal migration (migration of immature neurons from germinal zones into organized gray matter structures), and connectivity (formation of white matter tracts by extension of axons). Microtubules and their associated proteins are integral components of all of these processes in the developing brain; thus, their mutations can result in complex, overlapping imaging phenotypes. Diagnostically, these features can be useful because combinations of findings seen in other malformations of cortical development, when present together, can suggest a disorder of MT function. For example, in a patient with the combination of microcephaly, dysgyria, and a small corpus callosum and brain stem, the diagnosis of a tubulin mutation should be considered. It follows logically that while tubulin gene mutations often affect all categories (neurogenesis, migration and axonal pathfinding), mutations of MAPs often have more limited phenotypes, suggesting specialized or redundant functions. MAP gene mutations most notably caused errors in neuronal migration (particularly pachygyria and agyria), while axonal pathfinding abnormalities were much more common in the patients with tubulin mutations.

Disclosures: Annapurna Poduri—RELATED: Grant: National Institute of Neurological Disorders and Stroke K23 grant.\* Mustafa Sahin—UNRELATED: Grants/Grants Pending: Novartis,\* Shire,\* Comments: I am the Principal Investigator of the site of grants from Novartis related to tuberous sclerosis. I am the Principal Investigator of a grant from Shire related to spinal muscular atrophy. Christopher A. Walsh—RELATED: Grant: National Institute of Neurological Disorders and Stroke,\* National Institute of Mental Health,\* Howard Hughes Medical Institute; UNRELATED: Consultancy: Hoffman—La Roche, Third Rock Ventures; Grants/Grants Pending: National Institute of Mental Health, National Institute of Neurological Disorders and Stroke,\* Howard Hughes Medical Institute. Anthony James Barkovich—RELATED: Grant: National Institutes of Health/National Institute of Neurological Disorders and Stroke.\* \*Money paid to the institution.

## REFERENCES

1. Dobyns W, Reiner O, Carrozzo R, et al. **Lissencephaly: a human brain malformation associated with deletion of the LIS1 gene located at chromosome 17p13.** *JAMA* 1993;270:2838–42 CrossRef Medline
2. Gleeson JG, Allen KA, Fox JW, et al. **Doublecortin, a brain-specific gene mutated in human X-linked lissencephaly and double cortex syndrome, encodes a putative signaling protein.** *Cell* 1998;92:63–72 CrossRef Medline
3. Kitamura K, Yanazawa M, Sugiyama N, et al. **Mutation of ARX causes abnormal development of forebrain and testes in mice and**

- X-linked lissencephaly with abnormal genitalia in humans. *Nat Genet* 2002;32:359–69 CrossRef Medline
4. Barkovich AJ, Jackson DE Jr, Boyer RS. **Band heterotopia: a newly recognized neuronal migration anomaly.** *Radiology* 1989;171:455–58 CrossRef Medline
  5. Barkovich AJ, Ferriero DM, Barr RM, et al. **Micro-lissencephaly: a heterogeneous malformation of cortical development.** *Neuropediatrics* 1998;29:113–19 CrossRef Medline
  6. Poirier K, Keays DA, Francis F, et al. **Large spectrum of lissencephaly and pachygyria phenotypes resulting from de novo missense mutations in tubulin alpha 1A (TUBA1A).** *Hum Mutat* 2007;28:1055–64 CrossRef Medline
  7. Bahi-Buisson N, Poirier K, Boddaert N, et al. **Refinement of cortical dysgeneses spectrum associated with TUBA1A mutations.** *J Med Genet* 2008;45:647–53 CrossRef Medline
  8. Poirier K, Lebrun N, Broix L, et al. **Mutations in TUBG1, DYNC1H1, KIF5C and KIF2A cause malformations of cortical development and microcephaly.** *Nat Genet* 2013;45:639–47 CrossRef Medline
  9. Bahi-Buisson N, Poirier K, Fourniol F, et al; LIS-Tubulinopathies Consortium. **The wide spectrum of tubulinopathies: what are the key features for the diagnosis?** *Brain* 2014;137:1676–700 CrossRef Medline
  10. Cushion TD, Dobyns WB, Mullins JG, et al. **Overlapping cortical malformations and mutations in TUBB2B and TUBA1A.** *Brain* 2013;136:536–48 CrossRef Medline
  11. Doherty D, Millen KJ, Barkovich AJ. **Midbrain and hindbrain malformations: advances in clinical diagnosis, imaging, and genetics.** *Lancet Neurol* 2013;12:381–93 CrossRef Medline
  12. Dobyns WB, Truwit CL, Ross ME, et al. **Differences in the gyral pattern distinguish chromosome 17-linked and X-linked lissencephaly.** *Neurology* 1999;53:270–77 CrossRef Medline
  13. Franker MA, Hoogenraad CC. **Microtubule-based transport: basic mechanisms, traffic rules and role in neurological pathogenesis.** *J Cell Sci* 2013;126:2319–29 CrossRef Medline
  14. Kuijpers M, Hoogenraad CC. **Centrosomes, microtubules and neuronal development.** *Mol Cell Neurosci* 2011;48:349–58 CrossRef Medline
  15. Jaglin XH, Chelly J. **Tubulin-related cortical dysgeneses: microtubule dysfunction underlying neuronal migration defects.** *Trends Genet* 2009;25:555–66 CrossRef Medline
  16. Breuss M, Heng JI, Poirier K, et al. **Mutations in the  $\beta$ -tubulin gene TUBB5 cause microcephaly with structural brain abnormalities.** *Cell Rep* 2012;2:1554–62 CrossRef Medline
  17. Cushion TD, Paciorkowski AR, Pilz DT, et al. **De novo mutations in the beta-tubulin gene TUBB2A cause simplified gyral patterning and infantile-onset epilepsy.** *Am J Hum Genet* 2014;94:634–41 CrossRef Medline
  18. Chew S, Balasubramanian R, Chan WM, et al. **A novel syndrome caused by the E410K amino acid substitution in the neuronal  $\beta$ -tubulin isotype 3.** *Brain* 2013;136:522–35 CrossRef Medline
  19. Jaglin XH, Poirier K, Saillour Y, et al. **Mutations in the beta-tubulin gene TUBB2B result in asymmetrical polymicrogyria.** *Nat Genet* 2009;41:746–52 CrossRef Medline
  20. Kumar RA, Pilz DT, Babatz TD, et al. **TUBA1A mutations cause wide spectrum lissencephaly (smooth brain) and suggest that multiple neuronal migration pathways converge on alpha tubulins.** *Hum Mol Genet* 2010;19:2817–27 CrossRef Medline
  21. Morris-Rosendahl DJ, Najm J, Lachmeijer AM, et al. **Refining the phenotype of alpha-1a tubulin (TUBA1A) mutation in patients with classical lissencephaly.** *Clin Genet* 2008;74:425–33 CrossRef Medline
  22. Poirier K, Saillour Y, Bahi-Buisson N, et al. **Mutations in the neuronal  $\beta$ -tubulin subunit TUBB3 result in malformation of cortical development and neuronal migration defects.** *Hum Mol Genet* 2010;19:4462–73 CrossRef Medline
  23. Romaniello R, Tonelli A, Arrigoni F, et al. **A novel mutation in the  $\beta$ -tubulin gene TUBB2B associated with complex malformation of cortical development and deficits in axonal guidance.** *Dev Med Child Neurol* 2012;54:765–69 CrossRef Medline
  24. Kneussel M, Wagner W. **Myosin motors at neuronal synapses: drivers of membrane transport and actin dynamics.** *Nat Rev Neurosci* 2013;14:233–47 CrossRef Medline
  25. Kollman JM, Merdes A, Mourey L, et al. **Microtubule nucleation by  $\gamma$ -tubulin complexes.** *Nat Rev Mol Cell Biol* 2011;12:709–21 CrossRef Medline
  26. Slováková J, Speicher S, Sánchez-Soriano N, et al. **The actin-binding protein Canoe/AF-6 forms a complex with Robo and is required for Slit-Robo signaling during axon pathfinding at the CNS midline.** *J Neurosci* 2012;32:10035–44 CrossRef Medline
  27. Tanaka E, Ho T, Kirschner MW. **The role of microtubule dynamics in growth cone motility and axonal growth.** *J Cell Biol* 1995;128:139–55 CrossRef Medline
  28. Tanaka EM, Kirschner MW. **Microtubule behavior in the growth cones of living neurons during axon elongation.** *J Cell Biol* 1991;115:345–63 CrossRef Medline
  29. Huang J, Roberts Anthony J, Leschziner Andres E, et al. **Lis1 acts as a “clutch” between the ATPase and microtubule-binding domains of the dynein motor.** *Cell* 2012;150:975–86 CrossRef Medline
  30. Qu C, Dwyer T, Shao Q, et al. **Direct binding of TUBB3 with DCC couples netrin-1 signaling to intracellular microtubule dynamics in axon outgrowth and guidance.** *J Cell Sci* 2013;126:3070–81 CrossRef Medline
  31. Liu G, Dwyer T. **Microtubule dynamics in axon guidance.** *Neurosci Bull* 2014;30:569–83 CrossRef Medline
  32. Fallet-Bianco C, Laquerriere A, Poirier K, et al. **Mutations in tubulin genes are frequent causes of various foetal malformations of cortical development including microlissencephaly.** *Acta Neuropathol Commun* 2014;2:69 CrossRef Medline
  33. Bahi-Buisson N, Souville I, Fourniol FJ, et al; SBH-LIS European Consortium. **New insights into genotype-phenotype correlations for the doublecortin-related lissencephaly spectrum.** *Brain* 2013;136(pt 1):223–44 CrossRef Medline
  34. Uyanik G, Morris-Rosendahl D, Stiegler J, et al. **Location and type of mutation in the LIS1 gene do not predict phenotypic severity.** *Neurology* 2007;69:442–47 CrossRef Medline
  35. Goldowitz D, Hamre K, Przyborski S, et al. **Granule cells and cerebellar boundaries: analysis of Unc5h3 mutant chimeras.** *J Neurosci* 2000;20:4129–37 Medline
  36. Jen JC, Chan WM, Bosley TM, et al. **Mutations in a human ROBO gene disrupt hindbrain axon pathway crossing and morphogenesis.** *Science* 2004;304:1509–13 CrossRef Medline

# In Utero MR Imaging of Fetal Holoprosencephaly: A Structured Approach to Diagnosis and Classification

P.D. Griffiths and D. Jarvis



## ABSTRACT

**BACKGROUND AND PURPOSE:** Holoprosencephaly is a rare developmental brain abnormality with a range of severity. We describe our experience in diagnosing holoprosencephaly in the fetus with in utero MR imaging. We hypothesized that including in utero MR imaging in the diagnostic pathway will improve the detection of holoprosencephaly compared with ultrasonography and allow better assessment of the severity.

**MATERIALS AND METHODS:** We report on holoprosencephaly identified from ultrasonography and/or a diagnosis of holoprosencephaly made with in utero MR imaging. We compare the diagnoses made with sonography and in utero MR imaging in each case and compare the 2 methods of assessing the severity of holoprosencephaly.

**RESULTS:** Thirty-five fetuses are reported, including 9 in which the diagnosis of holoprosencephaly was made on ultrasonography but not confirmed on in utero MR imaging. Of the 26 cases of holoprosencephaly diagnosed on in utero MR imaging, 12 were not recognized on ultrasonography.

**CONCLUSIONS:** Our results show that in utero MR imaging has a major role in diagnosing or refuting a diagnosis of fetal holoprosencephaly made on ultrasonography. In utero MR imaging also assists in grading the severity of fetal holoprosencephaly.

**ABBREVIATIONS:** HPE = holoprosencephaly; iuMR = in utero MR imaging; MIHF = middle interhemispheric fusion variety of holoprosencephaly; US = ultrasonography

In utero MR imaging (iuMR) is now an accepted method of diagnosing fetal brain abnormalities and is an important adjunct to the diagnostic pathway alongside antenatal ultrasonography (US). Ultrafast iuMR methods (broadly defined as acquiring 1 image per second) are required to get good-quality imaging in utero because of movement from maternal and fetal sources. Heavily weighted T2 techniques are the mainstay of imaging the fetal brain and are usually acquired with single-shot fast spin-echo sequences. The nonmyelinated or poorly myelinated fetal brain is best imaged with T2-weighted sequences because of the improved tissue contrast between the different components of the fetal brain, which is particularly marked in the second trimester.<sup>1</sup> However, different methods

of acquiring T2-weighted images, such as steady-state sequences, offer other advantages.<sup>2,3</sup>

In this study, we describe our experience in applying these techniques in the diagnosis and classification of the severity of fetal holoprosencephaly (HPE). HPE is a relatively rare disorder with an estimated prevalence of 1 in 16,000 live births, though it is found in 1 of 250 spontaneous abortions.<sup>4</sup> HPE arises as a result of abnormal ventral induction, which causes impaired growth and failure of midline cleavage of the future cerebral hemispheres. The phenotype is exceptionally heterogeneous, and the clinical implications for a fetus/child are closely related to the severity of the malformation. The most severe forms of HPE are not consistent with long-term, extrauterine life, while the minor forms can produce relatively few symptoms.

We hypothesize that including iuMR in the diagnostic pathway will improve the detection of HPE compared with US and allow better assessment of the severity of HPE in an affected fetus.

## MATERIALS AND METHODS

### Study Population

This is a retrospective study of pregnant women referred to our Institution from fetomaternal units in England and Scotland,

Received July 22, 2015; accepted after revision August 17.

From the Academic Unit of Radiology, University of Sheffield, Sheffield, UK.

Please address correspondence to Paul Griffiths, FRCR, Academic Unit of Radiology, Floor C, Royal Hallamshire Hospital, Glossop Rd, Sheffield S10 2JF, UK; e-mail: p.griffiths@sheffield.ac.uk

Indicates article with supplemental on-line table.

<http://dx.doi.org/10.3174/ajnr.A4572>

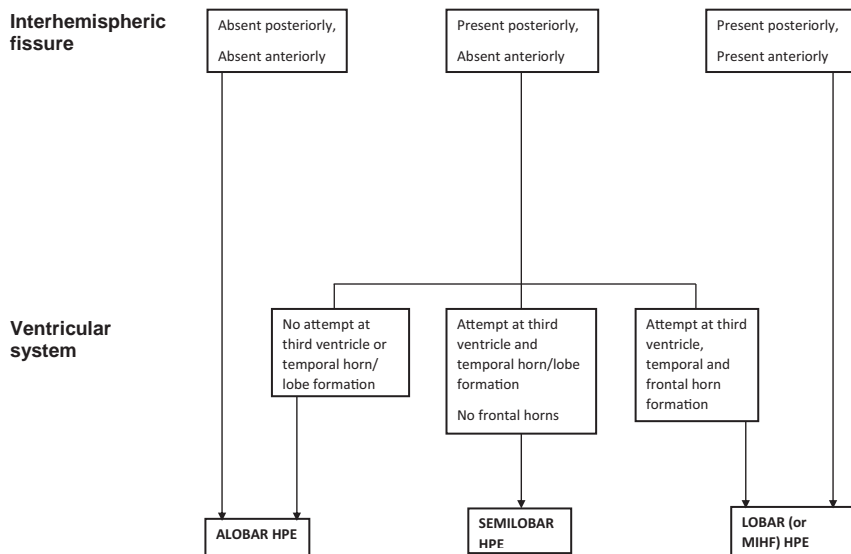


**FIG1.** A flowchart showing the classification of alobar, semilobar, and lobar holoprosencephaly in this article.

whose fetuses were either suspected of having HPE on US and/or were shown to have HPE following iuMR. Appropriate cases were located on the MR imaging data base of the institution during a 15-year period (2000–2014). All cases had US performed by a fetal-maternal expert from 1 of 11 tertiary centers before referral to our Institution for their iuMR study, and the full sonography report was available to the radiologist performing the iuMR study. Women were screened for contraindications to MR imaging, and iuMR examinations were not performed before 18 weeks' gestational age. Of the 35 cases found on the data base, 23 women were scanned as recruits into wider research studies of fetal iuMR, and they all provided informed written consent under the guidance and approval of Research Ethics Committees. Seven out of 23 of the research cases were referred from the Magnetic Resonance Imaging to Enhance the Diagnosis of Fetal Developmental Brain Abnormalities in Utero study.<sup>5</sup> These women were not paid for their involvement in the study, but travel expenses were offered. Relevant review was sought, and approval was obtained from the Institutional Clinical Effectiveness Unit and Research Department to allow the 12 cases with imaging performed for clinical purposes to be reported in this article as well.

### MR Imaging

In utero MR imaging was performed on whole-body 1.5T scanners (before 2008, Infinion; Philips Healthcare, Best, Netherlands; from 2008 onward, HDx; GE Healthcare, Milwaukee, Wisconsin). Maternal sedation was not used for any of the scans. The iuMR protocol changed during the course of the study as new methods became available; however, all subjects had ultrafast T2-weighted images of the fetal brain in the 3 orthogonal planes by using single-shot fast spin-echo sequences (4- to 5-mm thickness). Ultrafast T1-weighted and diffusion-weighted imaging in the axial plane were acquired routinely from 2007; and after 2011, 3D datasets were added by using a steady-state sequence (3D FIESTA). The imaging parameters for the 3D sequence are described in detail elsewhere<sup>2</sup> but are summarized

here: TR minimum, 4–5 ms; TE minimum, 2–3 ms; refocusing flip angle, 60°; NEX, 0.75; FOV, 340 × 270 mm; matrix size, 320 × 256 mm. The partition thickness varied between 1.8 and 2.2 mm with 28–32 scan locations per slab to allow full coverage of the fetal brain with maximum resolution; this was achieved in 18- to 23-second acquisitions.

The 3D datasets were transferred to a desktop PC and loaded into 3D Slicer software (<http://www.slicer.org>) for segmentation. This is an open source image processing and analysis software package. Each fetal brain was segmented manually by outlining the outer surface and ventricular margins on a section-by-section basis by a single trained operator (D.J.) with input from a neuroradiologist experienced in fetal brain imaging (P.D.G.) and

with reference to a fetal brain atlas.<sup>1</sup> Segmentation took approximately 60 minutes for a second trimester fetal brain and 90 minutes for more mature fetuses; the longer time was due to the increased complexity of sulcation/gyration. Reconstruction of that data allowed the creation of surface representations of the whole fetal brain and ventricular system.

### Analysis

All of the iuMR examinations were reported at the time of the study but were reviewed for the purpose of this study by a pediatric neuroradiologist experienced in fetal brain MR imaging (P.D.G.). In cases in which the diagnosis of HPE was not supported by the iuMR findings, the alternative diagnoses were recorded. Further detailed systematic anatomic analyses were made in the cases in which HPE was present on iuMR.

### DeMyer Classification

The first analysis was to ascribe a diagnosis of alobar, semilobar, and lobar HPE, based on the original descriptions of DeMyer and Zeman<sup>6</sup> and DeMyer,<sup>7</sup> and in the neuroradiologic literature of Simon et al<sup>8</sup> and Barkovich et al,<sup>9</sup> with some minor modifications (Fig 1). Three cases of fetal HPE did not fit into that standard description of ventral HPE but were classified as middle interhemispheric fusion varieties of HPE (MIHF). This variant was not described in the original works of DeMyer,<sup>6,7</sup> and our classification is based on the criteria suggested by Simon et al.<sup>10</sup>

### Severity Score

A more detailed secondary anatomic analysis was made by assessing the parts of the brain frequently affected by HPE, broadly following the approach of Simon et al<sup>8</sup> and Barkovich et al<sup>9</sup> in children. It was necessary to make some modifications to those assessments to customize them for fetal brains. These involved some simplification of the methods for reasons detailed in the "Discussion." "Present" or "absent" assessments were made of the posterior interhemispheric fissure, posterior falx, anterior inter-



**Antenatal US and iuMR information in 9 cases in which fetal holoprosencephaly had been diagnosed on US but was not confirmed on iuMR**

Case	Gestational Age at iuMR (wks)	Antenatal US Findings	iuMR Findings
A	24	Lobar HPE	Septo-optic dysplasia, schizencephaly
B	22	HPE (severity not specified)	Agenesis of corpus callosum
C	24	HPE (severity not specified)	Ventriculomegaly, disrupted cavum septum pellucidum probably secondary to hydrocephalus
D	27	HPE (severity not specified)	Septo-optic dysplasia, schizencephaly
E	21	HPE (severity not specified)	Agenesis of corpus callosum
F	27	Lobar HPE	Isolated absence of cavum septum pellucidum
G	18	HPE (severity not specified)	Ventriculomegaly, disrupted cavum septum pellucidum probably secondary to hydrocephalus
H	21	Lobar HPE	Septo-optic dysplasia, schizencephaly
I	24	HPE (severity not specified)	Ventriculomegaly, disrupted cavum septum pellucidum probably secondary to hydrocephalus

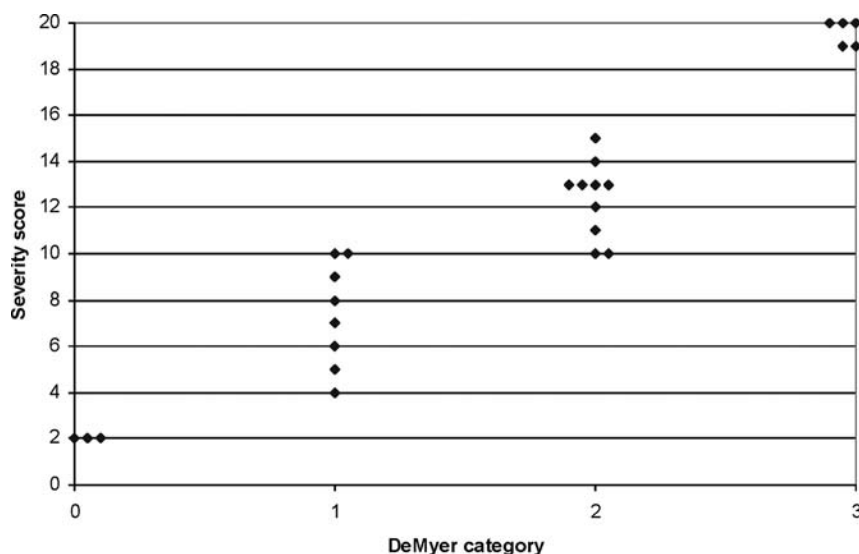


**FIG 2.** Scatterplot showing the correlation between the DeMyer classification and the severity score in 26 cases of fetal holoprosencephaly.

hemispheric fissure, anterior falx, third ventricle, temporal horns/lobes, and frontal horns. The structures did not have to be complete; some attempt at formation was sufficient to be scored as zero (present), whereas if the structure was not present at all, it was scored as 1. Similar binary scores were awarded for the hypothalamus (complete separation = 0, noncleavage = 1), the mid-brain (completely separated from the diencephalon = 0, some degree of nonseparation = 1), and the orbital portions of the frontal lobe, dorsomedial portions of the frontal lobes, and paracentral lobes (complete separation = 0, noncleavage = 1 for each of those regions). Assessments of the deep gray structures of the cerebral hemispheres (caudate, lentiform, and thalamic nuclei) were performed independently on a 3-point scale (as opposed to a 4-point scale by Simon et al<sup>8</sup>): complete separation = 0; <50% noncleavage or abnormally medially placed = 1; and  $\geq$ 50% noncleavage = 2. A similar 3-point scale was used to assess the corpus callosum: completely present = 0; >50% present but not fully formed = 1; and <50% present or absent = 2. The scores were added together to provide a severity score with a total of 20 points for each fetus. Note that the cavum septum pellucidum was not used in this analysis because it was absent in all cases and was considered nondiscriminatory.

## RESULTS

In 9/35 cases (26%), the diagnosis of HPE made on US was not supported by iuMR, and these cases are summarized in the Table. In all of these 9 cases, the cavum septum pellucidum was not demonstrated on US. On iuMR, the cavum septum pellucidum was shown to be either absent (4 cases, 1 with apparent isolated absence of the cavum septum pellucidum and 3 with possible septo-optic dysplasia based on a boxlike deformity of the frontal horns); disrupted (3 cases associated with ventriculomegaly probably due to hydrocephalus); or abnormally situated (2 cases of agenesis of the corpus callosum).

## DeMyer Classification

Twenty-six cases of HPE of any severity were depicted by iuMR, and a summary of the antenatal US and iuMR details of these cases is shown in the On-line Table. Most of these cases had relatively small head sizes. The median gestational age at the time of iuMR in that group was 21 weeks (interquartile range, 20–23 weeks; full range, 18–30 weeks). There were 5 cases of lobar HPE, 10 cases of semilobar HPE, and 8 cases of lobar HPE on iuMR based on the DeMyer and Zeman<sup>6</sup> and DeMeyer<sup>7</sup> classification and 3 cases of MIHF as described by Simon et al.<sup>10</sup> A diagnosis of HPE was made by US in 23 fetuses (all 9 fetuses in the Table and 14 fetuses in the On-line Table); and in 9/23 cases (39%), the diagnosis of HPE was not supported on iuMR (all those in the Table). A diagnosis of HPE was made on iuMR in 26 cases (all of those in the On-line Table); and in 12/26 cases (46%), HPE was not recognized on US.

In the 14 cases in which HPE was diagnosed by both US and iuMR, 8/14 US reports did not specify the severity of HPE. In 3/14 cases, the same severity was reported on both methods, and in 3/14 cases, the severity diagnosed by US and iuMR was different. The agreement in diagnosing HPE between US and iuMR was related to the severity of HPE, specifically ultrasonography diagnosed more cases of the more severe forms of

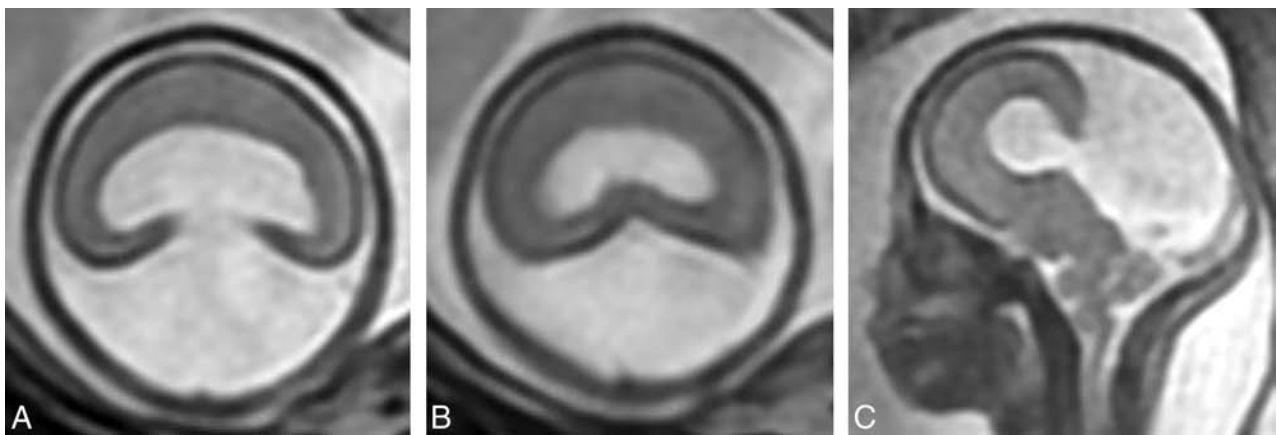


**FIG 3.** T2-weighted images (single-shot fast spin-echo) in a 24-week gestational age fetus with alobar holoprosencephaly according to the DeMyer classification and a severity score of 20/20 (case 2). Axial images of the supratentorial brain (A and B) show no attempt at formation of the interhemispheric fissure and a holoventricle and posterior cyst. Sagittal imaging (C) shows an abnormally kinked brain stem.

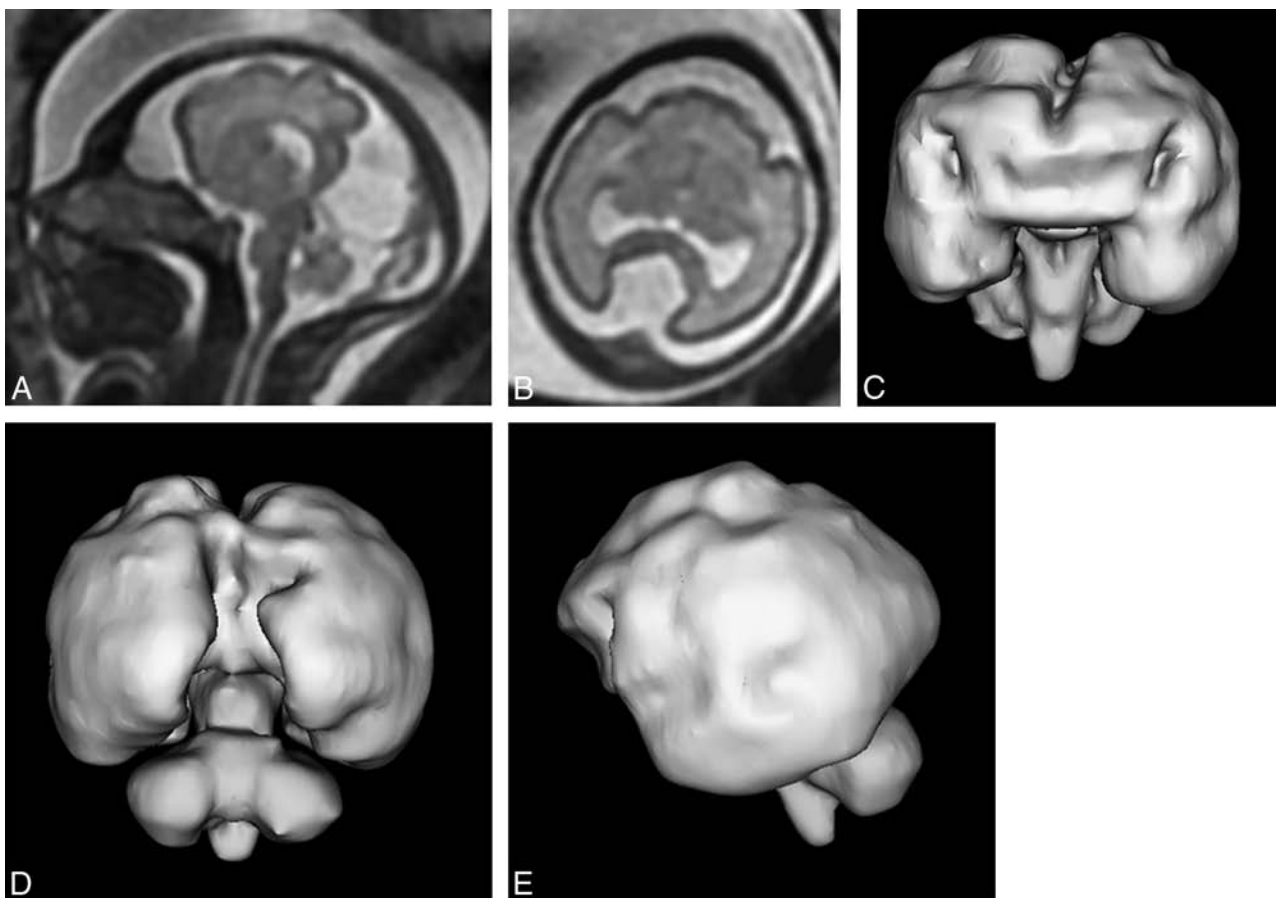


**FIG 4.** T2-weighted images (single-shot fast spin-echo, A and B) and surface reconstructions of 3D steady-state (FIESTA) data of a 26-week gestational age fetus with semilobar holoprosencephaly according to the DeMyer classification and a severity score of 13/20 (case 19). Axial images of the supratentorial brain (B) and posterior and anterior views of the brain (C and D) show some formation of the interhemispheric fissure posteriorly but not anteriorly. There is some attempt at formation of the third ventricle and temporal horns of the lateral ventricles. Lateral projections (E) show abnormal sulcation of the cerebral hemispheres and marked frontal lobe hypoplasia.

HPE correctly. HPE was diagnosed on iuMR in 5/5 cases (100%) of alobar HPE (US diagnoses: alobar [ $n = 3$ ], semilobar [ $n = 1$ ], and not specified [ $n = 1$ ]). In the 10 cases of semilobar HPE diagnosed on iuMR, HPE was the given diagnosis on US in 4/10 cases (40%) (US diagnoses: not specified

severity [ $n = 3$ ] and semilobar HPE [ $n = 1$ ]). In the 8 cases of lobar HPE diagnosed on iuMR, HPE was the given diagnosis on US in 4/8 cases (50%) (US diagnoses: not specified severity [ $n = 3$ ] and semilobar HPE [ $n = 1$ ]). Only 1/3 cases (33%) of MHHF were recognized as HPE on US (called “lobar HPE”).

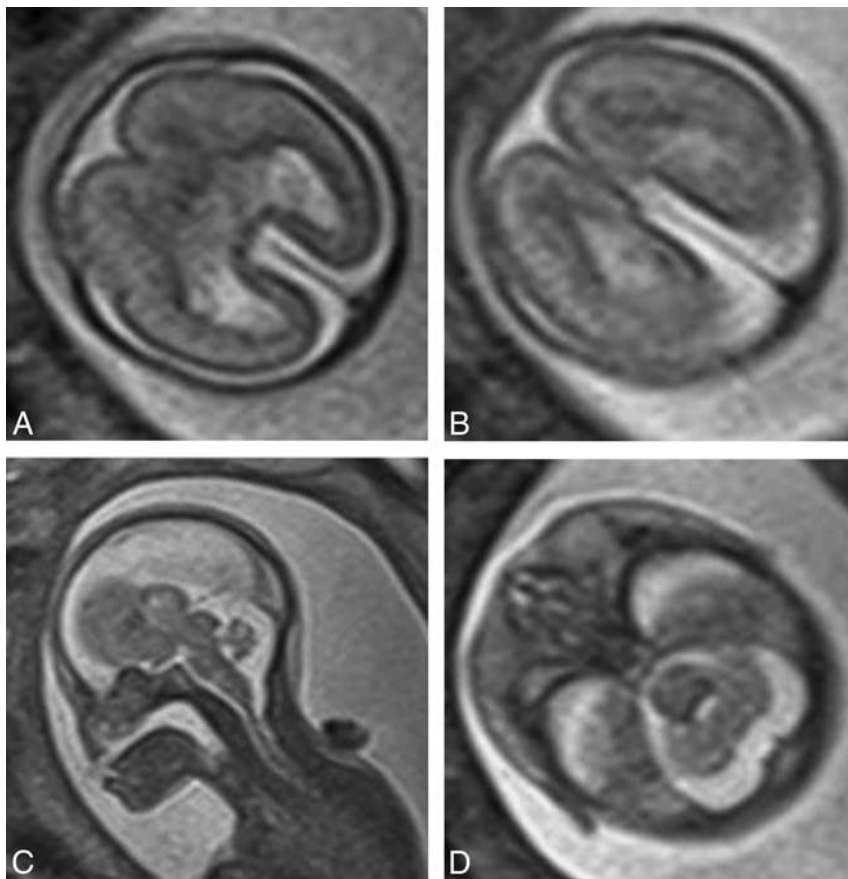


**FIG 5.** T2-weighted images (single-shot fast spin-echo) of a 21-week gestational age fetus with lobar holoprosencephaly according to the DeMyer classification and a severity score of 7/20 (case 15). Axial images of the supratentorial brain (A and B) show formation of the interhemispheric fissure posteriorly and anteriorly and some attempt at formation of the frontal horns of the lateral ventricles. The frontal lobes are fused anteriorly and inferiorly. Despite the relatively low severity score, brain development is markedly deranged, as shown by the corpus callosum anatomy, abnormal opercularization, and brain biometry. There is also a significant facial malformation with absence of the nose (C and D) and a midline cleft lip/cleft palate.

### Severity Score

The On-line Table shows the total severity scores based on the detailed assessment of the brain anatomy. There was a close correlation between the severity score and the DeMyer category of HPE as shown in Fig 2, and the importance of this is discussed in later sections. Representative images are shown in Figs 3–7.

### Other Brain Abnormalities

Brain abnormalities other than HPE, not including face or intracranial vascular abnormalities, were shown on iuMR in 9/26 fetuses (35%) with HPE. None of those were suspected on US. Other brain abnormalities were shown in 1/5 fetuses with alobar HPE, 5/10 fetuses with semilobar HPE, 3/8 fetuses with lobar HPE, and 0/3 fetuses with MIFH. Structural abnormalities of the posterior fossa content were notable and included cerebellar hypoplasia, Dandy-Walker malformation, rhombencephalosynapsis and brain stem malformations.

## DISCUSSION

HPE is a malformation that arises from abnormal ventral induction, a process that occurs 5–10 weeks after fertilization in hu-

mans, during which there is failure of normal growth and cleavage of the cranial end of the neural tube. Hence, the primary effects are on the prosencephalon/future cerebral hemispheres. Abnormal ventral induction can produce a range of anatomic abnormalities of the brain, and the severity is closely linked to prognosis. Detectable chromosomal abnormalities are found in 24%–45% of cases of HPE<sup>4</sup> and include numeric chromosomal abnormalities, most frequently trisomy 13 or 18 (only 1 case of a trisomy was demonstrated in our series, but not all fetuses had karyotyping). There is also an increased risk of HPE in fetuses with structural chromosomal abnormalities, particularly deletions of chromosomes 13, 18, and 7. HPE is thought to result from monogenic abnormalities in 18%–25% of cases,<sup>4</sup> which can produce autosomal dominant disorders such as Pallister-Hall and Rubinstein-Taybi syndromes, autosomal recessive disorders such as Smith-Lemli-Opitz and Meckel-Gruber syndromes (1 case in our series), or X-linked recessive disorders. In addition, there are a range of nongenetic associations that increase the risk of fetal HPE, including maternal diabetes and fetal exposure to retinoic acid, ethanol, and some anticonvulsants.

A woman whose pregnancy is complicated by possible HPE has a number of requirements from antenatal imaging, including the following: a confident diagnosis or exclusion of HPE, an accurate assessment of the anatomic severity

of HPE, and a description of associated brain abnormalities. In the absence of consistent reference outcome data for our cases, all we can say with certainty is that there are major differences between the US and iuMR results. This comment needs to be balanced against the accumulating published data suggesting that iuMR is more accurate than US in diagnosing fetal brain pathology in general, as shown in a recent meta-analysis.<sup>11</sup> Of the total 23 cases of US-diagnosed HPE described in this report, the chance of the diagnosis being incorrect was 39%. Conversely, in the 26 cases in which iuMR diagnosed HPE of any severity, the chance of the diagnosis being missed on US was 46% if iuMR is assumed correct. US performed better in the more severe forms of HPE as might be expected. Our results also show that when HPE was correctly diagnosed on US as an overarching classification, the severity was often either incorrect (3/14) or not attempted (8/14).

The cases of fundamental disagreement about the diagnosis of HPE between US and iuMR warrant further discussion. The 9 cases in which HPE was diagnosed on US but was not confirmed on iuMR had 1 common feature: The cavum septum pellucidum was not visualized on US. Although the cavum septum pellucidum (septum pellucidum after birth) has little or no functional significance, it is a vital landmark for normal brain development

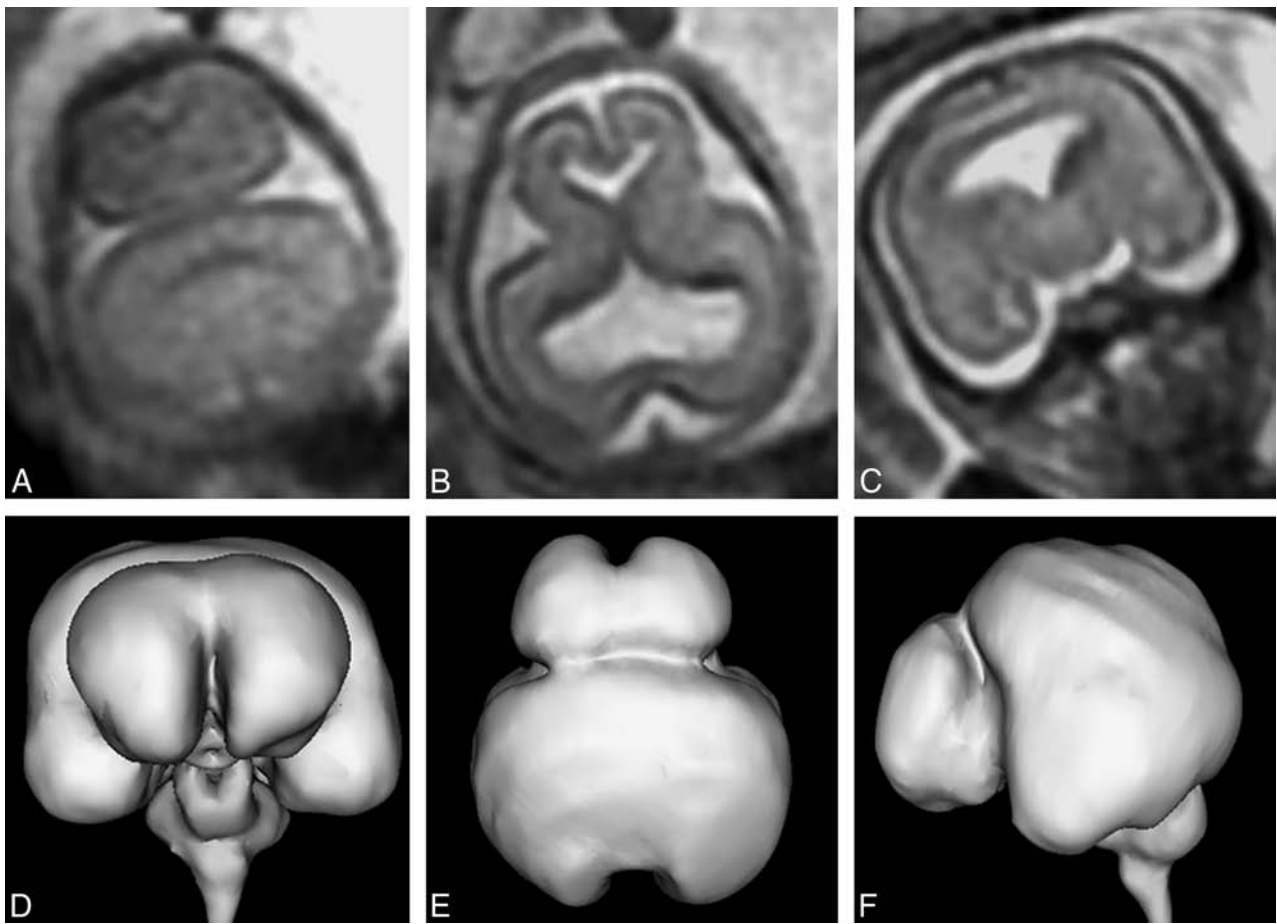


**FIG 6.** T2-weighted images (single-shot fast spin-echo, A–C) and surface reconstructions of 3D steady-state (FIESTA) data of the brain (D–F) in a 21-week gestational age fetus with lobar holoprosencephaly and a severity score of 9/20 (case 20). Axial images of the supratentorial brain (A and B) show interhemispheric fissure formation posteriorly and anteriorly. The third ventricle, temporal horns, and frontal horns of the lateral ventricles are separated. The coronal image (C) shows fusion of the frontal lobes, thalamus, and hypothalamus. The case is complicated by marked frontal lobe hypoplasia and bilateral abnormal frontal sulci shown on the surface reconstructions (D–F).

on antenatal and postnatal imaging.<sup>12,13</sup> Nonvisualization of the cavum septum pellucidum is an imaging feature in all severities of HPE. However, it is also found in other brain abnormalities, and there are a number of different explanations for nonvisualization of the cavum septum pellucidum. It may be that the cavum septum pellucidum never formed (as in HPE, septo-optic dysplasia, and isolated absent cavum septum pellucidum), it may have formed but been destroyed (raised intraventricular pressure from hydrocephalus), or it may have formed but in an abnormal position (agenesis of the corpus callosum where the leaf of the septum pellucidum is often closely applied to the inferior surface of the ipsilateral Probst bundle).<sup>13,14</sup> The alternative diagnoses on the basis of iuMR in the 9 false-positive cases all fit into these categories: The cavum septum pellucidum never formed (3 cases of septo-optic dysplasia and 1 case of isolated absent cavum septum pellucidum); or it formed but was secondarily disrupted (3 cases of ventriculomegaly probably due to hydrocephalus) or misplaced (2 cases of agenesis of the corpus callosum).

We also described 12 cases with false-negative findings in which the diagnosis of HPE on iuMR was not described on the referral from US. In 2 cases (cases 11 and 15), the diagnosis of HPE should have been strongly suspected from the US findings because of midline cleft lip and palate (1 with an absent cavum septum pellucidum), but in the other 10 cases, the diagnosis of

HPE on iuMR was unexpected. The US diagnoses varied in those 10 cases: 3 cases of agenesis or hypogenesis of the corpus callosum (cases 10, 19, and 24); 3 cases of isolated ventriculomegaly (17, 20, and 25); 2 cases of posterior interhemispheric cyst (cases 18 and 26); 1 case of a posterior cephalocele (case 5); and 1 case of cerebellar hypoplasia (case 21). It is difficult to make any specific observations or teaching points from those cases.

There was a high rate of brain abnormalities other than HPE in our cohort—that is, in 9/23 (39%) of the “classic” ventral HPE cases (ie, excluding the MIHF cases), most of which were cerebellar or brain stem malformations. No other brain abnormalities were found in the 3 cases of MIHF. If we assume that iuMR is more likely to provide the correct diagnosis, we suggest that there is a significant advantage in supplementing US with iuMR in the diagnostic pathway. This assumption is reasonable because though we are not aware of studies of diagnostic accuracy of iuMR, specifically in cases of HPE, the published literature suggests that it is true of fetal brain pathology in general as described above.

Our attempts to enhance the classification of fetal HPE were based on the previous work of Simon et al<sup>8,10</sup> and Barkovich et al,<sup>9</sup> who recognized the difficulty in apportioning a single DeMyer classification in pediatric cases of HPE. Their extensive experience and subsequent publications urge a more anatomically descrip-



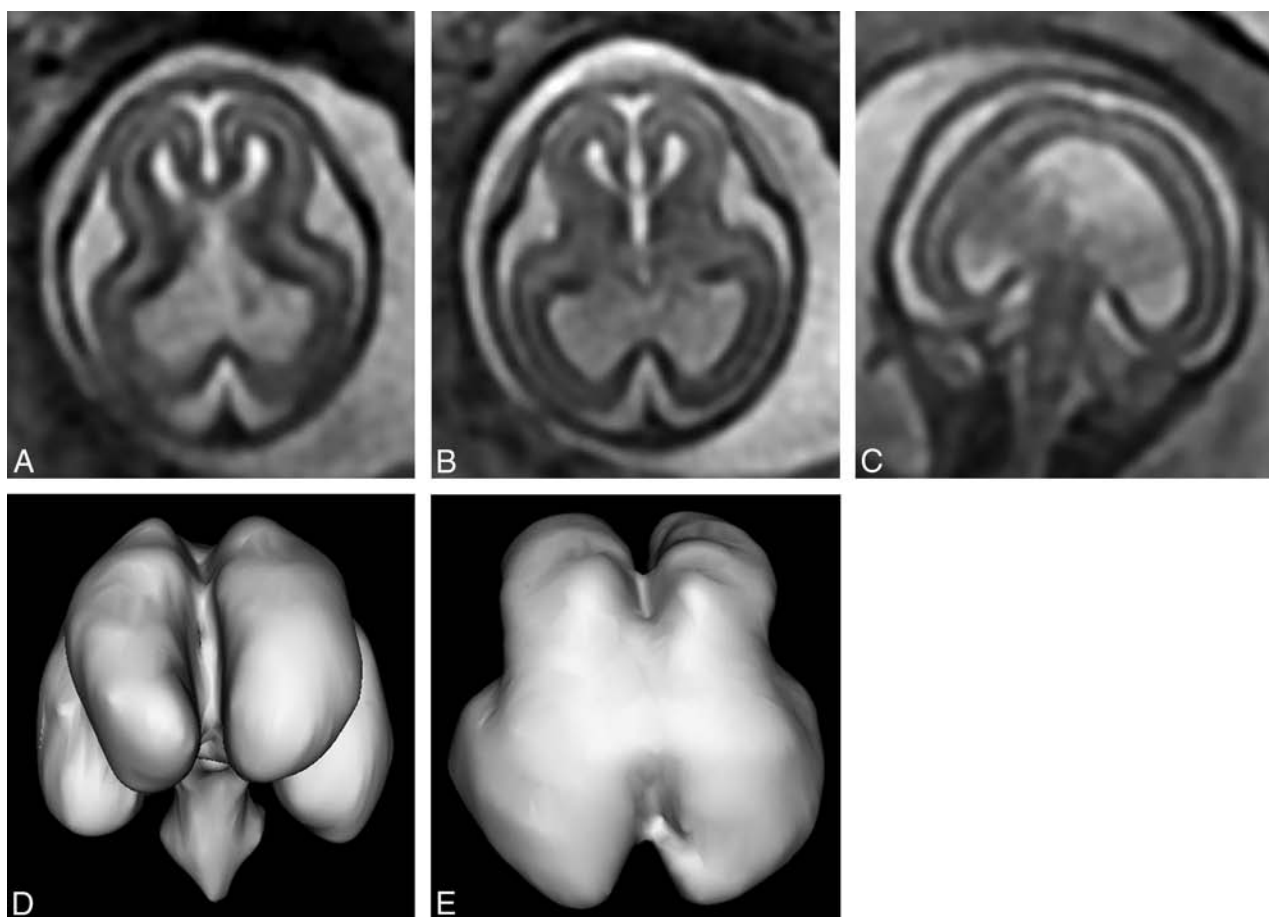


**FIG 7.** T2-weighted images (single-shot fast spin-echo, A–C) and surface reconstructions of 3D steady state (FIESTA) data of the brain (D and E) of a 19-week gestational age fetus with the interhemispheric fusion variety of holoprosencephaly and a severity score of 2/20 (case 25). Axial images of the supratentorial brain (A and B) show complete separation of the interhemispheric fissure and central gray structures, but the ventricles are large and dysmorphic. Coronal imaging (C) shows fusion of the paracentral lobules. These features are confirmed and better defined on the surface reconstructions.

tive approach, rather than relying on alobar, semilobar, and lobar classifications in pediatric practice. We attempted to reproduce their approach for fetuses in our study; there are several problems when one tries to apply their methods to iuMR, particularly in second trimester fetuses. Those authors most often used a 4-point scale to assess the sagittal separation of a particular anatomic structure: 0 = complete separation; 1 = minimal noncleavage or medial deviation; 2 = partial noncleavage; 3 = total noncleavage. We found assessment in such detail exceptionally difficult because of the small size of the fetal structures and opted for either a binary assessment, present or absent, or a 3-point scale for the larger structures: completely present = 0; >50% present but not fully formed = 1; <50% present or completely absent = 2. Simon et al and Barkovich et al considered the appearance of structures other than the deep gray nuclei to be important in describing HPE (eg, the corpus callosum and the Sylvian fissures). The corpus callosum can be assessed quite easily on iuMR, but the calculation of a Sylvian angle as suggested by Barkovich et al<sup>9</sup> is not practicable in second trimester cases. It was even difficult in third trimester cases, giving non-reproducible assessments, so we did not include it in our approach to analyzing the images.

Despite those limitations, our data show a close correlation between the DeMyer classification used in this study and the se-

verity score calculated in our study, but there were overlaps, particularly between the semilobar and lobar cases. For example, 4 cases had a severity score of 10, but 2 were classified as lobar, and 2, as semilobar. We believe that in most cases, the DeMyer classification is the most appropriate mechanism of relaying information based on the ease of assessment and the accessibility of the terms to non-neurology clinicians. There are cases in the mid-range of severity or unusual cases (such as the case in Fig 6), however, in which the more detailed anatomic information that forms the severity score would be useful.

A further weakness of our study was the change in imaging protocols that occurred during the 15-year period of data collection, but this is inevitable when a new and rapidly changing technique, such as iuMR, is used to study rare pathology. This point is well-illustrated when trying to image the fetal hypothalamus with iuMR, which, as stressed by Simon et al,<sup>8,10</sup> is an important anatomic feature of HPE in their publications concerning pediatric HPE.<sup>9</sup> Those authors were the first to bring the MIHF variety of HPE to the wider attention of the imaging community, and they highlighted the importance of involvement of the hypothalamus in distinguishing standard ventral HPE and MIHF, which affects the dorsal structures. They noted some degree of noncleavage of the hypothalamus in all 56 cases of standard ventral HPE that could be assessed. In contrast, the hypothalamus was normally

separated in all 21 of their cases of MIHF. They consider the hypothalamus to be a key structure in the assessment of pediatric HPE, and our findings from iuMR of the fetus concur with that view.

The fetal hypothalamus, however, is a very small structure, and reviewing the cases from the earlier part of recruitment highlighted a potential problem. At the time when only single-shot fast spin-echo sequences with 5-mm-thick sections were used, we thought that there was a real risk of overcalling hypothalamic fusion because of partial volume effects on the coronal images. Improvements in gradient performance and software allowed 2- to 3-mm partitions, but the most significant advance in our experience has been the introduction of 3D balanced steady-state imaging. Those sequences produce images with high signal-to-noise and permit fast imaging times due to a TR that is shorter than the T2 of the tissue in study. The T1/T2 ratios, rather than the T1/T2 differences, are responsible for image contrast and can be varied by changing the flip angle and are independent of the TR. The partition thickness on our current examinations can be reduced to 1.8 mm without major loss of signal/noise, and review of the base data of those acquisitions is very helpful when imaging the fetal brain. The production of individualized surface representations of the brain from the 3D datasets can also be helpful diagnostically but is perhaps more useful when explaining the findings to clinical colleagues and parents.

## CONCLUSIONS

We have shown that all aspects of the imaging diagnosis of fetal HPE are improved when antenatal US is supplemented with iuMR of the fetal brain. Advantages were found in confirming or refuting the diagnosis of HPE, classifying the severity of HPE, and recognizing associated brain abnormalities. All of these factors should improve the quality of information given to parents in terms of anatomic diagnosis and prognosis.

Disclosures: Paul D. Griffiths—**RELATED:** Other: GE Healthcare (research partnership)\*; **UNRELATED:** Medical Research Council,\* National Institute for Health Research—Health Technology Assessment,\* Wellcome Trust,\* GE Healthcare,\* **Comments:** awarded current grants. \*Money paid to the institution.

## REFERENCES

1. Griffiths PD, Reeves J, Larroche JC, et al. *Atlas of Fetal and Postnatal Brain MR Imaging*. Philadelphia: Mosby; 2010
2. Jarvis DA, Armitage P, Dean A, et al. **Surface reconstructions of foetal brain abnormalities using ultrafast steady state 3D acquisitions.** *Clin Radiol* 2014;69:1084–91 CrossRef Medline
3. Griffiths PD, Jarvis D, McQuillan H, et al. **MRI of the foetal brain using a rapid 3D steady-state sequence.** *Br J Radiol* 2013;86:20130168 CrossRef Medline
4. Chen H. *Atlas of Genetic Diagnosis and Counseling*. Totowa, NJ: Humana Press; 2006:493–501
5. Griffiths PD. **Protocol 11PRT/2491: Magnetic resonance imaging to enhance the diagnosis of fetal developmental brain abnormalities in utero (MERIDIAN) (1SRCTN27626961).** 2012. [www.thelancet.com/protocol-reviews/11PRT-2491](http://www.thelancet.com/protocol-reviews/11PRT-2491). Accessed October 15, 2015
6. DeMyer W, Zeman W. **Alobar holoprosencephaly (arhinencephaly) with median cleft lip and palate: clinical, electroencephalographic and nosologic considerations.** *Confin Neurol* 1963;23:1–36 Medline
7. DeMyer W. **Holoprosencephaly (cyclopia-arhinencephaly).** In: Myriantopoulos N, ed. *Malformations*. New York: Elsevier, 1987: 225–44
8. Simon EM, Hevner R, Pinter JD, et al. **Assessment of the deep gray nuclei in holoprosencephaly.** *AJNR Am J Neuroradiol* 2000;21:1955–61 Medline
9. Barkovich AJ, Simon EM, Clegg NJ, et al. **Analysis of the cerebral cortex in holoprosencephaly with attention to the Sylvian fissures.** *AJNR Am J Neuroradiol* 2002;23:143–50 Medline
10. Simon EM, Hevner RF, Pinter JD, et al. **The middle interhemispheric variant of holoprosencephaly.** *AJNR Am J Neuroradiol* 2002;23:151–56 Medline
11. Rossi AC, Prefumo F. **Additional value of fetal magnetic resonance imaging in the prenatal diagnosis of central nervous system anomalies: a systematic review of the literature.** *Ultrasound Obstet Gynecol* 2014;44:388–93 CrossRef Medline
12. Griffiths PD, Batty R, Reeves MJ, et al. **Imaging the corpus callosum, septum pellucidum and fornix in children: normal anatomy and variations of normality.** *Neuroradiology* 2009;51:337–45 CrossRef Medline
13. Griffiths PD, Batty R, Connolly DA, et al. **Effects of failed commissuration on the septum pellucidum and fornix: implications for fetal imaging.** *Neuroradiology* 2009;51:347–56 CrossRef Medline
14. Barkovich AJ, Raybaud CA. **Congenital malformations of the brain and skull.** In: Barkovich AJ, Raybaud CA, eds. *Pediatric Neuroimaging*. 5th ed. Philadelphia: Wolters Kluwer Health/Lippincott Williams & Wilkins; 2012:367–568

# Contrast Leakage Patterns from Dynamic Susceptibility Contrast Perfusion MRI in the Grading of Primary Pediatric Brain Tumors

C.Y. Ho, J.S. Cardinal, A.P. Kamer, C. Lin, and S.F. Kralik

## ABSTRACT

**BACKGROUND AND PURPOSE:** The pattern of contrast leakage from DSC tissue signal intensity time curves have shown utility in distinguishing adult brain neoplasms, but has limited description in the literature for pediatric brain tumors. The purpose of this study is to evaluate the utility of grading pediatric brain tumors with this technique.

**MATERIALS AND METHODS:** A retrospective review of tissue signal-intensity time curves from 63 pediatric brain tumors with preoperative DSC perfusion MR imaging was performed independently by 2 neuroradiologists. Tissue signal-intensity time curves were generated from ROIs placed in the highest perceived tumor relative CBV. The postbolus portion of the curve was independently classified as returning to baseline, continuing above baseline (T1-dominant contrast leakage), or failing to return to baseline (T2\*-dominant contrast leakage). Interobserver agreement of curve classification was evaluated by using the Cohen  $\kappa$ . A consensus classification of curve type was obtained in discrepant cases, and the consensus classification was compared with tumor histology and World Health Organization grade.

**RESULTS:** Tissue signal-intensity time curve classification concordance was 0.69 (95% CI, 0.54–0.84) overall and 0.79 (95% CI, 0.59–0.91) for a T1-dominant contrast leakage pattern. Twenty-five of 25 tumors with consensus T1-dominant contrast leakage were low-grade (positive predictive value, 1.0; 95% CI, 0.83–1.00). By comparison, tumors with consensus T2\*-dominant contrast leakage or return to baseline were predominantly high-grade (10/15 and 15/23, respectively) with a high negative predictive value (1.0; 95% CI, 0.83–1.0). For pilomyxoid or pilocytic astrocytomas, a T1-dominant leak demonstrated high sensitivity (0.91; 95% CI, 0.70–0.98) and specificity (0.90, 95% CI, 0.75–0.97).

**CONCLUSIONS:** There was good interobserver agreement in the classification of DSC perfusion tissue signal-intensity time curves for pediatric brain tumors, particularly for T1-dominant leakage. Among patients with pediatric brain tumors, a T1-dominant leakage pattern is highly specific for a low-grade tumor and demonstrates high sensitivity and specificity for pilocytic or pilomyxoid astrocytomas.

**ABBREVIATIONS:** rCBV = relative cerebral blood volume; TSITC = tissue signal-intensity time curves; WHO = World Health Organization

Primary brain tumors represent 29% of all childhood cancers, are the most common solid childhood tumor, and are the leading cause of cancer death in this age population.<sup>1</sup> With experienced pediatric neuroimaging specialists, presurgical diagnosis with anatomic MR imaging sequences can be accurate, especially with a classic appearance and location. However, many primary neoplasms do not follow the classic imaging appearance, and ad-

vanced imaging techniques such as perfusion imaging, diffusion-weighted imaging, and MR spectroscopy have been used to grade primary pediatric tumors.<sup>2–4</sup>

Dynamic susceptibility contrast perfusion MR imaging has demonstrated utility in the pretreatment evaluation of adult intracranial neoplasms for tumor grading, guiding biopsy, and prognosis. However, while the most common adult primary parenchymal neoplasms are of the astrocytic cell type, the most common pediatric primary brain tumors have diverse cellular origins, with astrocytic origin for pilocytic astrocytomas and embryonal neuroepithelial origin for medulloblastomas. Even within astrocytomas, outside of the classic “cyst and mural nodule” appearance of pilocytic astrocytomas, there is some overlap in the radiographic and histologic appearance of pilocytic astrocytomas and high-grade gliomas, with relative cerebral volume (rCBV) demonstrating usefulness in distinguish-

Received May 6, 2015; accepted after revision July 20.

From the Department of Radiology, Indiana University School of Medicine, Indianapolis, Indiana.

Paper previously presented in part at: American Society of Neuroradiology Annual Meeting and the Foundation of the ASNR Symposium, May 17–22, 2014; Montreal, Quebec, Canada.

Please address correspondence to Chang Ho, MD, 705 Riley Hospital Dr, MRI Department, Indianapolis, IN 46202; e-mail: cyho@iupui.edu

<http://dx.doi.org/10.3174/ajnr.A4559>

ing the 2 astrocytic entities.<sup>5</sup> However, when the most common pediatric primary brain tumors are evaluated, there is an overlapping range of rCBV values, particularly between pilocytic astrocytomas and medulloblastomas, limiting the usefulness of DSC perfusion in predicting low- versus high-grade tumors preoperatively.<sup>2</sup>

While rCBV has received the greatest attention in differentiating tumor grades from perfusion imaging in adult tumors,<sup>6–8</sup> tissue signal-intensity time curves (TSITC) have also demonstrated diagnostic utility, most notably in differentiating primary CNS lymphoma from glioblastoma multiforme and metastases.<sup>9–11</sup> We evaluated the interobserver agreement of the classification of DSC perfusion MR imaging TSITC and the utility of curve classification as a tool for grading pediatric brain tumors.

## MATERIALS AND METHODS

Following institutional review board approval, a retrospective radiology data base search from September 2009 to August 2013 identified 65 patients with pediatric brain tumors with pathology-proved diagnosis and assigned World Health Organization (WHO) grade who had undergone DSC perfusion MR imaging on the initial evaluation before chemotherapy, biopsy, or surgical resection. In most cases, a single dose of 2 mg/kg of IV dexamethasone was given emergently before MR imaging for the treatment of tumor-associated cerebral edema. Two cases were excluded leaving 63 cases for review. One case was excluded due to poor contrast bolus, and the second case, due to susceptibility artifacts generated by the patient's dental braces. This study population was previously reported.<sup>2</sup>

### MR Imaging

DSC perfusion MR images were obtained during the first pass of a bolus of gadobenate dimeglumine (MultiHance; Bracco Diagnostics, Princeton, New Jersey) on 1.5T and 3T MR imaging scanners (Magnetom, Avanto and Verio; Siemens, Erlangen, Germany) by using a gradient-echo echo-planar sequence (TR, 1410–2250 ms/TE, 30 and 45 ms; flip angle, 90°). Two different TEs were used on different scanners. A range of TRs was adjusted for tumor coverage. No scans were obtained with a preload of IV contrast. Following a precontrast phase to establish a baseline, a contrast medium dose of 0.1 mmol/kg of body weight was injected followed by a normal saline flush for a total volume of 32 mL. When possible, an 18- or 20-ga peripheral intravenous access was used with a power injector rate of 5 mL/s. In some cases, primarily with smaller children, only 24-ga peripheral intravenous access was possible. Contrast bolus adequacy was evaluated by 2 fellowship-trained board-certified neuroradiologists with a Certificate of Added Qualification (C.Y.H., 7 years' experience, and S.F.K., 3 years' experience) on the basis of TSITC and the patient scan was included or excluded in consensus.

### Data Analysis

Using a commercially available workstation (DynaSuite Neuro 3.0; InVivo, Gainesville, Florida), each neuroradiologist independently selected multiple 3- to 5-mm<sup>2</sup> ROIs within the tumor, placed at the locations of perceived highest rCBV by using Dyna-

Suite-generated rCBV maps, blinded to the pathologic diagnosis. Anatomic MR imaging sequences were used to help define tumor location and avoid major blood vessels or hemorrhage when placing the ROI. The resulting signal-intensity curve from the ROI with the highest rCBV was used for classification. This technique has been previously described in the literature.<sup>2</sup> Use of the maximum rCBV for characterization of the TSITC ensures that the most perfused portion of a heterogeneous tumor is evaluated, reducing sampling errors. Curves were assessed out to 50 TRs on the time axis. A y-axis value before the first-pass bolus was chosen to represent the average of the baseline and was compared with the final y-axis value at 50 TRs. The portion of the curve following the first pass of contrast medium bolus was characterized as returning to a level within  $\pm 10\%$  of the baseline with a plateau (return to baseline; Fig 1), overshooting at least 10% above the baseline without a plateau (T1-dominant contrast leakage; Fig 2), or failing to return to a level  $<10\%$  below baseline (T2\*-dominant contrast leakage; Fig 3). Interobserver agreement was assessed by using the Cohen  $\kappa$ . Blinded consensus opinion was obtained in cases with discrepant curve classification, and the resulting TSITC were compared with individual WHO tumor grades. TSITC results were also compared with the averaged rCBV maximum between the 2 observers. Histopathologic evaluation of surgical specimens for all tumors was performed by 1 of 2 board-certified neuropathologists who determined a diagnosis and assigned a WHO grade of I through IV.

A  $\chi^2$  test of independence was used to assess potential significant differences between 1.5T and 3T, 30- and 45-ms TE, the range of TRs, and dexamethasone administration. Diagnostic accuracy was assessed for specific curve patterns.

Statistical analysis was performed by using SPSS 21 (IBM, Armonk, New York) and an on-line statistical calculator (VassarStats, <http://vassarstats.net/>).

## RESULTS

Patient characteristics are summarized in Table 1. There were 38 low-grade (WHO grade I–II) tumors and 25 high-grade (WHO grade III–IV) tumors.

Independent classification of TSITC by 2 neuroradiologists had a Cohen  $\kappa$  of 0.69 (95% CI, 0.54–0.84), indicating good interobserver agreement. The proportion of agreement was highest with a T1-dominant pattern ( $K = 0.79$ , 95% CI, 0.56–0.91) compared with T2\*-dominant pattern ( $K = 0.60$ , 95% CI, 0.39–0.78) and return to baseline ( $K = 0.57$ , 95% CI, 0.35–0.76).

The  $\chi^2$  test for independence between 1.5T and 3T scanners ( $P = .63$ ), 30- and 45-ms TE ( $P = .55$ ), and TR range ( $P = .14$ ) failed to show significance, indicating that the null hypothesis is not rejected or that leakage patterns are not dependent on the differences in magnet strength, TE, or TR in our scanning parameters. Dexamethasone, however, did show some significant ( $P = .02$ ) effects. Further  $\chi^2$  analysis between tumors treated with dexamethasone ( $n = 41$ ) and without dexamethasone ( $n = 22$ ) showed a significant difference in all low-grade tumors ( $P = .03$ ) but not with pilocytic astrocytomas ( $P = .99$ ), pilomyxoid astrocytomas ( $P = 1.0$ ), or both piloid tumors together ( $P = .46$ ). For high-grade tumors, dexamethasone also did not show a significant effect ( $P = .09$ ).



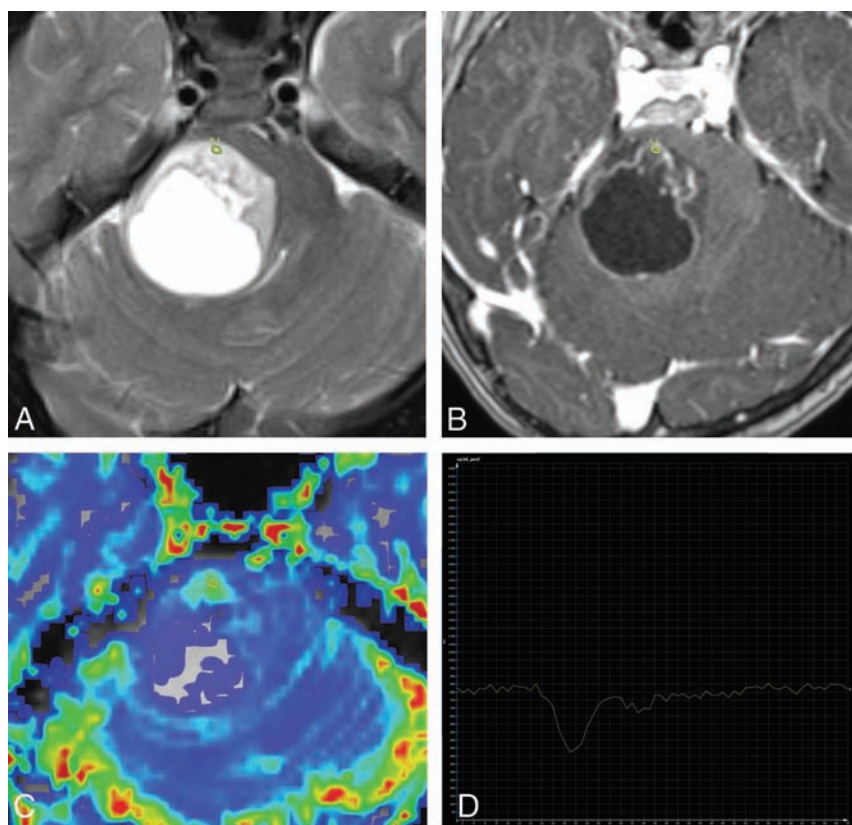


**FIG 1.** Axial T2 (A), axial T1-weighted postcontrast (B), axial DSC perfusion CBV map (C), and tissue signal-intensity time curve (D) of a glioblastoma. The tumor has T2 hyperintensity, cystic change, and minimal heterogeneous enhancement and has well-circumscribed margins suggesting a low-grade neoplasm such as a pilocytic astrocytoma. However, the TSITC from an ROI with the highest tumoral rCBV demonstrates a return to baseline pattern, which is highly sensitive for a high-grade tumor; there is low probability that this represents a pilocytic or pilomyxoid astrocytoma.

### All Tumors

Among 38 low-grade tumors, 25 had a consensus classification of T1-dominant contrast leakage, while 13 had a consensus curve classification other than T1-dominant leakage—either return to baseline or T2\*-dominant leakage. The 25 tumors with T1-dominant contrast leakage included the following: 15 pilocytic astrocytomas, 6 pilomyxoid astrocytomas, 1 low-grade glioneuronal tumor, 1 WHO grade II ependymoma, 1 desmoplastic infantile ganglioglioma, and 1 choroid plexus papilloma. Tumors showing a consensus curve classification with T2\*-dominant leakage or return to baseline were predominantly high-grade. Ten of 15 tumors identified as having a postbolus curve with T2\*-dominant leakage were high-grade (positive predictive value, 0.67; 95% CI, 0.39–0.87), and 15 of 23 tumors with curves identified as returning to baseline were high-grade (positive predictive value, 0.65; 95% CI, 0.43–0.83). Combining T2\* and return-to-baseline patterns for high-grade tumor yielded a high sensitivity (1.0, 95% CI, 0.83–1.0) and negative predictive value (1.0; 95% CI, 0.83–1.0) at the cost of specificity (0.66, 95% CI, 0.49–0.80). The most common high-grade tumors such as medulloblastoma, anaplastic ependymoma, and glioblastoma had both T2\* and baseline patterns. All 3 cases of atypical teratoid/rhabdoid tumor showed a return to baseline pattern. Conversely, the most common low-grade tumors, such as pilocytic astrocytoma and pilomyxoid

astrocytoma, demonstrated predominantly T1-dominant leakage: 15/17 for pilocytic astrocytoma and 6/6 for pilomyxoid astrocytoma. One case of 3 WHO II ependymomas showed T1-dominant leakage. For the diagnosis of pilocytic or pilomyxoid astrocytoma, a T1-dominant leakage pattern yields a high sensitivity (0.91, 95% CI, 0.70–0.98; negative predictive value, 0.95; 95% CI, 0.81–0.99) and specificity (0.90, 95% CI, 0.75–0.97; positive predictive value, 0.84; 95% CI, 0.63–0.95) (Table 2).

An analysis of variance showed no significant differences ( $P = .11$ ,  $F$  ratio = 2.32) between the means of the rCBV maximum for each leakage pattern (T1-dominant =  $3.25 \pm 3.3$ , baseline =  $3.25 \pm 2.2$ , T2\*-dominant =  $5.18 \pm 3.6$ ). A  $t$  test between the means of rCBV maximum for T1-dominant leakage ( $3.25 \pm 3.3$ ) and T2\*-dominant combined with baseline leakage patterns ( $4.02 \pm 2.93$ ) also yielded no significant difference ( $P = .33$ ).  $\chi^2$  tests were performed for significant differences between WHO grade and TSITC leakage results. Grade I-versus-II tumors were not significant ( $P = .38$ ) nor were grade III-versus-IV tumors ( $P = .93$ ). Only high (III and IV) versus low grade (I and II) were significant ( $P < .0001$ ).

### Dexamethasone Group

Among the 41 patients with tumors who received dexamethasone before DSC perfusion MR imaging, 19 had a consensus T1-dominant leakage, 12 had a consensus T2\*-dominant leakage pattern, and 10 had a consensus return to baseline pattern. All 19 with a T1-dominant leakage pattern were low-grade tumors while 5 other low-grade tumors had a leakage pattern other than T1-dominant leakage. Of 12 tumors with T2\*-dominant leakage, 9 were high-grade. Of 10 tumors with a return-to-baseline pattern, 8 were high-grade. Thirteen of 14 pilocytic astrocytomas and 3 of 3 pilomyxoid astrocytomas demonstrated T1-dominant leakage. Diagnostic accuracy for this cohort is summarized in Table 2. Within the entire dexamethasone group, no significant differences were seen between magnet strengths ( $P = .62$ ), TE ( $P = .32$ ), or TR ( $P = .20$ ).

### No Dexamethasone Group

Among the 22 patients with tumors who did not receive dexamethasone before DSC perfusion MR imaging, 6 had a consensus T1-dominant leakage, 3 had a consensus T2\*-dominant leakage, and 13 had a consensus return to baseline pattern. All 6 tumors with a T1-dominant leakage pattern were low-grade tumors. Eight low-grade tumors had a leakage pattern other

than T1-dominant leakage. Of the 3 tumors with T2\*-dominant leakage, only 1 was high-grade. Of 13 tumors with return-to-baseline patterns, 7 were high-grade. Two of 3 pilocytic astrocytomas and 3 of 3 pilomyxoid astrocytomas demonstrated T1-dominant leakage. Diagnostic accuracy is summarized in Table 2. Within the entire no dexamethasone group, no significant differences were seen among magnet strength ( $P = .08$ ), TE ( $P = .97$ ), or TR ( $P = .40$ ).

## DISCUSSION

In practice, hemodynamics, status of the blood-brain barrier, timing of the contrast bolus, and MR pulse sequence parameters affect the shape of the TSITC.<sup>12-16</sup> Disruption or lack of a blood-brain barrier results in leakage of contrast medium into the extravascular extracellular space. While in the intravascular space, paramagnetic contrast medium causes predominantly T2\* effects with loss of MR signal; however, once in the extravascular extra-

cellular space, T1-shortening effects compete with the T2\* effects.<sup>15,16</sup> Depending on the MR imaging parameters and biologic tissue environment, T1-shortening effects may predominate and cause a postbolus curve that returns to and then passes baseline, or T2\* effects may predominate and result in a postbolus curve that fails to return to baseline.<sup>15</sup> Another mechanism for a curve that fails to return to baseline was suggested by Kassner et al,<sup>13</sup> who showed that residual T2\* effects may reflect delayed passage of intravascular contrast medium due to vascular tortuosity, disorganization, and hypoperfusion in areas of increased neovascularity. They compared this effect with the tumor staining seen on conventional angiography.

Previous authors described the portion of the curve after the peak as "percent signal recovery,"<sup>9,17</sup> with a high percent signal recovery correlating with our T1-dominant leakage; a low percent signal recovery, T2\*-dominant leakage; or with smaller T2\* effects, a return to baseline. Cha et al<sup>17</sup> demonstrated a significant difference between metastatic brain tumors and glioblastoma and the associated surrounding abnormal white matter in adults, with greater T2\* effects and <50% return to baseline for metastatic tumors compared with >75% re-

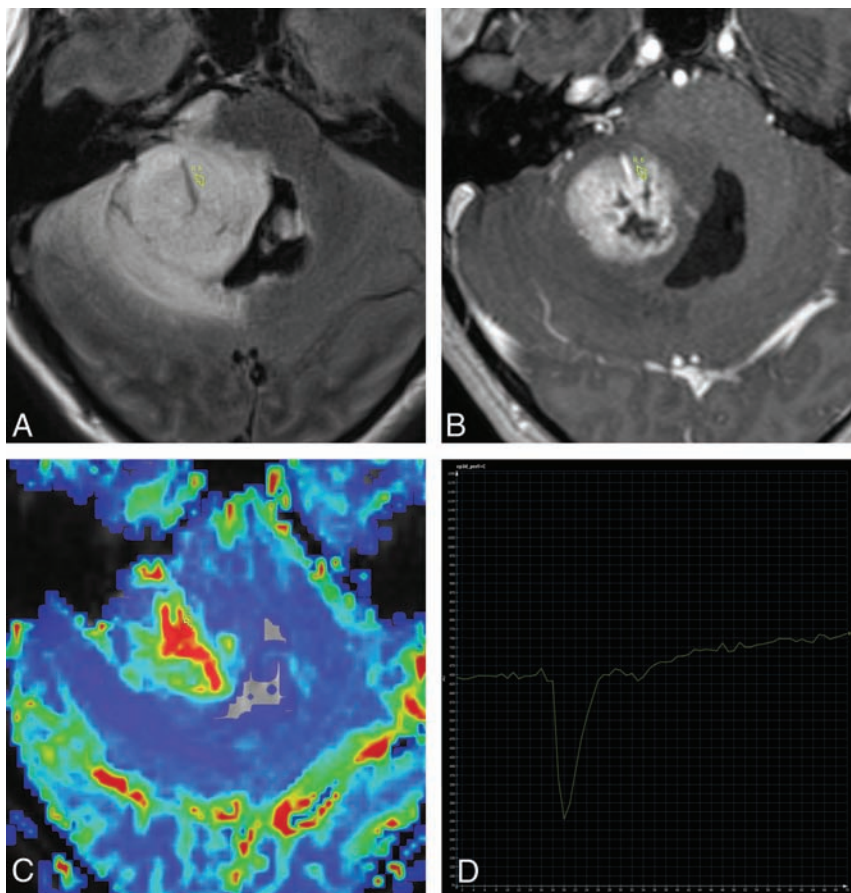


**FIG 2.** Axial T2 FLAIR (A), axial T1-weighted postcontrast (B), axial DSC perfusion rCBV map (C), and tissue signal-intensity time curve (D) of a pilocytic astrocytoma with atypical appearance. Despite apparent increased rCBV, poorly defined margins, central necrosis, and surrounding T2 hyperintensity suggesting a high-grade neoplasm, the T1-dominant leakage pattern suggests the correct interpretation of a low-grade tumor. The ROI is placed in the highest perfusing portion of the tumor, not including a dominant central vessel.

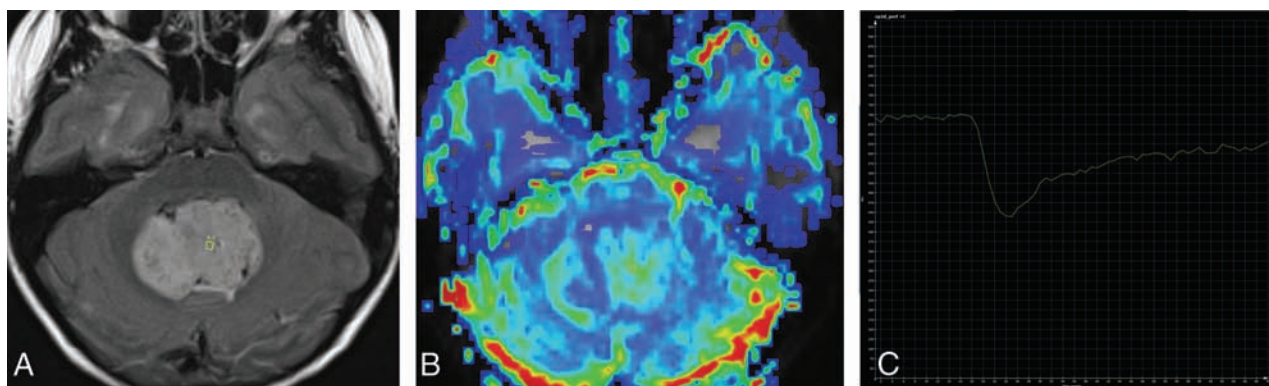


**FIG 3.** Axial T2 FLAIR (A), axial DSC perfusion rCBV map (B), and tissue signal-intensity time curve (C) in a patient with medulloblastoma. The tissue signal-intensity time curve demonstrates T2\*-dominant contrast leakage following the contrast bolus.



covery for glioblastomas. They suggested that this difference is due to the lack of a blood-brain barrier, leading to greater uniform vascular permeability and leakage in metastatic tumors compared with some presence of a blood-brain barrier in glioblastomas, with less uniform vascular permeability.<sup>17</sup> Last, the balance between T1 and T2\* effects is affected by varying MR imaging parameters, including the flip angle, TE, and TR in gradient-echo EPI DSC perfusion MR imaging.<sup>10,12,13,15-17</sup> We used a narrow range of TEs for similar T2\* effects across scanners and a uniform flip angle on all scanners for recovery from the peak. Previous authors have used a low flip angle to suppress T1 signal effects<sup>16,17</sup>; however in our study, our 90° flip angle did not suffi-

ciently suppress the T1 signal for our range of TRs to prevent overshooting the baseline in most low-grade tumors, which we categorized as T1-dominant leakage.

### Advances in Knowledge

A striking finding in our data was 100% positive predictive value (25 of 25) for low-grade tumors if a T1-dominant leakage pattern was identified. The converse is also true in that the lack of a T1 leakage pattern (T2\* or return to baseline) resulted in a 100% negative predictive value for high-grade tumors. T1-dominant leakage patterns were also sensitive and specific for either a pilocytic astrocytoma or pilomyxoid astrocytoma. In addition, good

interobserver agreement for identifying a T1-dominant leakage pattern was found, indicating potential clinical utility for grading pediatric brain tumors with TSITC from DSC perfusion.

Little prior data exist in the literature regarding the use of DSC perfusion MR imaging and signal-intensity curves in the evaluation of pediatric brain tumors. Similar to our findings, Grand et al<sup>18</sup> reported a series of 9 pilocytic astrocytomas evaluated with DSC perfusion MR imaging, in which all 9 tumors demonstrated an overshooting of the baseline or a T1-dominant contrast leakage pattern. Cha et al reported that pilocytic astrocytomas have >70% signal recovery, while medulloblastomas have <50% signal recovery, which is consistent with our findings.<sup>19</sup>

Before our study, a T1-dominant leakage pattern has most notably been demonstrated in primary CNS lymphoma and has been shown to be useful in distinguishing lymphoma from glioblastoma multiforme and CNS metastases.<sup>9-11</sup> Despite the lack of neoangiogenesis in CNS lymphoma, both glioblastoma and lymphoma have elevated rCBV but a significant difference in the high percent signal recovery for lymphomas. These features have been

**Table 1: Tumor pathology with patient age and TSITC results**

	Cases	Age (yr)		Tissue Signal-Intensity Time Curve Classification		
		Average	Range	T1	Baseline	T2
All cases	63	6.3	1.0–16.8	25	23	15
Infratentorial	39	5.6	1.2–14.2	16	13	10
Supratentorial	24	7.4	1.0–16.8	9	10	5
WHO I	25	7.1	1.1–15.0	18	5	2
WHO II	13	5.9	1.2–16.8	7	3	3
WHO III	9	4.6	1.4–12.0	0	6	3
WHO IV	16	6.4	1.0–16.2	0	9	7
Pilocytic astrocytoma	17	7.3	2.2–15.0	15	1	1
Medulloblastoma	9	6.8	2.3–13.3	0	4	5
Ependymoma WHO III	7	4.3	1.4–12.0	0	4	3
Pilomyxoid astrocytoma	6	2.9	1.2–5.8	6	0	0
Ependymoma WHO II	3	2.2	1.5–2.9	1	0	2
ATRT	3	1.4	1.0–1.9	0	3	0
GBM	3	6.9	4.2–9.5	0	2	1
Choroid plexus papilloma	2	4.1	3.1–5.2	1	1	0
Fibrillary astrocytoma	1	4.3		0	1	0
Craniopharyngioma	1	5.5		0	1	0
Desmoplastic infantile ganglioglioma	1	1.1		1	0	0
Ganglioglioma	1	12.9		0	1	0
Ganglion cell tumor	1	1.8		0	1	0
High-grade diffuse glioma	1	6.9		0	1	0
Low-grade glioma	1	12.8		0	0	1
Low-grade glioneuronal tumor	1	11.5		1	0	0
Low-grade oligoastrocytoma	1	16.8		0	1	0
Oligodendroglioma	1	15.5		0	1	0
Pineal parenchymal tumor WHO II	1	15.6		0	0	1
Supratentorial PNET	1	16.2		0	0	1
Anaplastic astrocytoma	1	4		0	1	0

**Note:**—ATRT indicates atypical teratoid rhabdoid tumor; GBM, glioblastoma multiforme; PNET, primitive neuroectodermal tumor.

**Table 2: Diagnostic sensitivity of leakage patterns and tumors with 95% confidence intervals**

	Sensitivity	Specificity	PPV	NPV
T1 leakage pattern for low-grade tumors	66% (49%–80%) <sup>a</sup> 79% (57%–92%) <sup>b</sup> 43% (19%–70%) <sup>c</sup>	100% (83%–100%) <sup>ba</sup> 100% (77%–100%) <sup>b</sup> 100% (60%–100%) <sup>c</sup>	100% (83%–100%) <sup>ba</sup> 100% (79%–100%) <sup>b</sup> 100% (52%–100%) <sup>c</sup>	66% (49%–80%) <sup>a</sup> 77% (54%–91%) <sup>b</sup> 50% (26%–74%) <sup>c</sup>
T2* leakage and baseline patterns for high-grade tumors	100% (83%–100%) <sup>a</sup> 100% (77%–100%) <sup>b</sup> 100% (60%–100%) <sup>c</sup>	66% (49%–80%) <sup>a</sup> 79% (57%–92%) <sup>b</sup> 43% (19%–70%) <sup>c</sup>	66% (49%–80%) <sup>a</sup> 77% (54%–91%) <sup>b</sup> 50% (26%–74%) <sup>c</sup>	100% (83%–100%) <sup>a</sup> 100% (79%–100%) <sup>b</sup> 100% (52%–100%) <sup>c</sup>
T1 leakage for pilocytic and pilomyxoid astrocytomas	91% (70%–98%) <sup>a</sup> 94% (69%–100%) <sup>b</sup> 83% (36%–99%) <sup>c</sup>	90% (75%–97%) <sup>a</sup> 88% (67%–97%) <sup>b</sup> 94% (68%–100%) <sup>c</sup>	84% (63%–95%) <sup>a</sup> 84% (60%–96%) <sup>b</sup> 83% (36%–99%) <sup>c</sup>	95% (81%–99%) <sup>a</sup> 95% (75%–100%) <sup>b</sup> 94% (68%–100%) <sup>c</sup>

**Note:**—PPV indicates positive predictive value; NPV, negative predictive value.

<sup>a</sup> All tumor results.

<sup>b</sup> Dexamethasone tumors results.

<sup>c</sup> Nondexamethasone tumors results.

attributed to the characteristic perivascular invasion of lymphoma cells, leading to disruption of the basement membrane and resulting vascular permeability. The hypercellularity of lymphoma with a small extravascular extracellular space has been suggested as a contributing factor, though the exact mechanism for T1-dominant leakage effects in lymphoma is not well-understood.<sup>9</sup> This finding contradicts the findings of Cha et al<sup>17</sup> in that the lack of a blood-brain barrier in metastatic disease, with resulting vascular permeability, results in a low percent recovery or a T2\*-dominant effect rather than the T1-dominant effect in CNS lymphoma.<sup>9,17</sup> Cha et al<sup>17</sup> used a flip angle of 35° compared with 80° for Mangla et al,<sup>9</sup> which may contribute to the differing TSITC results. Biologic factors may include differing rates of contrast leakage between CNS lymphoma and metastatic disease with a faster accumulation and concentration of extravascular contrast in metastatic disease leading to T2\*-dominant effects. The mechanism underlying the observed postbolus T1-dominant effects in low-grade pediatric brain tumors is not known but is also likely related to the balance between T1-shortening and T2\* effects of paramagnetic contrast medium that has leaked into the extravascular extracellular space. Other factors affecting the T1–T2\* balance may include characteristics of the extravascular space such as cellular attenuation, water content, and other molecular constituents, in addition to hemodynamic flow issues and capillary permeability.

Pilocytic astrocytomas and pilomyxoid astrocytomas account for 21 of the 25 tumors in our series demonstrating postbolus T1-dominant leakage. Pilocytic astrocytomas are described as having a biphasic histology with areas of loose glial tissue interposed with compacted piloid tissue composed of attenuated hypercellular sheets of elongated bipolar cells.<sup>20</sup> Distinguishing features of pilomyxoid astrocytomas include monomorphous piloid cells in a myxoid background with an angiocentric pattern, similar to perivascular pseudorosettes in ependymomas. While pilomyxoid astrocytomas tend to occur in younger children in the hypothalamic/chiasmatic pathway, with more aggressive behavior and a higher propensity for leptomeningeal spread, pilocytic and pilomyxoid astrocytomas have large morphologic and imaging overlap. There have been reports of recurrent pilomyxoid tumors demonstrating pilocytic features after several years, with some authors suggesting that pilomyxoid astrocytoma may be an infantile form versus an extreme subtype of pilocytic astrocytoma.<sup>21–23</sup> Because of this overlap and the lack of distinguishing imaging characteristics between the 2 tumors, we calculated diagnostic accuracy with both tumors rather than separately. Vascular proliferation can be seen in the solid component of both tumors but with more mature endothelial cells in a single layer compared with glioblastomas.<sup>24,25</sup> These single endothelial layers with open tight junctions and fenestrae and hyaline degeneration around vessels have been postulated to allow contrast medium extravasation and therefore vascular permeability.<sup>18</sup> Similar to CNS lymphomas, this level of increased vascular permeability likely plays a partial but crucial role in the T1-dominant leakage effects seen in both tumors. Further research between different pediatric tumors by using T1 signal–based dynamic contrast-enhanced MR imaging may be helpful in elucidating differences in vascular permeability.

### **Effect of Dexamethasone on Leakage Patterns**

We could not control for the administration of dexamethasone in pediatric patients with newly diagnosed brain tumors because corticosteroids are a first-line emergent therapy for controlling the cerebral swelling and the resultant mass effect from mass-occupying brain tumors. In a previous work on the same patient population, there was no significance between patients with and without dexamethasone treatment and rCBV measurements.<sup>2</sup> However, given the known rapid effects of dexamethasone in decreasing capillary permeability and reducing vasogenic edema,<sup>26,27</sup> the significance between patient populations is not surprising. However, only our low-grade tumor group was significant, and there was a larger proportion of T1-dominant and T2\*-dominant leakage patterns within the dexamethasone group. This result seems counterintuitive because high-grade tumors typically have greater vasogenic edema and mass effect, and decreasing capillary permeability should trend toward the return to baseline pattern because this pattern would best represent no leakage. In reality, multiple physiologic parameters likely affect the leakage pattern as indicated by our results. Despite the significance of dexamethasone on the low-grade tumor group, the 100% specificity of a T1-dominant leakage pattern for low-grade pediatric tumors and the high sensitivity and specificity for piloid astrocytomas remain unchanged for both groups with or without dexamethasone.

### **Implications for Patient Care**

Despite uncertainty in the exact underlying mechanism, a T1-dominant contrast leakage pattern on the signal-intensity curve obtained in the region of highest tumor rCBV is empirically highly predictive for low-grade brain tumor in the pediatric population, while a T2\*-dominant or baseline pattern has high sensitivity for a high-grade tumor. In addition to rCBV data,<sup>2</sup> TSITC from DSC perfusion potentially offer additional information not otherwise apparent with routine anatomic MR imaging sequences. Recognition of a T1-dominant leakage pattern may improve accuracy in preoperatively predicting the presence of a low-grade pediatric brain tumor. While experienced pediatric neuroradiologists can recognize low-versus-high-grade tumors in most cases, recognition of this pattern of perfusion leakage may be very helpful in the minority of cases in which low-grade pilocytic or pilomyxoid astrocytomas become large and heterogeneous, mimicking higher grade neoplasms and, conversely, when high-grade astrocytomas have benign imaging features (Figs 1 and 2). Furthermore, when complete surgical resection is not possible, knowing the likelihood of a high-grade or low-grade tumor can guide how aggressive a neurosurgeon should be in debulking the tumor, at the risk of morbidity and mortality.

### **Limitations**

The neuroradiologists evaluating the perfusion data were not blinded to the anatomic MR imaging sequences, some of which were highly suggestive of the tumor diagnosis. This scenario was unavoidable because the anatomic images provide information integral to the assessment of the perfusion images (eg, location of tumor, location of major vessels, and so forth). This limitation is reasonable however because it reflects the process in which MR



perfusion images are evaluated in clinical practice. As noted in the discussion, a T1-dominant contrast leakage pattern has been described in CNS lymphoma, and our series of 63 pediatric brain tumors included no cases of CNS lymphoma. While this represents a potential pitfall in using a T1-dominant leakage pattern to classify pediatric brain tumors as low grade, CNS lymphoma is rarely encountered in the pediatric population. Contrast medium infusion rate and peripheral intravenous catheter gauge are related issues that likely affect the quality of the perfusion study and are recognized challenges in performing DSC perfusion MR imaging on pediatric patients.<sup>28</sup> However, only 1 study of the 65 identified by the search criteria was excluded for poor contrast medium bolus, indicating that high-quality DSC perfusion MR imaging can be performed in pediatric patients with brain tumors. Differences in TR and TE parameters corresponded to those in studies obtained on different 1.5T and 3T scanners and theoretically have some effect on signal intensity and recovery/leakage patterns. However, our analysis demonstrates no significant differences in our results attributable to these different field strengths or parameters. There are no standardized criteria in the literature for T1 leak/T2\* leak or return to baseline. We arbitrarily chose the  $\pm 10\%$  range for the curve classification as a means of separation; consequently, curve classification could be altered if different thresholds are used. Similarly, as previously described, larger differences in technical parameters (flip angle, TE, TR) may result in greater differences in curve classification.

## CONCLUSIONS

There is good interobserver agreement in the classification of the DSC perfusion tissue signal-intensity time curves for pediatric brain tumors. Among our population of pediatric patients with brain tumors, a T1-dominant leakage pattern is 100% specific for a low-grade tumor and sensitive and specific for piloid astrocytomas, regardless of dexamethasone treatment. The addition of tissue signal-intensity time curves may help in cases in which low-grade tumors are large and heterogeneous, mimicking high-grade neoplasms.

Disclosures: Chen Lin—UNRELATED: Consultancy: CIVCO Medical Solutions\*; Grants/Grants Pending: Siemens.\*Money paid to the institution.

## REFERENCES

- Ostrom QT, de Blank PM, Kruchko C, et al. **Alex's Lemonade Stand Foundation Infant and Childhood Primary Brain and Central Nervous System Tumors Diagnosed in the United States in 2007–2011.** *Neuro Oncol* 2015;1(suppl 10):x1–x36 CrossRef Medline
- Ho CY, Cardinal JS, Kamer AP, et al. **Relative cerebral blood volume from dynamic susceptibility contrast perfusion in the grading of pediatric primary brain tumors.** *Neuroradiology* 2015;57:299–306 CrossRef Medline
- Kralik SF, Taha A, Kamer AP, et al. **Diffusion imaging for tumor grading of supratentorial brain tumors in the first year of life.** *AJNR Am J Neuroradiol* 2014;35:815–23 CrossRef Medline
- Panigrahy A, Nelson MD Jr, Blüml S. **Magnetic resonance spectroscopy in pediatric neuroradiology: clinical and research applications.** *Pediatr Radiol* 2010;40:3–30 CrossRef Medline
- de Fatima Vasco Aragao M, Law M, Batista de Almeida D, et al. **Comparison of perfusion, diffusion, and MR spectroscopy between low-grade enhancing pilocytic astrocytomas and high-grade astrocytomas.** *AJNR Am J Neuroradiol* 2014;35:1495–502 CrossRef Medline
- Law M, Yang S, Wang H, et al. **Glioma grading: sensitivity, specificity, and predictive values of perfusion MR imaging and proton MR spectroscopic imaging compared with conventional MR imaging.** *AJNR Am J Neuroradiol* 2003;24:1989–98 Medline
- Law M, Young R, Babb J, et al. **Histogram analysis versus region of interest analysis of dynamic susceptibility contrast perfusion MR imaging data in the grading of cerebral gliomas.** *AJNR Am J Neuroradiol* 2007;28:761–66 Medline
- Morita N, Wang S, Chawla S, et al. **Dynamic susceptibility contrast perfusion weighted imaging in grading of nonenhancing astrocytomas.** *J Magn Reson Imaging* 2010;32:803–08 CrossRef Medline
- Mangla R, Kolar B, Zhu T, et al. **Percentage signal recovery derived from MR dynamic susceptibility contrast imaging is useful to differentiate common enhancing malignant lesions of the brain.** *AJNR Am J Neuroradiol* 2011;32:1004–10 CrossRef Medline
- Hartmann M, Heiland S, Harting I, et al. **Distinguishing of primary cerebral lymphoma from high-grade glioma with perfusion-weighted magnetic resonance imaging.** *Neurosci Lett* 2003;338:119–22 CrossRef Medline
- Sugahara T, Korogi Y, Shigematsu Y, et al. **Perfusion-sensitive MRI of cerebral lymphomas: a preliminary report.** *J Comput Assist Tomogr* 1999;23:232–37 CrossRef Medline
- Hu LS, Baxter LC, Pinnaduwa DS, et al. **Optimized preload leakage-correction methods to improve the diagnostic accuracy of dynamic susceptibility-weighted contrast-enhanced perfusion MR imaging in posttreatment gliomas.** *AJNR Am J Neuroradiol* 2010;31:40–48 CrossRef Medline
- Kassner A, Annesley DJ, Zhu XP, et al. **Abnormalities of the contrast re-circulation phase in cerebral tumors demonstrated using dynamic susceptibility contrast-enhanced imaging: a possible marker of vascular tortuosity.** *J Magn Reson Imaging* 2000;11:103–13 Medline
- Jackson A, Kassner A, Annesley-Williams D, et al. **Abnormalities in the recirculation phase of contrast agent bolus passage in cerebral gliomas: comparison with relative blood volume and tumor grade.** *AJNR Am J Neuroradiol* 2002;23:7–14 Medline
- Paulson ES, Schmainda KM. **Comparison of dynamic susceptibility-weighted contrast-enhanced MR methods: recommendations for measuring relative cerebral blood volume in brain tumors.** *Radiology* 2008;249:601–13 CrossRef Medline
- Boxerman JL, Paulson ES, Prah MA, et al. **The effect of pulse sequence parameters and contrast agent dose on percentage signal recovery in DSC-MRI: implications for clinical applications.** *AJNR Am J Neuroradiol* 2013;34:1364–69 CrossRef Medline
- Cha S, Lupo JM, Chen MH, et al. **Differentiation of glioblastoma multiforme and single brain metastasis by peak height and percentage of signal intensity recovery derived from dynamic susceptibility-weighted contrast-enhanced perfusion MR imaging.** *AJNR Am J Neuroradiol* 2007;28:1078–84 CrossRef Medline
- Grand SD, Kremer S, Tropres IM, et al. **Perfusion-sensitive MRI of pilocytic astrocytomas: initial results.** *Neuroradiology* 2007;49:545–50 CrossRef Medline
- Cha S. **Dynamic susceptibility-weighted contrast-enhanced perfusion MR imaging in pediatric patients.** *Neuroimaging Clin N Am* 2006;16:137–47, ix CrossRef Medline
- Koeller KK, Rushing EJ. **From the archives of the AFIP: pilocytic astrocytoma: radiologic-pathologic correlation.** *Radiographics* 2004;24:1693–708 CrossRef Medline
- Chikai K, Ohnishi A, Kato T, et al. **Clinico-pathological features of pilomyxoid astrocytoma of the optic pathway.** *Acta Neuropathol* 2004;108:109–14 Medline
- Ceppa EP, Bouffet E, Griebel R, et al. **The pilomyxoid astrocytoma and its relationship to pilocytic astrocytoma: report of a case and a critical review of the entity.** *J Neurooncol* 2007;81:191–96 Medline
- Jeon YK, Cheon JE, Kim SK, et al. **Clinicopathological features and global genomic copy number alterations of pilomyxoid astrocytoma in the hypothalamus/optic pathway: comparative analysis with pilocytic astrocytoma using array-based comparative genomic hybridization.** *Mod Pathol* 2008;21:1345–56 CrossRef Medline

24. Brat DJ, Scheithauer BW, Fuller GN, et al. **Newly codified glial neoplasms of the 2007 WHO Classification of Tumours of the Central Nervous System: angiocentric glioma, pilomyxoid astrocytoma and pituicytoma.** *Brain Pathol* 2007;17:319–24 CrossRef Medline
25. Johnson MW, Eberhart CG, Perry A, et al. **Spectrum of pilomyxoid astrocytomas: intermediate pilomyxoid tumors.** *Am J Surg Pathol* 2010;34:1783–91 CrossRef Medline
26. Jarden JO, Dhawan V, Moeller JR, et al. **The time course of steroid action on blood-to-brain and blood-to-tumor transport of  $^{82}\text{Rb}$ : a positron emission tomographic study.** *Ann Neurol* 1989;25:239–45 CrossRef Medline
27. Sinha S, Bastin ME, Wardlaw JM, et al. **Effects of dexamethasone on peritumoural oedematous brain: a DT-MRI study.** *J Neurol Neurosurg Psychiatry* 2004;75:1632–35 CrossRef Medline
28. Yeom KW, Mitchell LA, Lober RM, et al. **Arterial spin-labeled perfusion of pediatric brain tumors.** *AJNR Am J Neuroradiol* 2014;35:395–401 CrossRef Medline

# GABA and Glutamate in Children with Primary Complex Motor Stereotypies: An $^1\text{H}$ -MRS Study at 7T

A.D. Harris, H.S. Singer, A. Horska, T. Kline, M. Ryan, R.A.E. Edden, and E.M. Mahone



## ABSTRACT

**BACKGROUND AND PURPOSE:** Complex motor stereotypies are rhythmic, repetitive, fixed, purposeful but purposeless movements that stop with distraction. They can occur in otherwise normal healthy children (primary stereotypies) as well in those with autism spectrum disorders (secondary stereotypies). The underlying neurobiologic basis for these movements is unknown but is thought to involve cortical-striatal-thalamo-cortical pathways. To further clarify potential neurochemical alterations, gamma-aminobutyric acid (GABA), glutamate, glutamine, *N*-acetylaspartate, and choline levels were measured in 4 frontostriatal regions by using  $^1\text{H}$  MRS at 7T.

**MATERIALS AND METHODS:** A total of 18 children with primary complex motor stereotypies and 24 typically developing controls, ages 5–10 years, completed MR spectroscopy at 7T. Single voxel STEAM acquisitions from the anterior cingulate cortex, premotor cortex, dorsolateral prefrontal cortex, and striatum were obtained, and metabolites were quantified with respect to Cr by using LCModel.

**RESULTS:** The 7T scan was well tolerated by all the participants. Compared with the controls, children with complex motor stereotypies had lower levels of GABA in the anterior cingulate cortex (GABA/Cr,  $P = .049$ ; GABA/Glu,  $P = .051$ ) and striatum (GABA/Cr,  $P = .028$ ; GABA/Glu,  $P = .0037$ ) but not the dorsolateral prefrontal cortex or the premotor cortex. Glutamate, glutamine, NAA, and Cho levels did not differ between groups in any of the aforementioned regions. Within the complex motor stereotypies group, reduced GABA to Cr in the anterior cingulate cortex was significantly associated with greater severity of motor stereotypies ( $r = -0.59$ ,  $P = .021$ ).

**CONCLUSIONS:** These results indicate possible GABAergic dysfunction within corticostriatal pathways in children with primary complex motor stereotypies.

**ABBREVIATIONS:** ACC = anterior cingulate cortex; CMS = complex motor stereotypies; DLPFC = dorsolateral prefrontal cortex; GABA = gamma-aminobutyric acid; Gln = glutamine; Glu = glutamate; PMC = premotor cortex

MR spectroscopy allows for the noninvasive assessment of tissue metabolite content. It recently became possible to perform such measurements at ultra-high field (7T), with the benefits of increased SNR and improved separation of metabolite

signals.<sup>1–3</sup> In particular, the overlapping signals of glutamate (Glu), the primary excitatory neurotransmitter, and glutamine (Gln), its metabolic precursor, can be differentiated and quantified at 7T. Gamma-aminobutyric acid (GABA), the primary inhibitory neurotransmitter, can also be resolved and quantified at 7T. To date, no previous studies applied ultra-high-field measurements in young pediatric populations (<10 years of age).

Complex motor stereotypies (CMS) are rhythmic, repetitive, fixed (in fashion, form, amplitude, and location) movements that appear purposeful but are purposeless (ie, serve no obvious adaptive function or purpose) and stop with sensory stimulation or

Received April 20, 2015; accepted after revision August 12.

From the Russell H. Morgan Department of Radiology and Radiological Science (A.D.H., A.H., R.A.E.E.), Department of Neurology (H.S.S., T.K.), Department of Pediatrics (H.S.S.), and Department of Psychiatry and Behavioral Sciences (E.M.M.), The Johns Hopkins University School of Medicine, Baltimore, Maryland; and Department of Neuropsychology (M.R., E.M.M.) and F.M. Kirby Center for Functional Brain Imaging (A.D.H., A.H., R.A.E.E.), Kennedy Krieger Institute, Baltimore, Maryland.

Supported by National Institutes of Health grants: 1R21 MH092693, P41 EB015909, U54 079123, and U11 RR025005 and the Nesbit-McMaster Foundation. The funding agencies were not involved in the design, data collection, data analysis, manuscript preparation, or publication design. The authors have stated that they had no interests that could be perceived as posing a conflict or bias.

Previously presented, in part, at: Annual Meeting of the Child Neurology Society, October 10–14, 2014; Columbus, Ohio; and Annual Meeting of the International Society for Magnetic Resonance in Medicine, May 10–16, 2014; Milan, Italy.

Please address correspondence to Ashley D. Harris, PhD, Russell H. Morgan Department of Radiology and Radiological Science, Johns Hopkins University School of Medicine, 600 North Wolfe St, Park 367C, Baltimore, MD 21287; e-mail: ashley.harris2@ucalgary.ca

Indicates open access to non-subscribers at [www.ajnr.org](http://www.ajnr.org)

<http://dx.doi.org/10.3174/ajnr.A4547>

distraction.<sup>4</sup> Motor stereotypies are defined clinically and are differentiated from tics by their patterned, coordinated, repetitive, rhythmic, and nonreflexive features, and developmental time course.<sup>5</sup> Episodes (eg, bilateral flapping and/or waving arm or hand movements, rotating the hands, and fluttering fingers in front of the face) last for periods of seconds to minutes, occur in clusters, and are associated with periods of excitement, engrossment, fatigue, boredom, and stress. Often occurring many times per day, these movements can adversely impact social, academic, and cognitive function.<sup>6</sup>

Although previously thought to only be associated with intellectual disability, sensory deprivation, or autism spectrum disorders, CMS are now recognized to occur as a “primary” form in as many as 3%–4% of otherwise typically developing children.<sup>7</sup> Primary CMS typically appear before the age of 3 years, have a persistent course, and respond poorly to pharmacologic intervention.<sup>8,9</sup> Stereotypies are not better described as tics or compulsions, though some degree of overlap and co-occurrence with other disorders that affect frontostriatal brain systems (attention deficit/hyperactivity disorder, obsessive compulsive disorder, tic disorders, developmental coordination disorder) is common.<sup>10</sup> Young children who present with CMS are at particular risk for social, cognitive, and academic difficulties. Earlier identification and a better understanding of the neurobiologic markers of CMS can potentially minimize the harmful impact of the disorder and lead to more targeted behavioral and pharmacologic treatments.

The underlying pathophysiologic mechanism of stereotypies has not been fully established; hypotheses range from psychological concerns to neurobiologic abnormalities.<sup>5,9,11</sup> The absence of premotor movement–related cortical potentials in children with primary CMS during these stereotypic movements indicates that motor stereotypies are initiated by different neural mechanisms than voluntary, purposeful movements.<sup>12</sup> Current research indicates that stereotypies, similar to many other movement disorders, likely involve cortico-striatal-thalamo-cortical circuits and their interconnecting brain regions. Distinct cortical-striatal pathways that support goal-directed (ventromedial prefrontal to caudate) and habitual (premotor to putamen) behaviors have been identified<sup>13</sup> and the limbic circuit (anterior cingulate cortex [ACC] to ventral striatum) is also involved in motor control<sup>13</sup> through its contributions to the anticipation of tasks, emotional, motivational, reward, attention, vigor, autonomic information, and impulse control.<sup>14</sup> In primary CMS, preliminary volumetric imaging results indicate a decreased volume of the putamen-caudate,<sup>15</sup> and recent findings from a deer mouse model of CMS demonstrate a loss of striatal volume with a particular reduction in GABAergic medium spiny neurons (H.S.S., oral communication, January 22, 2015).

Several neurotransmitters, including dopamine, Glu, GABA, serotonin, norepinephrine, acetylcholine, and opioids, have important roles in cortico-striatal-thalamo-cortical pathways. To date, there has been limited *in vivo* investigation into the link between specific neurotransmitter anomalies and motor symptoms in CMS. <sup>1</sup>H-MRS provides an opportunity to measure the major excitatory (Glu) and inhibitory (GABA) neurotransmitters involved in cortico-striatal-thalamo-cortical circuits *in vivo*. Glu and Gln are not as well resolved at 3T (and lower field strengths)

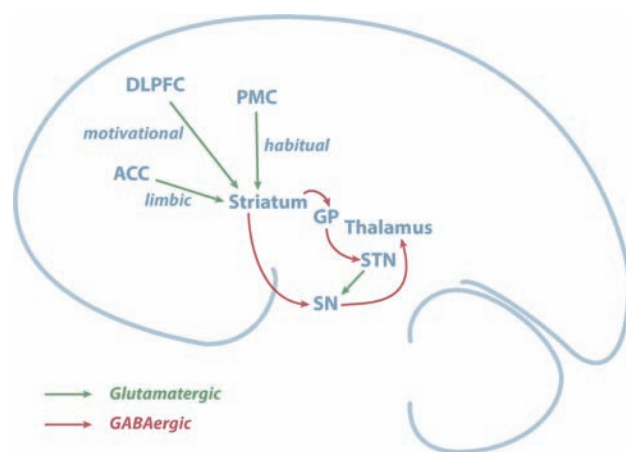


**FIG 1.** Illustration of the motor pathways and the neurotransmitter connections investigated in the current study. DLPFC, PMC, and ACC provide glutamatergic inputs to the striatum and outputs from the striatum to the globus pallidus and substantia nigra are GABAergic.

as at 7T and, therefore, are often reported as Glx. This may be problematic because both of these amino acids can influence neuronal functions and there are pathologic processes in which one amino acid can increase and the other decrease.<sup>16</sup> At higher field strengths (ie, 7T), Glu and Gln can more easily and reliably be differentiated.<sup>1,2</sup> Previous research on habitual behaviors has primarily hypothesized altered dopaminergic neurotransmission, and animal models have been developed to mimic this change.<sup>17</sup> Involvement of the glutamatergic system has been indicated based, in part, on the interaction between dopaminergic and glutamatergic activity in the corticostriatal system.<sup>13</sup> In Tourette syndrome, another childhood movement disorder with intermittent paroxysmal motor activity, animal models and human studies have indicated a role for GABA.<sup>18–20</sup>

Potential glutamatergic and GABAergic dysfunction in the goal-directed, habitual, and limbic pathways (Fig 1) were the focus of the present study. Specifically, we hypothesized that GABA and Glu levels in these pathways would be altered in primary CMS compared with healthy controls, with the greatest dysfunction observed in regions that support habitual circuitry (premotor-striatal). Examination of Gln, NAA, and Cho was also completed to provide a contrast for examination of GABA and Glu.

## MATERIALS AND METHODS

### Participants

This study was approved by the institutional review board of the Johns Hopkins Medical Institutions. Parents or legal guardians of all the participants provided informed, written consent, and all the participants provided assent before the study. Eighteen children diagnosed with nonautistic, primary CMS, age range 5–10 years, were recruited through the Pediatric Movement Disorders Clinic, Johns Hopkins Hospital; whereas 24 typically developing children were recruited through community advertisements to act as control participants. A pediatric neurologist (H.S.S.) made the diagnosis of CMS, with specific confirmation that movements were not better characterized as tics. Clinical characteristics used to distinguish motor stereotypies from chronic motor tics include the following: earlier age of onset, rhythmic movements of the upper extremities, a constant and fixed pattern of movements, a



continuous and prolonged duration, the absence of a premonitory urge, stereotypy exacerbation when engrossed in an activity, and suppression by distraction (ie, calling one's name).<sup>13</sup>

Exclusion criteria included current Full Scale IQ < 80, previous diagnoses of intellectual disability or autism spectrum disorders, and medication use in the past 3 months. In addition, all the participants in the CMS group were screened for autism spectrum disorders and excluded if they had a score of >13 when using the Autism Spectrum Screening Questionnaire.<sup>21</sup> Severity of stereotypy symptoms was rated by parents at the time of scanning by using the Stereotypy Severity Scale.<sup>22</sup> The Stereotypy Severity Scale is a 5-item caregiver questionnaire in which the parent rates the child's motor stereotypies with regard to the motor severity by rating the number, frequency, intensity, and interference of stereotypies (maximum, 18 points), and the global impairment (maximum, 50 points) during the past few days. Stereotypy Severity Scale motor and total stereotypy scores were used for brain-behavior analyses.

### **MR Imaging and MR Spectroscopy Acquisition**

All the children had a mock scan training session to improve comfort, decrease anxiety, and train them to lie still. No sedation was used. Structural MRI and MRS were performed by using a 7T scanner (Achieva; Philips Healthcare, Best, the Netherlands) equipped with a quadrature transmit head coil and 32-channel receive coil array (Nova Medical, Wilmington, Massachusetts). A high-quality T1-weighted MPRAGE structural brain image (TE/TR = 2.1/4.8 milliseconds; resolution,  $0.6 \times 0.6 \times 0.6 \text{ mm}^3$ ; total scan time, 6 minutes and 32 seconds) was acquired for planning of the MRS voxel locations and subsequent gray matter segmentation by using SPM (FIL Methods Group, UCL, London UK; <http://www.fil.ion.ucl.ac.uk/spm/>).<sup>23</sup> Spectra were acquired from 4 voxels: ACC, dorsolateral prefrontal cortex (DLPFC), premotor cortex (PMC), and striatum. The STEAM sequence was used for signal localization with the following parameters: TE, mixing time, TR = 14 milliseconds, 26 milliseconds, 3000 milliseconds, respectively, 96 averages, and VAPOR (variable power and optimized relaxation delays) water suppression. Voxel placement was performed by using a documented procedure and images for reference. The approximately 8-mL ACC voxel was placed in the left hemisphere on the ACC aligned tangential to the corpus callosum in the sagittal plane, with the posterior edge centered to the genu. This region of the ACC was selected to interrogate the premotor-striatal circuitry. The approximately 8-mL PMC voxel was placed on the left side, with the posterior face aligned to the precentral sulcus, and the inferior face above the level of the corpus callosum. The approximately 8-mL DLPFC voxel was placed on the left side, anterior to the premotor voxel, angulated so as to maximize GM content while avoiding the skull. The approximately 8-mL striatum voxel was placed on the left side, aligned in the sagittal plane with the principal axis of the striatum.

### **Postacquisition Image Analysis**

LCModel (<http://www.lcmodel.com/>)<sup>24</sup> was used to quantify both GABA and Glu by using an in-house basis set that includes a macromolecular basis spectrum. GABA, Glu, Gln, NAA, and Cho

were measured as a ratio to Cr within each voxel. GABA/Glu was also calculated to investigate inhibitory-excitatory balance.

### **Statistical Analysis**

Age, socioeconomic status, handedness, and sex balance between the groups were compared by using ANOVAs for continuous variables and  $\chi^2$  analyses for categorical variables. Distributions for metabolite ratios were examined for normality by using the Kolmogorov-Smirnov test, and those that showed significant skew were transformed by using square-root transformation (indicated in the text with superscript t).

To examine global metabolite differences between the groups, all voxel locations were pooled and a linear mixed-effects model with the Fisher least significant difference as a post hoc test was used to examine differences in regional metabolite concentrations in CMS compared with controls, controlling for age, sex, and GM fraction within the voxel. This test examines differences in metabolite levels across all brain regions and benefits from an increase in power when examining the fixed effects factors (age and sex). Subsequently, to address the primary aim of the study, regional differences in metabolites were tested by using a second set of linear mixed-effects models for each voxel (ACC, DLPFC, PMC, and striatum). These models were derived and tested independently; however, regional measurements within a single participant are not independent. Within each region, measurements from different individuals are assumed to be independent. As such, no corrections for multiple comparisons were performed. The association between symptom severity (Stereotypy Severity Scale motor and total scores) and metabolite levels was examined by using Pearson correlations or partial correlations as applicable (controlling for GM fraction).

## **RESULTS**

### **Demographics**

Eighteen participants with CMS were recruited. One participant in the CMS group had comorbid diagnosis of separation anxiety disorder. The mean Autism Spectrum Screening Questionnaire score across subjects with CMS was  $6.6 \pm 4.3$ , with an inner quartile range of 3–9.75, well below the threshold for a diagnosis of comorbid autism spectrum disorder. There were no significant differences between CMS and control groups in age ( $F[1,40] = 3.19, P = .082$ ), socioeconomic status ( $F[1,40] = 0.379, P = .542$ ), or handedness ( $\chi^2 = 0.062, P = .094, n = 42$ ); however, there was a significant difference between groups in sex distribution ( $\chi^2 = 7.41, P = .011, n = 42$ ). Most of the individuals in the CMS group (14/18) and the control group (22/24) were right-handed, with no significant differences between groups in proportion of right- versus left-handers ( $\chi^2 = 1.62, P = .375, n = 42$ ). For mixed-effects analyses that examined metabolite differences between groups, age, sex, and GM fraction were used as covariates in the model.

### **MR Spectroscopy Acquisition**

The MR imaging and/or MR spectroscopy protocol of 45–60 minutes of duration was well tolerated in both controls and children with CMS. Nevertheless, all 4 MR spectroscopy voxels were not acquired in all the children due to movement or child fatigue, which resulted in some missing data. Two children (both con-

trols) completed a second scanning session to acquire the remaining voxels. Table 1 summarizes the subject demographics for each voxel.

### Spectra

Example spectra from a participant with CMS are shown in Fig 2. Across regions, the distributions for GABA/Cr, Glu/Cr, Gln/Cr, NAA/Cr, and Cho/Cr were significantly skewed (Kolmogorov-Smirnov test,  $P < .05$  for each) and were thus transformed by using square-root transformation for subsequent analysis. The Kolmogorov-Smirnov tests confirmed the GABA/Glu data to be normally distributed. Due to the challenges of segmenting 7T pediatric images, GM fractions were available for the following number of participants (for the controls: ACC, 21/24; DLPFC, 17/20; PMC, 17/19; striatum, 13/16; and for the CMS group: ACC, 16/16; DLPFC, 13/13; PMC, 12/13; and striatum, 18/18). To facilitate linear mixed-effects analyses, missing data for each voxel were imputed by using the mean GM fraction for the respective voxels.

To test for global group differences in metabolites (ie, across the whole brain, when controlling for age, sex, and GM fraction),

**Table 1: Summary demographics for each voxel dataset**

	CMS			Controls		
	No.		Age, y (mean $\pm$ SD)	No.		Age, y (mean $\pm$ SD)
	n	Boys		n	Boys	
ACC	16	14	6.7 $\pm$ 1.4	24	9	7.5 $\pm$ 1.5
PMC	13	10	6.4 $\pm$ 1.5	18	9	7.4 $\pm$ 1.4
Striatum	18	15	6.7 $\pm$ 1.5	17	9	7.1 $\pm$ 1.2
DLPFC	13	11	6.7 $\pm$ 1.5	20	9	7.4 $\pm$ 1.5

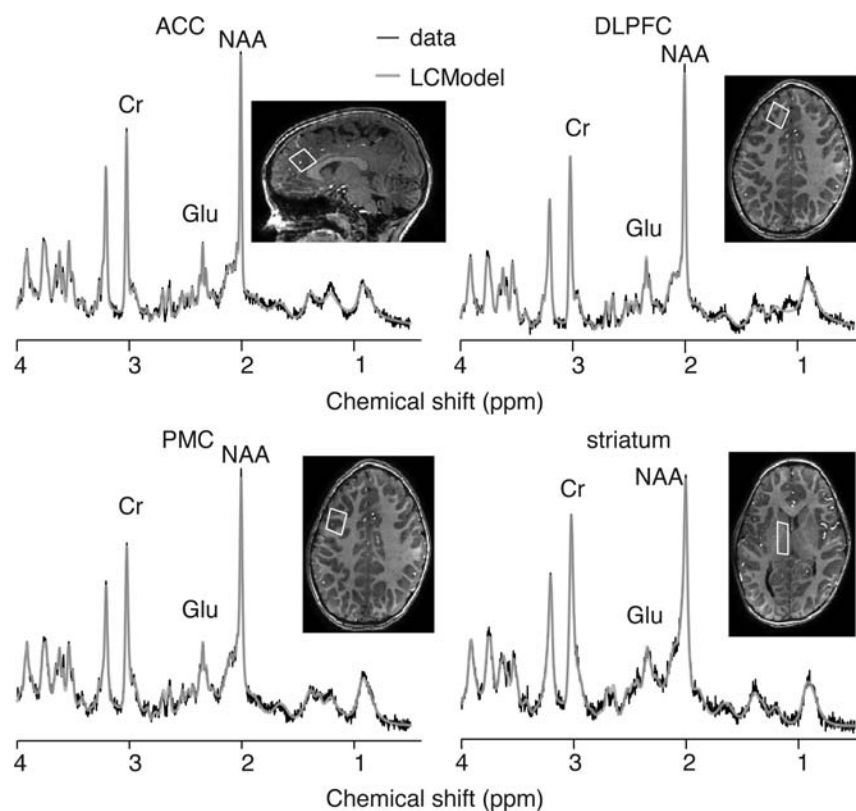


**FIG 2.** Example spectra and LCModel fit from each voxel.

data were pooled across all regions and did not differ between groups for GABA/Cr<sup>t</sup> ( $P = .119$ ), Glu/Cr<sup>t</sup> ( $P = .432$ ), Gln/Cr<sup>t</sup> ( $P = .697$ ), NAA/Cr<sup>t</sup> ( $P = .144$ ), or Cho/Cr<sup>t</sup> ( $P = .841$ ). Conversely, the overall group difference for GABA/Glu approached significance ( $P = .052$ ). Although age and sex were not associated with any of these metabolite ratios across all voxels or within any individual voxel, they, nevertheless, were retained in the model. Across the whole brain, the GM fraction was associated significantly with Glu/Cr<sup>t</sup> and NAA/Cr<sup>t</sup> (both  $P < .001$ ), and GABA/Glu ( $P = .021$ ), and was retained as a covariate for these models as well.

Data were subsequently analyzed in the individual voxels, controlling for age, sex, and GM fraction. Mean metabolite ratios within each voxel are presented in Table 2. There were no significant group differences in metabolite levels in any of the 4 voxels for Glu/Cr<sup>t</sup>, Gln/Cr<sup>t</sup>, NAA/Cr<sup>t</sup>, or Cho/Cr<sup>t</sup>. For GABA/Cr<sup>t</sup>, there were significant metabolite reductions among the CMS group within the ACC ( $F[1,35] = 4.163$ ,  $P = .049$ ,  $\eta_p^2 = 0.106$ ) and striatum ( $F[1,30] = 5.44$ ,  $P = .027$ ,  $\eta_p^2 = 0.154$ ) but not within DLPFC ( $F[1,26] = 0.526$ ,  $P = .475$ ,  $\eta_p^2 = 0.020$ ) or PMC ( $F[1,27] = 2.156$ ,  $P = .121$ ,  $\eta_p^2 = 0.087$ ). A similar pattern was seen for GABA/Glu, which showed reductions among the patients with CMS in ACC ( $F[1,35] = 4.07$ ,  $P = .051$ ,  $\eta_p^2 = 0.104$ ) and striatum ( $F[1,30] = 4.74$ ,  $P = .037$ ,  $\eta_p^2 = 0.137$ ), but not DLPFC ( $F[1,26] = 0.01$ ,  $P = .958$ ,  $\eta_p^2 < 0.001$ ) or PMC ( $F[1,27] = 1.48$ ,  $P = .234$ ,  $\eta_p^2 = 0.052$ ).

The association between GABA ratios (GABA/Cr<sup>t</sup>, GABA/Glu) and stereotypy severity (Stereotypy Severity Scale) were examined in the CMS group within the voxels, showing group differences (ACC, striatum). Within the ACC, the GABA/Cr<sup>t</sup> ratio was significantly negatively associated with the total motor Stereotypy Severity Scale ( $r = -0.59$ ,  $P = .021$ ,  $n = 15$ ) (Fig 3). Within the striatum, both GABA/Cr<sup>t</sup> ( $r = 0.50$ ,  $P = .039$ ,  $n = 17$ ) and GABA/Glu ( $r = 0.58$ ,  $P = .019$ ,  $n = 15$ ) showed significant positive associations with the total Stereotypy Severity Scale score.

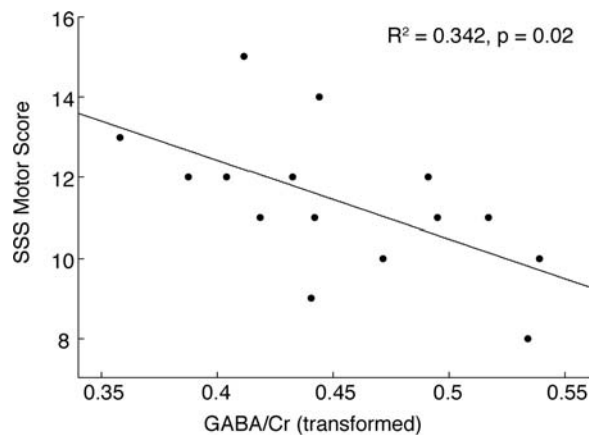
### DISCUSSION

To our knowledge, this is the first <sup>1</sup>H-MRS study performed at 7T in a young pediatric clinical population. Although the 7T MR system is classified as an investigational device, it is a nonsignificant-risk device per the FDA. Strict guidelines guard against excessive power deposition, which was continuously monitored, and the acquisitions used here stayed well within these limits. The combined experience at multiple institutions over the past 10 years in adults has not revealed any significant risks of 7T imaging. Some participants had experienced dizziness, and, for this reason, we do not recruit participants with a history of vertigo, seizure disorder, middle ear disorder, and double vision. Since

**Table 2: GABA and Glu levels across all voxels in the CMS and control groups**

	GABA/Cr		Glu/Cr		GABA/Glu	
	CMS	Controls	CMS	Controls	CMS	Controls
ACC	0.21 ± 0.052 <sup>a</sup>	0.28 ± 0.11 <sup>a</sup>	1.65 ± 0.10	1.64 ± 0.10	0.13 ± 0.029 <sup>a</sup>	0.17 ± 0.059 <sup>a</sup>
DLPFC	0.23 ± 0.10	0.22 ± 0.20	1.66 ± 0.10	1.60 ± 0.16	0.13 ± 0.066	0.13 ± 0.10
PMC	0.23 ± 0.13	0.26 ± 0.12	1.60 ± 0.13	1.67 ± 0.16	0.14 ± 0.077	0.15 ± 0.061
Striatum	0.24 ± 0.055 <sup>a</sup>	0.28 ± 0.049 <sup>a</sup>	1.29 ± 0.12	1.28 ± 0.15	0.18 ± 0.038 <sup>a</sup>	0.22 ± 0.048 <sup>a</sup>

<sup>a</sup>Significant differences between CMS and control groups are indicated ( $P < .05$ ).

**FIG 3.** Association between GABA/Cr (after square-root transformation) in the ACC and severity of motor stereotypy.

2009, our research team has scanned >100 children at 7T with no adverse effects. The MR spectroscopy protocol here was well tolerated in all 42 participants, with no report of dizziness, nausea, or other discomfort. The objective was to investigate GABA and Glu in the corticostriatal networks thought to be involved in the neurobiology of CMS.<sup>13,25</sup> The use of an ultra-high field affords increased SNR and spectra resolution, and enables the quantification of Glu rather than the mixed index of Glx.<sup>1-3</sup>

Although there is limited literature for comparison, the levels of GABA and Glu are consistent with a previous 7T study with a voxel in the ACC.<sup>3</sup> For this study, Cr was used as the reference signal. The implicit assumption that Cr does not change across the brain or with development is supported by finding only GABA and GABA/Glu differences in 2 voxels and no changes in other metabolites. Although water-signal referencing is becoming the standard in MR spectroscopy, it was not possible in the current study, and it is not clear how water-referenced metabolite quantification would be impacted by changes in water relaxation during childhood.<sup>26,27</sup> The primary findings were decreased GABA levels in CMS in the striatum and ACC but not in the PMC or DLPFC, and associations between ACC and striatal GABA and stereotypy severity. Similarly, decreases of GABA/Glu were detected in the ACC and striatum. These findings are likely driven by the decrease in GABA in these regions. No group differences in Glu, Gln, NAA, or Cho were detected. NAA and Cho analysis were included for completeness, not to investigate a specific hypothesis for these metabolites. This pattern of results indicates that inhibitory dysfunction in the ACC and striatum are associated with primary CMS. Of note, these measurements were obtained at rest, without accounting for the time from the last stereotypic behavior. Whether there are additional differences that present

during a stereotypy episode cannot be quantified by using this methodology.

Reduced striatal GABA in young children with CMS was identified in this study. Unfortunately, the limited spatial resolution of MR spectroscopy does not allow differentiation among putamen (habitual pathway), caudate (goal-directed pathway), and ventral (limbic pathway) striatum (Fig 1). The habitual motor network, composed of the PMC and putamen,<sup>13</sup> is involved in the development, learning, and control of habitual motor actions.<sup>28</sup> Functional connectivity analysis implicated the habitual circuit in slips of action (ie, extraneous behavior directed at no longer rewarding outcomes),<sup>29</sup> and a morphologic study detected reduced putamen volume in older children with CMS.<sup>10</sup> Hence, the current data could support a central role for the habitual pathway in CMS<sup>4,11,13</sup> based, in part, on decreased GABAergic inhibition either within or involving output from the putamen. Another small volumetric study in CMS identified a decrease in size and/or GM attenuation of the caudate,<sup>15</sup> which raises the possibility of a dysfunction in the goal-directed pathway. Regardless of whether the goal-directed or habitual pathway is involved, decreased levels of GABA in the striatum indicate that inhibitory output from the striatum is altered in childhood CMS.

The observation of decreased GABA and its association with stereotypy severity in the ACC raises the possibility that a dysfunction in CMS could be within the emotional-limbic circuit. The emotional-limbic circuit includes the ACC projections to the olfactory tubercle and nucleus accumbens (ventral striatum), as shown in Fig 1. Whether the behavioral alteration is related directly to the ACC involvement in conflict monitoring and response<sup>30</sup> or is secondary to increased, but undetected, glutamatergic activity from the ACC to the ventral striatum is unknown.

The combined results of this study indicate that CMS is not associated with direct alterations in Glu levels in children. Nevertheless, decreased GABA levels could result in poor GABAergic modulation and tuning of glutamatergic synapses rather than simply impairing GABAergic network components. Although 7T MR spectroscopy provides the ability to more easily and reliably differentiate Glu from its precursor Gln, it does not provide the ability to differentiate the metabolic and synaptic pools of Glu or GABA.<sup>31</sup> It, therefore, is possible that an imbalance between the metabolic and neurotransmitter Glu pools is present, which impacts glutamatergic function, but is not detected by MR spectroscopy. It is important to note that all statistical models were devised and tested independently. Measurements from different individuals are assumed to be independent; however, measurements from different regions within an individual are not independent. Thus, in this study, no corrections for multiple comparisons were applied, but significant results would not have survived a Bonferroni correction for multiple comparisons.



## CONCLUSIONS

To investigate the neurobiology of CMS, we successfully performed an MR spectroscopy study of children at 7T to examine GABA and Glu in multiple brain regions. We showed significantly lower GABA in the ACC and striatum in patients with CMS compared with healthy controls. These findings were consistent with abnormal function of corticostriatal networks in children with primary CMS.

Disclosures: Alena Horská—RELATED: Grant: National Institutes of Health (NIH).<sup>\*</sup> Comments: Dr. H. Singer, Principal Investigator. Matthew Ryan—RELATED: Supported by IR21 MH092693; the Nesbit-McMaster Foundation; U54 079123; and UL1 RR025005.<sup>\*</sup> The funding agencies were not involved in the design, data collection, data analysis, manuscript preparation, or publication design. Richard Edden—RELATED: Grant: This work was supported by NIH EB015909.<sup>\*</sup> E. Mark Mahone—RELATED: Grant: NIH IR21 MH092693.<sup>\*</sup> NIH P41 EB015909.<sup>\*</sup> NIH U54 079123.<sup>\*</sup> NIH UL1 RR025005.<sup>\*</sup> Nesbit-McMaster Foundation.<sup>\*</sup> Support for Travel to Meetings for the Study or Other Purposes: NIH IR21 MH092693. <sup>\*</sup>Money paid to the institution.

## REFERENCES

1. Tkac I, Oz G, Adriany G, et al. **In vivo 1H NMR spectroscopy of the human brain at high magnetic fields: metabolite quantification at 4T vs. 7T.** *Magn Reson Med* 2009;62:868–79 CrossRef Medline
2. Mekle R, Mlynárik V, Gambarota G, et al. **MR spectroscopy of the human brain with enhanced signal intensity at ultrashort echo times on a clinical platform at 3T and 7T.** *Magn Reson Med* 2009;61:1279–85 CrossRef Medline
3. Dou W, Palomero-Gallagher N, van Tol MJ, et al. **Systematic regional variations of GABA, glutamine, and glutamate concentrations follow receptor fingerprints of human cingulate cortex.** *J Neurosci* 2013;33:12698–704 CrossRef Medline
4. Singer HS. **Stereotypic movement disorders.** *Handb Clin Neurol* 2011;100:631–39 CrossRef Medline
5. Mahone EM, Bridges D, Prahme C, et al. **Repetitive arm and hand movements (complex motor stereotypies) in children.** *J Pediatr* 2004;145:391–95 CrossRef Medline
6. McCurdy MD, Bellows A, Ferrand J, et al. **Social cognition, repetitive behavior, and ADHD symptoms among children with primary complex motor stereotypies.** *J Int Neuropsychol Soc* 2014;20:12
7. Foster LG. **Nervous habits and stereotyped behaviors in preschool children.** *J Am Acad Child Adolesc Psychiatry* 1998;37:711–17 CrossRef Medline
8. Harris KM, Mahone EM, Singer HS. **Nonautistic motor stereotypies: clinical features and longitudinal follow-up.** *Pediatr Neurol* 2008;38:267–72 CrossRef Medline
9. Oakley C, Mahone EM, Morris-Berry C, et al. **Primary complex motor stereotypies in older children and adolescents: clinical features and longitudinal follow-up.** *Pediatr Neurol* 2015;52:398–403.e1 CrossRef Medline
10. Mahone EM, Crocetti D, Kline T, et al. **Anomalous putamen development in children with primary complex motor stereotypies.** *Annals Neurol* 2014;76(suppl 18):S227
11. Gao S, Singer HS. **Complex motor stereotypies: an evolving neurobiological concept.** *Future Neurol* 2013;8:273–85
12. Houdayer E, Walthall J, Belluscio BA, et al. **Absent movement-related cortical potentials in children with primary motor stereotypies.** *Mov Disord* 2014;29:1134–40 CrossRef Medline
13. Singer HS. **Motor control, habits, complex motor stereotypies, and Tourette syndrome.** *Ann N Y Acad Sci* 2013;1304:22–31 CrossRef Medline
14. Gruber AJ, McDonald RJ. **Context, emotion, and the strategic pursuit of goals: interactions among multiple brain systems controlling motivated behavior.** *Front Behav Neurosci* 2012;6:50 CrossRef Medline
15. Kates WR, Lanham DC, Singer HS. **Frontal white matter reductions in healthy males with complex stereotypies.** *Pediatr Neurol* 2005;32:109–12 CrossRef Medline
16. Novotny EJ Jr, Fulbright RK, Pearl PL, et al. **Magnetic resonance spectroscopy of neurotransmitters in human brain.** *Ann Neurol* 2003;54(suppl 6):S25–S31 CrossRef Medline
17. Aliane V, Perez S, Bohren Y, et al. **Key role of striatal cholinergic interneurons in processes leading to arrest of motor stereotypies.** *Brain* 2011;134:110–18 CrossRef Medline
18. Macri S, Onori MP, Roessner V, et al. **Animal models recapitulating the multifactorial origin of Tourette syndrome.** *Int Rev Neurobiol* 2013;112:211–37 CrossRef Medline
19. Puts NA, Harris AD, Crocetti D, et al. **Reduced GABAergic inhibition and abnormal sensory processing in children with Tourette syndrome.** *J Neurophysiol* 2015;114:808–17 CrossRef Medline
20. Draper A, Stephenson MC, Jackson GM, et al. **Increased GABA contributes to enhanced control over motor excitability in Tourette syndrome.** *Curr Biol* 2014;24:2343–47 CrossRef Medline
21. Ehlers S, Gillberg C, Wing L. **A screening questionnaire for Asperger syndrome and other high-functioning autism spectrum disorders in school age children.** *J Autism Dev Disord* 1999;29:129–41 CrossRef Medline
22. Miller JM, Singer HS, Bridges DD, et al. **Behavioral therapy for treatment of stereotypic movements in nonautistic children.** *J Child Neurol* 2006;21:119–25 CrossRef Medline
23. Ashburner J, Friston KJ. **Unified segmentation.** *NeuroImage* 2005;26:839–51 CrossRef Medline
24. Provencher SW. **Estimation of metabolite concentrations from localized in vivo proton NMR spectra.** *Magn Reson Med* 1993;30:672–79 CrossRef Medline
25. Balleine BW, O'Doherty JP. **Human and rodent homologies in action control: corticostriatal determinants of goal-directed and habitual action.** *Neuropsychopharmacology* 2010;35:48–69 CrossRef Medline
26. Kumar R, Delshad S, Macey PM, et al. **Development of T2-relaxation values in regional brain sites during adolescence.** *Magn Reson Imaging* 2011;29:185–93 CrossRef Medline
27. Paus T, Collins DL, Evans AC, et al. **Maturation of white matter in the human brain: a review of magnetic resonance studies.** *Brain Res Bull* 2001;54:255–66 CrossRef Medline
28. Tricomi E, Balleine BW, O'Doherty JP. **A specific role for posterior dorsolateral striatum in human habit learning.** *Eur J Neurosci* 2009;29:2225–32 CrossRef Medline
29. de Wit S, Watson P, Harsay HA, et al. **Corticostriatal connectivity underlies individual differences in the balance between habitual and goal-directed action control.** *J Neurosci* 2012;32:12066–75 CrossRef Medline
30. Botvinick MM, Cohen JD, Carter CS. **Conflict monitoring and anterior cingulate cortex: an update.** *Trends Cogn Sci* 2004;8:539–46 CrossRef Medline
31. Rae CD. **A guide to the metabolic pathways and function of metabolites observed in human brain 1H magnetic resonance spectra.** *Neurochem Res* 2014;39:1–36 CrossRef Medline



# Postoperative MR Imaging of Spontaneous Transdural Spinal Cord Herniation: Expected Findings and Complications

 S. Gaudino,  R. Colantonio,  C. Schiarella,  M. Martucci,  R. Calandrelli,  A. Botto,  M. Pileggi,  E. Gangemi,  G. Maira, and  C. Colosimo



## ABSTRACT

**BACKGROUND AND PURPOSE:** Spontaneous transdural spinal cord herniation is no longer a rare cause of myelopathy. The high frequency of diagnoses has led to an increase in the number of surgical procedures. The purpose of this study was to describe the spectrum of postoperative MR imaging findings concerning spontaneous transdural spinal cord herniation and to provide a practical imaging approach for differentiating expected changes and complications after an operation.

**MATERIALS AND METHODS:** We retrospectively reviewed MR images from 12 patients surgically treated for spontaneous transdural spinal cord herniation. Surgery comprised either dural defect enlargement or duraplasty procedures. Postoperative follow-ups included at least 3 (early, intermediate, late) MR imaging studies. MR images were analyzed with respect to 3 spinal compartments: intradural intramedullary, intradural extramedullary, and extradural. The meaning and reliability of changes detected on MR images were related to their radiologic and clinical evolution with time.

**RESULTS:** Spinal cord realignment has been stable since the early study, whereas spinal cord signal and thickness evolved during the following scans. Most extramedullary and extradural changes gradually reduced in later MR images. Three patients treated with dural defect enlargements experienced the onset of new neurologic symptoms. In those patients, late MR images showed extradural fluid collection and the development of pial siderosis.

**CONCLUSIONS:** Our findings demonstrate the spectrum of postoperative imaging findings in spontaneous transdural spinal cord herniation. Spinal cord thickness and signal intensity continued to evolve with time; most extramedullary postsurgical changes became stable. Changes observed in later images may be suggestive of complications.

**ABBREVIATIONS:** DDE = dural defect enlargement; E-MRI = early MR imaging; I-MRI = intermediate MR imaging; JOA = Japanese Orthopedic Association; L-MRI = late MR imaging; STSCH = spontaneous transdural spinal cord herniation

Spontaneous transdural spinal cord herniation (STSCH) is a rare, but potentially treatable cause of thoracic myelopathy that occurs in middle-aged adults, with a female preponderance.<sup>1</sup> It is defined as the herniation or prolapse of the spinal cord through an anterior or anterolateral dural defect. Clinical findings are nonspecific, and patients are typically affected by a slowly progressive, Brown-Séquard syndrome or paraparesis.<sup>2</sup> A variety

of theories have been postulated to explain the pathogenesis of this entity, but the exact cause of dural defects remains unclear.<sup>1</sup> Surgical treatment to restore a herniated cord to its normal intradural position is mandatory for maximum reversal of neurologic deficits.<sup>1</sup> The primary techniques for treating STSCH are dural defect enlargement (DDE) and duraplasty. In recent years, the increased frequency of STSCH has led to more surgical treatments. These increases may be due to a growing awareness among clinicians and radiologists and to improvements in MR imaging quality.<sup>2-4</sup>

A well-defined set of MR imaging diagnostic criteria has been established for STSCH<sup>2,4-6</sup>; however, little has been said about postoperative MR imaging of changes in the spinal cord and adjacent structures. Less than half of the cases reported in the literature have described postoperative MR imaging features after reduction of spinal cord herniation<sup>1,4,7-10</sup>; none provided descriptions of a rational analysis; and in cases of complications, few have performed time-related assessments

Received June 3, 2015; accepted after revision July 22.

From the Institute of Radiology (S.G., R. Colantonio, C.S., M.M., R. Calandrelli, A.B., M.P., E.G., C.C.) and Institute of Neurosurgery (G.M.), Catholic University of Rome, Rome, Italy.

Paper previously presented at: Annual Meeting of the Radiological Society of North America, November 25–30, 2012; Chicago, Illinois. Paper No. VSNR31-II.

Please address correspondence to Simona Gaudino, MD, Institute of Radiology, Catholic University, "A.Gemelli" Hospital, L.go A. Gemelli 1, 00168 Rome, Italy; e-mail: simona.gaudino@rm.unicatt.it



Indicates article with supplemental on-line table.

<http://dx.doi.org/10.3174/ajnr.A4537>

of the findings. The lack of a thorough knowledge of postoperative MR imaging findings and their evolution with time can lead to misinterpretations of normal postoperative changes and oversight of complications.

This study aimed to review the spectrum of postoperative MR imaging findings and provide a practical imaging approach for correctly differentiating normal postoperative findings and complications. This approach was based on our analysis of a case series of 12 patients who underwent surgery for STSCH and long-term follow-up with MR imaging and clinical assessment.

## MATERIALS AND METHODS

### Subjects

We analyzed 17 consecutive patients who underwent surgery for STSCH by the same surgeon between 1985 and 2012. Inclusion criteria were radiologic diagnosis of STSCH surgically demonstrated and the availability of both preoperative and at least 3 postoperative MR imaging studies, with the last study conducted at least 1 year after the operation. Of the 17 patients considered, 12 (4 men and 8 women) were included in this analysis. Eleven patients were treated at our institution, and 5 of them have been previously reported in the literature.<sup>1</sup> Clinical history, surgical outcomes, and radiographic findings were obtained for all patients. Medical records and MR imaging studies of the single patient not treated at our institution were collected by the surgeon during clinical follow-up. The mean age was 46 years (range, 29–61 years).

We have used 2 different surgical techniques: DDE for the first 3 patients and duraplasty for the other 9 patients. This difference is because after an initial experience with DDE, our surgeon preferred to repair the dural hole by using a dural patch, to reduce the risk of extradural fluid collection observed in patients whose dural defect was not repaired.<sup>1</sup> All patients underwent pre- and postoperative spine MR imaging, and 3 patients also underwent brain MR imaging in late follow-up, due to neurologic deterioration. The median follow-up period was 7.8 years (range, 2–23 years). Due to the lack of a predefined MR imaging protocol for follow-up and in light of the retrospective nature of the study, the number and timing of postoperative MR imaging studies varied for each patient. In addition, the change of the clinical picture, with the onset of new neurologic symptoms many years after surgery, led to a very late imaging follow-up in 3 patients (from 9 to 17 years after the operation). However, in all cases, these studies consisted of at least 3 serial examinations of the spine conducted as follows: early MR imaging (E-MRI), conducted 7–10 days after the operation; intermediate MR imaging (I-MRI), conducted 90–120 days after the operation; and late MR imaging (L-MRI), conducted >12 months after the operation. Postsurgical outcome was evaluated with the modified Japanese Orthopedic Association (JOA) score for thoracic myelopathy, an 11-point scale measuring lower extremity motor function, lower extremity and trunk function, and bladder function.<sup>11,12</sup>

Informed consent was obtained from all patients, and the local institutional review board approved this study. All data were anonymized for review and publication.

### MR Imaging Protocol

All postoperative MR imaging studies were performed with a 1.5T scanner (Signa Horizon, Signa Infinity; GE Healthcare, Milwaukee, Wisconsin) and a 4- or 8-channel, dedicated spine coil. The MR imaging protocol consisted at least of the following sequences: sagittal, axial, and coronal T2WI fast spin-echo (TR, >3000 ms; TE, >80 ms; NEX, 3); and sagittal and axial T1WI fast spin-echo (TR, <700 ms; TE, Minimum Full; NEX, 2–3) or spin-echo before and after intravenous administration of gadolinium (0.1 mmol/kg). Most MR imaging examinations also included fat-saturated T2WI and fat-saturated postcontrast T1WI; and 8 L-MRI also included gradient-echo T2\* images (TR, 500–600 ms; TE, 20 ms; flip angle, 20°; NEX, 3). Serial MR images were acquired at section thicknesses of 3–4 mm, with interimage gaps of 0.3–0.4 mm; the matrix size varied from 384 × 256 to 448 × 320. Steady-state free precession MR imaging sequences were obtained in the axial plane in all studies performed in 2003 or later. In addition, 3 patients underwent brain MR imaging studies that included gradient-echo T2\* images.

### Image Analysis

Pre- and postoperative MR images were retrospectively reviewed by 2 neuroradiologists (S.G. and C.S., with 10 and 2 years of experience, respectively); all determinations were made by consensus. For systematic image analysis, we used a compartmental approach, which followed the anatomic algorithm predicated on a myelographic interpretation<sup>13,14</sup>; consequently, the MR imaging findings were analyzed as follows:

- 1) In the intradural intramedullary compartment, we evaluated spinal cord realignment, dural adhesion of the spinal cord, abnormal thickness, abnormal signal intensity on the T2WI, and abnormal contrast enhancement of the spinal cord.
- 2) In the intradural extramedullary compartment, we evaluated the dural patch, the presence of siderosis on pial surfaces, intradural hemorrhage, and signs of CSF flow voids.
- 3) In the extradural compartment, we evaluated fluid collections.

A “spinal cord realignment” was defined as the repositioning of the spinal cord to its normal, intradural location, assessed on axial and sagittal T2WI. “Dural adhesion” was defined as a contact between the spinal cord and the ventral dura mater, without evidence of interposed CSF, assessed on axial T2WI and, when available, on steady-state free precession images. “Abnormal spinal cord thickness” was defined as a thinning or thickening of the spinal cord at the level of the operation, compared with the adjacent normal spinal cord, visible on T2WI and on at least 2 orthogonal planes. An “abnormal spinal cord signal intensity” on the T2WI was defined as a change in the spinal cord signal at the level of the operation, visible on at least 2 orthogonal planes (the conspicuity of the T2WI abnormality was further classified as either “faint” or “intense”). We also recorded abnormal spinal cord signal intensities on the T2WI that changed in longitudinal extension with time (classified as either “increased” or “decreased”). The dural patch was evaluated in terms of both the signal intensity on T2 and T1WI and the presence or absence of contrast enhancement. Extradural fluid collections were classified as either “anterior” or “posterior.” All these MR imaging findings were

evaluated across time to assess changes in terms of appearance, disappearance, progression, reduction, and stability.

## RESULTS

### Postoperative MR Imaging Findings

**Intradural Intramedullary Compartment.** In all patients, the E-MRIs demonstrated that the spinal cord was realigned to the normal intradural location. No recurrence of spinal cord herniation was observed during the MR imaging follow-up. However, despite realignment, in 10 cases, a focal anterior dural adhesion was observed on the E-MRIs, and in 8 cases, it persisted on the L-MRIs. The E-MRIs showed abnormal spinal cord thickness in all patients, but with different degrees of thinning at the site of surgery. Compared with the E-MRI, the I-MRIs showed that the spinal cord thickness had increased in 7 patients, remained stable in 3 patients, and decreased in 2 patients. Compared with the I-MRI, the L-MRIs showed that among the 7 spinal cords that had increased in thickness, 3 remained stable and 4 decreased; among the 3 spinal cords with a stable thickness, 1 remained stable and 2 decreased; and both spinal cords that had decreased thickness showed further thinning. Thus, at the end of the follow-up, 8 spinal cords showed progressive thinning and 4 remained stable.

On T2WI, the E-MRI showed abnormal spinal cord signal intensities in all patients at the level of the operation. During MR imaging follow-up, signal intensities increased in longitudinal extension in 4 patients: Two increases were observed between the E-MRI and I-MRI, and 2 were observed between the I-MRI and L-MRI. On the E-MRIs, the spinal cord signal intensity on T2WI was faint in 11 patients and intense in 1 patient; on the I-MRIs, it was faint in 7 and intense in 5 patients; and on the L-MRIs, it was faint in 3 and intense in 9 patients. Thus, 8 patients showed an overall modification in signal conspicuity at the end of the MR imaging follow-up. After administration of gadolinium, no patients showed abnormal contrast enhancement in the spinal cord.

**Intradural Extradural Compartment.** Among the 9 patients who underwent duraplasty, a dural patch was visible in 3 patients on E-MRIs and in 4 patients on I-MRIs and L-MRIs. The dural patch was a linear, T2 hyperintensity lying on the anterior surface of the dura, with variable signal intensity on T1WI (iso- to hypointensity). Dural patch contrast enhancement was observed in 1 case on the I-MRI. Posterior CSF flow artifacts were observed on the E-MRIs in 1 patient, on the I-MRIs in 8 patients, and on the L-MRIs in 9 patients. Intradural hemorrhage was observed on the E-MRIs in 2 patients at the level of the operation, but it completely resolved during the MR imaging follow-up. Spinal siderosis was observed in 1 patient on L-MRI.

**Extradural Compartment.** Posterior fluid collections were present in all patients on the E-MRI. They resolved in all except 2 on the I-MRIs, and they completely resolved in all patients on the L-MRIs. An anterior fluid collection adjacent to the site of previous herniation was present in 6 patients on the E-MRIs. In all cases, the anterior fluid collections were evident on preoperative MR images, and they began to show reductions on I-MRIs. In particular, they resolved on the I-MRIs in 3 patients and on the L-MRIs in the other 3 patients. An anterior extradural fluid col-

lection with a cervicothoracic extension appeared on the L-MRI in 3 patients.

### Brain Findings

Three patients had neurologic deterioration during follow-up (headache that worsened in the upright position, progressive sensorineural hearing loss, new-onset back pain). These patients required a brain MR imaging study. All 3 patients showed brain superficial siderosis.

### Postoperative Clinical Outcome

The preoperative JOA score of all patients ranged from 4 to 9 (average, 6.5), whereas the postoperative JOA score at 1-year follow-up ranged from 5 to 10 (average 8), with an average recovery rate of 36%. In particular, the postoperative score increased in 9 of 12 patients who showed a progressive improvement in spinal symptoms; in the remaining 3 patients, spinal symptoms and therefore the JOA score remained unchanged from the preoperative condition. There was no correlation between the postoperative JOA score and spinal cord changes. In fact, in our population, major spinal cord changes, in terms of cord thinning and T2WI signal extent, were present in 2 patients with an unvarying postoperative JOA score and in 3 patients with an increased postoperative JOA score. The 3 patients who had undergone DDE developed new clinical symptoms in the late clinical follow-up, including persistent headache that worsened in an upright position (2 cases), progressive sensorineural hearing loss (2 cases), and new-onset back pain (1 case).

## DISCUSSION

STSCCH is a rare, but treatable cause of slowly progressive thoracic myelopathy. It has been increasingly recognized and treated surgically in the past few years. Although great emphasis has been placed on the role of MR imaging in the diagnosis of STSCCH, postoperative MR imaging findings have been exhaustively described in only a small number of reports, to our knowledge. Furthermore, no previous study has considered the time evolution in a series of MR imaging studies or attempted to interpret the clinical significance of postoperative changes and complications. In this study, we investigated MR images acquired after surgical treatment of STSCCH in a series of MR imaging follow-ups. Our aim was to differentiate normal or expected postoperative changes and complications on the basis of their evolution in time and the onset of new neurologic symptoms.

The major MR imaging findings of the present study (On-line Table) were the following: 1) Spinal cord changes, such as thickness and signal intensity on T2WI, could continue to evolve until L-MRIs; 2) most extradural postsurgical changes became stable after the I-MRI; and 3) changes that developed in the late phase that were associated with new neurologic symptoms could be considered a complication, like extradural anterior fluid collections or spinal superficial siderosis. These changes indicated a need for brain MR imaging because they could be associated with brain superficial siderosis.

The aim of STSCCH surgery is to realign the spinal cord, to reposition it to its normal intradural location.<sup>15</sup> This aim was well-accomplished in all patients on the basis of the E-MRIs;

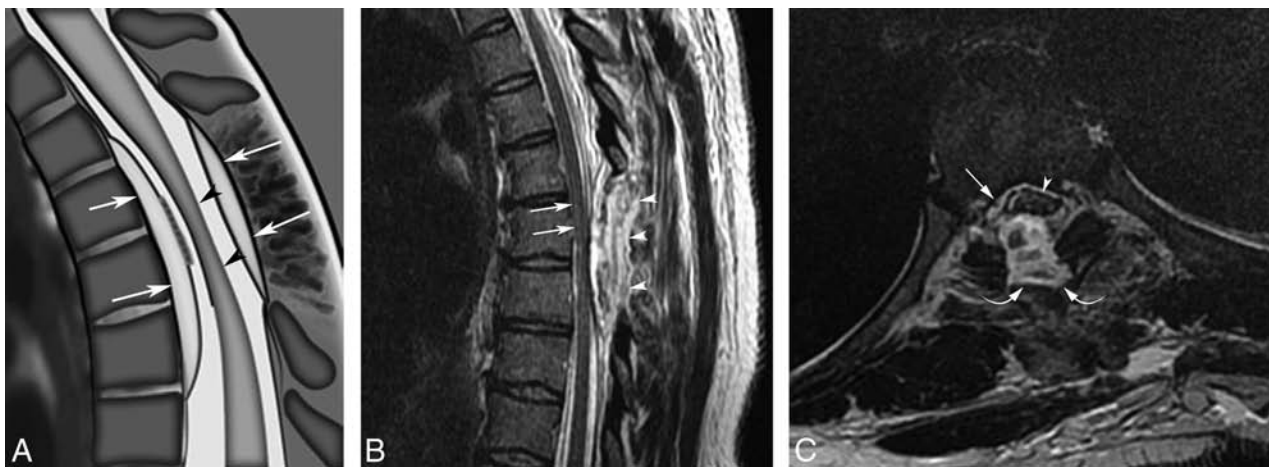


**FIG 1.** MR imaging findings after surgical treatment for STSCH. *A*, This drawing summarizes the expected MR imaging findings in early and intermediate MR imaging studies, including spinal cord realignment, reduced cord thickness at the site of herniation (*black arrowheads*), and anterior and posterior extradural fluid collections (*white arrows*). The *thick dotted line* along the anterior dura indicates the dural patch. *B* and *C*, Early postoperative findings. *B*, Sagittal T2WI demonstrates intradural realignment, reduced thickness, and signal hyperintensity of the spinal cord (*arrows*) at the T6–T7 level (site of herniation) and a posterior fluid collection along the laminectomy (*arrowheads*). *C*, Axial T2WI shows the position of the spinal cord in the intradural location, an anterior adhesion between the cord and the dura (*arrowhead*), a thin anterior fluid collection (*straight arrow*), and a thick posterior fluid collection (*curved arrows*) with consequent total effacement of the posterior subarachnoid space.

moreover, later MRIs showed that all realignments remained stable. Thus, evaluations of realignments could be reliably based on the early postoperative MR imaging study (Fig 1A). However, despite correct realignments, we observed a focal contact between the ventral dura mater and the spinal cord in 10 patients on the E-MRIs. In our opinion, this finding might be due to the presence of a posterior extradural fluid collection, which may have caused a persistent, mild anterior displacement of the spinal cord toward the ventral dura (Fig 1B, -C). Although complete resorption of posterior extradural fluid collections occurred in all patients, dural adhesions disappeared in only 2 patients on the I-MRI and in 2 other patients at the end of the MR imaging follow-up. We speculate that adhesion disappearance was probably due to a reparative or reactive process.

Spinal cord changes at the site of the operation occurred in all patients, with a remarkable variability in terms of signal intensity on T2WI and thickness during the MR imaging follow-up. Several authors have investigated the meaning and evolution across time of alterations in spinal cord T2WI signal intensity after different types of spinal surgery. Many authors have hypothesized that intramedullary T2WI hyperintensities might represent a variety of histologic changes, including edema, ischemia, demyelination, gliosis, and microcavities.<sup>16</sup> Yagi et al<sup>17</sup> reported intramedullary signal-intensity changes up to 1 year after cervical laminoplasty, and Sarkar et al<sup>18</sup> described the postoperative evolution of spinal cord T2WI, which changed in signal intensity and size, even after a long-term follow-up (mean duration, 28 months). Among our case series, some patients underwent a very long-term follow-up. In 2 patients, we detected T2WI signal intensity changes up to 10 years after the operation. In general, these signals tended to show progressive increases in both longitudinal extension and conspicuity; the conspicuity became intense in 9 patients at the end of follow-up. As recently proposed by Sarkar et al,<sup>18</sup> we assumed that in the early postoperative phase, a faint T2WI hyperintensity was mainly related to the presence of edema. Accordingly, a progres-

sive increase in conspicuity with time might be due to edema regression, which might unmask myelomalacia and/or gliosis. Therefore, in the setting of late postoperative spinal cord T2WI changes, the interpretation of these signal-intensity abnormalities should consider active pathogenic processes, such as alterations in venous circulation or arterial ischemia, which might indicate progression to myelomalacia and gliosis.

On E-MRIs, all patients showed decreases in spinal cord thickness at the site of the operation compared with adjacent areas of



**FIG 2.** Dural patch showing contrast enhancement. Sagittal T1WI after intravenous administration of gadolinium shows the dural patch as a linear hyperintensity lying on the anterior surface of the dura (*arrows*) at the level of the operation (D4–D5 vertebral bodies).



cord that appeared normal. On I-MRIs, 7 patients showed variable changes (increases or decreases in thickness), and on L-MRIs, 8 patients showed decreases in thickness. We speculated that these phenomena might be correlated with the processes that gave rise to the spinal cord signal-intensity abnormalities. We also hypothesized that increased cord thickness on I-MRIs might, in part, be related to the resorption of posterior extradural fluid collections and the consequent resolution of compression on the dural sac and spinal cord.

One final reflection on changes in spinal cord thickness after surgery merits our attention. On E-MRIs, spinal cord thickness at the level of the herniation always seemed increased (re-expanded) compared with preoperative images. This finding seemed to be related to evidence of immediate clinical benefit after the operation. However, it was not possible to assess this finding accurately because when the spinal cord was herniated through the dura mater, its deformation made it difficult to measure cord thickness correctly.

Spinal cord contrast enhancement was not detected in our population. This was an expected result because it rarely occurs during follow-up in patients with chronic degenerative processes of the spinal cord.<sup>19</sup> However, in our population, the administration of gadolinium showed dural patch contrast enhancement in 1 patient on the I-MRI (Fig 2). This finding may have indicated granulation tissue surrounding the patch, similar to scar tissue, which typically enhances in patients who have undergone prior a disc operation.<sup>20</sup>

Nine patients underwent duraplasty; among these, we detected the dural patch on the E-MRIs in 3 cases, and on I-MRIs

and L-MRIs, in 4 cases. The dural patch appeared as a linear dural hyperintensity on T2WI and as a variable linear iso- to hypointensity on T1WI. This variability in signal intensity may depend on the use of different grafting materials and on the size of the patch.

Posterior extradural fluid collections and intradural hemorrhage might be expected postoperatively. In fact, in all cases, these findings rapidly decreased or disappeared in the early postoperative phase. All posterior extradural fluid collections were located at the site of posterior laminectomy. On E-MRIs, all posterior collections displaced the dura anteriorly, resulting in a shrinking or total effacement of the normal amplitude of the subarachnoid space. This finding strictly correlated with the absence of CSF flow voids in 11 patients on E-MRIs and with the re-appearance of CSF flow voids in 8 patients on I-MRIs. In 1 patient, CSF flow voids reappeared on the L-MRI simultaneously with the resorption of a posterior extradural fluid collection.

Anterior extradural fluid collections have also been reported in patients with STSCH. These collections were considered a consequence of CSF leakage secondary to the dural defect.<sup>1,21</sup> Among our population, 6 patients showed anterior extradural fluid collections in the preoperative MR imaging study, with variable longitudinal extensions. Of these, 3 anterior collections had completely resolved on I-MRIs and the other 3 had resolved on L-MRIs. However, 3 patients treated with DDE showed no evidence of anterior fluid collection on preoperative MR imaging but had new neurologic symptoms at late clinic follow-up (Table) and showed evidence on L-MRIs of developing anterior extradural

collections with a cervicothoracic extension (Fig 3A, -B). In 1 case, these findings were associated with spinal cord siderosis, and in all cases, they were associated with brain siderosis, most extensively at the cerebellum surface and brain stem (Fig 3C).

Postoperative anterior extradural collection development was reported previously by Nakamura et al<sup>9</sup> in 16 pa-

**Postoperative L-MRI findings in patients with new onset of neurologic symptoms**

Patient No.	Anterior Fluid Collection	Spinal Superficial Siderosis	Brain Superficial Siderosis	Neurologic Symptoms
2	Yes	No	Yes	Persistent headache (worse in an upright position), progressive SNHL
5	Yes	Yes	Yes	Persistent headache (worse in an upright position), progressive SNHL
10	Yes	No	Yes	Low back pain

**Note:**—SNHL indicates sensorineural hearing loss.

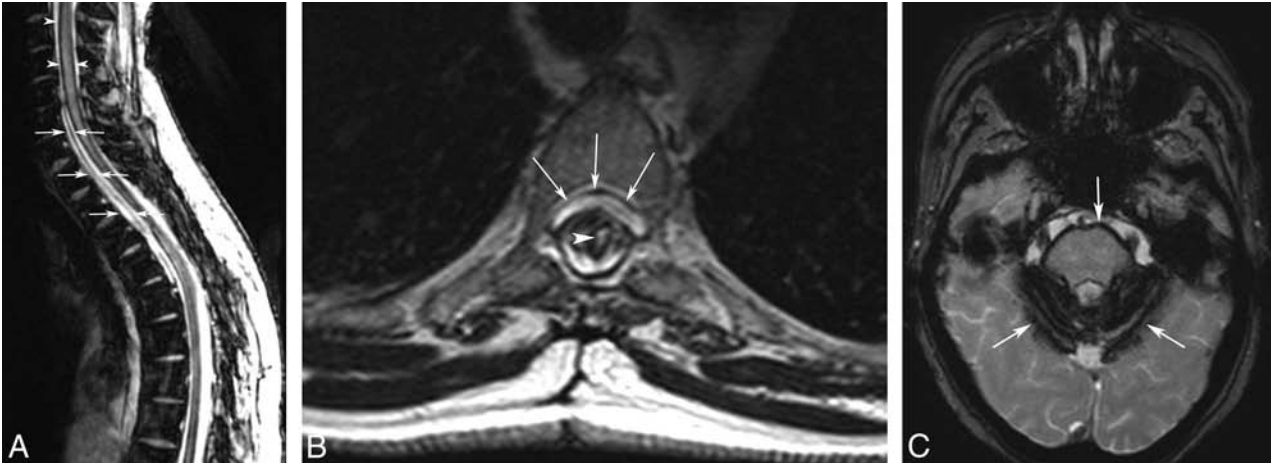


**FIG 3.** Anterior fluid collection and spinal and brain siderosis that developed 10 years after the operation for STSCH. A, Sagittal T2\*WI demonstrates hemosiderin deposition along the spinal cord (arrowheads) and a cervicothoracic, anterior extradural fluid collection (arrows). B, Axial T2WI confirms the anterior fluid collection (arrows) and shows an intramedullary hyperintensity (arrowhead) and reduced spinal cord thickness at the level of the operation (D3–D4 vertebral bodies). C, Axial T2\* of the brain demonstrates superficial siderosis (arrows).

tients with STSCH treated with DDE; however, those patients lacked symptomatology related to a persistent CSF leak. Superficial siderosis is thought to result from recurrent subarachnoid bleeds, though the source of bleeding is not typically identified with imaging.<sup>22</sup> The precise mechanism of bleeding in our cases remained unknown, but dural defects that were not repaired with duraplasty were probably the source of chronic or recurrent microhemorrhages. In fact, in a few reports of superficial siderosis, when a dural defect was detected, surgical repair of the dural tear with duraplasty stopped the bleeding.<sup>23</sup> Moreover, a recent study described “duropathies” as conditions, like craniospinal hypovolemia, multisegmental amyotrophy, and STSCH, in which the common denominator was the presence of a dural defect with an intraspinal fluid collection, accompanied by superficial siderosis.<sup>24</sup> To our knowledge, our 3 cases represent the first descriptions of superficial siderosis, which might indicate a long-standing complication of STSCH surgery.

The possible correlation between the duration of follow-up and the late MR imaging findings of fluid collection and siderosis deserves some consideration. L-MRI showed anterior fluid collection and siderosis from 2 to 10 years and between 8 and 17 years after surgery, respectively. These findings were observed in patients who had undergone DDE before the surgical technique was replaced by duraplasty. Due to the small sample of patients, we cannot conclude whether these MR imaging findings are related to the longer duration of follow-up and/or to the type of operation because in our population, the 2 factors coincided. Further studies with larger populations are needed to evaluate the possibility that these findings may actually correlate with longer follow-up duration, the type of operation, or both. Regarding spinal and/or intracranial pial siderosis, gradient-echo T2\*, which represents the optimal sequence to detect spinal siderosis, was performed in only 8 L-MRI examinations and in no preoperative MR imaging studies. No preoperative brain MR imaging studies were available. Thus, the evidence of spinal siderosis was based only on FSE T2WI for all preoperative studies and for most of the E-MRI and I-MRI studies. However, FSE can show pial siderosis, most likely in advanced stages, when the siderosis is extended and thick and the paramagnetic effect is marked, as reported by Boncoraglio et al,<sup>24</sup> who described presurgical siderosis in a patient with spinal cord herniation.

Our study had some limitations. First and foremost, our study population was small, particularly when the different types of surgical techniques are considered separately (duraplasty and DDE). A separate analysis that compares postoperative MR imaging findings and clinical outcome in patients treated with DDE or duraplasty would have been interesting, to better understand the nature of the relationship between pial siderosis, extradural anterior fluid collection, and surgical procedures for STSCH and to determine the most appropriate surgical technique for STSCH. However, our small sample size precluded any meaningful statistical analyses. Another limitation was that our study included patients treated at a single institution; therefore, our results might not be generalizable to other neurosurgical units. To determine the effectiveness of surgical interventions for STSCH, we encourage other groups to perform follow-up studies that include de-

tailed, comprehensive descriptions of postoperative MR imaging findings.

## CONCLUSIONS

In this study, we demonstrated that a systematic, rational analysis of postoperative MR images acquired during the follow-up after STSCH treatment allowed detection of a wide spectrum of MR imaging changes that involved the spinal cord, intradural space, dura mater, and epidural space. An understanding of these postoperative changes and their evolution with time will provide the radiologist with the means to recognize the normal postoperative appearance of the spine and adjacent structures and to identify changes that may represent early and late postoperational complications.

Disclosures: Cesare Colosimo—UNRELATED: Consultancy: Bayer HealthCare, Bracco Diagnostics.

## REFERENCES

1. Maira G, Denaro L, Doglietto L, et al. **Idiopathic spinal cord herniation: diagnostic, surgical, and follow-up data obtained in five cases.** *J Neurosurg Spine* 2006;4:10–19 CrossRef Medline
2. Parmar H, Park P, Brahma B, et al. **Imaging of idiopathic spinal cord herniation.** *Radiographics* 2008;28:511–18 CrossRef Medline
3. Sasani M, Ozer AF, Vural M, et al. **Idiopathic spinal cord herniation: case report and review of the literature.** *J Spinal Cord Med* 2009;32:86–94 Medline
4. Imagama S, Matsuyama Y, Sakai Y, et al. **Image classification of idiopathic spinal cord herniation based on symptom severity and surgical outcome: a multicenter study.** *J Neurosurg Spine* 2009;11:310–19 CrossRef Medline
5. Barrenechea JJ, Lesser JB, Gidekel AL, et al. **Diagnosis and treatment of spinal cord herniation: a combined experience.** *J Neurosurg Spine* 2006;5:294–302 CrossRef Medline
6. Haber MD, Nguyen DD, Li S. **Differentiation of idiopathic spinal cord herniation from CSF-isointense intraspinal extramedullary lesions displacing the cord.** *Radiographics* 2014;34:313–29 CrossRef Medline
7. Watanabe M, Chiba K, Matsumoto M, et al. **Surgical management of idiopathic spinal cord herniation: a review of nine cases treated by the enlargement of the dural defect.** *J Neurosurg* 2001;95(2 suppl):169–72 Medline
8. Anmar KN, Pritchard PR, Matz PJ, et al. **Spontaneous thoracic spinal cord herniation: three cases with long-term follow up.** *Neurosurgery* 2005;57:E1067 CrossRef Medline
9. Nakamura M, Fujiyoshi K, Tsuji O, et al. **Long-term surgical outcomes of idiopathic spinal cord herniation.** *J Orthop Sci* 2011;16:347–51 CrossRef Medline
10. Prada F, Saladino A, Giombini S, et al. **Spinal cord herniation: management and outcome in a series of 12 consecutive patients and review of the literature.** *Acta Neurochir (Wien)* 2012;154:723–30 CrossRef Medline
11. Kato S, Oshima Y, Oka H, et al. **Comparison of the Japanese Orthopaedic Association (JOA) score and modified JOA (mJOA) score for the assessment of cervical myelopathy: a multicenter observational study.** *PLoS One* 2015;10:e0123022 CrossRef Medline
12. Aizawa T, Sato T, Sasaki H, et al. **Results of surgical treatment for thoracic myelopathy: minimum 2-year follow-up study in 132 patients.** *J Neurosurg Spine* 2007;7:13–20 CrossRef Medline
13. Colosimo C, Cianfoni A, Di Lella GM, et al. **Contrast-enhanced MR imaging of the spine: when, why and how? How to optimize contrast protocols in MR imaging of the spine.** *Neuroradiology* 2006;48(suppl 1):18–33 CrossRef Medline
14. Grossman RI, Yousem DM. *Neuroradiology: The Requisites.* St Louis: Mosby; 1994:751–93

15. Groen RJ, Middel B, Meilof JF, et al. **Operative treatment of anterior thoracic spinal cord herniation: three new cases and an individual patient data meta-analysis of 126 case reports.** *Neurosurgery* 2009; 64(3 suppl):ons145–59; discussion ons159–60 CrossRef Medline
16. Chen CJ, Lyu RK, Lee ST, et al. **Intramedullary high signal intensity on T2-weighted MR images in cervical spondylotic myelopathy: prediction of prognosis with type of intensity.** *Radiology* 2001;221: 789–94 CrossRef Medline
17. Yagi M, Ninomiya K, Kihara M, et al. **Long-term surgical outcome and risk factors in patients with cervical myelopathy and a change in signal intensity of intramedullary spinal cord on magnetic resonance imaging.** *J Neurosurg Spine* 2010;12:59–65 CrossRef Medline
18. Sarkar S, Turel MK, Jacob KS, et al. **The evolution of T2-weighted intramedullary signal changes following ventral decompressive surgery for cervical spondylotic myelopathy: clinical article.** *J Neurosurg Spine* 2014;21:538–46 CrossRef Medline
19. Cho YE, Shin JJ, Kim KS, et al. **The relevance of intramedullary high signal intensity and gadolinium (Gd-DTPA) enhancement to the clinical outcome in cervical compressive myelopathy.** *Eur Spine J* 2011;20:2267–74 CrossRef Medline
20. Salgado R, Van Goethem JW, van den Hauwe L, et al. **Imaging of the postoperative spine.** *Semin Roentgenol* 2006;41:312–26 CrossRef Medline
21. Kumar N. **Beyond superficial siderosis: introducing “duropathies.”** *Neurology* 2012;78:1992–99 CrossRef Medline
22. Kumar N, Cohen-Gadol AA, Wright RA, et al. **Superficial siderosis.** *Neurology* 2006;66:1144–52 CrossRef Medline
23. Kumar N. **Neuroimaging in superficial siderosis: an in-depth look.** *AJNR Am J Neuroradiol* 2010;31:5–14 CrossRef Medline
24. Boncoraglio GB, Ballabio E, Erbetta A, et al. **Superficial siderosis due to dural defect with thoracic spinal cord herniation.** *J Neurol Sci* 2012;312:170–72 CrossRef Medline

# Normal Venous Phase Documented during Angiography in Patients with Spinal Vascular Malformations: Incidence and Clinical Implications

D. Eckart Sorte, M. Obrzut, E. Wyse, and P. Gailloud

## ABSTRACT

**BACKGROUND AND PURPOSE:** A key angiographic sign observed in patients with spinal vascular malformations is the absence of a normal venous phase. While this finding alone is often believed to rule out a lesion impacting the perimedullary venous drainage, the observation of a venous phase in several patients with vascular malformations led us to reconsider the validity of that sign.

**MATERIALS AND METHODS:** Eighty-one patients with 6 spinal arteriovenous malformations, 16 perimedullary arteriovenous fistulas, 61 spinal epidural or dural AVFs, and 1 paravertebral AVF (2 patients had multiple lesions) were reviewed. The venous phase was defined as normal, absent, or indeterminate. The venous phase timing was analyzed in patients with spinal dural or epidural AVFs.

**RESULTS:** The existence of a venous phase could not be determined for technical reasons in 23 patients. A venous phase was documented in 25 of 58 patients (43%), including 16 of 49 vascular malformations (40.0%) with perimedullary venous drainage. Twelve of the 30 patients (40.0%) with dural or epidural AVFs had a normal venous phase, appearing, on average, 10.1 seconds and best visualized 15.0 seconds after opacification of the artery of Adamkiewicz.

**CONCLUSIONS:** A normal venous phase was observed in 43% of patients with spinal vascular malformations, and within an acceptable delay (<18 seconds) in 40% of slow-flow AVFs. While it remains an important angiographic sign, the observation of a normal venous phase cannot be used to exclude the presence of a vascular malformation or justify interrupting a diagnostic spinal angiogram.

**ABBREVIATIONS:** SAVM = spinal AVM; SDAVF = spinal dural arteriovenous fistula; SEAVF = spinal epidural arteriovenous fistula; SpDSA = spinal digital subtraction angiography; SVM = spinal vascular malformation

Spinal digital subtraction angiography (SpDSA) is the criterion standard imaging technique for the evaluation of the spinal vasculature and remains essential for the diagnosis and management of spinal vascular malformations (SVMs).<sup>1</sup> The practice of SpDSA requires a sound understanding of the vascular anatomy of the spinal cord, notably its venous system.<sup>2,3</sup> A key angiographic sign observed in patients with SVMs is the absence of a normal venous phase, a phenomenon first reported in 2 cases of spinal dural arteriovenous fistulas (SDAVFs).<sup>2</sup> It was later suggested that a spinal angiogram could be terminated when “a nor-

mal venous phase is visualized and the veins correspond to the defects on the myelogram,” an approach based on the assumption that “if the venous phase of the spinal circulation is normal, this alone rules out DAVF [dural AVF] as the cause of the patient’s symptoms.”<sup>4</sup> While MR imaging has now supplanted myelography in the work-up of spinal vascular anomalies, the notion that the angiographic pursuit of an SVM can stop after the documentation of a normal venous phase is still widely accepted, though at times more cautiously. Some authors have, for example, suggested that a normal venous phase “usually”<sup>5</sup> or “reportedly”<sup>6</sup> allows terminating a diagnostic angiogram or that it only makes the “diagnosis of a fistula less likely.”<sup>7</sup> To our knowledge, there is, so far, only 1 reported instance of a normal venous phase associated with a vascular malformation draining into the perimedullary system, but this case involved a cranial dural arteriovenous fistula rather than an SVM.<sup>8</sup>

Several observations of a morphologically normal venous phase associated with lesions involving the perimedullary venous system have pushed us to reconsider the validity of this angiographic sign. The spinal venous phase was, therefore,

Received June 4, 2015; accepted after revision July 22.

From the Division of Interventional Neuroradiology, The Johns Hopkins Hospital, Baltimore, Maryland.

Paper previously presented in part at: American Society of Neuroradiology Annual Meeting and the Foundation of the ASNR Symposium, May 17–22, 2014; Montreal, Quebec, Canada.

Please address correspondence to: Philippe Gailloud, MD, Division of Interventional Neuroradiology, The Johns Hopkins Hospital, Bloomberg 7218, 1800 E Orleans St, Baltimore, MD 21287; e-mail: phg@jhmi.edu

<http://dx.doi.org/10.3174/ajnr.A4601>



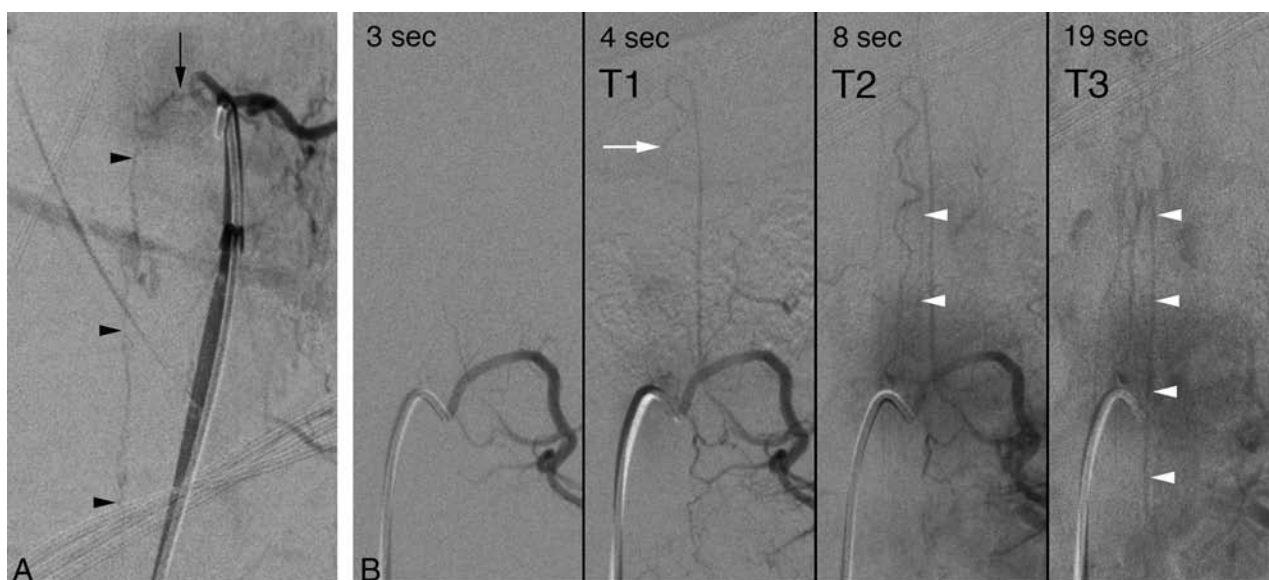


**FIG 1.** Timing of the spinal venous phase in a 51-year-old man with a progressive myelopathy secondary to a left T8 spinal dural arteriovenous fistula. A, SpDSA, left T8 injection, posteroanterior view, documents an SDAVF (black arrow) with perimedullary venous drainage (black arrowheads). B, SpDSA, left L1 injection, posteroanterior view, demonstrates the opacification sequence of the medullary circulation and the time stamps used to calculate the spinal venous phase: T1 indicates initial opacification of the anterior spinal artery (white arrow) (4 seconds); T2, initial detection of perimedullary structures, including the proximal segment of the left L2 radiculomedullary vein (white arrowheads) (8 seconds); and T3, best visualization of the spinal venous phase (19 seconds). In this case, the time to initial detection and best delineation was 4 and 15 seconds, respectively.

#### Spinal venous phase in slow-flow arteriovenous fistulas with perimedullary venous drainage

Feature	Overall	Venous Phase Absent	Venous Phase Present
No. of lesions	30 (100%)	18 (60.0%)	12 (40.0%)
SDAVF	11	8 (44.4%)	3 (25%)
SEAVF	17	9 (50.0%)	8 (66.7%)
SDAVF/SEAVF	2	1 (5.6%)	1 (8.3%)
Male predominance	26/30 (86.7%)	14/18 (77.8%)	12/12 (100%)
Age (average)	65	66.6	64.7
Symptomatic	29/30 (96.7%)	18/18 (100%)	11/12 (91.2%)
Flow voids on MRI	19 (63.3%)	10/18 (55.6%)	9/12 (75.0%)
Thoracic location	11	6 (33.3%)	5 (41.7%)
Lumbar location	11	8 (44.4%)	3 (25.0%)
Sacral location	8	4 (22.2%)	4 (33.3%)

evaluated in 81 patients diagnosed with an SVM in our practice during a 5-year period, with particular attention paid to SDAVFs and spinal epidural arteriovenous fistulas (SEAVFs).

#### MATERIALS AND METHODS

This study is based on 81 patients logged in an institutional review board–approved data base between February 2010 and February 2015, including 23 females (28%) and 58 males (72%), with ages ranging from 19 months to 89 years (average, 49 years; median, 23 years). Only lesions with arteriovenous shunting were considered. Seventy-nine patients had a single lesion, while 2 patients had 2 and 3 lesions respectively, for a total of 84 SVMs. The lesions included 39 SEAVFs, 20 SDAVFs, 1 paraspinal arteriovenous fistula, 6 spinal arteriovenous malformations (SAVMs), and 16 perimedullary arteriovenous fistulas. In 2 instances, a slow-flow fistula could not be clearly classified as SEAVF or SDAVF. The multiple lesions were all SEAVFs.

The angiographic venous phase was evaluated after opacification of the artery of Adamkiewicz and was classified as normal, absent, or indeterminate. The venous phase timing was analyzed in the subgroup of patients with slow-flow arteriovenous fistulas (SEAVF/SDAVF). We recorded 3 time stamps: initial opacification of the anterior spinal artery (t1), initial detection of perimedullary venous structures (t2), and best delineation of the spinal venous phase (t3). The times

at which the venous phase was first (t2 – t1) and best documented (t3 – t1) were then calculated (Fig 1).

#### RESULTS

The existence of a venous phase could not be determined for technical reasons (eg, short acquisitions, motion artifacts) in 23 patients (28.4%). A venous phase was seen in 25 of the remaining 58 patients (43%), including all 9 cases of SVM without perimedullary venous drainage, principally consisting of paraspinal arteriovenous fistulas or high-flow SEAVFs in children.

#### Spinal Venous Phase in SVMs with Perimedullary Venous Drainage

A normal venous phase was seen in 16 of the 49 patients (32.7%) with angiographically documented perimedullary venous drainage, including 1 of 14 perimedullary arteriovenous fistulas (7.1%), 3 of 5 SAVMs (all in cervical or cervi-

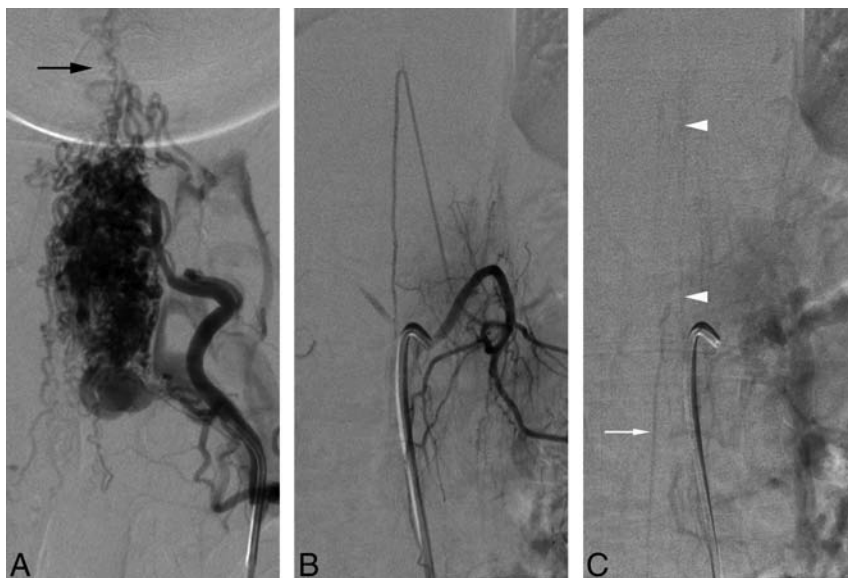


**FIG 2.** A 21-year-old man with a spinal arteriovenous malformation. A, DSA, left costocervical trunk injection, posteroanterior view, documents a large cervicothoracic SAVM nidus. Note that the venous drainage essentially occurs at the level of the lesion or in a cranial direction (black arrow). B, SpDSA, left T12 injection, posteroanterior view, arterial phase with opacification of the artery of Adamkiewicz. C, SpDSA, left T12 injection, posteroanterior view, later phase, documents the normal perimedullary venous drainage, including the visualization of spinal (white arrowheads) and radiculomedullary (white arrow) veins.

cothoracic locations) (60.0%), and 12 of 30 SEAVFs/SDAVFs (40.0%).

#### **Spinal Venous Phase in Slow-Flow Arteriovenous Fistulas with Perimedullary Venous Drainage**

The 30 patients with SEAVFs/SDAVFs draining into the perimedullary venous system are summarized in the Table. They included 4 women and 26 men, with ages ranging between 49 and 89 years (average, 65 years; median, 65 years). The lesions were located between T3 and S1; all were symptomatic except 1 SDAVF incidentally noted during preoperative tumor embolization. A normal venous phase was detected in 12 of these patients (40%). In particular, a lumbosacral radiculomedullary draining vein was documented in 9 of the 10 cases that included the lumbosacral region in the FOV. The type and topographic distribution of the fistulas were comparable between the groups with and without a venous phase. While our series is too limited for definitive statistical analysis, it appears that lesions located in the lumbar or sacral fistulas (54.5% and 50%, respectively) and that SDAVFs lacked a venous phase more often than SEAVFs (72.7% versus 52.9%). In all cases, the vertebral levels at which the abnormal perimedullary drainage and the normal venous phase were observed overlapped.

The average time for the beginning of the venous phase was 10.1 seconds (range, 4–29 seconds; median, 8 seconds), and the average time for the best delineation of the venous phase was 15.0 seconds (range, 7–39 seconds; median, 15 seconds). If 18 seconds is used as the upper limit for the observation of a normal venous phase,<sup>6</sup> a delayed venous phase was observed in 1 instance (29 seconds). When this outlying patient with respective values of 29 and 39 seconds was omitted (case illustra-

tion 5), the average times for the beginning and best delineation of the venous phase were 8.4 seconds (range, 4–14 seconds; median, 7.5 seconds) and 12.8 seconds (range, 7–18 seconds; median, 14.5 seconds), respectively.

#### **Case Illustrations**

Besides the patient demonstrating the method used to time the venous phase (Fig 1), 6 illustrative cases have been selected, including 1 SAVM, 2 SEAVFs, and 3 SDAVFs.

**Case 1.** A 21-year-old man with a 5-month history of progressive lower extremity weakness was diagnosed with a cervical SAVM after he had a posterior fossa hemorrhage. He was referred to our service 3 months later for further evaluation. SpDSA confirmed the diagnosis of SAVM supplied by the right vertebral artery and both costocervical trunks (Fig 2A). The injection of the artery of Adamkiewicz, found at the left

T12, showed a normal venous phase (Fig 2B, -C).

**Case 2.** A 64-year-old man presented with a 9-month history of leg weakness associated with urinary retention and constipation, progressively worsening until he became wheelchair-bound. MR imaging revealed an intramedullary T2 signal abnormality without perimedullary flow voids. SpDSA documented a right S1 SEAVF with extensive perimedullary venous drainage (Fig 3A). The injection of the artery of Adamkiewicz, found at the left T11, showed a normal venous phase (Fig 3B, -C).

**Case 3.** A 71-year-old man with an 8-month history of progressive lower extremity weakness, initially diagnosed as transverse myelitis, presented with a sudden deterioration of his bowel and bladder function before becoming wheelchair-bound. MR imaging showed intramedullary T2 signal abnormalities without perimedullary flow voids. SpDSA revealed a right S1 SEAVF with perimedullary drainage (Fig 4A, -B). The injection of the artery of Adamkiewicz, found at the left T8, showed a normal venous phase (Fig 4C, -D).

**Case 4.** A 58-year-old man was referred for preoperative embolization of a spinal metastasis from renal cell carcinoma. SpDSA incidentally documented an SDAVF supplied by the right L1 intersegmental artery (Fig 5A). The injection of the artery of Adamkiewicz, found at left L1, showed a normal venous phase (Fig 5B, -C).

**Case 5.** A 66-year-old man had a progressive right lower extremity weakness associated with paresthesias and pain. MR imaging showed intramedullary T2 signal abnormalities without perimedullary flow voids. A work-up for infectious and inflammatory etiologies remained negative. SpDSA revealed a

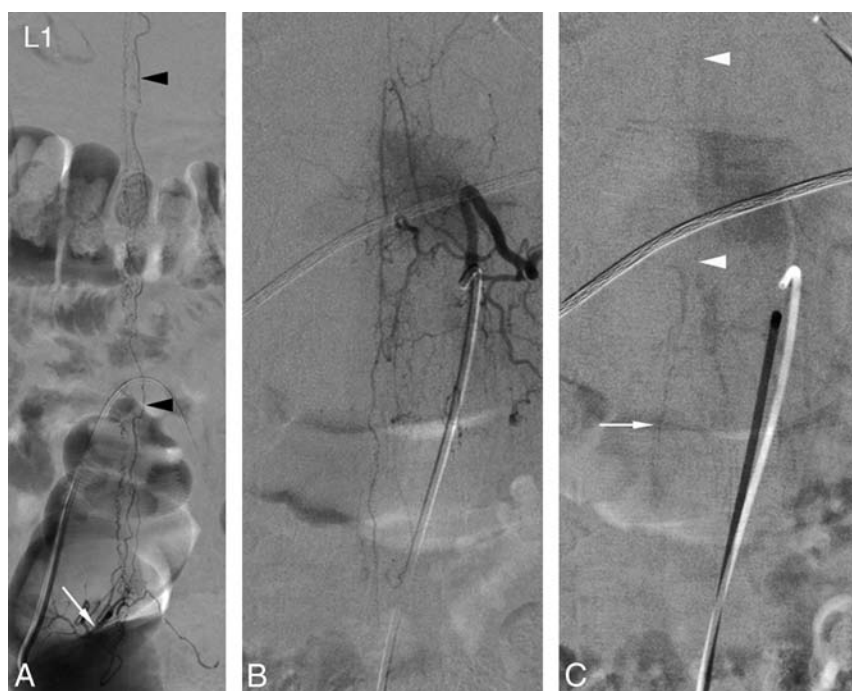


**FIG 3.** A 64-year-old man with a right S1 spinal epidural arteriovenous fistula. A, SpDSA, right S1 injection, posteroanterior view. The selective injection of the right S1 SEAVF (white arrow) reveals extensive perimedullary drainage (black arrowheads) from the sacral region up to about T5 (above L1 is not shown in this image). B, SpDSA, left T11 injection, posteroanterior view, arterial phase with opacification of the artery of Adamkiewicz. C, SpDSA, left T11 injection, posteroanterior view, later phase, documents the normal perimedullary venous drainage, including the visualization of spinal (white arrowheads) and radiculomedullary (white arrow) veins. Venous phase timing: first detection = 14 seconds, best delineation = 18 seconds.

right L1 SDAVF (Fig 6A). The injection of the artery of Adamkiewicz, found at the left T12, documented a normal venous phase (Fig 6B).

**Case 6.** A 65-year-old man with a recent history of heart transplantation and duodenal neuroendocrine tumor presented with rapidly worsening back pain, quadriplegia, and paresthesias. MR imaging showed perimedullary flow voids without definite intramedullary signal abnormality. SpDSA demonstrated a left T3 SDAVF (Fig 7A). The injection of the artery of Adamkiewicz, found at left T9, revealed a normal venous phase (Fig 7B, -C).

## DISCUSSION

### Classification and Diagnosis of Spinal Vascular Malformations

Spinal vascular anomalies with arteriovenous shunts can pragmatically be divided into 2 main categories. The high-flow lesions include the SAVMs, the fast perimedullary arteriovenous fistulas (Merland types 2 and 3),<sup>9</sup> and some high-output SEAVFs, generally of congenital or traumatic nature. The slow-flow lesions include SDAVFs,

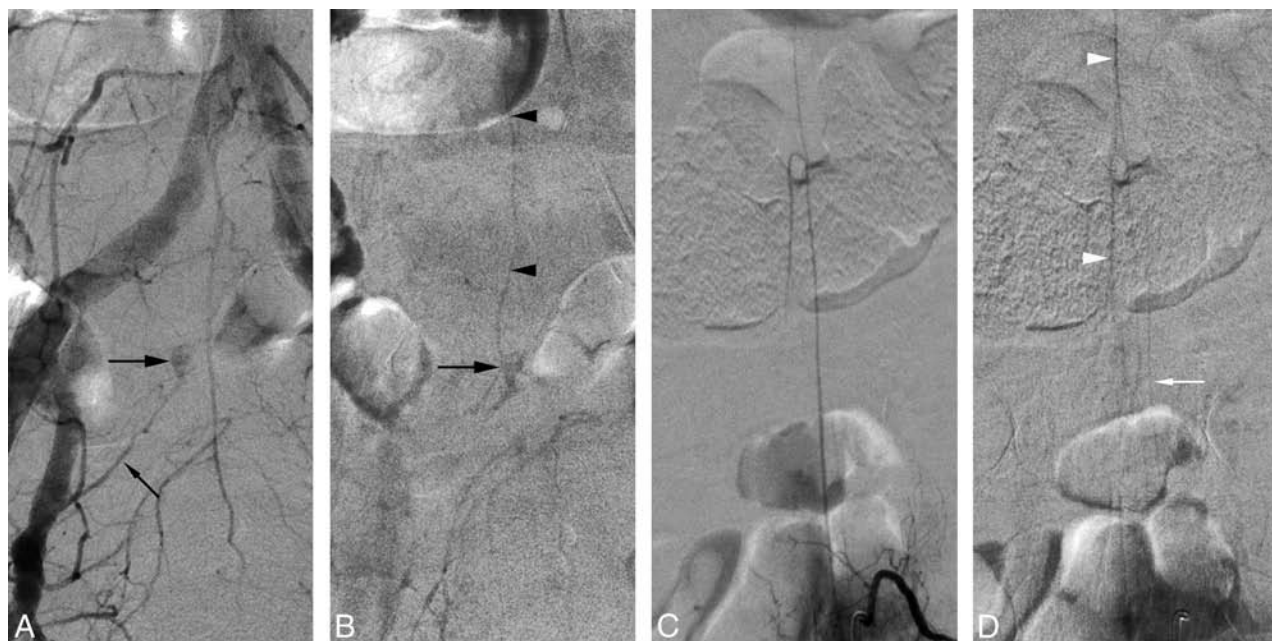


**FIG 4.** A 71-year-old patient with a right S1 spinal epidural arteriovenous fistula. A, SpDSA, right S1 injection, posteroanterior view; the selective injection of the right S1 radicular artery (small black arrow) opacifies the epidural venous pouch of the SEAVF (large black arrow). B, SpDSA right S1 injection, posteroanterior view; a slightly later phase shows the drainage of the isolated epidural pouch (large black arrow) into a right S1 radiculomedullary vein (black arrowheads). C, SpDSA, left T11 injection, posteroanterior view, arterial phase with opacification of the artery of Adamkiewicz. D, SpDSA, left T11 injection, posteroanterior view, later phase, documenting the normal perimedullary venous drainage, including the visualization of spinal (white arrowheads) and radiculomedullary (white arrow) veins. Venous phase timing: first detection = 7 seconds, best delineation = 13 seconds.





**FIG 5.** A 58-year-old man with a right L1 spinal dural arteriovenous fistula. A, SpDSA, right L1 injection, posteroanterior view, documents a right L1 SDAVF (black arrow) draining into the perimedullary venous system (white arrowheads). B, SpDSA, left L1 injection, posteroanterior view, arterial phase with opacification of prominent anterior and posterior radiculomedullary arteries (artery of Lazorthes). C, SpDSA, left L1 injection, posteroanterior view, later phase, documents the normal perimedullary venous drainage, including the visualization of spinal (white arrowheads) and radiculomedullary (white arrow) veins. Note that the opacified longitudinal spinal axis is identical to the one seen draining the SDAVF in A. Venous phase timing: first detection = 7 seconds, best delineation = 10 seconds.



**FIG 6.** A 66-year-old man with a right L1 spinal dural arteriovenous fistula. A, SpDSA, right L1 injection, posteroanterior view, documents a right L1 SDAVF (white arrow) draining into the perimedullary venous system (black arrowheads). B, SpDSA, left T12 injection, posteroanterior view, arterial phase with opacification of the artery of Adamkiewicz. C, SpDSA, left T12 injection, posteroanterior view, later phase, documents the normal perimedullary venous drainage, including the visualization of perimedullary veins (white arrowhead). A radiculomedullary vein is not clearly identified in this case. Venous phase timing: first detection = 29 seconds, best delineation = 39 seconds.

SEAVFs, and the slow perimedullary arteriovenous fistula (Merland type 1).

From a diagnostic viewpoint, high-flow SVMs are usually

easily identified by noninvasive imaging methods. On the other hand, the nonspecific MR imaging changes associated with slow-flow arteriovenous fistulas can be deceptive, particularly in the absence of typical flow voids. A recent study found that the sensitivity and positive predictive value of MR imaging for SVMs in general could be as low as 51% and 48%, respectively.<sup>10</sup> Our cohort similarly suggested a limited value for MR imaging, notably for slow-flow lesions, which were associated with an inaccurate initial diagnosis in 65% of cases.<sup>11</sup> This low predictive value may be related to the importance generally attributed to the absence of detectable flow voids, which were only noted in 49 of our 81 patients (60.5%). This situation is particularly relevant to our report because the angiographic documentation of a normal venous phase is generally used to rule out the presence of a slow-flow arteriovenous fistula in patients with inconclusive MR imaging findings.

#### Spinal Angiography Technique

The fundamental principles of selective spinal angiography established by its pioneers remain valid to this day.<sup>12-14</sup> While partial studies may be performed in certain circumstances (eg, the limited diagnostic portion of a therapeutic procedure or follow-up angiograms), a typical diagnostic study includes at least the selective catheterization of each pair of intersegmental arteries and a pelvic flush aortogram (documenting an SVM does not rule out the presence of additional lesions<sup>1</sup>), often complemented by selective injections of the internal iliac, subclavian, vertebral, supreme intercostal, and (in some instances) carotid arteries.<sup>4,6,15</sup> The appropriate technique and equipment allow performing a complete spinal angiogram with the patient under conscious sedation with short procedure durations, reasonable radiation and contrast agent doses, and extremely low complication rates.<sup>10</sup> However, a sign reliably permitting terminating the procedure

early, such as the observation of a normal venous phase, would carry an important clinical value. The emphasis placed on reliability is particularly important because it has been es-



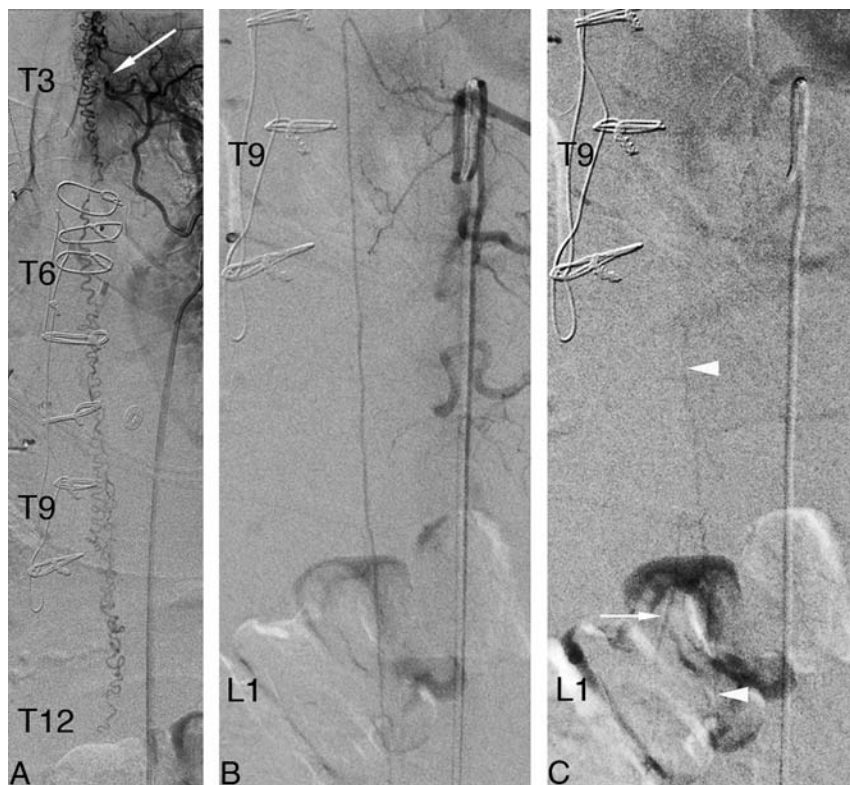


**FIG 7.** A 65-year-old man with a left T3 spinal dural arteriovenous fistula. A, SpDSA, left T3 injection, posteroanterior view, documents a left T3 SDAVF (white arrow) with extensive perimedullary venous drainage. B, SpDSA, left T9 injection, posteroanterior view, arterial phase with opacification of the artery of Adamkiewicz. C, SpDSA, left T9 injection, posteroanterior view, later phase, documents the normal perimedullary venous drainage, including the visualization of spinal (white arrowheads) and radiculomedullary (white arrow) veins. Venous phase timing: first detection = 11 seconds, best delineation = 15 seconds.

timated that about 50% of so-called false-negative findings on spinal angiograms result from a failure to investigate the vessel supplying the SVM.<sup>16</sup>

#### **Normal Venous Phase of Spinal Angiography**

Multiple factors influence the detectability of normal venous structures during the injection of the artery of Adamkiewicz, including the quality of the angiographic equipment, the patient's age and body habitus, the use of general anesthesia or conscious sedation (including the use of paralytic agents or the patient's ability to breath-hold when studied awake), and the presence of significant motion and/or bowel artifacts. The presence of a normal venous phase may, therefore, be underestimated by our retrospective study, in which a substantial portion of angiograms (28.4%) were technically inadequate for the detection of small venous structures, principally because of respiratory and gastrointestinal motion artifacts or limited angiographic sequences in patients generally studied under conscious sedation. It is possible that performing diagnostic SpDSA with the patient under general anesthesia (by using paralytics and pausing the ventilator during injections) would reduce motion artifacts, particularly at the end of long angiographic sequences, and increase the visibility of small venous structures and the number of normal venous phases identified in patients with spinal vascular malformations. Yet, despite these drawbacks, 43% of all the reviewed SVMs were associated

with a normal venous phase, including 40% of slow-flow lesions. The venous phase was analyzed at the lower thoracic and lumbosacral levels of the spinal cord (ie, the venous return of the anterior spinal artery after injection of the artery of Adamkiewicz). Some of the SVMs were, therefore, remotely located normal venous structures, such as a cervical cord SAVM (case 1) or an upper thoracic SDAVF (case 6), but most drained at the levels opacified during the observed normal venous phase. An interesting point made by Trop et al in 1998<sup>8</sup> in regard to their cranial arteriovenous fistula with perimedullary drainage but associated with a normal venous phase was the normal MR imaging appearance of the lower spinal cord in their patient, which led them to conclude that "venous compartmentalization accounted for the isolated abnormal signal of the cervical cord and the normal venous drainage of the lower cord at MR imaging." This idea of a "longitudinal compartmentalization" could certainly apply to our 3 cases with remotely located SVMs.

Cases in which the normal and abnormal venous phases were documented at the same vertebral levels

may suggest a relative functional independence of the anterior and posterior longitudinal venous systems, one preferentially participating in the drainage of the SVM while the other is involved in the visualization of a normal venous phase. Due to the 2D nature of SpDSA, however, the distinction between anterior and posterior spinal veins is generally not possible without the acquisition of lateral projections, which were generally not obtained in our patients. The existence of a "transverse compartmentalization" of the perimedullary venous drainage, therefore, remains hypothetical.

#### **The Mechanisms Underlying the Visualization or Nonvisualization of a Spinal Venous Phase in Perimedullary Venous Hypertension**

In our series, the lack of a spinal venous phase was slightly more common in SDAVFs than SEAVFs and in lesions located at the lumbar level. Both factors seem to favor a role for locoregional venous pressure variations. Hence, the observation of a venous phase, typically made at the level of the conus medullaris, would be more likely prevented by the pressure gradient produced by a closely rather than remotely located fistula (ie, lumbar versus sacral or thoracic). Similarly, the pressure gradient associated with an SDAVF, which consists of an arteriovenous shunt directly involving a radiculomedullary vein, should have a more significant locoregional impact than the gradient resulting from an

SEAVF, in which the arteriovenous shunt is located on an epidural venous pouch with secondary drainage into a radiculomedullary vein (and other possible venous outflow pathways).

Case illustration 5 (Fig 6) suggests that the visualization of a normal venous phase may also depend on the existence of a patent radiculomedullary vein locally available to drain the perimedullary venous blood. In terms of venous timing, this case was a clear outlier (first documentation at 29 seconds, best delineation at 39 seconds) and could have easily been considered as lacking a normal venous phase without a long angiographic acquisition. Most interesting, this “transitional case” is also the one in which a patent lumbosacral radiculomedullary vein was not documented. It is, therefore, reasonable to think that a disappearing venous phase correlates with increasing venous drainage impairment and venous hypertension, a phenomenon typical of slow-flow arteriovenous fistulas well-described by Merland et al in 1980:<sup>17</sup> “Hyperpressure is due to the presence of the shunt but also to impaired venous return, which in turn probably depends upon the absence of the veins normally draining into the epidural space.”

## CONCLUSIONS

A normal venous phase was observed in 43% of our patients, including all the SVMs without perimedullary drainage and all cervical or cervicothoracic junction SAVMs. More important, 40% of the slow-flow lesions (SEAVFs/SDAVFs) were associated with a normal venous phase as well. While the timing of the venous phase appeared to be delayed in that latter group, it was still within accepted normal limits (18 seconds) in all except 1 case. The principal implication of our report is that while it remains an interesting angiographic sign, the observation of a normal venous phase cannot be used to rule out the presence of an SVM or justify interrupting a diagnostic spinal angiogram.

Disclosures: Danielle Eckart Sorte—UNRELATED: Consultancy: Codman Neurovascular, Comments: nominal consulting fees for lectures; Payment for Lectures (including service on Speakers Bureaus): Codman Neurovascular (nominal consulting fees for lectures). Philippe Gailloud—UNRELATED: Consultancy: Codman Neurovascular; Grants/Grants Pending: Siemens\*; Stock/Stock Options: ArtVentive Medical. \*Money paid to the institution.

## REFERENCES

1. Koch C. Spinal dural arteriovenous fistula. *Curr Opin Neurol* 2006; 19:69–75 CrossRef Medline
2. Launay M, Chiras J, Bories J. Angiography of the spinal cord: venous

- phase—normal features. pathological application [in French]. *J Neuroradiol* 1979;6:287–315 Medline
3. Tadié M, Hemet J, Freger P, et al. Morphological and functional anatomy of spinal cord veins [in French]. *J Neuroradiol* 1985;12:3–20 Medline
4. Willinsky R, Lasjaunias P, Terbrugge K, et al. Angiography in the investigation of spinal dural arteriovenous fistula: a protocol with application of the venous phase. *Neuroradiology* 1990;32:114–16 CrossRef Medline
5. Krings T, Geibprasert S, ter Brugge K. *Case-Based Interventional Neuroradiology*. New York: Thieme; 2011
6. Hurst RW. Spinal angiography. In: Baum S, ed. *Abrams' Angiography Vascular and Interventional Radiology*. Boston: Little, Brown and Company; 1997:356–88
7. Harrigan MR, Deveikis JP. *Handbook of Cerebrovascular Disease and Neurointerventional Technique*. Totowa, NJ: Humana Press; 2009
8. Trop I, Roy D, Raymond J, et al. Craniocervical dural fistula associated with cervical myelopathy: angiographic demonstration of normal venous drainage of the thoracolumbar cord does not rule out diagnosis. *AJNR Am J Neuroradiol* 1998;19:583–86 Medline
9. Gueguen B, Merland JJ, Riche MC, et al. Vascular malformations of the spinal cord: intrathecal perimedullary arteriovenous fistulas fed by medullary arteries. *Neurology* 1987;37:969–79 CrossRef Medline
10. Chen J, Gailloud P. Safety of spinal angiography: complication rate analysis in 302 diagnostic angiograms. *Neurology* 2011;77:1235–40 CrossRef Medline
11. Sorte D, Wyse E, Orru E, et al. Initial MRI diagnosis in 132 cases of angiographically confirmed spinal vascular malformations [SNIS oral abstract O-014]. *J NeuroInterv Surg* 2015;7(suppl 1):A8 CrossRef
12. Di Chiro G, Doppman J, Ommaya AK. Selective arteriography of arteriovenous aneurysms of spinal cord. *Radiology* 1967;88:1065–77 CrossRef Medline
13. Djindjian R, Houdart R, Hurth M. Acquisitions récentes en angiographie médullaire. *Revue Neurologique* 1966;115:1068–69
14. Djindjian R, Hurth M, Houdart E. *Angiography of the Spinal Cord*. Baltimore: University Park Press; 1970
15. Gailloud P. Arterial anatomy of the spine and spinal cord. In: Mauro MA, Murphy KP, Thomson KR, et al, eds. *Image-Guided Interventions*. 2nd ed. Philadelphia: Saunders; 2014
16. Gailloud P, Wyse E, Greenberg B, et al. Analysis of 24 false negative spinal angiograms performed in 16 patients with vascular malformations subsequently documented by angiography: what went wrong and how to avoid it. In: *Proceedings of the 52nd Annual Meeting of the American Society of Neuroradiology*, Montréal, Quebec, Canada. May 17–22, 2014
17. Merland JJ, Riche MC, Chiras J. Intraspinal extramedullary arteriovenous fistulae draining into the medullary veins [in French]. *J Neuroradiol* 1980;7:271–320 Medline

# Using Body Mass Index to Predict Needle Length in Fluoroscopy-Guided Lumbar Punctures

A.P. Nayate, I.M. Nasrallah, J.E. Schmitt, and S. Mohan



## ABSTRACT

**BACKGROUND AND PURPOSE:** Predicting the appropriate needle length to use in oblique interlaminar-approach fluoroscopy-guided lumbar punctures in patients with a large body mass index is difficult. Using the wrong needle length can lead to an increased radiation dose and patient discomfort. We hypothesized that body mass index could help determine the appropriate needle length to use in patients.

**MATERIALS AND METHODS:** We randomly selected patients who underwent oblique interlaminar-approach fluoroscopy-guided lumbar punctures and had cross-sectional imaging of the lumbar spine within 1 year of imaging ( $n = 50$ ). The distance from the skin to the midlumbar spinal canal (skin-canal distance) at the level of the lumbar puncture was measured by using an oblique angle of  $8.6^\circ$ , which is an average of angles most often used to perform the procedure. A formula was devised using the skin-canal distance and body mass index to predict the appropriate needle length, subsequently confirmed in 45 patients.

**RESULTS:** The body mass index and skin-canal distance were significantly higher ( $P < .001$ ) in patients who underwent fluoroscopy-guided lumbar puncture with 5- or 7-inch needles ( $n = 22$ ) than in patients requiring 3.5-inch needles ( $n = 28$ ). Using linear regression, we determined the formula to predict the needle length as Skin-Canal Distance (inches) =  $0.077 \times \text{Body Mass Index} + 0.88$ . We found a strong correlation ( $P < .001$ ) between the predicted and actual skin canal distance in 45 patients, and our formula better predicted the skin-canal distance than others.

**CONCLUSIONS:** We designed a formula that uses body mass index to predict the appropriate needle length in oblique interlaminar-approach fluoroscopy-guided lumbar punctures and validated it by demonstrating a strong correlation between the predicted and actual skin-canal distance.

**ABBREVIATIONS:** BMI = body mass index; BMIC = BMI category; FGLP = fluoroscopy-guided lumbar puncture; LP = lumbar puncture; OIA = oblique interlaminar-approach; SCD = skin-canal distance

The palpation of bony landmarks required to successfully perform lumbar punctures (LPs)<sup>1</sup> can be masked in 33% of overweight patients and 68% of patients with obesity<sup>2</sup> due to overlying soft tissue and can lead to an LP failure rate of 19%<sup>3</sup> without image guidance. Sonography can be helpful for guidance but can only visualize pertinent bony landmarks in patients with obesity

74% of the time.<sup>2</sup> Fluoroscopy-guided LP (FGLP) can help alleviate this issue because fluoroscopy helps the operator visualize the bony structures, irrespective of the body habitus, and, in real time, can help the operator guide the needle from the soft tissues to the spinal canal.


An oblique interlaminar approach (OIA) is a common FGLP technique, which allows the operator to maximize visualization of the interlaminar space and bypass normal and abnormal osseous obstacles, such as spondylosis.<sup>4</sup> A 3.5-inch-long (8.9-cm) LP needle is most often used to perform this procedure in adults; however with the obesity epidemic in the United States,<sup>5</sup> the use of 5-inch-long (12.7 cm) and 7-inch-long (17.8 cm) needles is becoming increasingly common and has been estimated to be necessary in 13.8% of patients.<sup>6</sup> Predicting the appropriate needle length to use in OIA-FGLP in patients with a larger body mass index (BMI) is difficult and primarily relies on the operator's experience. A needle that is too long may lead to an increased risk

Received July 9, 2015; accepted after revision August 14.

From the Department of Radiology, Division of Neuroradiology, Hospital of the University of Pennsylvania, Philadelphia, Pennsylvania.

Findings from this research previously presented at: Annual Meeting of the American Society of Neuroradiology and the Symposium of the ASNR Foundation, April 25–30, 2015; Chicago, Illinois.

Please address correspondence to S. Mohan, MD, Hospital of the University of Pennsylvania, Department of Radiology, Division of Neuroradiology, 3400 Spruce St, 110 Donner Building, Philadelphia, PA 19104; e-mail: suyash.mohan@uphs.upenn.edu

 Indicates article with supplemental on-line table.

<http://dx.doi.org/10.3174/ajnr.A4579>

of piercing the anterior epidural space, which can cause a traumatic tap,<sup>7</sup> while a needle that is too short may not reach the spinal canal, requiring the insertion of a longer needle and potentially increasing patient discomfort and fluoroscopy time/radiation dose. An increased radiation dose is a particular concern in patients with obesity because increasing BMI is directly related to higher fluoroscopy times in patients undergoing FGLP.<sup>8</sup> In 2011, The Joint Commission expressed concern about the exposure of the American population to medical imaging ionizing radiation and recommended reviews of practices to reduce radiation exposure to as low as reasonably achievable without compromising patient care.<sup>9</sup>

Formulas to determine proper needle length in non-fluoroscopy-guided interspinous lumbar punctures have been investigated<sup>10–13</sup>; however, there is no established method to determine the appropriate needle length for OIA-FGLPs. The purpose of this study is to determine whether BMI could help predict the appropriate needle length in OIA-FGLPs.

## MATERIALS AND METHODS

This study was approved by the local institutional review board.

### Procedure Technique

Following informed consent, all patients underwent FGLP in the prone position by using a standard biplanar fluoroscopy machine in a neurointerventional suite. The procedures were performed by using techniques as dictated by the American College of Radiology–American Society of Neuroradiology–Society for Pediatric Radiology practice parameters.<sup>14</sup> LPs were performed by first-year neuroradiology fellows (fellows had little or no prior experience in performing FGLPs before the fellowship) under the supervision of attending neuroradiologists (experience in FGLPs ranged from 1 to 20+ years).

Under fluoroscopy, the lumbar levels were visualized and the x-ray tube was maneuvered to the right or left oblique orientation to optimize the view of the interlaminar space as determined by the operator. Using a 3.5-, 5-, or 7-inch beveled tip 22-ga needle, we accessed the lumbar spinal canal mostly at the L2–L3 or L3–L4 level as instructed by the American College of Radiology–American Society of Neuroradiology–Society for Pediatric Radiology practice parameters.<sup>14</sup> Briefly, these levels are favored because the distance of the skin to the subarachnoid space is shorter<sup>6</sup> and the thecal sac cross-sectional area is larger compared with L4–L5 or L5–S1,<sup>15</sup> while there is a higher rate of traumatic puncture<sup>7</sup> from LPs at L4–L5 and a higher incidence of degenerative changes and spinal canal stenosis at L4–L5 and L5–S1.<sup>16</sup> At our institution, LPs are rarely performed at L4–L5 or L5–S1. L1–L2 was never accessed due to the risk of injuring the spinal cord.

The choice of the needle length was determined by the operator on the basis of the patient's body habitus. Patient BMIs were not routinely checked before the LP. This check is not a standard practice at our institution or explicitly stated by the American College of Radiology–American Society of Neuroradiology–Society for Pediatric Radiology guidelines.<sup>14</sup>

The needle was advanced through the skin into the lumbar spine with intermittent pulsed fluoroscopy. Access into the

thecal sac was confirmed on egress of CSF after the removal of the stylet.

### Determination of Tube Angulation

The oblique angle of the x-ray tube used for FGLP at our institution from September 30 to November 4, 2014, was recorded in a consecutive subset of patients ( $n = 30$ ; age range, 19–69 years of age; 14 females and 16 males). In 5/30 patients, a single operator used a craniocaudal angle (range, 7°–27°) in addition to the lateral obliquity. The lumbar punctures were performed at L2–L3 in 14 patients, at L3–L4 in 15 patients, and at L4–L5 in 1 patient. The average oblique angle used to perform the lumbar punctures was  $8.6^\circ \pm 5.2^\circ$ .

### Patients with Imaging of the Lumbar Spine (Derivation Sample)

All patients who had FGLP at our hospital during 11 consecutive months from August 2013 to June 2014 were retrospectively reviewed. FGLP was performed on 322 patients (3.5-inch needle,  $n = 279$ ; 5-inch needle,  $n = 36$ ; and 7-inch needle,  $n = 7$ ). In all patients, age, sex, indication for lumbar puncture, anatomic level of lumbar puncture, and total fluoroscopy time were recorded.

We randomly selected 50/279 patients from the 3.5-inch needle set and included all the patients in the 5- ( $n = 36$ ) and 7-inch ( $n = 7$ ) needle sets for further analysis (total,  $n = 93$ ). All 50 patients had successful FGLP without adverse events. Our institutional PACS was queried to identify from these 93 patients those who had cross-sectional imaging of the abdomen or lumbar spine (CT, MR imaging, PET/CT covering the abdomen, or CT or MR imaging of the lumbar spine) performed within 1 year of the LP. Inclusion criteria for cross-sectional imaging were supine acquisition and inclusion of the flank skin and soft tissue, lumbar spinal canal, and lumbar vertebral bodies in the FOV. Fifty subjects of the 93 in the study met these criteria: 28/50 patients in the 3.5-inch group, 19/36 patients in the 5-inch group, and 3/7 patients in the 7-inch group. Additionally, the patient's BMI obtained closest to the day of the FGLP and lumbar or abdominal imaging and days between imaging and LP were recorded. BMI was categorized (BMI category [BMIC]) as underweight (BMI < 18.5), normal (BMI = 18.5–24.9), overweight (BMI = 25–29.9), obese (BMI = 30–39.9), and extremely obese (BMI  $\geq$  40), according to the obesity guidelines of the National Heart, Lung, and Blood Institute.<sup>17</sup>

### Measurement of Skin-to-Mid-Spinal Canal in the Patients with Lumbar Spine Imaging

We measured the distance from the skin to the midpoint of the spinal canal (skin-canal distance [SCD]) at the level where the lumbar puncture was performed in our cohort of 50 patients by using the standard measurement tools available on our PACS. To account for potential variations in needle approach, we measured the SCD at several angles, including parallel to and intersecting the spinous process (eg, standard bedside interspinous approach lumbar puncture angle, 0°) at the empirically determined mean oblique angle (8.6°) and at angles 1 SD from the mean angle (3.4° and 13.8°). We excluded the craniocaudal



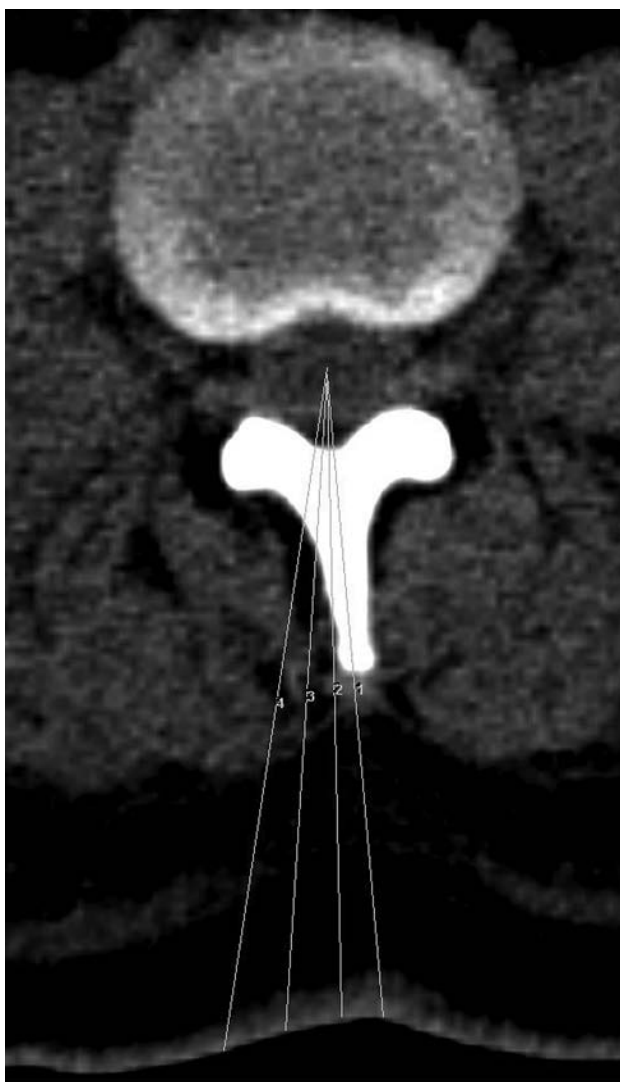


**FIG 1.** Angles used to measure skin to midlumbar spinal canal. Labels: 1 = 0°, 2 = 3.4°, 3 = 8.6°, 4 = 13.8°.

angles to simplify the measurements. Figure 1 summarizes the measurement process.

### Confirmation Sample

For confirmation, in a sample of 45 patients ( $n = 16$  at L2–L3;  $n = 21$  at L3–L4; and  $n = 8$  at L4–L5) who underwent OIA-FGLP from December 2014 to May 2015, the SCD was physically measured. Specifically, the tip of the needle was confirmed to be in the center of the spinal canal with a single lateral view. After the completion of the FGLP, the LP needle was marked at the skin and removed, and the distance from the skin surface to the tip of the needle was measured. BMIs obtained closest to the day of FGLP and other demographic measures were acquired from the electronic medical record as described above. To minimize selection bias, we required no inclusion criteria for our confirmation sample, including prior cross-sectional imaging. One patient was included in the confirmation sample and in the derivation sample; the remaining 44 patients were separate from the derivation sample.

### Statistical Analysis

Demographic information was summarized with means for continuous variables and proportions for discrete variables.  $T$  tests were performed to compare group differences in BMI and fluoroscopy time. To estimate the effect of potentially variant needle angles on the reliability of CT- and MR imaging–derived SCD measurements, we calculated the intraclass correlation coefficient among measurements at different angles (0°, 3.4°, 8.6°, 13.8°). Following graphic display of the data and assessment for normality, linear regression was used to explore the relationship between BMI and SCD. The  $\beta$  weights from the best-fit model were used to construct a formula for predicting needle length from BMI alone. On the basis of this formula, SCD was estimated for our confirmation sample on the basis of BMI and was compared with the actual measured SCD length via linear regression. Repeated-measures ANOVA was used to compare the deviation between the predicted and actual SCD between our formula and others. Multiple regression was used to examine the relationship between fluoroscopy time and needle length after accounting for BMI. For hypothesis tests, a 2-tailed  $\alpha$  of .05 was defined as the threshold for statistical significance.

## RESULTS

### Patients with Imaging of the Lumbar Spine (Derivation Sample)

In our sample of subjects with both LP and cross-sectional imaging data, there were 18 women and 32 men with a mean age of  $49.1 \pm 17.2$  years. Twenty-eight patients had LP at L2–L3; 17 patients, at L3–L4; 4 patients, at L4–L5; and 1 patient, at L5–S1. The indications for the LP were the following: 23 patients, intrathecal chemotherapy; 15 patients, CSF tumor cell detection; 1 patient, evaluation for neurosarcoidosis; 6 patients, detection of an infectious/inflammatory process in the CSF; 3 patients, concern for pseudotumor cerebri; 1 patient, indeterminate cervical spinal cord lesion; and 1 patient, concern for subarachnoid hemorrhage.

Patients had cross-sectional imaging of the abdomen or lumbar spine an average of 90 days (range, 1–353 days) before or after the LP. The cross-sectional imaging consisted of the following: 34 patients with CT of the abdomen, 9 patients with MR imaging of the lumbar spine, 5 patients with PET/CT, 1 patient with MR imaging of the abdomen, and 1 patient with CT of the lumbar spine.

In our sample of 50 patients, based on BMI, 2 patients (2%) were characterized as underweight; 11 patients (22%), as having normal weight; 11 patients (22%), as overweight; 19 patients (38%), as obese; and 7 patients (14%), as extremely obese. Patients, on average, had a BMI obtained within 12 days of their FGLP and within 17 days of their cross-sectional lumbar or abdominal imaging. These 2 BMI values were not significantly different (average difference in BMI, 1.4; range, 0–6.4;  $P = .78$ ), nor were the BMI of men (average BMI =  $30.7 \pm 11$ ) compared to women (average BMI =  $33.34 \pm 9.5$ ),  $P = .38$ .

The BMIs of the patients who underwent FGLP with a 5- or 7-inch needle ( $n = 22$ ; average,  $40.1 \pm 9.8$ ; BMIC, extremely obese; 11 women and 11 men) were significantly higher ( $P < .001$ ) than the BMIs of patients who underwent FGLP with a

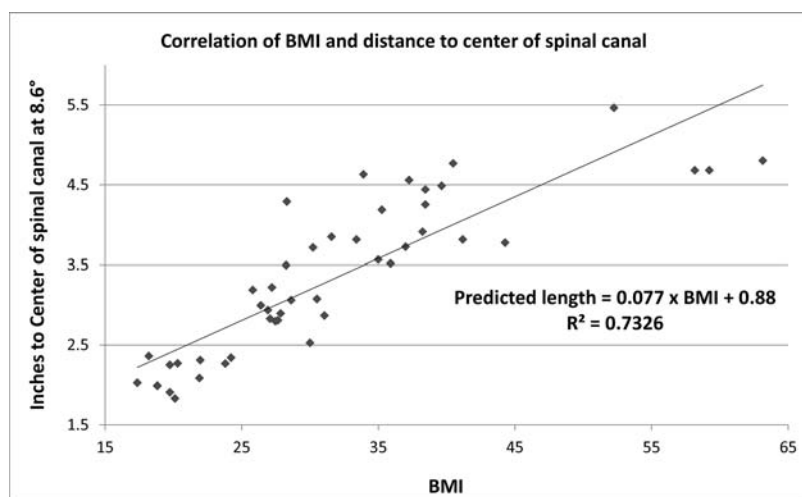


**FIG 2.** Correlation of 50 patient BMIs and the distance to the center of the spinal canal on cross-sectional imaging.

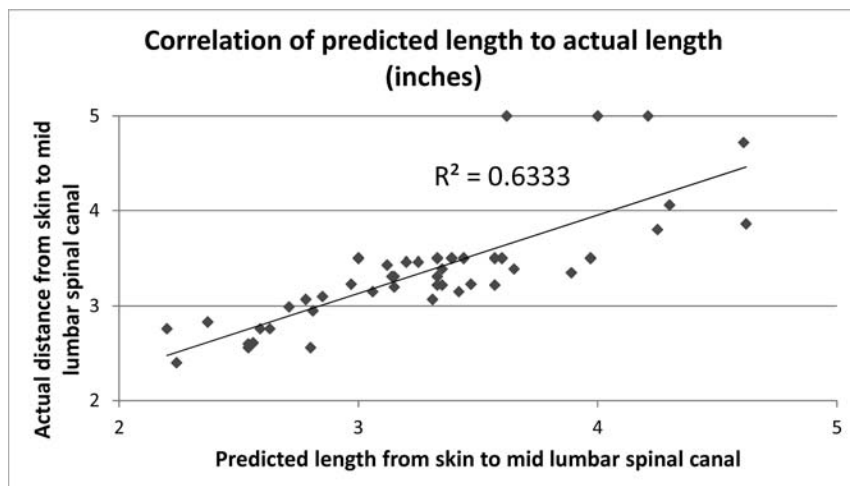


**FIG 3.** Correlation between actual and predicted SCDs.

3.5-inch needle ( $n = 28$ ; average,  $25 \pm 4.7$ ; BMIC, normal-overweight; 7 women and 21 men). The fluoroscopy time in patients who underwent FGLP with a 5- or 7-inch needle (average,  $1.32 \pm 0.89$  minutes) was significantly longer ( $P = .004$ ) than that in patients who underwent FGLP with a 3.5-inch needle (average,  $0.65 \pm 0.57$  minutes) and also in the entire cohort of patients (3.5-inch needle,  $n = 279$ ; 5- and 7-inch needle,  $n = 43$ ) who underwent FGLP ( $P = .004$ ). Multiple regression confirmed that needle length was an independent predictor of fluoroscopy time, even after accounting for BMI ( $P = .003$ ).

#### **Measurement of the Skin-to-Mid-Spinal Canal in Patients with Lumbar Spine Imaging**

SCD estimates were highly reliable between the measured-approach angles (intraclass correlation coefficient = 0.99). The distance measured on the cross-sectional imaging in the cohort of 50 patients at the mean FGLP right oblique angle of  $8.6^\circ$  was significantly higher ( $P < .001$ ) in patients who underwent FGLP with a 5- or 7-inch needle (average,  $4.1 \pm 0.6$  inches) compared with patients who underwent FGLP with a 3.5-inch needle (mean,  $2.7 \pm 0.6$  inches). Similar results were seen at other angle mea-

surements (all  $P < .001$ ). The data obtained from the cross-sectional imaging were plotted against the BMI, and with linear fit, we determined the following formula at an oblique angle of  $8.6^\circ$ : Skin to Center of Spinal Canal (inches) =  $0.077 \times \text{BMI} + 0.88$  (Fig 2).

#### **Confirmation Sample**

There was a strong correlation between predicted and actual SCD in our confirmation sample ( $r = 0.80$ ,  $R^2 = 0.63$ ,  $P < .001$ ), with a difference of  $8.0\% \pm 6.2\%$  (Fig 3). There was no significant difference ( $P = .76$ ) between the predicted and measured lengths if the procedure was performed at L2–L3 ( $n = 16$ ; average,  $8.4\% \pm 5.5\%$ ), at L3–L4 ( $n = 21$ ; average,  $8.3\% \pm 7.4\%$ ), or at L4–L5 ( $n = 8$ ; average,  $6.5\% \pm 4.0\%$ ). The average SCD was not significantly different between the predicted ( $3.27 \pm 0.60$  inches) and measured ( $3.36 \pm 0.61$  inches) length difference, 0.09 inches;  $P = .15$ . The average difference between the predicted and measured SCD length for women was  $11.5\% \pm 6\%$  ( $n = 15$ ) and was significantly higher ( $P = .001$ ) than that for men ( $6.23\% \pm 5.4\%$ ;  $n = 30$ ). Our formula more accurately predicted the needle length from the skin to the spinal canal than other published formulas, which were determined for ISLPs (On-line Table). Figure 4 compares the accuracy of existing formulas in predicting the actual SCD in our confirmation sample. The current model

was significantly more accurate ( $P < .0001$ ) compared with other formulas.

In the confirmation sample of 15 women and 30 men, the average age was  $47.1 \pm 16.9$  years and the average BMI was  $31.1 \pm 7.7$  (average BMI in men,  $30.6 \pm 6.7$ ; BMIC, overweight; average BMI in women,  $33.0 \pm 10.1$ ; BMIC, overweight). On the basis of the BMI, 2 patients (4%) were classified as underweight; 8 patients, as having normal weight (18%); 10 patients, as being overweight (25%); 18 patients, as being obese (40%); and 7 patients (16%), as being extremely obese. These values were similar to those seen in our cohort of 50 patients from which we determined the formula. The average oblique angle used was  $8.5^\circ \pm 4.8^\circ$  ( $n = 42$ ; for 3 patients, the angle was not recorded), similar to the  $8.6^\circ$  angle determined from the angle-determination cohort of 30 patients.

In 36/45 patients, a 3.5-inch needle was used; in 8/45 patients, a 5-inch needle was used; and in 1 patient, a 7-inch needle was used. In 1 of the patients requiring a 5-inch needle, originally a 3.5-inch needle was used; however, LP was unsuccessful and CSF was obtained after the use of a 5-inch needle. Our formula pre-

## Accuracy of BMI in predicting Source to Spinal Canal Distance

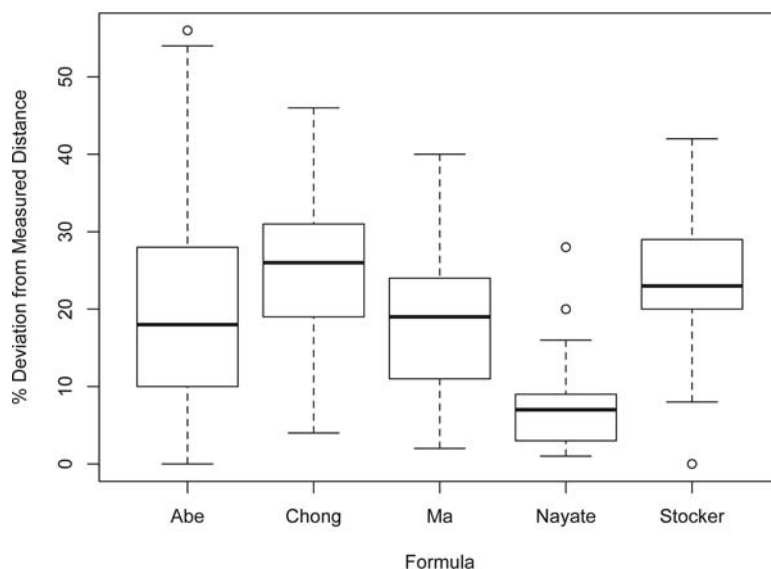


**FIG 4.** Boxplots demonstrating the accuracy in predicted SCD as a function of the formula. The predicted SCD from our method was closer to the actual SCD in our confirmation sample compared with the other formulas ( $P < .0001$  for all pair-wise comparisons, repeated measures ANOVA, Bonferroni correction).

**Table 1: Accuracy of formula to predict the appropriate needle length to use in the confirmation sample<sup>a</sup>**

Actual SCD	Correct	Incorrect
<3.5 inches	28/31 (90%) <sup>b</sup>	3/31 (10%) <sup>c</sup>
>3.5 inches	7/7 (100%) <sup>c</sup>	0 (0%)
Total	35/38 (92%)	3/38 (8%)

<sup>a</sup> Accuracy of formula needle-length prediction, 3.5 or 5 inches. In 7/45 patients, the actual SCD was 3.5 inches; our formula predicted a 5-inch needle in 3/7 (43%) patients and a 3.5-inch needle in 4/7 (57%) patients.

<sup>b</sup> Predicted 3.5-inch needle.

<sup>c</sup> Predicted 5-inch needle.

**Table 2: Accuracy of formula versus neuroradiologists at our institution (fellow or attending,  $n = 19$ ) in selecting the appropriate needle length<sup>a</sup>**

Actual SCD	Formula	Neuroradiologists
<3.5 inches	28/31 (90%) <sup>b</sup>	30/31 (97%) <sup>b</sup>
>3.5 inches	7/7 (100%) <sup>c</sup>	5/7 (71%) <sup>d</sup>
Total	35/38 (92%)	35/38 (92%)

<sup>a</sup> In 7/45 patients, the actual SCD is 3.5 inches. Our formula predicted a 5-inch needle in 3/7 (43%) patients and a 3.5-inch needle in 4/7 (57%) patients, and the neuroradiologists selected a 3.5-inch needle in 6/7 (86%) patients and a 5-inch needle in 1/7 (14%) patients.

<sup>b</sup> Predicted 3.5-inch needle.

<sup>c</sup> Predicted 5-inch needle.

<sup>d</sup> A 3.5-inch needle was unsuccessfully used in 1 patient, and a 7-inch needle, in another patient by 2 different neuroradiologists.

dicted that a 5-inch needle would be required in this patient. In the patient in whom a 7-inch needle was used, initially LP was unsuccessful with a 5-inch needle inserted at the L4–L5 level. Fluoroscopy showed the needle tip in center of the spinal canal, but there was no egress of CSF. LP with a 7-inch needle was successful at the L3–L4 level. The skin-to-mid-spinal canal measurement based on the LP needle was 4.72 inches, confirming that a 5-inch needle could also have been used at L3–L4; our formula predicted the SCD to be 4.5 inches. Similarly, in 1 patient, a 5-inch needle was used at L3–L4; however, our formula predicted that a

3.5-inch could have been used, and our prediction was confirmed with measurements on the LP needle (predicted, 3.06 inches; actual, 3.15 inches) (Online Table). Table 1 shows the accuracy of our formula in needle-length prediction, and Table 2 shows a comparison between the needle-length predictions by the formula and neuroradiologists' at our institution.

## DISCUSSION

Predicting lumbar puncture needle length in overweight patients and those with obesity is usually based on the operator's experience and can have a failure rate of 19%<sup>3</sup> without image guidance. Many of these patients with prior unsuccessful lumbar punctures are referred to the neuroradiology department for image-guided lumbar punctures under fluoroscopy. There are no established methods to help determine the appropriate needle length to use in

OIA-FGLPs, and this determination primarily relies on the operator's experience.

We derived a formula to predict the appropriate needle length to use in OIA-FGLP by using measurements from the skin to the midlumbar spinal canal on lumbar cross-sectional imaging, patients' BMIs, and oblique angles most commonly used to perform the procedure. The measurements we obtained from 4 angles (0°, 8.6°, 3.4°, and 13.8°) were very similar, suggesting that our formula can be used on a wide range of OIA angles and with the interspinous approach, which is much more commonly used without fluoroscopic guidance.

We validated our formula by measuring the distance from the skin surface to the needle tip in patients who underwent FGLP and found it highly predictive of actual SCD. The distance our formula predicted was, on average, 0.28 inches (8.0%) different, not statistically significantly different from that measured ( $P = .51$ ). Our formula overpredicted the needle length in 13/45 (29%) patients, underpredicted it in 22/45 (49%) patients, and precisely predicted (difference of <0.1 inch) it in 10/45 (22%) patients. The underpredictions never resulted in a needle too short to reach the spinal canal, while the overpredictions would have resulted in using a longer needle than needed in 3/45 (7%) patients (5 inch instead of 3.5 inch). In 7/45 (16%) patients, the SCD was 3.5 inches, so a 3.5- or 5-inch needle could be appropriately used.

The needle-length prediction from our formula would have guided the operator to use a 5-inch needle in a case that was unsuccessful with the use of a 3.5-inch needle and would have guided the operator to use a 5-inch needle instead of a 7-inch needle and a 3.5-inch instead of a 5-inch needle in 2 patients, appropriate changes as confirmed on measurements performed on the LP needles. Our formula correctly predicted the appropriate needle length to use in 92% of patients (3.5 inch,  $n = 28/31$ ; 5 inch,  $n = 7/7$ ) (Table 1) and more accurately predicted the

appropriate use of a 5-inch needle than the subjective assessment of 2 neuroradiologists (7/7 patients versus 5/7 patients, Table 2). Neuroradiologists more accurately predicted the use of a 3.5-inch needle than the formula, but overall (the 3.5- and 5-inch-needle groups included), the formula and neuroradiologists were equal in predicting the correct needle length (35/38, 92%). The high accuracy of subjective needle-length prediction by neuroradiologists at our institution may be related to the extensive experience in performing FGLP, because approximately 400+ FGLPs are performed at our institution yearly. Our formula may be particularly helpful to health care practitioners who perform FGLPs less frequently.

Our formula more accurately predicted the needle length in male patients than in female patients (6.23% versus 11.5%, respectively;  $P = .001$ ) and is probably due to sex differences in body fat distribution, with women having a more variable fat distribution with higher subcutaneous fat in the lower back and gluteal region, while men have more central adiposity.<sup>18,19</sup> However, less accuracy in female patients did not translate to errors in needle selection as our formula better predicted the correct needle length in women than in men. Our formula would have predicted the correct needle length in 14/15 (93%) female patients and selection of a needle that was too long (5 versus 3.5 inch) in 1 patient; while in men, our formula predicted the correct needle in 25/30 (83%) patients and selection of a needle that was too long (5 versus 3.5 inch) in 5 male patients.

There have been studies that have derived formulas to estimate SCD for interspinous approach LPs, including the formulas by Abe et al,<sup>10</sup> Ma et al,<sup>11</sup> Stoker and Bonsu,<sup>12</sup> and Chong et al,<sup>13</sup> which are often cited in the literature. The SCD that all 4 formulas predicted were significantly different from the actual SCD (all,  $P < .001$ ) measured in our cohort of 45 patients. The predicted SCD from our formula was 8% different from the actual one, while the predicted lengths from the formulas of Abe et al, Ma et al, Stoker and Bonsu, and Chong et al were 20%, 18%, 24%, and 25% different from the actual SCD, respectively (Fig 4). The use of the formulas of Ma et al, Stoker and Bonsu, and Chong et al in our cohort resulted in average predicted lengths of 0.56, 0.83, and 0.85 inches less than the actual distance, respectively; and using their formulas would have resulted in selection of a needle that was too short (3.5 versus 5 inches) in 2% (1/45) of patients with the formula of Ma et al, 13% (6/45) of patients with the formula of Stoker and Bonsu, and 11% (5/45) of patients with the formula of Chong et al. The formula of Abe et al predicted an average length of 0.62 inches higher than the actual distance. Most of the differences (41/45) were overpredictions and would have led to an unnecessary use of a longer needle length in 64% (29/45) of patients. The unnecessary use of a longer needle can be problematic because longer needles are independent predictors of longer fluoroscopic time ( $P = .003$ , in our cohort of 7 neuroradiology fellows), even after accounting for BMI, and there may be an increased risk of piercing the anterior epidural space, which can lead to a traumatic tap.<sup>7</sup> Furthermore, anecdotally, a longer needle is more difficult to guide from the skin into the spinal canal, particularly for less experienced operators; and there is often slower egress of CSF through longer needles, potentially causing a longer procedural time.

We believe our formula more accurately predicted the SCD length than the formula of Abe et al,<sup>10</sup> because the BMI in the cohort of 50 patients from which we derived our formula is more reflective of the adult US population. The patient population in the Abe et al study had a BMI of 22.6 (BMIC, normal) and included children and adults, while the BMI in our cohort of adult patients was 31.7 (BMIC, obese), which is more similar to the average BMI of 28.4 (BMIC, overweight) seen in the adult US population.<sup>20</sup> We believe our formula more accurately predicted the needle length than the formula of Ma et al<sup>11</sup> because in our cohort of 50 patients, the SD of weight (kilograms) of the patients was higher (24.2 versus 12.7 Kg). A formula derived from a wider range of patient weights suggests that the formula is potentially more applicable to a larger subset of the general population. We speculate that our formula more accurately predicted the needle length than the formulas of Stoker and Bonsu<sup>12</sup> or Chong et al<sup>13</sup> because children, who constituted their patient population, have shorter skin-to-mid-spinal canal measurements compared with adults and typically require 1.5-, 2.5-, or 3.5-inch needles.

Needle-length predictions from our formula are validated for FGLPs at L2–L3 and L3–L4 because 90% of the patients from whom we devised our formula underwent LPs at these levels. This finding is consistent with the practices of our institution and most other neuroradiology practices, where most of the FGLPs are performed at these 2 levels.<sup>20</sup> LPs are usually avoided at L4–L5 and L5–S1 due to the higher incidence of degenerative changes and spinal canal stenosis<sup>16</sup> and the smaller cross-sectional area of thecal sac compared with L2–L3 and L3–L4,<sup>15</sup> which could cause a lower success rate. In addition, lumbar punctures at L4–L5 are associated with twice the risk of traumatic lumbar puncture compared with L2–L3 and L3–L4,<sup>7</sup> which could lead to complications and confound results, especially in patients with concern for subarachnoid hemorrhage. In the limited patients in whom we performed FGLPs at L4–L5, our formula was accurate in predicting the needle length in 8/8 patients, with a 6.5% difference between the predicted and actual length. However, the average BMI in these patients was  $25.6 \pm 5.2$  (BMIC, normal-overweight), which was lower than the average BMI in our cohort of patients who underwent LPs at L2–L3 (average BMI,  $31.5 \pm 8.4$ ; BMIC, obese;  $n = 16$ ) and L3–L4 (average BMI,  $32.6 \pm 7.5$ ; BMIC, obese;  $n = 21$ ) because operators favored performing FGLPs at L2–L3 and L3–L4 in patients with large BMIs because the distance from the skin to the subarachnoid space is shorter at L2–L3 and L3–L4 compared with L4–L5.<sup>6</sup>

Our study has limitations. First, our sample size ( $n = 50$ ) from which we derived our formula was small; however, our patient population is reflective of the US population because the BMI of 31.7 (BMIC, obese) in our cohort is similar to the average BMI of 28.4 (BMIC, overweight) in the adult US population.<sup>21</sup> Second, our findings are based on the FGLPs performed at a single institution; though with a total of 14 neuroradiology fellows performing the FGLP under the supervision of 15 attending neuroradiologists, there was a range of operator skills. Third, our formula is designed to predict the appropriate needle length to use at the L2–L3 and L3–L4 levels and might not be accurate at L4–L5 or L5–S1, especially in patients with obesity (BMI > 30). Fourth, on cross-sectional imaging, we measured the distance from the skin



to the midspinal canal with the patient in a supine position, which can vary slightly (approximately 0.1 inch) from that determined from measurement in the prone position used for FGLP.<sup>22</sup> Fifth, lumbar puncture needles can bend while traversing from the skin to the spinal canal and could potentially affect the measured distance on the needle used as the reference standard. Sixth, the accuracy of prediction of SCD diminishes in patients with extreme obesity.

## CONCLUSIONS

We derived a formula ( $0.077 \times \text{BMI} + 0.88$ ) to predict the distance from the skin to the center of the spinal canal to determine the needle length (inches) to use in OIA-FGLPs in adults. We validated our formula by demonstrating only an 8% difference between the needle-length predictions and the actual distance from lumbar puncture needles used in patients. Our formula better predicted the SCD than other published formulas and can help guide operators in selecting the appropriate needle length for FGLPs.

Disclosures: James E. Schmitt—UNRELATED: Grants/Grants Pending: Radiological Society of North America (current) and National Institutes of Health (pending), Comments: 1) Imaging Genomics of the 22q11.2 Deletion Syndrome; Radiological Society of North America Fellow Grant (\$50,000), 2014–2015; 2) Integrated Neuroimaging Genomic Ontology Toolbox: a family of statistical computing algorithms for hypothesis-driven imaging genetic and longitudinal neuroimaging analysis; National Institutes of Health Mentored Career Development Award in Biomedical Big Data Science for Clinicians and Doctorally Prepared Scientists (K01, submitted); Payment for Lectures (including service on Speakers Bureaus): Registration waived for 3 invited lectures; no stipend or other compensation, Comments: 1) J.E. Schmitt, M.C. Neale, J.N. Giedd; "Genetically-Informative Multivariate Models of Brain Maturation," Imaging Genetics Symposium, Behavioral Genetics Association, San Diego, California (2015); 2) J.E. Schmitt; Outstanding Paper: The Dynamic Role of Genetics on Cortical Patterning During Childhood and Adolescence, American Society for Neuroradiology, Chicago, Illinois (2015); 3) T.S. Cook, J.E. Schmitt, J.C. Wildenberg: Introduction to Statistical Computing with R, Society for Imaging Informatics in Medicine, Washington DC (2015).

## REFERENCES

- Boon JM, Abrahams PH, Meiring JH, et al. **Lumbar puncture: anatomical review of a clinical skill.** *Clin Anat* 2004;17:544–53 CrossRef Medline
- Stiffler KA, Jwayyed S, Wilber ST, et al. **The use of ultrasound to identify pertinent landmarks for lumbar puncture.** *Am J Emerg Med* 2007;25:331–34 CrossRef Medline
- Edwards C, Leira EC, Gonzalez-Alegre P. **Residency training: a failed lumbar puncture is more about obesity than lack of ability.** *Neurology* 2015;84:e69–72 CrossRef Medline
- Williams MT. **The oblique interlaminar approach for fluoroscopy-guided lumbar puncture: keep the eye opened!** *Diagn Interv Imaging* 2014;95:629–32 CrossRef Medline
- Wang Y, Beydoun MA. **The obesity epidemic in the United States: gender, age, socioeconomic, racial/ethnic, and geographic characteristics—a systematic review and meta-regression analysis.** *Epidemiol Rev* 2007;29:6–28 CrossRef Medline
- Halpenny D, O'Sullivan K, Burke JP, et al. **Does obesity preclude lumbar puncture with a standard spinal needle? The use of computer tomography to measure the skin to lumbar subarachnoid space distance in the general hospital population.** *Eur Radiol* 2013;23:3191–96 CrossRef Medline
- Yu SD, Chen MY, Johnson AJ. **Factors associated with traumatic fluoroscopy-guided lumbar punctures: a retrospective review.** *AJNR Am J Neuroradiol* 2009;30:512–15 CrossRef Medline
- Boddu SR, Corey A, Peterson R, et al. **Fluoroscopic-guided lumbar puncture: fluoroscopic time and implications of body mass index: a baseline study.** *AJNR Am J Neuroradiol* 2014;35:1475–80 CrossRef Medline
- The Joint Commission. Sentinel Event Alert. Issue 47: Radiation risks of diagnostic imaging. 2011. [http://www.jointcommission.org/sea\\_issue\\_47/](http://www.jointcommission.org/sea_issue_47/). Accessed February 11, 2015
- Abe KK, Yamamoto LG, Itoman EM, et al. **Lumbar puncture needle length determination.** *Am J Emerg Med* 2005;23:742–46 CrossRef Medline
- Ma HP, Hung YF, Tsai SH, et al. **Predictions of the length of lumbar puncture needles.** *Comput Math Methods Med* 2014;2014:732694 CrossRef Medline
- Stocker DM, Bonsu B. **A rule based on body weight for predicting the optimum depth of spinal needle insertion for lumbar puncture in children.** *Acad Emerg Med* 2005;5:105–06
- Chong SY, Chong LA, Ariffin H. **Accurate prediction of the needle depth required for successful lumbar puncture.** *Am J Emerg Med* 2010;28:603–06 CrossRef Medline
- Kieffer S, Mukundan S, Rollins N. ACR–ASNR–SPR Practice Guideline for the Performance of Myelography and Cisternography. 2013. <http://www.acr.org/~media/f4c49aa1834d46a081f5f0ff20e1e26b.pdf>. Accessed February 12, 2015
- Chatha DS, Schweitzer ME. **MRI criteria of developmental lumbar spinal canal stenosis revisited.** *Bull NYU Hosp Jt Dis* 2011;69:303–07 Medline
- Saleem S, Aslam HM, Rehmani MAK, et al. **Lumbar disc degenerative disease: disc degeneration symptoms and magnetic resonance image findings.** *Asian Spine J* 2013;7:322–34 CrossRef Medline
- National Heart, Lung, and Blood Institute. How Are Overweight and Obesity Diagnosed? <http://www.nhlbi.nih.gov/health/health-topics/topics/obe/diagnosis.html>. Accessed August 6, 2015
- Dixon AK. **Abdominal fat assessed by computed tomography: sex difference in distribution.** *Clin Radiol* 1983;34:189–91 CrossRef Medline
- Toth MJ, Tchernof A, Sites CK, et al. **Effect of menopausal status on body composition and abdominal fat distribution.** *Int J Obes Relat Metab Disord* 2000;24:226–31 CrossRef Medline
- Abel AS, Brace JR, McKinney AM, et al. **Practice patterns and opening pressure measurements using fluoroscopically guided lumbar puncture.** *AJNR Am J Neuroradiol* 2012;33:823–25 CrossRef Medline
- Finucane MM, Stevens GA, Cowan MJ, et al; Global Burden of Metabolic Risk Factors of Chronic Diseases Collaborating Group (Body Mass Index). **National, regional, and global trends in body-mass index since 1980: systematic analysis of health examination surveys and epidemiological studies with 960 country-years and 9.1 million participants.** *Lancet* 2011;377:557–67 CrossRef Medline
- Carnie J, Boden J, Gao Smith F. **Prediction by computerised tomography of distance from skin to epidural space during thoracic epidural insertion.** *Anaesthesia* 2002;57:701–04 CrossRef Medline

# 3D T2 MR Imaging–Based Measurements of the Posterior Cervical Thecal Sac in Flexion and Extension for Cervical Puncture

M.P. Bazylewicz, F. Berkowitz, and A. Sayah

## ABSTRACT

**BACKGROUND AND PURPOSE:** The current standard technique for cervical puncture involves prone positioning with neck extension. The purpose of this study was to compare measurements of the posterior cervical thecal sac during neck flexion and extension in supine and prone positions by using high-resolution MR imaging to help determine the optimal positioning for cervical puncture.

**MATERIALS AND METHODS:** High-resolution T2-weighted MR imaging was performed of the cervical spine in 10 adult volunteers 18 years of age and older. Exclusion criteria included the following: a history of cervical spine injury/surgery, neck pain, and degenerative spondylosis. Images of sagittal 3D sampling perfection with application-optimized contrasts by using different flip angle evolutions were obtained in the following neck positions: supine extension, supine flexion, prone extension, and prone flexion. The degree of neck flexion and extension and the distance from the posterior margin of the spinal cord to the posterior aspect of the C1–C2 thecal sac were measured in each position.

**RESULTS:** The mean anteroposterior size of the posterior C1–C2 thecal sac was as follows: 4.76 mm for supine extension, 3.63 mm for supine flexion, 5.00 mm for prone extension, and 4.00 mm for prone flexion. Neck extension yielded a larger CSF space than flexion, independent of supine/prone positioning. There was no correlation with neck angle and thecal sac size.

**CONCLUSIONS:** The posterior C1–C2 thecal sac is larger with neck extension than flexion, independent of prone or supine positioning. Given that this space is the target for cervical puncture, findings suggest that extension is the ideal position for performing the procedure, and the decision for prone-versus-supine positioning can be made on the basis of operator comfort and patient preference/ability.

**ABBREVIATION:** SPACE = sampling perfection with application-optimized contrasts by using different flip angle evolution

Often the approach for accessing the thecal sac for CSF sampling or myelography is via lumbar puncture. There are subsets of patients, however, in whom lumbar puncture is not possible or is contraindicated. These include patients with severe lumbar spondylosis, extensive bony lumbar fusion, lumbar canal stenosis, spinal dysraphism, extensive lumbar hardware, and lumbar epidural abscess. In these cases, cervical puncture may be performed as an alternative. For cervical myelography, cervical puncture may actually be the preferred method for instillation of intrathecal contrast.

Although its use is being curbed by heavily T2-weighted, high-resolution MR imaging techniques, cervical myelography is still indicated in patients who have a contraindication to MR imaging or equivocal findings on MR imaging or who have failed MR imaging. Administering contrast via cervical puncture has several advantages, including less dilution of contrast within the cervical canal, better control of contrast to prevent intracranial spillage, and the ability to perform the procedure with the patient in a prone or supine position. Additionally, cervical puncture can be helpful to delineate the upper margin of an obstructive mass within the spinal canal below the cervical level. Disadvantages include a slightly increased risk of damage to nearby structures such as the spinal cord, vessels, or nerves.<sup>1,2</sup>

C1–C2 puncture for myelography is often performed with the patient in the prone position with the neck extended, though the procedure can be performed with patients in the lateral decubitus and supine positions.<sup>3,4</sup> Neck extension is helpful in the prevention of intrathecal contrast spilling into the intracranial space. This positioning may also be used for C1–C2 puncture for CSF

Received July 14, 2015; accepted after revision August 14.

From the Division of Neuroradiology, Department of Radiology, Medstar Georgetown University Hospital, Washington, DC.

Paper previously presented at: American Society of Neuroradiology Annual Meeting and the Foundation of the ASNR Symposium, May 17–22, 2014; Montreal, Quebec, Canada.

Please address correspondence to Anousheh Sayah, MD, Department of Radiology, Medstar Georgetown University Hospital, 3800 Reservoir Rd, NW, CG201, Washington, DC 20007; e-mail: anousheh.sayah@gunet.georgetown.edu

<http://dx.doi.org/10.3174/ajnr.A4564>

sampling, though there is no contrast as in myelography to warrant the extended neck position. Under fluoroscopic guidance, the needle is advanced into the posterior thecal sac between the C1 and C2 vertebrae at approximately the junction of the anterior two-thirds and posterior one-third of the spinal canal.<sup>3</sup> As a result, the size of the posterior thecal sac in various neck positions during puncture is of interest. That the diameter of the spinal canal varies on imaging with neck position, notably in flexion or extension, is well-documented; however, these studies are focused on the mid- and lower cervical spine in regard to stenosis from spondylotic change.<sup>5-7</sup> Measurements of the posterior cervical thecal sac are reported with x-ray myelography, with mention of a subjective change in dural configuration and lack of subjective movement of the cord at the C1–C2 level on flexion and extension.<sup>8</sup> Recently, thin-section MR imaging techniques have been used to assess cervical spinal canal dimensions in healthy volunteers.<sup>9</sup>

To our knowledge, no study has confirmed that there is more space in the posterior thecal sac at C1–C2 with neck extension over flexion or with prone-versus-supine positioning. The purpose of this study was to compare measurements of the posterior cervical thecal sac at C1–C2 during neck flexion and extension in the supine and prone positions by using high-resolution MR imaging in healthy volunteers, to determine which position allows the largest CSF space for cervical puncture.

## MATERIALS AND METHODS

### Patients

The Georgetown University Hospital institutional review board approved this prospective, Health Insurance Portability and Accountability–compliant study. The study included 10 healthy volunteers. The inclusion criterion was age older than 18 years. Exclusion criteria were the following: history of cervical spine injury, known cervical disc herniations, cervical canal or neuroforaminal stenosis, or cervical spine surgery; acute or chronic neck pain; and any contraindication to MR imaging. The mean age of the subjects was 30.3 years (range, 26–34 years). There were 6 male and 4 female subjects. Informed consent was obtained from all subjects for a noncontrast MR imaging of the cervical spine.

### MR Imaging Evaluation

Each subject underwent 3T MR imaging (Magnetom Verio; Siemens, Erlangen, Germany) of the cervical spine by using a 6-element body surface coil and a 16-element table spine coil. Sequences were obtained in the following 4 neck positions: prone flexion, prone extension, supine flexion, and supine extension. In each position, a single high-resolution sagittal T2 sampling perfection with application-optimized contrasts by using different flip angle evolution (SPACE; Siemens) sequence was performed through the cervical spine by using isotropic voxels. The SPACE sequence involved the following imaging parameters: TE, 123 ms; TR, 1200 ms; flip angle, 125°; partition thickness, 0.9 mm; FOV, 280 × 280 mm; matrix size, 320 × 317; receiver bandwidth, 744 Hz; parallel imaging factor, 2; 2 excitations. Each sequence was performed with the patient in the maximum amount of neck flexion or extension that could be maintained for the entire scan to



**FIG 1.** Sagittal T2 SPACE in the following neck positions: supine flexion (A) and prone extension (B).

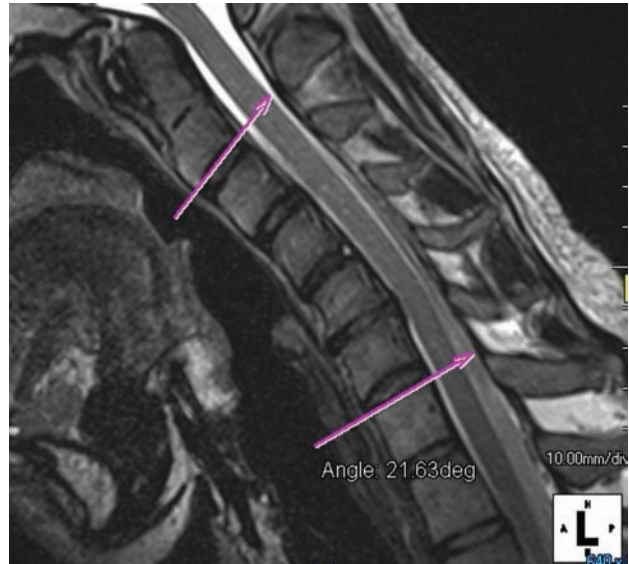


**FIG 2.** Sagittal T2 SPACE in the prone flexion position with angle measurements obtained from the lines drawn parallel to the inferior endplate of C2 and superior endplate of C7.

prevent motion (Fig 1). Scanning time was 5 minutes 18 seconds for each position.

### Image Analysis

All measurements were made on a true midline sagittal image of the cervical spine. The midline image was determined via 3D manipulation of the isotropic data on a separate workstation (AquariusNET; TeraRecon, San Mateo, California). The angle of cervical spine flexion and extension, defined as the angle between a line drawn parallel to the inferior endplate of C2 and a second line drawn parallel to the superior endplate of C7, was measured in each patient (Fig 2). The posterior thecal sac anteroposterior distance was measured in each subject with each neck position. These measurements were obtained by drawing a line from the dorsal spinal cord to the posterior wall of the spinal canal midway between the C1 and C2 spinous processes (Fig 3).

### Statistical Analysis

Measurements within patients were not considered independent. Therefore, we used a repeated measures ANOVA, assuming a covariance structure of compound symmetry among the 4 different positions. Each position was treated as a fixed effect and com-



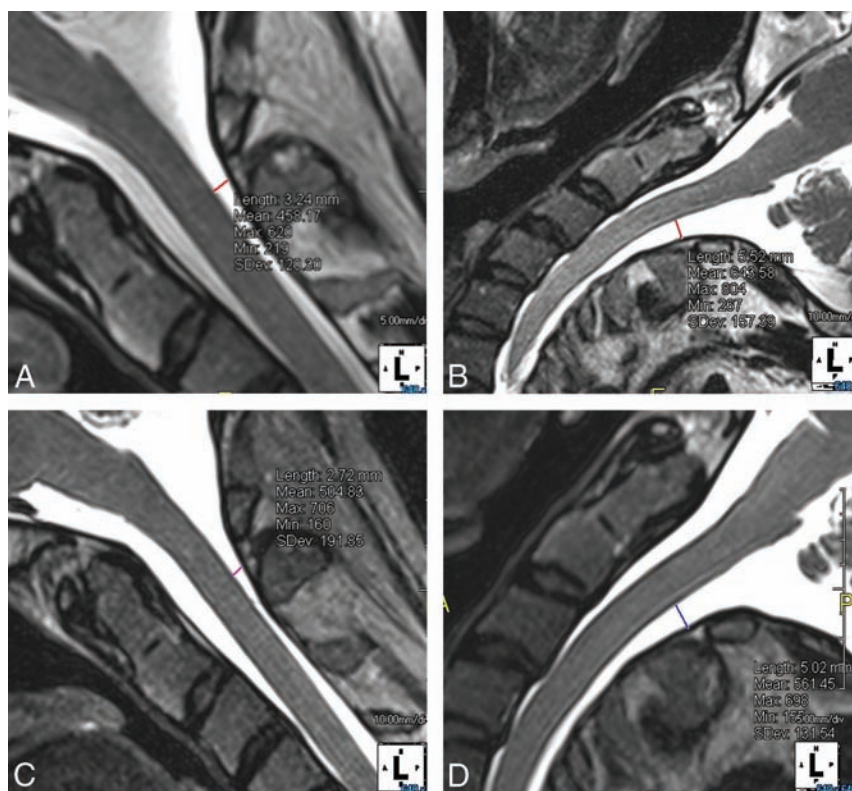


**FIG 3.** Anteroposterior measurements of the posterior C1–C2 thecal sac obtained off reformat-  
ted true midline images of the sagittal T2 SPACE in the same patient in prone flexion (A), prone  
extension (B), supine flexion (C), and supine extension (D).

#### Statistical analysis of C1–C2 posterior thecal sac measurements in various neck positions

Position	Analysis Variable: Distance (mm)					
	No.	Mean	Median	SD	Minimum	Maximum
Prone extension	10	5.00	4.69	1.29	3.19	7.16
Prone flexion	10	4.00	3.72	1.12	2.42	6.21
Supine extension	10	4.76	4.85	1.23	3.03	7.03
Supine flexion	10	3.62	3.18	1.25	1.56	5.56

pared with each of the other 3 positions. Correlative analysis of neck angle values and thecal sac size was also performed. A  $P$  value  $< .01$  was considered statistically significant. Analysis was performed by using SAS 9.3 software (SAS Institute, Cary, North Carolina).

#### RESULTS

The mean angle of extension was  $37.3^\circ$  for the supine and  $39.8^\circ$  for the prone position. The mean angle of flexion was  $28.6^\circ$  for the supine and  $28.8^\circ$  for the prone position. The mean anteroposterior dimensions of the posterior thecal sac at the C1–C2 level were as follows:  $4.00 \pm 1.12$  mm for prone flexion,  $5.00 \pm 1.29$  mm for prone extension,  $3.62 \pm 1.25$  mm for supine flexion, and  $4.76 \pm 1.23$  mm for supine extension (Table). There was a statistically significant difference in distances measured at different positions at  $P < .01$ .

The posterior thecal sac size for each position was held as a fixed variable and then compared with the measurements in each of the other 3 positions. Comparing with prone flexion, we calculated the following  $P$  values: prone extension at  $P = .0003$ , supine

extension at  $P = .004$ , and supine flexion at  $P = .128$ . Comparing with prone extension, we calculated the following  $P$  values: supine flexion at  $P = .0001$  and supine extension at  $P = .342$ . Compared with supine flexion, supine extension demonstrated  $P = .0001$ . In summary, statistically significant differences ( $P < .01$ ) were found between prone flexion and prone extension, prone flexion and supine extension, prone extension and supine flexion, and supine flexion and supine extension. Three of these significant correlations met even highly rigorous significance criteria at  $P < .0001$  (prone flexion versus prone extension; prone extension versus supine flexion; and supine flexion versus supine extension).

Additional correlative analysis between the distance and neck angle at each position resulted in the following  $P$  values: prone flexion at .963, prone extension at .983, supine flexion at .290, and supine extension at .257. There was no significant association between distance and neck angle at any position.

Overall results demonstrate that the posterior thecal sac is larger with the extension position compared with flexion but that there is no significant difference in the posterior thecal sac size between prone and supine imaging.

#### DISCUSSION

Cervical puncture is a very effective approach for CSF sampling and instillation of intrathecal contrast for myelography. Although lumbar puncture is often used for these purposes, myriad indications would warrant C1–C2 puncture into the thecal sac. These mostly include limited or contraindicated access at the level of the lumbar spine due to extensive bony fusion, epidural abscess, spondylosis, and so forth. Additionally one may prefer to inject intrathecal contrast into the cervical thecal sac for cervical myelography due to the advantages, such as less contrast dilution and better control of contrast to prevent intracranial spill.

The use of cervical puncture seems to be waning possibly due to growing inexperience with the technique and concern for the associated risks, mainly involving cervical cord injury. However, in 2009, Yousem et al<sup>1</sup> provided a discussion about the relevance of cervical puncture with regard to the current standard of practice and found that there are still reasonable indications for cervical puncture and that the complication rate is low when performed by experienced neuroradiologists. Additionally, a 2008 study of cervical myelography at 1 large center revealed that the authors' major approach was cervical puncture at a ratio of 6:1, with a slightly higher prevalence of documented minor adverse reactions over lumbar puncture.<sup>10</sup>

Complications of cervical puncture include the potential for



spinal cord puncture and injection of contrast into the cord parenchyma.<sup>11-13</sup> Another concern, albeit less common, is injury to nearby cervical nerves and major arteries such as the vertebral or posterior inferior cerebellar arteries, resulting in symptoms related to cord, brain stem, and brain infarcts. There are also case reports of spinal hematoma leading to a variety of complications, including cord compression and death.<sup>14-16</sup>

Cervical puncture can be performed with the neck flexed or extended and in either the prone or supine position. Standard positioning of the patient for cervical puncture involves placing the patient's neck in a prone extended position. In this study, we evaluated the anteroposterior size of the posterior cervical thecal sac in various neck positions to determine which yields the largest CSF space for access, theoretically decreasing the risk of cord injury. To our knowledge, there are no prior studies that measure the size of the posterior upper cervical thecal sac in these various positions. Orrison et al<sup>8</sup> performed a postmortem study and found that the average posterior thecal sac size at C1–C2 in the neutral position was 4.3 mm, in a range similar to that of measurements obtained in our study. Most interesting, Orrison et al also showed up to 1 cm of tenting of the dura ahead of the needle in cervical puncture before CSF was seen in the hub.

We used high-resolution 3D T2 SPACE MR imaging to reformat the data and determine the most accurate midline position of the spinal canal. This sequence has been reported by others to be of high quality and clinically acceptable for imaging of the spine and spinal canal.<sup>17,18</sup> Our measurement and analysis of healthy volunteers by using MR imaging of the cervical spine demonstrates that the posterior cervical subarachnoid space is approximately 25% larger with neck extension than with neck flexion. This result is independent of prone or supine positioning.

Prior studies have shown that the upper cervical levels from C2 to C4 (starting at the inferior edge of C2) demonstrate increases in the ventral subarachnoid space and decreases in the dorsal subarachnoid space on neck extension. Our measurements were obtained at the mid-C2 level (above the levels discussed in prior reports); in all subjects in both the prone and supine positions, the reverse was observed with decreases in the ventral subarachnoid space and increases in the dorsal space. On the basis of our evaluation of the images obtained in all of our subjects in the various positions, we postulate that the dynamics above the inferior margin of C2 vary from that observed in the remainder of the cervical spine. We theorize that the cervicomedullary cord remains in a relatively stable position between the flexed and extended positions in comparison with the bony spine and it is the upper cervical vertebral bodies that move closer to the anterior cord in extension, in effect widening the posterior thecal sac.

Although the study was limited by the small number of subjects, most of the differences between extension and flexion were highly statistically significant, meeting even the stringent criteria of  $P < .0001$ . A larger number of subjects would be required to see if the lack of a significant difference between the prone and supine position was due to a true lack of difference or the limited power of the study. Another possible limitation included small inconsistencies in placing calipers during measurements, given the relatively small size of the posterior thecal sac and mild motion artifacts. Additionally, we did not consider sex or height analyses,

mainly due to the number of subjects in the study, and this analysis may be a topic of interest in future studies.

Some may argue that the homogeneous, young, healthy nature of our subject group does not reflect that seen on a clinical basis. The strongest indications for cervical puncture in our institution are for CSF sampling and myelography in patients in whom lumbar puncture is not possible for reasons such as extensive lumbar bony fusion or lumbar epidural abscess. These indications occur in patients young and old, with or without cervical spondylosis. As such, our study population included healthy young volunteers to determine the effect of flexion and extension without other confounding factors.

We think that the increase in posterior thecal sac size in the extended neck position theoretically decreases the risk of the needle coming in contact with the spinal cord during cervical puncture. However, prolonged neck extension may be difficult in a subset of patients who have significant cervical disease. In cases in which prone positioning of the patient may not be possible due to anatomic limitations, medical conditions, and safety concerns, it is important to know that supine positioning does not have a significant impact on the space available for needle placement. This is of great importance in patients with cervical disease who may have problems with prone-versus-supine positioning.

Future studies could be performed including more subjects to increase the power of the analysis and possibly including patients who have clinical indications for cervical puncture to see if this patient population has results similar to those in healthy subjects.

## CONCLUSIONS

The posterior cervical thecal sac at C1–C2 is larger in extension than flexion, suggesting that extension is the ideal position for cervical puncture for CSF sampling or cervical myelography. There is no difference in posterior cervical thecal sac size in prone-versus-supine positioning.

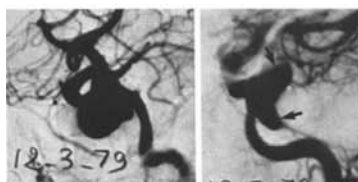
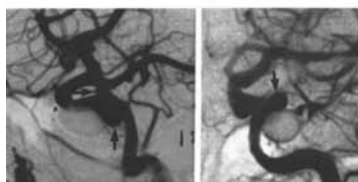
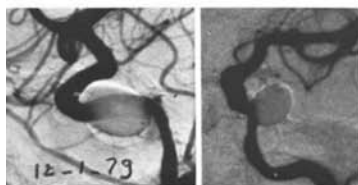
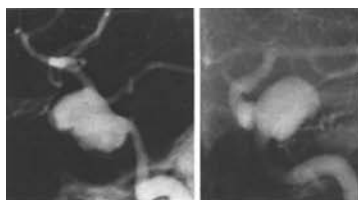
## REFERENCES

1. Yousem DM, Gujar SK. **Are C1–2 punctures for routine cervical myelography below the standard of care?** *AJNR Am J Neuroradiol* 2009;30:1360–63 CrossRef Medline
2. Robertson HJ, Smith RD. **Cervical myelography: survey of modes of practice and major complications.** *Radiology* 1990;174:79–83 CrossRef Medline
3. Orrison WW, Eldevik OP, Sackett JF. **Lateral C1–2 puncture for cervical myelography, part III: historical, anatomic, and technical considerations.** *Radiology* 1983;146:401–08 CrossRef Medline
4. ACR-ASNR-SPR practice parameter for the performance of myelography and cisternography. Updated 2014. <http://www.acr.org/~media/ACR/Documents/PGTS/guidelines/Myelography.pdf>. Accessed October 9, 2015
5. Muhle C, Wiskirchen J, Weinert D, et al. **Biomechanical aspects of the subarachnoid space and cervical cord in healthy individuals examined with kinematic magnetic resonance imaging.** *Spine (Phila Pa 1976)* 1998;23:556–67 CrossRef Medline
6. Muhle C, Metzner J, Weinert D, et al. **Classification system based on kinematic MR imaging in cervical spondylitic myelopathy.** *AJNR Am J Neuroradiol* 1998;19:1763–71 Medline
7. Bartlett RJ, Hill CA, Rigby AS, et al. **MRI of the cervical spine with neck extension: is it useful?** *Br J Radiol* 2012;85:1044–51 CrossRef Medline
8. Orrison WW, Sackett JF, Amundsen P. **Lateral C1–2 puncture for**

- cervical myelography, part II: recognition of improper injection of contrast material. *Radiology* 1983;146:395–400 CrossRef Medline
9. Ulbrich EJ, Schraner C, Boesch C, et al. Normative MR cervical spinal canal dimensions. *Radiology* 2014;271:172–82 CrossRef Medline
  10. Chin KR, Eiszner JR, Huang JL, et al. Myelographic evaluation of cervical spondylosis: patient tolerance and complications. *J Spinal Disord Tech* 2008;21:334–37 CrossRef Medline
  11. Johansen JG, Orrison WW, Amundsen P. Lateral C1–2 puncture for cervical myelography, part I: report of a complication. *Radiology* 1983;146:391–93 CrossRef Medline
  12. Nakstad PH, Kjartansson O. Accidental spinal cord injection of contrast material during cervical myelography with lateral C1–C2 puncture. *AJNR Am J Neuroradiol* 1988;9:410 Medline
  13. Servo A, Laasonen EM. Accidental introduction of contrast medium into the cervical spinal cord: a case report. *Neuroradiology* 1985;27:80–82 CrossRef Medline
  14. Rogers LA. Acute subdural hematoma and death following lateral cervical spinal puncture: case report. *J Neurosurg* 1983;58:284–86 CrossRef Medline
  15. Abba AA, Rothfus WE, Maroon JC, et al. Delayed spinal subarachnoid hematoma: a rare complication of C1–C2 cervical myelography. *AJNR Am J Neuroradiol* 1986;7:526–28 Medline
  16. Mapstone TB, Rekate HL, Shurin SB. Quadriplegia secondary to hematoma after lateral C-1, C-2 puncture in a leukemic child. *Neurosurgery* 1983;12:230–31 CrossRef Medline
  17. Lighvani AA, Melhem ER. Advances in high-field MR imaging of the spine. *Appl Radiol* 2009;38:18–27
  18. Meindl T, Wirth S, Weckbach S, et al. Magnetic resonance imaging of the cervical spine: comparison of 2D T2-weighted turbo spin echo, 2D T2\*-weighted gradient-recalled echo and 3D T2-weighted variable flip-angle turbo spin echo sequences. *Eur Radiol* 2009;19:713–21 CrossRef Medline

## Celebrating 35 Years of the AJNR

March 1981 edition



AJNR 2:167-173, March-April 1981  
0190-6106/81/0023-0167\$03.00  
© American Roentgen Ray Society

### Giant Unclippable Aneurysms: Treatment with Detachable Balloons

Nine cases of giant unclippable aneurysms treated with the detachable balloon technique are reported. Adjunctive surgical bypass procedures and arterial ligation were also carried out in four and one cases, respectively. All the patients tolerated occlusion of the carotid artery (eight cases) or of both vertebral arteries (one case). Three patients developed neurologic complications: two transient and one permanent (blindness in one eye). The complications occurred when attempts were made to occlude the aneurysm lumen only to preserve the carotid blood flow. Permanent occlusion of the carotid artery appears safer than aneurysm obliteration. Surgical procedures are necessary if the patient does not tolerate permanent occlusion of the artery or if occlusion of the artery is insufficient to obtain thrombosis of the aneurysm.

Some cavernous carotid artery aneurysms, giant ophthalmic artery aneurysms, giant aneurysms of the bifurcation of the internal carotid artery, and certain giant basilar artery aneurysms cannot be surgically clipped. Occlusion of the internal carotid artery by ligation or by a Silverstone clamp may produce thrombosis of such unclippable carotid aneurysms [1]. However, it may be easier to occlude the carotid artery with a detachable balloon positioned close to the neck of the aneurysm. The ideal would be to occlude the aneurysm itself with a detachable balloon while preserving the arterial blood flow. We report our experience with nine cases of unclippable giant aneurysms that were successfully treated with the detachable balloon technique. Five patients had adjunctive surgical procedures. This technique was first used by Gertsenko [2] and subsequently by one of us [3].

#### Materials and Methods

The nine patients are summarized in table 1. They were 12-56 years old (average, 34 years). There were six females and three males. Four aneurysms originated from the cavernous carotid artery, two from the ophthalmic artery, two were bifurcation carotid aneurysms, and one was a preprotonic basilar aneurysm according to the classifications of both Drake [1] and Pia [4].

The symptoms were classical. With cavernous carotid artery aneurysms were oculomotor nerve palsies or severe retroorbital pain. With one of the supraclinoid carotid aneurysms was progressive loss of vision. The two other carotid bifurcation aneurysms and the basilar aneurysm had subarachnoid hemorrhages. One ophthalmic aneurysm was unusual, with transient ischemic attacks and a small internal capsule infarct.

All procedures and angiographic examinations were carried out by the transarterial arterial route. The detachable balloon techniques used were described in a previous publication [3]. The balloons were attached to Teflon catheters with elastic ligatures and detached using a second, coaxial polyethylene catheter. Balloon size was 0.5-2.0 ml. The level of the carotid siphons was easily reached with the Teflon catheters.

Charles E. Seibert<sup>1</sup>  
James N. Dreisbach<sup>1</sup>  
Wendell B. Swanson<sup>2</sup>  
Robert E. Edgar<sup>3</sup>  
Paul Williams<sup>3</sup>  
Harry Hahn<sup>3</sup>

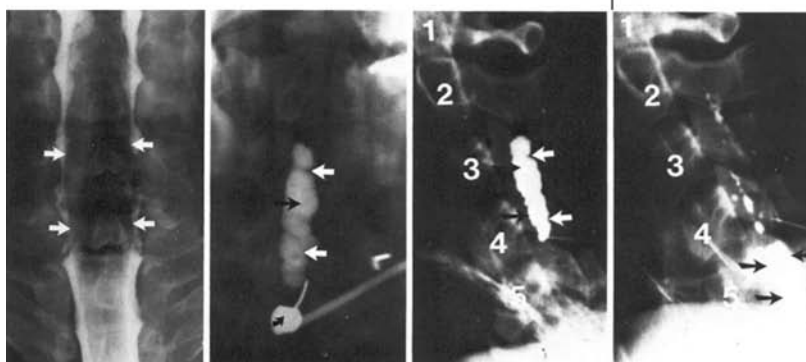
### Progressive Posttraumatic Cystic Myelopathy: Neuroradiologic Evaluation

The neuroradiologic evaluation and findings in 25 symptomatic patients with surgically proven progressive posttraumatic cystic myelopathy are reviewed. To follow patients with spinal cord injury, neuroradiologic algorithms were developed to confirm and define cystic myelopathy. The algorithm used in the early and mid 1970s relied on the myelographic demonstration of a large cord for suspicion of a cyst. Review of this material found that in progressively symptomatic patients 14 of 25 proven cysts were in large cords. A more recent algorithm used computed tomographic metrizamide myelography. In nine of 11 patients studied in this fashion, the cyst filled with contrast material 2-4 hr after injection, yet it did not communicate with the subarachnoid space at subsequent surgery. The origin of the cyst fluid and mechanism of cyst demonstration with metrizamide may be associated with transneuronal migration of fluid. This condition must be clinically suspected and radiologically confirmed for surgical treatment (cyst-shunt procedure) if neurologic preservation of function is to be maintained.

Progressive posttraumatic cystic myelopathy is an uncommon, but well documented complication of spinal cord injury. In a 1973 monograph, Barnett and Jousse [1] reviewed their findings in 17 cases and reported an additional 56 cases from the literature, but there has been little reference to this condition in neuroradiologic literature. Barnett and Jousse [1] reported that the posttraumatic cysts in their series did not communicate with subarachnoid space, central canal, or fourth ventricle, and that patients with this disorder may have progressive ascent of their level of loss of residual neurologic function. Recently, Edgar [2] described a shunt procedure for the cyst that was successful in arresting this progression. Technical advances in neuroradiologic evaluation methods, that is, the availability of both water-soluble contrast material for myelography and computed tomography (CT), have changed the workup of clinically suspected patients. Our review was designed to tabulate the neuroradiologic findings in a series of patients with posttraumatic myelopathy from Craig Hospital and Swedish Medical Center in Englewood, Colo., and to record a new unexplained observation: that the posttraumatic cyst fills with contrast material at metrizamide CT.

#### Materials and Methods

Craig Hospital admits about 350 new patients with spinal cord injury each year and about 500 more for follow-up evaluation. Neuroradiologic studies in 25 patients with surgically proven posttraumatic cystic myelopathy were reviewed. All 25 patients had symptoms and signs of progressive posttraumatic cystic myelopathy that prompted their evaluation and subsequent treatment. All were operated on by one of the authors (R. E. E.) with a technique described elsewhere consisting of a cyst shunting procedure [2]. Neuroradiologic studies reviewed included spine radiography, tomography, myelography with air or positive contrast agents (Pantopaque or metrizamide), CT of the spine with or without metrizamide, diagnostic percutaneous cyst punctures, and cystography with positive contrast injection (Pantopaque). Air myelography by a cervical approach was used in patients in whom a total block



## Re: The Benefits of High Relaxivity for Brain Tumor Imaging: Results of a Multicenter Intraindividual Crossover Comparison of Gadobenate Dimeglumine with Gadoterate Meglumine (The BENEFIT Study)



We have read with interest the publication by Vaneckova et al<sup>1</sup> reporting the results of a clinical study that assessed the diagnostic performances of 2 gadolinium-based contrast agents (GBCAs) used for brain tumor imaging. The authors performed a multicentric, prospective, randomized, intraindividual, crossover, 2-arm study. The objective of Arm 1 was to demonstrate the superiority of a full dose (0.1 mmol/kg) of gadobenate dimeglumine over the same dose of gadoterate meglumine, whereas in Arm 2, the aim was to ascertain whether a half dose (0.05 mmol/kg) of gadobenate provides diagnostic information similar to that of a full dose of gadoterate. GBCA administrations and image analyses were performed in a blinded manner. The primary end point was the overall diagnostic preference of the readers for one GBCA over the other. In Arm 1, a significant superiority was shown in favor of gadobenate, and in Arm 2, no significant differences could be found between the 2 GBCAs. The authors concluded that when administered at the approved dose of 0.1 mmol/kg, gadobenate is superior to gadoterate for qualitative and quantitative assessment of brain lesions, and that a half dose of the former agent is equivalent to a full dose of the latter. However, we consider that some biases limit the interpretation of the results and even lead to wrong assertions.

First, the statistical analysis was not adapted to the objectives of the study. To compute the sample size in each arm, the authors assumed that no difference in overall diagnosis preference would be found between the 2 GBCAs in half of the patients. In the other half, they hypothesized that the preference would be in favor of gadobenate in 80% of the patients who received the full dose (Arm 1) and in 75% of those who received the half dose (Arm 2). Then they applied the Wilcoxon signed rank test to demonstrate the superiority of gadobenate in both arms. The results showed a significant preference for this GBCA in Arm 1 but not in Arm 2. However, in Arm 1, the agreement among the 3 readers reached only 50.8%, with a  $\kappa$  value of 0.273. According to Landis and Koch,<sup>2</sup> this is

a moderate level of agreement, and it casts some doubt on the robustness of the interpretations. The second arm was clearly not designed as an equivalence or a noninferiority trial, as defined in the “Consolidated Standards of Reporting Trials” statement,<sup>3</sup> and failure to show a difference should not have been interpreted as an equivalence between both GBCAs. Therefore, when the authors concluded that “a half dose of gadobenate (0.05 mmol/kg body weight) is equivalent to a full dose (0.1 mmol/kg body weight) of gadoterate,”<sup>1</sup> they obviously made a biased interpretation of the results. The comparison in Arm 2 simply failed because the hypothesis of superiority was not met.

Second, the number of lesions subjected to signal intensity measurements with the T1-weighted gradient-echo (T1GRE) sequence differed from that of the T1-weighted spin-echo (T1SE) sequence. Most surprising, fewer lesions were considered with the T1GRE sequence, though they were all larger than 5 mm: In Arm 1, 63, 66, and 54 lesions were assessed by readers 1, 2, and 3 in T1SE and 60, 61, and 51 lesions in T1GRE; in Arm 2, 84, 89, and 78 lesions were assessed in T1SE and 82, 85, and 75 lesions in T1GRE. This discrepancy between sequences may have created a bias in the analysis of the images. As both GBCAs assessed the same number of lesions, it is likely that the choice of sequence is more important than differences in relaxivity between GBCAs.

In conclusion, the design of this multicenter randomized clinical trial had some important weaknesses that affected the comparability between the 2 GBCAs. Some of the conclusions are not supported by the results, especially the assumed equivalence of the half dose of gadobenate. As for the full dose, the low inter-reader agreement shows the variability of the interpretation of a qualitative end point such as the diagnostic preference of one GBCA over another. More important is the clinical impact of the diagnosis on patient management. Unfortunately, this end point was not assessed in the present study.

Indicates open access to non-subscribers at [www.ajnr.org](http://dx.doi.org/10.3174/ajnr.A4646)  
<http://dx.doi.org/10.3174/ajnr.A4646>

Conflict of interest: The authors of this letter declare that they currently have a conflict of interest because they are employed by Guerbet.



## REFERENCES

1. Vaneckova M, Herman M, Smith MP, et al. **The benefits of high relaxivity for brain tumor imaging: results of a multicenter intraindividual crossover comparison of gadobenate dimeglumine with gadoterate meglumine (the BENEFIT study).** *AJNR Am J Neuroradiol* 2015;36:1589–98 CrossRef Medline
2. Landis JR, Koch GG. **The measurement of observer agreement for categorical data.** *Biometrics* 1977;33:159–74 CrossRef Medline
3. Piaggio G1, Elbourne DR, Pocock SJ, et al. **Reporting of noninferiority and equivalence randomized trials: extension of the CONSORT 2010 Statement.** *JAMA* 2012;308:2594–604 CrossRef Medline

✉ E. Lancelot

✉ B. Piednoir

✉ P. Desché

Guerbet

Roissy CdG Cedex, France

## REPLY:

We thank Drs Lancelot, Piednoir, and Desché for their interest in our work and their comments regarding our recent article.<sup>1</sup> However, we disagree strongly with the critique presented in their letter. The necessity to comply with word count limitations when preparing manuscripts for publication means that the description of the statistical methodology is often too brief. We now address the points raised.

### Statistical Analysis and Sample Size

The study design and analysis described in our article<sup>1</sup> are similar to the methodology used in many previous intraindividual comparative studies.<sup>2-9</sup> The primary study end point was the overall diagnostic preference of each of 3 readers for one gadolinium-based contrast agent (GBCA) over the other. Other qualitative end points (determinations of lesion border delineation, definition of disease extent, visualization of lesion internal morphology, and lesion contrast enhancement) are accepted clinically relevant parameters that can directly impact patient management decisions and surgical planning, particularly for patients with glial tumors in whom macroscopically complete surgical removal is associated with improved prognosis and longer patient survival, and those with metastases, for whom determination of the precise number, size, and location of lesions can aid selection of the most appropriate treatment option.<sup>3,6-9</sup> Image assessment was performed by comparing images from the 2 MR imaging examinations side-by-side, with the readers blinded to the contrast agent used and all clinical information. Each reader expressed preference for examination 1 or 2 or determined that the 2 examinations were equal. The resulting data for each reader were 1 observation per patient (ie, 1 paired sample datum with an ordinal scale). Nonparametric analysis with a 2-sided Wilcoxon signed rank test is the appropriate statistical analysis method for assessment of overall diagnostic preference. The distribution of the preference between the 2 examinations was also tested by using a 1-sample  $\chi^2$  test for equal proportions. The results obtained were similar to those from the Wilcoxon signed rank test. This analysis was not included in the article due to the word restrictions.

The results for Study Arm 1 revealed a highly significant ( $P < .0001$ ) preference for gadobenate over gadoterate at an equivalent dose for each reader (Fig 1). Variation of measurements between readers is expected in a fully blinded read setting. Figure 1 shows that all 3 readers were in high agreement and consistent, especially concerning the very few assessments in which gadoterate was preferred over gadobenate (1.6%–3.2% of patients across 3 readers). The major reason for the 50.8% agreement among readers was the differential percentage of preferences for gadobenate across the 3 readers (49.2%, 82.3%, 69.4%). As already discussed in our article,<sup>1</sup> a  $\kappa$  value of 0.273 was due to the skewed distribution of preferences (very few preferences for gadoterate). Feinstein et al<sup>10</sup> demonstrated clearly that a low  $\kappa$  can result from a substantial imbalance in marginal totals.

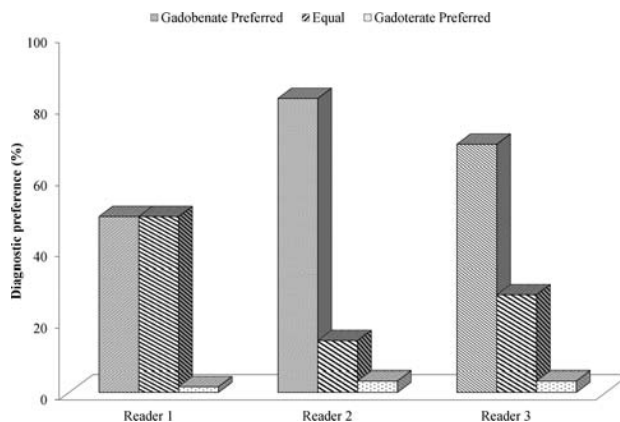


**FIG 1.** Distribution of overall diagnostic preference: gadobenate 0.1 mmol/kg versus gadoterate 0.1 mmol/kg.

The results for Study Arm 2 revealed no statistically significant differences between gadoterate at 0.1 mmol/kg and gadobenate at 0.05 mmol/kg of body weight.<sup>1</sup> In the abstract, we concluded, “No meaningful differences were recorded between 0.05 mmol/kg gadobenate and 0.1 mmol/kg gadoterate.” We understand from a statistical point of view that equivalence cannot be claimed if the test hypothesis is not prospectively defined as “noninferiority.” However, a conclusion of “no statistically significant difference” between treatments simply means that the evidence that the 2 treatments lead to different outcomes is not strong enough. As can readily be seen in Fig 2, all 3 readers determined that the images from most patients were diagnostically equal (ie, no diagnostic preference between the images with half-dose gadobenate and full-dose gadoterate).

The sample size calculation was based on the  $\chi^2$  test of specified proportions in 3 categories for paired 1-sample responses. Assumptions for the study were as follows: for Study Arm 1, an “equal” response for 50% of the patients and a ratio of superiority of either contrast agent of 4:1, with an effect size of 0.18; and for study Arm 2, an “equal” response for 50% of the patients and a ratio of superiority of either contrast agent of 3:1, with an effect size of 0.125. The sample size assumption should be based on the full distribution of the study population for the paired 1-sample data with the ordinal scale and cannot be divided in half; in addition, the hypothesis test was 2-sided and did not assume “that the preference would be in favor of gadobenate in 80% of the patients who received the full dose (Arm 1) and in 75% of those who received the half dose (Arm 2)” as stated in the comment/letter.

In summary, we believe that the statistical methods were correctly applied in line with the study objectives. The power determination and sample size consideration correctly reflected the primary analysis; the assumptions were evidence-based and reflected the information available from previous clinical trials with identical designs.<sup>6,8,9</sup>

### Quantitative Data

The methodology adopted for quantitative evaluation has been validated in several prior comparative studies of this type,<sup>5-9</sup> and there are absolutely no surprising or biased results.

Quantitative contrast parameters are an excellent metric for

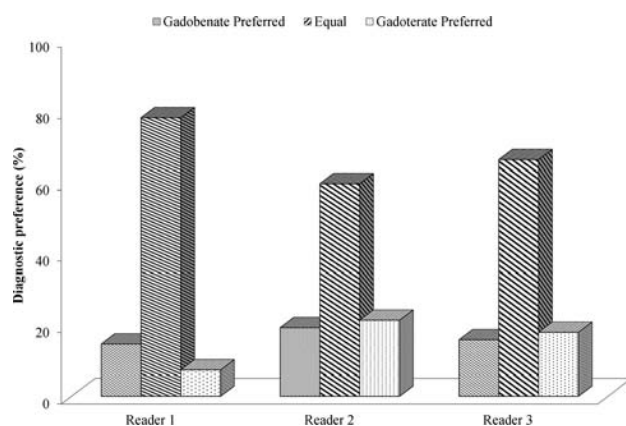


**FIG 2.** Distribution of overall diagnostic preference: gadobenate 0.05 mmol/kg versus gadoterate 0.1 mmol/kg.

lesion detection, which is certainly sequence-dependent. However, within-sequence inpatient intralesion analyses were performed in this study, which eliminated any possible opportunity for biased interpretation. Criteria for measurement and selection of lesions to measure were common across readers. Moreover, training sessions were conducted with each blinded reader before the assessment of study images to ensure a consistent approach to image assessment. To standardize the size and placement of ROIs within a subject, ROIs were positioned in a paired fashion on predose T1-weighted spin-echo (SE) images and the corresponding postdose T1-weighted SE images of both examinations 1 and 2. Round or elliptic ROIs were placed on the image frame, which provided the best visualization of the lesions. ROIs were as large as possible but included only homogeneous areas. The same lesions were measured on predose and postdose T1-weighted SE/fast SE sequences for both examinations 1 and 2. This same procedure was used for the placement of ROIs on T1-weighted gradient recalled-echo (GRE) images. ROIs of the same shape and size were used for the individual measurements (lesion, normal parenchyma, and background noise) on each sequence type. For patients with multiple lesions, a maximum of 3 lesions that met the measurability criteria (ie, a homogeneous enhancing area of  $>5$  mm, not having just very subtle rim enhancement, not being totally hemorrhagic, and not needing ROIs of  $<5$  mm<sup>2</sup>) were considered.

Most important, in light of the issue raised by Drs Lancelot, Piednoir, and Desché, each reader individually chose the total number of lesions to be measured in a patient with multiple lesions. This approach created situations in which one reader might have measured 3 lesions while the others measured only 1 or 2 in the same patient. Likewise, readers were free to measure different numbers of lesions across different sequence types (T1-weighted SE or T1-weighted GRE). In crossover studies of this type, the intraindividual comparison (ie, the comparison within the reader of the same lesions on the same sequence type) is important. Therefore, the minimal differences in the number of lesions on the 2 different T1-weighted sequences (from 2 to 5, depending on the reader) do not bias or influence the results of the study because the analysis was performed by sequence type. Quantitative findings confirmed the predictable superiority of gadobenate at the same dose of 0.1 mmol/kg of body weight and the lack of any

meaningful difference for half-dose gadobenate compared with full-dose gadoterate. In addition to confirming the results of previous large scale intraindividual comparative studies,<sup>6-9</sup> these quantitative results demonstrate once again the value of relaxivity as the only contributor to this specific outcome. The importance of relaxivity and the outcomes of previous trials that have compared gadobenate with other GBCAs<sup>6,8</sup> have been recognized by regulatory agencies in Europe in section 5.1 of the current Summary of Products Characteristics.<sup>11</sup>

While the study did not evaluate the impact of the diagnosis on patient management, such studies are extremely difficult to design because their interpretation presents the fundamental problem that the definition of accurate patient management based on either positive or negative test results may not be a single expected therapeutic choice and, more important, that a measured change in management does not necessarily translate into improved health outcomes. To date, there are no accepted guidelines for the design, reporting, and appraisal of patient-management studies.<sup>12</sup>

In conclusion, we believe that the design of this well-controlled clinical trial provides valuable information on the 2 GBCAs. First, it demonstrates that gadobenate is significantly superior to gadoterate for qualitative and quantitative enhancement of brain lesions when these agents are administered at an equivalent dose of 0.1 mmol/kg of body weight. This finding can be ascribed exclusively and unequivocally to the higher r1 relaxivity of gadobenate, which leads to superior contrast enhancement and significantly more clinically relevant morphologic information, which may be helpful for improved patient management and surgical planning. Second, it shows that there is no meaningful or relevant difference between a half dose of gadobenate and a full dose of gadoterate. The possibility of halving the amount of gadolinium administered is potentially extremely important for patients undergoing routine screening or follow-up examinations.

## REFERENCES

1. Vaneckova M, Herman M, Smith MP, et al. **The benefits of high relaxivity for brain tumor imaging: results of a multicenter intraindividual crossover comparison of gadobenate dimeglumine with gadoterate meglumine (The BENEFIT study).** *AJNR Am J Neuroradiol* 2015;36:1589–98 CrossRef Medline
2. Colosimo C, Knopp MV, Barreau X, et al. **A comparison of Gd-BOPTA and Gd-DOTA for contrast-enhanced MRI of intracranial tumors.** *Neuroradiology* 2004;46:655–65 Medline
3. Knopp MV, Runge VM, Essig M, et al. **Primary and secondary brain tumors at MR imaging: bicentric intraindividual crossover comparison of gadobenate dimeglumine and gadopentetate dimeglumine.** *Radiology* 2004;230:55–64 CrossRef Medline
4. Essig M, Tartaro A, Tartaglione T, et al. **Enhancing lesions of the brain: intraindividual crossover comparison of contrast enhancement after gadobenate dimeglumine versus established gadolinium comparators.** *Acad Radiol* 2006;13:744–51 CrossRef Medline
5. Rumboldt Z, Rowley HA, Steinberg F, et al. **Multicenter, double-blind, randomised, intraindividual crossover comparison of gadobenate dimeglumine and gadopentetate dimeglumine in MRI of brain tumors at 3 Tesla.** *J Magn Reson Imaging* 2009;29:760–67 CrossRef Medline
6. Maravilla KR, Maldjian JA, Schmalfuss IM, et al. **Contrast enhancement of central nervous system lesions: multicenter intraindividual**

- vidual crossover comparative study of two MR contrast agents. *Radiology* 2006;240:389–400 CrossRef Medline
7. Kuhn MJ, Picozzi P, Maldjian JA, et al. **Evaluation of intraaxial enhancing brain tumors on magnetic resonance imaging: intraindividual crossover comparison of gadobenate dimeglumine and gadopentetate dimeglumine for visualization and assessment, and implications for surgical intervention.** *J Neurosurg* 2007;106:557–66 CrossRef Medline
  8. Rowley HA, Scialfa G, Gao PY, et al. **Contrast-enhanced MR imaging of brain lesions: a large scale intraindividual crossover comparison of gadobenate dimeglumine versus gadodiamide.** *AJNR Am J Neuroradiol* 2008;29:1684–91 CrossRef Medline
  9. Seidl Z, Vymazal J, Mechl M, et al. **Does higher gadolinium concentration play a role in the morphologic assessment of brain tumors? Results of a multicenter intraindividual crossover comparison of gadobutrol versus gadobenate dimeglumine (the MERIT Study).** *AJNR Am J Neuroradiol* 2012;33:1050–58 CrossRef Medline
  10. Feinstein AR, Cicchetti DV. **High agreement but low kappa, I: the problems of two paradoxes.** *J Clin Epidemiol* 1990;43:543–49 CrossRef Medline
  11. MultiHance: Summary of Product Characteristics; last updated version December 4, 2015. Available at: <https://www.medicines.org.uk/emc/medicine/6132>. Accessed January 8, 2016
  12. Staub LP, Lord SJ, Simes RJ, et al. **Using patient management as a surrogate for patient health outcomes in diagnostic test evaluation.** *BMC Med Res Methodol* 2012;12:12 CrossRef Medline

**A. Spinazzi**

**G. Pirovano**

**N. Shen**

Global Medical and Regulatory Affairs

Bracco Diagnostics

Monroe, New Jersey

**M.A. Kirchin**

Global Medical and Regulatory Affairs

Bracco Imaging

Milan, Italy



## Cerebral Amyloid Angiopathy as an Etiology for Cortical Superficial Siderosis: An Unproven Hypothesis

We read with great interest a recent article by Inoue et al<sup>1</sup> on the diagnostic significance of cortical superficial siderosis (cSS) for Alzheimer disease in patients with cognitive impairment. The article focused on presymptomatic cases of cSS diagnosed by MR imaging.

The major finding of the article was that cSS was associated with a lobar location of microbleeds (MBs) and may be an initial radiologic finding of cerebral amyloid angiopathy (CAA) in patients with cognitive impairment. Lobar location includes both the cortical gray matter and the subcortical white matter. The imaging manifestations of hemosiderin deposition from cSS and MBs from CAA can be indistinguishable on gradient-echo T2-weighted images,<sup>2</sup> especially when MBs are seen on the surface of the cerebral cortex. There is even a suggestion that CAA can be an underlying cause of cSS.<sup>3</sup> In the current study, there was 72% correspondence between the location of cSS and that of MBs. The definition of cSS was only based on the shape of the signal abnormality on SWI (ie, linear). Because there are currently no widely recognized criteria to distinguish hemosiderin deposition from MBs on imaging, it may be helpful to show interobserver variability in the assignment of individual lesions to ensure agreement on the nature of the hypointensity seen on T2-weighted MR imaging.

Although its detection has increased with the advances in MR imaging technology, cSS is still a rare disease.<sup>4</sup> The most accepted hypothesis for its etiology has been chronic iron deposition in neuronal tissues associated with CSF.<sup>5</sup> Chronic bleeding into the subarachnoid space of the brain releases erythrocytes into the CSF. The chronic bleeding source can be a result of past brain surgery or CNS trauma.<sup>5</sup> Less common bleeding sources include CSF cavity lesions, tumors, vascular malformations, and so forth.<sup>4</sup> The authors stated that cSS related to previous symptomatic subarachnoid hemorrhage, traumatic subdural hematoma, or intracranial surgery was not included, but they did not provide infor-

mation on the number of patients excluded. According to the literature, the source of bleeding was never found in as many as half of all described cases.<sup>4</sup> Even for the 12 patients included in the analysis, it is possible that they still had an occult source of bleeding. Consequently, the relationship between cSS and CAA may be either overestimated or underestimated in the studied cohort, depending on how many patients were excluded due to a known bleeding source.

In conclusion, the pathogenesis of cSS from CAA is still an unproven hypothesis. An unidentified bleeding source may account for cSS in the studied cohort instead of CAA.

### REFERENCES

1. Inoue Y, Nakajima M, Uetani H, et al. **Diagnostic significance of cortical superficial siderosis for Alzheimer disease in patients with cognitive impairment.** *AJNR Am J Neuroradiol* 2015 Oct 8. [Epub ahead of print] CrossRef Medline
2. Kumar N. **Neuroimaging in superficial siderosis: an in-depth look.** *AJNR Am J Neuroradiol* 2010;31:5–14 CrossRef Medline
3. Linn J, Herms J, Dichgans M, et al. **Subarachnoid hemosiderosis and superficial cortical hemosiderosis in cerebral amyloid angiopathy.** *AJNR Am J Neuroradiol* 2008;29:184–86 CrossRef Medline
4. Fearnley JM, Stevens JM, Rudge P. **Superficial siderosis of the central nervous system.** *Brain* 1995;118:1051–66 CrossRef Medline
5. Kumar N. **Superficial siderosis: associations and therapeutic implications.** *Arch Neurol* 2007;64:491–96 CrossRef Medline

● H.X. Bai

Department of Radiology  
Hospital of the University of Pennsylvania  
Philadelphia, Pennsylvania

● H. Zhou

Department of Neurology  
Xiangya Hospital, Central South University  
Hunan, China

● X. Tan

● X. Huang

● L. Yang

Department of Neurology  
The Second Xiangya Hospital, Central South University  
Hunan, China

<http://dx.doi.org/10.3174/ajnr.A4652>

## REPLY:

We sincerely thank Harrison X. Bai and colleagues for their interest and comments regarding our recent article, in which we demonstrated the diagnostic significance of cortical superficial siderosis (cSS) for Alzheimer disease in patients with cognitive impairment.<sup>1</sup>

Regarding the methodologic issues of the present study that their letter raises, the diagnosis of cSS seen on susceptibility-weighted imaging was based on collegial discussion with experienced neuroradiologists, and no data are available for interobserver variability. We defined cSS as linear hypointensities on the surface of the cerebral gyri on SWI. The appearance of cSS on SWI was obvious in this study; fortunately, we had no difficulty in distinguishing cSS from lobar cerebral microbleeds (MBs). Very superficial clusters of multiple MBs can be mistaken for cSS, but these would be distinguished by their irregular appearance.<sup>2</sup>

In relation to exclusions, 4 patients with previous symptomatic subarachnoid hemorrhage, 23 patients with traumatic subdural hematoma, and 1 patient with an intracranial operation were excluded according to medical charts. We therefore presented 12 cases with cSS that did not seem to have occult sources of bleeding, as the authors pointed out.

We agree with their statement that elucidating the pathogenesis of cSS from cerebral amyloid angiopathy (CAA) warrants further analysis. However, imaging-histopathologic correlations

shown in cases with CAA might indicate that recurrent blood leakage of meningeal vessels leads to the propagation of cSS.<sup>3</sup> To confirm the progression of CAA-related cSS, prospective studies are needed that recruit patients with CAA based on the Boston criteria.<sup>4</sup>

## REFERENCES

1. Inoue Y, Nakajima M, Uetani H, et al. **Diagnostic significance of cortical superficial siderosis for Alzheimer disease in patients with cognitive impairment.** *AJNR Am J Neuroradiol* 2015 Oct 8. [Epub ahead of print] CrossRef Medline
2. Charidimou A, Linn J, Vernooij MW, et al. **Cortical superficial siderosis: detection and clinical significance in cerebral amyloid angiopathy and related conditions.** *Brain* 2015;138:2126–39 CrossRef Medline
3. Beitzke M, Enzinger C, Wünsch G, et al. **Contribution of convexal subarachnoid hemorrhage to disease progression in cerebral amyloid angiopathy.** *Stroke* 2015;46:1533–40 CrossRef Medline
4. Knudsen KA, Rosand J, Karluk D, et al. **Clinical diagnosis of cerebral amyloid angiopathy: validation of the Boston criteria.** *Neurology* 2001;56:537–39 CrossRef Medline

Y. Inoue

M. Nakajima

Department of Neurology

T. Hirai

Department of Diagnostic Radiology

Y. Ando

Department of Neurology

Graduate School of Medical Sciences

Kumamoto University

Kumamoto, Japan

<http://dx.doi.org/10.3174/ajnr.A4686>

## Hemorrhagic Pituitary Adenoma versus Rathke Cleft Cyst: A Frequent Dilemma

I read with interest the article of Park et al<sup>1</sup> published in the October issue of the *American Journal of Neuroradiology*. Differentiation with MR imaging of a cystic or hemorrhagic pituitary adenoma from a Rathke cleft cyst (RCC) remains a common issue. In daily practice, this situation may be particularly confusing in a young woman with mild hyperprolactinemia whose symptoms are frequently hidden by taking contraceptive pills. Moreover, parallelism between the prolactin level and tumoral volume is missing in hemorrhagic microprolactinomas. Then, diagnosis of hemorrhagic microprolactinoma versus T1 hyperintense intrasellar mucoid RCC is challenging.

Park et al reported that the main differentiating features of pituitary adenomas are off-midline location, tilting of the pituitary stalk, fluid-fluid level, T2 hypointense hemosiderin rim, and septations, while Rathke cleft cysts are more likely located on the midline and frequently present with a T2 hypointense characteristic nodule.

Nevertheless, pituitary adenomas may be on the midline, for instance corticotroph adenomas. The fluid-fluid level is inconstant, particularly with fresh hemorrhage and a peripheral hemosiderin rim because of the absence of blood-brain barrier in the pituitary gland; septations are inconstant. On the other hand, Rathke cleft cysts may be, rarely, in an off-midline location, and their T2 hypointense waxy nodules are detected in no more than 70% of cases.

Moreover, the diagnostic tree model proposed by Park et al seems difficult to apply to the strictly intrasellar infracentimetric

lesions, which are more and more frequently seen with high-resolution 3T scanners, either discovered fortuitously or in the assessment of hyperprolactinemia.

Ancillary signs are then welcome to differentiate RCCs from cystic or hemorrhagic pituitary adenomas.

The axial T1-weighted sequence is optimal for making the diagnosis of such RCCs: Strict midline location, regular convex symmetric anterior surface, and close contact with the posterior lobe are characteristic features.<sup>2</sup>

Furthermore, while intrasellar pituitary adenomas, even tiny ones, give rise to mass effect, such as bulging of the sellar diaphragm and eroding of the bony contours of the sella, intrasellar RCCs of equal volume give rise to a less important mass effect or even to no mass effect, most probably because of intracystic low pressure, at least with an asymptomatic RCC (Fig 1).

This observation is helpful in the presence of the not-so-rare concomitant intrasellar pituitary adenoma and RCC, in which the soft RCC is deformed by the firmer pituitary adenoma, even if the latter is smaller (Fig 2).

### REFERENCES

1. Park M, Lee SK, Choi J, et al. **Differentiation between cystic pituitary adenomas and Rathke cleft cysts: a diagnostic model using MRI.** *AJNR Am J Neuroradiol* 2015;36:1866–73 CrossRef Medline
2. Bonneville JF, Bonneville F, Cattin F. **Magnetic resonance imaging of pituitary adenomas.** *Eur Radiol* 2005;15:543–48 CrossRef Medline

●J.-F. Bonneville

Department of Radiology and Endocrinology  
University Hospital of Liège, University of Liège  
Liège, Belgium

<http://dx.doi.org/10.3174/ajnr.A4653>

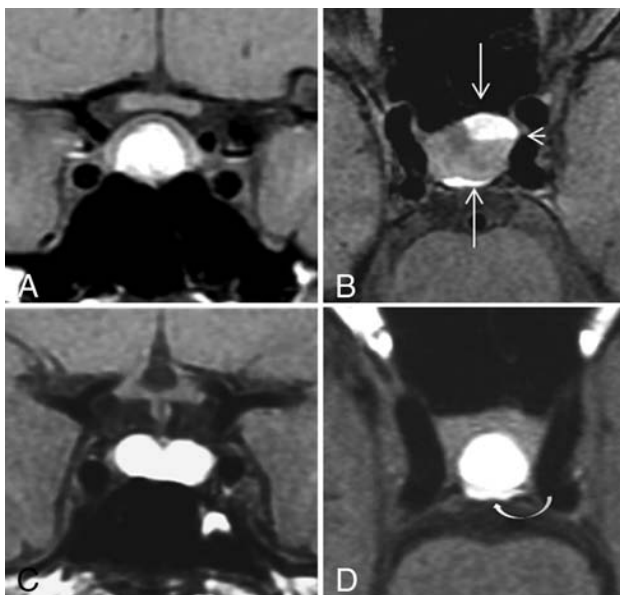


**FIG 1.** Hemorrhagic pituitary adenoma (A and B) versus mucoid RCC (C and D) on coronal and axial T1WI. This hemorrhagic pituitary adenoma (A and B) has fluid-fluid levels (*short arrow*) and mass effect on the sellar diaphragm, posterior lobe, and anterior wall of the sella (*long arrows*). In this RCC (C and D), note a mild imprint on the posterior lobe but no deformation of the sellar diaphragm or of the anterior wall.

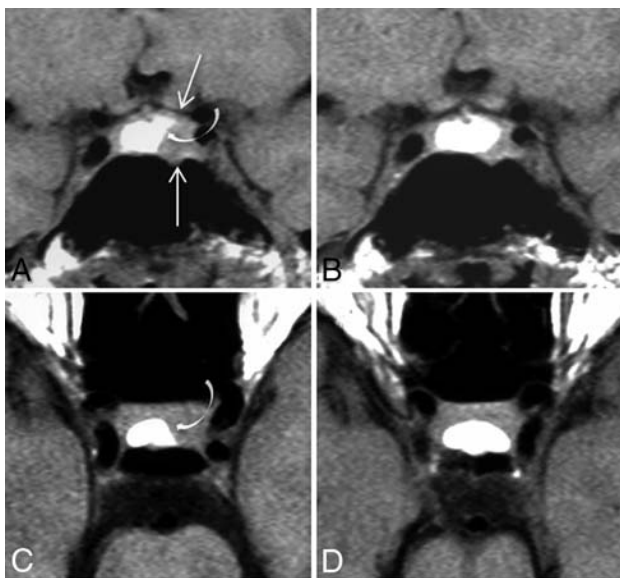


**FIG 2.** Concomitant pituitary adenoma and RCC. A and B, Coronal T1WI before and after cabergoline treatment. C and D, Corresponding axial T1WI. The T1 isointense pituitary microadenoma deforms the sellar floor, upraises the upper surface of the gland (*long arrows*), and imprints the lateral margin of a T1 hyperintense mucoid RCC (*curved arrow*). After treatment (B and D), shrinkage of the adenoma leads to a re-expansion of the RCC, whose pattern is pathognomonic in axial T1WI. D, Note again the absence of mass effect.



## REPLY:

We appreciate the comments from Jean-François Bonneville on our study entitled “Differentiation between Cystic Pituitary Adenomas and Rathke Cleft Cysts: A Diagnostic Model Using MRI.”<sup>1</sup> As Dr Bonneville mentioned, differentiating cystic or hemorrhagic adenoma and Rathke cleft cyst (RCC) is sometimes challenging, and preoperative differentiation of these conditions is important for treatment planning<sup>2-3</sup>; therefore, we suggested a diagnostic tree model for differentiating cystic pituitary adenoma from RCC by using preoperative MR imaging and reported an improved diagnostic accuracy when using the diagnostic tree model.<sup>1</sup>

We agree with Dr Bonneville that pituitary adenomas, especially corticotroph-secreting adenomas, may be on the midline as seen in Fig 5, and 16.7% of pituitary adenomas in our study were also located on the midline.<sup>1</sup> In addition, other imaging findings were seen with various frequencies: fluid-fluid levels in 68.5%, T2-hypointense rims in 75.9%, septations in 38.9% of pituitary adenomas, and intracystic nodules in 67.9% of RCCs. Therefore, we tried to develop a diagnostic tree model that included several imaging features because differential diagnoses are sometimes inconclusive with only 1 or 2 imaging findings. By applying the diagnostic tree model, we were also able to attain high diagnostic accuracy in the validation group (91.7%).<sup>1</sup>

Dr Bonneville also raised concerns about applying the diagnostic tree to subcentimeter lesions. In our study, we included cystic pituitary adenomas and RCCs that were confirmed histopathologically. Small asymptomatic RCCs showing typical imag-

ing features were not treated surgically; therefore, they were not included in our study. Although this omission can be considered a limitation of our study, we think that preoperative differentiation between cystic adenoma and RCC is important in patients who are considered for surgery due to hormonal or nonhormonal symptoms because different surgical procedures are required according to the different diagnoses. The diagnostic tree model may provide guidance to neurosurgeons for appropriate surgical planning.

We agree with Dr Bonneville that intrasellar pituitary adenoma can show mass effects such as a bulging sellar diaphragm and erosion of the body contours of the sella,<sup>4</sup> which we did not include in our diagnostic tree. Therefore, further studies that add these imaging features to the diagnostic tree model will be helpful in the differential diagnosis of cystic pituitary adenoma and RCC.

## REFERENCES

1. Park M, Lee SK, Choi J, et al. **Differentiation between cystic pituitary adenomas and Rathke cleft cysts: a diagnostic model using MRI.** *AJNR Am J Neuroradiol* 2015;36:1866–73 CrossRef Medline
2. Mehta GU, Jane JA Jr. **Pituitary tumors.** *Curr Opin Neurol* 2012;25:751–55 CrossRef Medline
3. Nishioka H, Haraoka J, Izawa H, et al. **Magnetic resonance imaging, clinical manifestations, and management of Rathke’s cleft cyst.** *Clin Endocrinol (Oxf)* 2006;64:184–88 CrossRef Medline
4. Bonneville JF, Bonneville F, Cattin F. **Magnetic resonance imaging of pituitary adenomas.** *Eur Radiol* 2005;15:543–48 CrossRef Medline

M. Park  
S.S. Ahn

Department of Radiology, Research Institute of Radiological Science  
Yonsei University, College of Medicine  
Seoul, Korea

<http://dx.doi.org/10.3174/ajnr.A4668>

## In Reply to Antiplatelet Therapy Prior to Temporary Stent-Assisted Coiling

**W**e would like to thank Drs Almekhlafi and Goyal for their comments<sup>1</sup> concerning our article, "Temporary Solitaire Stent-Assisted Coiling: A Technique for the Treatment of Acutely Ruptured Wide-Neck Intracranial Aneurysms."<sup>2</sup>

Almekhlafi et al noticed that we performed the procedures without preadministering antiplatelet therapy, and they would like to caution against the wide adoption of this technique without pretreatment with antiplatelet agents. They reported the endovascular treatment of 10 aneurysms (6 unruptured and 4 ruptured) in 8 patients by using temporary stent-assisted coiling. One of their patients with an unruptured aneurysm was not pretreated with dual antiplatelet therapy and presented with a procedural in-stent thrombosis with no clinical sequelae.

An antiplatelet regimen is usually administered before stent placement in selective cases. However, in our article,<sup>2</sup> we reported our experience in a different situation (acutely ruptured aneurysms). In this setting, to the best of our knowledge, it seems clear that adverse events happen more commonly and clinical outcomes are likely to be worse than those achieved without stent assistance<sup>3</sup>; thus, we did not use antiplatelet therapy in our series. Recently, Bechan et al<sup>4</sup> compared the rate of stent-placement complications in acutely ruptured versus unruptured aneurysms, and they have shown that the morbidity and mortality increased. Application of dual antiplatelet therapy in stent-assisted coiling of acutely ruptured aneurysms is associated with an increased risk of hemorrhagic complications following shunt placement,<sup>5</sup> especially in middle cerebral artery and anterior communicating artery aneurysms.<sup>6</sup> In our series, 4 of the 8 patients underwent emergent shunt placement and no hemorrhagic complication was noted.

As Drs Almekhlafi and Goyal noted, temporary stent-assisted coiling could be a helpful technique; however, it should be considered only when other endovascular techniques are not feasible, especially in the setting of acute ruptured aneurysms. The current

literature does not support using antiplatelet therapy in this setting because it associated with worse prognosis.

### REFERENCES

1. Almekhlafi MA, Goyal M. **Antiplatelet therapy prior to temporary stent-assisted coiling.** *AJNR Am J Neuroradiol* 2014;35:E6 CrossRef Medline
2. Signorelli F, Gory B, Turjman F. **Temporary Solitaire stent-assisted coiling: a technique for the treatment of acutely ruptured wide-neck intracranial aneurysms.** *AJNR Am J Neuroradiol* 2014;35:984–88 CrossRef Medline
3. Bodily KD, Cloft HJ, Lanzino G, et al. **Stent-assisted coiling in acutely ruptured intracranial aneurysms: a qualitative, systematic review of the literature.** *AJNR Am J Neuroradiol* 2011;32:1232–36 CrossRef Medline
4. Bechan RS, Sprengers ME, Majoie CB, et al. **Stent-assisted coil embolization of intracranial aneurysms: complications in acutely ruptured versus unruptured aneurysms.** *AJNR Am J Neuroradiol* 2015 Sep 24. [Epub ahead of print] CrossRef Medline
5. Kung DK, Policeni BA, Capuano AW, et al. **Risk of ventriculostomy-related hemorrhage in patients with acutely ruptured aneurysms treated using stent-assisted coiling.** *J Neurosurg* 2011;114:1021–27 CrossRef Medline
6. Yang P, Zhao K, Zhou Y, et al. **Stent-assisted coil placement for the treatment of 211 acutely ruptured wide-necked intracranial aneurysms: a single-center 11-year experience.** *Radiology* 2015;276:545–52 CrossRef Medline

✉ B. Gory

FHU IRIS, Department of Interventional Neuroradiology  
Hôpital Neurologique Pierre Wertheimer, Hospices Civils de Lyon  
Lyon, France

✉ F. Signorelli

Department of Neurosurgery  
Hôpital Neurologique Pierre Wertheimer, Hospices Civils de Lyon  
Lyon, France

Department of Experimental and Clinical Medicine

University Magna Graecia

Catanzaro, Italy

✉ F. Turjman

FHU IRIS, Department of Interventional Neuroradiology  
Hôpital Neurologique Pierre Wertheimer, Hospices Civils de Lyon  
Lyon, France

<http://dx.doi.org/10.3174/ajnr.A4661>